



HAL
open science

Synthèse et étude de nano-objets moléculaires multifonctionnels : vers des applications biomédicales

Guillaume Maurin-Pasturel

► **To cite this version:**

Guillaume Maurin-Pasturel. Synthèse et étude de nano-objets moléculaires multifonctionnels : vers des applications biomédicales. Material chemistry. Université Montpellier, 2015. English. NNT : 2015MONT093 . tel-01712705

HAL Id: tel-01712705

<https://theses.hal.science/tel-01712705>

Submitted on 19 Feb 2018

HAL is a multi-disciplinary open access archive for the deposit and dissemination of scientific research documents, whether they are published or not. The documents may come from teaching and research institutions in France or abroad, or from public or private research centers.

L'archive ouverte pluridisciplinaire **HAL**, est destinée au dépôt et à la diffusion de documents scientifiques de niveau recherche, publiés ou non, émanant des établissements d'enseignement et de recherche français ou étrangers, des laboratoires publics ou privés.

THÈSE

Pour obtenir le grade de
Docteur

Délivré par **L'université de Montpellier**

Préparée au sein de l'école doctorale Sciences
Chimiques
Et de l'Institut Charles Gerhardt, UMR 5253

Spécialité : CHIMIE ET PHYSICO-CHIMIE DES
MATERIAUX

Présentée par **Guillaume Maurin-Pasturel**

**SYNTHESIS AND STUDY OF MOLECULAR-
BASED MULTIFUNCTIONAL NANO-
OBJECTS: TOWARDS BIOMEDICAL
APPLICATIONS**

Soutenue le 02 décembre 2015 devant le jury composé de

Mr. Mir Wais HOSSEINI, Professeur, Université de Strasbourg	Rapporteur
Mr. Gabor MOLNAR, Directeur de recherche CNRS, Université de Toulouse	Rapporteur
Mr Joël CHOPINEAU, Professeur, Université de Nîmes	Examineur
Mme Joulia LARIONOVA, Professeur, Université de Montpellier	Directeur de thèse
Mr. Jérôme LONG, Maître de conférence, Université de Montpellier	Membre invité

Remerciements

Je tiens à exprimer mes sincères remerciements à toutes les personnes qui ont pu participer de près ou de loin à ce travail.

Je voudrais tout d'abord exprimer ma plus profonde gratitude aux personnes qui m'ont encadré et soutenu pendant ces trois années de thèse, le Pr. Joulia Larionova, les Dr. Jérôme Long et Dr. Yannick Guari. Un grand merci à Joulia pour sa disponibilité, son écoute, et qui a su me guider dans ma réflexion tout le long de ce travail. Un grand merci aussi à Jérôme qui a été mon interlocuteur privilégié durant toute cette période, qui a toujours été présent pour essayer de répondre à mes questions, et merci aussi pour avoir réalisé l'ensemble des mesures magnétiques. Un grand merci également à Yannick pour tous les conseils qu'il a pu me donner, notamment pour la microscopie électronique, et qui a su me motiver dans la réalisation de ce travail. Je tiens également à remercier Pr. Christian Guérin, qui m'a accueilli dans son bureau, qui m'a aiguillé à maintes reprises sur la littérature, et surtout qui m'a prodigué de précieux conseils tant dans le domaine scientifique que en matière de randonnées. Un grand merci à ces quatre personnes pour leur professionnalisme, et pour m'avoir tant appris dans cet univers de la recherche scientifique.

Je voudrais aussi remercier les personnes qui ont travaillé avec nous en collaboration. Je remercie les personnes du Laboratoire de Chimie de Coordination du CNRS de Toulouse, notamment les Dr. Gabor Molnar et Dr. Gautier Félix, qui fait maintenant partie de l'équipe, pour leur travail sur les nanoparticules d'analogues de Bleu de Prusse, avec en particulier les mesures de spectroscopie Raman et de spectroscopie Mössbauer. Merci au Dr. Marc-Georg Willinger du Fritz Haber Institute of the Max Planck Society de Berlin, en Allemagne, pour les images de HRTEM et de STEM-HAADF qu'il a réalisé. Je remercie aussi le Dr. Masashi Okubo de l'université de Tokyo, au Japon, pour les mesures d'insertion/extraction de Li-ion sur nos nanoparticules. Merci également à Estelle Rascol et au Pr. Joël Chopineau de l'équipe MACS de l'ICGM, pour les travaux qu'ils mènent sur le recouvrement des nanoparticules de Bleu de Prusse et des nanoparticules cœur-coquilles avec des bicouches lipidiques. Je remercie les Dr. Muriel Buisson et Samuel Sevestre de l'Institut de Recherche en Cancérologie de Montpellier, qui ont réalisé les mesures d'imagerie SPECT-CT in vivo. Je voudrais aussi remercier le Dr. Clarence Charnay pour son aide et son expertise dans la synthèse de nano-bâtonnets d'or.

Je tiens également à remercier toutes les différentes personnes, techniciens ou ingénieurs, qui m'ont aidé pour les diverses techniques de caractérisations. Tout d'abord, merci aux personnes du service commun de microscopie électronique, Franck Godiard, Frédéric Fernandez, Erwan Oliviero et Véronique Viguier-Richard, pour les mesures de TEM, de HRTEM, de STEM-HAADF et de quantification des éléments par EDX sur le MEB. Je remercie aussi Dominique Granier pour les mesures de DRX et Corine Reibel pour les mesures magnétiques. Je remercie José-Marie Ruiz et Léa Daenens pour les mesures de Spectroscopie Raman. Pour les mesures de DLS/potentiel Zéta, je remercie les Dr. Eliane Dumay et Dr. Claire Blayo pour les mesures au bâtiment 15 ainsi que Estelle Rascol pour les mesures à la faculté de Pharmacie de l'université de Montpellier.

Je remercie aussi l'ensemble des personnes du laboratoire pour l'aide qu'ils m'ont apportée, qu'elle soit scientifique ou non. Merci d'abord à Hubert Mutin de m'avoir accueilli dans le laboratoire, et ce depuis mon stage de Master. Je citerai ensuite tout particulièrement Serge Bertrand pour son aide technique et logistique, ainsi que pour les grands débats de paillasse digne des « Grandes Gueules » qui ont agrémenté mes journées. Je remercie aussi Christian Curtil pour son aide sur certains montages. Je remercie bien sûr les étudiants que j'ai côtoyés et qui ont pu aussi bien m'aider dans mon travail que partager des moments en toute sympathie. Je nommerai ainsi Marine, Charlène, Amandine, Mathieu, Saad, Giovanni, qui étaient là à mon arrivée, Céline qui est arrivée en même temps que moi, et avec qui j'ai partagé les infortunes administratives, ainsi que Chiara (ma petite Chiara, dont j'ai particulièrement apprécié de venir t'embêter dans ton bureau !), Rosa, Eléonore, Sandrine, Angel et Jean-François qui nous ont rejoints depuis. Merci aussi aux post-doctorants Maria Rodriguez Castillo et surtout à Maria Angeles Palaccio, qui a en partie travaillé avec moi sur ce projet et qui a apporté une certaine bonne humeur (dansante) à la paillasse. Je remercie aussi les stagiaires, Julien qui a travaillé avec moi, et Marylin, qui certes n'a pas travaillé avec moi mais avec qui j'ai un tant soit peu partagé mon expérience.

Je remercie aussi le Pr. Mir Wais Hosseini et le Dr Gabor Molnar, pour avoir accepté d'être les rapporteurs de ma thèse et d'évaluer ce manuscrit, ainsi que d'avoir bien voulu juger mon travail. Merci aussi au Pr. Joël Chopineau pour avoir accepté d'être le président de mon jury de thèse.

Je voudrais remercier aussi ma famille qui m'a soutenu tout le long de ce travail. Je pense tout d'abord à mes parents qui ont toujours été là pour moi, à ma sœur Chloé, que j'ai malencontreusement contaminée de mon goût pour la chimie, et aussi à Julien, mon beau-frère depuis cet été. Je remercie aussi mon Poupa (le seul et l'unique), qui m'a tant appris, ainsi que Hermine. Je remercie aussi le reste de la famille, mon parrain Jean-Marc, Stéphanie, pour son aide à la mise en page, et tous les cousins, cousines, oncles et tantes, et autres de la famille, qui m'ont soutenu.

Je voudrais aussi remercier tous mes amis qui ont été là, ceux qui le sont depuis le début comme ceux qui sont venus en cours de route. Je citerai entre autres (la liste étant longue) Christophe, Dorian, Alix, Mickael, Mathieu (les deux), Guilhem, Falco, Fred et Amandine, Jenny, Jennifer, Virginie, Julie,..., j'en oublie sûrement. Je voudrais particulièrement remercier Céline, que j'ai rencontré au tout début de la thèse, pour son exceptionnelle amitié et son soutien indéfectible tout le long de ces trois ans, ainsi que à sa merveilleuse petite Lisa qui est arrivée entre temps.

Je ne puis terminer sans avoir une pensée émue pour Toby, le chien de la famille, qui nous a quittés dans les derniers jours de rédaction de ce travail.

Table of contents

GENERAL INTRODUCTION	8
CHAPTER I- Introduction.....	11
Part 1: Prussian Blue and Analogous NPs.....	13
I.1.1 Introduction on the Prussian Blue and its Analogous.	14
I.1.2 Synthesis and properties of PB and its PBA NPs.....	16
I.1.3 Synthesis of core-shell PBA@PBA' NPs.....	26
I.1.4 Synthesis of hollow PB and its Analogous NPs.....	36
Part 2: Core@shell nano-heterostructures.....	40
I.2.1 Core@shell NPs: definition and interests.....	41
I.2.2 Synthesis and properties of inorganic core@shell NPs.....	42
I.2.2 Synthesis and properties of inorganic core@shell NPs: interest of gold.	45
Objectives of this work:	50
References	51
CHAPTER II-INITIAL WORK: SYNTHESIS OF $K^+/Ni^{2+}/[Fe(CN)_6]^{3-}/PEG-NH_2$ NPs	60
II.1 Introduction:	61
II.2 Synthesis and characterizations	63
II.2.1 First approach: synthesis of ultra-small $K^+/Ni^{2+}/[Fe(CN)_6]^{3-}/PEG-NH_2$ NPs	63
II.2.2 Second approach: synthesis of a series of $K^+/Ni^{2+}/[Fe(CN)_6]^{3-}$ NPs and post-synthetic grafting with PEG-NH ₂	64
II.2.3 Characterizations of the $K^+/Ni^{2+}/[Fe(CN)_6]^{3-}/PEG-NH_2$ NPs obtained using the two different approaches.	66
II.4 Study of the Fe ^{II} amount evolution as function of the size of the $K^+/Ni^{2+}/[Fe(CN)_6]^{3-}$ NPs and its influence on the structure by using Mossbauer spectroscopy.	83
II.5 Conclusion.....	87
References	89
Experimental part:.....	91
CHAPITRE III -Synthesis and study of core-shell $Au@K^+/Ni^{2+}/[Fe^{II}(CN)_6]^{4-}$ NPs	94
III.1 Introduction	95
III.2 Synthesis and characterization of $Au@K^+/Ni^{2+}/[Fe^{II}(CN)_6]^{4-}$ NPs	97
III.3 Studies of the mechanism of the formation of core-shell $Au@K^+/Ni^{2+}/[Fe^{II}(CN)_6]^{4-}$ NPs.	110
III.3.1 Investigation on the PBA anchoring process at the gold NPs surface.....	110
III.3.2 Investigation on the shell growth mechanism by TEM monitoring.	117
III.3.3 Discussion.....	119
III.4 Variation of the core and the shell size of $Au@K^+/Ni^{2+}/[Fe^{II}(CN)_6]^{4-}$ NPs	121
III.4.1 The gold core size control	121

II.4.2 control of the shell thickness.	127
III.5 Modification of the precursors used to synthesize core-shell Au@K ⁺ /Ni ²⁺ /[Fe ^{II} (CN) ₆] ⁴⁻ NPs.....	134
III.5.1 Variation of the nature of the counter-ion precursors.	134
III.5.2 Modification of the nature of the PBA layer.	139
III.6 Synthesis of Hollow nanoparticles	147
III.7 Conclusion	152
References	155
Experimental part.....	160
Chapter IV- Epitaxial growth of a PBA shell on Au@K ⁺ /Ni ²⁺ /[Fe ^{II} (CN) ₆] ⁴⁻ core-shell nanoparticles: a way to implement magnetic properties	163
V.1 Introduction.....	164
IV.2 Synthesis of double-layered core-shell Au@K ⁺ /Ni ²⁺ /[Fe ^{II} (CN) ₆] ⁴⁻ @PBA NPs where PBA = KNi ^{II} [Cr ^{III} (CN) ₆], KNi ^{II} [Fe ^{III} (CN) ₆], KCo ^{II} [Fe ^{II} (CN) ₆] and KFe ^{III} [Fe ^{II} (CN) ₆].	166
IV.2.1 Synthesis of double-layered core-shell Au@K ⁺ /Ni ²⁺ /[Fe ^{II} (CN) ₆] ⁴⁻ @ KNi ^{II} [Cr ^{III} (CN) ₆] NPs.....	167
IV.2.2 Synthesis of double-layered core-shell NPs Au@K ⁺ /Ni ²⁺ /[Fe ^{II} (CN) ₆] ⁴⁻ @PBA where PBA = KNi ^{II} [Fe ^{III} (CN) ₆], KCo ^{II} [Fe ^{II} (CN) ₆] and KFe ^{III} [Fe ^{II} (CN) ₆].	174
IV.2.3 Optical properties of the double-layered core-shell Au@K ⁺ /Ni ²⁺ /[Fe ^{II} (CN) ₆] ⁴⁻ @PBA NPs.....	184
IV.3 Study of the magnetic properties of the double-layered core-shell Au@K ⁺ /Ni ²⁺ /[Fe ^{II} (CN) ₆] ⁴⁻ @PBA NPs.....	189
IV.3.1 Effect of the PBA's shell size on the magnetic properties: study on double-layered Au@KNi ^{II} Fe ^{II} @KNi ^{II} Cr ^{III} NPs.....	189
IV.3.2 Magnetic properties of the double-layered core-shell Au@K ⁺ /Ni ²⁺ /[Fe ^{II} (CN) ₆] ⁴⁻ @PBA NPs.....	207
IV.4 Conclusion.....	211
References	213
Experimental part:.....	216
CHAPTER V	220
²⁰¹ Tl ⁺ -labeled Prussian Blue and core-shell Au@Prussian Blue NPs for bio-imaging.....	220
V.1 Introduction.....	221
V.2 Preparation, post-synthetic grafting and entrapment of Tl ⁺ of the ²⁰¹ Tl ⁺ nano-carriers.	223
V.2.1 Synthesis and characterization of the Na ⁺ /Fe ³⁺ /[Fe ^{II} (CN) ₆] ⁴⁻ NPs.	223
V.2.2 Post-synthetic grafting of the Na ⁺ /Fe ³⁺ /[Fe ^{II} (CN) ₆] ⁴⁻ and the Au@NaNi ^{II} Fe ^{II} @NaFe ^{II} Fe ^{III} NPs.	228

V.2.3 Post-synthetic sequestration of Tl ⁺ into the grafted Na ⁺ /Fe ³⁺ /[Fe ^{II} (CN) ₆] ⁴⁻ and Au@NaNi ^{II} Fe ^{II} @NaFe ^{II} Fe ^{III} NPs.	238
V.3 Use of the Na ⁺ /Fe ³⁺ /[Fe ^{II} (CN) ₆] ⁴⁻ /grafted and Au@NaNi ^{II} Fe ^{II} @NaFe ^{II} Fe ^{III} /grafted NPs as ²⁰¹ Tl ⁺ nano-carriers for SPECT/CT imaging.	243
V.3.1 Comparison between Na ⁺ /Fe ³⁺ /[Fe ^{II} (CN) ₆] ⁴⁻ NPs and Au@NaNi ^{II} Fe ^{II} @NaFe ^{II} Fe ^{III} NPs on CT imaging.	244
V.3.2 Use of the ²⁰¹ Tl-labelled NPs as tracking agents for <i>in vivo</i> SPECT/CT imaging on mice.....	245
V.4 conclusion	253
References	255
Experimental part:.....	257
General conclusion	261
Annexes.....	265
Annex 1: General instrumentation.	266
Annex 2: Supplementary information of chapter II.	267
2.1 Synthesis of ultra-small K ⁺ /Cu ²⁺ /[Fe(CN) ₆] ³⁻ /PEG-NH ₂ NPs using the first approach.	267
2.2: Calculation model of the K ⁺ /M ²⁺ /[Fe(CN) ₆] ³⁻ formula.	272
2.3 DLS/Zeta potential measurements.	273
Annex 3: Supplementary information of chapter III.	274
3.1 Study of the kinetic of the gold NPs formation: UV-Visible monitoring.	274
3.2 Modification of the nature and the shape of the core.....	276
References	281
Résumé Synthèse de nano-objets multifonctionnels à base moléculaire: vers des applications biomédicales	283
Bibliographie	295
ABSTRACT.....	296
RÉSUMÉ	297

GENERAL INTRODUCTION

Since the first discovery of nanoparticles, their elaboration has attracted a great deal of attention because of their interesting changes of the physical and chemical properties of the material occurring upon the size reduction to the nanoscale. These changes mainly originate from the increase of the surface area to volume ratio which induces the dominance of the surface atoms of the nanoparticle over those in its interior. For example, a nanoparticle with a mean diameter of 2 nm is composed by around 300 atoms with half are localized at the surface.

Because of the promising properties of these nanomaterials, researchers have first focused on the elaboration of nanoparticles composed by only one defined material. A large range of nanomaterial (silica, metal, metal oxide, coordination polymer) has been synthesized and developed for various applications such as catalysis, data storage, environmental remediation, sensors, photovoltaic devices, optical devices, biomedicine and others. Variations of some parameters permit to control the size and the shape of the nanoparticles, and thus allow to finely tune their properties, in relation with targeted applications.

More recently, the synthesis of heterogeneous composites has revealed to be a promising way to get a multifunctionality at the nanoscale, with the combination of two or more materials in a single nanoparticle exhibiting diverse responses when subjected to various external stimuli. Such intricate systems generally present the sum of the intrinsic properties originated from their different components. However, in some cases, the appearance of new properties or synergistic effects may be observed.

In this line of thought, we were interested in the design of heterostructures at the nanoscale combining two different materials to obtain magneto-optical nano-objects. In that aim, we have focused on gold and coordination polymers such as Prussian Blue and its analogues.

In the first chapter of this manuscript, we define the nature and structure of the Prussian Blue and its analogues, then we report the different synthetic processes permitting to obtain simple or complex nanoparticles of this class of materials, and their main properties and applications. Then, we also describe the different combinations of various materials to obtain core-shell nanoparticles, before to focus particularly on the nano-heterostructures involving gold, their properties and interests.

The second chapter concerns the elaboration of a series of Prussian Blue analogue nanoparticles, such as $\text{Ni}_3[\text{Fe}(\text{CN})_6]_2$, presenting different and controlled sizes. The evolution of their characteristics upon the size reduction is investigated, in order to better understand such systems.

In the third chapter, the design of core-shell nanoparticles combining both gold and Prussian Blue analogue, such as $\text{Ni}_2[\text{Fe}(\text{CN})_6]$, is described with using a new and rational approach. The growing mechanism of such intricate system has been investigated. Several variations on the synthesis have been performed, such as the variation of the gold core size, the Prussian Blue analogue shell thickness, or the precursors used. The used synthetic approach has been extended to other gold core containing heterostructures with varying the nature of the PBA selected as shell. An original way to design hollow nanoparticles with using the core-shell nanoparticles is also presented.

The fourth chapter presents the elaboration of double-layered core-shell nanoparticles obtained by subsequent growing of a second Prussian Blue analogous layer on the single-layered nanoparticles. The modification of their optical and magnetic properties as a function of the size and the nature of the Prussian Blue analogous shell has been investigated.

In the fifth chapter, we evaluate the potentiality of the core-shell nanoparticles for medical imaging. Firstly, Prussian Blue nanoparticles with similar size than the core-shell nanoparticles have been elaborated. The possibility to functionalize their surface with organic molecules or polymers and their ability to entrap thallium ions have been studied. Then, the nanoparticles has been tested as contrast agent *in vivo*.

Finally, we briefly conclude and present the future perspectives.

CHAPTER I

-

Introduction

The objective of our study consists in designing multifunctional nano-heterostructures combining properties of both gold and Prussian Blue Analogous (PBA). In this scope, it is necessary firstly well-understand each system separately. For this reason, we will describe in the first part the Prussian Blue and its Analogous in a macroscopic level, then we will focus on the synthesis of cyano-bridged coordination polymers NPs, describing different synthetic processes reported in the literature. The design of more intricate architecture at the nanoscale, such as PBA@PBA' core@shell NPs or PBA hollows NPs will also be considered. In the second part, description of nano-heterostructures will be presented, as well as a brief state-of-the-art on the elaboration of such nano-objects. Then, we will focus on the design of core@shell NPs involving gold, their properties and potential applications. Finally, we will present the objectives of this work with consideration of the recent research advances.

Part 1: Prussian Blue and Analogous NPs.

I.1.1 Introduction on the Prussian Blue and its Analogous.

Since the discovery in 1704 by Dippel and Diesbach of the oldest coordination polymer (CPs), Prussian Blue ($\text{Fe}_4[\text{Fe}(\text{CN})_6]_3 \cdot n\text{Solv}$), this important family of molecule-based materials has attracted the interest of numerous researchers for their interesting physical and chemical properties, including magnetic, optical, photo-switchable, catalytic and intercalation properties. From this date, and their first use as pigments, to now, a large variety of coordination polymer have been synthesized and studied. These cyano-bridged coordination polymers have the general formula $\text{A}_x\text{M}_y[\text{M}'(\text{CN})_6]_z$, where M and M' are transition metal ions or lanthanides and A is the counter cation. The cyanometallate moiety $[\text{M}'(\text{CN})_6]^{n-}$ can change according to the number of cyano groups present to complete the coordination sphere of the metal ion. The dimensions of the materials depend on the cyanometallate moiety geometry (linear, trigonal, square planar, tetrahedral, octahedral, ect) and the number of possible connections. In the aim to design cyano-bridged coordination polymer material, such as nanostructures, we focus our study on a tridimensional network at a macroscopic level.

To obtain tridimensional cyano-bridged coordination polymers, in most cases a cyanometallate moiety with at least six bridging cyano groups should be used. Since the structural resolution of the PB crystalline structure in 1970^{1,2} (figure 1, a)) of $\text{Fe}_4[\text{Fe}(\text{CN})_6] \cdot 14\text{H}_2\text{O}$ formula³, it is known that the analogous compounds of a general formula $\text{M}_x[\text{M}'(\text{CN})_6]$ (M= Fe, Co; Cu, Mn, Ga, Bi; M'= Fe, Cr, Co) have a cubic structure of NaCl (figure 1, b and c)), with regular succession of M-C≡N-M' linkages, which can be linear or angular according to the ligand coordination mode, and which may be determined by Infrared spectroscopy. An isomerization of the bridging cyano groups may occurs, leading to the simultaneous presence of both M-CN-M' and M'-CN-M coordination⁴⁻⁶. Water molecules can be inserted in the structure to complete the coordination sphere of the bivalent metal ion, due to several vacancies originated from lacunar cyanometallate moieties, it is the vacancy-type structure (figure 1, b)). Water molecules non coordinated can be present in the network. The PB and its analogous structure can also be completed by monovalent cations (as K^+ , Na^+ , NH_4^+ ...) situated in the tetrahedral sites, which is the 1:1:1-type structure (figure 1, c)). However, the structure generally observed is intermediate of these two boundaries structures, with a general formula of $\text{A}_{1-x}\text{M}(\text{M}'(\text{CN})_6)_{1-x/3}$. The general synthesis method consists on a "soft" chemistry method with the self-assembly reaction between a bivalent salts of a transition metal ion and a hexacyanometallate ion.

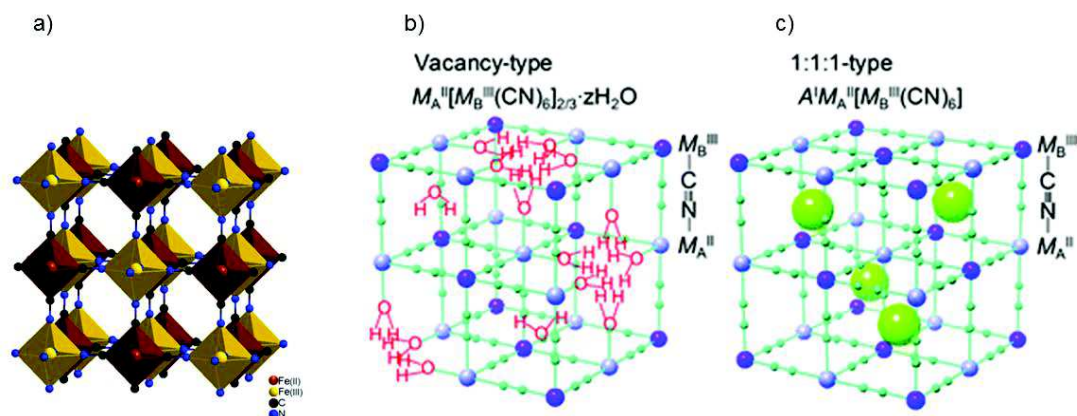


Figure 1: a) NaCl type cubic structure of the PB, b) Vacancy type of the PBA cubic structure with water molecules and c) NaCl type PBA cubic structure with alkali ions A (green spheres in the figure)⁷.

PB and its Analogous present interesting intrinsic properties. One of the most use of these compound originates from its porosity and its ability to exchange the cations presented in the structure with other monovalent cations, such as Cs^+ ^{8,9}, Tl^+ ^{10,11} or Rb^+ ¹². Then, it is possible to use PBA to selectively entrap these ions and to treat radioactive Tl^+ and Cs^+ poisoning. This is already possible with using commercial PB capsules (Radiogardase®), which is a FDA-approved medical treatment for the Cs^+ poisoning of humans¹³. On the other hand, PB and its analogous also present magnetic properties which can be modulated by varying the nature of the metal ions used. For example, a high Curie temperatures have been obtained for several compounds: 376 K for $\text{KV}[\text{Cr}(\text{CN})_6] \cdot 2\text{H}_2\text{O}$ PBA¹⁴ and 315 K for $\text{V}[\text{Cr}(\text{CN})_6]_{0.86} \cdot 2.8\text{H}_2\text{O}$. Photo-magnetic effects have also been reported on PBA, as for $\text{K}_{0.14}\text{Co}[\text{Fe}(\text{CN})_6] \cdot 4.9\text{H}_2\text{O}$ ¹⁵. The irradiation in the metal-metal charge transfer band centered at around 550 nm^{15,16} at low temperature induces an electron transfer: $\text{Co}^{III}(\text{BS}, {}^6t_{2g}^0e_g) - \text{Fe}^{II}(\text{BS}, {}^6t_{2g}^0e_g) \rightarrow \text{Co}^{II}(\text{HS}; {}^5t_{2g}^2e_g) - \text{Fe}^{III}(\text{BS}, {}^5t_{2g}^0e_g)$, where BS and HS represent respectively the High Spin and Low Spin configuration. These properties may be used for a large range of applications.

For the last twenty years, the interest for PBA have been extended to the design of nanomaterials. Indeed, the cyano-bridged coordination polymers present interesting advantages, such as determined and flexible molecular structures, determined and adjustable physical and chemical properties, porosity, and the possibility to obtain such nanostructures by “soft” chemistry methods, making them promising for the design of nano-objects. Moreover, the investigations on materials at the nanoscale have revealed an appearance of new phenomena arising from the size reduction, which are potentially promising for future applications. With the size reduction, size-dependent electrical, optical, magnetic and chemical properties different their PBA bulk analogous are accesible, due to the high surface-to-volume, quantum size effect and electrodynamic interactions¹⁷⁻²⁰. Thus, the interest in the synthesis and studies of cyano-bridged coordination polymer materials at the nano-size level is in constant expansion, and we have particularly focused on this field in the next sections.

I.1.2 Synthesis and properties of PB and its PBA NPs

The first synthesis of cyano-bridged coordination polymers nano-objects was first reported by Moulik and al.²¹ and by Mann and al.²² around fifteen years ago. Since, an important number of studies have been devoted to the elaboration of such NPs, using different synthetic approaches with varying the nature of the transition metal ions used and controlling the size and the shape, which permits to modulate the properties. From all the synthetic processes used, we can distinguish three main different approaches. First, the synthesis of PBA NPs with using organic molecules (polymers, biopolymers, ionic liquids, surfactants) as stabilizing agents to control the size and the morphology of the nano-objects. Secondly, the use of inorganic or organic matrices as hosts to form PBA NPs, with the obtaining of nanocomposite materials containing the confined NPs. Thirdly, the surfactant-free synthesis of PBA NPs, where the control of the size and the morphology is only performed by electrostatic interactions through adjustment of the experimental conditions.

I.1.2.a Synthesis of PB and its PBA NPs by using stabilizing agents.

The main developed approach to synthesize cyano-bridged coordination polymers NPs consists in a co-precipitation procedure in an aqueous or an organic solution with using organic molecules (such as polymers, biopolymers, ionic liquids, surfactants). These organic molecules serve as stabilizing agents, *i.e.* they stabilize PBA precursors and/or PBA NPs to control the growth of the NPs, avoiding the NPs aggregation and thus controlling their shape and morphology. This stabilization is usually ensured by donor groups of the organic molecules, able to bind to the metal ions situated at the NPs surface; the main difference in the diverse synthetic methods being in the strength of the binding. Then, the main different techniques to obtain PBA NPs can be divided according to the nature of the stabilizing agent used, and to their precise role in the formation of the NPs.

- Water-in-oil microemulsion.

The first technique used to obtain PBA NPs consists to form water-in-oil, or reverse microemulsion of the PBA precursors by mixing aqueous precursors solutions in a surfactant to form nanoscaled (~) water droplets. Then, by mixing of the two respective reverse microemulsions, PBA NPs are formed and growth when water droplets meet, playing the role of nanoreactor. With these method, several PBA NPs have been synthesized, such as $\text{Cu}_2[\text{Fe}(\text{CN})_6]$ NPs²¹, $\text{Fe}_4[\text{Fe}(\text{CN})_6]_3$ NPs²²⁻²⁴, $\text{Co}_2[\text{Fe}(\text{CN})_6]$ NPs²⁵, $\text{Cr}_3[\text{Cr}(\text{CN})_6]_2$ NPs²⁵, $\text{Ni}_3[\text{Cr}(\text{CN})_6]_2$ NPs²⁶, $\text{Ni}_3[\text{Fe}(\text{CN})_6]_2$ NPs²⁷, $\text{Co}_3[\text{Co}(\text{CN})_6]$ NPs²⁸ and $\text{KFe}[\text{Cr}(\text{CN})_6]$ NPs²⁹.

In the general procedure, the surfactant used to form the reverse micelles is the anionic surfactant bis(2-ethylehexyl)sulfosuccinate (Aerosol OT, AOT), but cetylmethylammonium bromide (CTAB)^{28,29} and didodecyldimethylammonium bromide (DDAB)²⁵ have already been used. Moreover, several co-surfactant can be used, as PVP²⁴ (figure 2) or p-nitrobenzylpyridine²⁷. The organic solvent can also change, n-heptane, isooctane and cyclohexane being the most used.

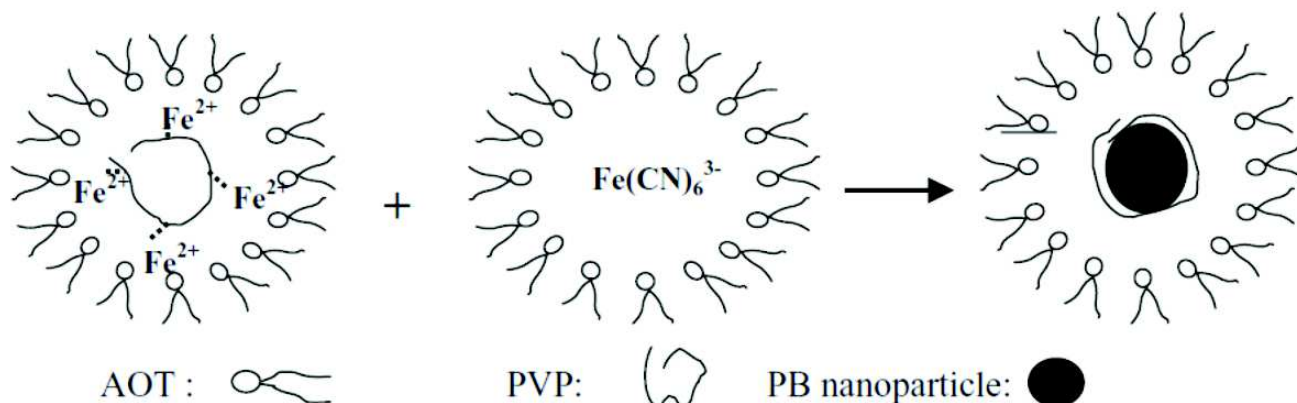


Figure 2: Schematic representation of PVP-protected PB formed in reverse microemulsion²³.

The size and shape control of the PBA nano-objects is provided by the variation of the precursors' concentration and the molar ratio of $[H_2O]/[surfactant]$ (w)³⁰. The size of the NPs is dependent on the precursor's concentration and the number of precursor's ions in the water droplets, their size being modulated by decreasing w , permitting to obtain NPs with a size range of 5 to 50 nm. Moreover, the water droplets size can affect the shape of the NPs, the confined reaction media constraining the crystal growth processes, leading to cubic or spherical shapes (figure 3).

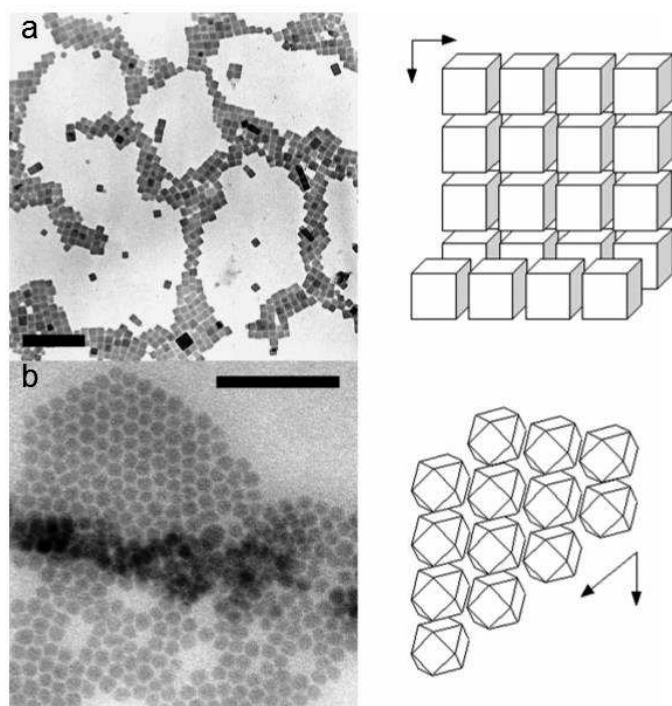


Figure 3: TEM images of $Co_2[Fe(CN)_6]$ NPs with a) cubic and b) spheroidal shapes and their corresponding square or hexagonal superlattices²⁵. Scale bars are 200 nm.

- Organic molecules and polymers.

The synthesis of PBA NPs can also be performed by using organic molecules or polymers as stabilizing agents in aqueous or organic media. These stabilizers possess a polar group able to coordinate to the metal atoms of the precursors and/or at the NPs surface, conferring solubility and permitting to control the size of the particles with the limitation of the shell-growth process.

The main common methods to obtain PBA NPs with using stabilizing agents consists to mixing of two aqueous solutions containing the PBA precursors (transition metal or lanthanide ion and hexacyanometallate) in the presence of the stabilizer, generally a polymer or a biopolymer, such as poly(N-vinyl-2-pyrrolidone) (PVP)³¹⁻³³, poly(diallyldimethylammonium chloride) (PDDA)³³, poly(ethylene glycol) (PEG; $M_w=400$ or 1000 g/mol) or poly(ethylene glycol) bis-(3-aminopropyl)-terminated (PEG-NH₂, $M_w=1500$ g/mol)³⁴ and N-acetyl-D-glucosamine (NADG)³⁴. Stabilizing agents anchor to the metal ion precursor *via* the polar groups, as amide, ammonium, ethylene glycol or hydroxyl-groups, limiting the growth process and then favoring the nucleation, and also ensuring the dispersion of the NPs in solution (figure 4).

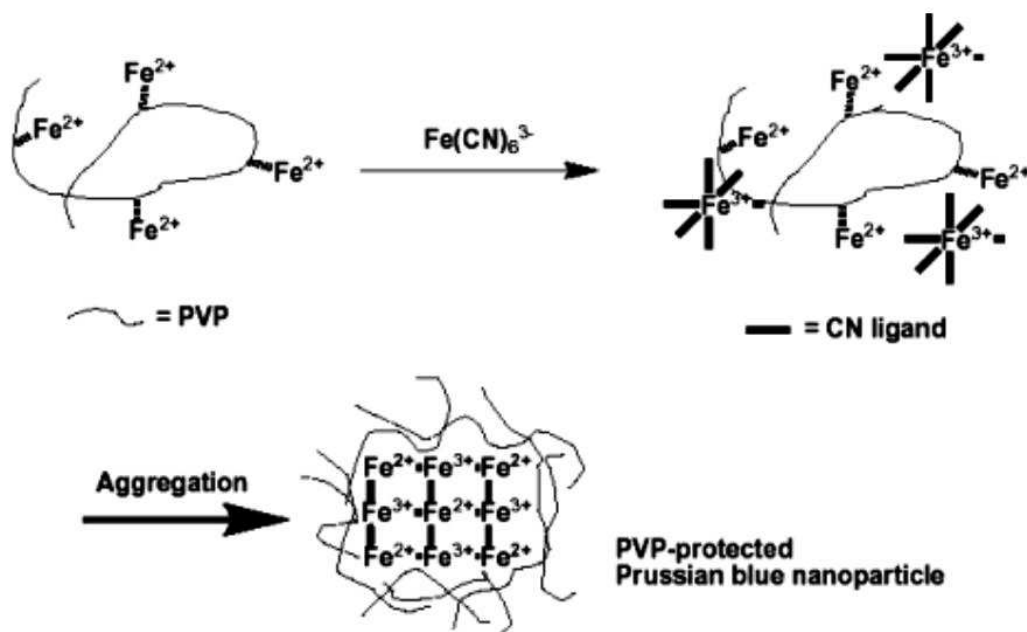


Figure 4: Schematic representation of the synthesis of PB NPs with using PVP to stabilize the Fe²⁺ ions before a self-assembly process permitting to obtain PVP-protected PB NPs stable in solution³¹.

A large variety of $M_x[M'(CN)_6]_y$ PBA NPs has been obtained by this method with $M = Gd^{3+}, Y^{3+}, Tb^{+3}, Ni^{2+}, Cu^{2+}, Fe^{2+}, Fe^{3+}, Co^{2+}$ and $M' = Fe^{2+}, Fe^{3+}, Co^{2+}$. The nano-objects have size ranging from 2 to 50 nm, however this method is mainly used to design small and ultra-small cyano-bridged NPs (figure 5). The size can be modulated by varying the concentration of the PBA precursors and the $[stabilizer]/[M]$ ratio³³. Higher is the $[stabilizer]/[M]$ ratio, smaller the PBA NPs are, due to the important limitation of the growing process. The initial concentration of the transition metal ions M also influences the NPs size: the decrease of the concentration gives smaller particle size.

Only one synthetic methodology to obtain cyano-bridged coordination polymers NPs in organic solvent using stabilizing agents has been reported³⁵. It consists on a sequential two-step reaction: i) the self-assembly between the bivalent metal ion and the cyanometallate moiety in presence of a fatty acid, which is a poor ligand but sufficient to stabilize the formed NPs, and ii) the addition of a long alkyl or aryl amine chain to reinforce the stabilization of the NPs in the solution (figure 6). A significant advantage of this method is that the NPs can be recovered by precipitation then dispersed on polar or non-polar solvents without further addition of any ligands or surfactants, which is not the case for PBA NPs obtained *via* a reverse microemulsion process. Moreover, this permits to obtain a large range of ultra-small $[M_x[M'(CN)_6]_y]$ NPs where $M = Mn^{2+}, Ni^{2+}, Fe^{2+}, Eu^{3+}, Tb^{3+}, Sm^{3+}$ and $M' = Fe^{3+}, Cr^{3+}$, with the size ranging from 2.2 to 5.1 nm.

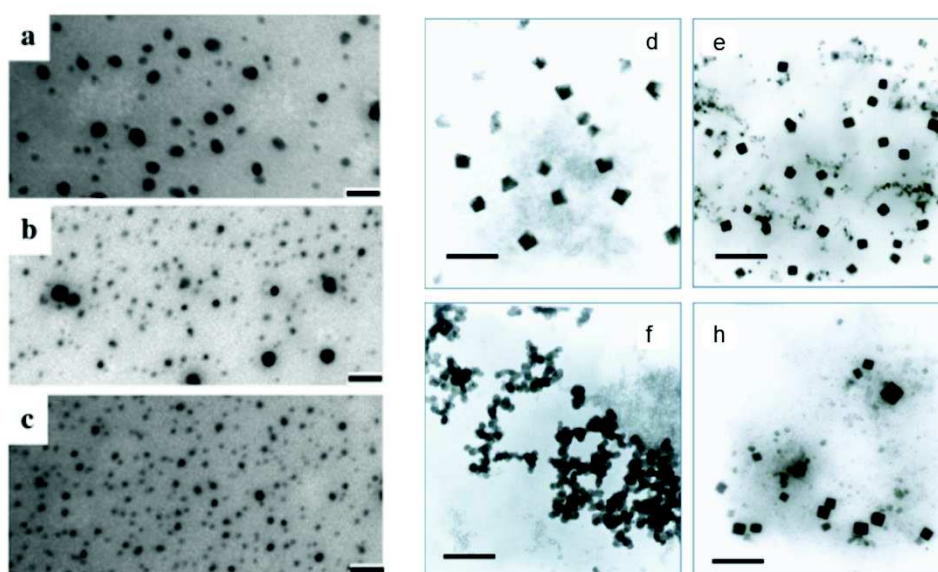


Figure 5: TEM images of PVP-protected PB NPs prepared with $[PVP]/[Fe^{2+}] = 20$ (a), 50 (b) and 100 (c)³³. Scale bars = 100 nm. TEM images of PVP-protected BP NPs (d) $Co_3[Fe(CN)_6]_2$ NPs (e), $Ni_3[Fe(CN)_6]_2$ NPs (f) and $Cu_3[Fe(CN)_6]_2$ NPs (g)³¹. Scale bars = 200 nm.

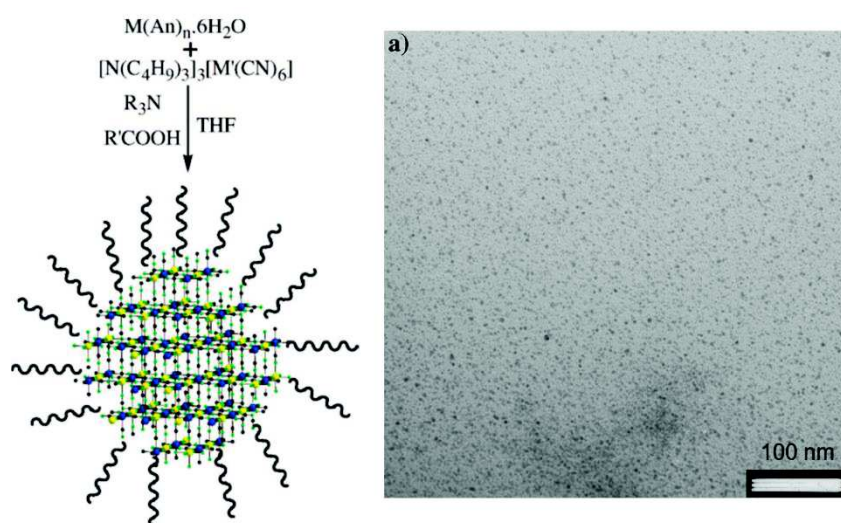


Figure 6: Schematic Representation of the organic phase synthesis of the NPs made of M^{n+} and $[M'(CN)_6]^{3-}$. TEM image of $Ni^{2+}/[Fe(CN)_6]^{3-}$ NPs³⁵.

- Ionic liquids.

Ionic liquids (ILs) are organic compounds composed of organic cations with a variety of substituents such as quaternary ammonium cations, pyrrolidinium, phosphonium or sulfonium cations. These compounds are interesting for their physico-chemical properties, such as low melting point, good solubility characteristics, relatively low viscosity, high fluidity and excellent thermal and chemical stability, but they also can be used as solvents for the synthesis and stabilization of nano-objects. ILs can play the role of “nanosynthetic template”³⁶ by stabilizing the metal NPs, the stabilization being originated from the high ionic charge and the high polarity plus the steric bulk of these salts. Indeed, this effect creates electrostatic and steric colloid-type stabilization and forms a “protective shell”, permitting the NPs synthesis extra stabilizing molecules or solvents. The synthesis of cyano-bridged coordination polymers have been performed by using 1-R-3-methylimidazolium salts $(Cn\text{-MIM})^+$ ($n = 4\text{-}12$), acting both as stabilizing agents for the NPs and reaction media to synthesize soluble PBA NPs of $M_x[M'(\text{CN})_6]_y/(Cn\text{-MIM})[\text{An}]$ ($Mn^+ = \text{Ni, Cu, Co, Mn, Eu, Tb, Gd}$; $M' = \text{Fe, Cr}$; $n = 4, 10, 12$; $\text{An} = \text{BF}_4^-, \text{Cl}^-$)³⁷⁻⁴⁰.

The typical synthetic procedure consists in a) the metathesis synthesis of $(Cn\text{-MIM})_3[M'(\text{CN})_6]$ cyanometallate precursors (ionic liquid playing the role of the counter cation), and b) the self-assembly reaction of bivalent metallic salt or lanthanide salts with these cyanometallate precursors (Figure 7).

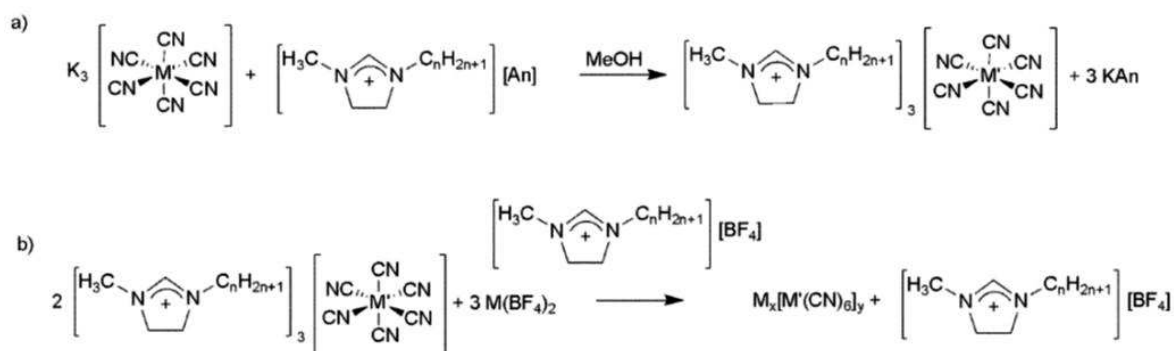


Figure 7: Schematic representation of a) the metathesis reaction to obtain the cyanometallate precursor $(Cn\text{-MIM})_3[M'(\text{CN})_6]$ and b) the self-assembly reaction with the second metal ion to form cyano-bridged coordination polymers NPs $M_x[M'(\text{CN})_6]_y/(Cn\text{-MIM})[\text{An}]$ ³⁶.

This method permits to prepare 3-4 nm spherical NPs at room temperature. Moreover, this method is highly versatile and by varying the reaction conditions, different shapes and the sizes ranging from few nanometers to 100 nm can be obtained³⁶. For example, the increase of the reaction temperature to 50°C permits to double increase the NPs size without any modification of their shape and dispersion properties, but the temperature increase to 80°C leads to the formation of 100 nm crystallites (figure 8, a), b), c)). The use of the microwave treatments (inducing a rapid heating of the reaction mixture) leads to the formation of NP superstructures (figure 8, d)). On the other hand, the addition of a few amount of alcohols with 5% of water induces the system destabilization and modify thus the shape of the particles, permitting to obtain cubic NPs (figure 8, f)).

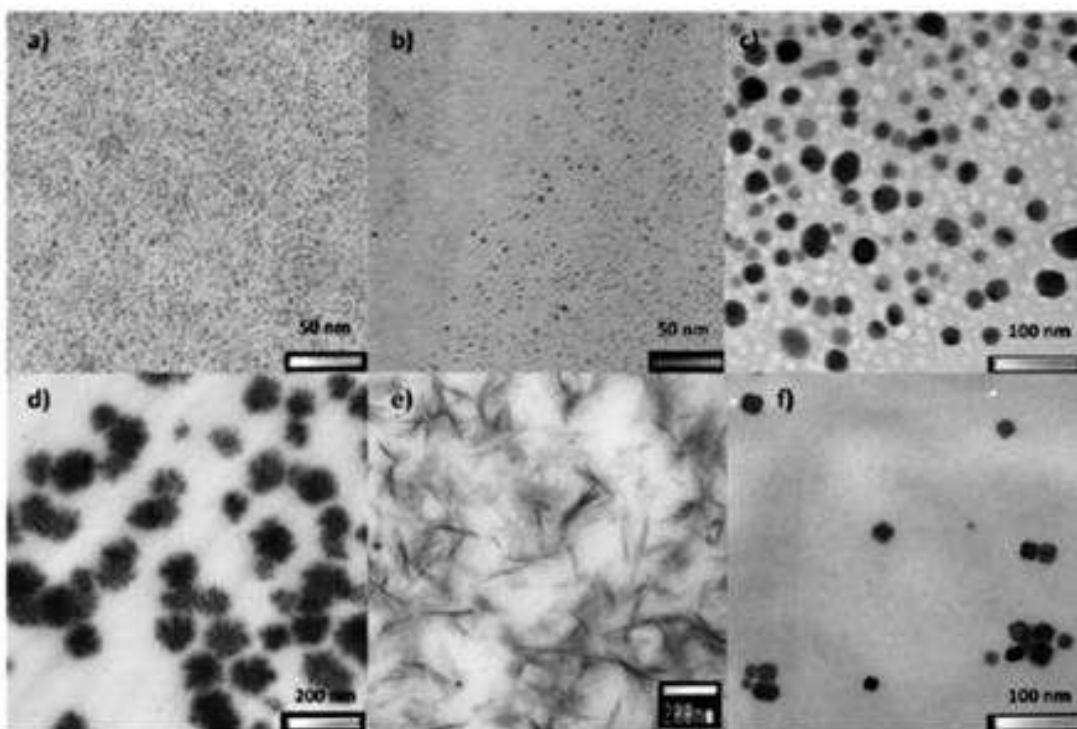


Figure 8: TEM images of $\text{Cu}^{2+}/[\text{Fe}(\text{CN})_6]$ NPs synthesized at a) 20°C, b) 50°C, c) 80°C, d) with microwave treatment, e) using an excess of $[\text{Fe}(\text{CN})_6]^{3-}$, f) after precipitation with MeOH-H₂O (95 : 5)³⁶.

I.1.2.b Synthesis of PB and PBA NPs with using organic or inorganic matrices.

Cyano-bridged coordination polymers NPs have also been obtained by using organic or inorganic matrixes, the later define the reaction space and permit to obtain large amounts of nanocomposite materials containing the confined nano-objets. This approach generally involves the use of porous matrices such as mesostructured silica, alumina and organic polymers (chitosan beads), in which the growth of the PBA network is achieved by a successive multi-step growth, at the opposite to the co-precipitation process used by the other synthetic processes. The confinement of the NPs in the host matrices alloys the size and shape control, induced by the size and the shape of the hosts' pores and the internal/external surface properties. Concretely, the synthesis consists in the sequential step-by-step coordination of the metal ions and cyanometallates (with several cycles of successive impregnation with the PBA precursor's solutions) insides the matrix pores, which play the role of a mesoscopic or nanoscopic reaction chamber to grow the NPs of a given size. The size is usually determined by the matrix' pores size, but also can be controlled by varying the number of deposition cycles⁴¹. Moreover, by inserting appropriate functionalities inside the pores, it is possible to stabilize the precursors and to attach the NPs, ensuring the formation of well-dispersed PBA NPs.

The use of alumina membrane as matrix permits to design PBA nanotubes^{41,42} with the presence of well-defined nanopores of 60-200 nm. To ensure the anchoring of the NPs inside the pores, Pd NPs were deposited at the surface to serve as nucleation sites⁴¹. The NPs can be recovered by etching of the alumina membrane. However, variable length of the nanotubes were obtained and the aggregation of the NPs after the etching of the matrix were observed. To overcome this problem, a solution consists to fix an organic molecule as an amino-acid inside the pores of the alumina matrix. Using Histidine as “anchoring sites” for the nickel ions, well-defined nanotubes of $\text{KNi}[\text{Fe}(\text{CN})_6]$ have been synthesized (figure 9, e)), with the length of 10 μm and the wall thickness of 30 nm⁴².

Silica appears also as a good material to obtain cyano-bridged coordination polymer NPs, and then design nanocomposites. Incorporation of the PBA precursors into the solution phase of the synthesis of a xerogel permits to obtain homogeneous $\text{K}^{\text{I}}\text{Co}^{\text{II}}[\text{Fe}^{\text{II}}(\text{CN})_6]$ silica xerogel containing nanocomposites, which presents interesting photomagnetic properties⁴³. To prepare PBA-containing silica materials, the most used silica matrices are mesostructured silica, as SBA-15 or MCM-41⁴⁴⁻⁴⁶, which are excellent hosts due to the presence of open hexagonal pores permitting the easy diffusion of precursors. The size of the pores may easily be modified without modification of the silica structure, allowing the control of the NPs size. The pores can be functionalized by grafting appropriate organic groups able to coordinate the PBA transition metal precursors, ensuring the anchoring the NPs inside the matrix. Using this method, a wide range of cyano-bridged networks of a general formula $\text{M}^{\text{n}+}[\text{M}'(\text{CN})_m]^{3-}$ (where $\text{M}^{\text{n}+} = \text{Ni}^{2+}, \text{Fe}^{2+}, \text{Co}^{2+}, \text{Fe}^{3+}$ and $\text{M}' = \text{Fe}^{3+}, \text{Co}^{3+}$ ($m = 6$); Mo^{5+} ($m = 8$)) were synthesized with a repeated successive impregnation of the PBA precursors. The anchoring of the metal ions and thus of the NPs was provided by a covalent bond using functionalities such as pyridine (figure 10). Moreover, the PBA NPs can be recovered by HF treatment of the silica matrix. The NPs obtained present spherical shape and have a size ranging from 2 to 7.5 nm (figure 10).

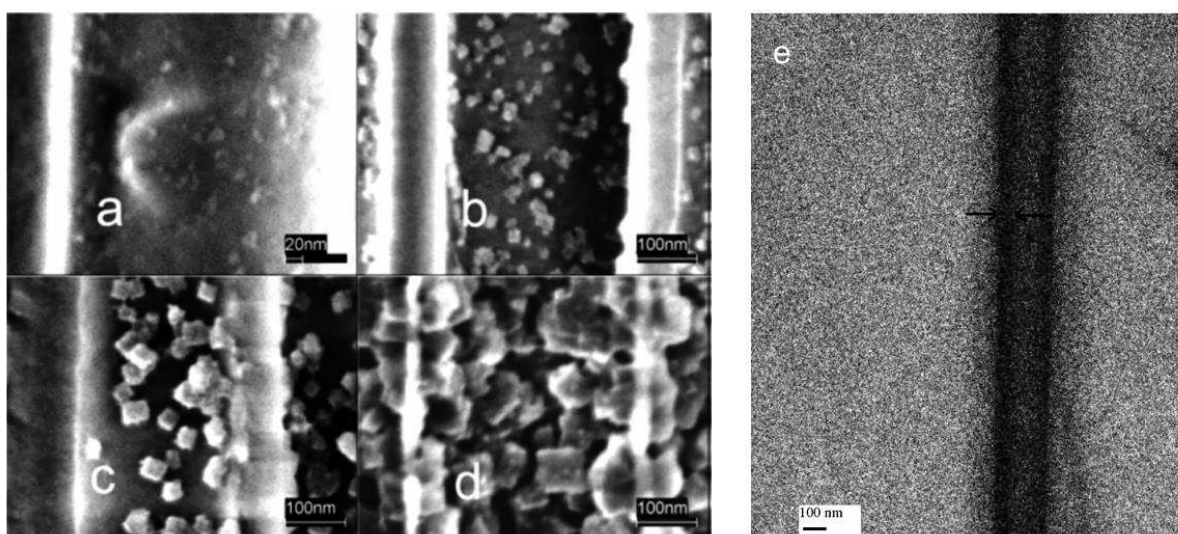


Figure 9: Cross-sectional SEM images of PB NPs deposited using 1 (a), 3 (b), 5 (c) and 10 (d) deposition cycles⁴¹. TEM image (e) of the liberated nanotube $\text{KNi}[\text{Fe}(\text{CN})_6]$ ⁴².

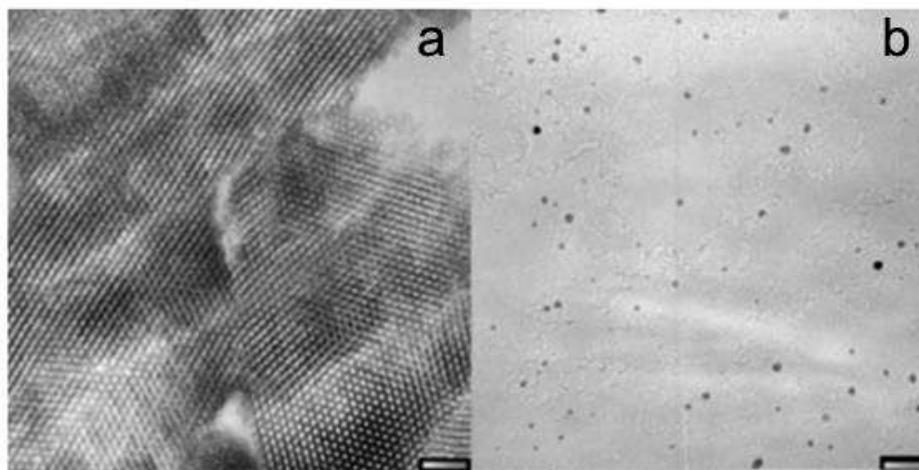
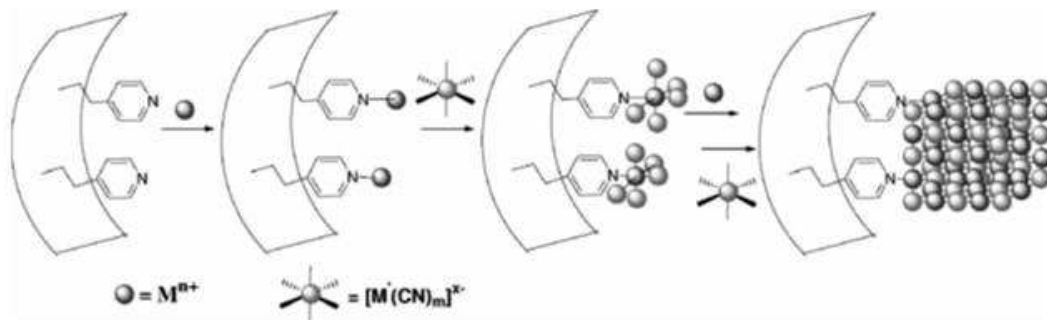


Figure 10: Schematic representation of the synthesis of PBA NPs inside the silica matrix with anchoring to pyridine groups⁴⁶. TEM images of a) $Ni^{2+}/[Fe(CN)_6]^{3-}/silica$ nanocomposite and b) the NPs obtained after removal of silica using HF treatment³¹.

The synthesis of PBA NPs was also performed by using porous organic polymers, such as chitosan beads^{47,48} or alginate beads and films⁴⁹. Chitosan and alginate are hydrophilic polysaccharides, biocompatible polymers which present high micrometric porosity and functional groups (amino-groups for chitosan and carboxylate groups for alginate) able to anchor the NPs inside the pores. By using porous chitosan beads obtained by using CO_2 supercritical drying, the sequential impregnation of the metal ions and cyanometallates was developed to grow PBA NPs of a general formula $M^{n+}[M'(CN)_m]^{3-}$ (where $M^{n+} = Ni^{2+}, Fe^{2+}, Co^{2+}, Fe^{3+}, Gd^{3+}$ and $M' = Fe^{3+}$) (figure 11). Spherical and non-aggregated NPs with the sizes of 2-3 nm were obtained inside the matrix, and were recovered by solubilisation of the chitosan in a slightly acidic water (figure 11). By using porous alginate beads or films, PBA NPs of general a general formula $M^{n+}/[M'(CN)_m]^{3-}/alginate$ (where $M^{n+} = Ni^{2+}, Cu^{2+}, Mn^{2+}, Fe^{2+}, Eu^{3+}$ and $M' = Fe^{3+}, Cr^{3+}(m = 6), Mo^{5+}(m = 8)$) were obtained, presenting uniformly dispersed NPs of 3-7 nm.

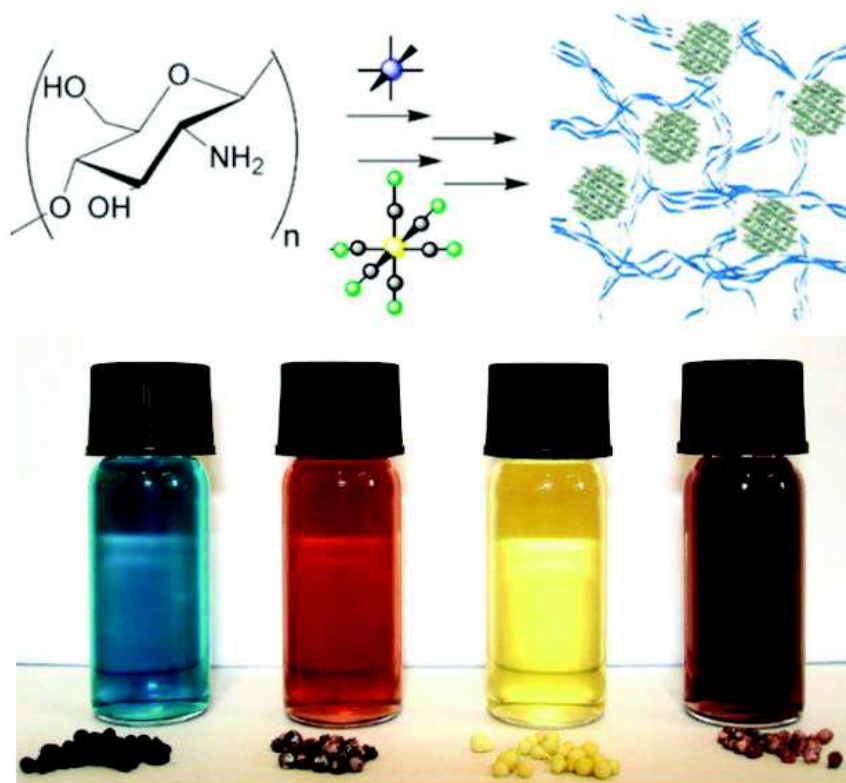


Figure 11: Schematic representation of CPN growth within chitosan beads by successive impregnation with a cyanometallate and a metal salt. Photograph of water colloidal solutions of Fe²⁺/[Fe(CN)₆]³⁻, Cu²⁺/[Fe(CN)₆]³⁻, Ni²⁺/[Fe(CN)₆]³⁻ and Co²⁺/[Fe(CN)₆]³⁻ NPs and the corresponding chitosan beads (from left to right)⁴⁶.

I.1.2.c Synthesis of PB and PBA NPs without stabilizing agents.

Cyano-bridged coordination polymers NPs can also be obtained without stabilizing agents, via a “free surfactant” procedure. Such stabilization of the NPs in an aqueous solution is only provided by electrostatic interactions, originated from the negative charged surface originated from the terminating [M'(CN)₆]ⁿ⁻ moieties. By self-precipitation of the PBA precursors in water, PBA NPs are obtained with size ranging from 6 to 200 nm⁵⁰. The size control is performed by modulation of the concentration and the addition rate of the precursors. Fast addition and high concentrations promote the nucleation process, and then the formation of small NPs. At the opposite, low concentrations and addition rates promote the growth of the PBA network, permitting to access large-sized NPs. Moreover, by increasing the electrostatic stabilization with the presence of a Cs⁺ ions excess, it is possible to obtain smaller NPs. Since the first synthesis of 6.5 nm CsNi[Cr(CN)₆] NPs performed by Catala and al.⁵⁰, several examples of free-surfactant PBA NPs have been reported, as KNi[Fe(CN)₆] NPs^{51,52} (figure 12), KNi[Cr(CN)₆] NPs⁵³, RbCo[Fe(CN)₆] NPs⁵⁴, or ternary metal PBA K_{4y-3+x}Mn^{II}_xIn^{III}_{1-x}[Fe^{II}(CN)₆]_y⁵⁵ and Na_αNi_{1-x}Co_x[Fe(CN)₆]_β·nH₂O NPs⁵⁶. Such NPs present an advantage to remain reactive at the surface, due to the terminating [M'(CN)₆]ⁿ⁻ moieties which ensure the stabilization of the NPs, and permits to consider the possibility to perform more intricate structure or morphologies.

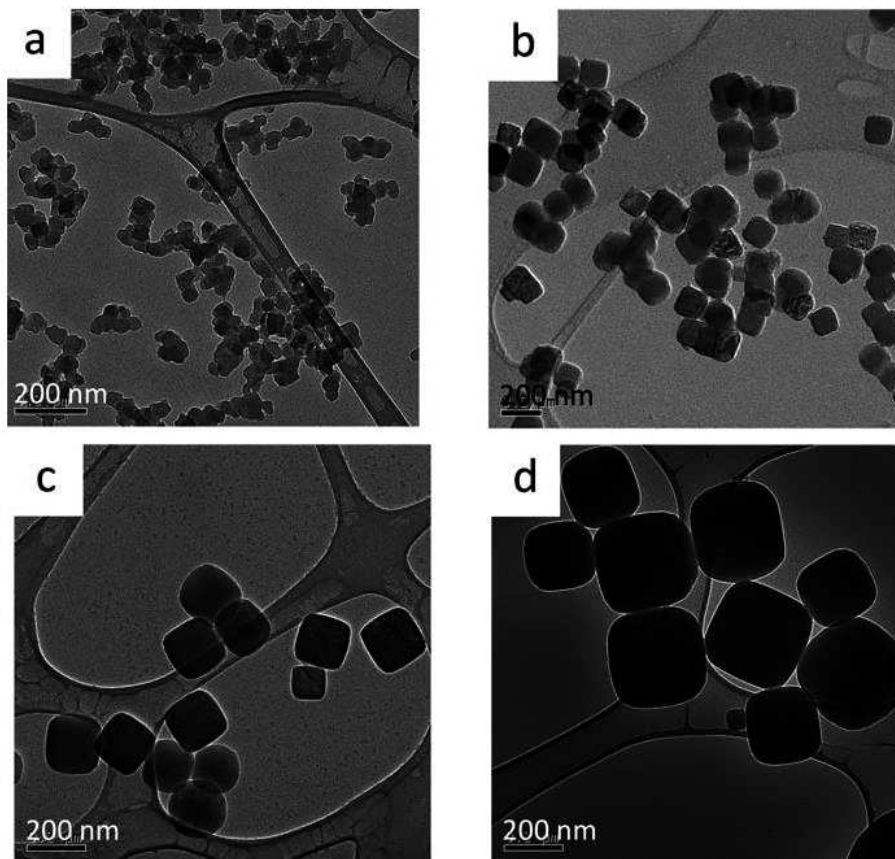


Figure 12: Examples of PBA NPs obtained via free surfactant procedure: HRTEM images of the $\text{KNi}[\text{Fe}(\text{CN})_6]$ particle samples of four different sizes. (a) 38 ± 4 nm; (b) 140 ± 13 nm; (c) 176 ± 18 nm; (d) 295 ± 33 nm⁵².

I.1.2.d Properties and applications of the PBA NPs.

The interest in the synthesis of PBA NPs concerns the modification of the intrinsic properties of the cyano-bridged coordination polymers networks. Indeed, it is well known that the size reduction of a material to nano-level induces radical modification of its properties. For the cyano-bridged coordination polymers, the main modification for instance concerns their magnetic properties. Indeed, bulk PBA is constituted by different paramagnetic ions in which the spins interact through the cyano-bridges, inducing the presence of a long-range magnetic ordering. Numerous PBA compounds present long-range ferro-, ferri- and antiferromagnetic ordering, the nature of the metal ions in the structure being responsible of the magnetic behavior, the sign of the magnetic interactions and the value of the critical temperature. The size reduction prevents the propagation of the magnetic correlation in three directions. Thus, for PBA NPs possessing strongly interacting paramagnetic centers, important size effects are observed, such as an appearance of a short range magnetic ordering as it was observed for small and ultra-small PBA NPs, as for $\text{CsNi}[\text{Cr}(\text{CN})_6]$ NPs⁵¹. Such magnetic properties present interest for several applications, as for information storage or bioimaging PBA NPs also possess other interesting properties, which can be used for other applications. For instance, due to their intrinsic porosity, and the possibility to insert alkali ions in the tetrahedral sites of their structures, PBA appear as a promising material for cathode in batteries with inserting Li^+ ions^{52,53}. On the other hand, the optical properties of the Prussian Blue, originated from its

strong intervalence charge-transfer band $\text{Fe}^{\text{III}}\text{-NC-Fe}^{\text{II}} \rightarrow \text{Fe}^{\text{II}}\text{-NC-Fe}^{\text{III}}$, is a promising agent for bioimaging, as photoacoustic or photothermal imaging, and may also be used for photothermal therapy, behaving as a nano-theragnostic agent⁵⁷⁻⁵⁹. However, PBA NPs rarely present multifunctional properties, which require the combination of different material in more intricate architecture.

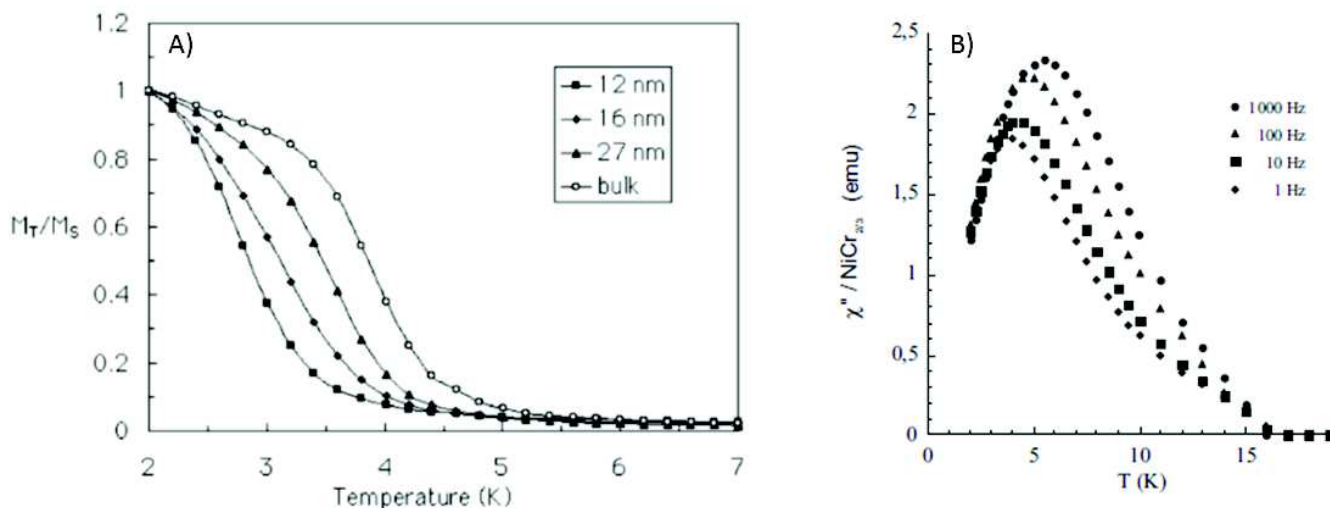


Figure 13: A) field-cooled magnetization versus temperature curves for PB NPs (average diameters = 12, 16 and 27 nm) and bulk at an external magnetic field of 50 G⁴². B) Thermal variation of the out-of-phase susceptibility with a zero DC field at different frequencies of the oscillating magnetic field (1 Oe) for CsNi[Cr(CN)₆] NPs²⁶.

I.1.3 Synthesis of core-shell PBA@PBA' NPs

Current research on nanosized cyano-bridged coordination polymers is not only focusing on the synthesis of simple PBA NPs, but also on combining of two or more of these coordination polymers to design intricate multifunctional materials, such as core-shell PBA@PBA' NPs. It is possible to vary the nature of the metal ions composing both, the core and the shell, and finely modulate their properties. These nano-structures can originate from a simple combination of the physical and chemical properties of the different PBA constitutive components (core and shell(s)) or display new properties originated from mutual interactions between the core and the shell components, revealing synergistic effects.

The first description of PBA@PBA' core@shell NPs was reported by Catala and al.⁶⁰ in 2009 with the synthesis of bi-layered particles of $\text{Cs}^{\text{I}}\text{Fe}^{\text{II}}[\text{Cr}^{\text{III}}(\text{CN})_6] @ \text{Co}^{\text{II}}[\text{Cr}^{\text{III}}(\text{CN})_6]$ and $\text{Co}^{\text{II}}[\text{Cr}^{\text{III}}(\text{CN})_6] @ \text{Cs}^{\text{I}}\text{Fe}^{\text{II}}[\text{Cr}^{\text{III}}(\text{CN})_6]$, and tri-layered particles of $\text{Cs}^{\text{I}}\text{Co}^{\text{II}}[\text{Cr}^{\text{III}}(\text{CN})_6] @ \text{Cs}^{\text{I}}\text{Fe}^{\text{II}}[\text{Cr}^{\text{III}}(\text{CN})_6] @ \text{Cs}^{\text{I}}\text{Ni}^{\text{II}}[\text{Cr}^{\text{III}}(\text{CN})_6]$. The design of these heterostructures is performed by using an epitaxial growth seed-mediated procedure on surfactant free PBA NPs, which is essential to obtain the targeted core-shell nano-objects. Indeed, as shown previously, the general synthesis of PBA NPs requires the use of a stabilizing agent permitting to control the growth of the particles (size, shape), precluding their aggregation and ensuring their dispersion in different solvents. However, the presence of these protective agents at the NPs surface weakens its reactivity, avoiding the possibility of any subsequent growth of a new PBA shell. At the opposite, the stabilization of the surfactant-free nanoparticles by

self-stabilization, as described previously⁴⁹, make possible to perform a coordination chemistry at the particles surface, the $[M'(CN)_6]^{n-}$ moieties at the surface remaining reactive. Thus, the preparation of pure core-shell PBA@PBA' NPs requires: 1) the synthesis of well-dispersed and well-defined crystalline surfactant-free charged PBA NPs, which are used as seeds, then 2) the control of the PBA shell side nucleation by controlling the addition rate and the concentration of the components. Then, the general procedure consists on the simple growth process on the charged core present in solution with the slow and controlled addition of the diluted PBA' precursors solution (figure 14), in order to avoid any nucleation of simple PBA NPs.

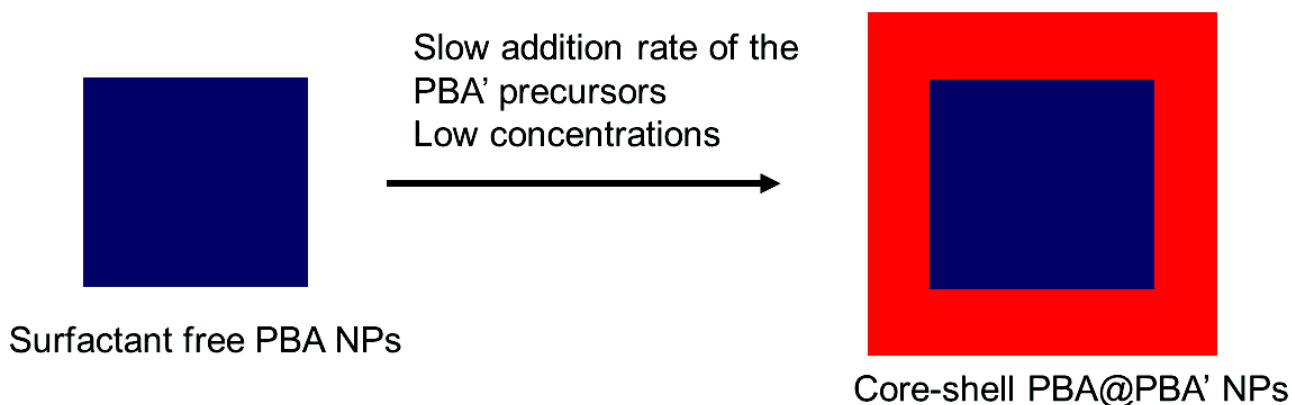


Figure 14: Schematic representation of the general procedure permitting the obtaining of core-shell according those described by Catala and al⁶⁰.

For the design of PBA@PBA' core-shell NPs, the control of the morphology is particularly dependent on the concept of epitaxial growth. The presence of such growth mode can be confirmed by a HRTEM image of a core-shell particle. The continuity of the lattice fringes through the interface, with a single-orientation of the crystallites that form the shell are characteristic of a heteroepitaxial growth⁵⁴ (figure 15, a). Moreover, by using a Fourier transformation of HRTEM image, the indexing of the Fourier spots can permits the determination of the termination facets. If these facets are parallel in both, the shell and the primary particles, then an epitaxial growth corresponding to a cube-on-cube growth mode is occurred, leading to well-defined cubic heterostructures⁵³ (figure 15,b). Epitaxial growth is particularly dependent of the different PBAs used for the core and the shell of the heterostructure. Indeed, epitaxial growth defects are minimized and growth is favored if the characteristic intermetallic distances of the two PBAs are closed enough to any lattice mismatch to be compensated by the limited flexibility of the lattice. If the lattice mismatch is too important to be compensated, other morphologies than cubic shape are obtained, as reported by Talham and al⁶¹. A pseudomorphic layer growth leading to cubic shape was observed for KNiCo@KNiFe and KNiCo@KNiCr core-shell NPs with lattice misfit lower than 3.5% (figure 16, a), b) and c)). At the opposite, an island growth mechanism was observed with the preferential growth at the corners for lattice misfit higher than 3.9%, as for KNiCo@KCoCr and KNiCo@KFeCr, (figure 16, d) e) and f)). Then the control of the morphology is dependent of the elastic properties of both, the core and the shell, and particularly of the difference of the respective PBA lattices.

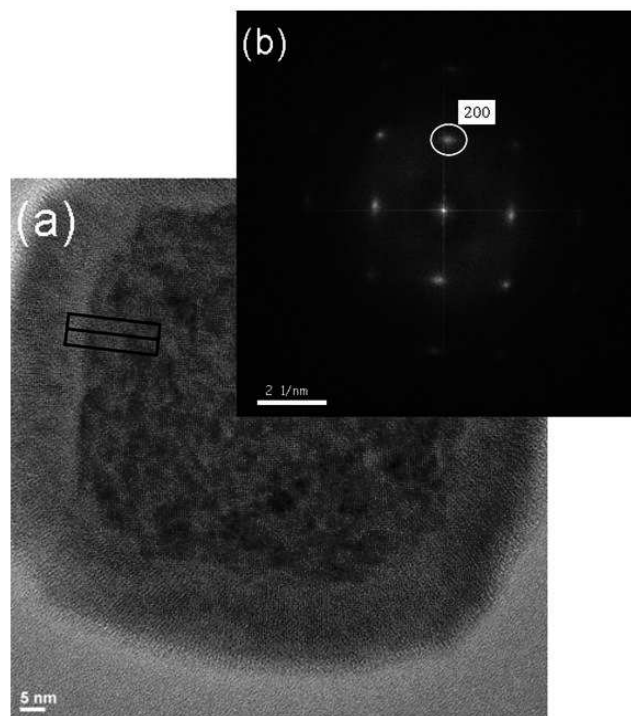


Figure 15: a) HRTEM image of RbCoFe@RbNiCr particle recorded in low-dose mode and b) Fourier transform of the same image using DigitalMicrograph, reported by M. Presle and al^{54,62}.

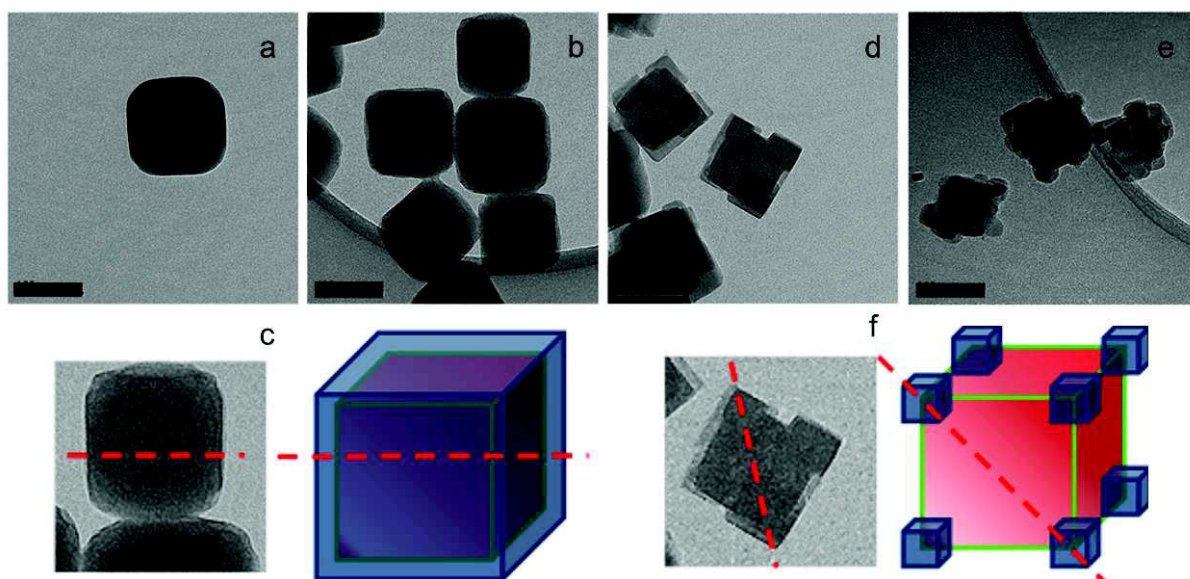


Figure 16: TEM images of KNiCo@KNiFe NPs a) and KNiCo@KNiCr NPs b) showing the core-shell morphology c). TEM images of KNiCo@KCoCr NPs d) and KNiCo@KFeCr NPs e) showing the core-island morphology f)⁶¹. (Scale bar: 100 nm).

The epitaxial growth seed-mediated procedure with using PBA NPs as seeds can have two main interests. On one hand, it is possible to grow a new PBA shell with the same PBA used for the core. On the other hand, the growth of a new PBA' shell on the PBA core permits to design a heterostructured PBA@PBA' NPs presenting a multifunctionality.

The growth of the same PBA shell on PBA NPs using a seed-shell procedure can be performed: i) to precisely control the shell size, then finely tune the properties of the NPs or ii) to access NPs size difficult to access with using a classical co-precipitation method. The first approach was achieved by Mallah and al.^{63,64} to obtain a series of ferromagnetic CsNi[Cr(CN)₆] NPs with a shell of the desired thickness ranging from 6 to 30 nm from the initial 6 nm CsNi[Cr(CN)₆] NPs (figure 17, left). After dilution in PVP matrix, these ferromagnetic NPs have permitted to determine the single domain critical size of the CsNi[Cr(CN)₆], found to be around 22 nm, a uniform reversal of the magnetization being observed below this size. Using the second approach, KNi[Fe(CN)₆] NPs with a mean size of 387 nm were obtained by Talham and al.⁵² with using two successive seed-shell procedure (figure 17, right). Indeed, the synthesis of particles greater than 300 nm by a single co-precipitation method is difficult, and lead to very large size distributions. Li⁺ and Na⁺ ions were inserted in the PBA structure of these particles, to investigate their rate capability. These NiFe NPs present an important charge capacity and rate capability regardless on the particle size, but the capacity at high cycle rate is limited by the Li-ion diffusion into the particles due to their large size. Such systems present interest for potential applications as cathode material in electrochemical energy storage schemes.

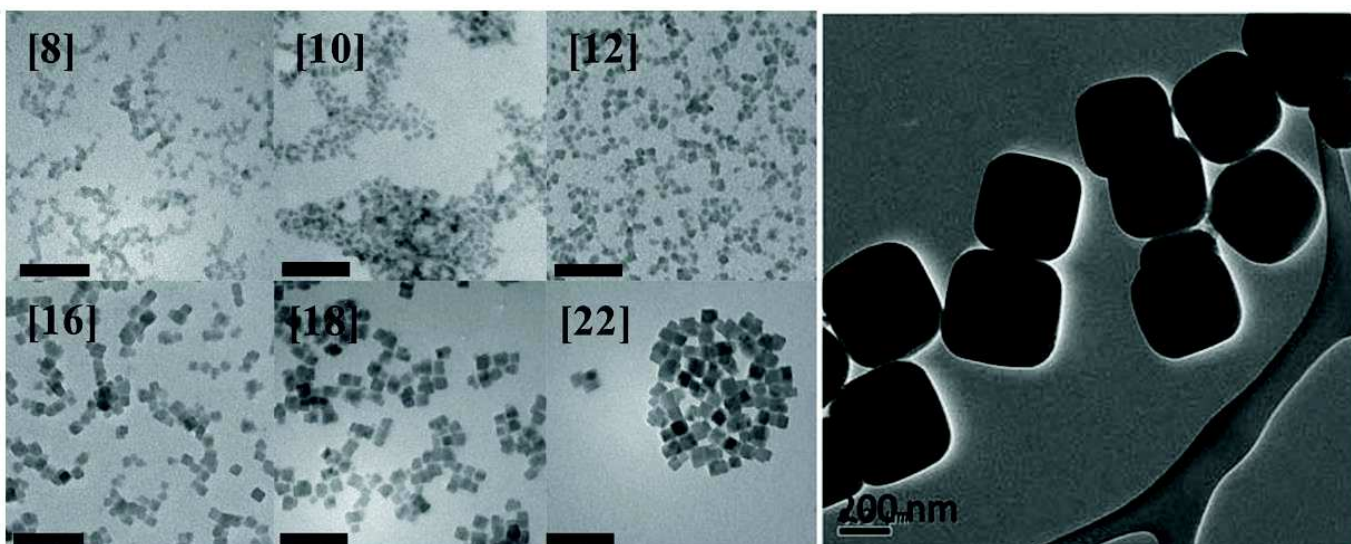


Figure 17: Right: TEM images of the CsNi[Cr(CN)₆] NPs of 8 nm [8], 10 nm [10], 12 nm [12], 16 nm [16], 18 nm [18] and 22 nm [22] obtained by Mallah and al.⁶⁴ (scale bar: 100 nm). Left, TEM image of 387 nm sized KNi[Fe(CN)₆] NPs synthesized by Talham and al.⁵².

Since the first description of PBA@PBA' nano-heterostructures, several examples of core-shell NPs have been reported in the literature. The combination of the properties of both the PBA core and the PBA shell, with sometimes an apparition of interesting phenomenon modifying the properties, such as synergistic effects, permit to target a large range of potential applications.

Such PBA heterostructured nano-objects can be used for Li-ion storage, PBA being recently proposed as cathode material for low-cost, long-cycle-life and high-power batteries. In that aim, core-shell particles combining K_{0.1}Cu[Fe(CN)₆]_{0.7} PBA as core for its high-capacity and K_{0.1}Ni[Fe(CN)₆]_{0.7} PBA for its high stability have been obtained^{65,66}. The core-shell Cu[Fe(CN)₆]@Ni[Fe(CN)₆] present an interesting reversible Li-ion charging and discharging due to the Cu[Fe(CN)₆] core and the Ni[Fe(CN)₆] shell facilitates the ions transport to the core. Moreover, simple Cu[Fe(CN)₆] NPs are subjected to a loss of the

electrochemical reversibility and a rapid decrease of the capacity originated from the modification of the cell parameter upon lithiation, but no similar effect is observed for the heterostructure, which is the sign of a synergy between the core and the shell. This may be originated from the potential strain at the interface which limit the structural phase change. The efficiency of the Li-ion insertion can also be provided by the evolution of the magnetic properties. Indeed, the progressive insertion of Li-ion leads to the stepwise reduction of the Fe^{3+} ion in the structure into Fe^{2+} ion, first in the CuFe core (figure 18, 1 a)) then in the NiFe shell (figure 18, 1 b)). The reduction of the CuFe core induces a slight shrink of the lattice and an increase in the NiFe shell domain size, visible with the increase of the coercive field H_c (Figure 18, 2, c)). Then the reduction of the NiFe shell leads to a loss of the ferromagnetic order with the decrease of H_c (Figure 18, 2, d)). Such synergy may be interesting to control the magnetism in cyano-bridged coordination polymer by controlling the electrochemically guest ion insertion in the structure.

Core-shell PBA@PBA' NPs can also be used for hydrogen storage applications, as shown for $\text{Mn}[\text{Cr}(\text{CN})_6] \cdot m\text{H}_2\text{O} @ \text{Ni}[\text{Cr}(\text{CN})_6] \cdot n\text{H}_2\text{O}$ ⁶⁷ (figure 19, a)). By comparison with simple $\text{Mn}[\text{Cr}(\text{CN})_6] \cdot m\text{H}_2\text{O}$ and $\text{Ni}[\text{Cr}(\text{CN})_6] \cdot n\text{H}_2\text{O}$ NPs, these heterostructures present an interesting enhancement of the hydrogen storage capacity, which is performed by removing the coordinated and non-coordinated water in the structure to be replaced by hydrogen (figure 19, b). This is due to the higher specific surface area and the lower dehydration of the core-shell compound and may be originated from the synergistic effect between the core and the shell, particularly at their interface.

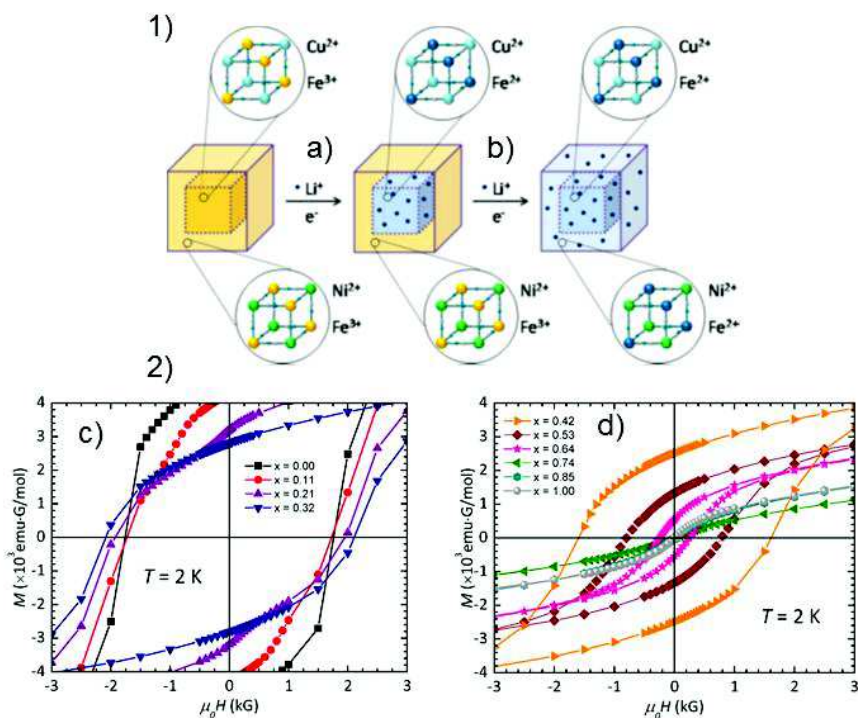


Figure 18: 1) Schematic illustration of the stepwise reduction of the Fe centers in the CuFe@NiFe core-shell heterostructure during the electrochemical Li-insertion Process. 2) Evolution of the coercive field H_c for different concentrations x of inserted Li-ion⁶⁶.

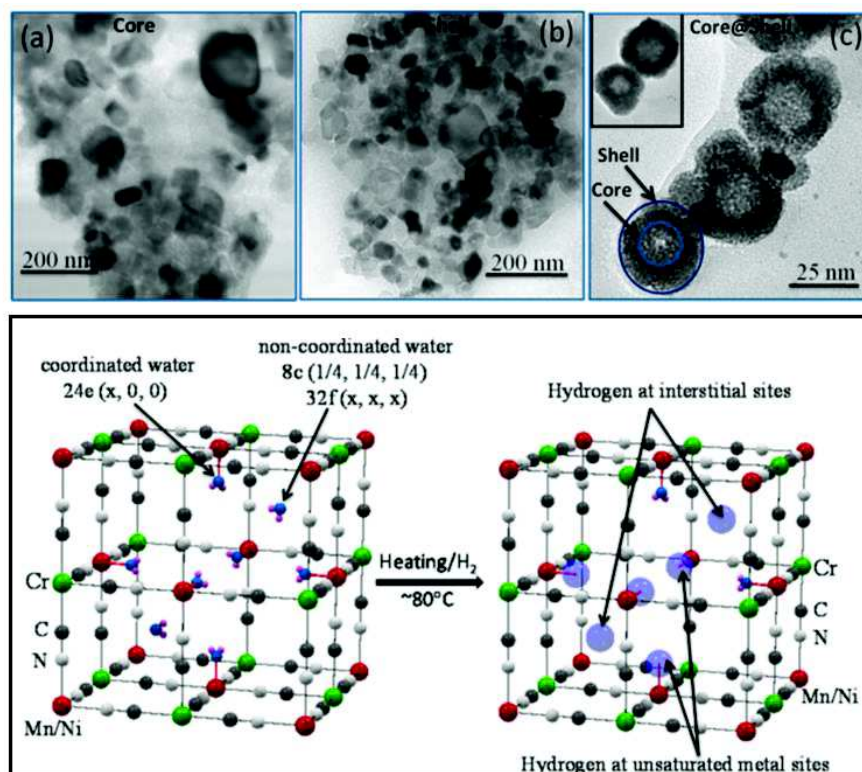


Figure 19: TEM images of Mn[Cr(CN)₆] \cdot mH₂O NPs a), Ni[Cr(CN)₆] \cdot nH₂O NPs b) and core-shell Mn[Cr(CN)₆] \cdot mH₂O@Ni[Cr(CN)₆] \cdot nH₂O NPs developed by Yusuf and al. for hydrogen storage. Schematic representation of the unit cell of the core-shell compound with the removing of the coordinated water and non-coordinated water under heating to create active sites of hydrogen in the structure⁶⁷.

The first synergistic effect reported in PBA@PBA' nano-heterostructures concerns the combination of two different ferromagnetic PBAs to form multifunctional core-shell NPs, such as CsNiCr@CsCoCr nano-heterostructures (figure 20, a) and b))⁶⁰. Indeed, while the coercive fields of separated CsNiCr and CsCoCr were found equal respectively to 80 and 600 Oe, the core-shell CsNiCr@CsCoCr NPs present a larger hysteresis cycle with a coercive field of 2500 Oe (figure 20, c). Such enhancement of the magnetic properties is clearly originated from a synergistic effect, due to the interface between the CsNiCr-PBA core and the CsCoCr-PBA shell.

The main synergistic effect studied in heterostructured systems consists on the combination of a CoFe photomagnetic/photostrictive PBA and a NiCr ferromagnetic /piezomagnetic PBA in the core-shell nano-objects. Double-layered core-shell RbCoFe@RbNiCr NPs⁶² (99 nm, figure 20), KNiCr/RbCoFe⁵⁴ NPs (266 nm, figure 21, b)), RbCoFe/KNiCr⁶⁸ NPs (502 nm, figure 21, a)), core/shell/shell KNiCr /RbCoFe/KNiCr (493 nm, figure 21, c)) and RbCoFe/KNiCr/RbCoFe NPs⁵³ (785 nm, figure 21, d)) have been synthesized using the growth seed-mediated procedure.

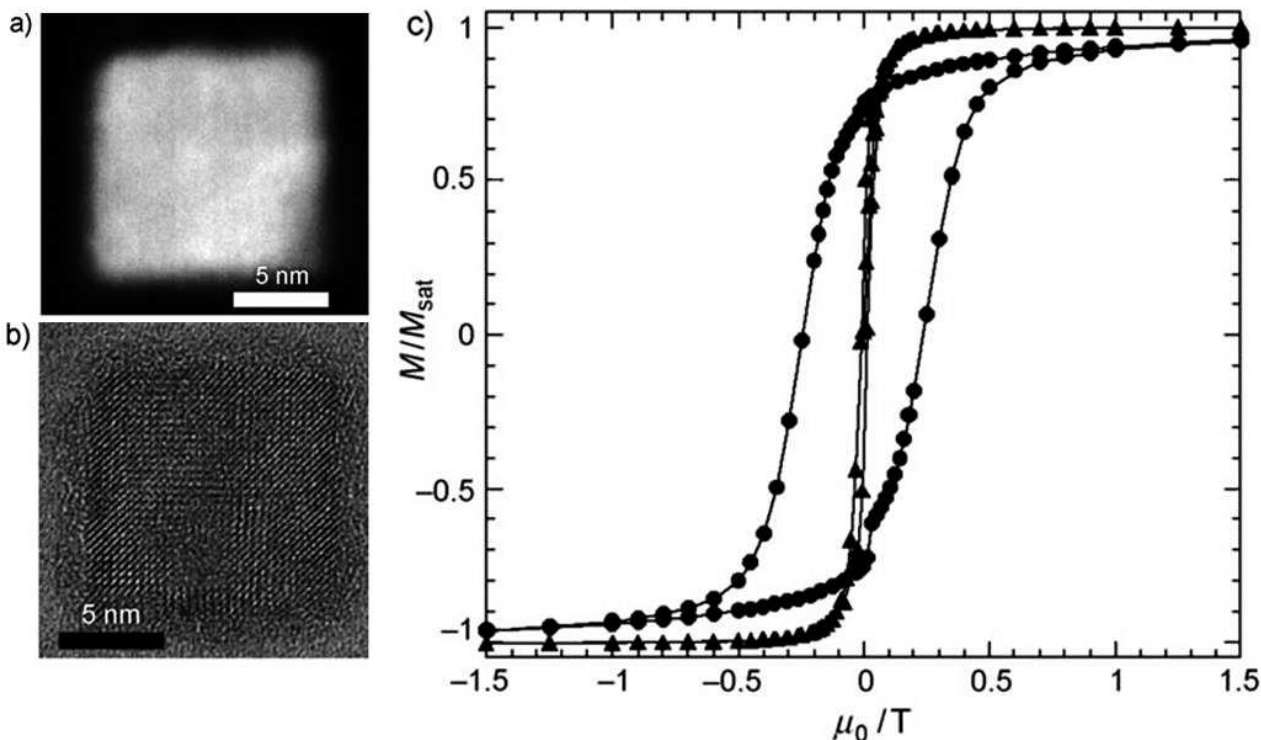


Figure 20: HAADF-STEM a) and HRTEM b) images of a CsNiCr@CsCoCr particle. Plot of magnetization versus field for CsNiCr@CsCoCr NPs (12 nm, circles) and CsNiCr NPs (12 nm, triangles)⁶⁰.

All these examples present magnetic properties corresponding to the sum of both PBAs, however after light-irradiation, an interesting modification of the magnetic properties occurs on the KNiCr PBA contribution (figure 22), with the decrease of the T_C by comparison with similar sized KNiCr NPs ($T_C \sim 70$ K). This synergy is originated from the light induced charge transfer occurring from $Fe^{II}-CN-Co^{III}$ (LS) pairs to $Fe^{III}-CN-Co^{II}$ (LS) pairs, followed by a spin transition giving the $Fe^{III}-CN-Co^{II}$ (HS) pairs. The photoactive RbCoFe transitions from the LS state to the HS state is accompanied by an increase of the metal-to-metal bond length for ~ 0.2 Å (from 9.9 for the non-magnetic RbCoFe to 10.33 Å for the photoinduced magnetic RbCoFe), as shown by DRX studies⁶⁹. The expansion of the lattice volume of the RbCoFe part (core or shell) exerts a mechanical strain on the adjacent of the KNiCr part (core or layer) at the interface (figure 23) inducing large field-cooled magnetization changes in the low-temperature ordered state of this PBA, known to be sensitive to pressure (piezomagnetism)⁷⁰. Then, such synergy allows a control of the ferromagnetic properties of a KNiCr PBA structure *via* a photomagnetic/photostrictive RbCoFe structure, by using light-irradiation.

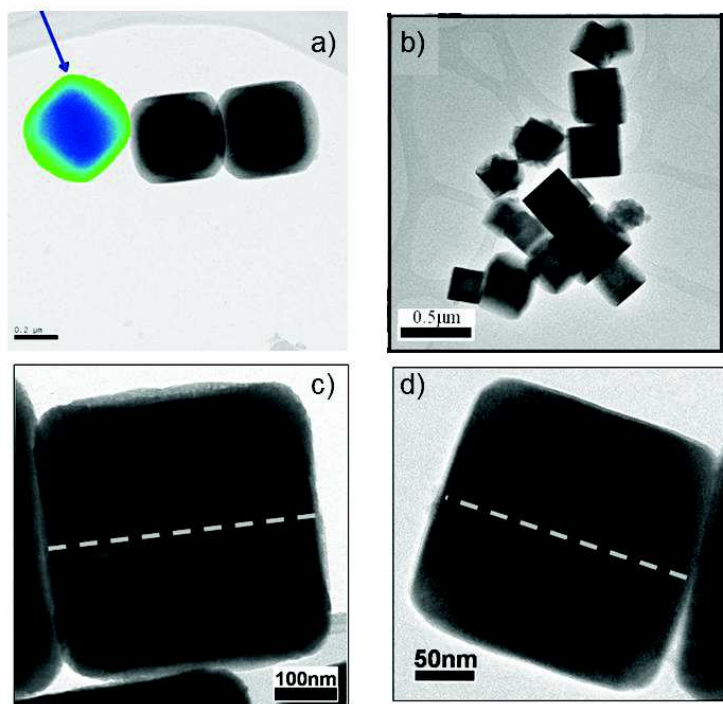


Figure 21 TEM images of a) RbCoFe/KNiCr single-layered core-shell NPs⁶⁸, b) KNiCr/RbCoFe single-layered core-shell NPs⁵⁴, c) KNiCr/RbCoFe/KNiCr double-layered core-shell NPs⁵³ and d) RbCoFe/KNiCr/RbCoFe double-layered core-shell NPs⁵³.

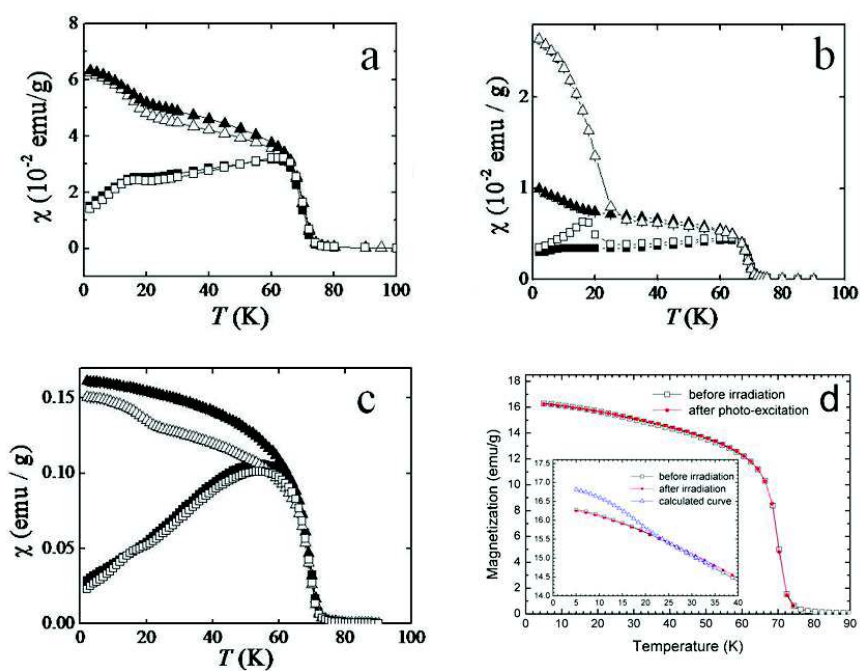


Figure 22: The field cooled magnetic susceptibility χ , $H=100$ G as a function of temperature before irradiation (\blacktriangle , "dark") and with the light off after 11 hours of irradiation with visible white light (Δ , "light") for RbCoFe/KNiCr/RbCoFe NPs a), KNiCr/RbCoFe NPs c) and KNiCr/RbCoFe/KNiCr NPs c)⁶⁹. Magnetization change during irradiation at 35 K for RbCoFe@RbNiCr d)⁵³.

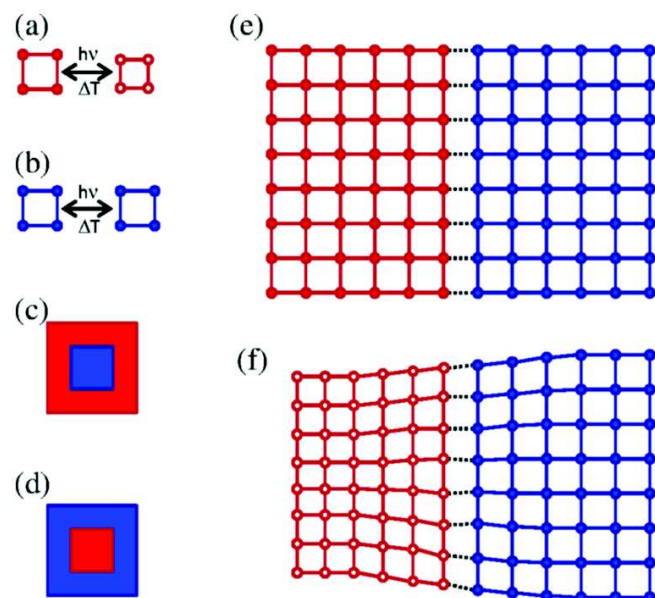


Figure 23: Coupling of photoinduced structural changes in core@shell particles. (a) The Co-Fe PBA undergoes a structural transformation that can be controlled using temperature or applied light. (b) The Ni-Cr PBA does not have an appreciable response to either of these stimuli. These materials may be incorporated into core@shell particles as either (c) Ni-Cr@Co-Fe or (d) Co-Fe@Ni-Cr. (e) At room temperature, or in the photoexcited metastable state at low temperature, Co-Fe PBA (red) and Ni-Cr PBA (blue) have similar lattice constants. (f) In the low-temperature ground state, there is a substantial mismatch between the contracted Co-Fe PBA (red) and Ni-Cr PBA (blue), and there is expected to be a region of strain in the vicinity of the interface before the particles may relax to their equilibrium lattice constants⁶⁹.

However, several parameters can influence the magnetic response of the piezomagnetic PBA structure, as the presence of structural defects, the respective proportion of the two materials in the heterostructure or the presence of Ni-Fe pairs at the Co-Fe/Ni-Cr interface. The remaining of a reduced fraction of $\text{Co}^{\text{III}}\text{-Fe}^{\text{II}}$ converted pairs may also be responsible of the differences observed on the magnetization variation (3.5% for RbCoFe@RbNiCr NPs obtained by Presle and al.⁵⁴, 20% for RbCoFe@KNiCr NPs obtained by Talham and al.⁵³) (figure 24). To avoid the presence of Ni-Fe pairs at the Co-Fe/NiCr interface, a solution consists to wash the RbCoFe-PBA NPs used as core with using a solution containing $[\text{M}'(\text{CN})_6]^{n-}$ ions (which are precursors to the shell), to ensure the stabilization of the NPs and to avoid the contamination of $[\text{Fe}^{\text{III}}(\text{CN})_6]^{3-}$ moieties during the growth stage of the new PBA' layer⁷¹.

Furthermore, the valence of state of the heterostructures has a critical role on the photomagnetic properties, necessary to design photomagnetic/ferromagnetic PBA nano-heterostructures. Indeed, the synthesis of $\text{CsNiCr@CoFe@CsNiCr}$ and $\text{CsNiCr@CsCoFe@CsNiCr}$ core-multishell NPs by growth seed-mediated procedure have revealed that the presence of Cs^+ ion inserted in the PBA structure modify the valence of the Co-Fe pairs, increasing the numbers of photoswitchable $\text{Co}^{\text{III}}\text{-NC-Fe}^{\text{II}}$ pairs and affecting the lattice parameter (9.9 Å for CsCoFe and 10.3 Å for CoFe)⁷² (figure 24). This permits the light induced charge transfer $\text{Fe}^{\text{II}}\text{-CN-Co}^{\text{III}}$ (LS) \rightarrow $\text{Fe}^{\text{III}}\text{-CN-Co}^{\text{II}}$ in the case of CsCoFe PBA and not for CoFe PBA. On other hand, the effect of the photoactive shell thickness on the synergistic effect have been reported in the same study by comparison of the magnetic responses after light-irradiation of different core-shell NPs with different sizes of the CsCoFe PBA layer⁷².

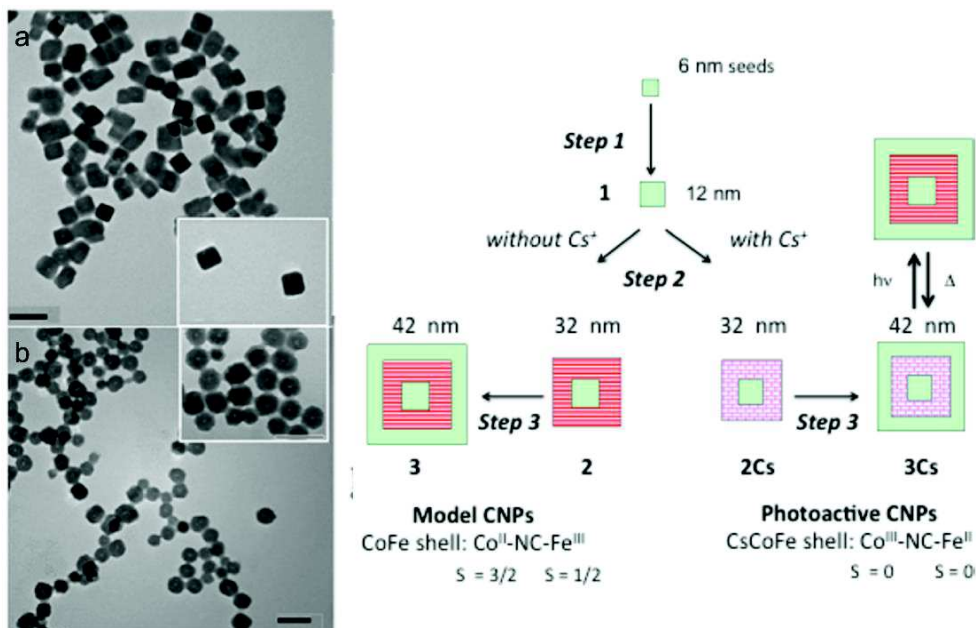


Figure 24: TEM images of CsNiCr@CoFe@CsNiCr double-layered core-shell NPs a) and CsNiCr@CsCoFe@CsNiCr double-layered core-shell NPs b), scale bars = 100 nm. Synthetic strategy of the synthesis of CsNiCr@CoFe@CsNiCr double-layered core-shell NPs and CsNiCr@CsCoFe@CsNiCr double-layered core-shell NPs. (CsNiCr, green, CsCoFe, violet, CoFe, red). The mentioned sizes correspond to the overall diameter⁷².

Such synergistic effects can also be observed with using other magnetic PBAs. Indeed, a similar synergy arising from the interface have been observed with using the photomagnetic RbCoFe PBA and the ferromagnetic (and insensitive to light) KCoCr PBA to obtain RbCoFe@KCoCr core-shell heterostructures⁷³ (figure 25). That provides the possibility to extend this approach to other ferromagnetic PBA to design photomagnetic/ferromagnetic heterostructures presenting similar synergies.

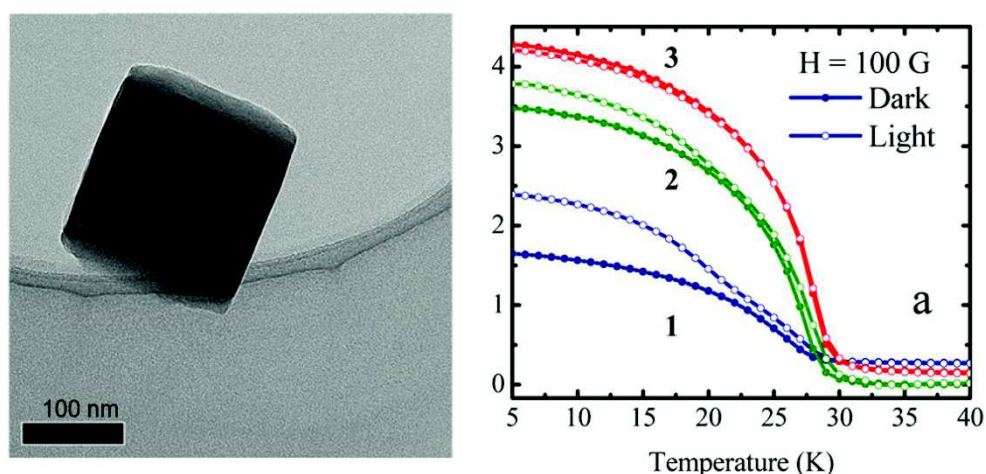


Figure 25: Left, TEM image of RbCoFe@KCoCr core-shell NPs. Right, Field-cooled magnetization vs temperature for RbCoFe@KCoCr of different size (1, 11 nm; 2, 23 nm; 3, 37 nm) under an applied field of 100 G in the dark state (filled dots) and in the light state after irradiation at 5 K (empty dots)⁷³.

I.1.4 Synthesis of hollow PB and its Analogous NPs

The synthesis of hollow nanostructures of coordination polymers, as PBA, have been developed these last years for potential applications in catalysis, sensing, separation or drug delivery. The creation of larger cavities in the structure by hollowing up the core of PBA NPs, coupled to the presence of the uniformly sized pores intrinsic to the framework of this material, bring high surface area, with the possibility to diffuse molecules or ions inside the remaining shell. Moreover, the presence of an empty cavity in the structure can lead to a modification of physical properties, such as magnetism.

The typical strategy to design the crystalline hollow PBA NPs, consists in the control of an etching process of the cyano-bridged coordination polymer NPs. The chemical etching of these nanostructures depends on the nature of the PBA itself. The main described etching process consists in creating the interior hollow cavity by etching mesoporous PB nanocrystals with an acidic solution (HCl)⁷⁴⁻⁷⁶. The mixture is stirred 2h in a Teflon vessel, then transferred into a stainless autoclave and heated at 140 °C for 4h in an electric oven. Hollow PB NPs of 110nm and 190 nm were obtained (figure 27), presenting respectively cavities of 80 nm and 130 nm. The control of the selective etching of the PB NPs core is performed by the presence of PVP molecules at the NPs surface, adsorbed due to the binding of their amide units to irons ions, which protect the shells. However, the difficulty remains to totally control the reaction, otherwise the coordination framework can be entirely decomposed. One of the interest of this method is to be transposed to other PBA, as for example the synthesis of cubic hollow CoFe or MnFe NPs, which size of respectively 200 nm and 400 nm, presenting both an important porosity (respectively 237 m².g⁻¹ and 71 m².g⁻¹)⁷⁷.

By comparison with the initial PB mesoporous NPs, the PB hollow NPs present a modification of magnetic behaviour, with a modification of the hysteresis shape (figure 27) and the increase of the remanant magnetization (M_r), from 7.0 emu.g⁻¹ for solid PB mesocrystal to 21.3 emu.g⁻¹ for hollow PB mesocrystal⁷⁴ (figure 28). Based in their high surface area (324 m².g⁻¹) such hollow PB NPs have been used drug delivery systems. PB hollow NPs containing large amount of anti-cancer agent, such as cisplatin⁷⁵ or doxorubicin⁷⁶ have also been reported (figure 29). The combination of drug delivery with the properties of the PB NPs interesting for ultrasound/photoacoustic imaging and photothermal therapy, originated from the large intervalence charge-transfer band $Fe^{III}-NC-Fe^{II} \rightarrow Fe^{II}-NC-Fe^{III}$, appears as a promising therapeutic agents for nanotheragnostic. Moreover, the release of encapsulated n-perfluoropentane⁷⁶ in these hollow NPs under the heating is susceptible to enhance the signal of B-mode ultrasound imaging by mismatching the tissue impedance.

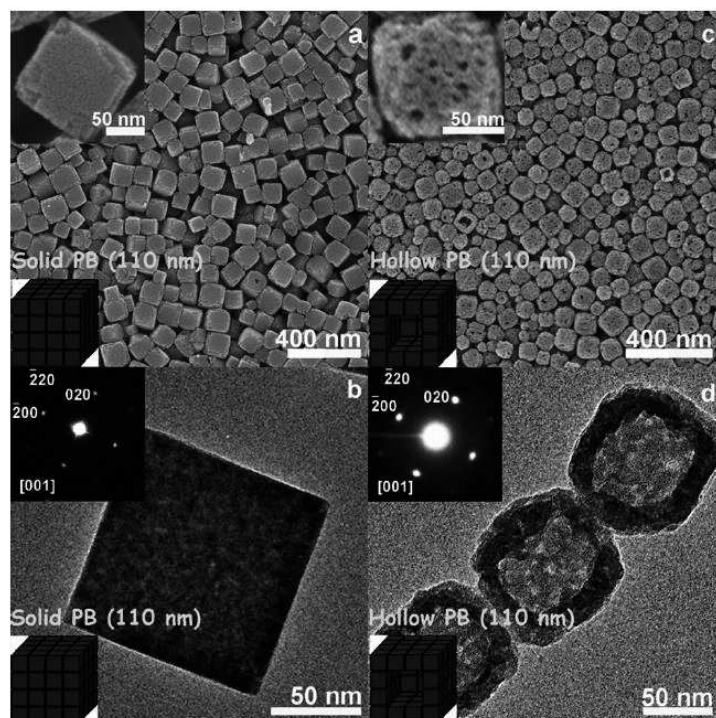


Figure 27: a) SEM and b) TEM images of the solid PB mesocrystals (average particle size: 110 nm) and c) SEM and d) TEM images of the hollow PB mesocrystals synthesised by chemical etching as described by Yamauchi and al.⁷⁴ Inset, a), c) enlarged SEM images of one particle and b), d) the corresponding selected-area electron diffraction (ED) patterns of one particle.

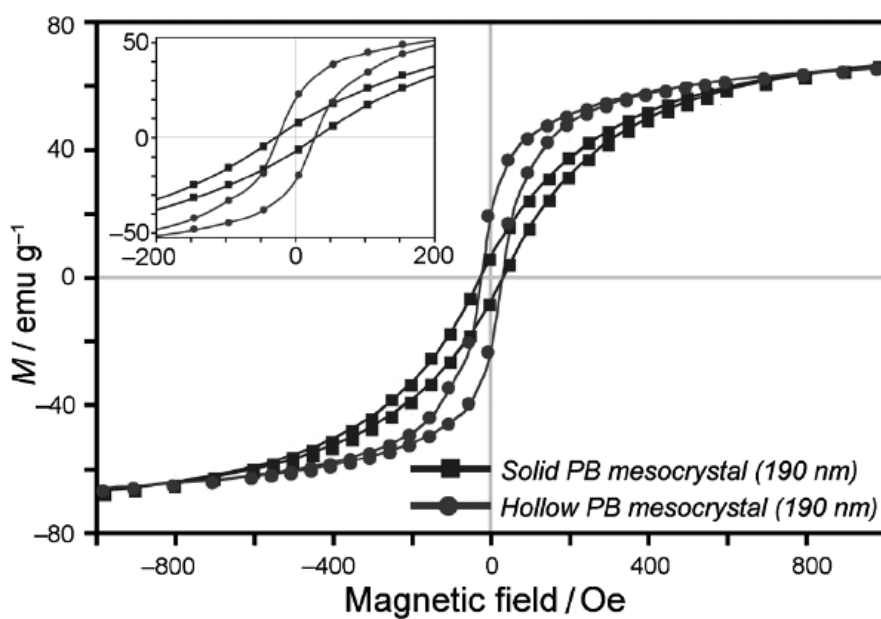


Figure 28: Field dependence of the magnetization at 2.0 K of the Solid PB NPs and the hollow PB NPs synthesized by Yamauchi and al⁷⁴.

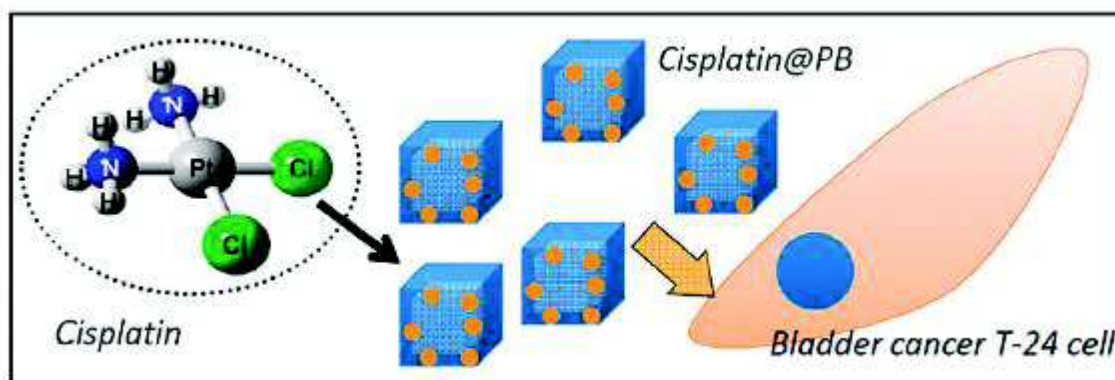


Figure 29: Example of application of hollow PB NPs: use as drug delivery systems containing Cisplatin for cancer chemotherapy, as described by Wu and al.⁷⁵.

Another original method to prepare core@shell heterostructures reported by Talham and al.⁷⁸ consists in the synthesis of RbMnFe core as sacrificial template and RbMFe (M= Co, Ni) as a shell (figure 30). Then, taking advantage of the increased solubility of RbMnFe PBA compared to others members of the PBA family (known to be insoluble), the RbMnFe core is removed by dissolution in very mild conditions (washing in water at 45 °C for 45 min).

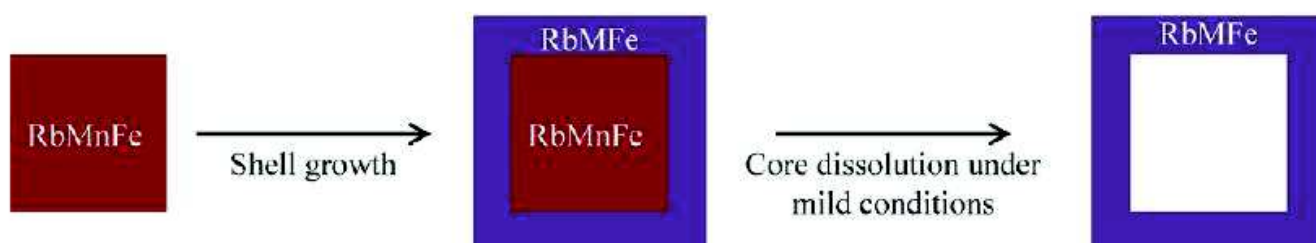


Figure 30: Synthetic strategic developed by Talham⁷⁸ and al. to design hollow PBA NPs which consists to prepare core@shell heterostructure with RbMnFe core as template and RbMFe (M= Co, Ni) as a shell, then the template is dissolved under mild conditions to form well-preserved hollow shells.

The hollow RbCoFe and RbNiFe NPs obtained present a well-defined cubic shape and a size of respectively 53 ± 12 nm and 52 ± 10 nm (figure 31). These hollow NPs have hierarchical pores, as indicated by N_2 adsorption-desorption isotherms measures, and their specific surface area has been calculated to be $694 \text{ m}^2\text{g}^{-1}$ for RbCoFe and $786 \text{ m}^2\text{g}^{-1}$ for RbNiFe. Moreover, the NPs have been obtained using a surfactant free process, then the PBA NPs surface remains reactive, with the presence of the terminal cyanides of the $[M^{III}(\text{CN})_6]^{3-}$ moieties. By performing a subsequent growing of another PBA, hollow PBA@PBA' NPs can be obtained, such as hollow RbCoFe@NiCr NPs⁷⁸. Such intricate heterostructure presents two ordering temperatures, $T_c = 20$ K and 75 K, respectively due to the ferrimagnetic ordering of RbCoFe and ferromagnetic ordering of NiCr (figure 32). Such porous and magnetic heterostructure are promising for applications in adsorptive/magnetic separation.

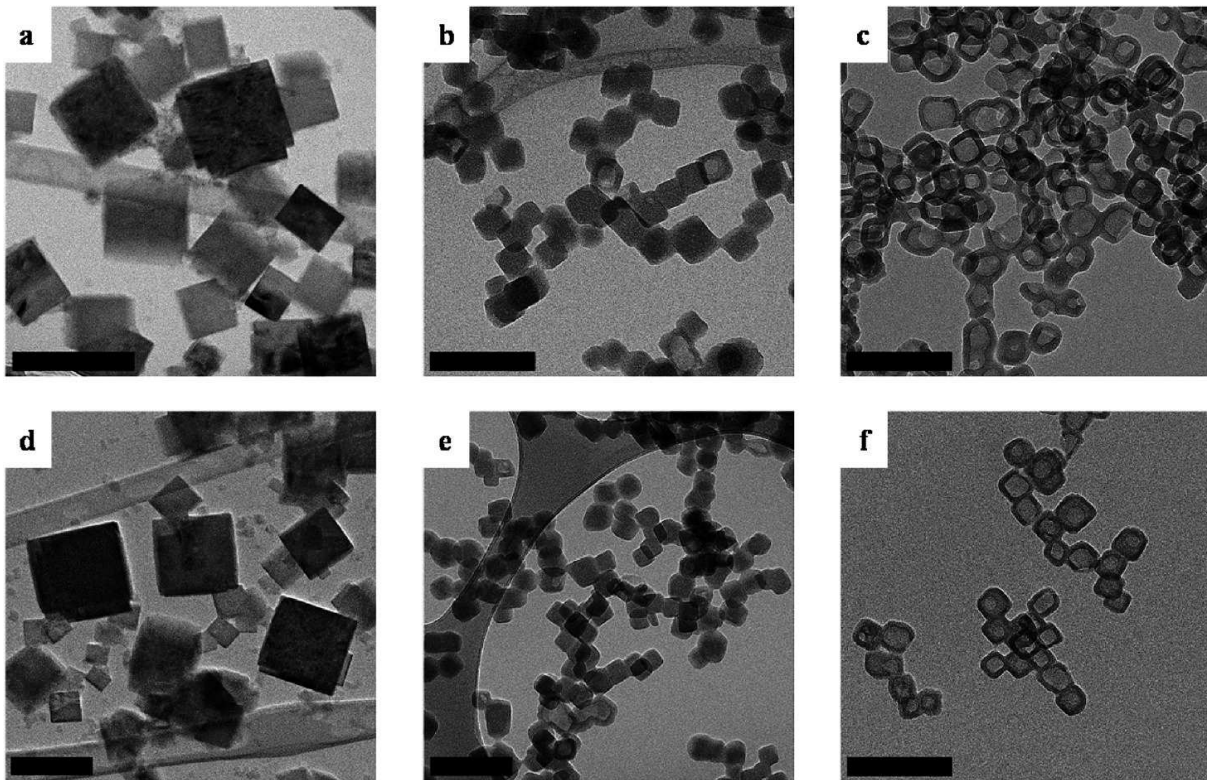


Figure 31: TEM images of the hollow PBA NPs described by Talham and al.⁷⁸ with RbMnFe cores (a, d) showing polydispersed cubes with a size range of 50 to 300 nm; (b) uniform cubic core@shell particles of RbMnFe@RbCoFe and (e) RbMnFe@RbNiFe; (c) RbCoFe and (f) RbNiFe hollow shells with shape and size preserved upon removal of the template. Shell thickness ranges from 9 to 15 nm. Scale bars for each images are 200 nm.

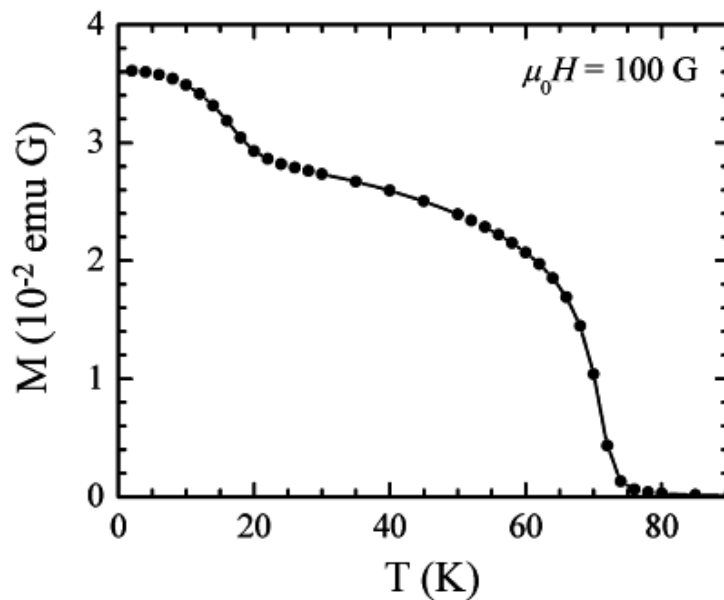


Figure 32: Magnetization vs temperature plot in an applied magnetic field $0H = 100$ G exhibiting two ordering temperature characteristic of the RbCoFe ($T_c = 20$ K) and NiCr ($T_c = 75$ K) shells of hollow RbCoFe@NiCr NPs⁷⁸.

Part 2: Core@shell nano-heterostructures

I.2.1 Core@shell NPs: definition and interests

In the recent years, synthesis of heterogeneous composite have revealed a promising way to improve a multifunctionality at the nanoscale, with the combination of two or more materials in intricate nano-objects and then the combination of their intrinsic properties, with in some cases the appearance of new properties⁷⁹ or synergistic effects, arising from interactions at the interface. Today, with the perpetual advances in this field, the synthetic techniques permitting to control the size and the morphology of the nano-objects, and then a large variety of shape is accessible: not only spherical shape, but also shapes such as cube⁸⁰, prism⁸¹, hexagon⁸², octahedron⁸³, disk⁸⁴, wire⁸⁵, rod⁸⁶, tube⁸⁷, ect. It is now well-know that the NPs properties are dependent of their size, however certain properties have revealed also dependent of the shape. For example, anisotropic gold NPs, such as nanorods or nanostars⁸⁸, present two or more Surface Plasmon Resonance (SPR) modes, which are dependent of the numbers of different dimensions (as length and width for nanorods), while symmetrical (spherical) gold NPs only exhibit a single SPR mode⁸⁹. In general, a core@shell nanoparticle is composed by two or more materials, one as the core (inner material) and the other(s) as the shell(s). These can consist of different combinations, including inorganic@inorganic, inorganic@organic, organic@inorganic and organic@organic materials. Even if the concentric core@shell nanoparticles are the most common (figure 33, a), different shaped core@shell nano-heterostructures are accessible (figure 32, b) to e)), generally when the core is non spherical, its morphology inducing those of the shell.

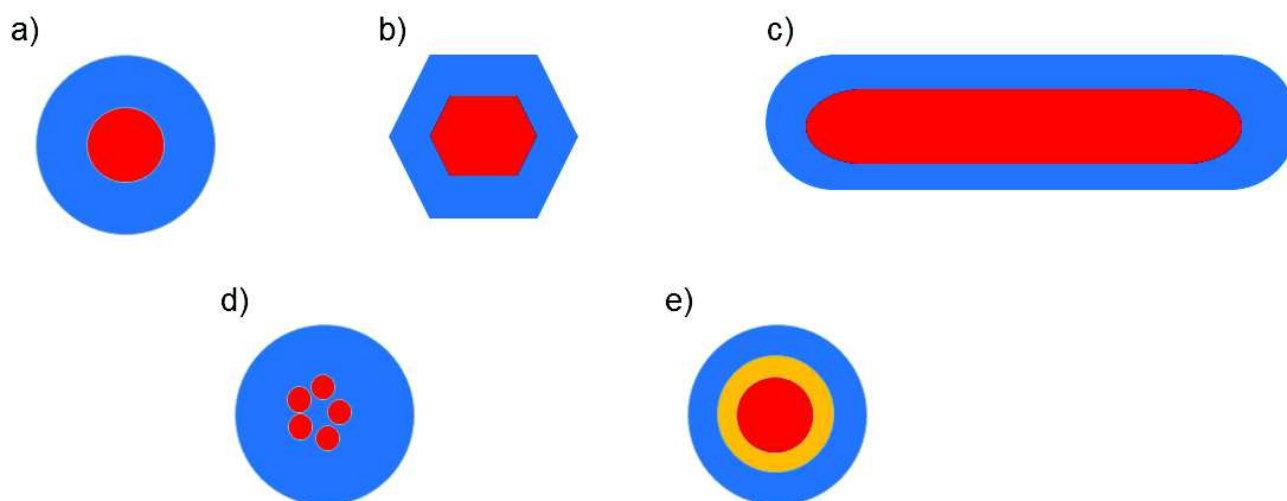


Figure 32: Different core@shell nanoparticles: a) spherical core@shell NPs; b) hexagonal core@shell NPs; Core@shell nanorods; d) multiple small core materials coated by single shell materials; d) nanomaterial with a red core, a yellow intermediate shell, and a blue outer shell.

Core@shell nano-heterostructures are really interesting for a wide range of applications, due to the possibility to finely tune their properties by varying the nature of the materials used, the size and the morphology according to the targeted use. Current applications include catalysis⁹⁰, electronic⁹¹, pharmaceutical applications⁹², biomedical, with different used as contrast agent for bioimaging⁹³, controlled drug release⁹⁴, targeted drug delivery⁹⁵, cell labeling⁹⁶ and tissues engineering applications⁹⁷.

In the context of our work, we are particularly interested in designing inorganic/inorganic core@shell nano-heterostructures. Firstly, we briefly present a state-of-the-art on the obtention of such intricate systems, with describing the main materials combinations reported in the literature and their potential applications. Then we focus on design of core@shell NPs involving gold. Indeed, gold NPs exhibit catalytic properties and strong optical features arising from the SPR phenomenon, which allow them a promising use to prepare multifunctional nano-devices. A special emphasis is given on description of synergistic effects, as for example in magneto-plasmonic nano-objects.

1.2.2 Synthesis and properties of inorganic core@shell NPs.

In the quest of the multifunctionality at the nanoscale, a large variety of materials have been used to design nano-heterostructures, such as metal (Ag, Pt, Pd, Ni, Fe, Co, Cu, Zn), metal oxide (Fe_3O_4 , ZnO, TiO_2 , CuO_2), semiconductor (quantum dots: CdTe, CdS, ZnS, ZnTe), silica or coordination polymers (MOFs, PBA), in a wide range of combination, such as semiconductor@semiconductor, metal@ semiconductor, metal@metal, metal@metal oxide, metal oxide@metal and metal or metal oxide@silica NPs.

One of the mostly used material as a shell is a silica. In comparison with other materials, silica presents certain advantages, as the increase of the suspension stability of the core particles, the reduction of the bulk conductivity, the optical transparency, or also its chemical inertia. Different metals, as Ag⁹⁸, Ni, Co or Fe⁹⁹, and metal oxides, as for instance Fe_3O_4 ^{100,101} have been coated by SiO_2 shell, generally synthesized according to a Stöber (or sol-gel) process in the presence of the NPs used as core. Ag@ SiO_2 NPs present interesting optical properties which can be modulated by varying the shell thickness. On the other hand, magnetic properties of M@ SiO_2 (M=Ni, Fe, Co) or Fe_3O_4 @ SiO_2 have been studied, and the presence of the inert shell induces a modification of the magnetic properties, such as a decrease of the saturation magnetization M_s . Such NPs can be used for biomedical applications, as bioimaging (MRI) contrast agents or as a drug delivery vehicle, by incorporating bioactive molecules inside the silica shell.

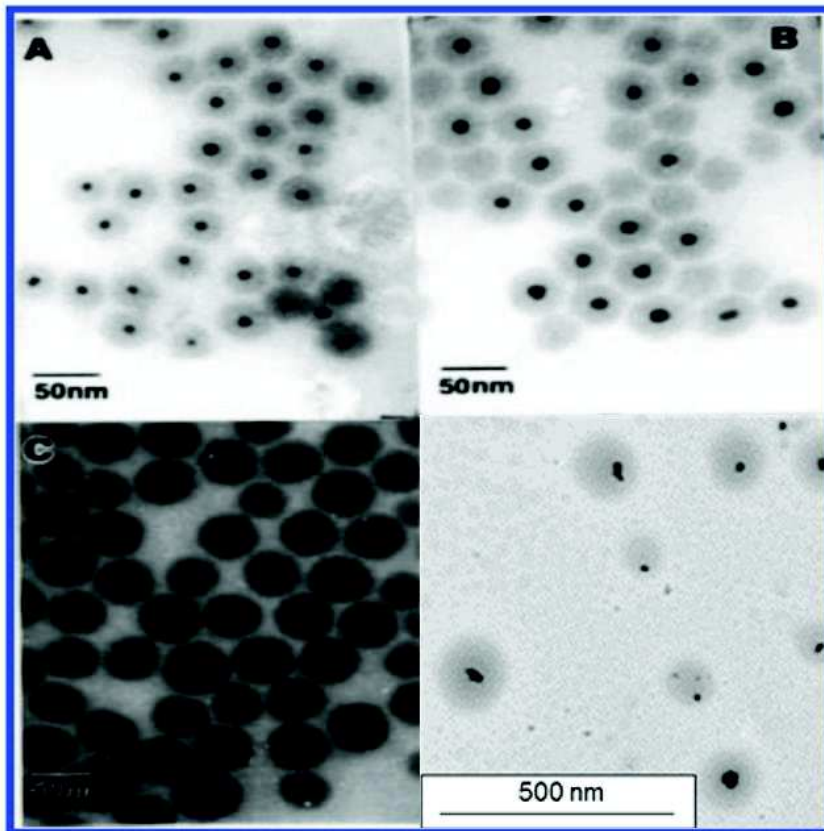


Figure 33: TEM micrographs of Ag@SiO₂ NPs synthesized at different water contents: a) R = 2; b) R = 4; C) R = 6⁹⁸. TEM image of Fe₃O₄@SiO₂ NPs d)¹⁰¹.

Semiconductor nanoparticles, also called Quantum Dots (QDs) have attracted an interest for their interests in applications as light-emitting devices¹⁰², nonlinear optics¹⁰³, catalysis¹⁰⁴, enhancement of optical properties¹⁰⁵. We can distinguish two types of core@shell heterostructures, Semiconductor@Nonsemiconductor or Nonsemiconductor@Semiconductor NPs and Semiconductor@Semiconductor NPs. The interest of using a nonsemiconductor material as core or shell is to bring other properties¹⁰⁶, as magnetism for example, which can increase the photocatalytic effect of magnetic core semiconductor shell NPs (Fe₂O₃@TiO₂ NPs). Moreover, these systems present interesting photoluminescence properties which can be tuned by changing the particle size. On the other hand, combination of a semiconductor as a core and a shell permits to increase optical activity and photooxidation stability¹⁰⁷. It is also possible to obtain core/multishell semiconductor NPS with the presence of two or more shell on the core, as CdSe/CdS/ZnS, CdS/CdSe/CdC or CdSe/ZnS/CdCe. Multilayer semiconductor NPs present higher quantum yield, higher photoluminescence efficiency or improved optical properties.

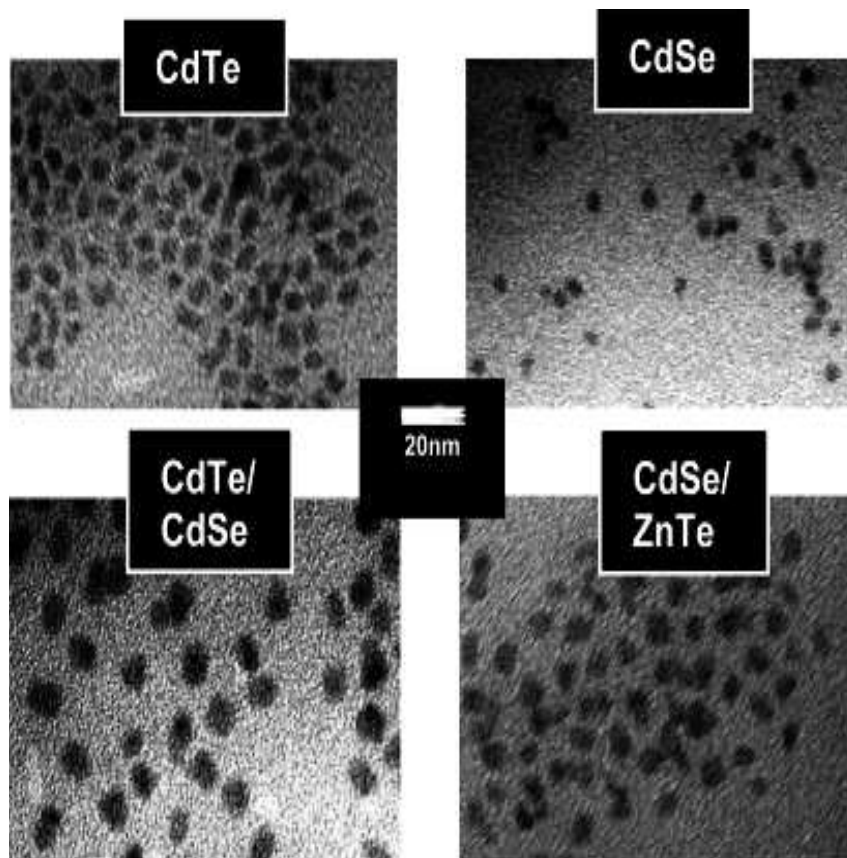


Figure 34: TEM images of CdTe, CdSe, CdTe@CdSe and CdSe@ZnTe QDs NPs¹⁰⁸.

Recently, the use of coordination polymers, such as Metal Organic Frameworks (MOFs) or Prussian Blue Analogous (PBA), has revealed promising for design multifunctional core-shell NPs. These nano-systems profit all advantages of a molecular chemistry, such as flexibility of molecular structures, tunable properties, and often soft synthetic routes for self-assembly reactions¹⁰⁹. As observed for PBA NPs (described previously) the epitaxial growth of the shell on a well-defined MOFs core gives heterogeneous core-shell MOFs or “MOFs on MOFs” crystal, such as $\{[Zn_2(ndc)_2(dabco)]_n\}@[Cu_2(ndc)_2(dabco)]_n$ NPs (with $ndc = 1,4$ -naphthalene dicarboxylate and $dabco = diazabicyclo [2.2.2]octane$)¹¹⁰, $\{Zn_2(bdc)_2(dabco)\}_n @Zn_2(adc)_2(dabco)\}_n$ shell ($adc = 9,10$ -anthracene, $ndc = 1,4$ -naphthalene dicarboxylate)¹¹¹, $Cu@MOF-5$ NPs¹¹² and $MOF-5@IRMOF-3$ ¹¹³. Such nano-heterostructures present optimized porosity and enhanced storage capacity. On the other hand, it is possible to combine coordination polymers with different inorganic material, such as metal NPs (Pt, Ag, Pd, Ru, Cu, Ni)¹¹⁴, which were embedded in various MOFs matrixes by using several technologies such as precursors' infiltration¹¹⁵, solid grinding¹¹⁶ surface grafting¹¹⁷ and metal–organic chemical vapor deposition (MOCVD)¹¹⁸. These Metal@MOFs heterostructures present an important potential as catalysts with enhancing durability, selectivity, reactivity or additional functionality¹¹⁹. Furthermore, metal oxide (Fe_3O_4) were also inserted in the MOFs¹²⁰ or PB¹²¹ for an association of the magnetic or optical properties of inorganic NPs with MOFs porosity, electrochemical or magnetic properties of the coordination polymers.

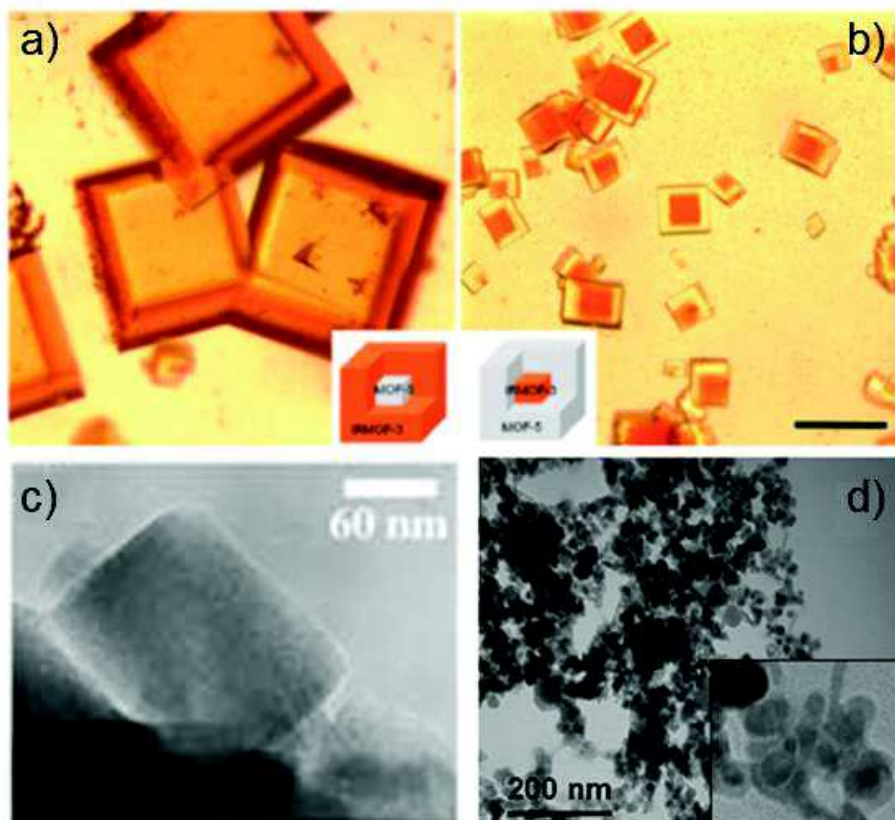


Figure 35: Microscope images of a) core@shell MOF-5@IRMOF-3¹¹⁵, b) IRMOF-3@MOF-5¹¹⁵, c) Cu@MOF-5 NPs¹¹² and d) TEM image of the Fe₃O₄@PB NPs¹²⁰.

1.2.2 Synthesis and properties of inorganic core@shell NPs: interest of gold.

In the field of nanotechnology, numerous researches has been devoted to the synthesis and investigation of the gold NPs. Indeed they present exiting properties, such as catalytic activity, biocompatibility¹²², bio affinity through functionalization of amine/thiol terminated groups¹²³, and the optical properties originated from the Surface Plasmon Resonance phenomenon (SPR)^{89,124}. This latter property can be finely tuned by modification of the size and the shape of the nano-objects, and a large variety of shapes for gold at nanoscale have been reported, such as nanorods, nanoprisms, nanoshells, nanocubes, nanostars, nano-triangular pyramids, ect^{88,89,122} (figure 36). Then, gold appears as an interesting material to design multifunctional NPs by combining with other materials for a large range of applications in catalysis, sensing, optics, and particularly in biomedicine, as diagnostic or therapic agents^{88,89,122,124}. In this aim, a large range of core@shell NPs involving gold as core or shell has already been reported in the literature, such as Au@Metal or M@Au, Au@Silica or Silica@Au, Au@Metal oxide or Metal oxyde@Au, or Au@CPs (MOFs/ PBA).

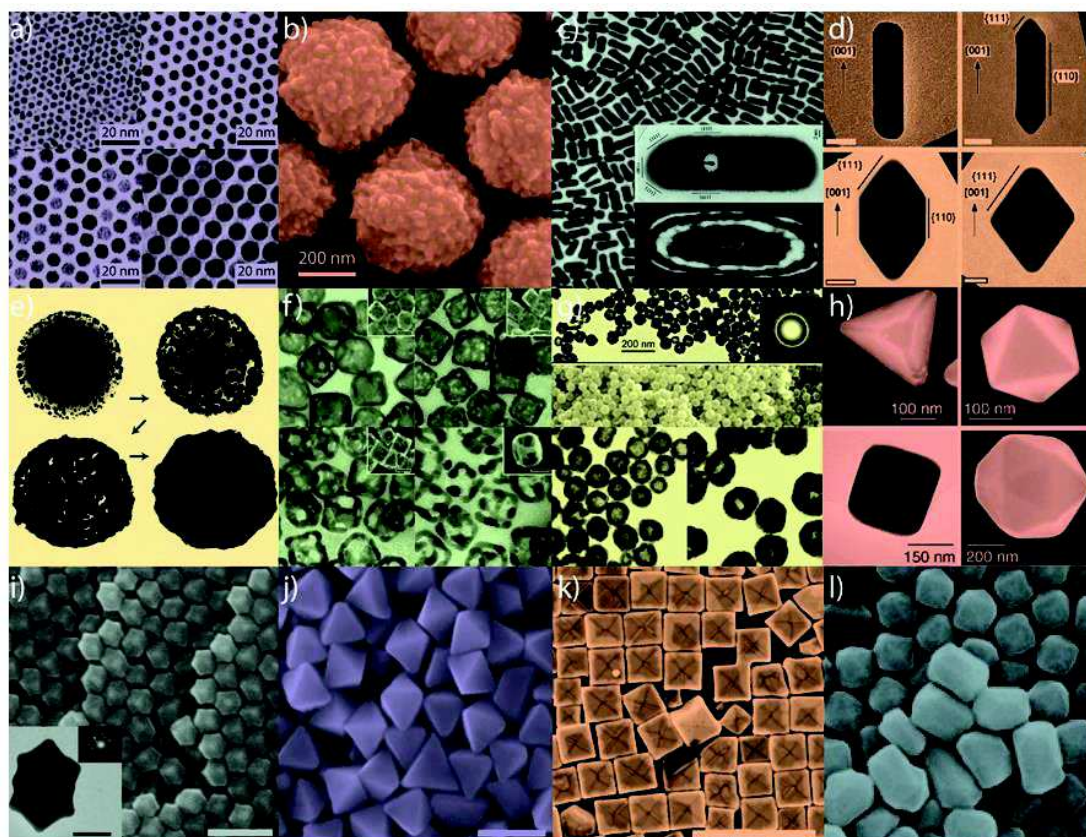


Figure 36: Examples of different shaped gold NPs, as small (a) and large (b) nanospheres, (c) nanorods, (d) sharpened nanorods, (e) nanoshells, (f), nanocages/ frames, (g) hollow nanospheres, (h) tetrahedra/octahedra/cubes/icosahedra, (i) rhombic dodecahedra, (j) octahedra, (k) concave nanocubes, (l) tetrahexahedra⁸⁹.

Among those, the combination of gold and silica have been reported on the elaboration of nano-heterostructures as Au@SiO₂^{125,126} (figure 37) or SiO₂@Au¹²⁷. Generally, Au@Silica are prepared by using a sol-gel process to form the SiO₂ shell around the gold NPs. The thermal-decomposition of the gold precursor permits to form a gold shell around SiO₂ NPs. Both systems exhibit varying optical properties (figure 37), which dependent on both, the relative size of core as well as the shell thickness^{125,127}. Then, by controlling the core size and the shell thickness, a large range of optical responses from the visible to the near-infrared can be reached. These core-shell NPs may prove useful for biomedical applications, in bioimaging.

The combination of the gold with other metal to form Metal@Metal NPs, such as Au@Ag and Ag@Au¹²⁸⁻¹³⁰, or Au@Pt¹³¹, is interesting for different accessible shapes, and thus possibility to finely modulate their optical properties originated from the SPR phenomenon of gold. We can distinguish two different synthetic approaches to control the size of the NPs. On one hand, a shape template (core) nano-object, generally a gold particle, serve to control the shape of the shell during the growth process, generally performed by reduction or reduction-transmetalation¹²⁸⁻¹³¹. On the other hand, a capping agent, as a surfactant or polymer, is used to control the direction and the dimension of the NPs growth¹³². The interest for such heterostructures lies to modulation of the optical properties originated from the SPR phenomenon, by controlling the shape. Moreover, the presence of a shell at the core surface also induces modification of the optical properties, which can be modulated by varying the shell thickness. These objects also present an

interest for catalytic applications, the variation of the metal nature at the surface permitting the access to different reactivity. Magneto-plasmonic multifunctionality can also be obtained with using magnetic metal. Metal@Metal NPs, such as for instance Co@Au NPs, present a significant coercivity and a blocking temperature at 45 K with optical properties due to gold¹³³. Applications as bioimaging may be targeted for these systems.

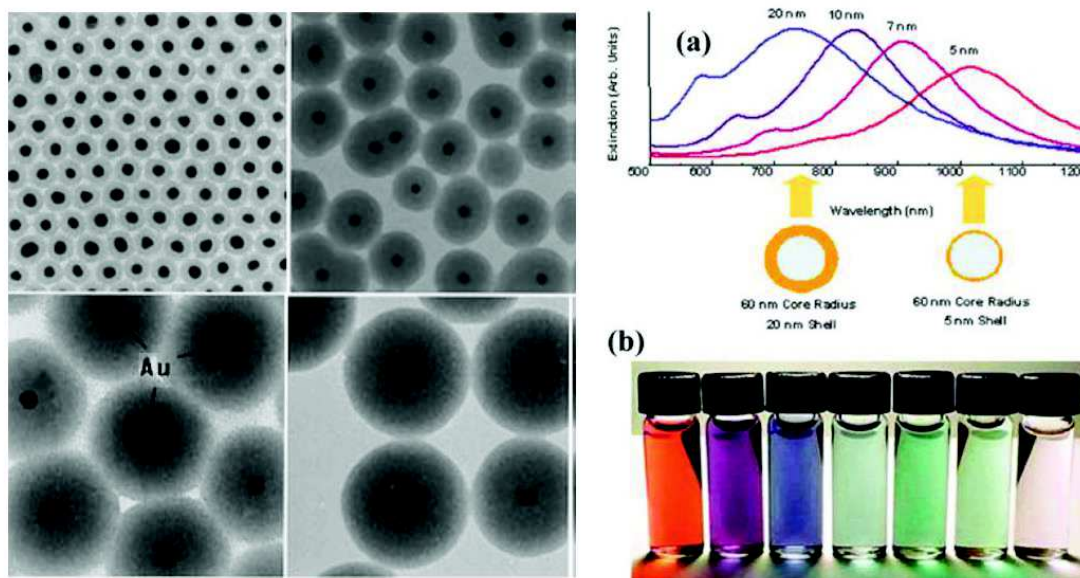


Figure 37: Transmission electron micrographs of silica-coated gold particles produced during the extensive growth of the silica shell around 15 nm Au particles with various SiO₂ shell thickness¹²⁵. Optical resonances of SiO₂@Au core nanoshells as a function of their core/shell ration a) and visual appearance of gold nanoshells with different thickness b)¹²⁷.

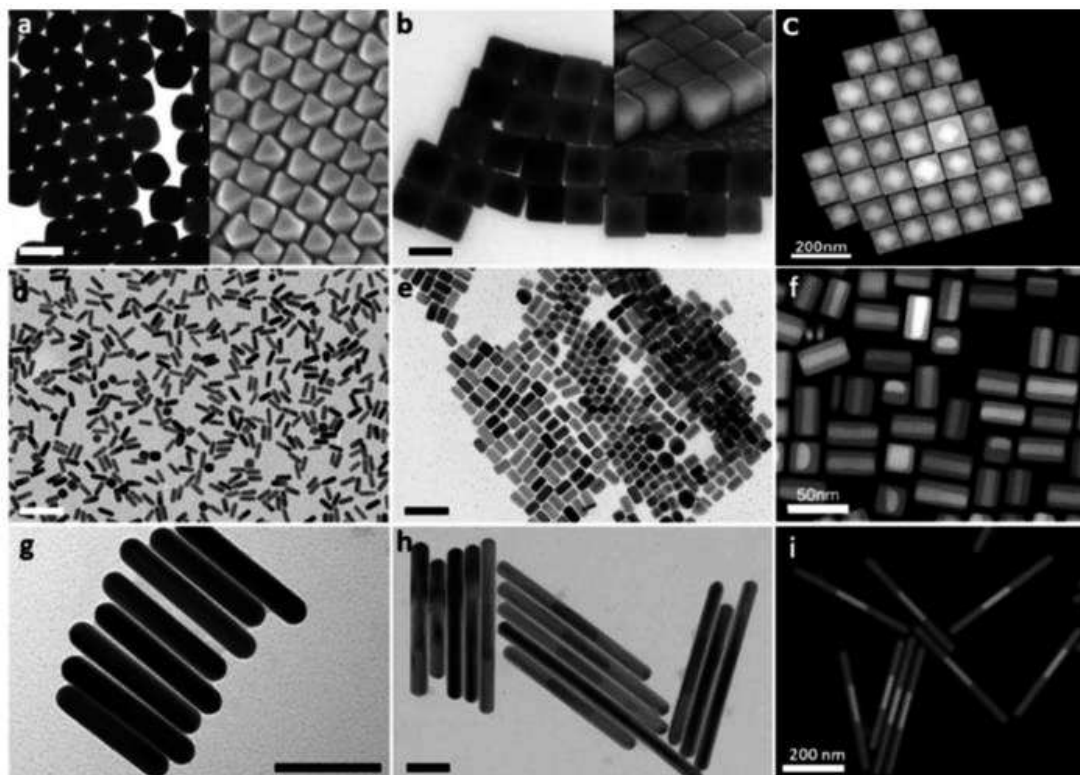


Figure 38: Representative TEM and SEM images of the different gold nanoparticles used as seeds (left column, scale bars: 100 nm) and the corresponding Au@Ag counterparts after silver growth (middle column, scale bars: 100 nm). The right column displays HAADF-STEM images of the same core@shell particles, where the silver shells can be easily discerned from the gold cores¹²⁹.

Other heterostructured systems involving gold also exhibit magneto-optical properties, such as Au@Fe₃O₄^{134,135} or Fe₃O₄@Au NPs¹³⁶⁻¹³⁹. As for metal@metal NPs, it is possible to induce the morphology of the shell by using different shaped gold NPs, such as nanorods¹³⁵ or tetracubic NPs¹³⁸. Generally, the synthetic processes used to growth the shell are reduction or thermal decomposition, and can be made with following a surfactant-assisted seeded-growth technique¹³⁴⁻¹³⁸. Such systems exhibit both plasmonic properties originated from the gold and magnetic properties due to the iron oxide phase; their properties can be modulated by varying the core size or/and the shell thickness. Interesting synergic effects appear^{134,136-139}, as the modification of the magnetic properties due to the electromagnetic field associated to the SPR phenomenon, or modification of the optical properties occurring with the presence of the magnetic part, such as transfer polarization or Kerr effect. These systems are particularly promising for applications such as bioimaging (MRI contrast agents, biosensing) or spintronic.

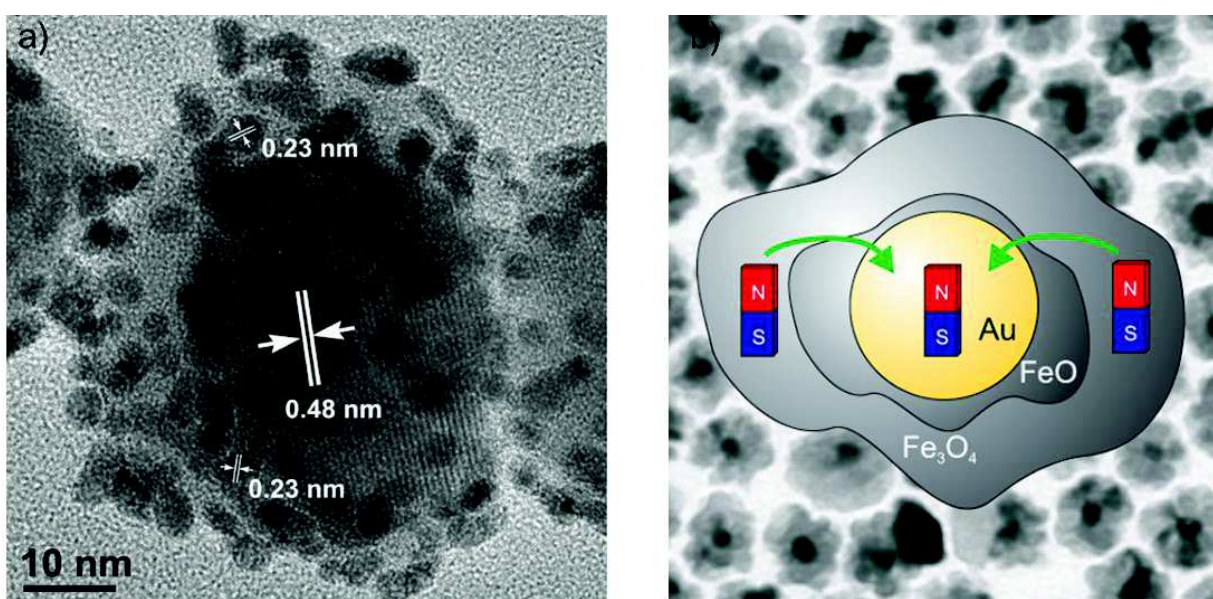


Figure 39: a) HRTEM image of core-shell structured Fe₃O₄@Au nanocomposites¹³⁹. b) TEM images of Au@iron-oxide core@shell NPs, with the schematic representation of the heterostructure and the synergistic effects occurring from the combination of the properties of gold and Fe₃O₄¹³⁴.

Since few years, the design of Au-core containing nano-heterostructures has been extended to the coordination polymers, particularly to the MOFs. Several examples have been reported in the literature, as MOF (with MOF = Zn₄O(BDC)₃, BDC=1,4-benzenedicarboxylate) decorated gold NPs presenting selectivity for CO₂ entrapment¹⁴⁰, Au NPs encapsulated by MIL-100(Fe)¹⁴¹, by ZIF-8 (Zn²⁺-based imidazolate framework)¹⁴², shell or by porous coordination polymer Cu₂(pzdc)²(pyz) presenting enhanced catalytic activity *via* a synergic effect¹⁴³. Generally, these heterostructures are obtained by soft decomposition of the gold precursors impregnated in the pores of the MOFs host¹⁴⁴. The main challenge for such systems lies with the design of core@shell heterostructure where only a single gold core is coated by an uniform and a well-defined MOF shell, and only one example has been reported up to now¹⁴⁰. Concerning nano-heterostructures of the gold core and the PBA shell, only one example has been reported. Au NPs were obtained by

reduction of the hydrogen tetrachloroaurate (HAuCl_4) with the trisodium citrate and the tannic acid, then modified with a slow addition of the PB precursors¹⁴⁵. These nanostructures have been proposed as contrast agent for photoacoustic/CT bimodal imaging and a photothermal ablation of the cancer¹⁴⁶. However, the morphology of the nano-objects appears as a less-defined. To the best of our knowledge, no core-shell Au@PBA have been reported with a single gold NPs as a core coated by a uniform PBA shell.

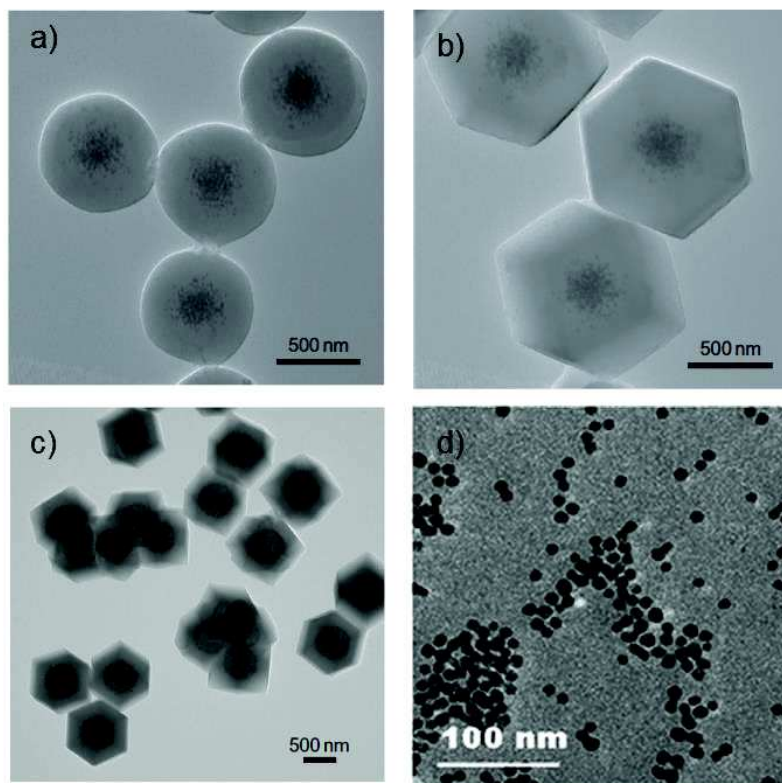


Figure 40: TEM images of Au NPs in ZIF-8 crystals collected at different times, a) 30 min, b) 3h and c) at the end of the reaction¹⁴². d) TEM image of Au@PB NPs¹⁴⁶.

Objectives of this work:

In this work, we have focused on the design of heterostructured nano-objects combining both the optical properties of gold and the magnetic properties of PB and its Analogous. As described previously, the elaboration of such magneto-optical heterostructures present real interest for applications such as bioimaging or magneto-optical devices. With consideration to the previous systems reported, the combination of gold and coordination polymers (such as MOFs) mainly concerns the elaboration of core-shell nano-objects presenting enhanced catalytic properties. Only one combination of gold and PB has been reported¹⁴⁵, but that concerns the respective optical properties originated from the SPR band for gold and the intervalence charge-transfer band of PB, and designed for potential use as photoacoustic/CT bimodal imaging and a photothermal ablation of the cancer¹⁴⁶.

In the design of magneto-optical materials, several modifications of the properties are expected. On one hand, the core-shell morphology may induce modifications of the properties, due to the complexity and the anisotropy of the shape. On the other hand, interesting synergistic effects, originated from interactions arising at the interface between the two materials, can be observed and may allow the control of the magneto-optical properties. For example, the decrease of the temperature below the T_C of the magnetic material may induce the modification of the SPR phenomenon. Other example, magnetic properties may be modified by irradiating at the wavelength corresponding to the SPR phenomenon.

Thus, the design of magneto-optical Au@PBA heterostructure must be investigated. In that aim, we first have to select the PBA used, and thus a well-understanding of these systems is required. Then, we have to develop a synthetic approach permitting the obtention of such Au@PBA heterostructure. Both the optical and magnetic properties of these core-shell NPs have to be investigated. The implementation of diverse magnetic properties according to the different PBA used was studied. Finally, their potential use as contrast agent for bioimaging have to be evaluated.

References

1. F. Herren, P. Fisher, A. Ludi, *Inorg. Chem.*, **1980**, *19*, 956.
2. L. R. Walker, G. K. Wertheim, V. Jacarino, *Phys. Chem. Lett.*, **1961**, *6*, 98.
3. H. J. Buser, D. Scharfenbach, W. Petter, A. Ludi, *Inorg. Chem.*, **1961**, *6*, 98.
4. D. F. Shriver, S. A. Shriver, S. E. Handerson, *Inorg. Chem.*, **1965**, *4*, 725.
5. D. B. Brown, D. F. Shriver, L. H. Swartz, *Inorg. Chem.*, **1968**, *7*, 77.
6. D. B. Brown, D. F. Shriver, *Inorg. Chem.*, **1969**, *8*, 37.
7. H. Tokoro, S.-i Ohkishi, *Dalton Trans.*, **2011**, *40*, 6825.
8. K. Jain, R. P. Singh, C. Bala, *J. Radioanal. Chem.*, **1981**, *75*, 85.
9. S. Ayrault, B. Jimenez, E. Garnier, M. Fedoroff, D.J. Jones, C. Loos-Neskovic, *J. Solid State Chem.*, **1998**, *141* (2) 475.
10. H. Heydlauf, *Eur. J. Pharmacol.*, **1969**, *6*, 340.
11. H. H. Kamerbeek, A. G. Rauws, M. ten Ham and A. N. P. van Heijst, *Acta med. scand.* **1971**, *189*, 321.
12. L. Catala, F. Volatron, D. Brinzei, T. Mallah, *Inorg. Chem.*, **2009**, *48* (8), 3360.
13. U.S Food and Drug Administration (FDA, FDA approved Drug Product list, No. 021626, 2003.
14. S. M. Holmes, G. S. Girolami, *J. Am. Chem. Soc.*, **1999**, *121*, 5593.
15. O. Sato, T. Lyoda, A. Fujishima, K. Hasimoto, *Science*, **1996**, *272*, 704.
16. O. Sato, T. Einaga T. Lyoda, A. Fujishima, K. Hasimoto, *Inorg. Chem.*, **1999**, *38*, 4405.
17. T. Hyeon, *Chem. Commun.*, **2003**, 927.
18. K. J. Klabunde, in *Nanoscale Materials in Chemistry*, ed. K. J. Klabunde, Wiley Intersciences, New York, **2001**.
19. M. R. Diehl, J.-Y. Yu, J. R. Heath, G. A. Doyle, S. Sun and C. B Murray, *J. Phys. Chem. B*, **2001**, *105*, 7913.
20. D. L. Leslie-Pelescky and R. D. Rieke, *Chem. Mater.*, **1996**, *8*, 1770.

21. S. P. Moulik, G. C. De, A. K. Panda, B. B. Bhowmik, and A. R. Das, *Langmuir* **1999**, *15*, 8361.
22. S. Vaucher, M. Li, and S. Mann, *Angew. Chem. Int. Ed.*, **2000**, *39* (10), 1793.
23. Z. Li, J. Zhang, T. Mu, J. Du, Z. Liu, B. Han, *Colloids Surf., A*, **2004**, *243*, 63.
24. M. Taguchi, K. Yamada, K. Suzuki, O. Sato, and Y. Einaga *Chem. Mater.* **2005**, *17*, 4554.
25. S. Vaucher, J. Fielden, M. Li, E. Dujardin, and S. Mann, *Nano Lett.*, **2002**, *2*, 225.
26. L. Catala, T. Gacoin, J.-P. Boilot, R. Riviere, C. Paulsen, E. Lhotel, and T. Mallah, *Adv. Mater.*, **2003**, *15* (10), 826.
27. Gutiérrez-Becerra, M. Barcena-Soto, V. Soto, J. Arellano-Ceja, N. Casillas, S. Prévost, L. Noirez, M. Gradzielski and J. I Escalante, *Nanoscale Res. Lett.* 2012, *7*, 83.
28. M. Cao, X. Wu, X. He and C. Hu, *Chem. Commun.*, **2005**, 2241.
29. M. F. Dumont, O. N. Risset, El. S. Knowles, T. Yamamoto, D. M. Pajerowski, M. W. Meisel, and D. R. Talham, *Inorg. Chem.*, **2013**, *52*, 4494.
30. E. Dujardin and S. Mann, *Adv. Mater.*, **2004**, *16*, 1126.
31. T. Uemura and S. Kitagawa, *J. Am. Chem. Soc.*, **2003**, *125*, 7814.
32. Q. Kong, X. Chen, J. Yao and D. Xue, *Nanotechnology*, **2005**, *16*, 164.
33. T. Uemura, M. Ohba, and S. Kitagawa, *Inorg. Chem.*, **2004**, *43* (23), 7339.
34. M. Perrier, S. Kenouche, J. Long, K. Thangavel, J. Larionova, C. Goze-Bac, A. Lascialfari, M. Mariani, N. Baril, C. Guérin, B. Donnadieu, A. Trifonov, and Y. Guari *Inorg. Chem.*, **2013**, *52*, 13402.
35. E. Chelebaeva, Yannick Guari, J. Larionova, A. Trifonov, and C. Guérin, *Chem. Mater.*, **2008**, *20* (4), 1367.
36. J. Larionova, Y. Guari, C. Sangregorio and Christian Guérin, *New J. Chem.*, **2009**, *33*, 1177.
37. J. Larionova, Y. Guari, A. Tokarev, E. Chelebaeva, C. Luna, C. Sangregorio, A. Caneschi, C. Guérin, *Inorg. Chim. Acta*, **2008**, *361*, 3988.
38. G. Clavel, J. Larionova, Y. Guari, and C. Guérin, *Chem. Eur. J.*, **2006**, *12*, 3798.
39. J. Larionova, Y. Guari, C. Blanc, P. Dieudonné, A. Tokarev, and C. Guérin, *Langmuir*, **2009**, *25*, 1138.
40. J. Larionova, Y. Guari, H. Sayegh, C. Guérin, *Inorg. Chim. Acta*, **2007**, *360*, 3829.

41. Johansson, E. Widenkvist, J. Lu, M. Boman, and U. Jansson, *Nano Lett.*, **2005**, *5* (8), 1603.
42. M. Yang, J. Jiang, Y. Lu, Y. He, G. Shen, R. Yu, *Biomaterials*, **2007**, *28*, 3408.
43. J. G. Moore, E.J. Lochner, C. Ramsey, N. S. Dalal, and A. E. Stiegman, *Angew. Chem. Int. Ed.*, **2003**, *42*, 2741.
44. B. Folch, Y. Guari, J. Larionova, C. Luna, C. Sangregorio, C. Innocenti, A. Caneschi and C. Guérin, *New J. Chem.*, **2008**, *32*, 273.
45. B. Folch, J. Larionova, Y. Guari, L. Datas and C. Guérin, *J. Mater. Chem.*, **2006**, *16*, 4435.
46. G. Clavel, Y. Guari, J. Larionova and C. Guérin, *New J. Chem.*, **2005**, *29*, 275.
47. Y. Guari, J. Larionova, K. Molvinger, B. Folch and C. Guérin, *Chem. Commun.*, **2006**, 2613.
48. E. Chelebaeva, Thesis of Université Montpellier II, Montpellier, France, **2009**.
49. A. Tokarev, P. Agulhon, J. Long, F. Quignard, M. Robitzer, R. A. S. Ferreira, L. D. Carlos, J. Larionova, C. Guerin and Y. Guari, *J. Mater. Chem.*, **2012**, *22*, 20232.
50. D. Brinzei, L. Catala, N. Louvain, G. Rogez, O. Stephan, A. Gloter and T. Mallah, *J. Mater. Chem.*, **2006**, *16*, 2593.
51. Y. Mizuno, M. Okubo, K. Kagesawa, D. Asakura, T. Kudo, H. Zhou, K. Oh-ishi, A. Okazawa, and N. Kojima, *Inorg. Chem.*, **2012**, *51*, 10311.
52. C.H. Li, Y. Nanba, D. Asakura, M. Okubo and D. R. Talham, *RSC Adv.*, **2014**, *4*, 24955.
53. M. F. Dumont, E. S. Knowles, A. Guet, D. M. Pajerowski, A. Gomez, S. W. Kycia, M. W. Meisel, and D. R. Talham, *Inorg. Chem.*, **2011**, *50*, 4295.
54. M. Presle, I. Maurin, F. Maroun, R. Cortès, L. Lu, R. S. Hassan, E. Larquet, J.-M. Guigner, E. Rivière, J. P. Wright, J.-P. Boilot, and T. Gacoin, *J. Phys. Chem. C*, **2014**, *118*, 13186.
55. D. M. Pajerowski, J. E. Gardner, D. R. Talham, and M. W. Meisel, *J. Am. Chem. Soc.*, **2009**, *131*, 12927.
56. G. Paul, Y. Prado, N. Dia, E. Riviere, S. Laurent, M. Roch, L. Vander Elst, R. N. Muller, L. Sancey, P. Perriat, O. Tillement, T. Mallah and Laure Catala, *Chem. Commun.*, **2014**, *50*, 6740.
57. X. Liang, Z. Deng, L. Jing, X. Li, Z. Dai, C. Li and M. Huanga *Chem. Commun.*, **2013**, *49*, 11029.
58. X. Jia, X. Cai, Y. Chen, S. Wang, H. Xu, K. Zhang, M. Ma, H. Wu, J. Shi, and H. Chen, *ACS Appl. Mater. Interfaces*, **2015**, *7*, 4579.

59. X. Cai , X. Jia , W. Gao , K. Zhang , M. Ma , S. Wang , Y. Zheng ,J. Shi , and H. Chen, *Adv. Funct. Mater.*, **2015**, DOI: 10.1002/adfm.201403991.
60. L. Catala, D. Brinzei, Y. Prado, A. Gloter, O. Stephan, G. Rogez and T. Mallah, *Angew. Chem.*, **2009**, *48*, 183.
61. O. N. Risset and D. R. Talham, *Chem. Mater.*, **2015**, *27*, 3838.
62. M. Presle, Thesis of Ecole Polytechnique, Palaiseau, France, **2011**.
63. Y. Prado, L. Lisnard, D. Heurtaux, G. Rogez, A. Gloter, O. Stephan, N. Dia, E. Riviere, L. Catala and Talal Mallah, *Chem. Commun.*, **2011**, *47*, 1051.
64. Y. Prado, S. Mazerat, E. Riviere, G. Rogez, A. Gloter, O. Stephan, L. Catala and T. Mallah, *Adv. Funct. Mater.*, **2014**, *24*, 5402.
65. D. Asakura, C. H. Li, Y. Mizuno, M. Okubo, H. Zhou, and D. R. Talham, *J. Am. Chem. Soc.*, **2013**, *135*, 2793.
66. C. H. Li, M. K. Peprah, D. Asakura, M. W. Meisel, M. Okubo, and D. R. Talham, *Chem. Mater.*, **2015**, *27*, 1524.
67. P. Bhatt, S. Banerjee, S. Anwar, M. D. Mukadam, S. S. Meena, and S. M. Yusuf, *ACS Appl. Mater. Interfaces*, **2014**, *6*, 17579.
68. E. S. Knowles, C. H. Li , M. F. Dumont, M. K. Peprah, M. J. Andrus, D. R. Talham, M. W. Meisel, *Polyhedron*, **2013**, *66*, 153.
69. D. M. Pajerowski, B. Ravel, C. H. Li, M. F. Dumont, and D. R. Talham, *Chem. Mater.*, **2014**, *26*, 2586.
70. M. Zentková, Z. Arnold, J. Kamarád, V. Kavečanský, M. Lukáčová, S. Mat'áš, M. Mihalik, Z. Mitròová, A. Zentko, *J. Phys.: Condens. Matter.*, **2007**, *19*, 266217.
71. M. Presle, J. Lemainque, J.-M. Guigner, E. Larquet, I. Maurin, J.-P. Boilot and T. Gacoin, *New J. Chem.*, **2011**, *35*, 1296.
72. N. Dia, L. Lisnard, Y. Prado, A. Gloter, O. Stéphan, F. Brisset, H. Hafez, Z. Saad, C. Mathonière, L. Catala, and T. Mallah, *Inorg. Chem.*, **2013**, *52*, 10.
73. O. N. Risset, P. A. Quintero, T. V. Brinzari, M. J. Andrus, M. W. Lufaso, Mark W. Meisel, and D. R. Talham, *J. Am. Chem. Soc.*, **2014**, *136*, 15660.
74. M. Hu, S. Furukawa, R. Ohtani, H. Sukegawa, Y. Nemoto, J. Reboul, S. Kitagawa and Y. Yamauchi, *Angew. Chem. Int. Ed.*, **2012**, *51*, 984.
75. H.-Y. Lian, M. Hu, C.-H. Liu, Y. Yamauchi, K. C.-W. Wu, *Chem. Commun.*, **2012**, 5151.
76. X. Cai , X. Jia , W. Gao , K. Zhang , M. Ma , S. Wang , Y. Zheng ,J. Shi and H. Chen, *Adv. Funct. Mater.*, **2015**, *25* (17), 2520.
77. M. Hu, N. L. Torad and Y. Yamauchi, *Eur. J. Inorg. Chem.*, **2012**, *30*, 4795.

78. O. Risset, E. S. Knowles, S. Ma, M. W. Meisel, D. R. Talham, *Chem. Mater.*, **2013**, 25, 42.
79. A. Henglein, *Chem. Rev.*, **1989**, 89, 1861. L. Spanhel, H. Weller, A. Henglein, *J. Am. Chem. Soc.*, **1987**, 109, 6632. H.-C. Youn, S. Baral, J. H. Fendler, *J. Phys. Chem.*, **1988**, 92, 6320.
80. J. Ahmed, S. Sharma, K. V. Ramanujachary, S. E. Lofland, A. K. Ganguli, *J. Colloid Interface Sci.*, **2009**, 336, 814; S. A. El-Safty, *J. Colloid Interface Sci.*, **2008**, 319, 477; Q. Song, Z. J. Zhang, *J. Am. Chem. Soc.*, **2004**, 126, 6164; G. Salazar-Alvarez, J. Qin, V. Sepelak, I. Bergmann, M. Vasilakaki, K. N. Trohidou, J. D. Ardisson, W. A. A. Macedo, M. Mikhaylova, M. Muhammed, M. D. Baro, J. Nogues, *J. Am. Chem. Soc.*, **2008**, 130, 13234; E. Schmidt, A. Vargas, T. Mallat, A. Baiker, *J. Am. Chem. Soc.*, **2009**, 131, 12358; Z. L. Wang, T. S. Ahmad, M. A. El-Sayed, *Surf. Sci.*, **1997**, 380, 302; X. W. Wei, G. X. Zhu, Y. J. Liu, Y. H. Ni, Y. Song, Z. Xu, *Chem. Mater.*, **2008**, 20, 6248; M. Yamada, S. Kon, M. Miyake, *Chem. Lett.*, **2005**, 34, 1050.
81. J. S. Hu, Y. G. Guo, H. P. Liang, L. J. Wan,; L. Jiang, *J. Am. Chem. Soc.*, **2005**, 127, 17090. M. Jitianu, D. V. Goia, *J. Colloid Interface Sci.*, **2007**, 309, 78.
82. T. Z. Ren, Z. Y. Yuan, W. Hu, X. Zou, *Microporous Mesoporous Mater.* **2008**, 112, 467; X. Ren, D. Han, D. Chen, F. Tang, *Mater. Res. Bull.*, **2007**, 42, 807; N. J. Suematsu, Y. Ogawa, Y. Yamamoto, T. Yamaguchi, *J. Colloid Interface Sci.*, **2007**, 310, 648.
83. Z. L. Wang, T. S. Ahmad, M. A. El-Sayed, *Surf. Sci.*, **1997**, 380, 302; X. W. Wei, G. X. Zhu, Y. J. Liu, Y. H. Ni, Y. Song, Z. Xu, *Chem. Mater.*, **2008**, 20, 6248.
84. X. Qu, L. Omar, T. B. Le, L. Tetley, K. Bolton, K. W. Cjooi, W. Wang, I. F. Uchegbu, *Langmuir*, **2008**, 24, 9997.
85. G. Cao, D. Liu, *Adv. Colloid Interface Sci.*, **2008**, 136, 45. T. R. Kline, M. Tian, J. Wang, A. Sen, M. W. H. Chan, T. E. Mallouk, *Inorg. Chem.*, **2006**, 45, 7555; M. Li, T. S. Mayer, J. A. Sioss, C. D. Keating, R. B. Bhiladvala, *Nano Lett.*, **2007**, 7, 3281; J. A. Sioss, C. D. Keating, *Nano Lett.*, **2005**, 5, 1779; Y. Wu, T. Livneh, Y. X. Zhang, G. Cheng, J. Wang, J. Tang, M. Moskovits, G. D. Stucky, *Nano Lett.*, **2004**, 4, 2337.
86. H. M. Bok, S. Kim, S. H. Yoo, S. K. Kim, S. Park, *Langmuir*, **2008**, 24, 4168; H. M. Bok, K. L. Shuford, S. Kim, S. K. Kim, S. Park, *Nano Lett.*, **2008**, 8, 2265; S. Park, S. W. Chung, C. A. Mirkin, *J. Am. Chem. Soc.*, **2004**, 126, 11772.
87. A. Michailowski, D. Almawlawi, G. Cheng, M. Moskovits, *Chem. Phys. Lett.*, **2001**, 349, 1; K. B. Shelimov, M. Moskovits, *Chem. Mater.*, **2000**, 12, 250.
88. L. Dykman and N. Khlebtsov, *Chem. Soc. Rev.*, **2012**, 41, 2256.
89. E. C. Dreaden, A. M. Alkilany, X. Huang, C. J. Murphy and M. A. El-Sayed, *Chem. Soc. Rev.*, **2012**, 41, 2740.
90. M. C. Daniel, D. Astruc, *Chem. Rev.*, **2004**, 104, 293.

91. S. Phadtare, A. Kumar, V. P. Vinod, C. Dash, D. V. Palaskar, M. Rao, P. G. Shukla, S. Sivaram, M. Sastry, *Chem. Mater.*, **2003**, *15*, 1944; A. R. Kortan, R. Hull, R. L. Opila,; M. G. Bawendi, M. L. Steigerwald, P. J Carroll, L. E. Brus, *J. Am. Chem. Soc.*, **1990**, *112*, 1327.
92. F. Caruso, *Adv. Mater.*, **2001**, *13*, 11.
93. L. Babes, B. Denizot, G. Tanguy, J. J. Le Jeune, P. Ballet, *J. Colloid Interface Sci.* **1999**, *212*, 474 ; P. M. A. De Farias, B. S. Santos, F. D. Menezes, A. G. Brasil Jr, R. Ferreira, M. A. Motta, A. G. Castro-Neto, A. A. S. Vieira, D. C. N. Silva, A. Fontes, C. L. Cesar, *Appl. Phys. A: Mater. Sci. Process.*, **2007**, *89*, 957; F. D. de Menezes, A. G. Brasil Jr., W. L. Moreira, L. C. Barbosa, C. L. Cesar, R. D. C. Ferreira, P. M. A. de Farias, B. S. Santos, *Microelectron. J.*, **2005**, *36*, 989; A. K. Gupta, M. Gupta, *Biomaterials*, **2005**, *26*, 3995; B. Schreder, T. Schmidt, V. Ptatschek, L. Spanhel, A. Materny, W. J. Kiefer, *Cryst. Growth*, **2000**, *214*, 782.
94. N. Sounderya, Y. Zhang, *Recent Pat. Biomed. Eng.*, **2008**, *1*, 34.
95. A. K. Gupta, M. Gupta, *Biomaterials*, **2005**, *26*, 3995.
96. J. K. Jaiswal, H. Mattoussi, J. M. Mauro, S. M. Simon, *Nat. Biotechnol.*, **2003**, *21*, 47. X. Michalet, F. F. Pinaud, L. A. Bentolila, J. M. Tasy, S. Doose, J. J. Li, G. Sundaresan, A. M. Wu, S. S. Gambhir, S. Weiss, *Science*, **2005**, *307*, 538.
97. N. Sounderya, Y. Zhang, *Recent Pat. Biomed. Eng.*, **2008**, *1*, 34.
98. T. Li, J. Moon, A. A. Morrone, J. J. Mecholsky, D. R. Talham, and J. H. Adair *Langmuir*, **1999**, *15*, 4328.
99. Y. Qi, M. Chen, S. Liang, W. Yang, J. Zhao, *Appl. Surf. Sci.*, **2008**, *254*, 1684; Y. Qi, M. Chen, S. Liang, J. Zhao, W. Yang, *Colloids Surf. A.*, **2007**, *302*, 383; L. M. Liz-Marzan, M. Giersig, P. Mulvaney, *Langmuir*, **1996**, *12*, 4329.
100. J. Lee, Y. Lee, J. K. Youn, H. B. Na, T. Yu, H. Kim, S. M. Lee, Y. M. Koo, J. H. Kwak, H. Park, H. N. Chang, M. Hwang, J. G. Park, J. Kim, T. Hyeon, *Small*, **2008**, *4*, 143; F. G. Aliev, M. A. Correa-Duarte, A. Mamedov, J. W. Ostrander, M. Giersig, L. M. Liz-Marzan, N. A. Kotov, *Adv. Mater.*, 1999, **11**, 1006; Y. H. Lien, T. M. Wu, *J. Colloid Interface Sci.*, **2008**, *326*, 517.
101. V. Sundaresan, J. U. Menon, M. Rahimi, K. T. Nguyen, A. S. Wadajkar, *Int. J. Pharm.*, **2014**, *466*, 1.
102. V. L. Colvin, M. C. Schlamp, A. P. Alivisatos, *Nature*, **1994**, *370*, 354.
103. V. I. Klimov, A. A. Mikhailovsky, S. Xu, A. Malko, J. A. Hollingsworth, C. A. Leatherdale, H.-J. Eisler, M. G. Bawendi, *Science*, **2000**, *290*, 314.
104. L. Spanhel, M. Haase, H. Weller, A. Henglein, *J. Am. Chem. Soc.*, **1987**, *109*, 5649.
105. W. Lu, B. Wang, J. Zeng, X. Wang, S. Zhang, J. G. Hou, *Langmuir*, **2005**, *21*, 3684.

106. M. A. Correa-Duarte, M. Giersig, L. M. Liz-Marzan, *Chem. Phys. Lett.*, **1998**, 286, 497.
107. R. Kortan, R. Hull, R. L. Opila, M. G. Bawendi, M. L. Steigerwald, P. J. Carroll, L. E. Brus, *J. Am. Chem. Soc.*, **1990**, 112, 1327; A. Mews,; A. Eychmeuller, M. Giersig, D. Schooss, H. Weller, *J. Phys. Chem.*, **1994**, 98, 934.
108. S. Kim, B. Fisher, H.-Ju Eisler, and M. Bawendi, *J. Am. Chem. Soc.*, **2003**, 125, 11466.
109. S. Kotagawa, R. Kitaura, S.I. Noro, *Angew. Chem. Int. Ed.* **2004**, 43, 2334.
110. S. Furukawa, K. Hirai, K. Nakagawa, Y. Takashima, R. Matsuda, T. Tsuruoka, M. Kondo, R. Haruki, D. Tanaka, H. Sakamoto, S. Shimomura, O. Sakata, and S. Kitagawa, *Angew. Chem. Int. Ed.*, **2009**, 48, 1766.
111. E. A. Fleugel, A. Ranft, F. Haase and B. V. Lotsch, *J. Mater. Chem.*, **2012**, 22, 10119.
112. S. Hermes, M.-K. Schröter, R. Schmid, L. Khodeir, M. Muhler, A. Tissler, R. W. Fischer, and R. A. Fischer, *Angew. Chem. Int. Ed.*, **2005**, 44, 6237.
113. Y. Wei, S. Han, D. A. Walker, P. E. Fuller, and B. A. Grzybowski, *Angew. Chem. Int. Ed.*, **2012**, 51, 74.
114. Y. Y. Pan, B. Z. Yuan, Y. W. Li and D. H. He, *Chem. Commun.*, **2010**, 46, 2280; T. Ishida, M. Nagaoka, T. Akita and M. Haruta, *Chem. Eur. J.*, **2008**, 14, 8456; Y. K. Hwang, D. Y. Hong, J. S. Chang, S. H. Jhung, Y. K. Seo, J. Kim, A. Vimont, M. Daturi, C. Serre and G. Ferey, *Angew. Chem., Int. Ed.*, **2008**, 47, 4144; J. Hermannsdorfer, M. Friedrich, N. Miyajima, R. Q. Albuquerque, S. Kummel and R. Kempe, *Angew. Chem., Int. Ed.*, **2012**, 51, 11473.
115. Y. Y. Pan, B. Z. Yuan, Y. W. Li and D. H. He, *Chem. Commun.*, **2010**, 46, 2280.
116. T. Ishida, M. Nagaoka, T. Akita and M. Haruta, *Chem. Eur. J.*, **2008**, 14, 8456.
117. Y. K. Hwang, D. Y. Hong, J. S. Chang, S. H. Jhung, Y. K. Seo, J. Kim, A. Vimont, M. Daturi, C. Serre and G. Ferey, *Angew. Chem., Int. Ed.*, **2008**, 47, 4144.
118. J. Hermannsdorfer, M. Friedrich, N. Miyajima, R. Q. Albuquerque, S. Kummel and R. Kempe, *Angew. Chem., Int. Ed.*, **2012**, 51, 11473–11477.
119. *ACS Catalysis*, **2014**, 4, 4409.
120. F. Ke, L.-G. Qiu, Y.-P. Yuan, X. Jiang, J.-F. Zhu, *J. Mater. Chem.* **2012**, 22, 9497.
121. G. Fu, W. Liu, Y. Li, Y. Jin, L. Jiang, X. Liang, S. Feng, and Z. Dai, *Bioconjugate Chem.*, **2014**, 25, 1655.
122. N. Li, P. Zhao, and D. Astruc, *Angew. Chem. Int. Ed.*, **2014**, 53, 2.

123. R. I. Mout, D. F. Moyano, S. Rana and V. M. Rotello, *Chem. Soc. Rev.*, **2012**, *41*, 2539.
124. K. M. Mayer, and Jason H. Hafner, *Chem. Rev.*, **2011**, *111*, 3828.
125. L. M. Liz-Marzan, M. Giersig, and P. Mulvaney, *Langmuir*, **1996**, *12*, 4329.
126. N. Sui, V. Monnier, Y. Zakharko, Y. Chevolot, S. Alekseev, J.-M. Bluet, V. Lysenko, E. Souteyrand, *Plasmonics*, 2013, *8*, 85; P. Reineck, D. Gomez, S. Hock, M. Karg, T. Bell, P. Mulvaney, and U. Bach, *ACS Nano*, **2013**, *7* (8), 6636.
127. C. Loo, A. Lin, L. Hirsch, M. Lee, J. Barton, N. Halas, J. West, R. Drezek, *Technol. Cancer Res. Treat.*, **2004**, *3*, 33.
128. V. K. Pustovalov, W. Fritzsche, *Plasmonics*, **2013**, *8*, 983.
129. S. Gómez-Graña, B. Goris, T. Altantzis, C. Fernández-López, E. Carbó-Argibay, A. Guerrero-Martínez, N. Almora-Barrios, N. López, I. Pastoriza-Santos, J. Pérez-Juste, S. Bals, G. Van Tendeloo, and L. M. Liz-Marzán, *J. Phys. Chem. Lett.*, **2013**, *4*, 2209.
130. J. Gong, F. Zhou, Z. Li, and Z. Tang, *Langmuir*, **2012**, *28*, 8959.
131. M. Min, C. Kim, Y. In Yang, J. Yib and H. Lee, *Chem. Commun.*, **2011**, *47*, 8079.
132. X. Chen, H. Pan, H. Liu, M. Du, *Electrochim. Acta*, **2010**, *56*, 636.
133. G. Bahmanrokh, M. Hashim, N. Soltani, I. Ismail, P. Vaziri, M. Navaseri, M. Erfani, S. Kanagesan, *Mater. Res. Bull.*, **2013**, *48*, 4039.
134. F. Pineider, C. de Julian Fernandez, V. Videtta, E. Carlino, A. al Hourani, F. Wilhelm, A. Rogalev, P. Davide Cozzoli, P. Ghigna, C. Sangregorio, *ACS Nano*, **2013**, *7*, 857.
135. Gole, J. W. Stone, W. R. Gemmill, H.-C. zur Loye, and C. J. Murphy, *Langmuir*, **2008**, *24*, 6232.
136. L. Wang, J. Luo, Q. Fan, M. Suzuki, I. S. Suzuki, M. H. Engelhard, Y. Lin, N. Kim, J. Q. Wang, and C.-J. Zhong, *J. Phys. Chem. B*, **2005**, *109*, 21593.
137. D. A. Wheeler, S. A. Adams, T. López-Luke, A. Torres-Castro, and J. Z. Zhang, *Ann. Phys.*, **2012**, *524* (11), 670.
138. C. S. Levin, C. Hofmann, T. A. Ali, A. T. Kelly, E. Morosan, P. Nordlander, K. H. Whitmire, and N.J. Halas, *ACS Nano*, **2009**, *3* (6), 1379.
139. L. Lou, K. Yu, Z. Zhang, R. Huang, Y. Wang, Z. Zhu, *Appl. Surf. Sci.*, **2012**, *258* 8521.
140. L. He, Y. Liu, J. Liu, Y. Xiong, J. Zheng, Y. Liu, and Z. Tang, *Angew. Chem. Int. Ed.*, **2013**, *52*, 3741.
141. F. Ke, J. Zhu, L.-G. Qiu and X. Jiang, *Chem. Commun.*, 2013, **49**, 1267.

142. G. Lu, S. Li, Z. Guo, O. K. Farha, B. G. Hauser, X. Qi, Y. Wang, X. Wang, S. Han, X/Liu, J. S. DuChene, H. Zhang, Q. Zhang, X. Chen, J. Ma, S. Chye, J. Loo, W. D. Wei, Y. Yang, J. T. Hupp, and F. Huo, *Nat. Chem.*, **2012**, *4*, 310.
143. T. Ishida, M. Nagaoka, T. Akita and M. Haruta, *Chem. Eur. J.*, **2008**, *14*, 8456.
144. M. Meilikhov, K. Yusenko, D. Esken, S. Turner, G. Van Tendeloo, and R. A. Fischer, *Eur. J. Inorg. Chem.*, **2010**, 3701.
145. J.-D. Qiu, H.-Z. Peng, R.-P. Liang, J. Li, and X.-H. Xia, *Langmuir*, **2007**, *23*, 2133.
146. L. Jing, X. Liang, Z. Deng, S. Feng, X. Li, M. Huang, C. Li, Z. Dai, *Biomaterials*, **2014**, *35*, 5814.

CHAPTER II

-

INITIAL WORK: SYNTHESIS OF
 $\text{K}^+/\text{Ni}^{2+}/[\text{Fe}(\text{CN})_6]^{3-}/\text{PEG-NH}_2$ NPs

II.1 Introduction:

As shown in the first chapter, PBA's NPs may be obtained by self-assembly reaction between two precursors, di- or trivalent transition metal ions (M^{2+} or M^{3+}) and hexacyanometallate precursors $[M'(CN)_6]^{n-}$ ($M' = Fe, Cr; n = 2$ or 3). In this chapter, we have chosen to focus our study on $M^{II}_3[Fe^{III}(CN)_6]_2$ ($M = Ni$ or Cu) PBA NPs with the aim to control the morphology and the size of these NPs as well as their surface state in order to acquire a fine understanding of such systems. Indeed, the size decrease of materials leads at the nanoscale to the evolution of the intrinsic properties, switching from a bulk behavior to a nanoparticle ones. The size limit between these two matter states is known for other materials but not for PBA systems. Then, the study of the evolution of the material characteristics with the decrease of the size will permit the comprehension of several phenomena, as the magnetic behavior modification with the size decrease. In this aim, two different approaches were used to obtain the NPs with the size ranging from few to several hundred nanometers.

The first approach consists in the use of the self-assembly reaction in the presence of organic molecules or polymers as stabilizing agents¹⁻⁹. Due to the presence of functional groups, these stabilizers can either coordinate to the metal ions, or form weak interactions stopping the growth of the cyano-bridged coordination polymer network. That permits to control the size of the NPs, and to obtain indeed ultra-small NPs with the size usually lower than 10 nm. Furthermore, the presence of the stabilizers offers usually a good dispersibility in various solvents depending on the nature of the stabilizer (hydrophilic or hydrophobic).

PBA NPs of larger size may be synthesized by using the second two steps approach consisting in the self-assembly reaction between the appropriate precursors without stabilizing agents. Then the anchoring of the stabilizers at the NPs surface is performed post-synthetically. The control of the size and the morphology in this case may be achieved in the first step of this approach by varying of the precursor's addition rate¹⁰⁻¹⁴, their respective concentration and by the presence or not of ionic salts such as for instance CsCl. The variation of the addition rate and the precursor's concentration can promote preferentially either nucleation or growing phenomenon which are the two main steps of the formation of the NPs. In the first case, the nucleation favors the formation of the homogeneous seeds leading to small NPs; in the second case, the Ostwald maturation phenomenon favors the growth of the PBA network leading to formation of large-sized NPs. Generally, the use of a high precursor's concentration and a fast addition rate promotes a nucleation process, and then leads to small NPs. At the opposite, a slow precursor's concentration and a low addition rate encourage Ostwald ripening and lead to the formation of larger NPs. We can modulate also both the nucleation and the growth phenomena empirically with the use of intermediate precursor's concentrations and intermediate addition rates, leading to medium-sized NPs. But, due to the absence of stabilizers in the first reaction step, this approach can lead to a loss of the shape control and an aggregation phenomenon, including sometimes the formation of the parent bulk material. For this reason, the challenge of this approach consists in the choice of good conditions to obtain well-defined and size controlled NPs.

In this chapter, we describe the synthesis and characterizations of a series of $\text{K}^+/\text{Ni}^{2+}/[\text{Fe}(\text{CN})_6]^{3-}$ NPs having different size ranging from 3 to 180 nm obtained by using these two above approaches. Thus, at first, we present the synthesis of the ultra-small $\text{K}^+/\text{Ni}^{2+}/[\text{Fe}(\text{CN})_6]^{3-}/\text{PEG-NH}_2$ (PEG-NH₂ 1500 g/mol) NPs having the size of around 3 nm by using the first approach. Then we describe the synthesis of a series of larger $\text{K}^+/\text{Ni}^{2+}/[\text{Fe}(\text{CN})_6]^{3-}$ NPs ranging from 14 to 180 nm by using the second approach. These later NPs were post-synthetically grafted with the same stabilizer that we used in the first approach, PEG-NH₂ 1500. These NPs were characterized in order to define their structural properties and their morphologies. Finally, in collaboration with the Laboratoire de Chimie de Coordination (University Toulouse III, France), we investigate the evolution of the NPs structural characteristics, such as the $\text{Fe}^{\text{III}}/\text{Fe}^{\text{II}}$ ratio as a function of their size.

II.2 Synthesis and characterizations

II.2.1 First approach: synthesis of ultra-small $K^+/Ni^{2+}/[Fe(CN)_6]^{3-}/PEG-NH_2$ NPs

Ultra-small NPs of cyano-bridged coordination polymers were obtained by a self-assembly reaction in water between the hexacyanometallate precursor, $K_3[Fe(CN)_6]$, and the divalent transition metal ion, $[Ni(H_2O)_6]^{2+}$, in the presence of a stabilizing agent, a polyethylene glycol with terminal amino groups PEG-NH₂ (figure 1)^{10, 11}; this stabilizer is able to coordinate to the NPs surface. The interest in the presence of a stabilizing agent during the synthesis consists in the reduction of infinite growth of the tridimensional cyano-bridged network by coordination of the metal ions situated at the NPs surface leading to formation of ultra-small NPs stable in water¹⁻¹¹. The used stoichiometry of PEG-NH₂/M²⁺ is equal to 0.5/1. The synthesis consists in adding the aqueous solution of $Ni(NO_3)_2 \cdot 6H_2O$, containing half of the amount of PEG-NH₂ into the aqueous solution of $K_3[Fe(CN)_6]$ containing another half amount of PEG-NH₂. The reaction leads to a yellow-brown solution for $K^+/Ni^{2+}/[Fe(CN)_6]^{3-}/PEG-NH_2$ NPs (sample 1-1). After reaction, the solution was filtered through a filter syringe (0.45 μm , PTFE), then the NPs were precipitated with acetone, centrifuged, washed several times in water to eliminate any trace of the unreacted precursors, centrifuged again and dried under vacuum.

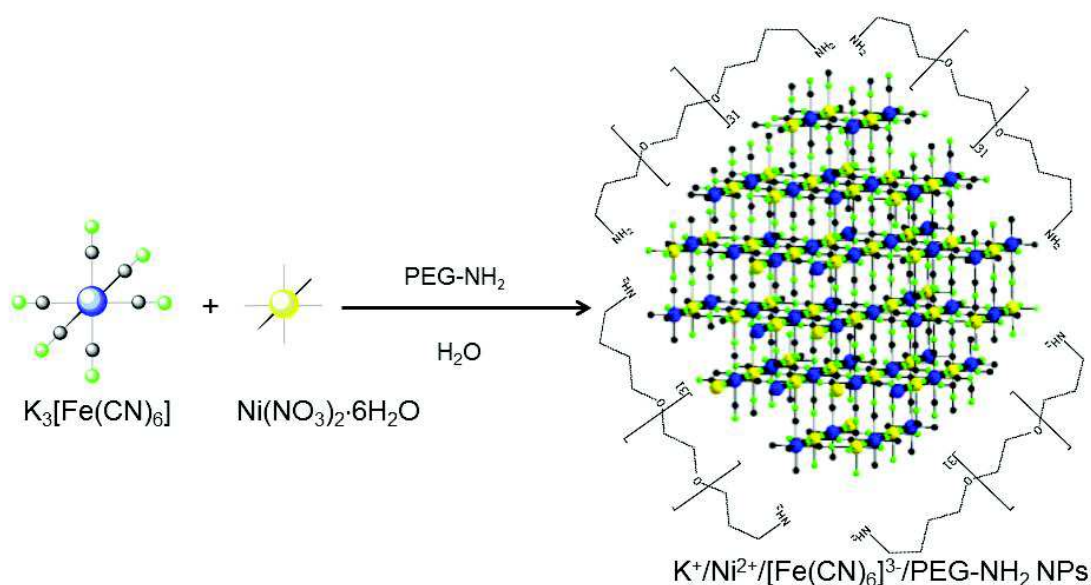


Figure 1: Schematic representation of the synthesis of $K^+/Ni^{2+}/[Fe(CN)_6]^{3-}/PEG-NH_2$ NPs.

II.2.2 Second approach: synthesis of a series of $K^+/Ni^{2+}/[Fe(CN)_6]^{3-}$ NPs and post-synthetic grafting with PEG-NH₂.

A series of the larger $K^+/Ni^{2+}/[Fe(CN)_6]^{3-}$ NPs was obtained by a two-step reaction consisting, first in the self-assembly reaction between $NiCl_2 \cdot 6H_2O$, and $K_3[Fe(CN)_6]$ in water at 25°C without stabilizing agents (figure 2), and secondly by a post-synthetic anchoring of the stabilizing agent at the NPs surface (figure 3). In the first step, the self-assembly reaction consists in the dropwise addition of the aqueous solutions of precursors simultaneously in a defined volume of ultrapure water. A specific device, a syringe pump, has been used to control the quantity and the precursor addition rate providing indeed a good reproducibility of the synthesis (Figure 4).

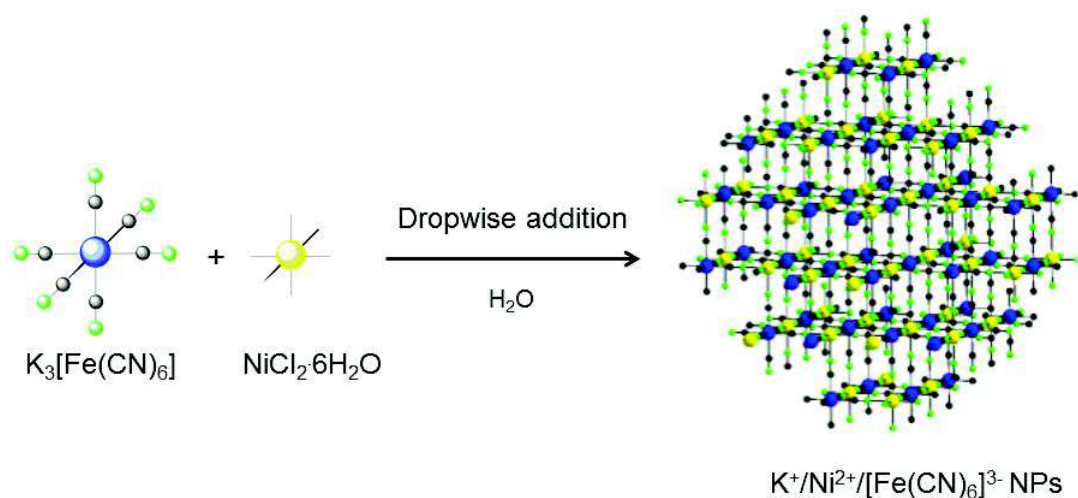


Figure 2: Schematic representation of the self-assembly reaction for the synthesis of $K^+/Ni^{2+}/[Fe(CN)_6]^{3-}$ NPs by using the second approach.

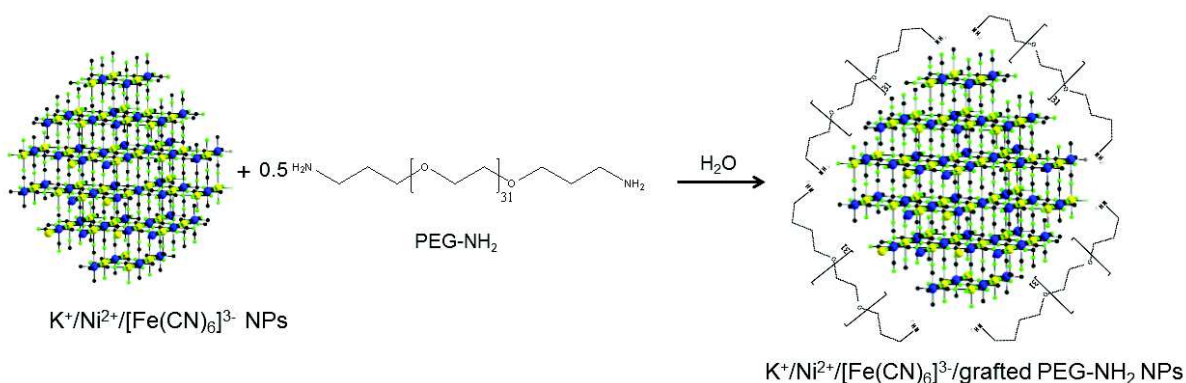


Figure 3: Schematic representation of the post-synthetic grafting of $K^+/Ni^{2+}/[Fe(CN)_6]^{3-}$ /PEG-NH₂ NPs.

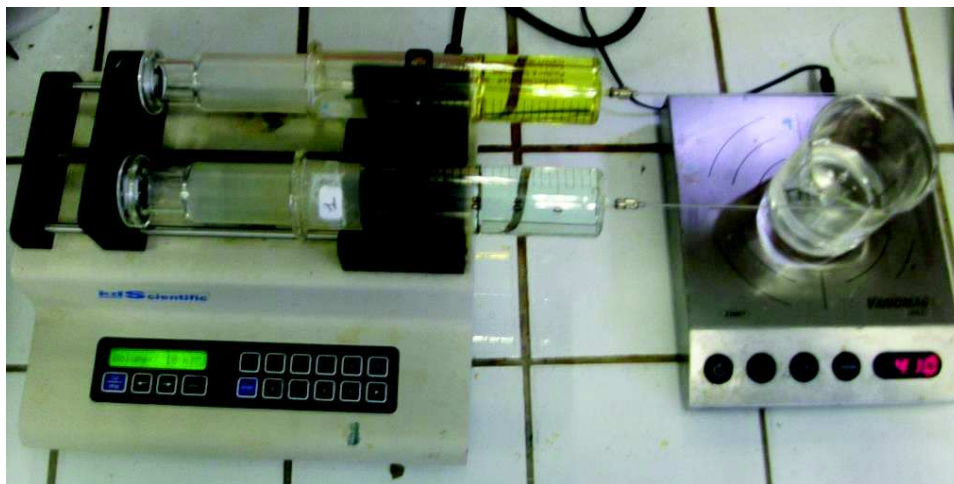


Figure 4: Image of a syringe pump adding precursors during a synthesis of $K^+/Ni^{2+}/[Fe(CN)_6]^{3-}$ NPs.

The modulation of the synthetic conditions, such as the precursors' addition rate, the precursors addition concentration and the volume of the added precursors and/or the volume of the reaction aqueous media (table 1) permits to modulate the NPs size. Furthermore, the use of an excess of CsCl in the precursor solutions leads to the decrease of the size, by increasing the electrostatic stabilization of the NPs, due to the excess of Cs^+ ions. Indeed, the electrostatic bonding of a slight excess of the $[Fe(CN)_6]^{3-}$ moieties by Cs^+ induces the formation of charged NPs, which increases the electrostatic repulsions between the seeds and the metal transition precursor, leading to the suppression of the Oswald ripening phenomenon¹⁵.

In all cases, the appearance of a turbid yellow-brown suspension indicates the formation of the $K^+/Ni^{2+}/[Fe(CN)_6]^{3-}$ NPs. These suspensions are stable in water for several hours. After completion of the addition, the solution was stirred one hour and the NPs were isolated by centrifugation, washed with water and ethanol, and finally dried under vacuum. These NPs are re-dispersible in water and the as-obtained suspensions are stable in water for several hours.

Samples	Size of NPs (nm)	Volume of precursors added (mL)	Addition rate (mL/min)	$[NiCl_2 \cdot 6H_2O]$ (mM)	$[K_3[Fe(CN)_6]]$ (mM)	$[CsCl]$ (mM)	Initial volume of water (mL)
1-2	14.4 ± 1.8	50	4	16	17	18	100
1-3	38.2 ± 5.6	50	4	16	17		100
1-4	67.1 ± 12.1	50	1.5	8	9		100
1-5	112.5 ± 22.5	100	1.5	4	4.5		200
1-6	177.1 ± 42.7	100	0.5	4	4.5		200

Table 1: Table presenting different parameters used in the synthesis of $K^+/Ni^{2+}/[Fe(CN)_6]^{3-}$ NPs with sizes ranging from 14 to 200 nm.

As previously detailed, the synthesis of $K^+/Ni^{2+}/[Fe(CN)_6]^{3-}$ is realized without stabilizers, leading to NPs with a “nude” surface and stabilized in water by electrostatic interactions due to the presence of terminal hexacyanoferrates terminations of the cyano-bridged network. In order to improve the good redispersability in aqueous solution, the post-synthetic grafting with PEG-NH₂ was performed in the second step of the approach. The coordination of the lone pair of the nitrogen atom of amino group with the metal ions of the PBA network should permit to covalently anchor the stabilizer to the surface, ensuring the stability of the grafting. This method presents the advantage to be easily applicable on any $K^+/Ni^{2+}/[Fe(CN)_6]^{3-}$ NPs, whatever its original size.

The post-synthetic grafting of $K^+/Ni^{2+}/[Fe(CN)_6]^{3-}$ NPs (we focalized on samples **1-3** and **1-4**) was achieved by mixing NPs with PEG-NH₂, in the $M^{2+}/PEG-NH_2 = 1/0.5$ stoichiometry, in water, under stirring for 24h. Preliminary, the NPs were dispersed in water by sonication, in order to maximize available surface leading to a better grafting. Then, the $K^+/Ni^{2+}/[Fe(CN)_6]^{3-}$ / grafted PEG-NH₂ NPs were centrifuged and washed several times with water to remove any trace of ungrafted PEG-NH₂, precipitated and dried under vacuum.

II.2.3 Characterizations of the $K^+/Ni^{2+}/[Fe(CN)_6]^{3-}$ /PEG-NH₂ NPs obtained using the two different approaches.

The structural characteristics of the NPs were obtained first by using Infrared spectroscopy (IR). The formation of the PBA cyano-bridged network is confirmed for the series of $K^+/Ni^{2+}/[Fe(CN)_6]^{3-}$ /PEG-NH₂ NPs by the presence of the stretching vibration of the bridging cyano-groups in the 2000-2200 cm^{-1} spectral window^{1,2,12-14,16} (figures 6 and 7). The broad bands, located at 2165 and 2100 cm^{-1} are characteristic of respectively $Fe^{III}-C\equiv N-Ni^{II}$ and $Fe^{II}-C\equiv N-Ni^{II}$ linkages and are situated at the same values as in the bulk analogous¹⁶ (table 2). That indicates the presence of both Fe^{III} and Fe^{II} ions in the structure, due to the reduction of a part of the ferricyanide ions, $[Fe^{III}(CN)_6]^{3-}$ in the PBA's network into ferrocyanide ions $[Fe^{II}(CN)_6]^{4-}$. This reduction is also confirmed for samples **1-2** to **1-6** by the presence of two sharp bands at 592 and 543 cm^{-1} , corresponding respectively to $Fe^{II}-C\equiv N$ and $Fe^{III}-C\equiv N$ linkages in the metal-carbon bond stretching region (Figure 6)^{16,17}. Additionally, the presence of a non-symmetric band at 438 cm^{-1} , corresponding to the $Fe^{III}-CN$ linkage in the metal-carbon bond bending region, with a shoulder at 461 cm^{-1} (Figures 6 and 7) was attributed to $Fe^{II}-CN$ linkage according to the literature^{17,18}, which is a new proof of the presence of both Fe^{III} and Fe^{II} ions in NPs. However no trace of the bands corresponding to the $Fe^{III}-CN$ linkages (the metal-carbon stretching and bending vibrations) are observed for sample **1-1**, indicating a large amount of Fe^{II} in the tridimensional cyano-bridged network¹⁶⁻¹⁸. However, it is not possible to precisely quantify the ratio Fe^{III}/Fe^{II} by using IR spectroscopy, only on the basis of the respective bands intensity; each different linkage seems to have different value of the absorption coefficient. This will be confirmed later with using ⁵⁷Fe Mossbauer spectroscopy. Indeed, bands corresponding to the stretching vibration of $Fe^{II}-C\equiv N-Ni^{II}$ and $Fe^{II}-C\equiv N$ linkages are more intense than the ones corresponding to the stretching of $Fe^{III}-C\equiv N-Ni^{II}$ and $Fe^{III}-C\equiv N$; in the opposite, bands corresponding to the bending

vibrations of the $\text{Fe}^{\text{III}}-\text{C}\equiv\text{N}$ linkage is clearly more intense than the ones of the $\text{Fe}^{\text{II}}-\text{C}\equiv\text{N}$ linkage, which is only visible as a shoulder.

In the other hand, the presence of the characteristic bands located in the range $3700\text{-}3000\text{ cm}^{-1}$, corresponding to $-\text{OH}$ stretching vibrations, shows the presence of both coordinated and crystallized water molecules in all samples. A very broad band at 3417 cm^{-1} is attributed to crystallized water molecules, involved in a hydrogen-bonded network¹⁷. A sharp band at 3646 cm^{-1} corresponds to water molecules coordinated to the metallic ions of the cyano-bridged network¹⁷ (Figures 6 and 7). This water is part of the $\text{K}^+/\text{Ni}^{2+}/[\text{Fe}(\text{CN})_6]^{3-}$ NPs structure because it presents several vacancies, due to the some $[\text{Fe}(\text{CN})_6]^{3-}$ moieties vacancies and the Ni^{2+} ions coordinating one or more water molecules to complete their coordination sphere. The crystallized water molecules can be relatively easy removed by heating, but the removing of the coordinated water required comparatively higher temperatures and vacuum conditions. The presence of the band in the $1640\text{-}1600\text{ cm}^{-1}$ region, is attributed to the bending vibration of H-O-H linkage of crystallized water molecules.

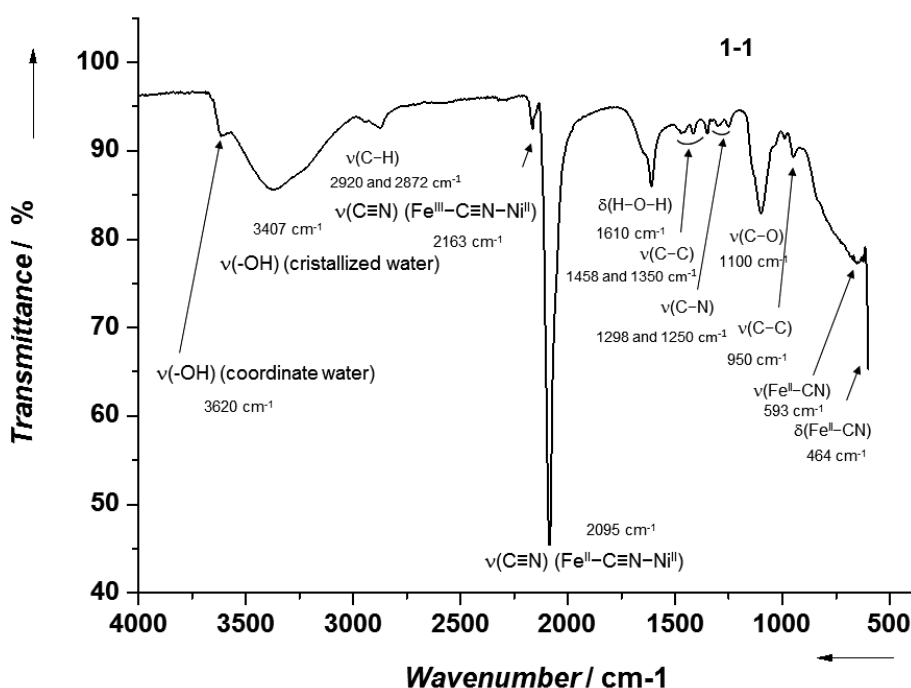


Figure 5: IR spectrum of the $\text{K}^+/\text{Ni}^{2+}/[\text{Fe}(\text{CN})_6]^{3-}/\text{PEG-NH}_2$ NPs obtained using the first approach

IR attribution	1-1	1-2	1-3	1-4	1-5	1-6
$\nu(-OH)$ coordinate water (cm^{-1})	3620	3645	3644	3646	3644	3644
$\nu(-OH)$ crystallized water (cm^{-1})	3407	3424	3418	3417	3417	3417
$\nu(Fe^{III}-C\equiv N-Ni^{II})$ (cm^{-1})	2163	2165	2166	2167	2167	2167
$\nu(Fe^{II}-C\equiv N-Ni^{II})$ (cm^{-1})	2095	2100	2100	2100	2100	2100
$\delta(H-O-H)$ crystalized water (cm^{-1})	1610	612	1611	1611	1611	1611
$\nu(Fe^{II}-CN)$ (cm^{-1})	593	593	592	592	592	592
$\nu(Fe^{III}-CN)$ (cm^{-1})	Not observed	543	543	541	544	544
$\delta(Fe^{II}-CN)$ (cm^{-1})	464	460	461	460	460	463
$\delta(Fe^{III}-CN)$ (cm^{-1})	Not observed	433	437	438	436	438

Table 2: Table summarizing the different IR band's values corresponding to the PBA network, obtained for samples 1-1 to 1-6, with their respective attributions.

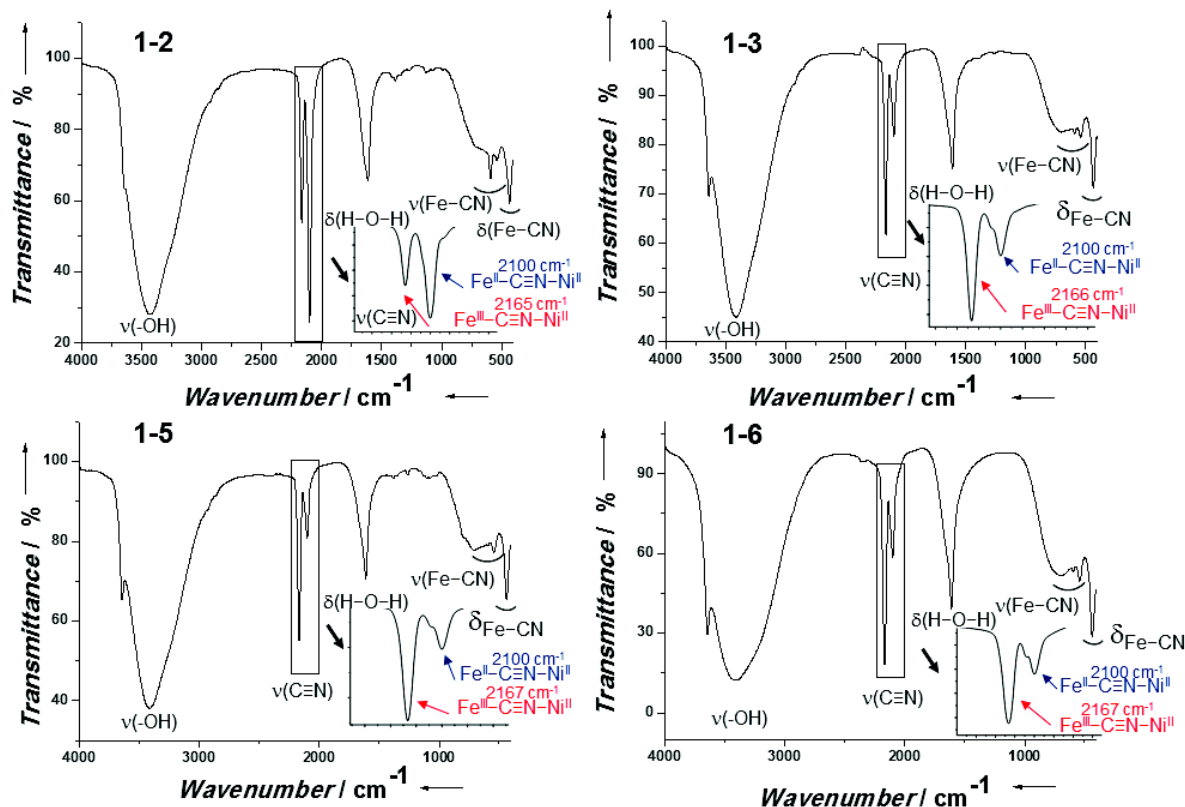


Figure 6: IR spectra of $\text{K}^+/\text{Ni}^{2+}/[\text{Fe}(\text{CN})_6]^{3-}$ NPs for samples 1-2, 1-3, 1-5 and 1-6. In inset, magnifications of their respective cyanide stretching regions with the attributions.

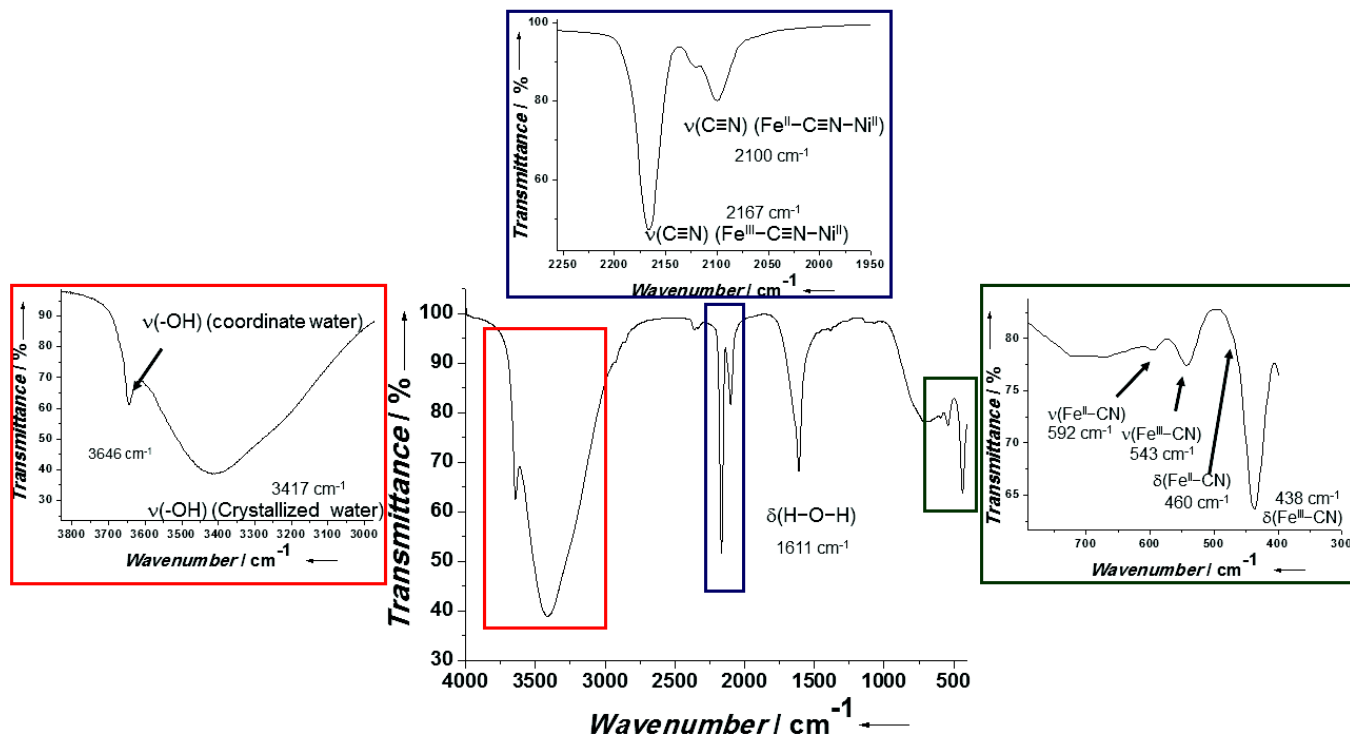


Figure 7: IR spectrum of $\text{K}^+/\text{Ni}^{2+}/[\text{Fe}(\text{CN})_6]^{3-}$ NPs for sample 1-4. In inset, magnification of 3700-3000 cm^{-1} region (red), 2200-2000 cm^{-1} region (blue) and 700-400 cm^{-1} region (green).

For sample **1-1** obtained with the first approach (figure 5), the presence of the PEG-NH₂ as stabilizer is confirmed by IR. Two bands are observed in the 2800-2950 cm⁻¹ range and correspond to CH₂ and CH₃ stretching vibration. Several bands, corresponding to C-C stretching vibration, are located in the 1500-800 cm⁻¹ region (table 3)^{10,11}. The C-N stretching vibrations observed at 1298 and at 1254 cm⁻¹, prove the presence of the terminal-amino groups of PEG-NH₂. The bands located around 1100 cm⁻¹ were assigned to the C-O stretching vibration band, corresponding to the polyethylene glycol groups in the PEG-NH₂.

For samples **1-3** and **1-4**, obtained from the second approach, the IR spectra performed after the post-synthetic grafting step confirm the presence of the cyano-bridged network corresponding to the K⁺/Ni²⁺/[Fe(CN)₆]³⁻ NPs (figure 8) with the presence of the same bands previously found. The appearance of new bands, at similar values than for sample **1-1** (table 3) confirmed the presence of the polymeric chains of the stabilizer. Thus, the modification of the NPs surface with the PEG-NH₂ was effective. The grafting may also be experimentally observed by a better dispersion of the NPs in water.

Label	IR $\nu(\text{C-H})$, cm ⁻¹	IR $\nu(\text{C-C})$, cm ⁻¹	IR $\nu(\text{C-N})$, cm ⁻¹	IR $\nu(\text{C-O})$, cm ⁻¹
1-1	2920 and 2872	1458, 1350 and 950	1298 and 1250	1100
1-3 grafted	2954 and 2923	1497, 1350 and 955	1270	1099
1-4 grafted	2918 and 2849	1460, 1355 and 1020	1260	1103

Table 3: Table summarizing the different IR band's values corresponding to the PEG-NH₂ of the K⁺/Ni²⁺/[Fe(CN)₆]³⁻ NPs, obtained for samples **1**, **3** and **4**, with their respective attributions.

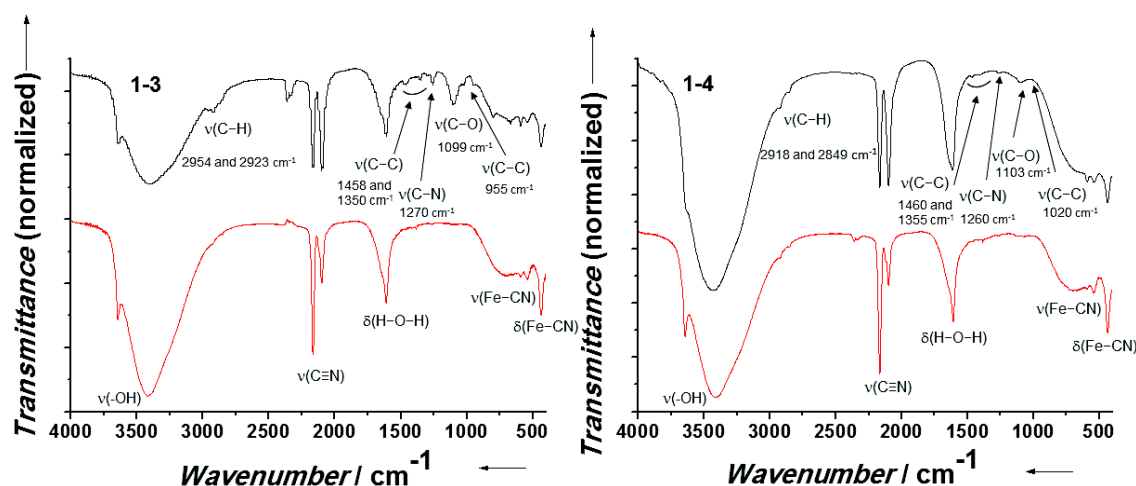


Figure 8: IR spectra the / grafted PEG-NH₂ NPs in black for sample **1-4** (37 nm) on left and sample **1-5** (70 nm) on right. For comparison K⁺/Ni²⁺/[Fe(CN)₆]³⁻ NPs before post-synthetic grafting in red for their respective sizes.

We have to point out the modification of the respective intensity of two bands corresponding respectively to the $\text{Fe}^{\text{III}}-\text{C}\equiv\text{N}-\text{Ni}^{\text{II}}$ and $\text{Fe}^{\text{II}}-\text{C}\equiv\text{N}-\text{Ni}^{\text{II}}$ linkages. Indeed, by comparing the IR spectra before and after grafting (figure 10), the band located at 2165 cm^{-1} ($\text{Fe}^{\text{III}}-\text{C}\equiv\text{N}-\text{Ni}^{\text{II}}$) is more intense than the band at 2100 cm^{-1} ($\text{Fe}^{\text{II}}-\text{C}\equiv\text{N}-\text{Ni}^{\text{II}}$) before grafting. After grafting, the two bands have similar intensity for both samples. Then the $\text{Fe}^{\text{II}}/\text{Fe}^{\text{III}}$ ratio was modified, with an increase of the Fe^{II} ion amount in the NPs. To quantify this evolution, the areas of the respective bands were calculated before and after grafting and then, the $\text{Fe}^{\text{II}}/\text{Fe}^{\text{III}}$ ratio was estimated for both cases. For samples **1-3** and **1-4**, this ratio turns from 0.76 before grafting to 1.33 and to 0.60 before grafting to 1.50 after grafting respectively. Then an increase of the amount of Fe^{II} is clearly observed. We can conclude that the post-synthetic grafting induces the further reduction of the iron ions located at the surface. This reduction is probably due to the presence of amino groups at the terminations of the PEG-NH₂ chains; amines are known to be reducing agents and the reduction of $\text{K}_3[\text{Fe}(\text{CN})_6]$ by a primary amine has already been reported¹⁹ ($\text{RCH}_2\text{NH}_2 + 4 [\text{Fe}(\text{CN})_6]^{3-} + 4 \text{OH}^- \rightarrow \text{RC}\equiv\text{N} + 4 [\text{Fe}(\text{CN})_6]^{3-} + 4 \text{H}_2\text{O}$). Moreover, the previous observation seems to be in agreement with the fact that the amount of Fe^{II} is localized at the surface, where the polymer may be anchored as indicated by the IR spectra.

This series of $\text{K}^+/\text{Ni}^{2+}/[\text{Fe}(\text{CN})_6]^{3-}/\text{PEG-NH}_2$ NPs and their bulk analogue (sample **7**) were characterized using Raman spectroscopy^{20,21}. For all samples, the Raman spectra indicate the presence of the band located at around 2188 cm^{-1} corresponding to the stretching vibrations of the $\text{Fe}^{\text{III}}-\text{C}\equiv\text{N}-\text{Ni}^{\text{II}}$ linkage (figure 9)²². For all samples except sample **1-1** corresponding to the ultra small $\text{K}^+/\text{Ni}^{2+}/[\text{Fe}(\text{CN})_6]^{3-}/\text{PEG-NH}_2$ NPs, this band is the most intense band, comparatively to the short band located at around 2120 cm^{-1} , and assigned to the $\text{Fe}^{\text{II}}-\text{C}\equiv\text{N}-\text{Ni}^{\text{II}}$ linkage. It clearly reveals a high amount of Fe^{III} ions in these NPs. For sample **1**, two low-wavenumber bands are observed at 2104 and at 2146 cm^{-1} , characteristic of the $\text{Fe}^{\text{II}}-\text{C}\equiv\text{N}$ linkage²². Moreover, these bands are clearly more intense than those characteristic of the $\text{Fe}^{\text{III}}-\text{C}\equiv\text{N}$ linkage. It indicates a high amount of Fe^{II} for the ultra small $\text{K}^+/\text{Ni}^{2+}/[\text{Fe}(\text{CN})_6]^{3-}/\text{PEG-NH}_2$ NPs. This is also confirmed by the stretching vibrations of the metal-carbon linkages.

For the ultra small $\text{K}^+/\text{Ni}^{2+}/[\text{Fe}(\text{CN})_6]^{3-}/\text{PEG-NH}_2$ NPs, this band is located at 254 cm^{-1} , attributed to $\text{Fe}^{\text{II}}-\text{C}$ stretching vibrations, and at around 240 cm^{-1} for the others samples, corresponding to the $\text{Fe}^{\text{III}}-\text{C}$ stretching vibrations. Consequently, the Raman spectroscopy clearly indicates the same increase of the amount in Fe^{II} observed in IR.

The chemical composition of the $\text{K}^+/\text{Ni}^{2+}/[\text{Fe}(\text{CN})_6]^{3-}$ NPs were determined by Energy Dispersive X-ray Spectroscopy (EDS), giving the metals ratio (Ni, Fe). The expected $\text{Ni}^{2+}/\text{Fe}^{3+}$ ratio which value is close to 1.5 for the bulk material of the formula $\text{Ni}_3[\text{Fe}(\text{CN})_6] \cdot \text{XH}_2\text{O}$ or $\text{Ni}[\text{Fe}(\text{CN})_6]_{0.66} \cdot \text{XH}_2\text{O}$ ²³. However, the found experimental $\text{Ni}^{2+}/\text{Fe}^{3+}$ ratio is different from the theoretical ratio for all NPs and varied from 1.23 for sample **1-2** to 1.74 for sample **1-3** (table 4). The difference with the expected value can be explained by the presence of a non-negligible amount of Fe^{II} instead of Fe^{III} in the NPs as shown by the IR spectra and Raman spectroscopy. Then, by using the calculations model described in annexes, the $\text{K}^+/\text{Ni}^{2+}/[\text{Fe}(\text{CN})_6]^{3-}$ NPs compositions were determined and summarized in table 4.

Samples	Size of NPs (nm)	Ni ²⁺ /Fe ³⁺ ratio calculated	K ⁺ /Ni ²⁺ ratio calculated	Estimated formula
1-1	3	1.60	0.72	K _{0.72} Ni[Fe ^{II} (CN) ₆] _{0.4} [Fe ^{III} (CN) ₆] _{0.37}
1-2	14	1.23	0.10	K _{0.01} Cs _{0.48} Ni[Fe ^{II} (CN) ₆] _{0.06} [Fe ^{III} (CN) ₆] _{0.75}
1-3	35	1.74	0.04	K _{0.04} Ni[Fe ^{II} (CN) ₆] _{0.33} [Fe ^{III} (CN) ₆] _{0.24}
1-4	70	1.61	0.04	K _{0.04} Ni[Fe ^{II} (CN) ₆] _{0.19} [Fe ^{III} (CN) ₆] _{0.43}
1-5	110	1.61	0.04	K _{0.04} Ni[Fe ^{II} (CN) ₆] _{0.18} [Fe ^{III} (CN) ₆] _{0.44}
1-6	180	1.60	0.40	K _{0.04} Ni[Fe ^{II} (CN) ₆] _{0.21} [Fe ^{III} (CN) ₆] _{0.40}

Table 4 : Table giving ratio of theoretical Ni²⁺/Fe³⁺ ratio calculated by EDS (considering case of Ni₃[Fe(CN)₆]₃·XH₂O formula) and estimated formula for all size of K⁺/Ni²⁺/[Fe(CN)₆]³⁻ NPs.

Comparing these formulas, we correlate a possible size effect with the increase of the amount in Fe^{II}. Except sample **1-2** which presents a high Cs⁺ content, the reduction of the NPs size leads to an increase of the Fe^{II} ions amount. This fact is also confirmed by the IR spectra and by calculating the Fe^{II}/Fe^{III} ratio with the respective areas of the bands corresponding of the Fe^{II}-C≡N-Ni^{II} and Fe^{III}-C≡N-Ni^{II} linkages (figure 10). The increase of Fe^{II}/Fe^{III} ratio while the size decrease clearly shows the increase of the Fe^{II} amount with the size reduction of the NPs. However, in the case of sample **1-2**, the amount of Fe^{II} is clearly underestimated, as shown with the IR spectrum, while the band characteristic of the Fe^{II}-C≡N-Ni^{II} linkage is more intense than those corresponding to the Fe^{III}-C≡N-Ni^{II} linkage (figure 6, **1-2**). The calculation of the Fe^{II}/Fe^{III} ratio with the IR bands areas for this sample gives 2.26, which is higher than those estimated by calculation (0.08). It indicates that the amount of Fe^{II} is higher than those estimated by calculation. Then divergence between the results obtained using IR spectroscopy and the formula calculated using our model reveals its limits. This difference may be due to the excess of cesium in the sample, which false the calculation.

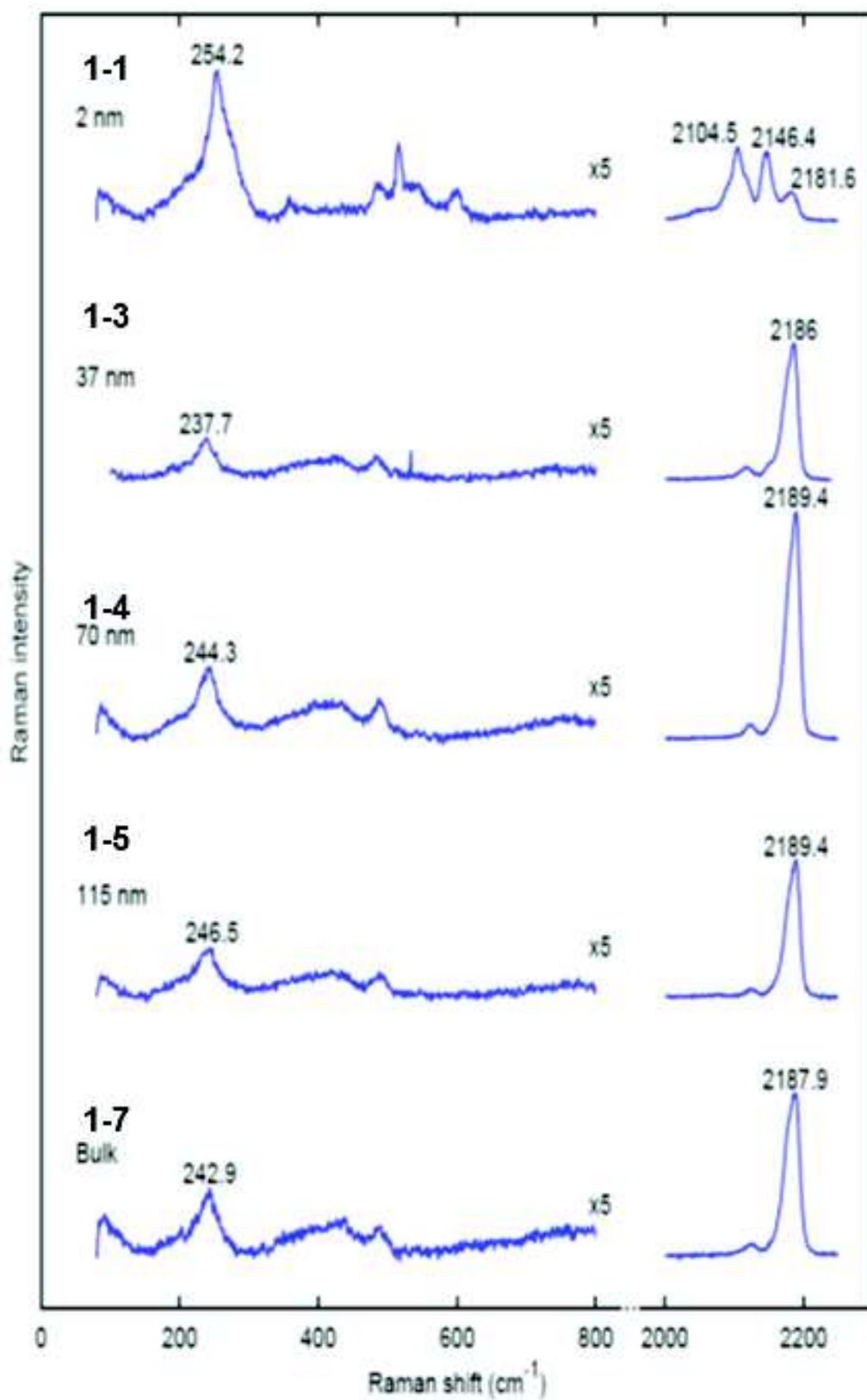


Figure 9: Raman spectra for NPs with different sizes (2 nm, 37 nm, 70 nm, 115 nm) and the analogous bulk material of $\text{Ni}_3[\text{Fe}(\text{CN})_6]$ at room temperature²¹.

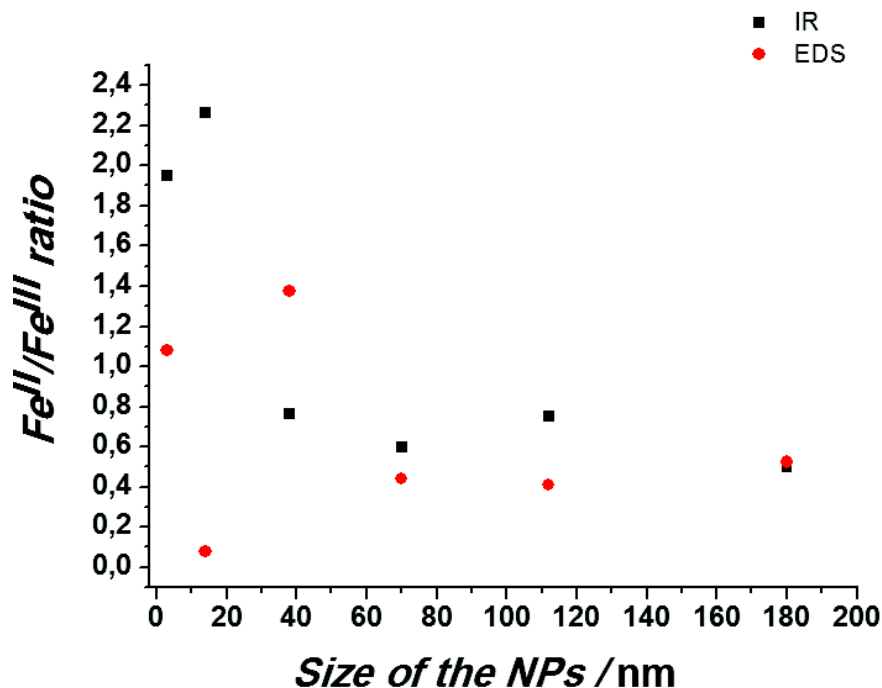


Figure 10: Evolution of the Fe^{II}/Fe^{III} ratio calculated with the IR band areas corresponding to the Fe^{II}-C≡N-Ni^{II} and Fe^{III}-C≡N-Ni^{II} linkages (black) and Fe^{II}/Fe^{III} EDS ratio as a function of size.

Indeed, the part of ions located at the surface is higher for small NPs than for large NPs and that induces an increase of Fe^{II}/Fe^{III} ratio for small particles, due to the large amount of Fe^{II} ions at the surface. This conclusion should be confirmed by others characterization techniques permitting to differentiate Fe^{II} and Fe^{III} such as Mössbauer spectroscopy. For the ultra-small K⁺/Ni²⁺/[Fe(CN)₆]³⁻ NPs obtained using the first approach, the reducing agent may be the PEG-NH₂, which coordinates to the surface. This has been already showed with the IR spectra of the K⁺/Ni²⁺/[Fe(CN)₆]³⁻ NPs post-synthetically grafted (figure 8). Nevertheless, the PEG-NH₂ is not present during the first step of the second approach, while the K⁺/Ni²⁺/[Fe(CN)₆]³⁻ NPs were synthesized, and the reduction of Fe^{III} in Fe^{II} is already observed. To our knowledge no reducing agent is present in the reaction media. However, due to the closeness of the redox potential of the redox couple O₂/OH⁻ (E° = 0.40 V) and [Fe^{III}(CN)₆]³⁻/[Fe^{II}(CN)₆]⁴⁻ (E° = 0.36 V), it is possible that phenomenon at the interface modify the value of the redox potential, permitting the reduction of a part of the [Fe^{III}(CN)₆]³⁻ with the OH⁻ ions naturally present in the aqueous media. Such reduction may also occur by the photoreduction of the cyanometallate precursor during the synthesis. Indeed, the sensibility of the [Fe^{III}(CN)₆]³⁻ moieties to light is well-known²⁴.

We have performed powder X-ray diffraction to obtain structural informations on the K⁺/Ni²⁺/[Fe(CN)₆]³⁻/PEG-NH₂ NPs. For all the K⁺/Ni²⁺/[Fe(CN)₆]³⁻/PEG-NH₂ NPs and the analogous bulk material Ni₃[Fe(CN)₆]₂, XRD patterns indicate the presence of the diffraction peaks corresponding to the *fcc* structure of Ni₂[Fe(CN)₆] PBA (01-075-0037), as described in the literature²³, which were indexed with the $F\bar{4}3m$ space group. (Figure 11). The cell parameters obtained are close for all NPs indicating no modification of the structure with the increase of the size of the particles (table 5). From sample 1-5 to sample 1-1, the widths of the peaks are enlarging. This phenomenon is characteristic to the size reduction of the particles. However, the peaks of the analogous bulk material are

unexpectedly broad. This may be explained by its intrinsic nature. Indeed, the bulk material refers to a mixing of particles ranging from several nm to several μm . The size distribution of these particles may be extremely broad, which is the origin of the wide peaks observed.

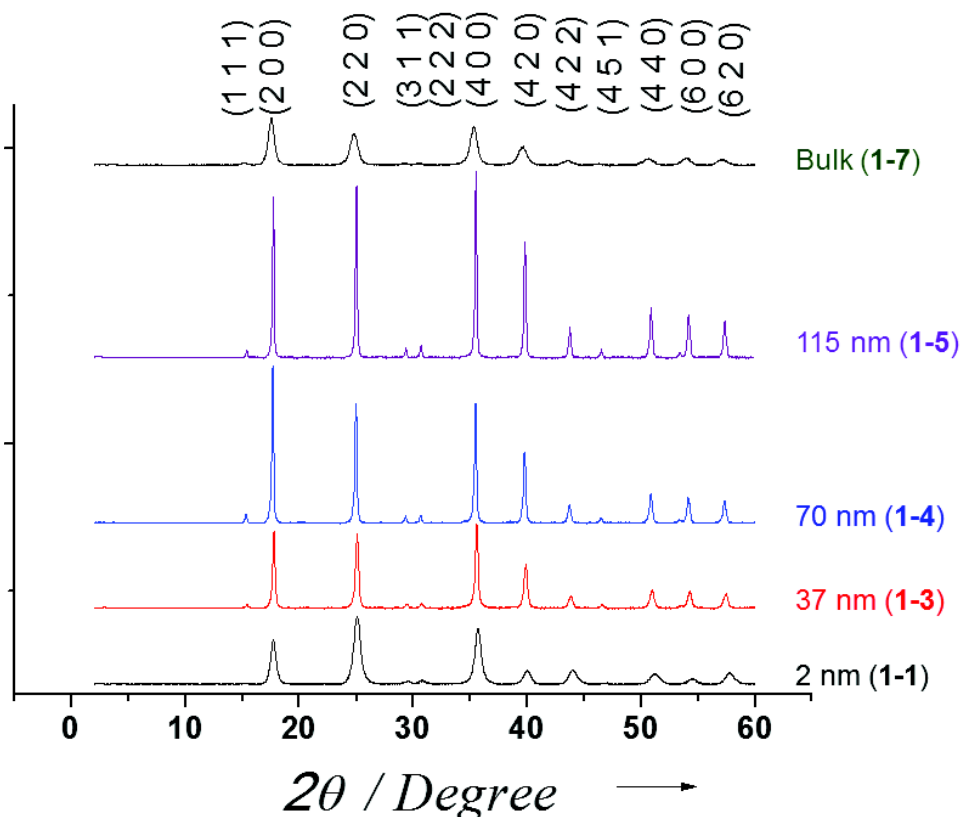


Figure 14: Powder X-Ray diffraction patterns for different particle size of $\text{Ni}_3[\text{Fe}(\text{CN})_6]_2$ at room temperature²¹.

The experimental XRD patterns of the $\text{K}^+/\text{Ni}^{2+}/[\text{Fe}(\text{CN})_6]^{3-}$ NPs show significant difference by comparison with the $\text{Ni}_2[\text{Fe}(\text{CN})_6]$ PBA reference. Indeed, a shift of the peaks occurs as a function of the size of the NPs (figure 15). For example, the peak corresponding to the (2 0 0) plane is located at 17.7° for the ultra-small NPs (sample **1-1**), which is closed to the value observed for $\text{Ni}^{\text{II}}[\text{Fe}^{\text{II}}(\text{CN})_6]$ (17.7°), then with the increase of the size the peak is gradually shifted until 17.5° for the bulk material (sample **1-7**), which is closer to the value (17.3°) observed for $\text{KNi}^{\text{II}}[\text{Fe}^{\text{III}}(\text{CN})_6]$ (00-051-1897). Moreover, the difference with the measured data and the two references patterns was quantified with the degrees of “fit”, which correspond to the degree of accordance between the data and the reference. The matching score is clearly in accordance with $\text{Ni}^{\text{II}}[\text{Fe}^{\text{II}}(\text{CN})_6]$ reference for sample **1-1**, and with $\text{KNi}^{\text{II}}[\text{Fe}^{\text{III}}(\text{CN})_6]$ for the others. That seems to corroborate the presence of an important amount of Fe^{II} for the ultra-small NPs. Then this amount decreases gradually and at the opposite, the amount of Fe^{III} increases with the size increase of the particles, which was observed by the previous characterizations.

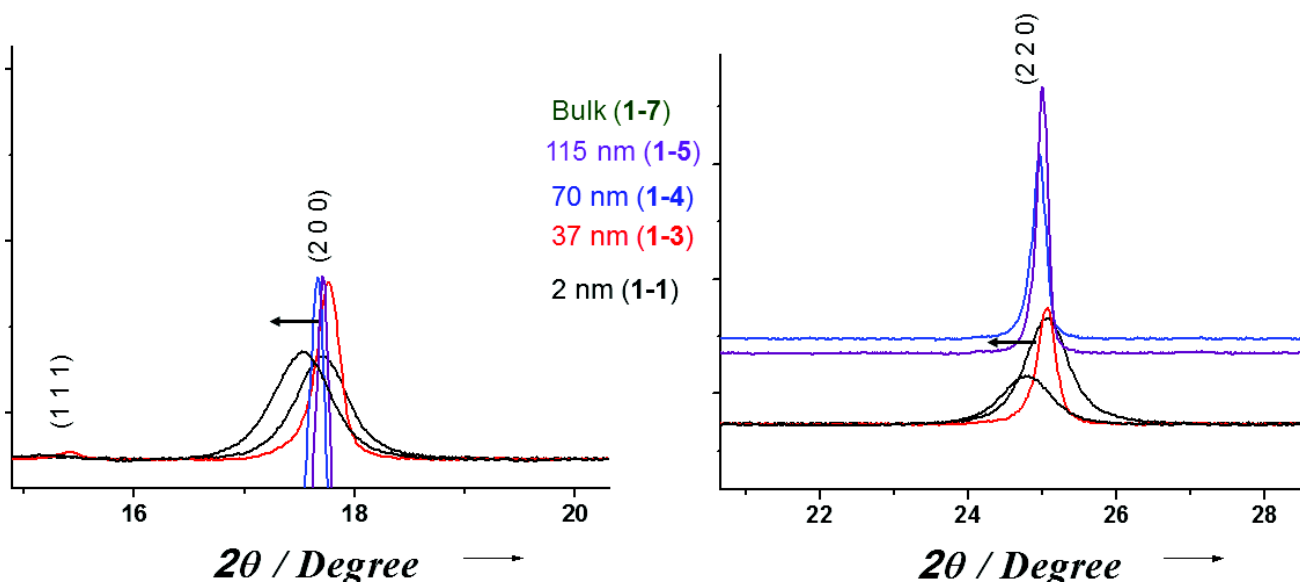


Figure 15: Shift of the peaks with the size increase observed for (2 0 0) and (2 2 0) planes.

Label	Size (nm)	Cell parameter (Å)	Value of the score by comparison with the	
			Ni ^{II} [Fe ^{II} (CN) ₆] reference	KNi ^{II} [Fe ^{III} (CN) ₆]
1-1	2	10.102	70	60
1-3	37	10.007	48	60
1-4	70	10.035	18	47
1-5	115	9.982	17	40
1-7	Bulk material	10.016	39	68

Table 5: Table presenting the evolution of the cell parameter for the respective K⁺/Ni²⁺/[Fe(CN)₆]³⁻ NPs.

The images obtained by Transmission Electronic Microscopy (TEM) bring size information about the K⁺/Ni²⁺/[Fe(CN)₆]³⁻ NPs (Figure 15). For sample **1-1**, TEM analysis revealed the formation of ultra-small “spherical” K⁺/Ni²⁺/[Fe(CN)₆]³⁻/PEG-NH₂ NPs. For samples **1-3** to **1-6**, the morphology is well-defined, and appears as truncated cubes. For sample **1-3**, we observed the presence of both cubic and “spherical” NPs. As described in the literature, the crystal morphology is determined by extrinsic and intrinsic factors, such as the crystal structure or the surface and interfacial energy during the growth^{25,26}. During the growth, the system tends to minimize its surface energy. The Wulff’s theorem²⁵ shows that this minimum should be obtained for a polyhedron for which the length of a vector drawn normal to a crystal face is proportional to its surface energy.

The higher surface tension faces tends to grow along its normal direction to minimize its energy. Then, according to this theorem, the most stable shape for smaller size (< 10 nm) is the icosahedron, because it's the shape the most dense, maximizing the cohesion energy with a shape quite close to a sphere and presenting only (1 1 1) faces, which have the lower surface energy²⁶. The shape observed for sample **1-1** and **1-2** may be parented to icosahedra. Then during the growth, when the critical size is attained, the shape is influenced by the intrinsic crystal structure of the material^{25,26}. The Ni^{II}[Fe^{III}(CN)₆] PBA crystalizes in a face-centered cubic structure (*fcc*) with a cubic lattice. Thus, the shape of the nano-objects is cubic at the larger size, what is observed for sample **1-3** to **1-6**. This morphology is also determined by the crystal growth along preferential facets²⁶.

For the *fcc* structure, the growth is kinetically favored for the (1 1 1) facets, because their energy is higher than that of the (1 0 0) facets. Then these faces grow, to form the cubes bounded by the six (1 0 0) planes²⁵. In our case, the observation of truncated cubes seems to indicates that the (1 1 1) faces remain present. Sample **1-2** is interesting because both icosahedron and cubic shape are present. This indicates that this size corresponds to the limit between one shape and the other, which is the critical size. Then for the Ni^{II}[Fe^{III}(CN)₆] PBA, we can estimate this critical size around 15 nm. This is concordant with results obtained on CsNi^{II}[Cr^{III}(CN)₆] PBA NPs, where the critical size was found to be 16 nm²⁸.

After the post-synthetic grafting step, the results from TEM measurements indicate the presence of particles with similar size for samples **1-3** and **1-4** (figure 18). Comparatively to the initial K⁺/Ni²⁺/[Fe(CN)₆]³⁻ (figure 15), which are "nude", the presence of an organic material is visible at the surface of the K⁺/Ni²⁺/[Fe(CN)₆]³⁻/grafted PEG-NH₂ NPs, indicating the anchoring of PEG-NH₂ chains at the PBA NPs surface.

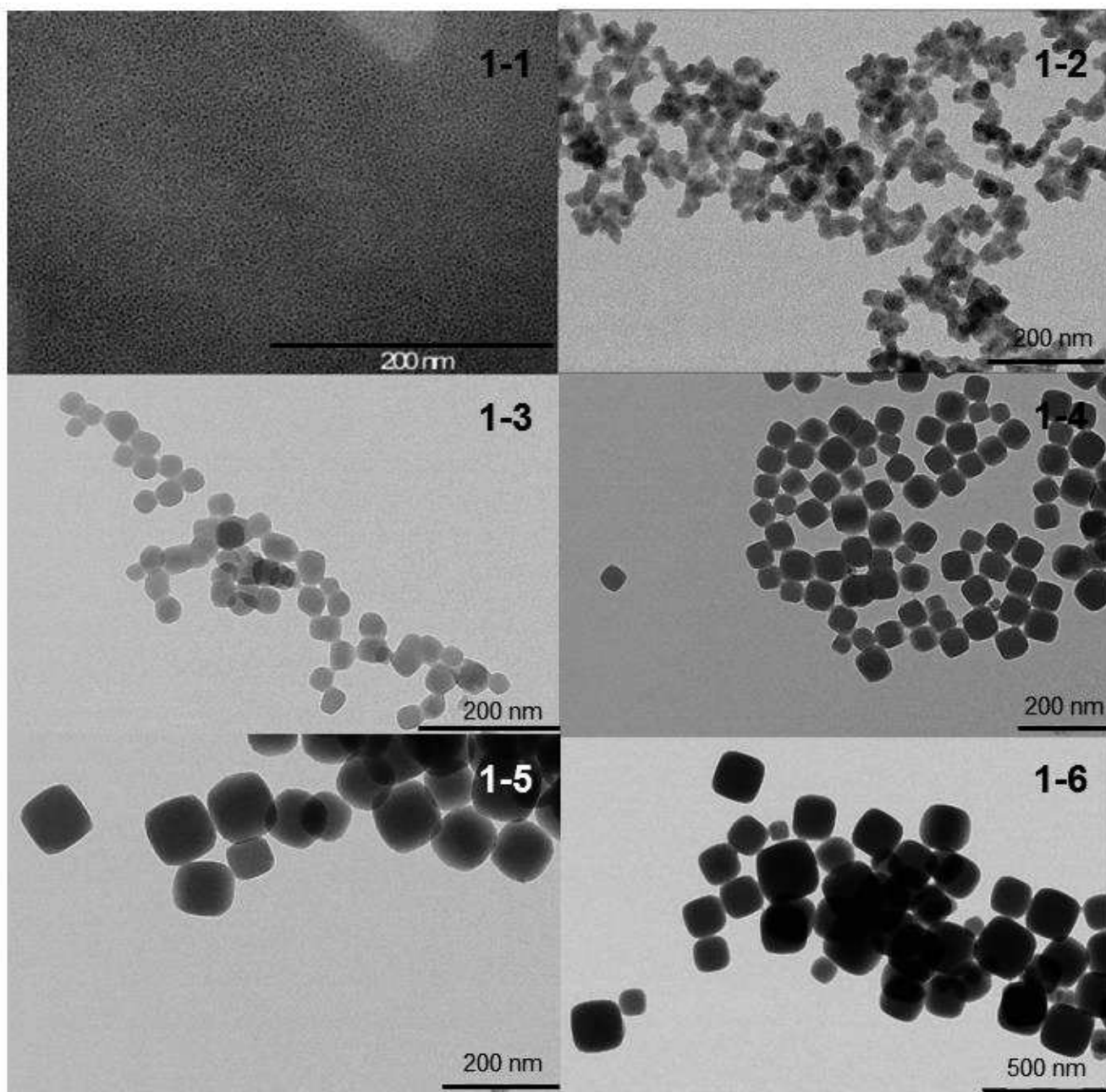


Figure 15: TEM images of $K^+/Ni^{2+}/[Fe(CN)_6]^{3-}$ NPs.

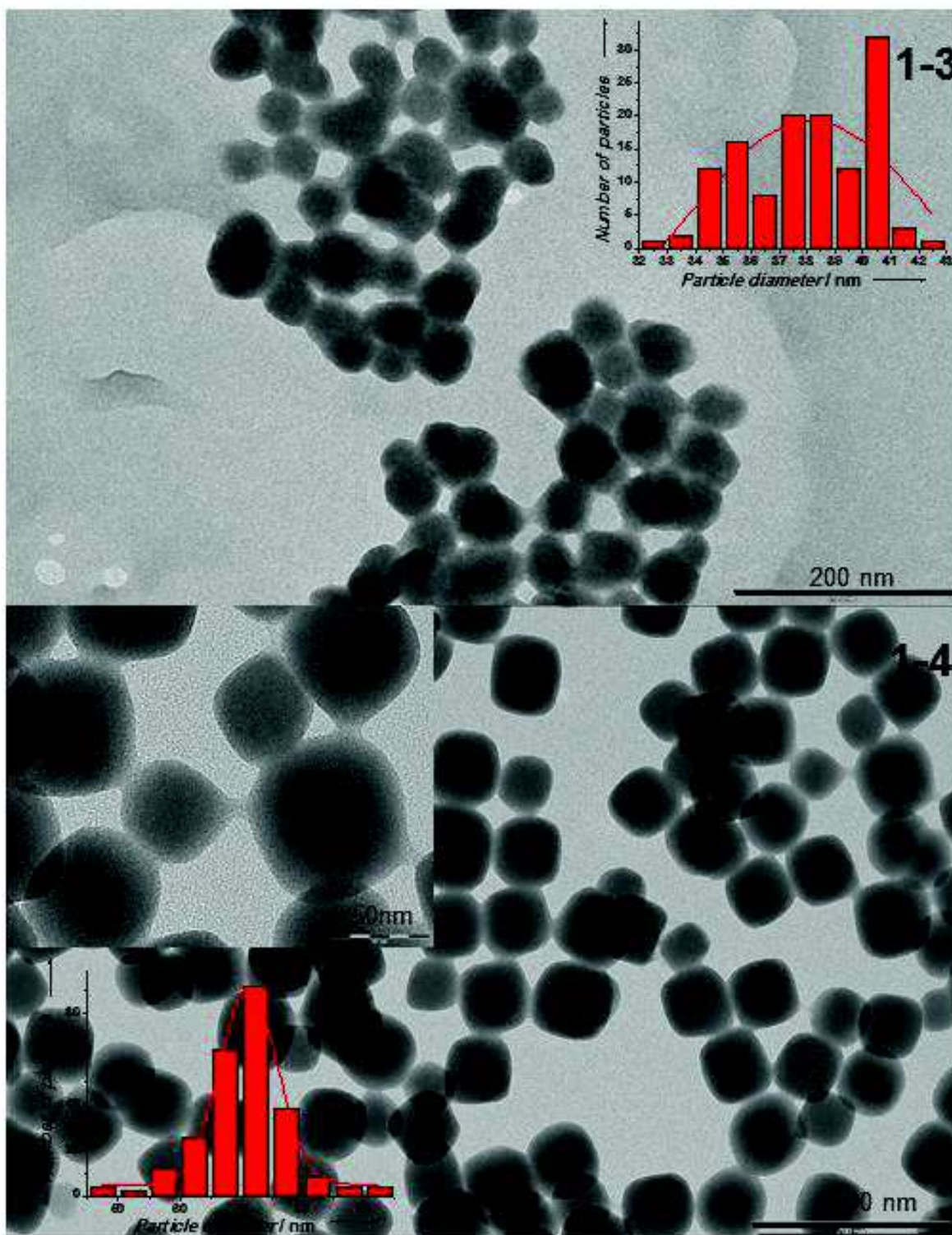


Figure 16: TEM images of $K^+/Ni^{2+}/[Fe(CN)_6]^{3-}$ /grafted PEG-NH₂ NPs, in left sample **1-3** (35 nm) and in right sample **1-4** (70 nm), with in inset a magnification on several NPs. In inset for both images, corresponding histograms of the NPs's size distribution.

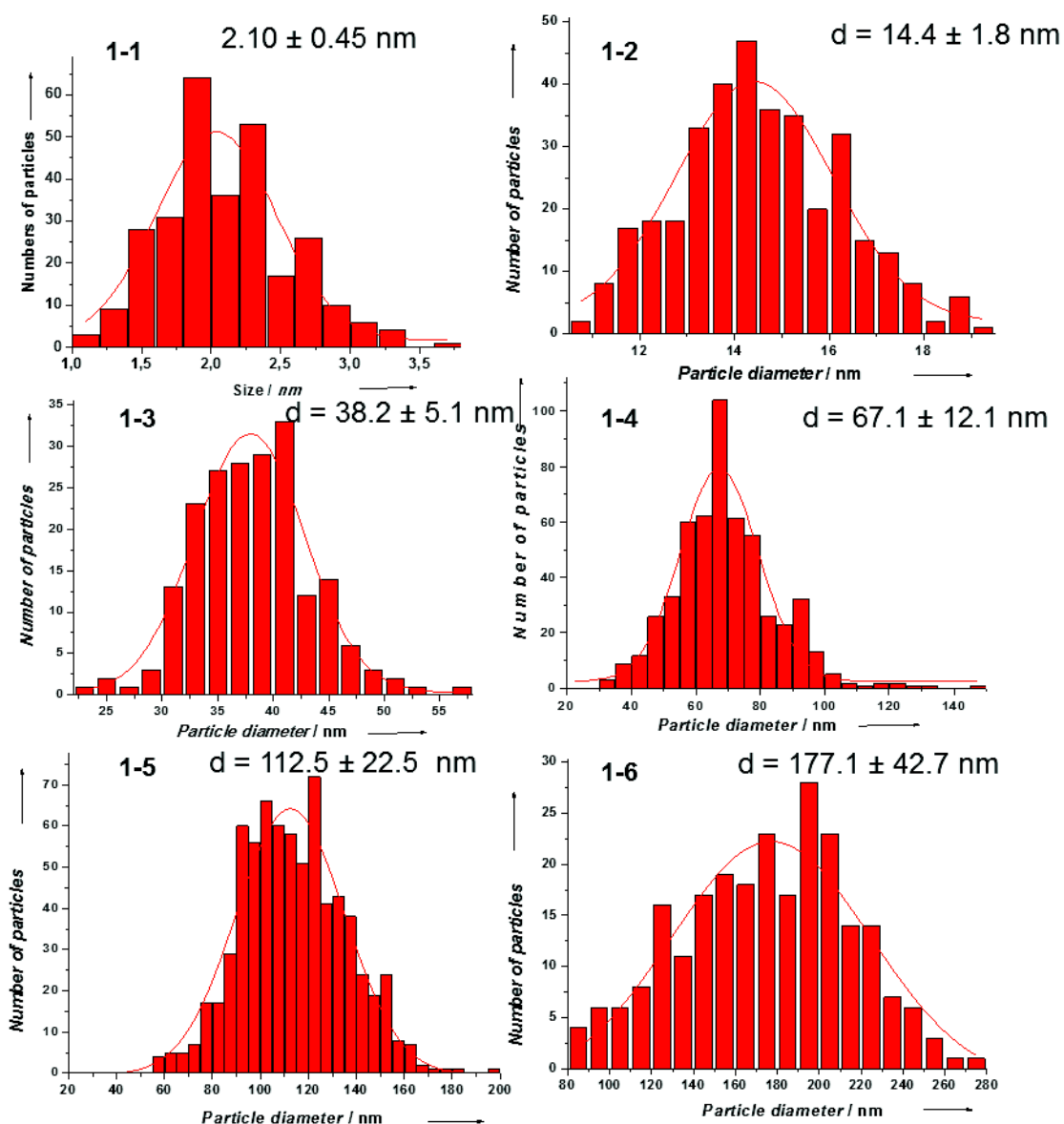


Figure 17: Histograms presenting the size distribution of the $\text{K}^+/\text{Ni}^{2+}/[\text{Fe}(\text{CN})_6]^{3-}$ NPs with their respective mean diameters.

Moreover, the size distributions were obtained from TEM images, giving the mean diameter of the nanoparticles, respectively equal to 2.10 ± 0.45 nm, 14.4 ± 1.8 nm, 38.2 ± 5.6 nm, 67.1 ± 12.1 nm, 112.5 ± 22.5 nm and 177.1 ± 42.7 nm for samples from **1-1** to **1-6**, respectively (figure 17). For the $\text{K}^+/\text{Ni}^{2+}/[\text{Fe}(\text{CN})_6]^{3-}$ /grafted PEG-NH₂ NPs, the size distribution (figure 16) is equal to 38.2 ± 5.6 nm and 67.1 ± 12.1 nm (figure 18), respectively for sample **1-3** and sample **1-4** after post-synthetic grafting, that shows no significant size modification upon grafting.

A point to note is that the standard deviation increases with the size increase. This phenomenon is statistically normal; however, for sample **1-6**, a relatively large standard deviation indicates the difficulty to obtain NPs greater than 300 nm using this approach. As shown in the literature¹⁴, a solution permitting to obtain particles larger than 300 nm in size consists in realizing an epitaxial growth on the NPs previously obtained. Indeed, the terminal cyanides of the $[\text{Fe}^{\text{III}}(\text{CN})_6]^{3-}$ building blocks at the surface of the NPs are still reactive¹³. Taking advantage of this surface reactivity, previously synthesized $\text{K}^+/\text{Ni}^{2+}/[\text{Fe}(\text{CN})_6]^{3-}$ NPs can be used as seeds for further precipitation. This seed-shell procedure permit to increase gradually the size of the NPs, several growth cycles can be performed, leading to very large NPs up to 400 nm¹³.

By correlation of the different synthetic parameters (table 1) with the size of NPs (figure 17), we observe a dependence between the size of the NPs and the experimental conditions, such as the precursors concentrations and the precursors addition rate. Indeed, with the higher concentration and a higher addition rate, a smaller size of the NPs is obtained. On the contrary, NPs size became larger with a low concentration and a slow rate. This observation is in agreement with other systems reported in literature, where the authors describe a dependence of the NPs size as a function of the number of nucleation sites^{12,13,28-30}.

With a high concentration and a fast addition rate, a lot of precursors is available in the same time in the reaction media (Figure 17, zone 1), and since the critical threshold is attained, the nucleation process occurs (Figure 17, zone 2), with the fast formation of seeds in an important amount. If the precursors' concentration comes close to the supersaturation concentration C_{max} , the kinetic of the seeds nucleation becomes very high and the germination lowers the precursors' concentration necessary to the formation of new seeds. When the sursaturation (concentration of dissolved precursors / solid phase solubility ratio) is close to C_{min} , the formation of new seeds is very slow, and under C_{min} , completely non-existent. Then, the precursors added in the reaction media react on the surface of the NPs already formed to grow them (Figure 18, zone 3), which corresponds to the Oswald ripening phenomenon, until the solid phase solubility is attained, where the NPs can only be the subject to a possible aging phenomenon³¹. In the case of the ultra-small $\text{K}^+/\text{Ni}^{2+}/[\text{Fe}(\text{CN})_6]^{3-}$ NPs (sample **1-1**), the process is limited to the nucleation (Figure 17, zone 2) due to the effect of the PEG-NH₂, which limits the formation of the tridimensional network, avoiding any growth step.

For the series of $\text{K}^+/\text{Ni}^{2+}/[\text{Fe}(\text{CN})_6]^{3-}$ NPs, the smaller sizes, obtained for high concentration and addition rate are corresponding to the zone 2 where the precursors concentration is close to C_{min} , with the formation of an important amount of seed and only a limited growth. For larger NPs, synthesized with a low concentration and a slow rate, the precursors' concentration is under C_{min} (Figure 18, zone 3) which corresponds to the growth step. Then the size of the NPs is dependent of the slow rate, i.e. the addition time of the precursors. Lower is the speed, more the time addition is extended, favoring the growth phenomenon and leading to larger NPs. However, the size is limited by the solid solubility, which avoids the growth process. For $\text{K}^+/\text{Ni}^{2+}/[\text{Fe}(\text{CN})_6]^{3-}$ NPs, the size limit is close to 300 nm. To access larger size than 300 nm, the best method consists to perform a subsequent growing using 250 nm sized NPs as seeds.

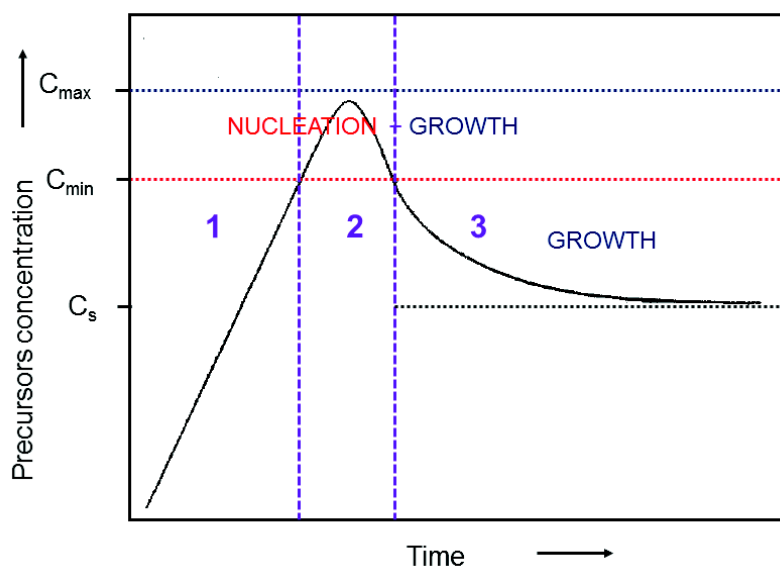


Figure 18: Simplified representation of the evolution of the precursors concentration as a function of the time during the precipitation of a solid phase, as described by LaMer and Dinegar³².

Dynamic Light-Scattering (DLS) and zeta-potential measurements were performed to prove the grafting of the $K^+/Ni^{2+}/[Fe(CN)_6]^{3-}$ NPs with the PEG-NH₂ chains. DLS gives information on the NPs size distribution in solution, and more especially on the NPs hydrodynamic radius, which may be defined as the volume moved by the particles and the solvated water molecules around it. The measurements were effectuated on two different NPs sizes, 35 nm (sample **1-3**) (figure 12) and 70 nm (sample **1-4**) (figure 13). For both samples, a dominant peak was observed, indicating no sign of NPs aggregation in aqueous media (figures 7 and 8, annex 3). For **1-3**, the hydrodynamic radius increases from 93 nm to 153 nm due to the presence of organic moieties around the inorganic core NPs (table 6). Similarly, an increase was observed for **1-4** from 108 nm to 172 nm. Indeed, by coating the NPs with PEG-NH₂ chains, the hydrophilicity of the surface is improved. That increases the number of the solvated water molecules, therefore modifying the hydrodynamic radius.

The quality of the grafting can also be evaluated by the Zeta potential which shows the nature of the charges present at the surface of the NPs. The non-coated $K^+/Ni^{2+}/[Fe(CN)_6]^{3-}$ NPs are charged negatively at the surface, with a value of the Zeta potential of -20 mV for both samples (table 6, figures 7 and 8, annex 3). This negative charge is due to the presence of the negatively charged $[Fe(CN)_6]^{3-}$ moieties located at the surface of the PBA network and then stabilizing the NPs. After grafting, the polymer chains may hide these charges, inducing then an increase of the Zeta potential value. More the Zeta potential increases and become close to zero and more the grafting is effective and coats the NPs surface. For sample **1-3**, the measured Zeta potential has a value of -18.7 mV after grafting, that indicates a thin and probably incomplete grafting of the PEG-NH₂ at the NPs surface (figures 29 and 30, annex 3). For sample **1-4**, the coating of the NPs is more visible, with the increase of the Zeta potential from -20 mV to -13.2 mV after grafting (figure 21). The Zeta potential increases after grafting, proving the coating of the NPs surface. However, the Zeta potential difference between before and after grafting remains far from zero, indicating an important amount of negative charges on the surface. This seems to indicate that the grafting is not complete. Moreover, the Zeta potential difference

is more important for sample **1-4** than for sample **1-3**. This seems to indicate the polymer coating is more thick for the $K^+/Ni^{2+}/[Fe(CN)_6]^{3-}$ NPs size of 70 nm than for 35 nm.

Label	TEM size (nm)	Hydrodynamic radius (nm)	Zeta potential (mV)
1-3	38.2 ± 5.6	93.0 ± 29.6	-20.0
1-3 grafted PEG-NH ₂	38.2 ± 5.6	153.0 ± 46.1	-18.7
1-4	67.1 ± 12.1	108.0 ± 37.5	-20.0
1-4 grafted PEG-NH ₂	67.1 ± 12.1	172.0 ± 49.4	-13.2

Table 6: Table summarizing the TEM size, the hydrodynamic radius and the Zeta potential of samples **1-3** and **1-4** before and after grafting.

II.4 Study of the Fe^{II} amount evolution as function of the size of the $K^+/Ni^{2+}/[Fe(CN)_6]^{3-}$ NPs and its influence on the structure by using Mossbauer spectroscopy.

Previously, we have seen that the size reduction of the $KNi/[Fe(CN)_6]$ NPs seems lead to an increase of the Fe^{II}/Fe^{III} ratio, according to the results obtained from EDS analysis and IR spectroscopy visibly due to the reduction of the Fe^{III} to Fe^{II} ions located at the NPs surface. In order to confirm the validity of this hypothesis, Mössbauer spectroscopy was performed on the series of $K^+/Ni^{2+}/[Fe(CN)_6]^{3-}$ NPs, in collaboration with the LCC (University Toulouse III, France)^{20,21}.

The ⁵⁷Fe Mössbauer spectroscopy is able to differentiate the different valence states of an element in the sample²², in our case the Fe^{II} and the Fe^{III}, and permits to quantify their relative amount by determining the surface area of the band. The spectrum of sample **1-1** exhibits a singlet, characteristic of Fe^{II} ions (figure 19). In the case of sample **1-3**, the presence of both a doublet, characteristic of Fe^{III} ions, and a singlet indicate that the two oxidation states Fe^{III} and Fe^{II} are present in the NPs structure. At the opposite, only a doublet is observed for the samples **1-4** and **1-5** (70 and 115 nm) and the analogous bulk material (sample 7), indicating the presence of only Fe^{III} in these samples. Then only a subtle or maybe no reduction occurs for larger NPs. But with the size reduction, the progressive appearance of the singlet indicates a progressive increase of the reduced iron ion ratio (figure 15). This increase is concordant with the increase of the

number of atoms at the surface. Then, that confirms our previous observations on the reduction of Fe^{III} to Fe^{II} at the surface of the NPs.

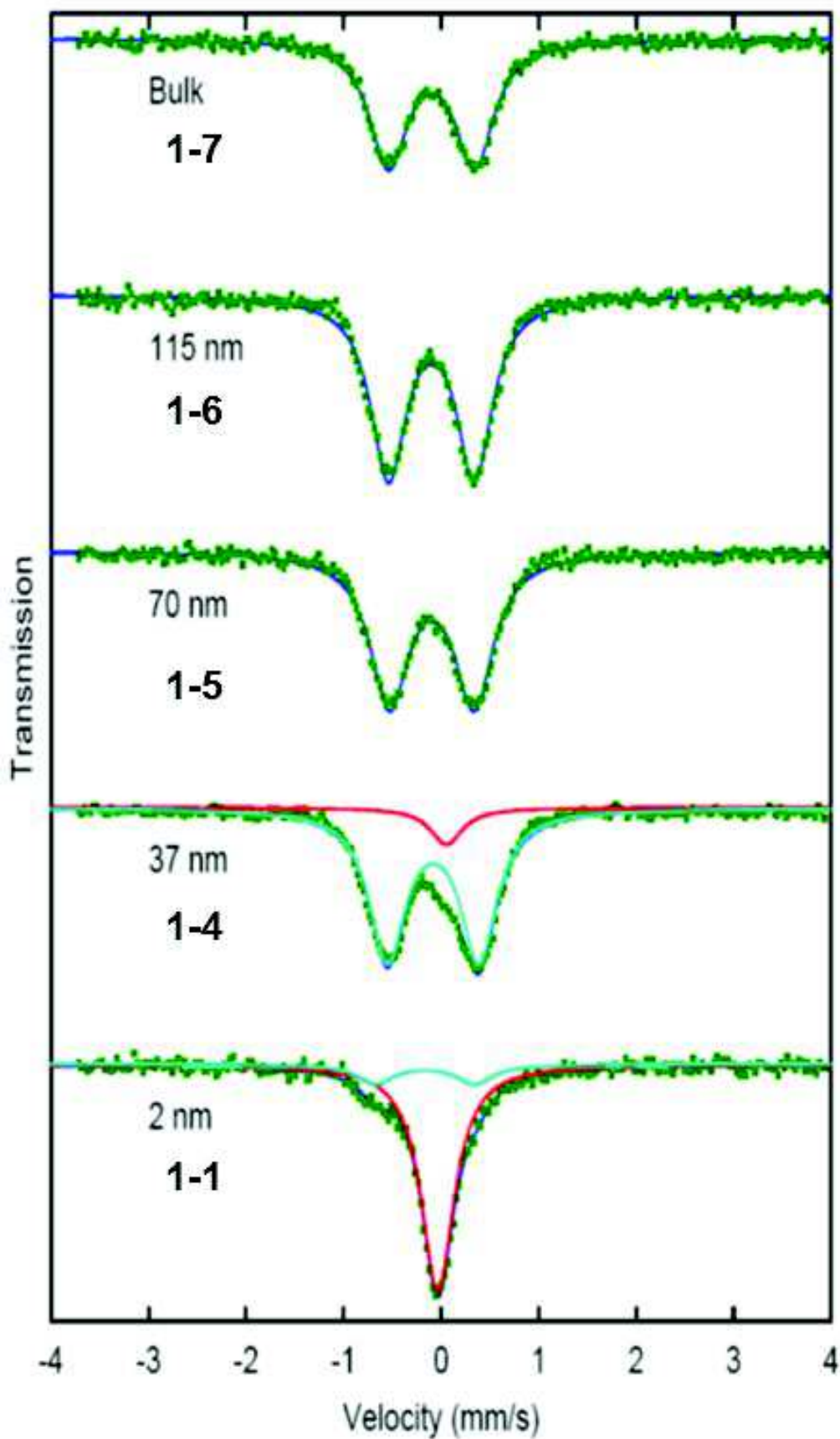


Figure 19: Mössbauer spectrum of $K^+/Ni^{2+}/[Fe(CN)_6]^{3-}$ at 80 K for different particle sizes (2 nm, 37 nm, 70 nm, 115 nm, and bulk)²¹.

Using the ^{57}Fe Mössbauer spectroscopy, it is possible to estimate the Debye Temperature Θ_D . This factor is related to the rigidity of the material i.e. its opposition to deform under the strain. A modification of the rigidity with the size decrease may indicate several modifications in the structure, as the intrinsic strain due to the shape or the surface energy, which can affect the properties. To obtain the Debye Temperature Θ_D of the material, the method consists in measuring the spectrum area at several temperatures. In our case, the spectra were recorded between 80 K and 300 K. Then, by fitting the temperature dependence with the following equation²³ (figure 20), we obtained the value of the Debye Temperature Θ_D for the respective material:

$$\log(A) \approx \log(f) = -\frac{E_R}{2k_B\Theta_D} \left(1 + \left(\frac{\Theta}{\Theta_D} \right)^2 \int_0^{\frac{\Theta_D}{\Theta}} \frac{x dx}{e^x - 1} \right)$$

With the Debye-Waller factor, k_B the Boltzmann constant, E_R the recoil kinetic energy of ^{57}Fe , Θ the temperature, Θ_D the Debye Temperature and x a non-dimensional parameter.

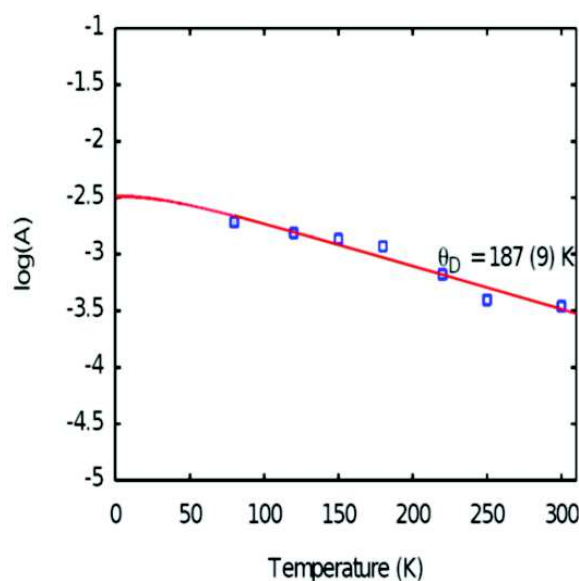


Figure 20: Area of Mössbauer spectra as a function of the temperature for the $\text{Ni}_3[\text{Fe}(\text{CN})_6]$ bulk material. The curve was fitted by the equation described previously²¹.

The estimation of the Debye Temperature of the different $\text{K}^+/\text{Ni}^{2+}/[\text{Fe}(\text{CN})_6]^{3-}$ reveals a similar behavior for all samples, except sample 1-1 and the bulk material. By comparison with these samples, an important increase of the Debye Temperature is observed for the very small NPs (figure 21). This increase is consequently due to the difference of stiffness between the atoms present at the surface and those present in the core of the NP. Then the rigidity of the structure is function of the size of the particles and the surface atom differ from the bulk, their contributions on the global elastic properties increases with the size decrease.

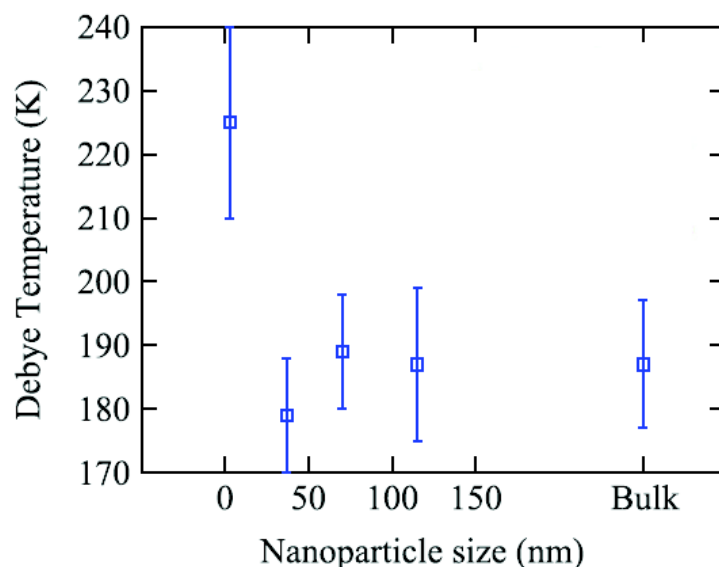


Figure 21: Evolution on the Debye temperature for $K^+/Ni^{2+}/[Fe(CN)_6]^{3-}$ PBA particles as a function of their average size (2 nm, 37 nm, 70 nm, 115 nm, bulk material)²⁰.

The influence of the increased rigidity may be important and permits to explain several phenomena. Indeed, it is the first time that the Debye temperature is measured for PBA. The difference of the Debye Temperature observed for the ultra-small NPs clearly shows a “nano” behavior for a size lower to 10 nm. Such phenomenon can be correlated for example to the different magnetic behavior observed for $CsNi[Cr(CN)_6]$ NPs with the appearance of superparamagnetic behavior for NPs size lower to 16 nm²⁸. Moreover, the Debye Temperature has permitted to obtain the phenomenological parameter, Γ , which has been used in a theoretical model, based on a thermodynamical calculation. This core-shell model allows explaining the reopening of the hysteresis loop for materials exhibiting spin-crossover phenomenon²⁰.

To resume, we have proven using several techniques that the size reduction increases the amount in Fe^{II} in the $K^+/Ni^{2+}/[Fe(CN)_6]^{3-}$ PBA NPs, as suspected. This size reduction is controlled using several parameters, such as the concentration of the precursors’ solutions, the additional rate and the possible use of stabilizing agents, as summarized in figure 22. The reduction of the Fe^{III} to Fe^{II} occurs at the surface of the particles, due to the increase of the atom’s amount at the surface with the decrease of the size.

The increase of the Fe^{II} amount in the NPs with decreasing the size has permitted to determinate the Debye Temperature, which indicates the hardening of the surface atoms with the size decrease, and is concordant with a “nano” behavior. According to the theoretical model elaborated by the LCC team (University Toulouse III, France), that permits to model the phenomenon of the reopening of the hysteresis loop with the size reduction for materials exhibiting spin-crossover phenomenon.

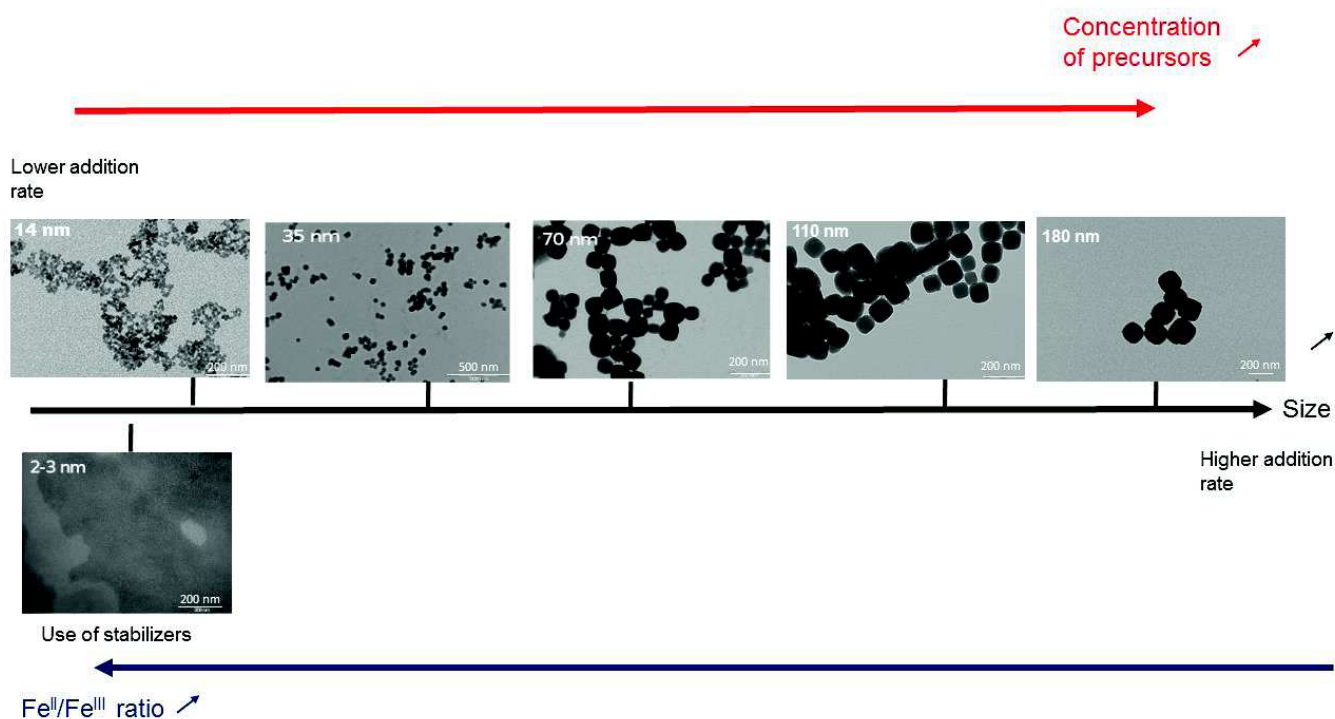


Figure 22: Evolution of the NPs's size and the Fe^{II}/Fe^{III} ratio in function of several parameter (Concentration in added precursors, rate of addition and use of stabilizers).

II.5 Conclusion

In this chapter, we present the synthesis of a series of $K^+/Ni^{2+}/[Fe(CN)_6]^{3-}$ NPs, by using two different approaches. The first approach consists in a self-assembly reaction in water between the hexacyanometallate precursor, $K_3[Fe(CN)_6]$, and the divalent transition metal ion, $[Ni(H_2O)]^{2+}$, in the presence of a stabilizer, PEG-NH₂ in order to prevent the infinite growth of the tridimensional PBA network; it permits to obtain ultra-small $K^+/Ni^{2+}/[Fe(CN)_6]^{3-}/$ PEG-NH₂ of the size of 2.10 ± 0.45 nm. The second approach is composed by two steps. The first step consists in a similar self-assembly reaction in water between the hexacyanometallate precursor, $K_3[Fe(CN)_6]$, and the divalent transition metal ion, $[Ni(H_2O)]^{2+}$ without any stabilizers. By varying several parameters, such as the precursors concentration and the addition rate, the size of the $K^+/Ni^{2+}/[Fe(CN)_6]^{3-}$ NPs was modulated. Then the second step consists in the post-synthetic grafting of the NPs surface by stabilizer chains, such as PEG-NH₂, to obtain $K^+/Ni^{2+}/[Fe(CN)_6]^{3-}/$ grafted PEG-NH₂ of larger size ranging from 14.4 ± 1.8 nm to 177.1 ± 42.7 nm.

The structural and the textural characteristics of these $K^+/Ni^{2+}/[Fe(CN)_6]^{3-}$ NPs were obtained using several techniques, IR, Raman, EDS, TEM, DLS and Zetametry. IR spectroscopy confirms the formation of the cyano-bridged coordination polymer network, and the presence of PEG-NH₂ at the NPS surface. Moreover, it reveals the presence of both Fe^{III} and Fe^{II} oxidation states in the structure of the NPs. Their respective formula was indeed proposed using the metals ratio given by EDS analysis, indicating the decrease of the Fe^{II}/Fe^{III} ratio with the increase of the NPs size. This observation is also confirmed by Raman spectroscopy, which indicates the increase of the amount in Fe^{II} with the size reduction. The XRD patterns confirms the formation of the $Ni_2[Fe(CN)_6]$ PBA network, and gives the values of the lattice parameter, which is close to 10.1 Å for all NPs, with a *fcc*

structure indexed with the $F\bar{4}3m$ space group. That also seems to indicate the presence of a large amount in Fe^{II} for the ultra-small NPs.

The TEM images give the size and the morphology of the NPs. Then the first approach permits to obtain ultra-small NPs with a size of 2.10 ± 0.45 nm. The second approach permits to synthesize a series of $K^+/Ni^{2+}/[Fe(CN)_6]^{3-}$ NPs ranging from 14.4 ± 1.8 nm to 177.1 ± 42.7 nm. The morphology of the NPs changes with the size. For small NPs, we observed sphere-like shape, which may be icosahedron shape, the most stable shape at such size. For larger sized NPs, the nature of the lattice, cubic for this PBA, influences the shape, leading to formation of truncated cubes. The presence of both icosahedron and cubes for 14 nm sized NPs indicates that the critical size is close to this value. TEM images also confirm the post-synthetic grafting of the NPs with PEG-NH₂ with the presence of organic material on the NPs. This is also confirmed by the DLS measurements, which show the increase of the hydrodynamic radius of the NPs with the modification of the surface state. The Zeta potential measurements indicate that the surface is negatively charged, due to the presence of $[Fe(CN)_6]^{3-}$ moieties at the surface. However, this negative value is partially modified by the PEG-NH₂ coating, indicating that the grafting is clearly incomplete.

In collaboration with the LCC, the series of the $K^+/Ni^{2+}/[Fe(CN)_6]^{3-}/PEG-NH_2$ have been characterized with ⁵⁷Fe Mössbauer spectroscopies. The data confirmed the increase of the amount in Fe^{II} at the surface of the particles with the decrease of the size. Moreover, the ⁵⁷Fe Mössbauer spectroscopy has been used to quantify it, permitting to estimate the Debye Temperature of all samples. The increase of the Debye Temperature for the ultra-small NPs reveals the increase of the rigidity with the size reduction, and the appearance of a “nano” behavior. This observation has been used in a theoretical model, permitting to model the phenomenon of the reopening of the hysteresis loop with the size reduction, for nano-objects exhibiting spin-cross over transition.

To summarize, this study clearly demonstrates the possibility to control the size of the $K^+/Ni^{2+}/[Fe(CN)_6]^{3-}$ NPs by modifying some parameters, such as the concentrations in precursors and the rate of addition. This control of the size can be extended for other PBA's NPs, such as $Ni_3[Cr(CN)_6]_2$, but not to all. Indeed, this is due to an important difference in the kinetic of the formation of the different PBA. The state of the NPs surface can also be modified, using the post-synthetic grafting step. By modulating the nature of the stabilizing agents, it is possible either to increase the stability of the dispersion in water, either to promote the dispersion in organic solvents.

The fine understanding of this system allows to use it for designing more intricate systems, such as core-shell NPs. That includes homogeneous PBA@PBA' core-shell NPs, obtained by subsequent growth, or heterogeneous structures, combining PBA and other materials, such as noble metal.

References

- 1 J. Larionova, Y. Guari, C. Sangregorio and C. Guerin, *New J. Chem.*, **2009**, 33, 1177.
- 2 E. Chelebaeva, Y. Guari, J. Larionova, A. Trifonov and C. Guerin, *Chem. Mater.*, **2008**, 20, 1367.
- 3 L. Catala, T. Gacoin, J. P. Boilot, E. Riviere, C. Paulsen, E. Lhotel, T. Mallah, *Adv. Mater.*, **2003**, 15, 826.
- 4 D. Brinzei, L. Catala, C. Mathoniere, W. Wernsdorfer, A. Gloter, O. Stephan, T. Mallah, *J. Am. Chem. Soc.*, **2007**, 129, 3778.
- 5 S. Vaucher, M. Li, S. Mann, *Angew. Chem. Int. Ed.*, **2000**, 112, 1863
- 6 L. Catala, C. Mathoniere, A. Gloter, O. Stephan, T. Gacoin, J. P. Boilot, T. Mallah, *Chem. Commun.*, **2005**, 746.
- 7 L. Catala, A. Gloter, O. Stephan, G. Rogez, T. Mallah, *Chem. Commun.*, **2006**, 1018.
- 8 Y. Guari, J. Larionova, K. Molvinger, B. Folch, C. Guerin, *Chem. Commun.*, **2006**, 2613.
- 9 B. Folch, Y. Guari, J. Larionova, C. Luna, C. Sangregorio, C. Innocenti, A. Caneschi, C. Guerin, *New J. Chem.*, **2008**, 32, 273.
- 10 M. Perrier, S. Kenouche, J. Long, K. Thangavel, J. Larionova, C. Goze-Bac, A. Lascialfari, M. Mariani, N. Baril, C. Guérin, B. Donnadiou, A. Trifonov, and Y. Guari, *Inorg. Chem.*, **2013**, 52, 13402.
- 11 M. Perrier, M. Busson, G. Massasso, J. Long, V. Boudousq, J. P. Pouget, S. Peyrottes, C. Perigaud, C. Porredon-Guarch, J. de Lapuente, M. Borrás, J. Larionova and Y. Guari, *Nanoscale*, **2014**, 6, 13425.
- 12 C.H. Li, Y. Nanba, D. Asakura, M. Okubo and D. R. Talham, *RSC Adv.*, **2014**, 4, 24955.
- 13 D. Asakura, C. H. Li, Y. Mizuno, M. Okubo, H. Zhou and D. R. Talham, *J. Am. Chem. Soc.*, **2013**, 135, 2793.
- 14 O. N. Risset, E. S. Knowles, S. Ma, M. W. Meisel and D. R. Talham, *Chem, Mater.*, **2013**, 25, 42.
- 15 D. Brinzei, L. Catala, N. Louvain, G. Rogez, O. Stephan, A. Gloter and T. Mallah, *J. Mater. Chem.*, **2006**, 16, 2593.
- 16 S. N. Gosh, *J. Inor. Nucl. Chem.*, **1974**, 36, 2465.
- 17 J. Lejeune, J. B. Brubach, P. Roy and A. Bleuzen, *C. R. Chimie*, **2014**, 17, 534.
- 18 P. Higuél, F. Villain, M. Verdaguer, E. Rivière and A. Bleuzen, *J. Am. Chem. Soc.*, **2014**, 136, 6231.
- 19 G. I. Nikishin, E. I. Troyanskii and V. A. Ioffe, *B ACAD SCI USSR CH+*, **1982**, 31 (12), 2437.

- 20 G. Félix, W. Nicolazzi, L. Salmon, G. Molnar, M. Perrier, G. Maurin-Pasturel, J. Larionova, J. Long, Y. Guari, and A. Bousseksou, *Phys. Rev. Lett.*, **2013**, *110*, 235701.
- 21 Supplementary material of (20)
- 22 K. M. Jeerage, W. A. Steen, and D. T. Schwartz, *Chem. Mater.*, **2002**, *14*, 530.
- 23 Y. Mizuno, M. Okubo, K. Kagesawa, D. Asakura, T. Kudo, H. Zhou, K. Oh-ishi, A. Okazawa, and N. Kojima, *Inorg. Chem.*, **2012**, *51*, 10311.
- 24 M. Oku, *J. Electron. Spectrosc. Relat. Phenom.*, 1994, *67*, 401.
- 25 M. Lahmani, C. Bréchinac, P. Houdy, *Les nanosciences*, Belin, **2006**, Vol.2, *Nanomateriaux et nanochimie*.
- 26 S. Xu, X. Qian, G. Li, *Mater. Res. Bull.*, **2008**, *43*, 135.
- 27 Y. Prado, L. Lisnard, D. Heurtaux, G. Rogez, A. Gloter, O. Stephan, N. Dia, E Riviere, L. Catala and T. Mallah, *Chem. Commun.*, **2011**, *47*, 1051.
- 28 L. Catala, D. Brinzei, Y. Prado, A. Gloter, O. Stephan, G. Rogez and T. Mallah, *Angew. Chem.*, **2009**, *48*, 183.
- 29 N. Dia, L. Lisnard, Y. Prado, A. Gloter, O. Stephan, F. Brisset, H. Hafez, Z. Saad, C. Mathoniere, L. Catala and T. Mallah, *Inorg. Chem.*, **2013**, *52*, 10264.
- 30 M. F Dumont, E. S. Knowles, A. Guiet, D. M. Pajerowski, A. Gomez, S. W. Kycia, M. W. Meisel and D. R. Talham, *Inorg. Chem.*, **2011**, *50*, 4295.
- 31 M. Presle, Thesis of Ecole Polytechnique, Palaiseau, France, **2011**.
- 32 V. K. LaMer and R. H. Dinegar, *J. Am. Chem. Soc.*, **1950**, *72*, 4847.

Experimental part:

The syntheses were carried out using commercially available reagents. All chemical reagents were purchased and used without further purification. Potassium ferricyanide ($K_3[Fe(CN)_6]$, 99%) and Copper nitrate trihydrate ($Cu(NO_3)_2 \cdot 3H_2O$) were purchased from Acros Organics, Poly(ethylene glycol) bis(3-aminopropyl) terminated (PEG-NH₂, Mw=1500g/mol) Nickel nitrate hexahydrate ($Ni(NO_3)_2 \cdot 6H_2O$, 98.5%) were purchased from Aldrich, Nickel(II) chloride hexahydrate ($NiCl_2 \cdot 6H_2O$, 99%) was purchased from Chimica, and Cesium chloride was purchased from Alfa Aesar.

Synthesis of 3 nm $K^+/Ni^{2+}/[Fe(CN)_6]^{3-}/PEG-NH_2$ NPs (1-1):

At room temperature, an aqueous solution of $Ni(NO_3)_2 \cdot 6H_2O$ (32 mmol, 5 mL) with 4.03 mmol of PEG-NH₂ was added to an aqueous solution of $K_3[Fe(CN)_6]$ (2.1 mmol, 5 mL) with 4.03 mmol of PEG-NH₂. After stirring for 2 hours, the solution was filtered through a filter syringe (0.45 μm). Then, the NPs were precipitated with acetone, centrifuged for 10 min, at 20000 rpm, washed twice with acetone and dried under vacuum.

Characterizations:

FT-IR (KBr, ν , cm^{-1}): $\nu(-OH)$ (coordinate water) = 3620 cm^{-1} , $\nu(-OH)$ (crystalized water) = 3407 cm^{-1} , $\nu(C-H)$ = 2920 and 2872 cm^{-1} , $\nu(C\equiv N)$ = 2163 cm^{-1} ($Fe^{III}-C\equiv N-Ni^{II}$) and 2095 cm^{-1} ($Fe^{II}-C\equiv N-Ni^{II}$), $\delta(H-O-H)$ (crystalized water) = 1610 cm^{-1} , $\nu(C-C)$ = 1458 and 1350 cm^{-1} , $\nu(C-N)$ = 1298 and 1250 cm^{-1} , $\nu(C-O)$ = 1100 cm^{-1} , $\nu(C-C)$ = 950 cm^{-1} , $\nu(Fe^{II}-CN)$ = 593 cm^{-1} , $\delta(Fe^{II}-CN)$ = 464 cm^{-1} .

EDS: 29/31/40 (K/Fe/Ni). Estimated formula: $K_{0.72}Ni[Fe^{II}(CN)_6]_{0.4}[Fe^{III}(CN)_6]_{0.37}$.

Synthesis of 3 nm $K^+/Cu^{2+}/[Fe(CN)_6]^{4-}/PEG-NH_2$ NPs (16):

At room temperature, an aqueous solution of $Cu(NO_3)_2 \cdot 3H_2O$ (1.7 mmol, 40 mL) with 0.86 mmol of PEG-NH₂ was added to an aqueous solution of $K_3[Fe(CN)_6]$ (1.14 mmol, 40 mL) with 0.86 mmol of PEG-NH₂. After stirring for 2 hours, the solution was filtered through a filter syringe (0.45 μm). Then, the NPs were precipitated with acetone, centrifuged for 10 min, at 20000 rpm, washed twice with acetone and dried under vacuum.

Characterizations:

FT-IR (KBr, ν , cm^{-1}): $\nu(-OH)$ (coordinate water) = 3588 cm^{-1} , $\nu(-OH)$ (crystalized water) = 3426 cm^{-1} , $\nu(C-H)$ = 2918 and 2888 cm^{-1} , $\nu(C\equiv N)$ = 2170 cm^{-1} ($Fe^{III}-C\equiv N-Cu^{II}$) and 2098 cm^{-1} ($Fe^{II}-C\equiv N-Cu^{II}$), $\delta(H-O-H)$ (crystalized water) = 1612 cm^{-1} , $\nu(C-C)$ = 1473, 1456 and 1349 cm^{-1} , $\nu(C-N)$ = 1298 and 1254 cm^{-1} , $\nu(C-O)$ = 1084 cm^{-1} , $\nu(C-C)$ = 946 cm^{-1} , $\nu(Fe^{II}-CN)$ = 593 cm^{-1} , $\delta(Fe^{II}-CN)$ = 493 cm^{-1} .

EDS: 13.6/33.2/53.2 (K/Fe/Cu). Estimated formula: $K_{0.25}Cu[Fe^{II}(CN)_6]_{0.39}[Fe^{III}(CN)_6]_{0.23}$.

Synthesis of 14 nm $K^+/Ni^{2+}/[Fe(CN)_6]^{3-}$ NPs (1-2):

The NPs are obtained using the same protocol than for 35 nm $KNi/[Fe(CN)_6]$ NPs with addition of CsCl (1.8 mM) in the solution of $NiCl_2 \cdot 6H_2O$.

Characterizations:

FT-IR (KBr, ν , cm^{-1}): $\nu(-OH)$ (coordinate water) = 3645 cm^{-1} , $\nu(-OH)$ (crystalized water) = 3424 cm^{-1} , $\nu(C\equiv N)$ = 2165 cm^{-1} ($Fe^{III}-C\equiv N-Ni^{II}$) and 2100 cm^{-1} ($Fe^{III}-C\equiv N-Ni^{II}$), $\delta(H-O-H)$ (crystalized water) = 1612 cm^{-1} , $\nu(Fe^{II}-CN)$ = 593 cm^{-1} , $\nu(Fe^{II}-CN)$ = 543 cm^{-1} , $\delta(Fe^{II}-CN)$ = 460 cm^{-1} , $\delta(Fe^{III}-CN)$ = 433 cm^{-1} .

EDS: 0.45/20.9/35.3/43.35 (K/Cs/Fe/Ni). Estimated formula: $K_{0.01}Cs_{0.48}Ni[Fe(CN)_6]_{0.81}$.

Synthesis of 35 nm K⁺/Ni²⁺/[Fe(CN)₆]³⁻ NPs (1-3):

At 25°C, an aqueous solution of NiCl₂·6H₂O (16 mM, 50 mL) and K₃[Fe(CN)₆] (17 mM, 50 mL) were added simultaneously to 100 mL of pure water at a 4 mL/min rate, using a syringe pump. After completion of the addition, the mixture was stirred one hour before being centrifuged at 20000 rpm during 10 minutes. The supernatant was removed and the NPs were washed with water and centrifuged once more at 20000 rpm during 10 minutes. The supernatant was removed and the NPs were washed with ethanol and centrifuged at 20000 rpm during 10 min, and finally dried under vacuum.

Characterizations:

FT-IR (KBr, ν , cm⁻¹): ν (-OH) (coordinate water) = 3644 cm⁻¹, ν (-OH) (crystalized water) = 3418 cm⁻¹, ν (C≡N) = 2166 cm⁻¹ (Fe^{III}-C≡N-Ni^{II}) and 2100 cm⁻¹ (Fe^{II}-C≡N-Ni^{II}), δ (H-O-H) (crystalized water) = 1611 cm⁻¹, ν (Fe^{II}-CN) = 592 cm⁻¹, ν (Fe^{III}-CN) = 543 cm⁻¹, δ (Fe^{II}-CN) = 461 cm⁻¹, δ (Fe^{III}-CN) = 437 cm⁻¹.

EDS: 2.6/35.55/61.85 (K/Fe/Ni). Estimated formula: K_{0.04}Ni[Fe^{II}(CN)₆]_{0.33}[Fe^{III}(CN)₆]_{0.24}.

Synthesis of 70 nm K⁺/Ni²⁺/[Fe(CN)₆]³⁻ NPs (1-4):

The NPs are obtained using the same protocol than for 35 nm KNi/[Fe(CN)₆] NPs by changing the concentration of NiCl₂·6H₂O (8 mM, 50 mL) and K₃[Fe(CN)₆] (9 mM, 50 mL) and the rate, at 1.5 mL/min.

Characterizations:

FT-IR (KBr, ν , cm⁻¹): ν (-OH) (coordinate water) = 3646 cm⁻¹, ν (-OH) (crystalized water) = 3417 cm⁻¹, ν (C≡N) = 2167 cm⁻¹ (Fe^{III}-C≡N-Ni^{II}) and 2100 cm⁻¹ (Fe^{II}-C≡N-Ni^{II}), δ (H-O-H) (crystalized water) = 1611 cm⁻¹, ν (Fe^{II}-CN) = 592 cm⁻¹, ν (Fe^{III}-CN) = 541 cm⁻¹, δ (Fe^{II}-CN) = 460 cm⁻¹, δ (Fe^{III}-CN) = 438 cm⁻¹.

EDS: 2.7/37.2/60.1 (K/Fe/Ni). Estimated formula: K_{0.04}Ni[Fe^{II}(CN)₆]_{0.19}[Fe^{III}(CN)₆]_{0.43}.

Synthesis of 110 nm K⁺/Ni²⁺/[Fe(CN)₆]³⁻ NPs (1-5):

The NPs are obtained using the same protocol than for 35 nm KNi/[Fe(CN)₆] NPs by changing the concentration and volume of NiCl₂·6H₂O (4 mM, 100 mL) and K₃[Fe(CN)₆] (4.5 mM, 100 mL), added simultaneously to a 200 mL of pure water at a 1.5 mL/min rate.

Characterizations:

FT-IR (KBr, ν , cm⁻¹): ν (-OH) (coordinate water) = 3644 cm⁻¹, ν (-OH) (crystalized water) = 3417 cm⁻¹, ν (C≡N) = 2167 cm⁻¹ (Fe^{III}-C≡N-Ni^{II}) and 2100 cm⁻¹ (Fe^{II}-C≡N-Ni^{II}), δ (H-O-H) (crystalized water) = 1611 cm⁻¹, ν (Fe^{II}-CN) = 592 cm⁻¹, ν (Fe^{III}-CN) = 544 cm⁻¹, δ (Fe^{II}-CN) = 460 cm⁻¹, δ (Fe^{III}-CN) = 436 cm⁻¹.

EDS: 2.7/37.05/59.8 (K/Fe/Ni). Estimated formula: K_{0.04}Ni[Fe^{II}(CN)₆]_{0.18}[Fe^{III}(CN)₆]_{0.44}.

Synthesis of 200 nm K⁺/Ni²⁺/[Fe(CN)₆]³⁻ NPs (1-6):

The NPs are obtained using the same protocol than for 105 nm KNi/[Fe(CN)₆] NPs by changing the rate at 0.5 mL/min.

Characterizations:

FT-IR (KBr, ν , cm^{-1}): $\nu(\text{-OH})$ (coordinate water) = 3644 cm^{-1} , $\nu(\text{-OH})$ (crystalized water) = 3417 cm^{-1} , $\nu(\text{C}\equiv\text{N})$ = 2167 cm^{-1} ($\text{Fe}^{\text{III}}\text{-C}\equiv\text{N-Ni}^{\text{II}}$) and 2100 cm^{-1} ($\text{Fe}^{\text{II}}\text{-C}\equiv\text{N-Ni}^{\text{II}}$), $\delta(\text{H-O-H})$ (crystalized water) = 1611 cm^{-1} , $\nu(\text{Fe}^{\text{II}}\text{-CN})$ = 592 cm^{-1} , $\nu(\text{Fe}^{\text{III}}\text{-CN})$ = 544 cm^{-1} , $\delta(\text{Fe}^{\text{II}}\text{-CN})$ = 463 cm^{-1} , $\delta(\text{Fe}^{\text{III}}\text{-CN})$ = 438 cm^{-1} .

EDS: 2.4/37.65/60.55 (K/Fe/Ni). Estimated formula: $\text{K}_{0.04}\text{Ni}[\text{Fe}^{\text{II}}(\text{CN})_6]_{0.21}[\text{Fe}^{\text{III}}(\text{CN})_6]_{0.4}$.

Post-synthetic grafting of $\text{K}^+/\text{Ni}^{2+}/[\text{Fe}(\text{CN})_6]^{3-}$ NPs with PEG-NH₂

The NPs were grafted with PEG-NH₂ ($M_w=1500 \text{ g/mol}$) with a stoichiometry 1:0.5 in water for 24 hours, before being centrifuged at 20000 rpm during 10 minutes. The supernatant was removed and the NPs were washed with water and centrifuged again at 20000 rpm during 10 minutes. The supernatant was removed and the NPs were washed with ethanol and centrifuged at 20000 rpm during 10 min and were dried under vacuum.

Characterizations:

FT-IR (KBr, ν , cm^{-1}): $\nu(\text{-OH})$ (coordinate water) = 3641 cm^{-1} , $\nu(\text{-OH})$ (crystalized water) = 3424 cm^{-1} , $\nu(\text{C-H})$ = 2926 and 2853 cm^{-1} , $\nu(\text{C}\equiv\text{N})$ = 2165 cm^{-1} ($\text{Fe}^{\text{III}}\text{-C}\equiv\text{N-Ni}^{\text{II}}$) and 2100 cm^{-1} ($\text{Fe}^{\text{II}}\text{-C}\equiv\text{N-Ni}^{\text{II}}$), $\delta(\text{H-O-H})$ (crystalized water) = 1612 cm^{-1} , $\nu(\text{C-C})$ = 1468 and 1401 cm^{-1} , $\nu(\text{C-N})$ = 1257 cm^{-1} , $\nu(\text{C-O})$ = 1100 cm^{-1} , $\nu(\text{Fe}^{\text{II}}\text{-CN})$ = 593 cm^{-1} , $\nu(\text{Fe}^{\text{III}}\text{-CN})$ = 543 cm^{-1} , $\delta(\text{Fe}^{\text{II}}\text{-CN})$ = 460 cm^{-1} , $\delta(\text{Fe}^{\text{III}}\text{-CN})$ = 433 cm^{-1} .

EDX: 5.25/36.55/58.2 (K/Fe/Ni). Estimated formula: $\text{K}_{0.09}\text{Ni}[\text{Fe}^{\text{II}}(\text{CN})_6]_{0.2}[\text{Fe}^{\text{III}}(\text{CN})_6]_{0.42}$.

CHAPITRE III

-

Synthesis and study of core-shell
 $\text{Au}@K^+/\text{Ni}^{2+}/[\text{Fe}^{\text{II}}(\text{CN})_6]^{4-}$ NPs

III.1 Introduction

Previously we have developed an approach consisting in the self-assembly reaction to synthesize PBA NPs of different sizes with and without using stabilizers, given as $K^+/Ni^{2+}/[Fe^{III}(CN)_6]^{3-}$. For this system, the size control is performed by varying the reaction parameters, such as the precursors' addition rate and their respective concentrations. Moreover, ultra-small NPs (with a size smaller than 10 nm) are obtained by using a stabilizing agent, PEG-NH₂ which prevents the infinite growth of the PBA network by coordinating the transition metal ions. This leads us to consider the possibility to design more complex systems, such as metal core-PBA shell NPs for designing multifunctional nano-objects.

The design of core-shell nano-heterostructures, combining at least two inorganic materials meeting at their interface is one of the main subjects of research devoted to nanoscience during the last years. Such intricate systems present exciting physical and chemical properties, which may result from the association of the intrinsic properties of each constitutive material, or may exhibit an appearance of a new phenomenon or a synergistic effect. These effects strongly depend on the interface between the core and the shell, their structural and chemical compatibilities, their reactivity and their electronics properties. Moreover, the final hybrid material, by combining several properties inherent from their respective constituents, may present a multifunctionality and thus a great interest for a large range of applications, including electronic, photonic, sensors, light emitting devices, catalysis, biology and medicine. In this line of thought, a large range of nano-heterostructures with various core@shell combinations, exhibiting advanced catalytic¹, electronic², pharmaceutical applications³ or biomedical applications⁴ have been reported, as described in the first chapter.

A particular attention has been paid to the synthesis of various heterostructures involving gold as the core due to its exciting optical properties, the Surface Plasmon Resonance (SPR)⁸. Such phenomenon arises from the resonance of conduction electrons driven by an electromagnetic field, and the SPR response is dependent on different parameters, such as size and shape of the nano-objects⁸⁻¹⁰. By designing Au core@shell heterostructures, it may be possible to tune the position and the intensity of the spectral SPR responses by varying the shell nature, its electronic properties and its thickness¹¹⁻¹². Furthermore, the design of magneto-plasmonic nano-heterostructures¹³⁻²⁵ combining both, a gold core and a metal or a metal oxide shell may lead to exciting magneto-optical synergistic effects, such as a Kerr effect enhancement, spin polarization transfer and others²¹⁻²⁸. However, they are highly controversial and new materials are highly needed to confirm and explain these phenomena.

On the other hand, coordination polymer NPs, including Metal Organic Framework (MOFs)^{29,30} or Prussian Blue analogous (PBA)³¹, have attracted a great deal of attention for the last decade. This interest is mainly due to the intrinsic characteristics of these materials, such as flexibility of molecular structures, tunable properties and often soft

synthetic routes through self-assembly reactions³². Thus, several heterostructured systems combining inorganic materials with these coordination polymers have been investigated. Multiple metal NPs were embedded in various porous coordination polymers or MOF matrixes using diverse synthetic approaches, as already described. These metal@MOFs NPs are interesting for potential applications, such as catalysts with enhancing durability, selectivity or reactivity. Moreover, several examples of the combination between the gold core and the MOFs shell have been reported, as described in the first chapter. However, note that the design of core-shell heterostructures presenting a single inorganic NP coated by a uniform and a well-defined coordination polymer layer to give strictly individual nano-heterostructures is extremely rare^{33,34} and represents a real challenge.

Then, in this chapter, we describe a new and rational synthetic approach for the design of a single-layer Au@K⁺/Ni²⁺/[Fe^{II}(CN)₆]⁴⁻ NPs³⁵. This approach consists in taking advantage of the nature of the PBA, *i.e.* a cyano-bridged coordination polymer, to grow a layer at the surface of cyanide-stabilized gold NPs. The previous chapter allowed us a fine understanding on the K⁺/Ni²⁺/[Fe^{III}(CN)₆]³⁻ PBA NPs, for this reason we have chosen this one for the shell growth at the gold surface. Note that, only few examples of the combination of gold and PB nano-heterostructures have been reported, however these heterostructures are poorly-defined. The obtained core-shell heterostructures were characterized using different techniques with a special emphasis given on the mechanism of the shell growth at the gold surface. The control of the size of both, the gold core and the PBA layer by different parameters, including temperature and the concentration of molecular precursors added, was performed. The variations in the gold core precursors and of the Ni^{II}[Fe^{II}(CN)₆] PBA precursors were investigated, just as the variation of the PBA used for the shell, in order to extend the approach to others PBA. Finally, the core-shell Au@K⁺/Ni²⁺/[Fe^{II}(CN)₆]⁴⁻ NPs were used to design hollow PBA NPs by Au core dissolution.

III.2 Synthesis and characterization of Au@K⁺/Ni²⁺/[Fe^{II}(CN)₆]⁴⁻ NPs

The synthesis of Au@K⁺/Ni²⁺/[Fe^{II}(CN)₆]⁴⁻ NPs (sample 2) was performed by using a two-step approach, consisting in: 1) the synthesis of the cyanide-stabilized gold NPs in aqueous solution,³⁶ and 2) the subsequent time-controlled growth of the coordination polymer shell at the surface of these gold NPs (figure 1). Firstly, the primary gold NPs were obtained in pure water by reduction of the dicyanoaurate precursor [Au(CN)₂]⁻ with potassium borohydride at 25°C under vigorous stirring. This reaction is realized without any stabilizers and only the cyanide ions present at the NPs surface stabilize the Au particles avoiding their aggregation. The appearance of a characteristic red color indicates the formation and the gradual growth of the Au NPs³⁶ (figure 1). The NPs are stable in solution for few hours; however they readily dissolve to reform the gold dicyanoaurate complex, due to an important affinity between the gold and the free cyanide ions still present in the solution. Indeed, in the presence of dioxygen in the basic aqueous media, the Au⁰ NPs are oxidized according to the etching process³⁷ (which corresponds to the equation: $\text{Au} + 8 \text{CN}^- + \text{O}_2 + 2 \text{H}_2\text{O} \rightarrow 4 [\text{Au}(\text{CN})_2]^- + 4 \text{OH}^-$) to reform the [Au(CN)₂]⁻ which is the most stable Au^I species ($K = 10^{37} \text{ M}^{-2}$)³⁷. The dissolution is visible with a gradual decrease of the intense ruby color, time window in which the shell can grow at the surface of the gold NPs. Then, 20 min after formation of the Au NPs, two aqueous solutions, K₃[Fe(CN)₆] and NiCl₂·6H₂O, were directly added dropwise in the gold NPs solution, to start the formation of the cyano-bridged coordination shell. The control of the precursors' addition rate (2mL/h) by using a syringe pump is essential to obtain well-defined core-shell NPs and to control their size. Indeed, a slow addition permits the growth of the PBA network directly at the gold NPs surface and avoids any side nucleation of K⁺/Ni²⁺/[Fe^{III}(CN)₆]³⁻ NPs. After completing the addition (5h), the purple solution of the Au@K⁺/Ni²⁺/[Fe^{II}(CN)₆]⁴⁻ NPs (figure 2) was maintained under stirring 1h to complete the formation of the coordination polymer layer. Then the core-shell NPs were recovered by centrifugation, washed with water and ethanol, and dried under vacuum. The obtained solid appears as a purple powder, with a yield of 52 % (12 mg).

The formation of these heterostructures is mainly conditioned by the control of the gold NPs formation, which is the decisive step to obtain well-defined and uniform sized NPs. Indeed, these NPs are used as seeds to grow the PBA shell, and while the formation of the cyano-bridged coordination polymer layer is controlled by using low precursors concentration and slow addition rate, the experiments have revealed that the synthesis of such gold NPs is very sensitive to several parameters: i) pH of the aqueous solution; ii) the temperature of the media; iii) the light exposure, and iv) the presence of dissolved dioxygen.

First, pH should be fixed at 5 by adding hydrochloric acid. At the beginning of the reaction, pH value increases due to the formation of OH⁻ ions during the oxidation of the KBH₄ and the solution color became yellow or dark purple instead of ruby color which is indicative of NPs aggregation.

Secondly, the temperature has an important role to control the reaction kinetic and especially governs the size of the gold NPs. To ensure the reproducibility of the synthesis, whatever the room temperature, the temperature of the aqueous media is controlled from the starting of the reaction to the end, 6 hours later, using a jacketed bowl connected to a cryostat/thermostat set to 25°C.

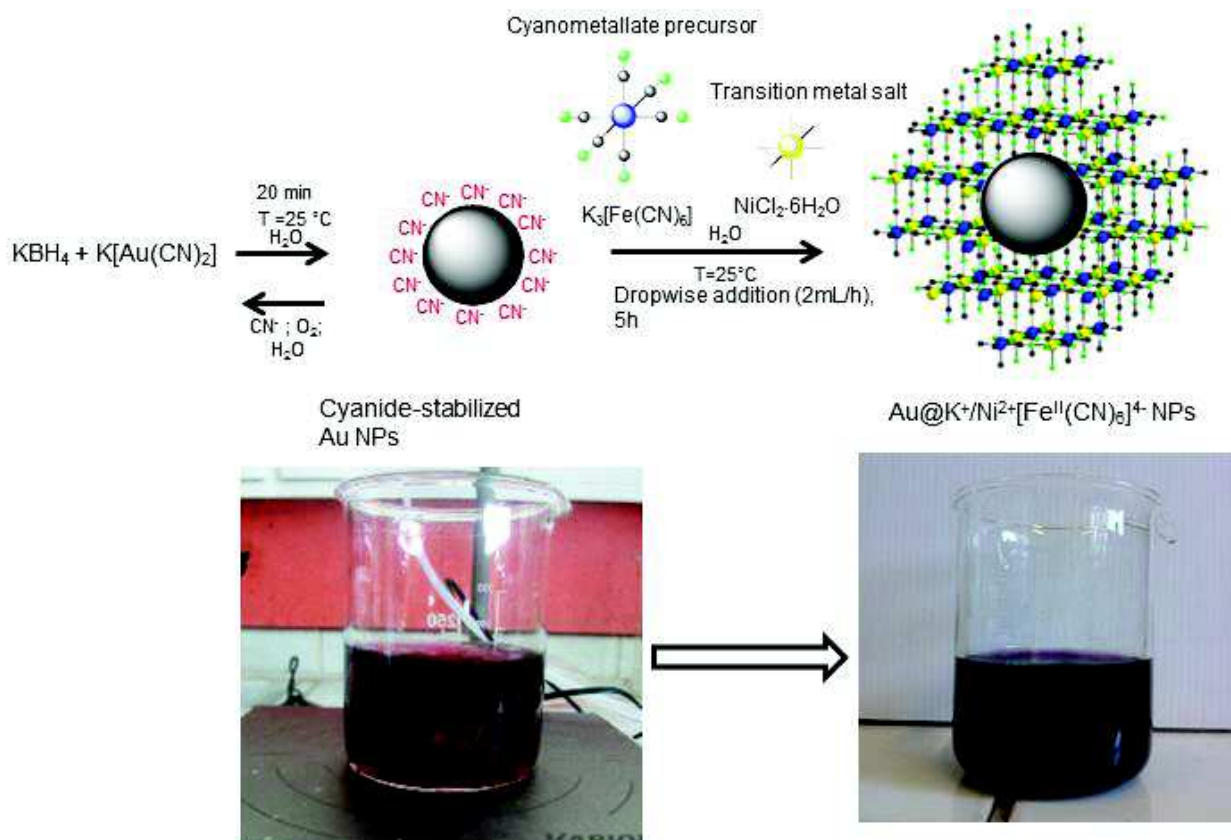


Figure 1: Schematic representation of the synthesis of the Au@K⁺/Ni²⁺/[Fe^{II}(CN)₆]⁴⁻ NPs with the two successive steps. Evolution of the color of the solution before and after the formation of the PBA layer on the gold NPs is illustrated.

Thirdly, several attempts were performed using deoxygenate water, leading to a slower appearance of the ruby color with a maximum coloration at approximately one hour, indicating the important role of dioxygen on the reaction kinetic. Moreover, even if the gold (I) precursor is less sensitive than gold(III) precursors, the solution must be placed out of sunlight to avoid any reduction of the dicyanoaurate precursor $[\text{Au}(\text{CN})_2]$ to Au(0), which can be observed by the presence of few little gold specks in solution.

The obtained core-shell NPs were characterized by IR spectroscopy. The IR spectrum confirmed the formation of the cyano-bridged network with a single broad band observed in the cyanide stretching region, located at 2094 cm^{-1} , which is characteristic of the $\text{Fe}^{\text{II}}-\text{C}\equiv\text{N}-\text{Ni}^{\text{II}}$ linkage (figure 2)³⁸⁻⁴³. The absence of the typical band expected at 2165 cm^{-1} corresponding to the $\text{Fe}^{\text{III}}-\text{C}\equiv\text{N}-\text{Ni}^{\text{II}}$ reveals the reduction of the $[\text{Fe}^{\text{III}}(\text{CN})_6]^{3-}$ cyanometallate moiety to $[\text{Fe}^{\text{II}}(\text{CN})_6]^{4-}$ during the shell growth process⁴². This effect can be explained by the presence of residual reducing agent KBH_4 in the reaction mixture ($([\text{Fe}^{\text{III}}(\text{CN})_6]^{3-}/[\text{Fe}^{\text{II}}(\text{CN})_6]^{4-}) = 0.36 \text{ V}$; $(\text{B}(\text{OH})_4^-/\text{BH}_4^-) = -1.24 \text{ V}$). This reduction is also confirmed by the presence of two bands in the metal-carbon bond region (figure 2)^{42,43}. The metal-carbon stretching vibration corresponding to the $\text{Fe}^{\text{II}}-\text{CN}$ linkage is observed at 586 cm^{-1} , the metal-carbon bending band attributed to the $\text{Fe}^{\text{II}}-\text{CN}$ at 461 cm^{-1} . No trace of

a $\text{Fe}^{\text{III}}\text{-CN}$ bending band, expected at 440 cm^{-1} is detected in this region, also indicating the presence of only Fe^{II} ions in the coordination polymer shell.

The presence of crystallized water molecules, involved in a hydrogen-bonded network, is detected with the presence of a broad band at 3410 cm^{-1} , characteristic of $\nu(\text{-OH})$ stretching vibrations⁴³ (figure 2) and an intense band localized at 1622 cm^{-1} , corresponding to the bending vibration of H-O-H linkage. A shoulder, at 3600 cm^{-1} , can be attributed to the water molecules coordinated to the Ni^{2+} ions in the coordination polymer shell, due to the absence of a part of the hexacyanoferrate moieties⁴³. This observation indicates that the structure of the PBA shell for $\text{Au@K}^+/\text{Ni}^{2+}/[\text{Fe}^{\text{II}}(\text{CN})_6]^{4-}$ NPs presents several vacancies, as observed for $\text{K}^+/\text{Ni}^{2+}/[\text{Fe}(\text{CN})_6]^{3-}$ NPs.

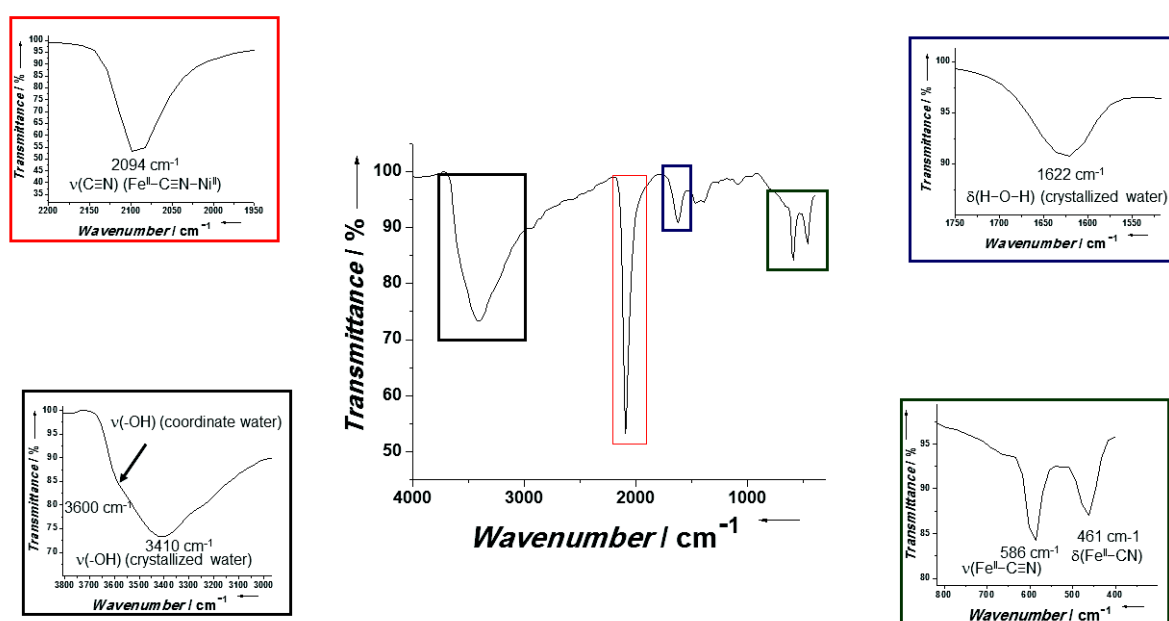


Figure 2: IR spectrum of the core-shell $\text{Au@K}^+/\text{Ni}^{2+}/[\text{Fe}^{\text{II}}(\text{CN})_6]^{4-}$ NPs. Inset, magnifications of $3700\text{-}3000\text{ cm}^{-1}$ region (black), $2200\text{-}2000\text{ cm}^{-1}$ region (red), $1700\text{-}1500\text{ cm}^{-1}$ region (blue) and $700\text{-}400\text{ cm}^{-1}$ region (green).

To complete the informations given by the IR spectroscopy, Raman spectroscopy was performed. The spectra show two bands located at 2106 cm^{-1} and at 2142 cm^{-1} , which are characteristic of the stretching vibration of the $\text{Fe}^{\text{II}}\text{-C}\equiv\text{N-Ni}^{2+}$ linkage⁴⁴ (figure 3). No band at 2190 cm^{-1} , characteristic of the $\text{Fe}^{\text{III}}\text{-C}\equiv\text{N-Ni}^{\text{II}}$ linkage is observed, confirming the reduction of all $[\text{Fe}^{\text{III}}(\text{CN})_6]^{3-}$ in $[\text{Fe}^{\text{II}}(\text{CN})_6]^{4-}$ moieties. In the metal-carbon stretching region, the band located at 250 cm^{-1} may be observed which corresponds to the $\text{Fe}^{\text{II}}\text{-C}$ stretching vibrations, confirming the presence of $[\text{Fe}^{\text{II}}(\text{CN})_6]^{4-}$ moieties⁴⁵. Another band visible at 388 cm^{-1} may be attributed to the $\text{Au}^{\text{I}}\text{-CN}$ linkage, corresponding to the anchoring bond at the interface gold core/PBA shell⁴⁷. That may indicate that the formation of the PBA shell on the gold NPs occurs by anchoring the cyanide coordinated metal (Ni^{2+}) at the interface with the formation of $\text{Au-CN-M}^{\text{II}}$ bond.

The composition for the $\text{Au@K}^+/\text{Ni}^{2+}/[\text{Fe}^{\text{II}}(\text{CN})_6]^{4-}$ NPs was determined by elemental analysis: 41.3 wt % for Au, 9.11 wt % for K, 11.4 wt % for Ni, 8.67 wt % for Fe, 11.2 wt% for C, 13.1 wt% for N and 0.65 wt% for H. Then the formula for core-shell NPs is deduced, to be $\text{Au}_{1.08}@\text{K}_{1.20}\text{Ni}[\text{Fe}(\text{CN})_6]_{0.80}$.

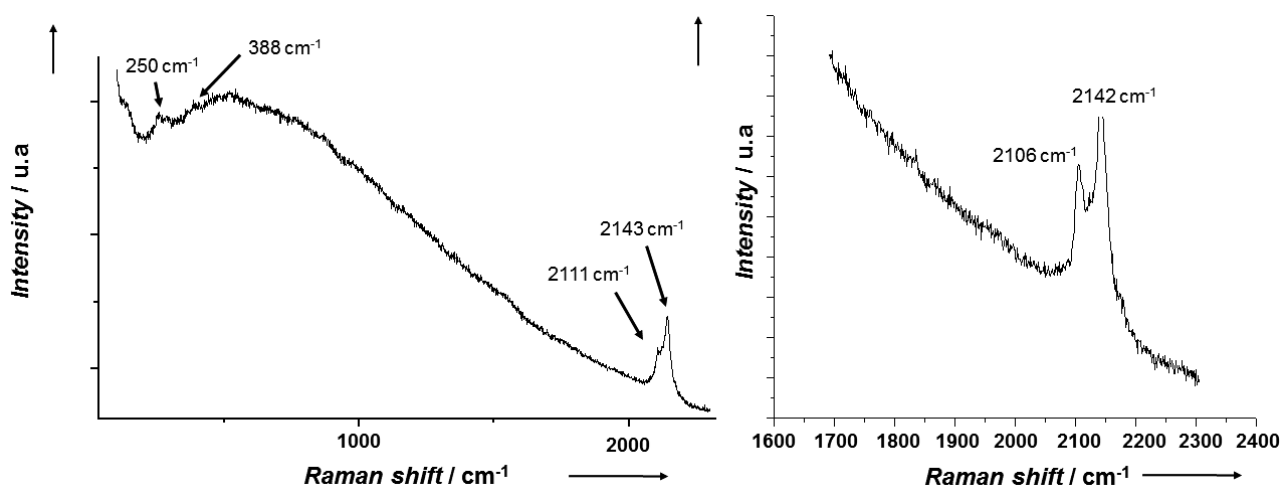


Figure 3: Left: Raman spectrum of core-shell $\text{Au@K}^+/\text{Ni}^{2+}/[\text{Fe}^{\text{II}}(\text{CN})_6]^{4-}$ NPs. Right: Raman spectrum performed in the cyanide stretching region with a high definition.

The formation of the targeted heterostructure is corroborated by powder X-ray diffraction (PXRD) pattern, with the presence of peaks attributed for both, gold and $\text{Ni}_2[\text{Fe}^{\text{II}}(\text{CN})_6]$ PBA structures (figure 4). The PXRD pattern exhibits peaks at 38.2, 44.4, 64.7 and 77.7°, corresponding to the *fcc* gold metal structure (00-004-0784). They are indexed in the space group $Fm\bar{3}m$, with a cell parameter $a_{\text{gold}} = 4.08 \text{ \AA}$. The Scherrer formula permits to calculate the size of the crystalline domain. The value of the peak position and the full width at half maximum for a determined peak gives an average value of approximately 15 nm for the gold. Moreover, peaks are observed at 17.7, 25.1, 37.7, 51.2, 55.6 and 58.9°, characteristic of $\text{Ni}_2[\text{Fe}^{\text{II}}(\text{CN})_6]$ structure, and indexed in the $F4-3m$ space group (01-075-0037), with a cell parameter of $a_{\text{NiFe}} = 10.07 \text{ \AA}$. Using the Scherrer formula, a crystalline domain size of approximately 26 nm is estimated, on the first peak corresponding to the PBA pattern (d_{200} reflection).

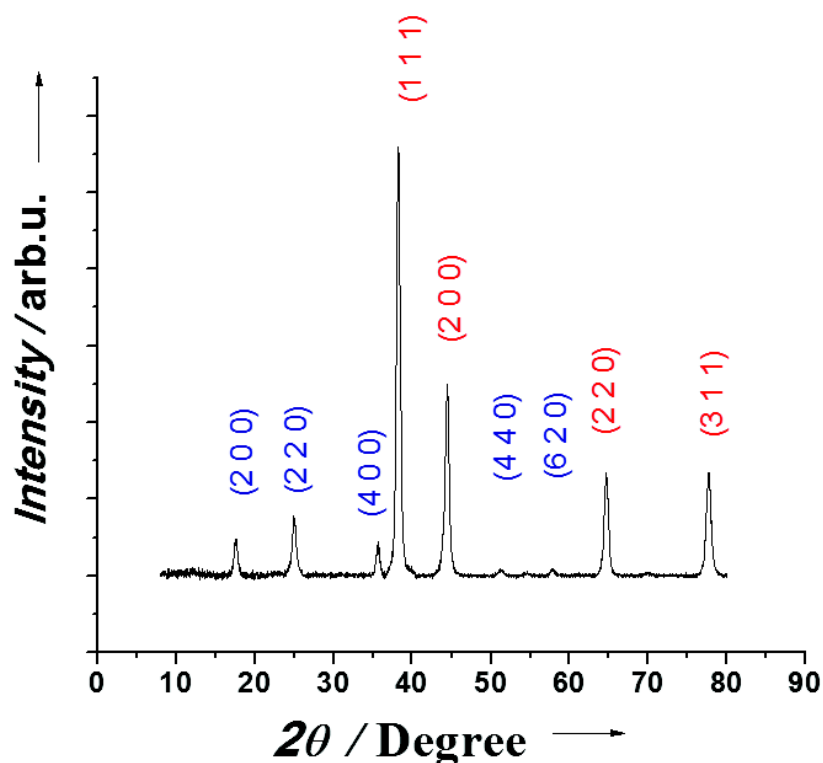


Figure 4: Room temperature PXRD pattern for the Au@K⁺/Ni²⁺/[Fe^{II}(CN)₆]⁴⁻ NPs. Miller indices (h k l) are related to the gold phase in red and PBA in blue.

The formation of Au@K⁺/Ni²⁺/[Fe^{II}(CN)₆]⁴⁻ heterostructures is clearly confirmed by Transmission Electronic Microscopy (TEM) and High Resolution Transmission Electronic Microscopy (HRTEM) measurements. The images show well-defined core-shell NPs uniform in size and shape, with the presence of the gold core, denser and therefore more contrasting, in the center of the structure, and the PBA shell (figure 5). Especially, we observed that each gold NP is coated by a regular coordination polymer shell. We observed that 97% of the NPs in the samples are core-shell NPs, which proves that the formation of the heterostructures is really well-controlled. The size of the gold core and the PBA shell is given by the size distribution performed from the TEM images (figure 5). We obtain for the core a mean diameter of 19.5 ± 4.3 nm, which is consistent with the value obtained from PXRD. All the heterostructures have a diameter of 52.4 ± 8.6 nm. Thus the thickness of the K_{1.20}Ni[Fe(CN)₆]_{0.80} shell has a size of 16.6 ± 2.7 nm.

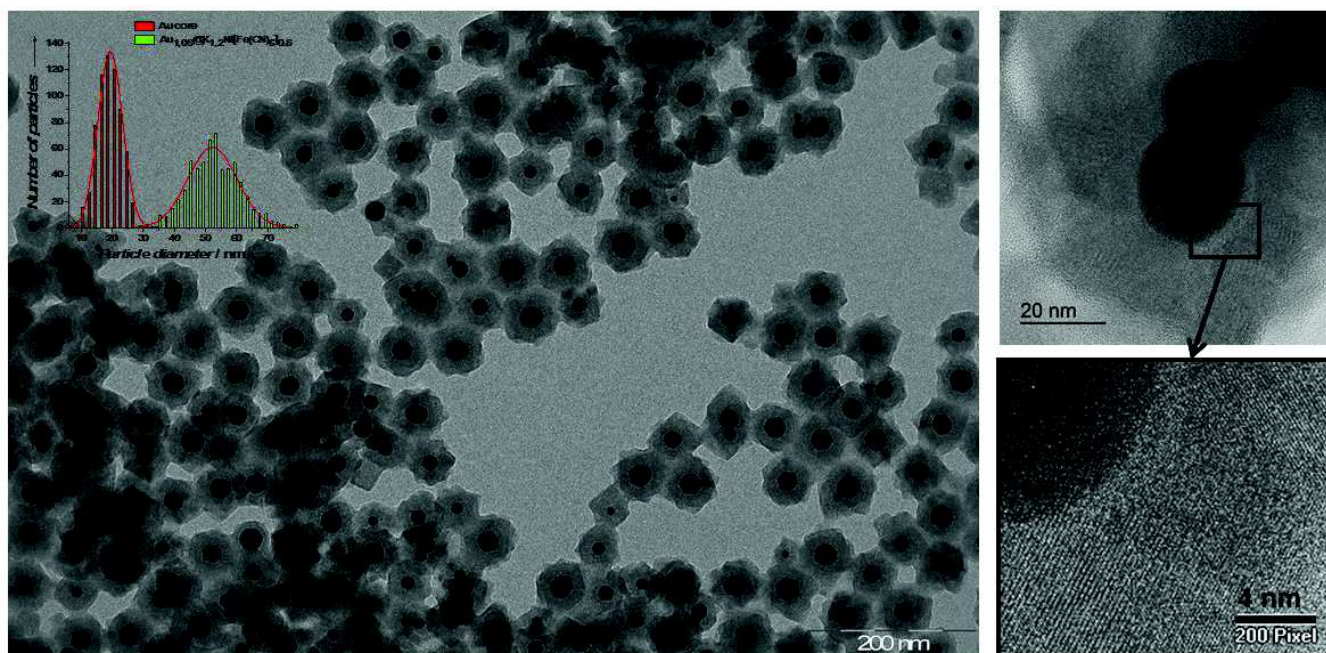


Figure 5: Left: TEM image of the core-shell Au@K⁺/Ni²⁺/[Fe^{II}(CN)₆]⁴⁻. Inset, size distribution of the whole NPs and the gold core. Right: the HRTEM image (up) and magnification of a part of the NP to show the lattice planes of the different materials (down).

The shape of the core-shell NPs is relatively complex, as shown on TEM, HRTEM images and by Scanning Transmission Electronic Microscopy in High Angle Annular Dark Field mode (STEM-HAADF) (Figures 6 and 7). The shape of the gold core is not really spherical, but presents several facets. A three-dimensional reconstruction of a core-shell NPs was performed using HRTEM in tomography mode (figure 7). That has revealed a particular shape for the PBA shell, which appeared rather as a result of several cubic parts interlocked to form the faceted cube. By the way, it is rational to think that the faceted shape of the layer is induced by the shape of the gold core. HRTEM study at the interface between the two materials is currently underway.

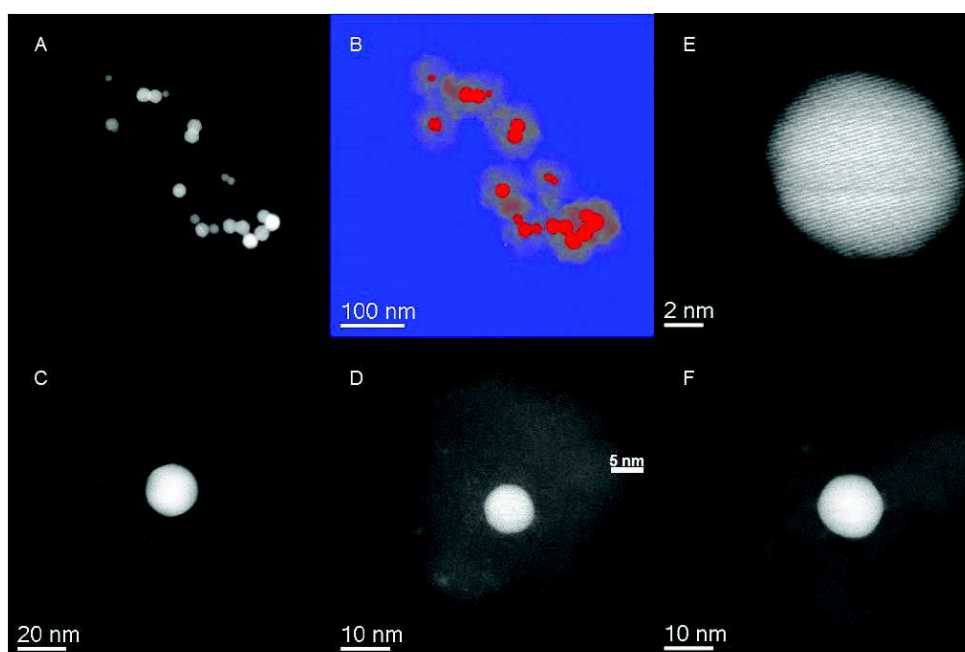


Figure 6: Scanning Transmission Electronic Microscopy – High Angle Annular Dark field (STEM-HAADF) images of a collection of core@shell Au@K⁺/Ni²⁺/[Fe^{II}(CN)₆]⁴⁻ NPs (A and B) and an individual one (C and D). Right, magnifications showing the lattice structures of the gold core (E) and the PBA layer (F).

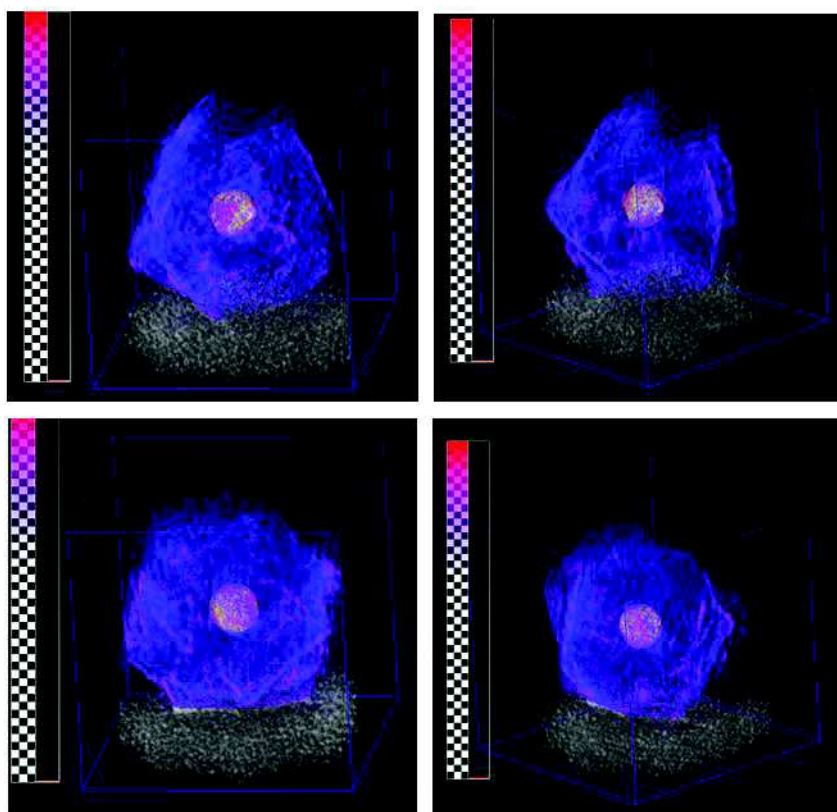


Figure 7: Images of the 3D reconstruction obtained in HRTEM in tomography modes, revealing the different facets of the PBA layer.

Structural informations are also given by TEM, HRTEM and STEM-HAADF analyses. Indeed, it is possible to observe the lattice plane of the gold and the coordination polymer shell structures (figures 6 and 7). Using TEM, a Selected Area Electron Diffraction (SAED) pattern is realized on an individual NP (figure 8). The most intense diffraction lines are attributed to a crystalline phase of both gold and $\text{Ni}_2[\text{Fe}(\text{CN})_6]$, confirming the results obtained from PXRD.

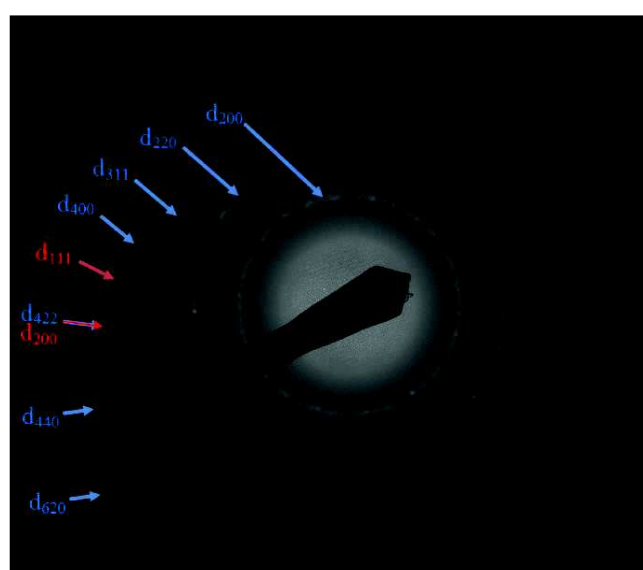


Figure 8: Single Area Electron Diffraction (SAED) on an individual core@shell $\text{Au}@K^+/\text{Ni}^{2+}/[\text{Fe}^{\text{II}}(\text{CN})_6]^{4-}$ NPs with corresponding Miller indices d_{hkl} in red for the gold core and d_{hkl} in blue for the $\text{Ni}_2[\text{Fe}^{\text{II}}(\text{CN})_6]$ shell.

TEM images gave us the dimensions of the Au@K⁺/Ni²⁺/[Fe^{II}(CN)₆]⁴⁻ NPs. However, due to the preparing method of the samples by deposition of a single drop of the NPs dispersed in water on the TEM grid, the NPs appear aggregated. Then it is necessary to characterize the quality of the dispersion of the NPs in water. This is possible by using Dynamic Light Scattering (DLS), which permits the access to the size dispersion in solution and bring informations about the hydrodynamic diameter of the particle. On the other hand, informations on the surface state can be obtained by Zeta potential measurements which characterizes the electrical charges present at the surface of colloidal suspensions. This charge is due to the presence of the water molecules and the counter-ions around the particles. The value of the Zeta potential can bring informations about the nature of the ions at the surface, and the stability of the dispersion.

Then, we measured the size and the Zeta potential of both the gold NPs and the core-shell Au@K⁺/Ni²⁺/[Fe^{II}(CN)₆]⁴⁻ NPs. The measures on the gold NPs were performed on the freshly synthesized NPs and 0.2 mL was taken off the reaction media at 20 min and diluted in water. For the Au@K⁺/Ni²⁺/[Fe^{II}(CN)₆]⁴⁻ NPs, 2-3 mg of the powder were dispersed in 5 mL of water and sonicated until obtaining a solution without any visible aggregate.

The DLS measurements show for gold NPs a majority peak at 48.3 ± 26.1 nm, corresponding to the hydrodynamic diameter of the gold NPs; the peak observed at low size seems to be an artefact, being below the detection limit of the device (figure 9, **1**). For the core-shell NPs, a single peak is observed for a value of the hydrodynamic diameter at 190 ± 74 nm (figure 9, **2**). For both samples, the presence of only one intense peak proves the narrow dispersion of the particle's size in aqueous solution. Comparatively to the TEM size (19.5 ± 4.3 nm for gold core and 52.4 ± 8.6 nm for the core-shell NPs), the sizes obtained by DLS measurements give the hydrodynamic diameter, which is larger than the size of the particles, because this takes into account the volume of water close to the particle, and the counter-ions permitting the equilibrium of the electrostatic charges, with their respective solvated water molecules (figure 10). However, the refractive indexes of the material measured must also be taken in account to obtain an indicative value, and for the PBA, they are unknown. Then the refractive index used was the index of gold. Consequently, the value of hydrodynamic diameter given by DLS for the Au@K⁺/Ni²⁺/[Fe^{II}(CN)₆]⁴⁻ NPs should be considered as an indicative information, the most important being the size dispersion, revealing no formation of large aggregates.

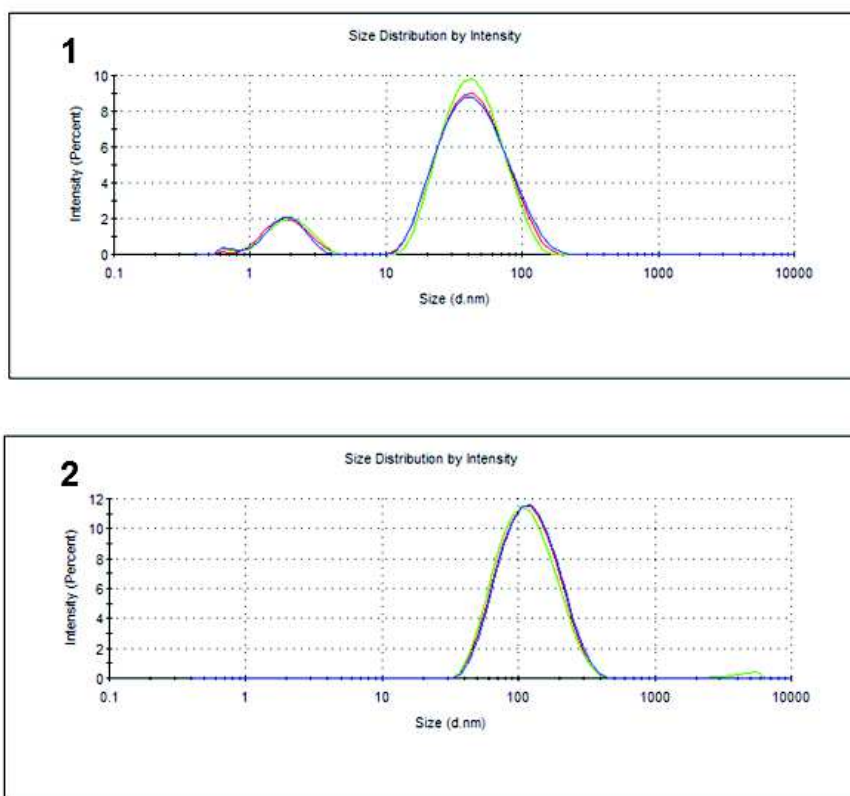


Figure 9: Size distribution of the hydrodynamic radius given by DLS measurements for gold NPs (1) and core-shell Au@K⁺/Ni²⁺/[Fe^{II}(CN)₆]⁴⁻ NPs (2).

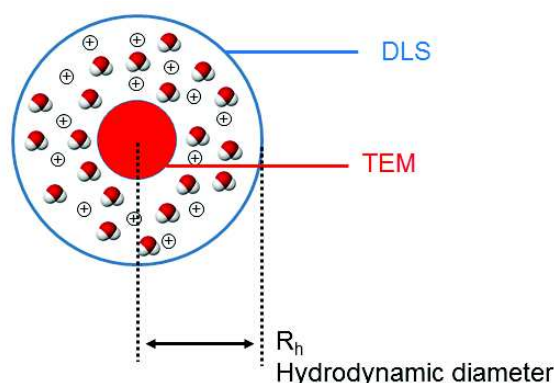


Figure 10: Schematic representation of the hydrodynamic diameter of a particle.

The Zeta potential on the gold has a mean value of -33.9 ± 7.0 mV, indicating an important density of negative charges on their surface (figure 11, 1). That clearly proves the presence of cyanide ions coordinated to the gold surface and thus stabilizing the NPs in aqueous solution, as it will be observed by Raman spectroscopy of the gold NPs, described later. These cyanide ions may be used as anchoring points permitting the formation of the PBA layer at the interface by coordinating the metal precursors of the cyano-bridged coordination polymer. The Zeta potential of the Au@K⁺/Ni²⁺/[Fe^{II}(CN)₆]⁴⁻ is at -23.6 ± 4.3 mV, which is in accordance with the values generally observed for such systems⁴⁷, revealing a negative charge less important than the mean value of the cyanide-stabilized gold NPs (figure 11, 2). This may be explained by the lower density of the cyanide ions at the surface due to the coating of the gold surface by the PBA layer;

however the surface remains negatively charged, which is in agreement with the presence of the $[\text{Fe}(\text{CN})_6]^{3-}$ moieties at the surface of the coordination polymer network.

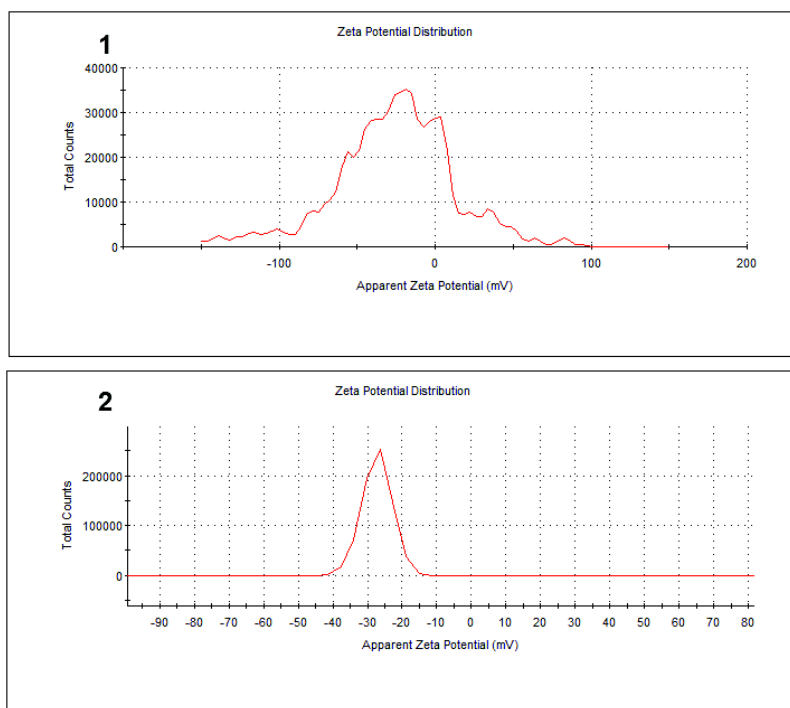


Figure 11: Zeta potential spectra of gold NPs (1) and core-shell Au@K⁺/Ni²⁺/[Fe^{II}(CN)₆]⁴⁻ NPs (2).

The optical properties of the core-shell Au@K⁺/Ni²⁺/[Fe^{II}(CN)₆]⁴⁻ NPs have been investigated using UV-Visible spectroscopy (UV-Vis). They exhibit an intense surface plasmon resonance (SPR) absorption band in the visible region, located at 540 nm, due to the presence of the gold core (figure 12). Comparatively, the red-color solution of the uncoated gold NPs displays a similar intense SPR band, but the maximum absorption wavelength is located at 520 nm⁹. It is important to note that the exact position and the width of this band is extremely sensitive to any perturbation of the gold surface, and in particular to the shape and the size of the NPs^{8,10}. The red shift effect of SPR band in the case of the Au core-optically transparent shell was previously predicted by the Mie theory⁸ and already observed for spherical gold NPs coated with a thin layer (< 60nm) of silica¹⁰, ZrO₂ or TiO₂¹¹. The main origin of this shift is explained by the modification of the dielectric constant, *i.e.* the modification of the local refractive index around the gold NPs due to the presence of the shell.

For the Au@SiO₂ NPs, silica is electronically inert, but its refractive index is different from the solvent (usually water or ethanol) and the gold¹⁰. Thus the silica layer influences the optical properties. It was demonstrated that the increase of the silica shell first induces a red shift in the position of the absorption maximum, from 518 nm for uncoated gold NPs to 525 nm for Au@SiO₂ NPs (shell thickness = 35.5 nm), due to the increase in the local refractive index around the gold core. However, when the silica shell becomes sufficiently larger, an important increase in the absorbance at shorter wavelength occurs, resulting from the scattering phenomenon. This effect induces a blue shift of the SPR band, from 525 for shell thickness of 35.5 nm to 515 nm for shell thickness of 75 nm, and an increase of the band width, leading eventually at shell thicknesses above 80 nm to vanishing of SPR.

For the Au@Metal Oxide NPs (Metal Oxide = TiO₂, ZrO₂)¹¹, the increase in the shell thickness also induces a red shift, due to the increase of the local refractive index as well as the increase of the band width, as observed for Au@ZrO₂ with a red shift from 520 nm for uncoated gold NPs to 560 nm for the larger Au@ZrO₂ NPs. However, while the band width increase is due to the scattering phenomenon for Au@SiO₂ NPs (resulting from the shell thickness increase), other phenomena occur for Au@Metal Oxide NPs. For smaller particles (bellow 25 nm for gold NPs, as for the Au@K⁺/Ni²⁺/[Fe^{II}(CN)₆]⁴⁻ NPs), *i.e.* where the particle dimension is much smaller than the wavelength of electrons, the increase of the band width with the shell thickness increase is due to the confinement of the free electrons within the metal core. For larger particles, the increase of the band width with the shell thickness increase is attributed to inhomogeneous polarization of the particle in the electromagnetic field, originated from the increase in the particle dimension in the extrinsic size range.

Then, for Au@SiO₂ NPs and Au@Metal Oxide NPs (Metal Oxide = TiO₂, ZrO₂), different phenomena explain the increase of the band width with the shell thickness increase, due to the different material nature of the shell. However, in all cases, the position of the absorption maximum, which is red-shifted with the shell thickness increase, has the same origin *i.e.* the increase of the local refractive index around the gold core.

For the Au@K⁺/Ni²⁺/[Fe^{II}(CN)₆]⁴⁻ NPs, the red shift occurs with the modification of the refractive index, due to the presence of the cyano-bridged coordination polymer shell. The size distribution of the gold cores (bellow 25 nm for gold NPs) permits to compare this system to Au@Metal Oxide NPs. As for the Au@Metal Oxide NPs, Au@K⁺/Ni²⁺/[Fe^{II}(CN)₆]⁴⁻ NPs exhibit an increase in width, from 37 nm for gold NPs to 58 nm. This phenomenon may be originated from the confinement of the free electrons within the core, or also from the scattering phenomenon due to the presence of the shell. To conclude, it is necessary to observe the evolution of the SPR band for different shell thicknesses, which will be describe later. Whatever, the presence of the optical properties observed for these heterostructured NPs opens the way to biological and chemical detection analysis applications⁴⁸.

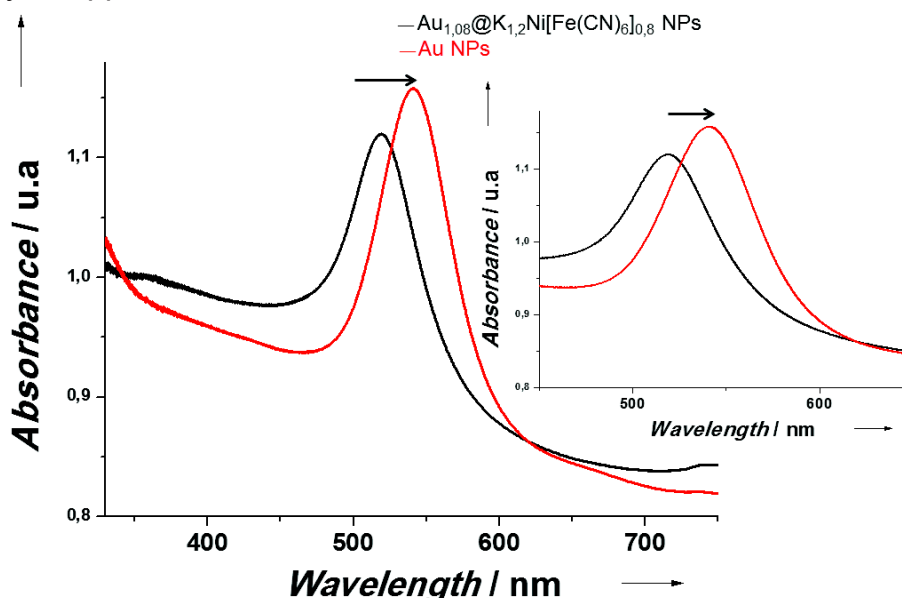


Figure 12: UV-Visible spectrum of Au and Au@K⁺/Ni²⁺/[Fe^{II}(CN)₆]⁴⁻ NPs in the visible region. In inset, magnification of the SPR band of the gold centers.

The magnetic properties of the $\text{Au}@K^+/Ni^{2+}/[Fe^{II}(CN)_6]^{4-}$ NPs were investigated using a SQUID-MPMS magnetometer working in the temperature range 1.8 – 350 K up to 7 T. The magnetic measurements indicate no significant magnetization evolution as a function of the temperature from 25 K to 300 K in the mode of Zero Field-Cooled - Field-Cooled (ZFC-FC) procedures. No hysteresis loop is observed on the magnetization vs. applied field curve (figure 13). The coordination polymer layer behaves as a paramagnetic compound, due to the total reduction of the $[Fe^{III}(CN)_6]^{3-}$ to $[Fe^{II}(CN)_6]^{4-}$ moieties during the shell-growth process because of the presence of residual borohydride, as already described (figure 2). This reduction leads to a modification of the Fe spin, from $S = 1/2$ for Fe^{III} to $S=0$ for Fe^{II} . Then the paramagnetic behavior is supported by Ni^{II} , with a spin $S = 1$. A sharp increase on the ZFC curve (figure 10) at low temperature may be explained by magnetic interactions between neighbor paramagnetic Ni^{II} ions through the diamagnetic $[Fe^{II}(CN)_6]^{4-}$ bridges. Moreover, a representative $1/\chi$ vs T curve performed for the sample 2 with an applied magnetic field of 100 Oe follows the Curie-Weiss law demonstrating predominant antiferromagnetic interactions (figure 14). The main characteristics of the $\text{Au}@K^+/Ni^{2+}/[Fe^{II}(CN)_6]^{4-}$ NPs (sample 2) are given table 1.

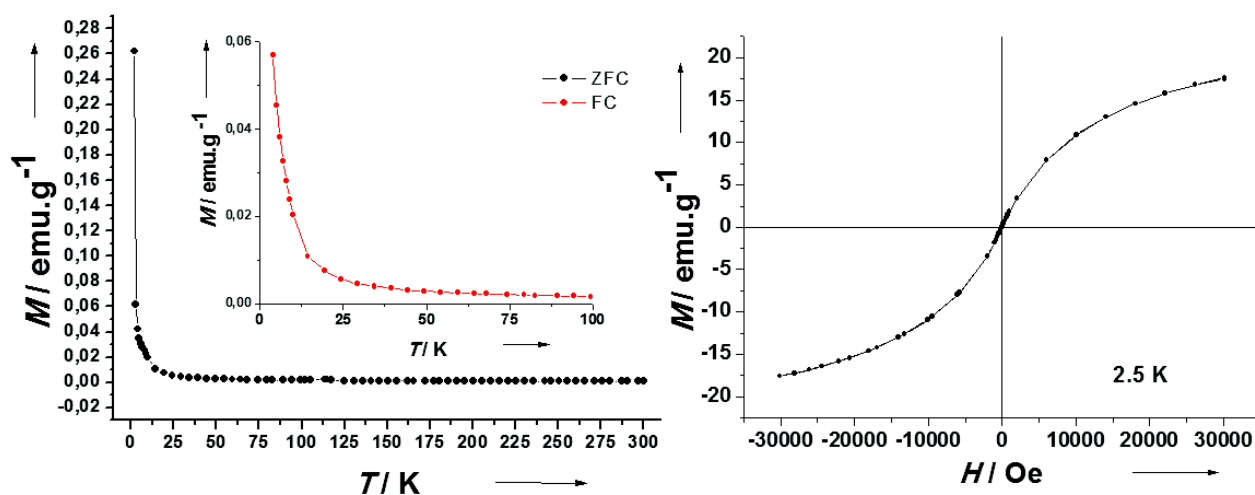


Figure 13: Left: ZFC-FC magnetization curves performed for the $\text{Au}@K^+/Ni^{2+}/[Fe^{II}(CN)_6]^{4-}$ NPs with an applied field of 50 Oe. Right: Field dependence of the magnetization performed at 2.5 K

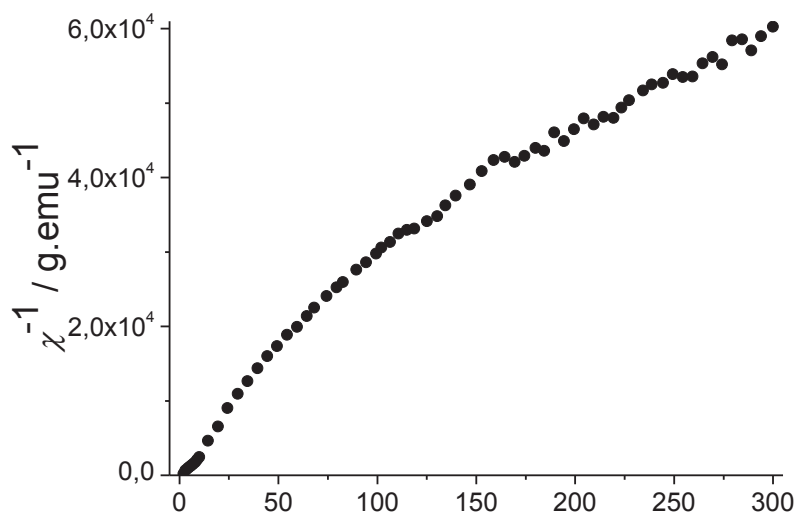


Figure 14: Temperature dependence of the inverse susceptibility measured under a 100 Oe DC field for the $\text{Au}@K^+/Ni^{2+}/[Fe^{II}(CN)_6]^{4-}$ NPs.

Main characteristics	Au@K ⁺ /Ni ²⁺ /[Fe ^{II} (CN) ₆] ⁴⁻ NPs
IR ν (-OH) coordinate water (cm ⁻¹)	3600
IR ν (-OH) free water (cm ⁻¹)	3410
IR ν (Fe ^{II} -C \equiv N-Ni ^{II}) (cm ⁻¹)	2094
IR δ (H-O-H) free water (cm ⁻¹)	1622
IR ν (Fe ^{II} -CN) (cm ⁻¹)	586
IR δ (Fe ^{II} -CN) (cm ⁻¹)	461
Raman ν (Fe ^{II} -C \equiv N-Ni ^{II}) (cm ⁻¹)	2106 and 2142
Raman ν (Au-CN) (cm ⁻¹)	388
Raman ν (Fe ^{II} -CN) (cm ⁻¹)	250
Anal. Found (At %)	Au, 6.5 ; K, 7.2; Ni, 5.9; Fe, 4.6; C, 28; N, 28 ; H, 19.8.
Estimated formula	Au _{1.08} @K _{1.20} Ni[Fe(CN) ₆] _{0.80}
Lattice parameter (Å)	a _{gold} = 4.08 a _{NiFe} = 10.07
Debye-Scherrer size (nm)	d _{gold} = 15 d _{NiFe} = 26
TEM size of gold core (nm)	19.5 ± 4.3
TEM size of shell thickness (nm)	16.6 ± 2.7
TEM size of total NPs (nm)	52.4 ± 8.6
Hydrodynamic diameter (nm)	190 ± 74
Zeta potential (mV)	-23.6 ± 4.3
Maximum of absorption of the SPR band (nm)	540

Table 1: Summary of the main characteristics of the Au@K⁺/Ni²⁺/[Fe^{II}(CN)₆]⁴⁻ NPs (sample 2).

III.3 Studies of the mechanism of the formation of core-shell Au@K⁺/Ni²⁺/[Fe^{II}(CN)₆]⁴⁻ NPs.

The design of the core-shell Au@K⁺/Ni²⁺/[Fe^{II}(CN)₆]⁴⁻ NPs has been successfully performed, as described above. However, the mechanism of the formation of such heterostructures remains unclear. The Zeta potential measurements have indicated a negative potential which is consistent with our hypothesis involving the cyanides ions at the surface of the gold NPs. These cyanide ions may play a role in the formation of the PBA shell. However, no tangible proves were given about. Furthermore, some questions about the formation of the cyano-bridged network layer of the gold remain unexplained. Then, in order to have a well-understanding, several techniques have been used to investigate the formation of these core-shell Au@K⁺/Ni²⁺/[Fe^{II}(CN)₆]⁴⁻, such as DLS/ Zeta potential measurements, UV-visible spectroscopy, Raman spectroscopy for the understanding of the PBA anchoring at the gold NPs surface, or TEM monitoring for the comprehension of the shell growth.

III.3.1 Investigation on the PBA anchoring process at the gold NPs surface.

III.3.1.a DLS/ zeta potential monitoring.

The values of the hydrodynamic diameter and the Zeta potential of the cyanide-stabilized gold NPs must be modified with the addition of the first drops of the PBA bivalent metal precursors. Then it should be possible to use DLS and Zeta potential measurements to observe the effect of the coordination of the metal salt coordination at the surface of the gold. In this aim, the addition of quantities (0.1, 0.25 and 0.5 μmol) of either a NiCl₂·6H₂O or a CoCl₂·6H₂O aqueous solution (5 mM) in gold NPs solution was followed by DLS and Zeta potential measurements. The DLS measurements clearly show an increase of the hydrodynamic radius of the NPs, as a function of the amount of the metal salt added (figure 15, **A**), visibly due to the coordination of the bivalent transition metal at the surface of the gold through the cyanides. The increase observed for Ni²⁺ is more important than the one observed for Co²⁺, indicating a particular affinity between Ni²⁺ and the cyanide-stabilized gold NPs. The Zeta potential measurements (figure 15, **B**) indicate a non-linear evolution of the Zeta potential as a function of the amount of the metal salts added. For both metal ions, the Zeta potential increases, then decreases, presents a minimum and increases again, indicating a complex modification of the charge at the gold surface. With a significant amount of Ni²⁺ added (0.5 μmol), the Zeta potential becomes positive, indicating a coordination of the Ni²⁺ ions to the cyanides and confirming the particular affinity between this metal ion and the cyanide-stabilized gold NPs. However, for Co²⁺, the Zeta potential at a higher amount added remains negative. Then it is rational to think that the coordination of the metal ion precursors may occur at the surface of the cyanide-stabilized gold NPs. This can explain the aggregation occurring at 0.5 μmol observed with the DLS measurements, which may be the result of the coordination of the metal ion

precursors at the gold NPs surface, the excess of Ni^{2+} added inducing the destabilization of the dispersion.

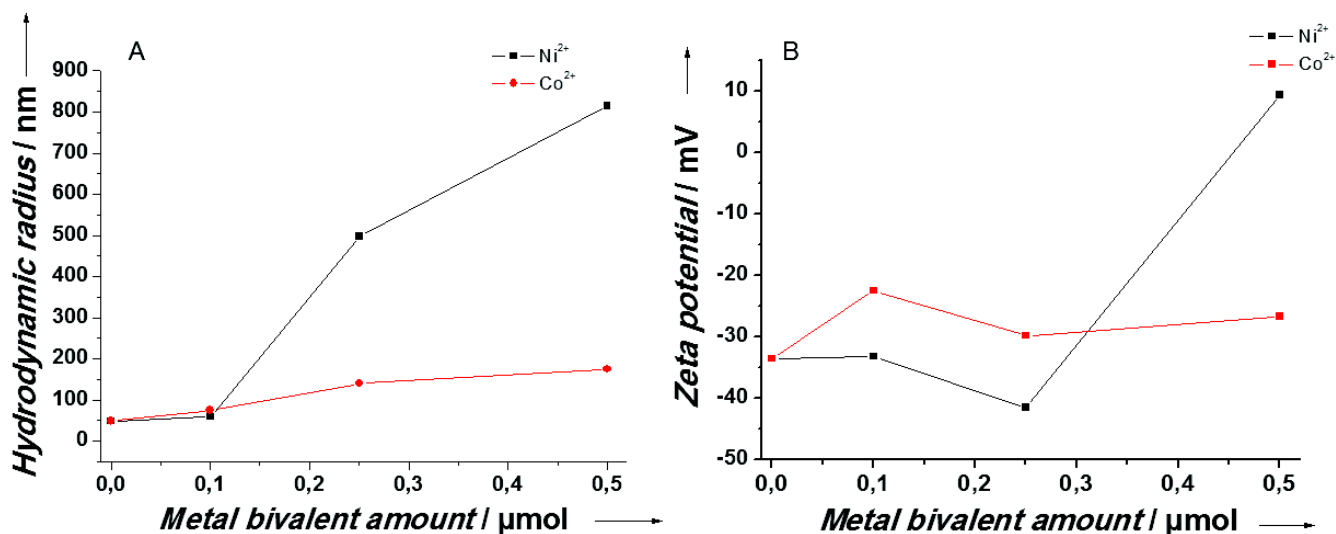


Figure 15: Evolution of the hydrodynamic diameter (A, left) and the Zeta potential (B, right) of the cyanide-stabilized NPs as a function of the amount of metal salt added.

III.3.1.b UV-visible monitoring.

The aqueous solution of the pristine gold NPs stabilized by cyanide anions exhibits the SPR band at 517 nm. A large range of metal precursors were investigated. As for DLS and Zeta potential measurement, 0.1 μmol of the metal ion solution (where the metal ion used was: Co^{2+} ($\text{Co}(\text{NO}_3)_2 \cdot 3\text{H}_2\text{O}$ and $\text{CoCl}_2 \cdot 6\text{H}_2\text{O}$), Cu^{2+} ($\text{CuCl}_2 \cdot 2\text{H}_2\text{O}$), Mn^{2+} ($\text{MnCl}_2 \cdot 4\text{H}_2\text{O}$), Ni^{2+} ($\text{NiCl}_2 \cdot 6\text{H}_2\text{O}$ and $\text{Ni}(\text{NO}_3)_2 \cdot 6\text{H}_2\text{O}$), Zn^{2+} (ZnCl_2), Fe^{2+} ($\text{FeCl}_2 \cdot 6\text{H}_2\text{O}$), Fe^{3+} ($\text{K}_3[\text{Fe}(\text{CN})_6]$), Cr^{3+} (CrCl_3), Gd^{3+} ($\text{Gd}(\text{NO}_3)_3 \cdot 6\text{H}_2\text{O}$), Pd^{2+} (PdCl_2), Pt^{2+} (PtCl_2) at concentration of 5.00 mM, was added to the gold NPs solution, and after one minute of stirring, measured on UV-visible spectroscopy.

Comparatively to the cyanide-stabilized gold NPs, only the nickel ion Ni^{2+} ($\text{NiCl}_2 \cdot 6\text{H}_2\text{O}$ and $\text{Ni}(\text{NO}_3)_2 \cdot 6\text{H}_2\text{O}$), cobalt ion Co^{2+} ($\text{CoCl}_2 \cdot 6\text{H}_2\text{O}$ and $\text{Co}(\text{NO}_3)_2 \cdot 6\text{H}_2\text{O}$) and zinc ion Zn^{2+} (ZnCl_2) exhibit a red-shift of the SPR band (figure 16). For Ni^{2+} ion, the SPR band is red-shifted at 522 nm, and at 520 nm for both Co^{2+} and Zn^{2+} ion. The red-shift observed may originate from the coordination at the surface of these ions at the gold NPs surface. All other metal ions used induce no modification of the SPR band, indicating probably much lower affinity to coordination at the surface of the gold NPs. That confirms the affinity of the Ni^{II} and Co^{II} with the cyanide stabilized gold NPs, as observed with DLS/ Zeta potential measurements.

To observe the effect of the precursor quantity on the red-shift of the SPR band, we have investigated more deeply by performing the same experiment with additional amounts of metal ion (0.01, 0.1, 0.15, 0.25, 0.5 μmol), for Ni^{II} , Co^{II} and Zn^{II} . The measurements show that the SPR band is rapidly shifted in presence on Ni^{2+} , from 517 to 525 nm at 0.1 μmol, then remains constant until 0.25 μmol then increases again to 532 nm at 0.5 μmol (figure 17). For Co^{2+} , the SPR band is red-shifted gradually from 517 to 522 nm

after 0.05 μmol , and until 540 nm at 0.5 μmol (figure 18). For the Zn^{2+} , a red-shift occurs from 517 nm to 521 nm at 0.05 μmol and 522 nm at 0.25 μmol , and then remain constant until 0.5 μmol (figure 19). In all cases, the progressive red-shift of the SPR band with the increase of the bivalent metal ion amount may be the consequence of the coordination at the surface of the gold NPs. The significant red-shift occurring with the addition of Ni^{2+} at lower quantity comparatively to those observed for Co^{2+} seems confirm that the Ni^{2+} ion has a better affinity with the gold surface, the amount of precursor necessary to observe the same shift being less higher. The red-shift observed for the Zn^{2+} ion is weak which seems indicate a low affinity with the gold surface, by comparison with the other bivalent ions.

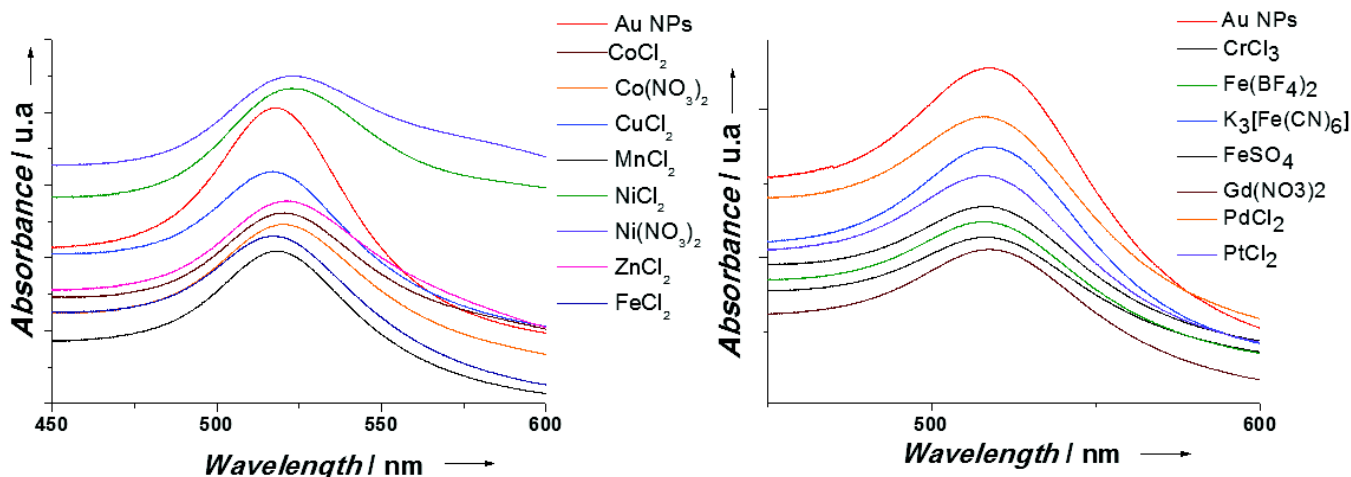


Figure 16: Evolution of the SPR band of the cyanide-stabilized NPs at the addition of 0.1 μmol of a metal ion (for a best clearness, the different SPR bands have been separated).

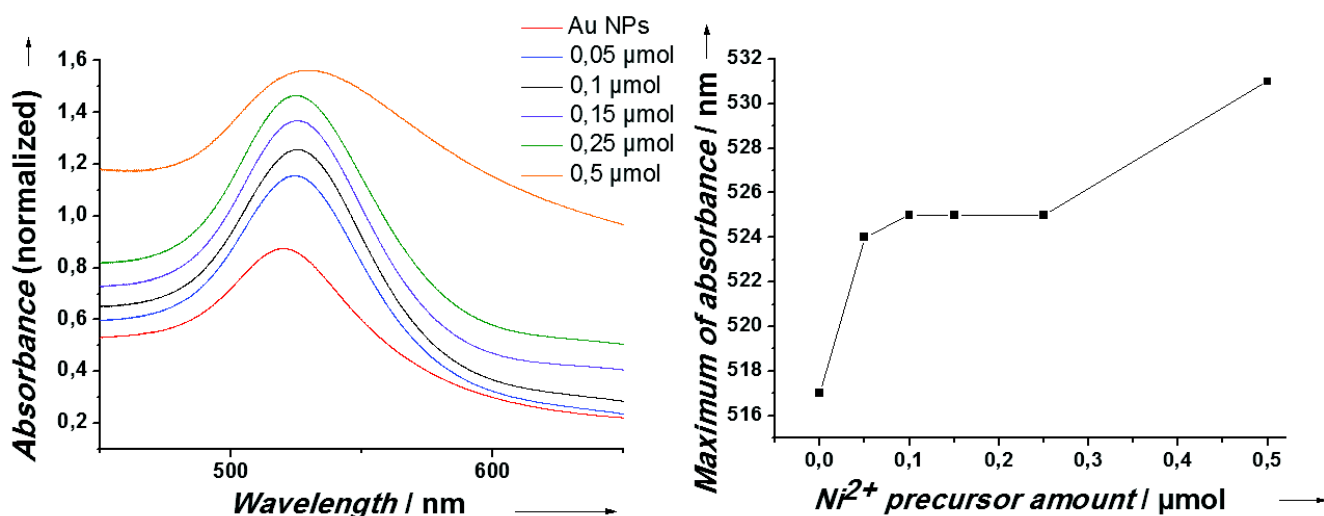


Figure 17: Left: evolution of the SPR band of the cyanide-stabilized NPs at the addition of a quantity of $\text{NiCl}_2 \cdot 6\text{H}_2\text{O}$ (for a best clearness, the different SPR bands have been separated). Left: evolution of the maximum of absorbance of the SPR band as a function of the amount of Ni^{2+} added.

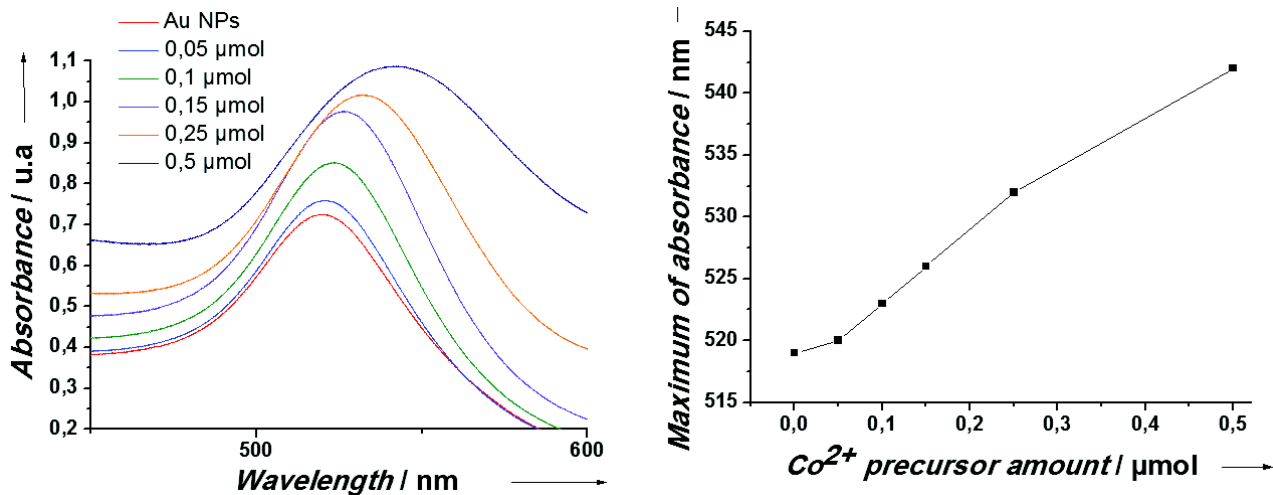


Figure 18: Left: evolution of the SPR band of the cyanide-stabilized NPs at the addition of a quantity of $\text{CoCl}_2 \cdot 6\text{H}_2\text{O}$ (for a best clearness, the different SPR bands have been separated). Right: evolution of the maximum of absorbance of the SPR band as a function of the amount of Co^{2+} added.

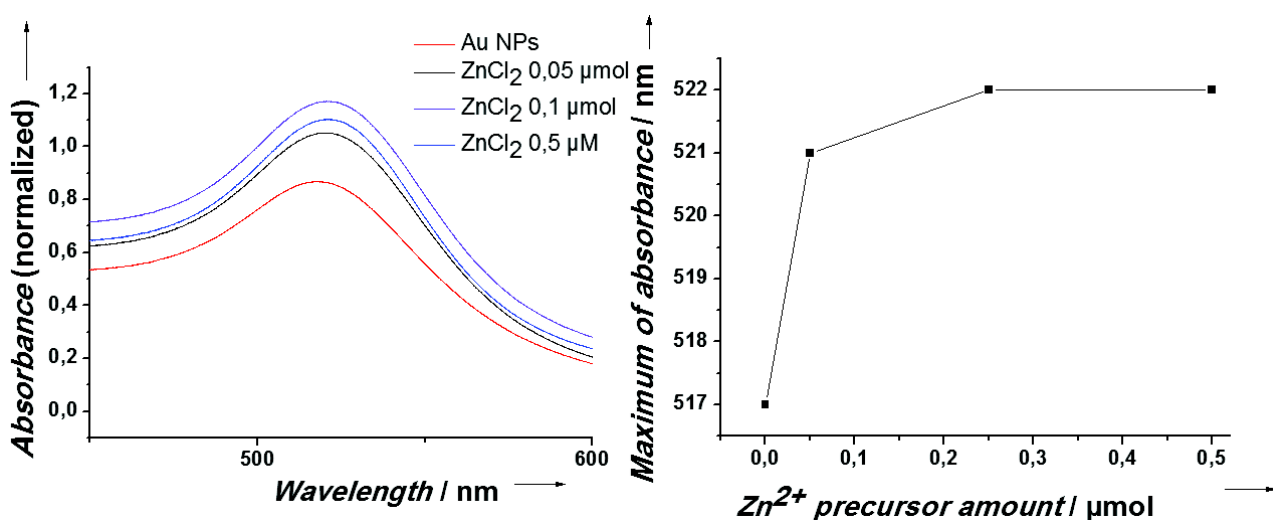


Figure 19: Left: evolution of the SPR band of the cyanide-stabilized NPs at the addition of a quantity of $\text{ZnCl}_2 \cdot 6\text{H}_2\text{O}$ (for a best clearness, the different SPR bands have been separated). Right: evolution of the maximum of absorbance of the SPR band as a function of the amount of Zn^{2+} added.

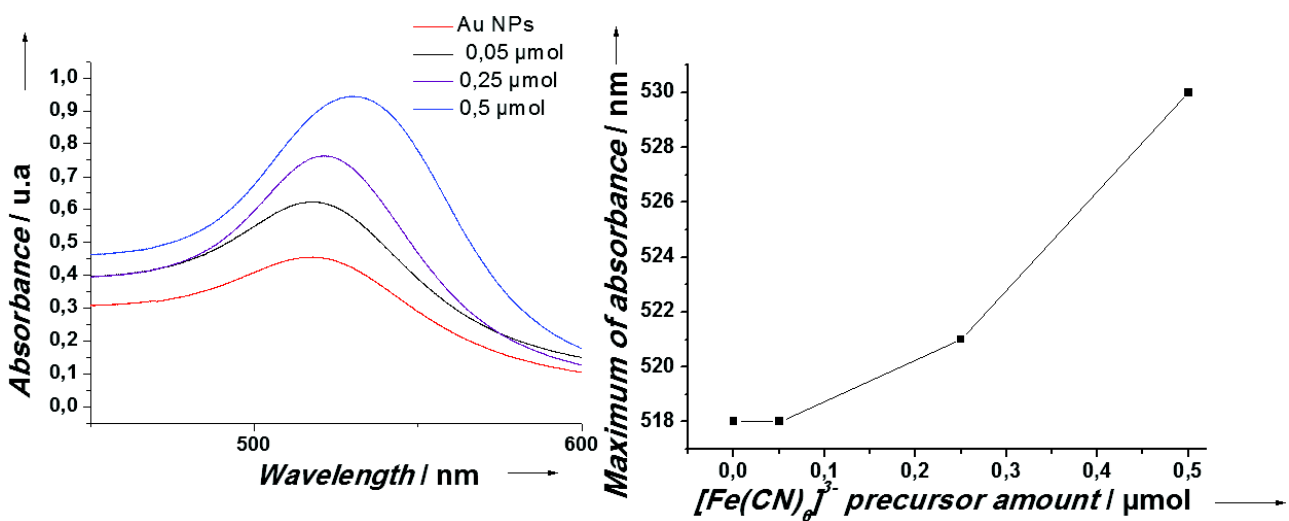


Figure 20: Left: evolution of the SPR band of the cyanide-stabilized NPs at the addition of a quantity of $\text{K}_3[\text{Fe}(\text{CN})_6]$ (for a best clearness, the different SPR bands have been separated). Right: evolution of the maximum of absorbance of the SPR band as a function of the amount of $\text{K}_3[\text{Fe}(\text{CN})_6]$ added.

The effect of the $[\text{Fe}(\text{CN})_6]^{3-}$ moiety on the SPR band was also studied (figure 20). The addition of a sufficient concentration of $\text{K}_3[\text{Fe}(\text{CN})_6]$ modifies the SPR band, with a shift from 521 nm after the mixing of 0.01 μmol to 530 nm after the addition of 0.5 μmol . Then an interaction should be created between the cyanometallate precursor and the gold surface, possibly by coordination of the nitrogen atom of the cyanide ions coordinated at the Fe^{III} after exchange with the cyanide ions coordinated at the gold surface, which may be at the origin of the formation of the PBA shell. However, the red-shift occurs at higher amount added in comparison with the Ni^{2+} , and then it's rational to think that the Ni^{2+} ion plays a prevailing role in the formation of coordination bond with the surface of the cyanide-stabilized gold NPs, due to its particular affinity with the gold surface. Finally, the use of a KCl solution as reference does not show any modification; it confirms that the presence of ions such as K^+ and Cl^- induces no modification of the SPR band, which eliminates a possible effect of ionic strength (figure 21).

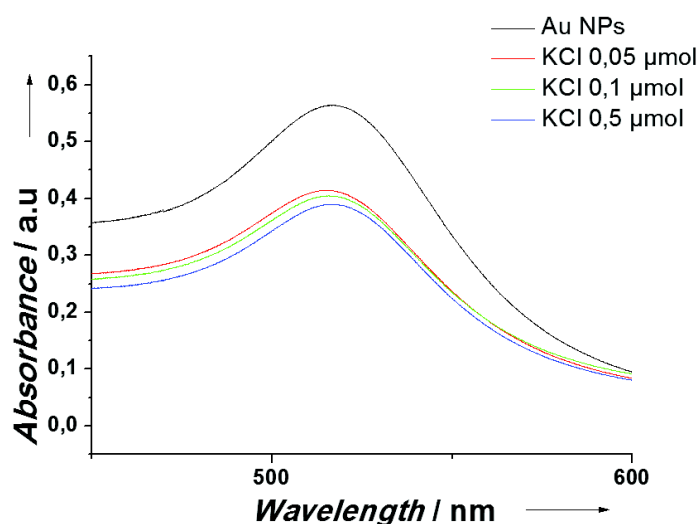


Figure 21: Evolution of the SPR band of the cyanide-stabilized NPs at the addition of a quantity of KCl (for a best clearness, the different SPR bands have been separated).

To conclude, UV-visible brings interesting information. The extreme sensitivity of the SPR band to any perturbation on the surface has been used to show a particular affinity to Ni^{2+} , Co^{2+} a lesser affinity to Zn^{2+} and $[\text{Fe}(\text{CN})_6]^{3-}$ moiety, and no affinity with the Au NPs surface with other metal ions and KCl. This particular affinity should correspond to the coordination of the metal precursor to the gold surface, *via* the cyanide ligands. Moreover, the most important affinity is observed for Ni^{2+} . However, the hypothesis of the formation of coordination bonds with the gold surface, such as $\text{Au}-\text{C}\equiv\text{N}-\text{Ni}^{2+}$, must be confirmed by a technique able to show structural information, such as Raman spectroscopy.

III.3.1.c Raman monitoring.

The comprehension of the mechanism of the $\text{Au}@K^+/Ni^{2+}/[Fe^{II}(CN)_6]^{4-}$ nano-heterostructures formation needs to go through the understanding of the coordination bond formed during the synthesis. However, the difficulty consists in the measurements during reaction, requiring a technique permitting to follow the reaction *in situ*. Raman spectroscopy is an ideal candidate, with the possibility to perform the measurements in solution which may give information on the phenomenon occurring at the surface of cyanide-stabilized gold NPs, as the formation of coordination bonds with the Ni^{2+} ion. Indeed, several studies^{49,50} on gold cyanide complexes have shown the extreme sensibility of the $\nu(CN)$ frequencies of $[Au(CN)_2]^-$ based coordination polymers. In particular, the coordination of the metal ion to the nitrogen of the cyanide coordinated to the gold atom is always visible by a blue-shift of the $\nu(C\equiv N)$ band⁵⁰.

To this aim, we have realized a series of measurements in aqueous solutions. First, we performed the spectrum of the dicyanoaurate precursor in powder. The $K[Au^I(CN)_2]$ powder exhibits a very intense band at 2163 cm^{-1} , in the cyanide stretching region, which correspond to the cyanide ion coordinated to the gold atom ($Au^I-C\equiv N$) (figure 22)⁴⁵. Moreover, the coordination is confirmed also by the presence of the metal-carbon bond⁴⁵ Au^I-C with the stretching band at 310 cm^{-1} . We have also performed the spectrum of the dicyanoaurate precursor in aqueous media, to compare with the cyanide-stabilized gold NPs in solution. The stretching vibration band observed at 325 cm^{-1} corresponds to the metal-carbon bond Au^I-C , and two bands located at 222 cm^{-1} and 272 cm^{-1} also may rationally attributed to the bending vibration of Au^I-C linkage⁵¹. However, it was not possible to observe the band in the cyanide stretching region ($2000-2200\text{ cm}^{-1}$) due to the presence of a really large fluorescence band.

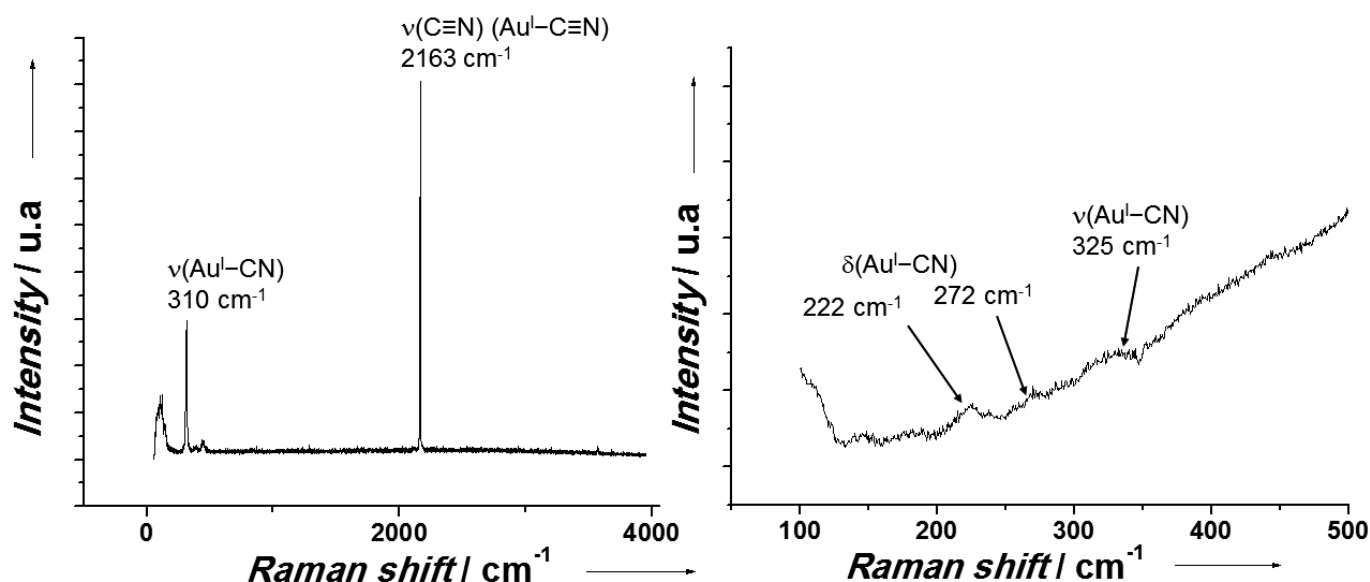


Figure 22: Raman spectra of the $K[Au(CN)_2]$ precursor, in powder (left) and in aqueous media (right).

In a second time, we have realized a Raman monitoring on a solution of the cyanide-stabilized gold NPs. The measurements were performed on freshly prepared NPs after 20 minutes by scanning in solution. In this case, the band corresponding to the cyanide stretching vibration is observed at 2125 cm^{-1} and was attributed to the $Au^I-C\equiv N$

(figure 23, a))⁴⁶. It is not possible to compare with the cyanide stretching vibration band of the precursor in solution; however comparatively to the gold precursor in powder a red-shift occurs. At the opposite, a blue-shift was observed for the stretching band corresponding to the metal-carbon bond, from 352 cm⁻¹ for the gold precursor to 383 cm⁻¹ for the gold NPs. The band attributed to bending vibration of Au-C is also blue-shifted from 272 cm⁻¹ for the gold precursor to 286 cm⁻¹ for the gold NPs. Then, the modification of the values of the bands, characterizing the formation of Au^I-C bond, is clearly due to the formation of the cyanide-stabilized gold NPs⁴⁶.

Several drops of an aqueous solution of NiCl₂·6H₂O (5.00mM) were added in the solution. Rapidly, an enlargement of the band is observed, and then a blue-shift occurs at 0.25 μmol from 2125 cm⁻¹ to 2132 cm⁻¹ (figure 23, b)). The addition of more Ni²⁺ ion produces the splitting of the band with two maxima located respectively at 2121 cm⁻¹ and 2140 cm⁻¹ for 0.4 μmol of Ni²⁺ ion added and 2119 cm⁻¹ and 2142 cm⁻¹ for 0.55 μmol of Ni²⁺ ion added. The bands located at 2121 cm⁻¹ and 2119 cm⁻¹ are close to those corresponding of the cyanide-stabilized gold NPs, located at 2125 cm⁻¹. However, a significant blue-shift is observed from 2125 to 2132, 2140 and finally 2142 cm⁻¹ as a function of the amount of Ni²⁺ ion added.

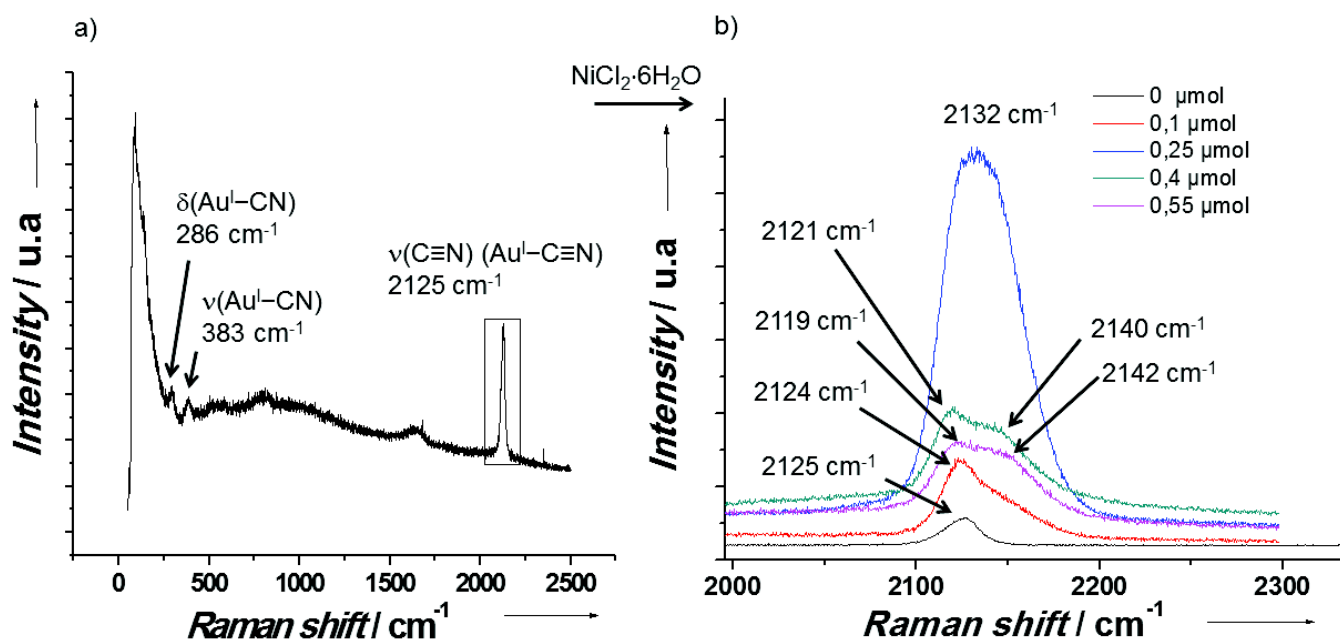


Figure 23: a) Raman spectrum of the gold NPs in aqueous solution. b) Evolution of the cyanide stretching vibration band with the addition of NiCl₂·6H₂O aqueous solution.

This shift clearly indicates that the addition of Ni²⁺ ion has induced a modification of the Au^I-C≡N bond. This blue-shift may be the sign of the coordination of the Ni²⁺ to cyanide bonded to the gold, as described in the literature^{49,50}, to form a Au^I-C≡N-Ni²⁺ bond. However, that also may correspond with the formation of [Ni(CN)₄]²⁻ ion⁴⁵, for which the bands of the Ni²⁺-C≡N linkage are observed at 2143, 2134 and 2123 cm⁻¹, but this specie may also be able to coordinate with the gold surface. Nevertheless, the addition of more Ni²⁺ ion in the reaction media led to the aggregation of the NPs in absence of stirring, as observed visually with the sedimentation of the NPs, inducing a loss of the signal. We have tried to obtain fine spectra; however the aggregation process was too fast. Several

times, the focusing point was set more deeply in the solution but the time to set and the signal was again lost, due to the sedimentation of the NPs. This aggregation was observed previously for similar concentration of precursor added, and may be originated by the presence of an excess of Ni^{2+} ions. Moreover, by correlation with the Zeta potential measurements, the maximum intensity of the signal is observed for a concentration of 25 μM , when the value of the Zeta potential is at its minimum, before to increase until a positive charge value (figure 15). It is possible that this indicates the total coating of the cyanide-stabilized gold NPs surface by the Ni^{2+} ions, and the next addition of Ni^{2+} , now in excess at the surface, induces the increase of the Zeta potential.

Then, the Raman spectroscopy confirms us the formation of a coordination bond between the cyanide-stabilized gold surface and the Ni^{2+} . It is now clear that the formation of this $\text{Au}^0\text{-C}\equiv\text{N-Ni}^{\text{II}}$ linkage is one of the phenomena at the interface permitting to grow a PBA shell of the gold NPs.

III.3.2 Investigation on the shell growth mechanism by TEM monitoring.

The PBA shell growth on the Au NPs surface could be due to a regular increase of the PBA shell, or to the anchoring of PBA nano-structures at the surface of the gold, *via* the metal coordination at the surface, which would play the role of “molecular adhesive”. Then, to resolve the PBA shell growth mechanism at the gold NPs surface, TEM monitoring was performed. TEM grids were prepared at several times during the PBA shell growth, from 20 minutes to 5 hours.

A series of TEM images reveals a regular increase of the shell thickness during the shell growing period (figures 24 and 25), but the size of the gold core remained stable, figures 25 and 25). The shell growth is regular but not uniform (the PBA shell can present a structural anisotropy during the first hours). Then the shell growth become more homogenous, the PBA layer grows more uniformly to lead to well-formed core shell $\text{Au@K}^+/\text{Ni}^{2+}/[\text{Fe}^{\text{II}}(\text{CN})_6]^{4-}$ NPs.

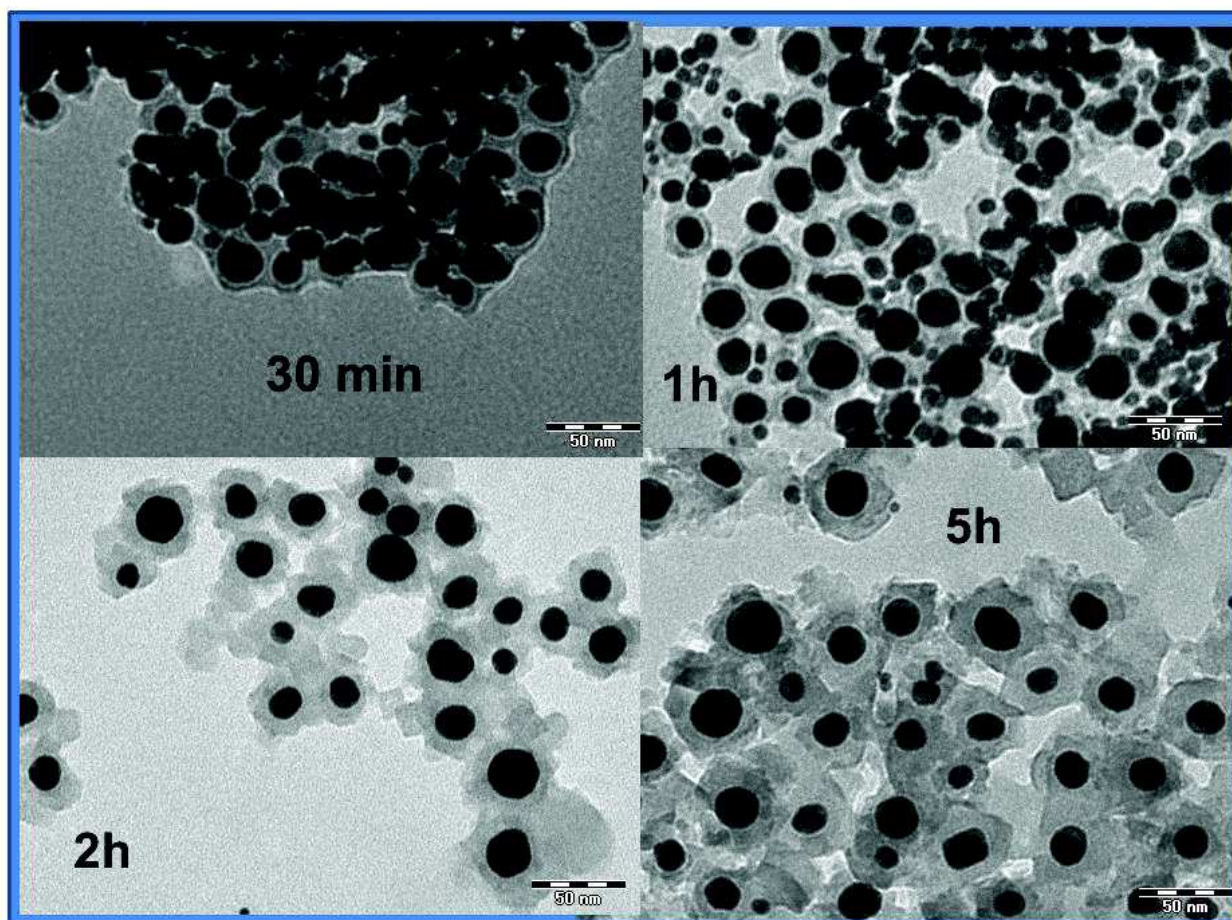


Figure 24: TEM images of $K^+/Ni^{2+}/[Fe^{II}(CN)_6]^{4-}$ shell growth followed in times for $Au@K^+/Ni^{2+}/[Fe^{II}(CN)_6]^{4-}$ NPs.

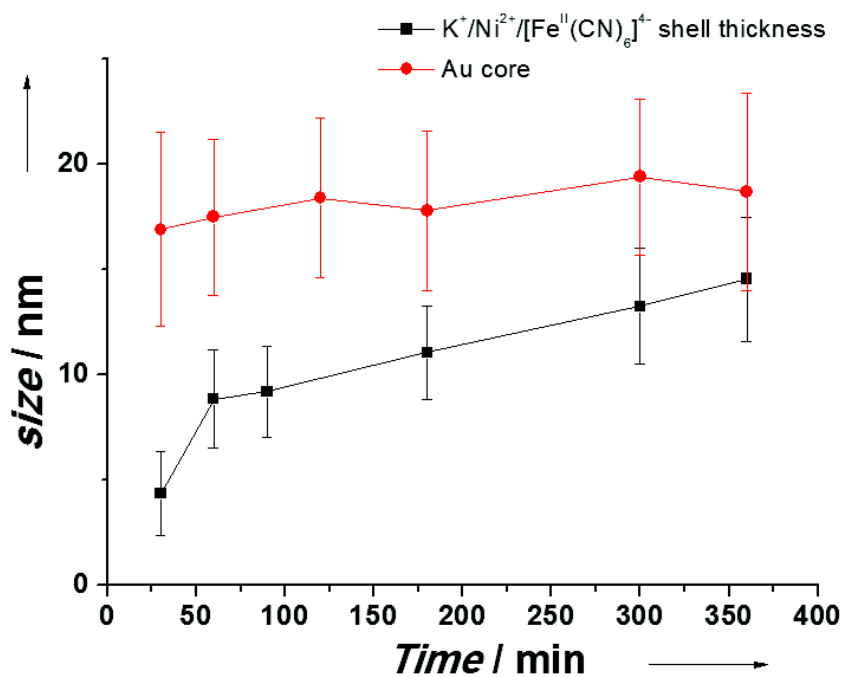


Figure 25: $K^+/Ni^{2+}/[Fe^{II}(CN)_6]^{4-}$ shell thickness dependence and Au core size dependence as a function of reaction time for $Au@K^+/Ni^{2+}/[Fe^{II}(CN)_6]^{4-}$ NPs.

III.3.3 Discussion.

Previously, several techniques have been used to investigate the formation of the core-shell nano-heterostructures, and particularly the formation of the PBA shell by coordination of the bivalent ions at the gold NPs surface and the PBA shell growth mechanism. On one hand, the coordination of the bivalent ions at the NPs surface was followed by DLS, to observe the modification of the hydrodynamic radius, and by Zeta potential measurements, to observe the evolution of the Zeta potential as a function of the addition of a metal salt precursor (Ni^{2+} and Co^{2+}). The evolution of the SPR band with the addition of metal precursors was performed to evidence the coordination of the metal ions at the gold NPs surface. Then, Raman spectroscopy on the gold NPs in solution was used to look for the bands characteristic of the coordination of the metal at the gold NPs surface. On other hand, the shell growth mechanism was observed by TEM-monitoring. These investigations bring useful information's permitting to better understand the mechanism of the PBA layer formation on the gold NPs.

The results show that the cyanide ions on the gold surface play an essential role to design nano-heterostructures. Indeed, the modification of the zeta-potential, the red-shift observed for SPR band and the blue-shift of the cyanide stretching band^{49,50} in Raman spectra consequently to the addition of Ni^{2+} corroborate with the coordination of the metal ion to the cyanides at the gold surface, creating a $\text{Au}^{\text{I}}-\text{C}\equiv\text{N}-\text{Ni}^{\text{II}}$ bond. This bond permits to anchor the metal at the surface of gold, and fixes the cyano-bridged coordination polymer shell. The formation of such $\text{Au}^{\text{I}}-\text{C}\equiv\text{N}-\text{M}^{\text{II}}$ bond by coordination of the nitrogen from the cyanide molecule to the M^{2+} seems to be a crucial step to obtain the core-shell NPs. This coordination occurs only for Ni^{2+} , Co^{2+} and Zn^{2+} which may indicate a particular affinity with the cyanide-stabilized gold NPs, as shown by UV-visible measurements. Moreover, the Ni^{2+} seems to have the most important effect, as shown by UV-Visible and DLS/ Zeta potential measurements. While the formation of the $\text{Au}^{\text{I}}-\text{C}\equiv\text{N}-\text{M}^{\text{II}}$ bond with several transition metals ($\text{M} = \text{Cu}^{2+}$, Mn^{2+} , Fe^{2+} , Ni^{2+} , Co^{2+}) or lanthanides (Gd^{3+} , Tb^{3+} , Eu^{3+} , Nd^{3+}) was observed for cyanoaurate-based coordination polymers^{49,50,51,53}, it is not the case using the cyanide at the gold NPs surface, except for Ni^{2+} , Co^{2+} and Zn^{2+} ions. For now, this specific affinity of these ions for the gold NPs surface has not been explained and the solution remains open. The nature of the metal could be the cause of this particular affinity, due to their own electronic configuration. The effect of the reducing media also could avoid the formation of the coordination bond with the cyanide ligand on the gold surface except for Ni^{2+} , Co^{2+} and Zn^{2+} . However, the impossibility to grow the PBA layer to form core-shell $\text{Au}@K^+/\text{Ni}^{2+}/[\text{Fe}^{\text{II}}(\text{CN})_6]^{4-}$ NPs without the reducing agent does not permit to conclude on the effect of the reaction conditions. Nevertheless, the formation of the heterostructures seems clearly to be dependent of the particular affinity between the Ni^{2+} ions and the cyanide-stabilized gold NPs. The kinetic of the formation of the PBA may be also an important parameter affecting the shell formation around the gold core.

The mechanism of the formation of the $\text{Au}@K^+/\text{Ni}^{2+}/[\text{Fe}^{\text{II}}(\text{CN})_6]^{4-}$ NPs at the nanoscale was demonstrated by TEM monitoring. The growth of the PBA shell around the gold core seems to be regular, but not totally symmetrical. Indeed, for small sized core-shell NPs, a preferential growth of the PBA shell on certain gold facets is observed, giving

large distribution for the shell thickness. However, the size becomes more homogeneous for larger size. Then, the growth process occurs according to a progressive growing of the PBA at the surface of the gold core, and not the result of an aggregation of small PBA NPs at the surface of the cyanide-stabilized gold NPs to form the shell.

Then, the better comprehension of the formation of the core-shell $\text{Au}@K^+/Ni^{2+}/[Fe^{II}(CN)_6]^{4-}$ NPs permits us to propose a general mechanism (figure 24). Firstly, the Ni^{2+} added may be coordinated to the cyanide-stabilized surface (figure 24, 1). Then, the $K_3[Fe(CN)_6]$ added may react with the Ni^{2+} on the gold surface to form a thin layer of the $K^+/Ni^{2+}/[Fe^{II}(CN)_6]^{4-}$ PBA (figure 24, 2), which may be the anchoring point to form the shell. Then this layer grows regularly with the addition of the PBA precursors (figure 24, 3 and 4) to finally form the large core-shell $\text{Au}@K^+/Ni^{2+}/[Fe^{II}(CN)_6]^{4-}$ NPs. However, this mechanism remains hypothetical, and the origin of several phenomena, such as the particular affinity for Ni^{2+} , Co^{2+} and Zn^{2+} ions, has not been explained.

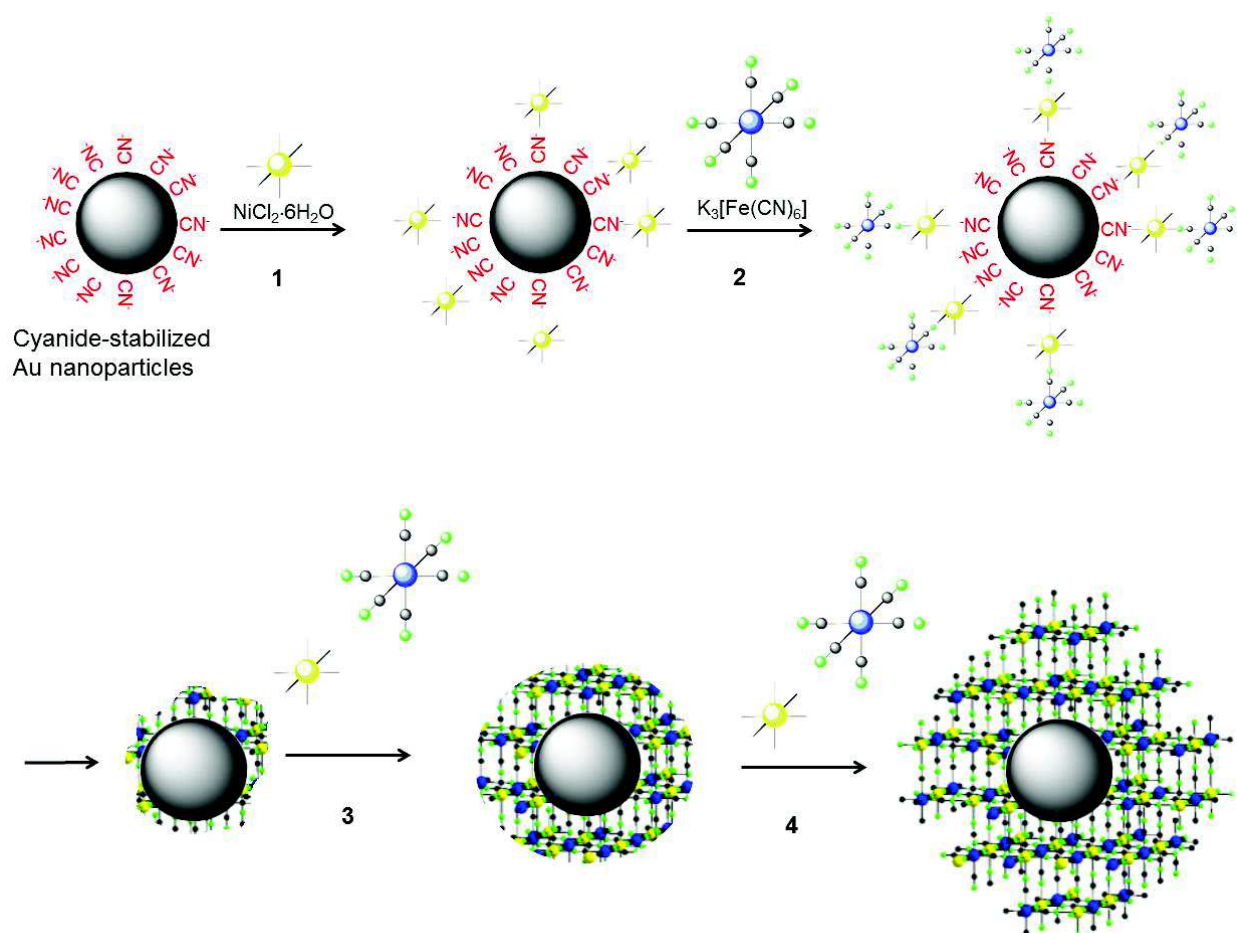


Figure 26: schematic representation of the proposed mechanism of the formation of core-shell $\text{Au}@K^+/Ni^{2+}/[Fe^{II}(CN)_6]^{4-}$ NPs, with the different steps of the growth of the PBA layer.

III.4 Variation of the core and the shell size of $\text{Au}@K^+/\text{Ni}^{2+}/[\text{Fe}^{\text{II}}(\text{CN})_6]^{4-}$ NPs

This section is devoted to the variation of the gold core and the PBA shell size and investigation of these effect on the optical properties of the heterostructured NPs.

III.4.1 The gold core size control

A variation of the gold core size was performed according to the same protocol than for the initial core-shell $\text{Au}@K^+/\text{Ni}^{2+}/[\text{Fe}^{\text{II}}(\text{CN})_6]^{4-}$ NPs, with the temperature fixed at 18, 25, 32 and 40°C during the synthesis of the pristine cyanide-stabilized gold NPs (figure 27). When the precursors of the PBA layer are added, the temperature is gradually turned to 25°C in order to control the growth of the cyano-bridged coordination polymer shell. After reaction, the NPs were isolated by centrifugation, washed with water and ethanol and dried under vacuum.

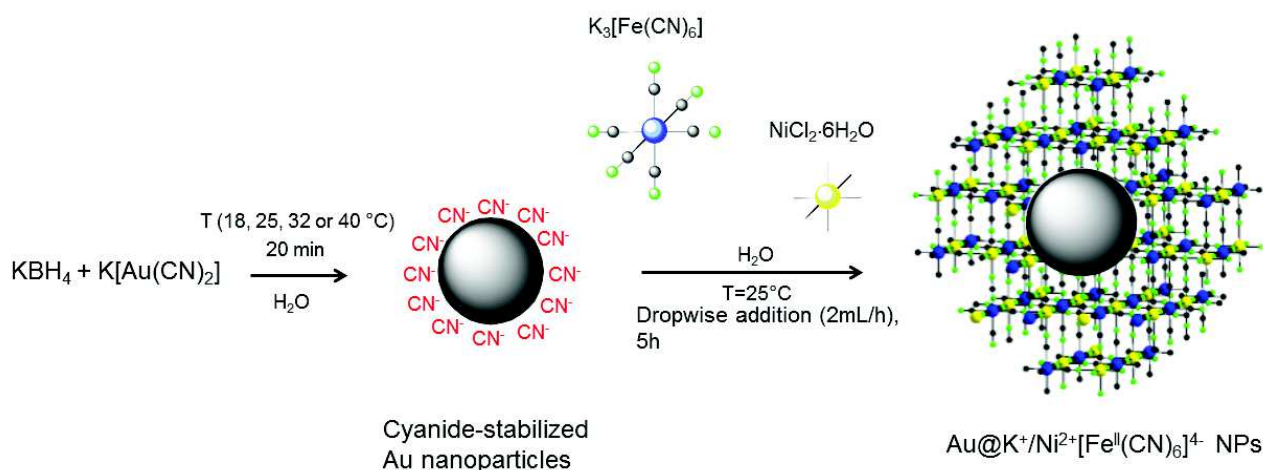


Figure 27: Schematic representation of the core-shell $\text{Au}@K^+/\text{Ni}^{2+}/[\text{Fe}^{\text{II}}(\text{CN})_6]^{4-}$ NPs synthesis with varying the gold core size by modulation of the temperature.

The IR spectra of $\text{Au}@K^+/\text{Ni}^{2+}/[\text{Fe}^{\text{II}}(\text{CN})_6]^{4-}$ NPs obtained at different temperatures (**2**, **2-18**, **2-32**, **2-40**) indicate no significant difference in the cyanide stretching region or in the other characteristic region according to the initial core-shell NPs (**2**) obtained at 25°C (figure 28). For all of them, the formation of the PBA network is confirmed, particularly by the presence of the cyanide stretching band located at 2094 cm^{-1} , characteristic of the $\text{Fe}^{\text{II}}-\text{C}\equiv\text{N}-\text{Ni}^{\text{II}}$ linkage³⁸⁻⁴³. All the bands and their respective attributions are summarized in table 2. As expected, the modification of the temperature during the synthesis of the gold core does not influence the structure of the PBA network.

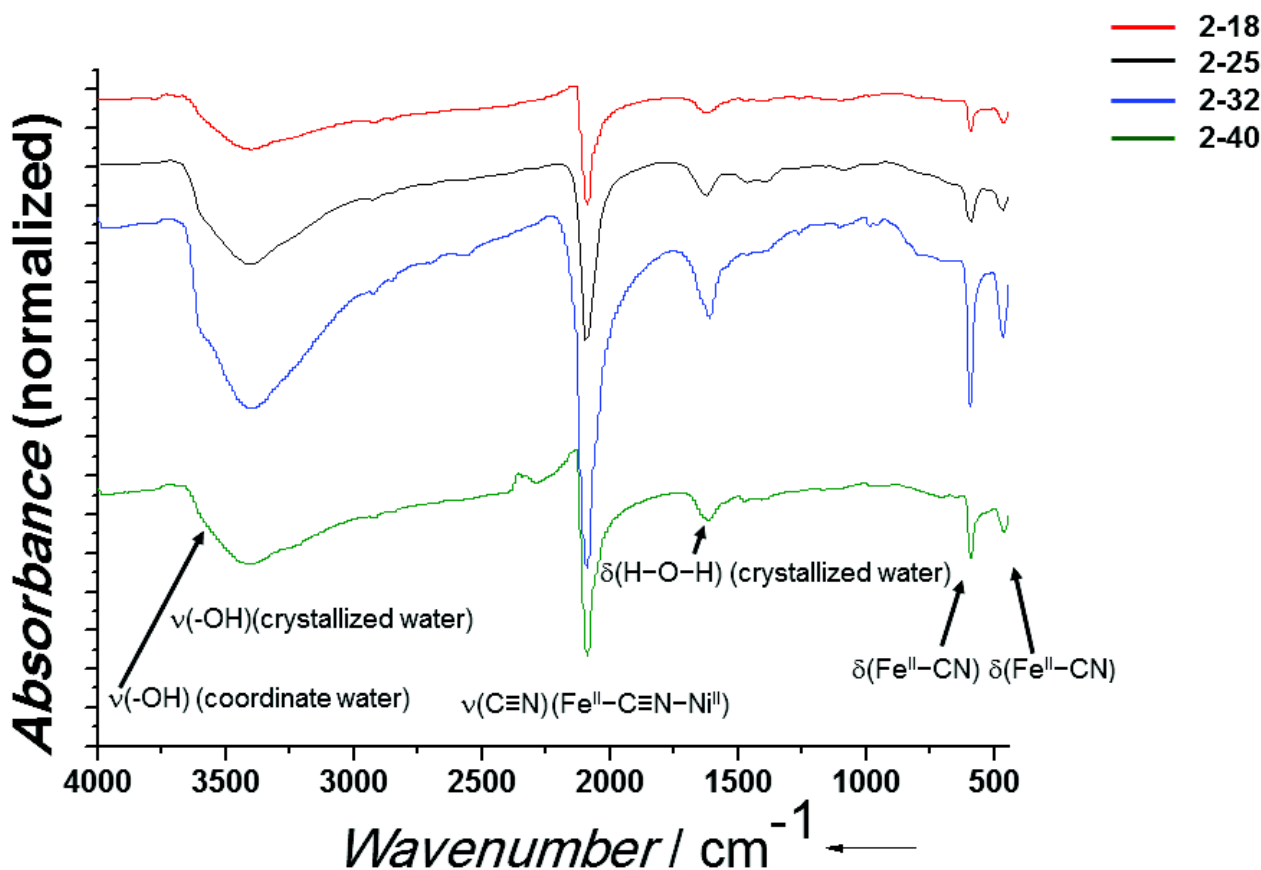


Figure 28: IR spectra of the core-shell Au@K⁺/Ni²⁺/[Fe^{II}(CN)₆]⁴⁻ NPs synthesized with varying the temperature during the formation of the gold NPs.

EDX measurements permit to calculate the formula for these core-shell NPs (table 2). The formulas clearly show an increase on the stoichiometric coefficient for the gold, which is consistent with the increase of the core size as a function of temperature.

TEM images confirm the formation of the core-shell Au@K⁺/Ni²⁺/[Fe^{II}(CN)₆]⁴⁻ NPs for all temperatures used (figure 29). The size distributions revealed the increase of the gold core size as a function of the temperature from 15.0 ± 3.8 nm for 18°C to 26.3 ± 5.0 nm for 40°C (figures 30, 31 and table 2). However, the reduction of the dicyanoaurate at higher temperature leads to an enlargement of the size distributions of the core. Note also that the Au synthesis performed at temperatures higher than 25°C induces an inhomogeneity in the Au core morphology and the appearance of some cubes and triangles as minor shapes besides the spherical NPs. This observation is in accordance with literature³⁷. On the other hand, the PBA shell size is the same for all samples (50 nm) except the one for which the gold core was obtained at 18°C, which is lower in comparison with others (31.8 ± 4.9 nm) (see Fig 30 and 31). This is probably due to a slow temperature increase from 18°C to 25°C at the beginning of the shell growth. However, the PBA shell thickness varies clearly according to the different temperatures (table 2). Then the thickness of the layer is also affected by the variation of the temperature.

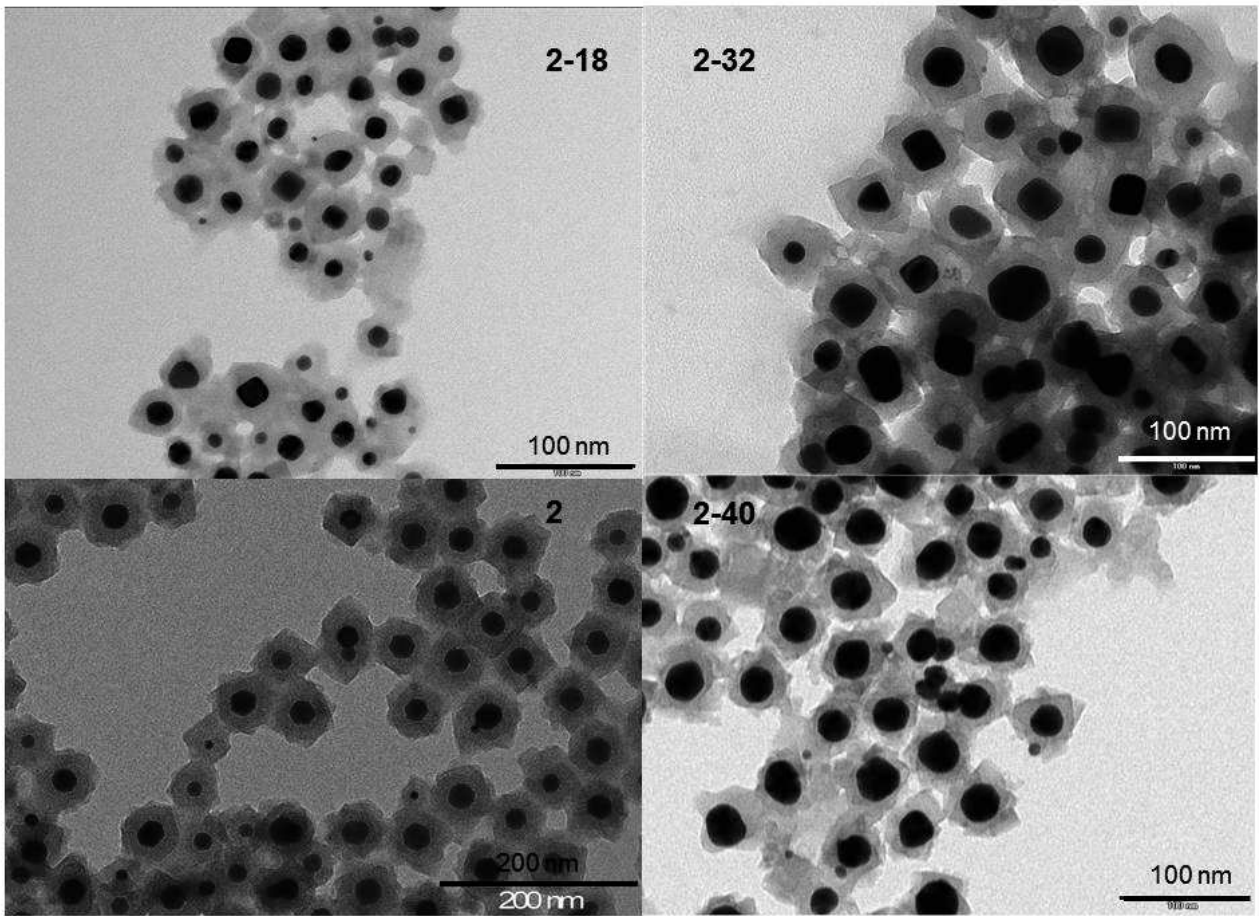


Figure 29: TEM images for of the Au@K⁺/Ni²⁺/[Fe^I(CN)₆]⁴⁻ NPs obtained from different reaction's temperatures.

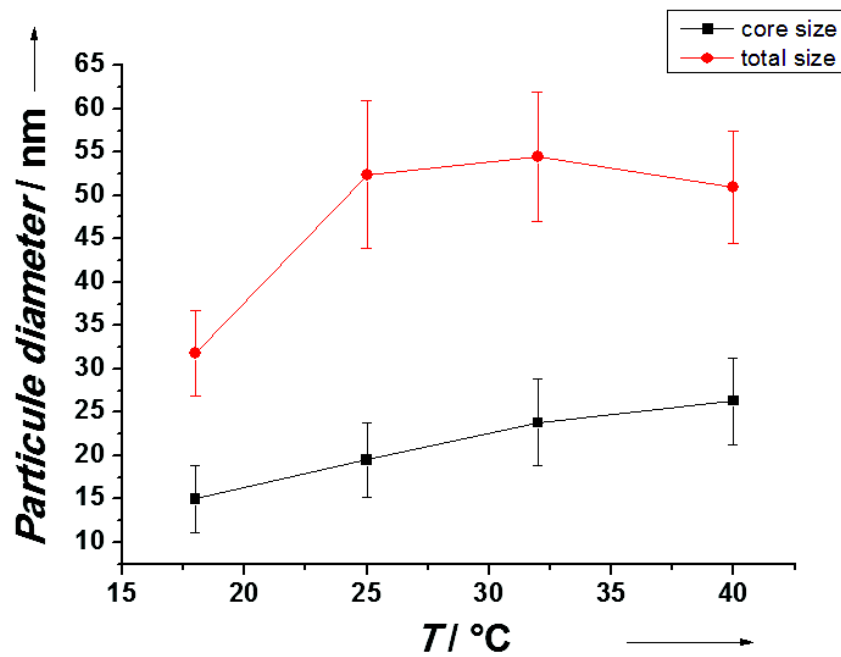


Figure 30: Temperature dependence of the gold core size (black) and the total NPs size (red).

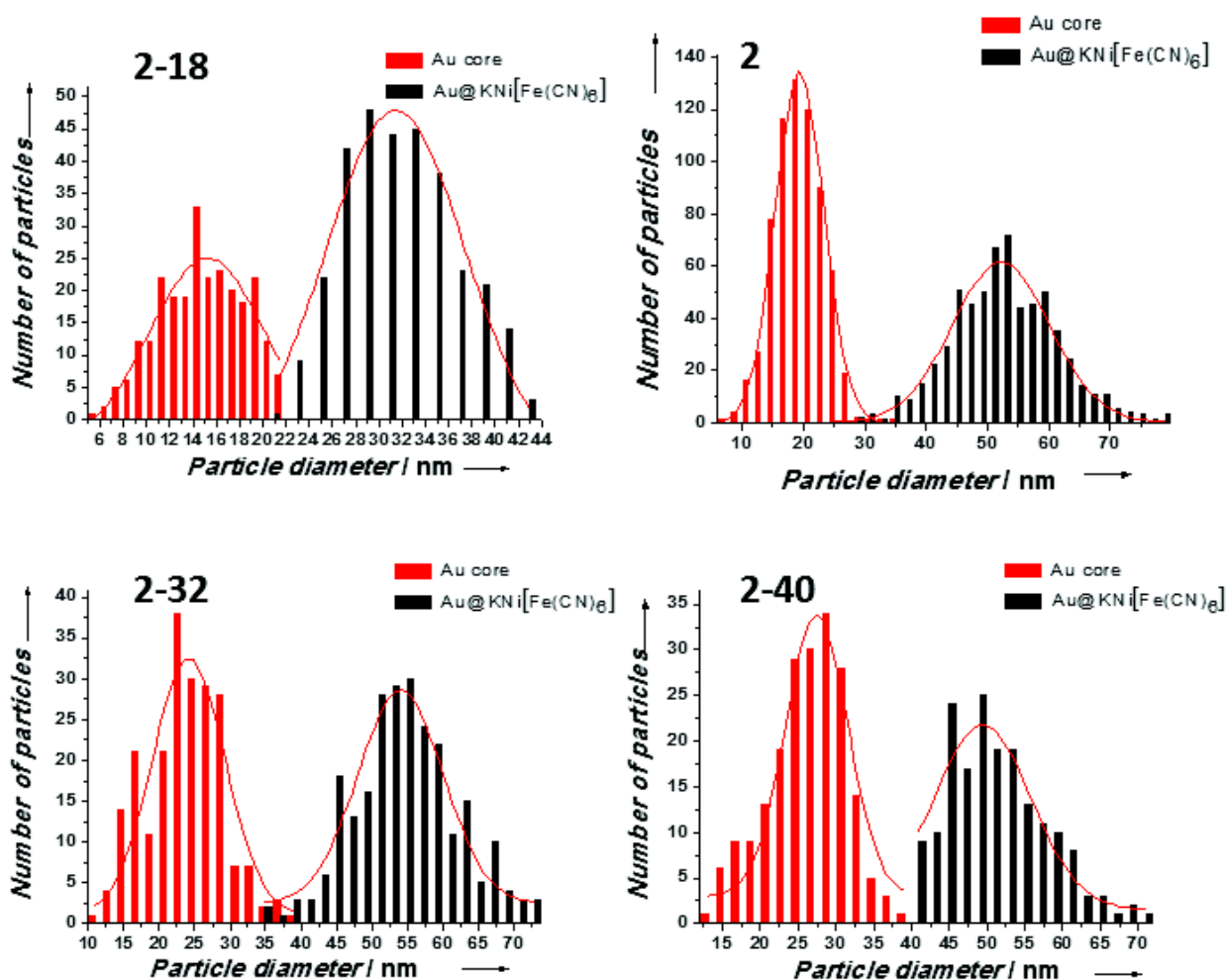


Figure 31: Size distributions of the gold core and the total size of the core-shell Au@K⁺/Ni²⁺/[Fe^{II}(CN)₆]⁴⁻ NPs obtained from different reaction's temperature.

The influence of the gold core size on the SPR phenomenon was studied by electronic spectroscopy. These core-shell NPs exhibit a SPR band localised between 537 and 540 nm (figure 32). Except for those obtained at 32°C, the band is weakly red-shifted with the increase of the gold core size (only 4 nm). These results seem to indicate that the SPR band is dependent of the gold size. However, it is difficult to compare the optical properties of these samples because in all cases, both gold core and PBA shell thickness are modified with the modification of the temperature (table 2). Then, the evolution of the SPR band may be originated from the core size, from the PBA shell thickness, or more rationally by both, which prevents to conclude on an effect of the gold core only. For that, it is necessary to measure the SPR band of core-shell NPs with different gold core sizes, but with a similar PBA shell thickness. However, the control of both gold core and PBA shell thickness still remains difficult.

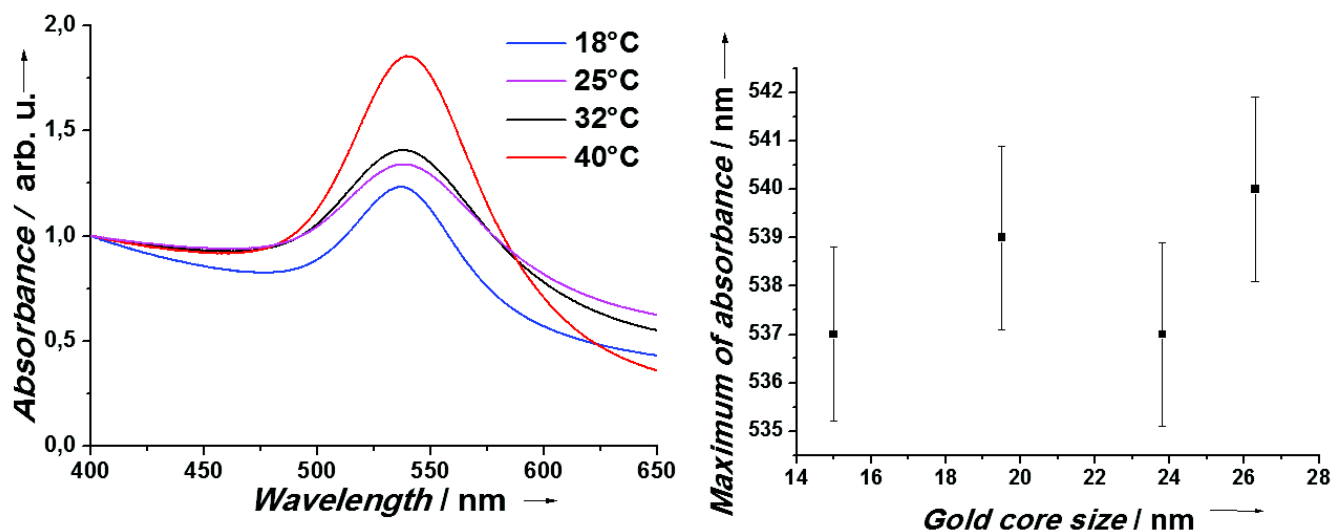


Figure 32: Left, evolution of the SPR band for core-shell Au@K⁺/Ni²⁺/[Fe^{II}(CN)₆]⁴⁻ NPs for several temperature. Right, evolution of the maximum of absorbance as a function of the gold core diameter.

To conclude, the synthesis of the Au@K⁺/Ni²⁺/[Fe^{II}(CN)₆]⁴⁻ NPs with temperature varying during the formation of the gold core permits a certain control of their mean core size; however large size distributions are observed, especially at high temperatures. The evolution of the SPR band is weakly dependent of the gold core size.

Main characteristics	Samples Au@K ⁺ /Ni ²⁺ /[Fe ^{II} (CN) ₆] ⁴⁻ NPs			
	2-18	2	2-32	2-40
Temperature during gold NPs synthesis (°C)	18	25	32	40
IR ν (-OH) (cm ⁻¹) Coordinate water	3580	3600	3593	3583
IR ν (-OH) (cm ⁻¹) Crystallized water	3422	3410	3405	3413
IR ν (Fe ^{II} -C≡N-Ni ^{II}) (cm ⁻¹)	2090	2094	2093	2093
IR δ (H-O-H) (cm ⁻¹) free water	1619	1622	1607	1615
IR ν (Fe ^{II} -C≡N) (cm ⁻¹)	590	586	590	590
IR δ (Fe ^{II} -CN) (cm ⁻¹)	462	461	462	462
Core size (nm)	15.0 ± 3.8	19.5 ± 4.3	23.8 ± 5.3	26.3 ± 5.0
Shell thickness (nm)	8.0 ± 2.2	16.6 ± 3.8	13.6 ± 2.8	11.3 ± 3.1
Total size (nm)	31.8 ± 4.9	52.4 ± 8.5	54.5 ± 7.5	51.0 ± 6.5
Estimated formula	Au _{0.5} @ K _{1.35} Ni[Fe ^{II} (CN) ₆] _{0.85}	Au _{1.08} @ K _{1.20} Ni[Fe ^{II} (CN) ₆] _{0.80}	Au _{1.65} @ K _{1.45} Ni[Fe ^{II} (CN) ₆] _{0.88}	Au _{1.9} @ K _{1.44} Ni[Fe ^{II} (CN) ₆] _{0.86}

Table 2: Main characteristics of the Au@K⁺/Ni²⁺/[Fe^{II}(CN)₆]⁴⁻ NPs obtained with varying the temperature.

II.4.2 control of the shell thickness.

Previously, we have seen by TEM monitoring that the PBA layer grows regularly on the cyanide-stabilized gold NPs to form the nanosized heterostructures. The core-shell NPs observed seems to be well-defined and then it should be rational to control the shell thickness by modulating the quantity of precursors added (*i.e.* the precursors volume added), and thus modulate the optical properties. Indeed, the increase of the PBA layer should modify the shell refractive index, changing the SPR band. The synthesis is strictly the same than for the $\text{Au}@K^+/\text{Ni}^{2+}/[\text{Fe}^{\text{II}}(\text{CN})_6]^{4-}$ NPs, with varying the quantity of PBA precursors added (*i.e.* the volume) (figure 33). Note that the NPs obtained with a small volume of precursors ($V \leq 2$ mL) can't be isolated by centrifugation, the excess of borohydride causing their aggregation. In this case, the borohydride is eliminated by hydrolysis by the addition of an hydrochloric acid solution (1M) monitored with pH-meter. The pH of the solution is turned from approximately 9.5 to 4, with the bubbling of dihydrogen which confirmed the acid hydrolysis of the KBH_4 , before the centrifugation ($\text{BH}_4^- + \text{H}_3\text{O}^+ + 2 \text{H}_2\text{O} \rightarrow 4 \text{H}_2(\uparrow) + \text{B}(\text{OH})_3$). Note that a decrease of the pH below 3 also leads to the aggregation of the NPs. After centrifuging, the NPs are washed with water and ethanol and dried under vacuum.

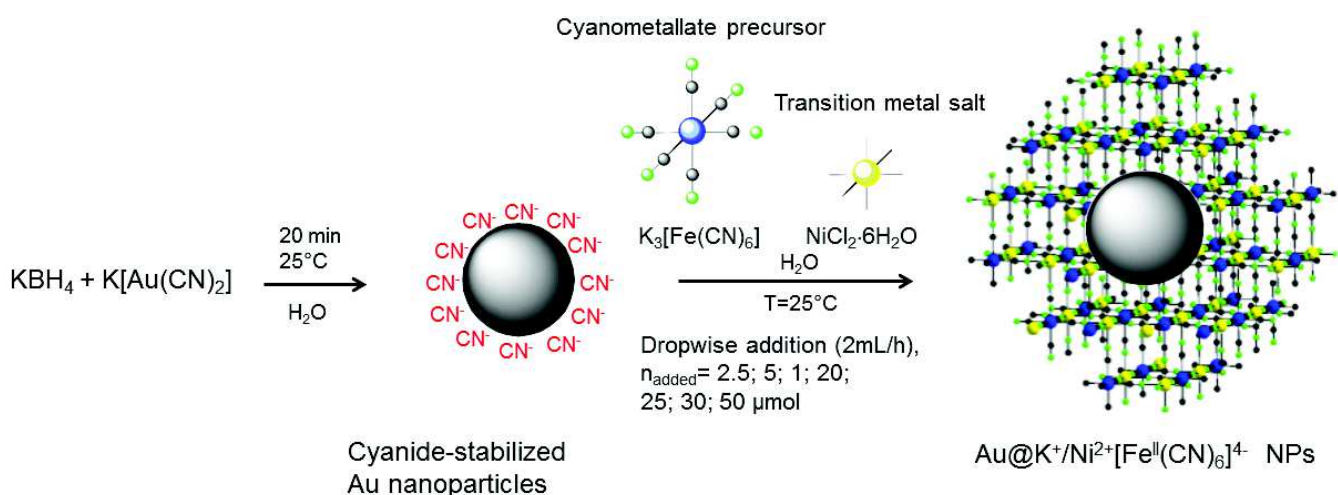


Figure 33: Schematic representation of the synthesis of core-shell $\text{Au}@K^+/\text{Ni}^{2+}/[\text{Fe}^{\text{II}}(\text{CN})_6]^{4-}$ NPs with varying of the shell thickness by modulation of the PBA precursors concentration added.

The IR spectra confirmed the formation of the cyano-bridged network (figure 34). Several bands observed are characteristic of the PBA structure, especially the cyanide stretching band located at 2094 cm^{-1} , typical of the $\text{Fe}^{\text{II}}-\text{C}\equiv\text{N}-\text{Ni}^{\text{II}}$ linkage³⁸⁻⁴³, and the metal carbon bond stretching and bending vibration bands located respectively at 590 cm^{-1} and 460 cm^{-1} , corresponding to the $\text{Fe}^{\text{II}}-\text{C}$ linkage. All the bands corresponding to the different samples are summarized in table 3. By comparing the IR spectra, the increase of the shell thickness shows no significant difference, whether the cyano-bridged network or the water molecules present in the framework, indicating that the structure of the PBA layer is not dependent of the volume of precursors added.

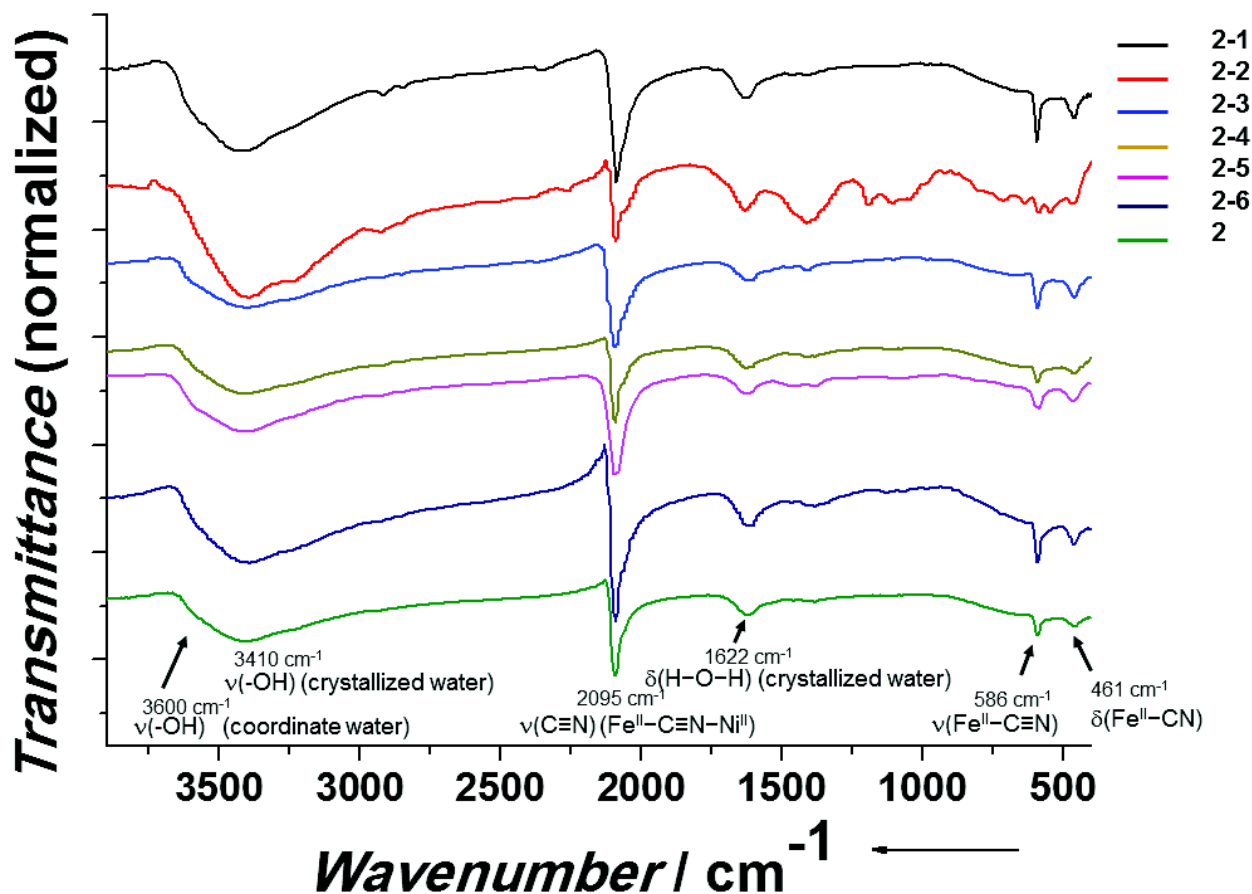


Figure 34: IR spectra of the core-shell Au@K⁺/Ni²⁺/[Fe^{II}(CN)₆]⁴⁻ NPs obtained by varying the PBA precursors concentration added

The EDX analyses permit to calculate the respective formula for the different core-shell NPs (table 3). By comparing these formulas, we can observe that the amount of gold decrease with the increase of the volume of PBA precursors added. This is concordant with the increase of the size of the PBA shell. Indeed, the relative amount of the gold remains the same in the samples because the core keeps the same size. However, the amounts of the cyano-bridged coordination polymer change because the layer grows as a function of time, which modifies their relative ratio. In appearance, the amount of the gold decreases, but it is a result of the coordination polymer layer growth.

TEM images confirm the formation of the targeted heterostructures Au@K⁺/Ni²⁺/[Fe^{II}(CN)₆]⁴⁻, with well-defined core-shell NPs incorporating a single gold core (figure 35). All the sizes (gold core, shell thickness and total size of the NPs) are presented in table 3. For all the samples, the size of the gold core remains the same, at an average diameter of 20 nm (figure 36). However, the entire size of the NPs increases as a function of the quantity of concentration added, from 25 to 52.4 nm. This is consistent with the regular increase of the PBA layer. Indeed, the size distribution of the coordination polymer shell thickness increases linearly with the amount of molecular precursor added, from 4 to 16.6 nm after 300 min (5 hours) of addition. Obtaining well-defined core-shell nano-objects with a narrow size distribution and a good reproducibility ensures a real control of the PBA shell thickness. Then it is possible to design core-shell Au@K⁺/Ni²⁺/[Fe^{II}(CN)₆]⁴⁻ nano-structures with a tunable PBA layer, if needed for different applications.

Main characteristics	2-1	2-2	2-3	2-4	2-5	2-6	2
Concentration of precursors added (μM)	2.5	4.9	9.6	18.5	22.7	26.7	41.6
IR $\nu(-\text{OH})$ (cm^{-1}) Coordinate water	3559	3559	3568	3580	3600	3593	3600
IR $\nu(-\text{OH})$ (cm^{-1}) water	3427	3427	3417	3411	3413	3416	3410
IR $\nu(\text{Fe}^{\text{II}}-\text{C}\equiv\text{N}-\text{Ni}^{\text{II}})$ (cm^{-1})	2090	2098	2098	2098	2093	2094	2095
IR $\delta(\text{H}-\text{O}-\text{H})$ cm^{-1} free water	1631	1631	1616	1623	1621	1623	1622
IR $\nu(\text{Fe}^{\text{II}}-\text{C}\equiv\text{N})$ (cm^{-1})	598	584	594	590	594	590	586
IR $\delta(\text{Fe}^{\text{II}}-\text{CN})$ (cm^{-1})	457	467	457	461	457	461	461
Gold core size (nm)	20.1 ± 4.2	20.2 ± 3.0	19.1 ± 4.6	19.5 ± 2.9	18.1 ± 3.0	19.2 ± 8.0	19.5 ± 4.3
Shell thickness (nm)	4.0 ± 1.3	$5.5 \pm 1,3$	$5.9 \pm 1,5$	$6.8 \pm 1,5$	$7.9 \pm 1,7$	9.2 ± 2.0	16.6 ± 2.7
Total size (nm)	25.3 ± 6.0	29.0 ± 4.0	31.0 ± 4.0	30.4 ± 4.2	33.9 ± 2.6	36.6 ± 4.5	52.4 ± 8.5
Estimated formula	$\text{Au}_{20.2}@\text{K}_{0.8}\text{Ni}[\text{Fe}^{\text{II}}(\text{CN})_6]_{0.7}$	$\text{Au}_{14.7}@\text{K}_{0.92}\text{Ni}[\text{Fe}^{\text{II}}(\text{CN})_6]_{0.76}$	$\text{Au}_{3.4}@\text{K}_{0.7}\text{Ni}[\text{Fe}^{\text{II}}(\text{CN})_6]_{0.68}$	$\text{Au}_{2.87}@\text{K}_{0.93}\text{Ni}[\text{Fe}^{\text{II}}(\text{CN})_6]_{0.72}$	$\text{Au}_{2.16}@\text{K}_{0.63}\text{Ni}[\text{Fe}^{\text{II}}(\text{CN})_6]_{0.65}$	$\text{Au}_{1.72}@\text{K}_{0.88}\text{Ni}[\text{Fe}^{\text{II}}(\text{CN})_6]_{0.69}$	$\text{Au}_{1.08}@\text{K}_{1.20}\text{Ni}[\text{Fe}^{\text{II}}(\text{CN})_6]_{0.80}$

Table 3: Main characteristics of the $\text{Au}@\text{K}^+/\text{Ni}^{2+}/[\text{Fe}^{\text{II}}(\text{CN})_6]^{4-}$ NPs obtained with varying the volume of precursors added.

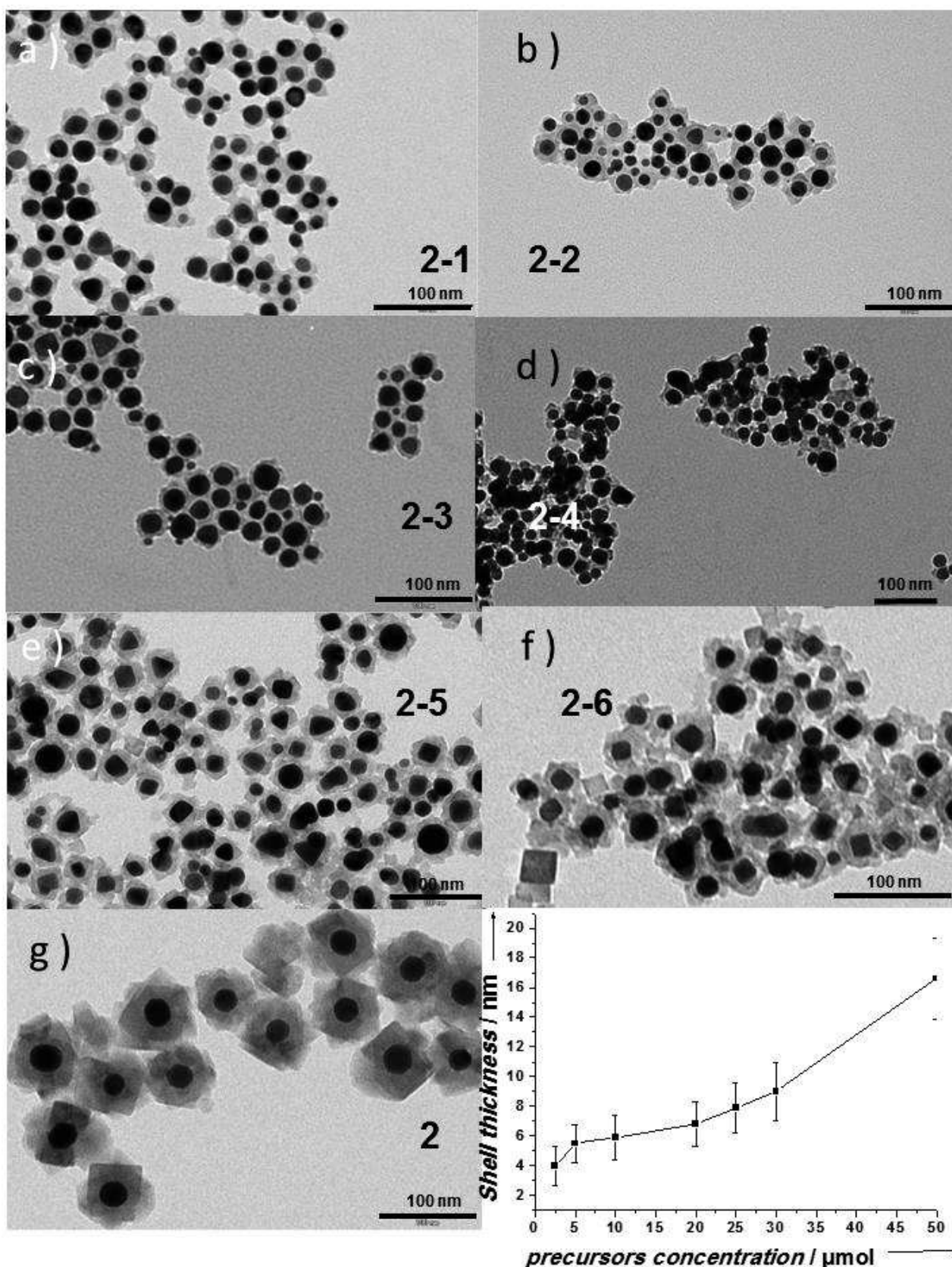


Figure 35: TEM images for of the $\text{Au}@K^+/\text{Ni}^{2+}/[\text{Fe}^{\text{II}}(\text{CN})_6]^{4-}$ NPs after different addition time of the molecular precursors. Time dependence of the shell thickness size measured by TEM. Line is a guide for eyes.

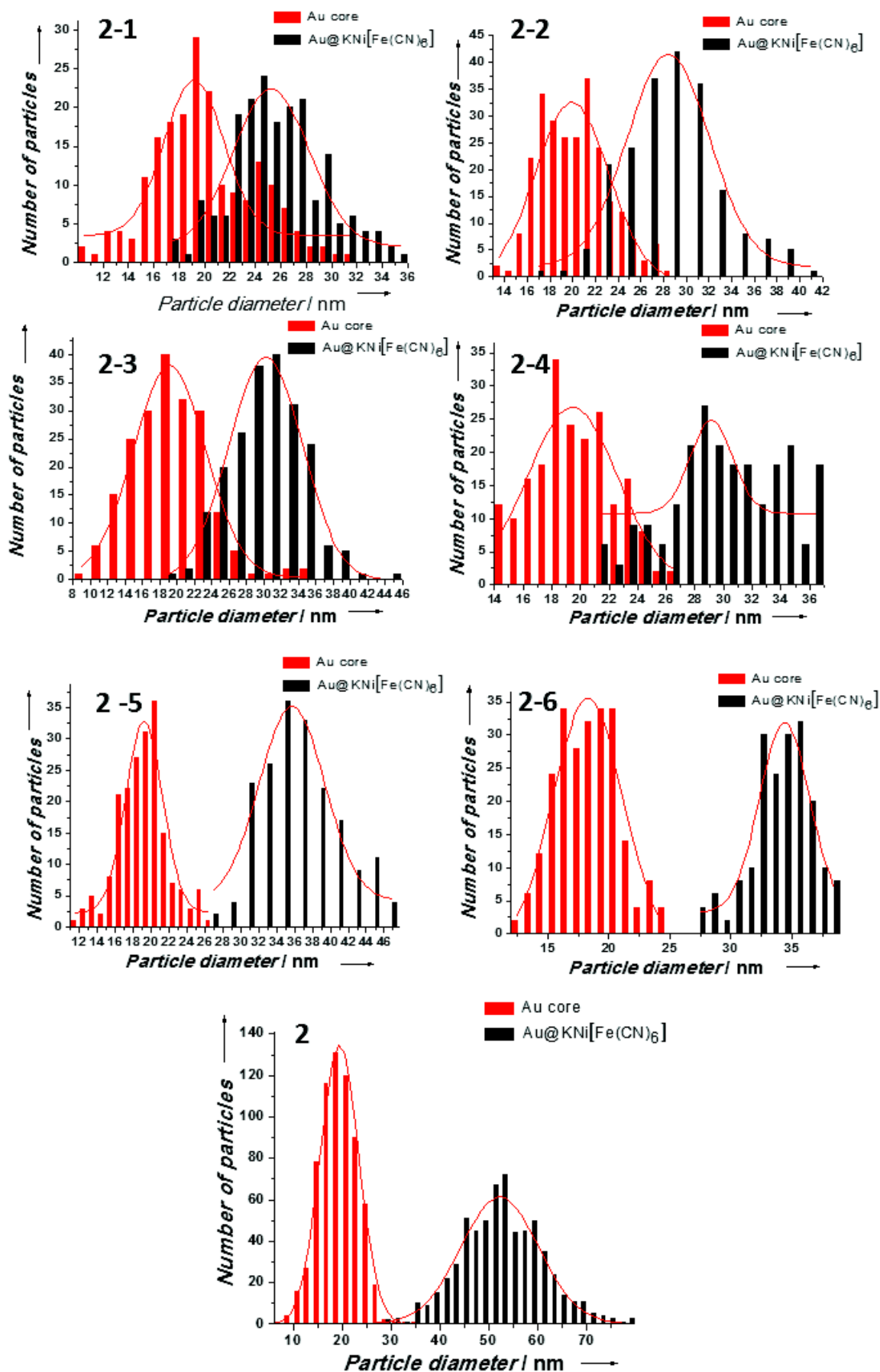


Figure 36: Size distributions of the gold core and the total size of the core-shell Au@K⁺/Ni²⁺/[Fe^{II}(CN)₆]⁴⁻ NPs obtained from different precursor concentration added.

The as-obtained Au@K⁺/Ni²⁺/[Fe^{II}(CN)₆]⁴⁻ NPs exhibit a SPR band in UV-visible spectroscopy (figure 37). A red-shift of the SPR band is observed from 520 to 539 nm, corresponding to the regular growth of the PBA shell on the surface of the gold core. This is due to the increase of the local refractive index around the gold core with the regular increase of the shell, which confirms the Mie theory prediction⁸⁻¹⁰ as observed in literature for core-shell Au@silica NPs⁴. However, comparatively to these systems, no blue-shift, resulting of the scattering phenomenon, is observed with the increase of the shell up to 16.6 nm. Note that for Au@silica NPs, this blue shift only occurs after a shell thickness of 35.5 nm. Nevertheless, the S-shaped curve shows a tendency to saturation starting from 9.2 nm (figure 37). This saturation indicates that change in the local dielectric environment beyond that distance (*i.e* 9.2 nm) to the surface no longer affects the electron oscillation of the gold NPs. For larger shell thicknesses, the electromagnetic field consists mainly of the scattering components, which determine the optical properties of the nanoparticles. This thickness limit found for the Au@KNi[Fe^{II}(CN)₆] nanoheterostructures is smaller than that found for the SiO₂ shell (15 nm) with a similar gold core size. Nevertheless, the significant enlargement of the band with the increase of the shell thickness is visible, as for core-shell Au@silica NPs⁴ and Au@Metal oxide NPs¹¹ (table 4). This width band enlargement may occur from the scattering phenomenon, as for Au@silica NPs¹⁰, or may originate from the confinement of the free electrons within the metal core with the shell size increase, as for the Au@Metal oxide NPs¹¹. Then, the control of the PBA shell thickness allows to precisely tune the maximum absorption wavelength. This could be interesting for future applications, with the possibility to modulate the size of the PBA's layer, permitting to target a selected wavelength.

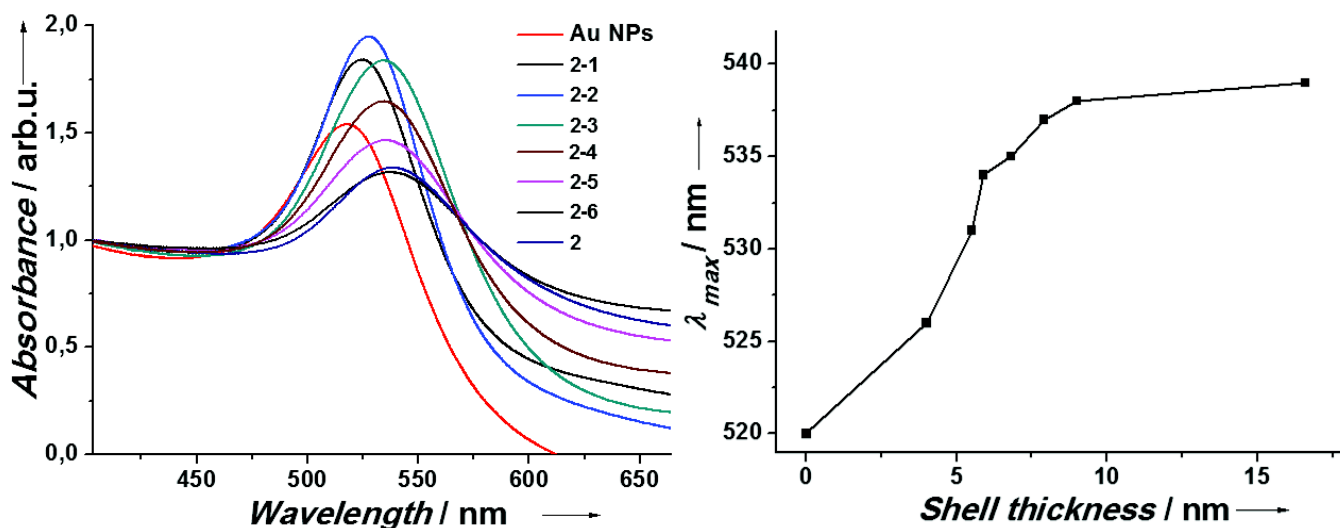


Figure 37: Left: Evolution of the SPR band for the NPs obtained for different precursors concentration. For a better visibility, the different spectra have been normalized to clearly show the red-shift. Right: The evolution of the maximum absorption wavelength of the SPR band as a function of the shell thickness. Line is a guide for eyes.

	Au NPs	Sample 2-1	Sample 2-2	Sample 2-3	Sample 2-4	Sample 2-5	Sample 2-6	Sample 2
Maximum of absorbance (nm)	520	526	531	534	535	537	538	539
Width of the band at half maximum (nm)	37	45	55	55	45	57	59	58

Table 4: table presenting the evolution of the maximum of absorbance and the width of the SPR band for the Au@K⁺/Ni²⁺/[Fe^{II}(CN)₆]⁴⁻ NPs with the different PBA shell thickness.

III.5 Modification of the precursors used to synthesize core-shell Au@K⁺/Ni²⁺/[Fe^{II}(CN)₆]⁴⁻ NPs.

III.5.1 Variation of the nature of the counter-ion precursors.

Some minor variations of the synthetic conditions of the core-shell NPs were performed, in order to investigate the possible influence of the K⁺ counter cation and the presence of counter anions on the NPs shell growth. Then, the synthesis of the core-shell NPs was performed by using precursors with Na⁺ as counter-ion instead of K⁺ (samples **2a** to **2d**). On the other hand, the interest of the use of Cl⁻ as counter-ion of the transition metal salt was investigated by replacing it by NO₃⁻ (sample **2e**). Finally, the role of cyanide from the dicyanoaurate salt was also studied by using a Au^{III} precursor, HAu^{III}Cl₄ (sample **2f**). All the combinations of the precursors used are summarized in table 5.

Label	Gold precursor	Reducer precursor	Metal transition salt	Cyanometallate salt
2a	K[Au ^I (CN) ₂]	KBH ₄	NiCl ₂ ·6H ₂ O	Na ₃ [Fe(CN) ₆]
2b	K[Au ^I (CN) ₂]	NaBH ₄	NiCl ₂ ·6H ₂ O	Na ₃ [Fe(CN) ₆]
2c	Na[Au ^I (CN) ₂]	KBH ₄	NiCl ₂ ·6H ₂ O	Na ₃ [Fe(CN) ₆]
2d	Na[Au ^I (CN) ₂]	NaBH ₄	NiCl ₂ ·6H ₂ O	Na ₃ [Fe(CN) ₆]
2e	K[Au ^I (CN) ₂]	KBH ₄	Ni(NO ₃) ₂ ·6H ₂ O	K ₃ [Fe(CN) ₆]
2f	HAu ^{III} Cl ₄	KBH ₄	NiCl ₂ ·6H ₂ O	K ₃ [Fe(CN) ₆]

Table 5: Different combinations of the precursors used to synthesize core-shell Au@Ni²⁺/[Fe^{II}(CN)₆]⁴⁻ NPs.

TEM images indicate that the variation of the synthetic precursors leads to similar core-shell heterostructures except for sample **2f**, prepared with the HAuCl₄ precursor (figure 38). The variation of the counter-cation nature (K⁺ or Na⁺), as the use of Na₃[Fe(CN)₆] instead of K₃[Fe(CN)₆] (sample **2a**) for the PBA precursors, or as the use of NaBH₄ instead of KBH₄ as reducing agent (**2b**) permits to design similar heterostructures. Moreover, the replacement of K[Au(CN)₂] with Na[Au(CN)₂] (**2c**) also leads to core-shell heterostructures when the reducing agent is KBH₄. However the combination of Na[Au(CN)₂] and NaBH₄ (**2d**) induces the formation of poorly-defined core-shell NPs, with a large amount of single gold NPs and K⁺/Ni²⁺/[Fe^{II}(CN)₆]⁴⁻ NPs, indicating a loss of the morphology control (**2e**). This seems to indicate that the presence of the K⁺ plays a role in the formation of the core-shell NPs, and exclude a “full Na⁺ synthesis” route. Otherwise, the replacement of K⁺ with Na⁺ induces for samples **2a** and **2c** the increase of the nucleation of single K⁺/Ni²⁺/[Fe^{II}(CN)₆]⁴⁻ NPs, which represents 20 % of the samples.

The variation of the counter-anion of the Ni²⁺ salt (Cl⁻ (**2**) or N(O₃)⁻ (**2e**)) also leads to the targeted core-shell heterostructures, indicating that the nature of this anion doesn't modify the morphology of the NPs.

On the other hand, the importance of the use of a dicyanoaurate salt was confirmed this time via synthetic approach. Indeed, replacing K[Au^I(CN)₂] by HAu^{III}Cl₄ as the gold precursor did not yield to the heterostructured NPs, only to two separated populations of gold and PBA NPs (sample **2f**). This is in agreement with our previous observations, and

supports the critical role of the cyanide ions in the formation of Au^I-CN-Ni coordination bond, which may be the anchoring point for the PBA shell growth.

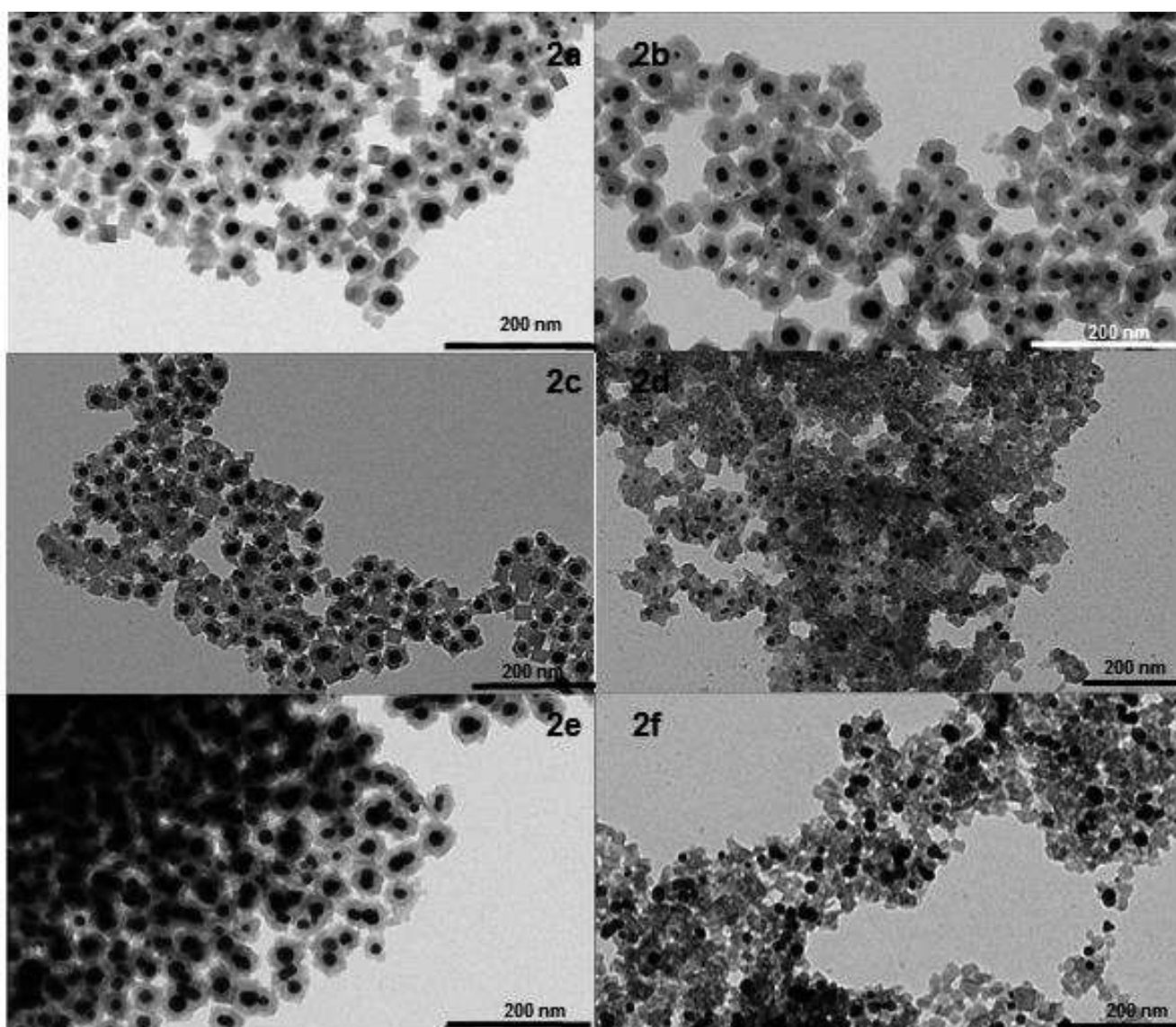


Figure 38: Core-shell Au@Ni²⁺/[Fe^{II}(CN)₆]⁴⁻ NPs obtained with varying the nature of the synthetic precursors.

For the samples presenting similar and well-defined core-shell heterostructures, the TEM distributions reveal that the nature of the counter-ions doesn't influence the gold core size (figure 39 and table 6), with a mean size close to 20 nm. However, the size of the PBA shell thickness is clearly affected by the variation of the counter-ions nature, with value of 8.8 ± 1.8 nm, 12.6 ± 2.5 nm, 9.2 ± 1.8 nm and 7.9 ± 1.7 nm for samples **2a**, **2b**, **2c** and **2e**, respectively. Then, a significant decrease of the shell thickness is observed comparatively to the original core-shell Au@K⁺/Ni²⁺/[Fe^{II}(CN)₆]⁴⁻ NPs (shell thickness = 16.6 ± 2.7 nm), indicating that the counter-ions nature may modify the kinetic of the PBA shell formation.

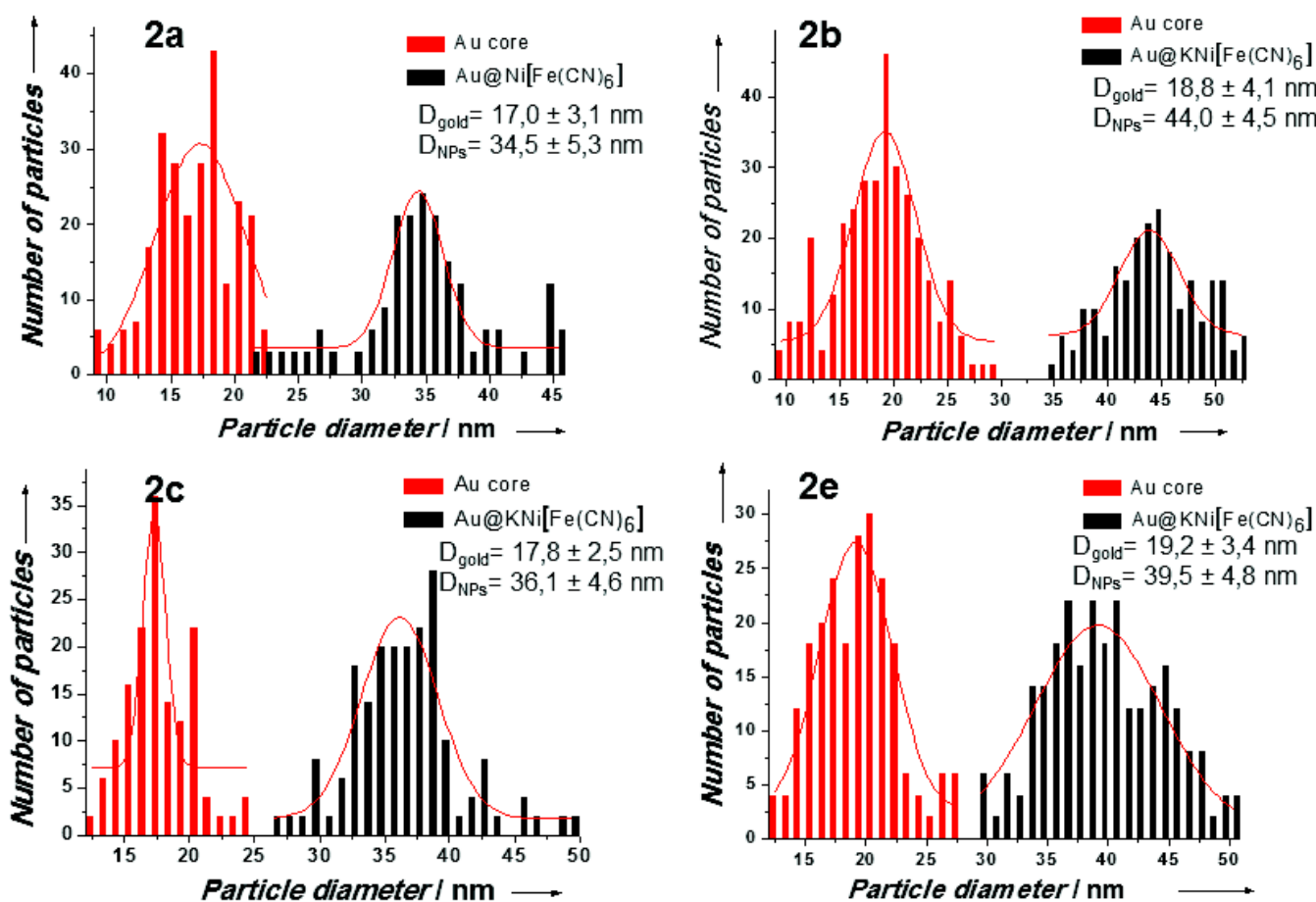


Figure 39: Size distribution for the core-shell heterostructures obtained with varying of the synthetic precursors.

IR spectroscopy confirms the formation of the cyano-bridged network for samples **2a**, **2b**, **2c** and **2e** (figure 40), with the presence of several bands characteristic of the PBA structure. The cyanide stretching band, typical of the $\text{Fe}^{\text{II}}-\text{C}\equiv\text{N}-\text{Ni}^{\text{II}}$ linkage³⁸⁻⁴³ is observed at 2094 cm^{-1} , and the metal carbon bond stretching and bending vibration bands corresponding to the $\text{Fe}^{\text{II}}-\text{C}$ linkage are located respectively at 594 cm^{-1} and 461 cm^{-1} . All the bands corresponding to the different samples are summarized in table 6. By comparing the IR spectra, no significant difference is observed indicating that the structure of the PBA layer is not dependent of the counter-ions of the precursors added.

EDX measurements gave us the elements' amounts for these core-shell NPs, permitting to calculate their respective formula (table 6). Their comparison revealed that the amount of potassium is lower for sample **2b**, *i.e.* when the reducing agent used is NaBH_4 instead of KBH_4 . Then the main origin of the K^+ inserted in the PBA shell structure may be originated from the excess of KBH_4 in the reaction media.

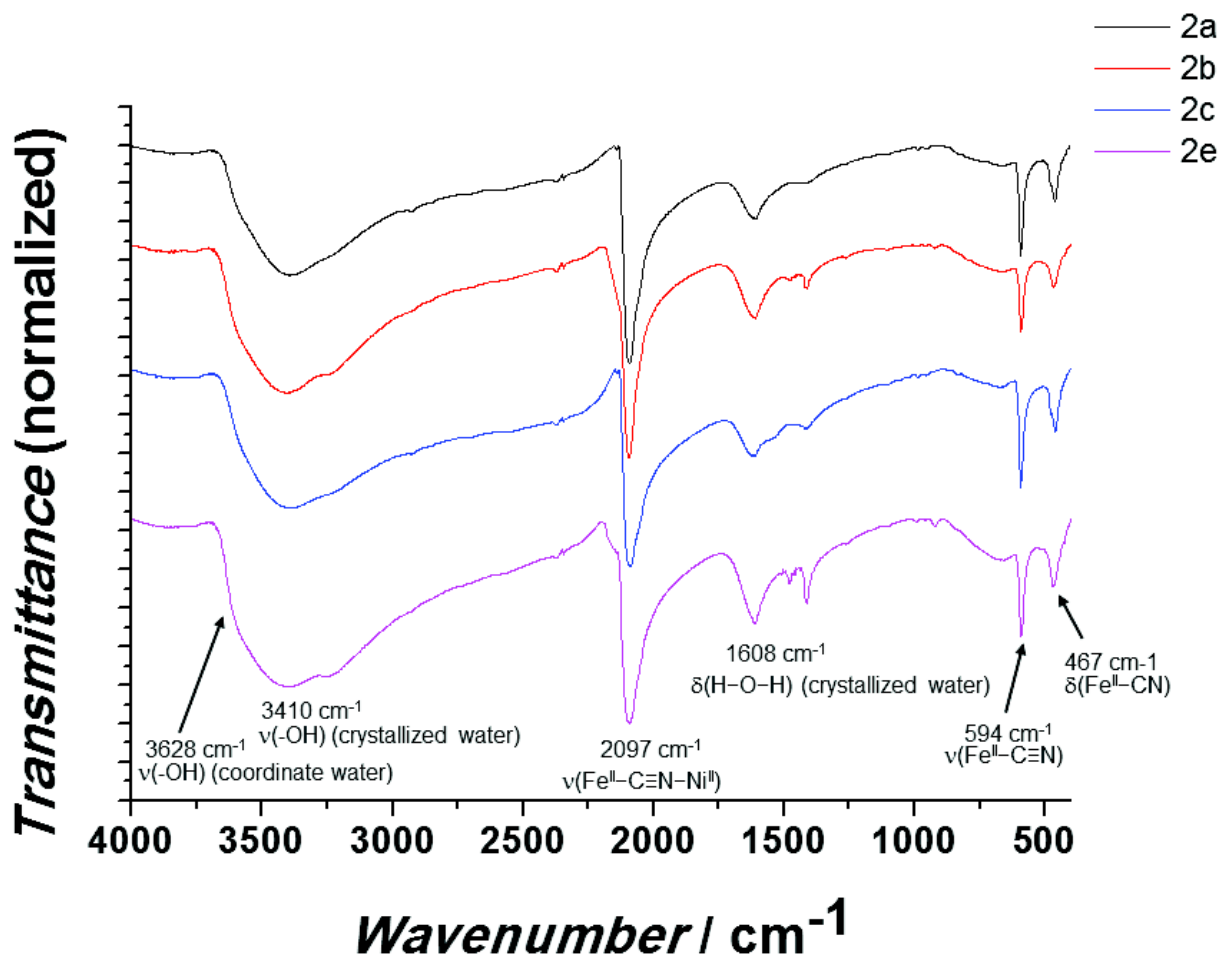


Figure 40: IR spectra of the core-shell NPs obtained by varying the counter-ions of the precursors used for the synthesis.

Main characteristics	2a	2b	2c	2e
IR $\nu(-OH)$ (cm^{-1}) Coordinate water	3606	3512	3594	3628
IR $\nu(-OH)$ (cm^{-1}) crystallized water	3403	3420	3403	3410
IR $\nu(Fe^{II}-C\equiv N-Ni^{II})$, (cm^{-1})	2090	2098	2094	2097
IR $\delta(H-O-H)$ (cm^{-1}) crystallized water	1606	1610	1623	1608
IR $\nu(Fe^{II}-C\equiv N)$ (cm^{-1})	595	590	590	594
IR $\delta(Fe^{II}-CN)$ (cm^{-1})	461	465	461	467
Gold core size (nm)	17.0 \pm 3.1	18.8 \pm 4.1	17.8 \pm 2.5	19.2 \pm 3.4
Shell thickness (nm)	8.8 \pm 1.8	12.6 \pm 2.5	9.2 \pm 1.8	7.9 \pm 1.7
Total size (nm)	34.5 \pm 5.3	44.0 \pm 4.5	36.1 \pm 4.6	39.5 \pm 4.8
EDX ratio Na/K/Fe/Ni/Au	3.1/10.7/15.8/22.4/48.0	5.55/13.1/20.45/31.4/29.5	0.45/23.8/15.55/18.3/41.9	0/27.2/17.4/21.9/33.1
Estimated formula	Au _{2.1} @ Na _{0.1} K _{0.6} [Fe ^{II} (CN) ₆] _{0.7}	Au _{0.94} @ Na _{0.18} K _{0.4} Ni[Fe ^{II} (CN) ₆] _{0.65}	Au _{2.3} @ Na _{0.2} K _{1.3} Ni[Fe ^{II} (CN) ₆] _{0.84}	Au _{1.1} @ K _{1.1} Ni[Fe ^{II} (CN) ₆] _{0.75}

Table 6: Main characteristics of the Au@Ni²⁺/[Fe^{II}(CN)₆]⁴⁻ NPs obtained with varying the synthetic precursors

III.5.2 Modification of the nature of the PBA layer.

The core-shell Au@K⁺/Ni²⁺/[Fe^{II}(CN)₆]⁴⁻ NPs synthesized by the approach previously described exhibit both optical and magnetic properties, as expected in the quest of the multifunctionality at the nanoscale. However, while their optical properties are interesting, the paramagnetic properties do not target future applications, which require strong response from an external stimulus. Then, the two-step approach permitting to obtain the core-shell Au@K⁺/Ni²⁺/[Fe^{II}(CN)₆]⁴⁻ NPs was revisited by changing the nature of the PBA precursors in order to modify shell nature and then properties of these heterostructured NPs. The main objective was to implement ferromagnetic properties, to synthesize magneto-plasmonic heterostructures, using as example the [Cr^{III}(CN)₆]³⁻ moiety⁵⁶⁻⁵⁹, selected for the spin S = 3/2 of the Cr^{III}. Moreover, its redox potential of -1.14 V is closer to the redox potential value of the reducer ((B(OH)₄/BH₄⁻) = -1.24 V), comparatively to the value of 0.36 V for the [Fe^{III}(CN)₆]³⁻, ensuring its higher stability against reduction.

On the other hand, the modification of the PBA nature may permit to access different properties, intrinsic to the selected PBA structure. For example, Prussian Blue (Fe^{III}₄[Fe^{II}(CN)₆]₃) is known for its host-guest property in the capture of Cs⁺⁶⁰⁻⁶³ and Tl⁺^{64,65}, and already has been used to treat the poisoning of these two radioactive ions^{66,67}. As an other example, the use of Rb_xCo_y[Fe(CN)₆]_z should permit to access photomagnetic properties^{56-59,68}. Thus, the modification of the PBA nature may permit to design diverse Au@M²⁺/[M'(CN)₆]³⁻ heterostructures exhibiting different multifunctionalities, and then a large range of applications could be considered.

The same synthesis than for Au@K⁺/Ni²⁺/[Fe^{II}(CN)₆]⁴⁻ NPs was performed with the replacement of the precursors nature, the concentrations (5.65 mM for the hexacyanometallate and 5.00 mM for the transition metal salt) and the addition rate (2 mL/h) being unchanged (figure 41). Several couples of M²⁺/[M'(CN)₆]³⁻ were investigated, and summarized in table 7. As described previously, Ni²⁺ and Co²⁺ present an important affinity with the gold NPs surface, and also Zn²⁺ in a lesser extent. Then for this reason, these bivalent metals ions were selected and associated to different hexacyanometallate precursors.

Name of sample	Transition metal salt used	Hexacyanometallate used	PBA layer targeted
3	Ni ^{II} Cl ₂ ·6H ₂ O	K ₃ [Cr ^{III} (CN) ₆]	Ni ^{II} ₃ [Cr ^{III} (CN) ₆] ₂
4	Ni ^{II} Cl ₂ ·6H ₂ O	K ₃ [Co ^{III} (CN) ₆]	Ni ^{II} ₃ [Co ^{III} (CN) ₆] ₂
5	Cu ^{II} Cl ₂ ·2H ₂ O	K ₃ [Fe ^{III} (CN) ₆]	Cu ^{II} ₃ [Fe ^{III} (CN) ₆] ₂
6	Fe ^{II} Cl ₂ ·6H ₂ O	K ₃ [Fe ^{III} (CN) ₆]	Fe ^{II} ₄ [Fe ^{III} (CN) ₆] ₃
7	Co ^{II} (NO ₃) ₂ ·3H ₂ O	K ₃ [Fe ^{III} (CN) ₆]	Co ^{II} ₃ [Fe ^{III} (CN) ₆] ₂
8	Co ^{II} Cl ₂ ·6H ₂ O	K ₃ [Fe ^{III} (CN) ₆]	Co ^{II} ₃ [Fe ^{III} (CN) ₆] ₂
9	Mn ^{II} Cl ₂ ·4H ₂ O	K ₃ [Fe ^{III} (CN) ₆]	Mn ^{II} ₃ [Fe ^{III} (CN) ₆] ₂
10		Zn ^{II} Cl ₂	K ₃ [Fe ^{III} (CN) ₆]
			Zn ^{II} ₃ [Fe ^{III} (CN) ₆] ₂

Table 7: Table presenting the different couples of transition metal salt/hexacyanometallate used, and their respective PBA expected to form the coordination polymer layer of the Au@M²⁺/[M'(CN)₆]³⁻ NPs.

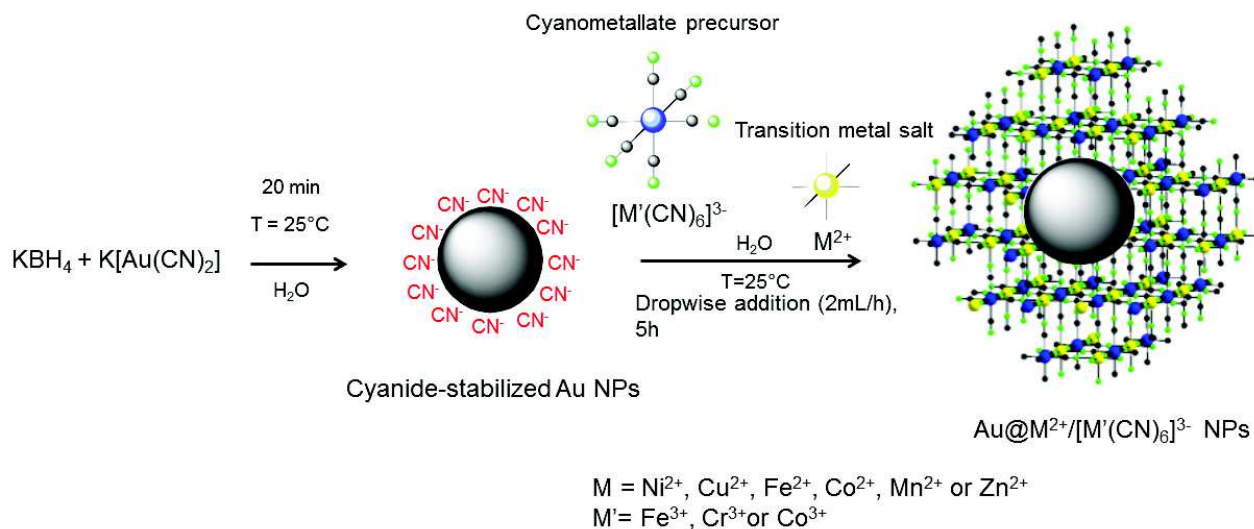


Figure 41: schematic representation of the approach to obtain $\text{Au@[M}^{2+}/\text{[M'(CN)}_6\text{]}^{3-}$ NPs.

The TEM images of the different samples clearly show that no well-defined core-shell NPs are obtained for all PBA except for samples **7** and **8** (figure 42), *i.e.* with using Co^{2+} precursors as bivalent metal precursor and $\text{[Fe(CN)}_6\text{]}^{3-}$ as hexacyanometallate precursor (table 7). The targeted heterostructures are observed only for these two samples, with an important population of $\text{K}^+/\text{Co}^{2+}/\text{[Fe}^{\text{II}}(\text{CN)}_6\text{]}^{4-}$ NPs (figure 42, **e**) and **f**). The use of Cu^{2+} leads to $\text{K}^+/\text{Cu}^{2+}/\text{[Fe}^{\text{II}}(\text{CN)}_6\text{]}^{4-}$ (**5**, figure 42, **e**) with cubic shape, and only few gold NPs. A similar result is observed when using Fe^{II} as bivalent metal precursor, with a less defined cubic shape of the $\text{K}^+/\text{Fe}^{2+}/\text{[Fe}^{\text{II}}(\text{CN)}_6\text{]}^{4-}$ NPs (figure 42, **d**). The use of Mn^{2+} and Zn^{2+} (figure 42, **g**) and **h**) leads for both cases to large PBA NPs (higher than 200 nm), with a well-defined cubic shape for the $\text{K}^+/\text{Mn}^{2+}/\text{[Fe}^{\text{II}}(\text{CN)}_6\text{]}^{4-}$ NPs (**9**), and a truncated cubic shape for the $\text{K}^+/\text{Zn}^{2+}/\text{[Fe}^{\text{II}}(\text{CN)}_6\text{]}^{4-}$ NPs (**10**). Moreover, a large amount of aggregated gold NPs are observed in both samples. Note that several heterostructures may be obtained for **10**, nevertheless a significant amount but however minority of the gold NPs also may be only on the PBA NPs and not in the structure. These observations are in agreement with the previous results. Indeed, we have observed that only an addition of bivalent metal ions such as Ni^{2+} and Co^{2+} , led to red-shift of the SPR band of the gold NPs suggesting the formation of $\text{Au}^{\text{I}}\text{-C}\equiv\text{N}-\text{Co}^{2+}$ coordination bond. Moreover, the combination of both, M^{2+} and $\text{[M}^{\text{III}}(\text{CN)}_6\text{]}^{3-}$ precursors has an important role in the formation of the heterostructures. For now, no rational explanation is advanced to explain the preferential formation of such $\text{Au}-\text{C}\equiv\text{N}-\text{M}^{2+}$ (with $\text{M} = \text{Ni}^{2+}$ or Co^{2+}) coordination bond at the surface of the gold NPs.

The variation of the hexacyanometallate precursor also does not lead to the targeted nano-heterostructures. Indeed, only few core-shell $\text{Au@[K}^+/\text{Ni}^{2+}/\text{[Cr}^{\text{III}}(\text{CN)}_6\text{]}^{3-}$ NPs are detected for sample **3**, but they remain a minority comparatively to the $\text{K}^+/\text{Ni}^{2+}/\text{[Cr}^{\text{III}}(\text{CN)}_6\text{]}^{3-}$ PBA NPs, which present an amorphous morphology (figure 42, **a**). For sample **4**, it is difficult to conclude on the heterostructure morphology, due to the aggregation of the NPs; however it is rational to think that the NPs observed are a mix of PBA and gold NPs (figure 42, **b**). Note that the $\text{K}^+/\text{Ni}^{2+}/\text{[Co}^{\text{III}}(\text{CN)}_6\text{]}^{3-}$ NPs observed present a similar amorphous aspect than for sample **3**. We can observe that only the synthesis with $\text{[Fe}^{\text{III}}(\text{CN)}_6\text{]}^{3-}$ moiety gives a satisfactory results. This may be explained by difference

of the formation's kinetic of the PBA shell, which depends on the nature of the precursors. The reduction of the $[\text{Fe}^{\text{III}}(\text{CN})_6]^{3-}$ moiety to the $[\text{Fe}^{\text{II}}(\text{CN})_6]^{4-}$ moiety during the reaction may also have an effect on the formation of the targeted heterostructures.

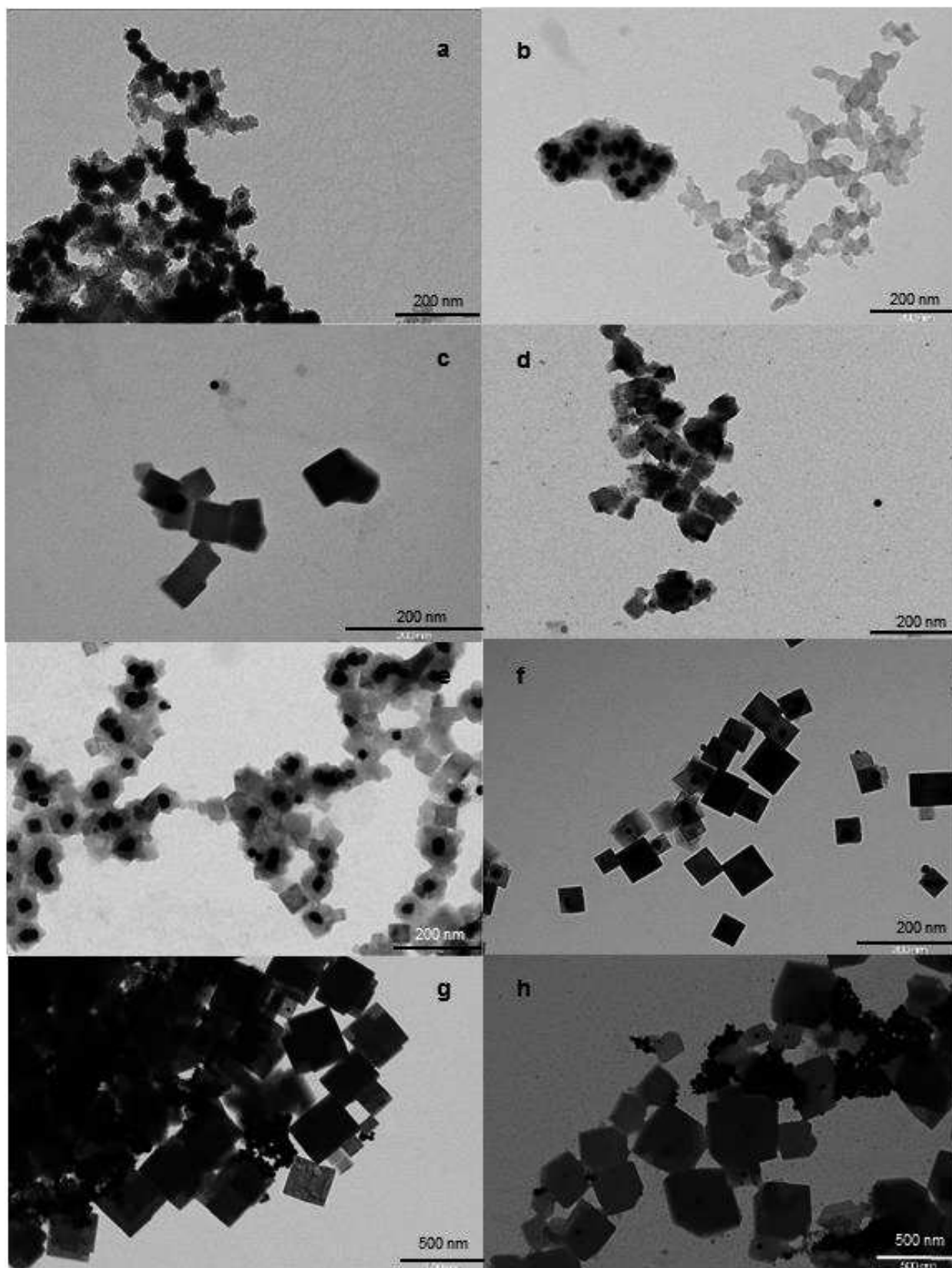


Figure 42: TEM images of the different attempts to obtain $\text{Au}@M^{2+}/[\text{Fe}^{\text{II}}(\text{CN})_6]^{4-}$ NPs with a) corresponding to sample 3, b) to 4, c) to 5, d) to 6, e) to 7, f) to 8, g) to 9 and h) to 10.

Due to the interesting results obtained with using Co^{2+} salts as bivalent metal precursors and $[\text{Fe}^{\text{III}}(\text{CN})_6]^{3-}$ as hexacyanometalate to form $\text{Au}@K^+/\text{Co}^{2+}/[\text{Fe}^{\text{II}}(\text{CN})_6]^{4-}$ NPs (**7** and **8**), the synthesis was optimized to reduce the amount of $K^+/\text{Co}^{2+}/[\text{Fe}^{\text{II}}(\text{CN})_6]^{4-}$ NPs observed with the targeted nano-heterostructures. The formation of an important amount of these PBA NPs, by comparison with the $\text{Au}@K^+/\text{Ni}^{2+}/[\text{Fe}^{\text{II}}(\text{CN})_6]^{4-}$ NPs (**2**) which present only 3% of PBA NPs, may be originated from a different kinetic of the formation of the PBA shell on the gold core. For the $\text{Au}@K^+/\text{Ni}^{2+}/[\text{Fe}^{\text{II}}(\text{CN})_6]^{4-}$ NPs, the growth of the $K^+/\text{Ni}^{2+}/[\text{Fe}^{\text{II}}(\text{CN})_6]^{4-}$ shell is predominantly promoted than the nucleation of single $K^+/\text{Ni}^{2+}/[\text{Fe}^{\text{II}}(\text{CN})_6]^{4-}$ NPs. By comparison, the nucleation of $K^+/\text{Co}^{2+}/[\text{Fe}^{\text{II}}(\text{CN})_6]^{4-}$ NPs seems to be favored in the case of the $\text{Au}@K^+/\text{Co}^{2+}/[\text{Fe}^{\text{II}}(\text{CN})_6]^{4-}$. Then, this is not enough to have a sufficient control of the design of such intricate structures. Previously, UV-visible measurements had shown that the addition of Co^{2+} induces a red-shift of the SPR band, but the quantity required is more important than for Ni^{2+} ion. Then, to promote the formation of the $K^+/\text{Co}^{2+}/[\text{Fe}^{\text{II}}(\text{CN})_6]^{4-}$ shell and optimize the synthesis of core-shell heterostructure, the same synthesis was performed starting with the addition of the Co^{2+} precursor at 20 min after the beginning of the reaction, as previously, and the starting of the $\text{K}_3[\text{Fe}(\text{CN})_6]$ addition was delayed (10 min (**7-1**); 30 min (**7-2**) ; 60 min (**7-3**)). This may favored the coordination of the Co^{2+} at the gold surface and may induce the preferential formation of core-shell heterostructure.

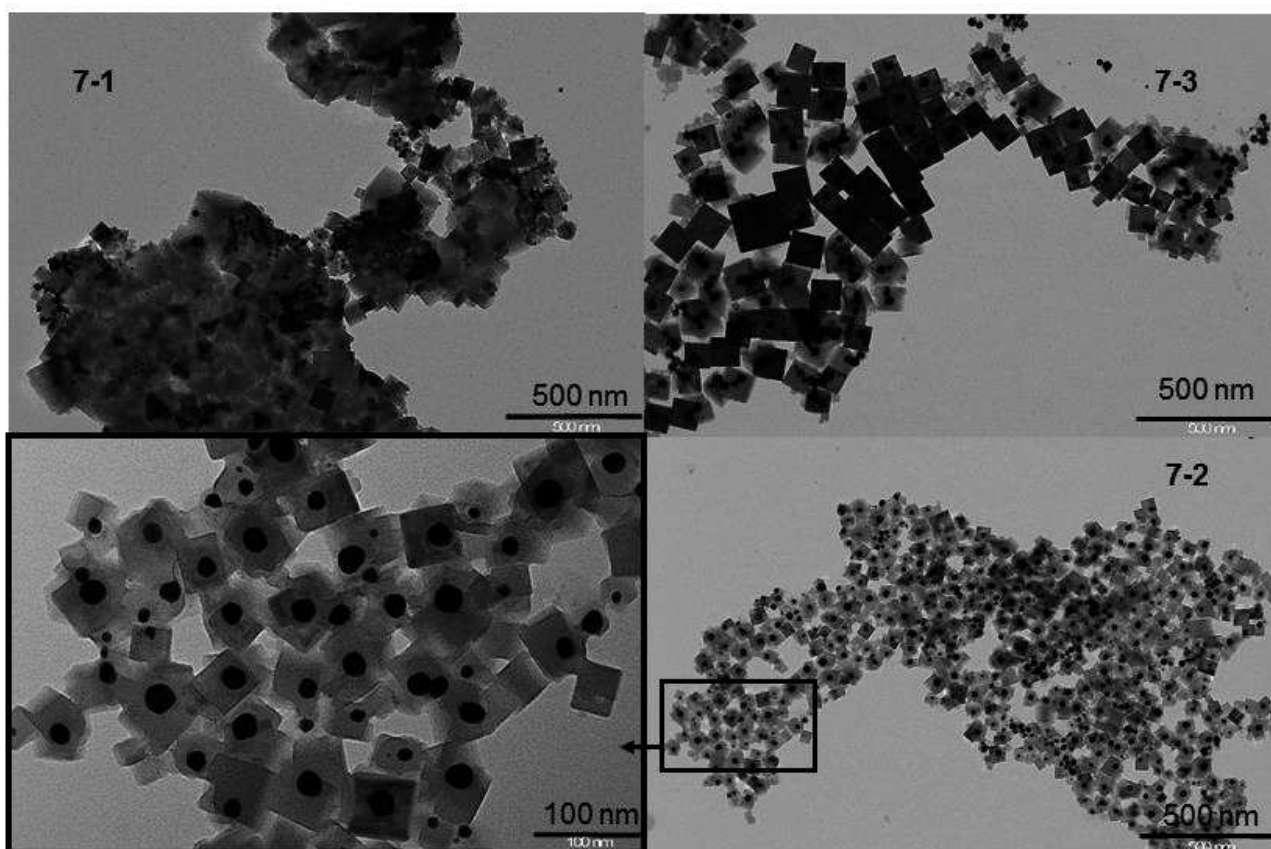


Figure 43 : TEM images of the $\text{Au}@K^+/\text{Co}^{2+}/[\text{Fe}^{\text{II}}(\text{CN})_6]^{4-}$ NPs, with their respective delays. In left the box image is a magnification on the $\text{Au}@K^+/\text{Co}^{2+}/[\text{Fe}^{\text{II}}(\text{CN})_6]^{4-}$ NPs with 30 min in time interval between the addition of the two precursors.

TEM images revealed that an effect of the addition precursors' delay occurs for an optimized time interval of 30 min (7-2) (figure 43). The Au@K⁺/Co²⁺/[Fe^{II}(CN)₆]⁴⁻ NPs obtained are well-defined and present a majority of population (80 %). Note however, than single K⁺/Co²⁺/[Fe^{II}(CN)₆]⁴⁻ NPs are still present as 20% of the total population. The addition with 10 (7-1) and 60 (7-3) min delays seems to largely promote the formation of single K⁺/Co²⁺/[Fe^{II}(CN)₆]⁴⁻ NPs, leading to two populations of K⁺/Co²⁺/[Fe^{II}(CN)₆]⁴⁻ and gold NPs. As for the Au@K⁺/Ni²⁺/[Fe^{II}(CN)₆]⁴⁻ NPs (2), the Au@K⁺/Co²⁺/[Fe^{II}(CN)₆]⁴⁻ NPs (7-2) have a gold core with a mean diameter of 20.0 ± 3.3 nm and a total size of 52.3 ± 7.0 nm (figure 44). The Co²⁺/[Fe^{II}(CN)₆]⁴⁻ shell thickness has a value of 16.2 ± 3.5 nm, which is also close to the K⁺/Ni²⁺/[Fe^{II}(CN)₆]⁴⁻ shell thickness for the larger Au@K⁺/Ni²⁺/[Fe^{II}(CN)₆]⁴⁻.

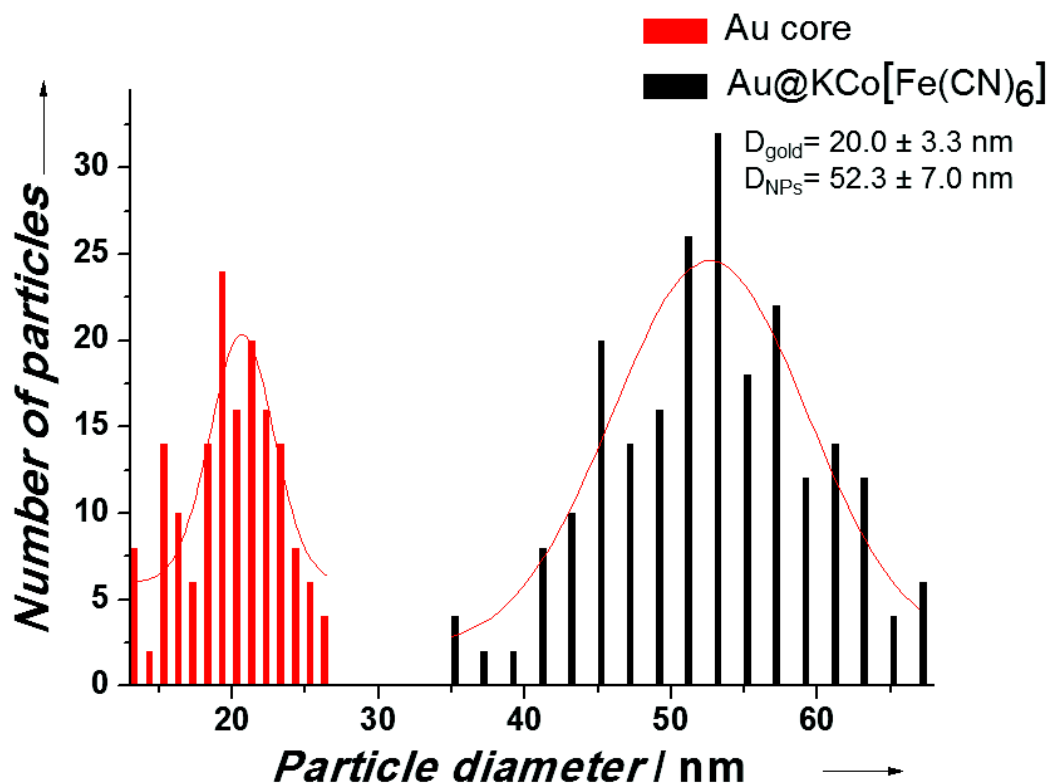


Figure 44: Size distribution of the gold core and the total size of the Au@K⁺/Co²⁺/[Fe^{II}(CN)₆]⁴⁻ NPs (7-2).

The optimized Au@K⁺/Co²⁺/[Fe^{II}(CN)₆]⁴⁻ NPs (7-2) were characterized using IR spectroscopy (figure 45). The formation of the structure of the PBA is confirmed by the presence of a band in the cyanide stretching region with a broad band located at 2081 cm⁻¹, attributed to Fe^{II}-C≡N-Co^{II} linkage³⁸⁻⁴³. No vibration band is observed at 2118 cm⁻¹ revealing the reduction of the [Fe^{III}(CN)₆]³⁻ to [Fe^{II}(CN)₆]⁴⁻ moiety similarly as for Au@K⁺/Ni²⁺/[Fe^{II}(CN)₆]⁴⁻ NPs. Furthermore, the presence of two bands corresponding respectively to the stretching vibration at 598 cm⁻¹ and the bending vibration at 460 cm⁻¹ of the Fe^{II}-CN linkage attests the formation of the Co^{II}[Fe^{II}(CN)₆] network^{42,43}. The presence of the stretching vibration band, at 3415 cm⁻¹ and the bending vibration band at 1635 cm⁻¹ indicates the presence of crystallized water molecules in the PBA structure. Moreover, the presence of a subtle shoulder at 3615 cm⁻¹ attributed to water molecules coordinated to metal ions, confirms the lacunar structure of the PBA. All the bands are summarized in table 8.

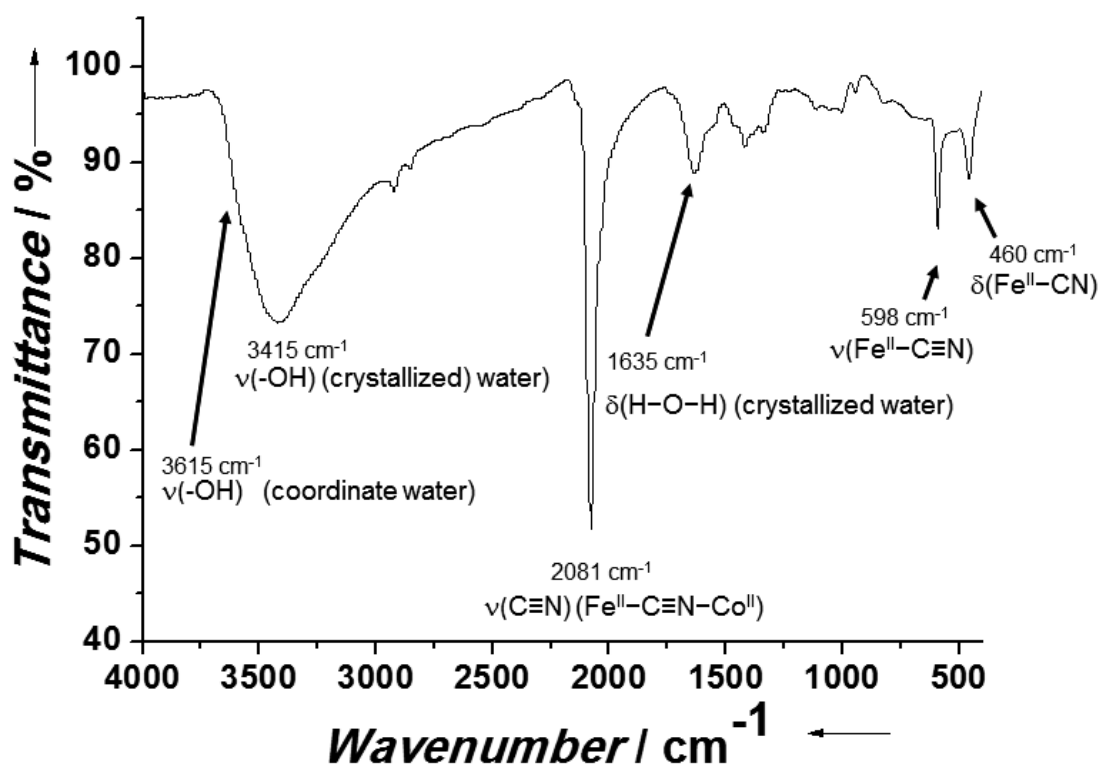


Figure 45: IR spectrum of the Au@K⁺/Co²⁺/[Fe^{II}(CN)₆]⁴⁻ NPs.

EDX analysis give us the amount of the different elements (K, 38.7; Co, 22.65; Fe, 20.45; Au, 18.2) permitting to deduce the formula of the core-shell NPs, which is Au_{0.88}@K_{1.36}Co_{0.8}[Fe^{II}(CN)₆]_{0.72}.

The formation of the heterostructure Au@K⁺/Co²⁺/[Fe^{II}(CN)₆]⁴⁻ NPs (7-2) is corroborated by PXRD with the presence of peaks attributed to both gold and KCo[Fe^{II}(CN)₆] structures (figure 46). PXRD pattern exhibit peaks at 38.2, 44.4, 64.9 77.6° and 81.9°, corresponding to the *fcc* gold metal structure (00-004-0784). They are indexed in the space group $F\bar{4}3m$, with a cell parameter $a_{\text{gold}} = 4.07 \text{ \AA}$. Moreover, peaks are observed at 17.6, 25.1, 28.4, 35.6, 51.4, 54.6, 57.8 and 69.5°, characteristic of KCo[Fe^{II}(CN)₆] structure, and indexed in the $F4\bar{3}m$ space group (01-075-0038), with a cell parameter of $a_{\text{CoFe}} = 10.04 \text{ \AA}$, which is in accordance with the value obtained in the literature⁵⁹. The Scherrer formula gives values of the crystallite size of 14.3 nm for gold and 30 nm for the PBA shell, which is in the same order than the values obtained by the size distribution performed on the TEM images.

The Au@K⁺/Co²⁺/[Fe^{II}(CN)₆]⁴⁻ NPs (7-2) exhibit optical properties, with the presence of the SPR band of the gold core (figure 47). The maximum of absorbance of the SPR band is observed at 542 nm, which is red-shifted comparatively to the initial gold NPs (517 nm). As for the Au@K⁺/Ni²⁺/[Fe^{II}(CN)₆]⁴⁻ NPs, such phenomenon occurs with the increase of the local refractive index around the gold core, due to the K⁺/Co²⁺/[Fe^{II}(CN)₆]⁴⁻ shell, as described in the literature^{4,5}.

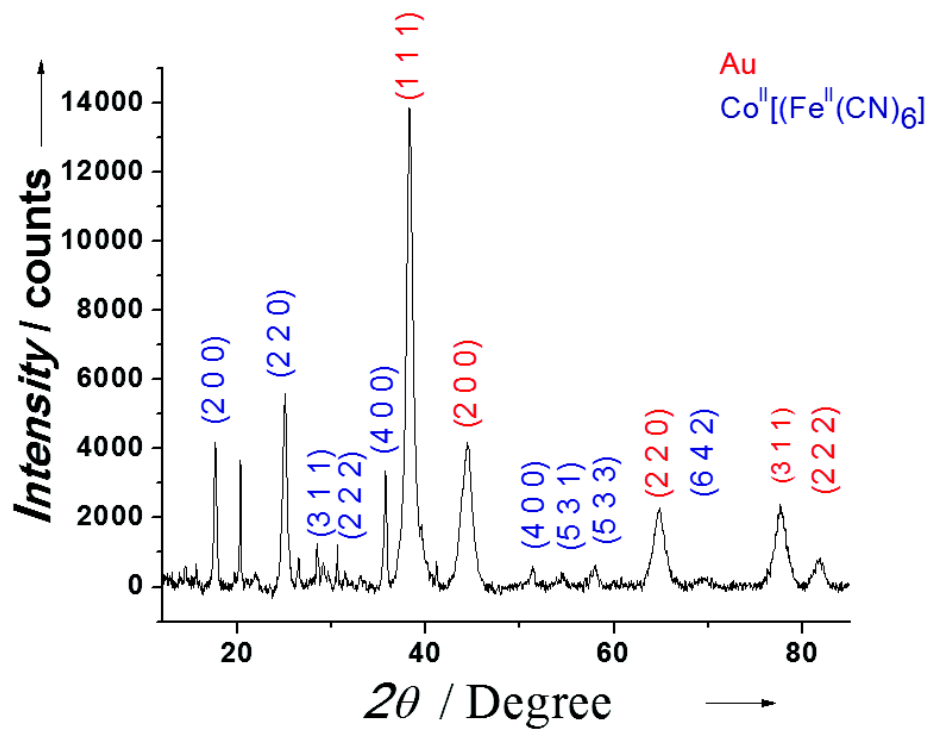


Figure 46: PXRD of Au@K⁺/Co²⁺/[Fe^{II}(CN)₆]⁴⁻ NPs (7-2).

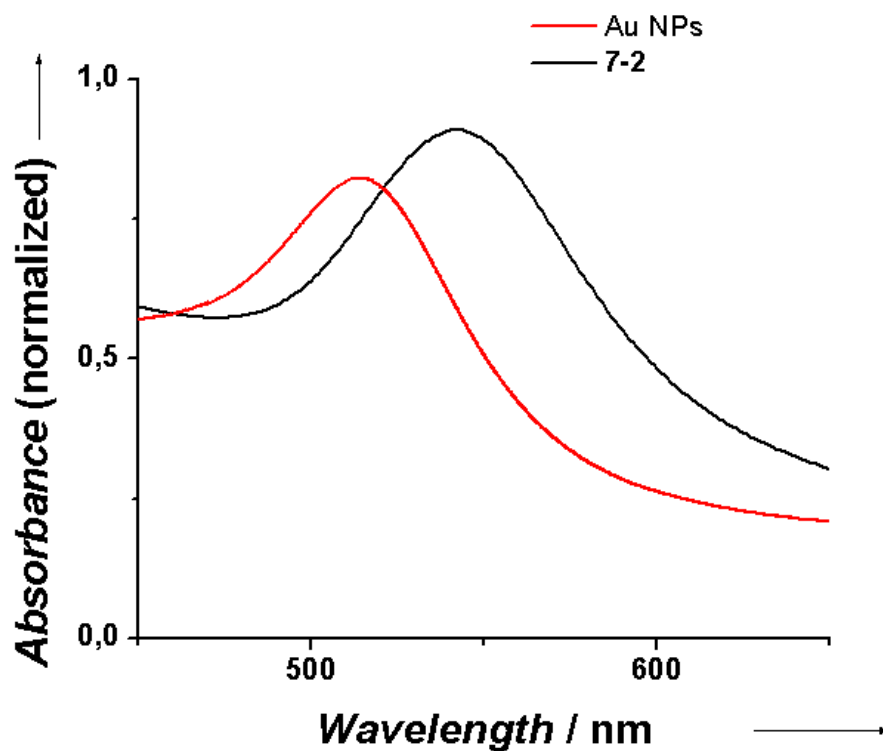


Figure 47: SPR band of the Au@K⁺/Co²⁺/[Fe^{II}(CN)₆]⁴⁻ NPs (7-2) and the initial gold NPs.

To conclude, we attempt to extend our approach leading to Au@K⁺/Ni²⁺/[Fe^{II}(CN)₆]⁴⁻ NPs to obtain Au@M²⁺/[M^{II}(CN)₆]⁴⁻ NPs.

For the case consisting in modification of the hexacyanometallate $[M^{III}(\text{CN})_6]^{3-}$ where $M = \text{Cr}^{3+}$ or Co^{3+} , no combination with the Ni^{2+} works to obtain heterostructured NPs.

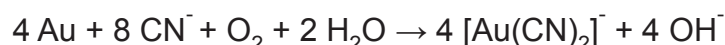
In the case consisting in modification of the bivalent metal ion, only the combination $M^{II}/[\text{Fe}^{III}(\text{CN})_6]^{3-}$ where $M^{II} = \text{Ni}^{2+}$ or Co^{2+} works well giving rise to a design of well-defined heterostructures, confirming the particular affinity of the cyanide-stabilized gold NPs to these metal ions as described previously. However, even if the synthesis of the core-shell $\text{Au}@K^+/\text{Co}^{2+}/[\text{Fe}^{II}(\text{CN})_6]^{4-}$ NPs has been successfully optimized by delaying the addition of the $[\text{Fe}^{III}(\text{CN})_6]^{3-}$ precursor (30 min, **7-2**) according to the addition of the Co^{2+} precursor, the formation of a 20 % of single $K^+/\text{Co}^{2+}/[\text{Fe}^{II}(\text{CN})_6]^{4-}$ NPs besides the heterostructural NPs has also been observed. Note also that the reduction of the cyanometallate moiety occurs during the synthesis as it was observed for $\text{Au}@K^+/\text{Ni}^{2+}/[\text{Fe}^{II}(\text{CN})_6]^{4-}$ NPs (**2**). Thus, the core-shell $\text{Au}@K^+/\text{Co}^{2+}/[\text{Fe}^{II}(\text{CN})_6]^{4-}$ may exhibit only paramagnetic properties, supported by the Ni^{2+} centers. Then, this method seems to not be the right route to implement properties such as ferromagnetism. A solution to avoid the reduction of the cyanometallate precursor $[M^{III}(\text{CN})_6]^{3-}$ moieties consists to perform a subsequent growing on the $\text{Au}@K^+/\text{Ni}^{2+}/[\text{Fe}^{II}(\text{CN})_6]^{4-}$ NPs, using the remaining of the $[\text{Fe}^{II}(\text{CN})_6]^{4-}$ moieties reactivity at the NPs surface. It will be presented in the chapter IV.

Main characteristics	$\text{Au}@K^+/\text{Co}^{2+}/[\text{Fe}^{II}(\text{CN})_6]^{4-}$ NPs (7-2)
IR $\nu(-\text{OH})$ coordinate water (cm^{-1})	3615 cm^{-1}
IR $\nu(-\text{OH})$ free water (cm^{-1})	3415 cm^{-1}
IR $\nu(\text{C}\equiv\text{N})$ $\text{Fe}^{II}-\text{C}\equiv\text{N}-\text{Ni}^{II}$ (cm^{-1})	2081 cm^{-1}
IR $\delta(\text{H}-\text{O}-\text{H})$ free water (cm^{-1})	1622 cm^{-1}
IR $\nu(\text{Fe}^{II}-\text{CN})$ (cm^{-1})	598 cm^{-1}
IR $\delta(\text{Fe}^{II}-\text{CN})$ (cm^{-1})	460 cm^{-1}
Lattice parameter (\AA)	$a_{\text{gold}} = 4.07 \text{ \AA}$ $a_{\text{NiFe}} = 10.04 \text{ \AA}$
Debye-Scherrer size (nm)	$d_{\text{gold}} = 14.3$ $d_{\text{CoFe}} = 30$
TEM size of gold core (nm)	$20.0 \pm 3.3 \text{ nm}$
TEM size of shell thickness (nm)	$16.2 \pm 3.5 \text{ nm}$
TEM size of total NPs (nm)	$52.3 \pm 7.0 \text{ nm}$
EDX ratio (K/Co/Fe/Au)	38.7/22.65/20.45/18.2
Estimated formula	$\text{Au}_{0.65}@K_{1.7}\text{Co}[\text{Fe}^{II}(\text{CN})_6]_{0.9}$
Maximum of absorbance	542 nm

Table 8: Table summarizing the main characteristics of the $\text{Au}@K^+/\text{Ni}^{2+}/[\text{Fe}^{II}(\text{CN})_6]^{4-}$ NPs (**7-2**).

III.6 Synthesis of Hollow nanoparticles

An interesting use of the $\text{Au}@K^+/Ni^{2+}/[Fe^{II}(CN)_6]^{4-}$ NPs is to obtain hollow NPs by removing the gold core³⁶. As reported in the first chapter, the synthesis of hollow nanostructures of coordination polymers, as PBA, has been developed during the last years for potential applications in catalysis, sensing, separation or drug delivery. To design hollow PBA NPs, the typical strategy consists in controlling an etching process of the cyano-bridged coordination polymer NPs^{69,70,71}. However, the strict experimental conditions (hydrochloric acid, 140°C)^{70,71} often lead to the total dissolution of the NPs. In our case, obtaining PBA hollow NPs can be performed by removing the gold core. It is well known that in presence of cyanide and oxygen, gold NPs are exposed to an etching process³⁸ leading to the formation of $[\text{Au}(\text{CN})_2]^-$, according to this equation:



The dissolution of the gold NPs is due to the high stability constant of the $[\text{Au}(\text{CN})_2]^-$ complex ($K=10^{37} \text{ M}^{-2}$). Then, the idea consists to remove the gold core using this etching process by taking advantage of the intrinsic microporosity of the PBA shell, which could permit the diffusion of the cyanide ions into the nano-heterostructures. Concretely, the hollow NPs (**2-h**) were obtained by dispersing the core-shell $\text{Au}@K^+/Ni^{2+}/[Fe^{II}(CN)_6]^{4-}$ NPs in a KCN aqueous solution ($2 \cdot 10^{-3} \text{ M}$) (figure 48). The reaction was easily followed by the disappearance of the characteristic red color, as the consequence of the gold core dissolution. Then the NPs were isolated by centrifugation and dried.

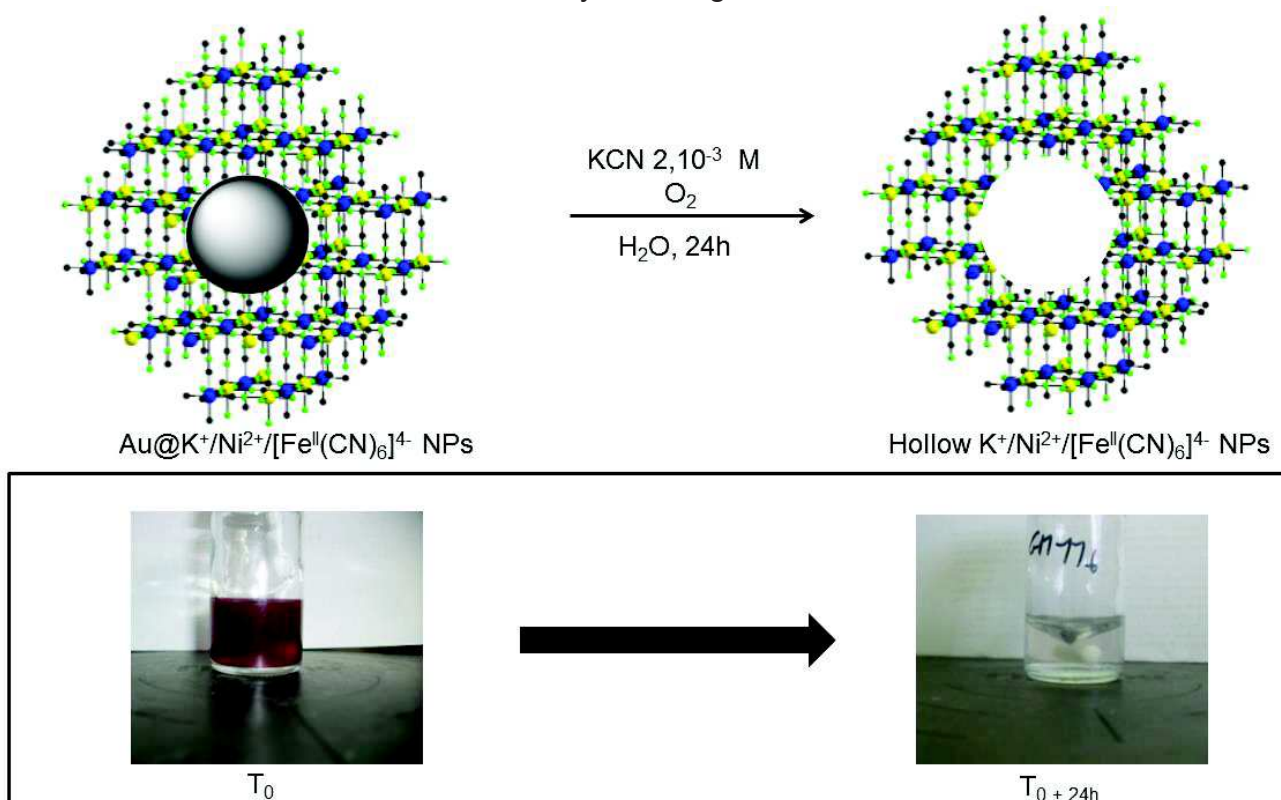


Figure 48: Up: schematic representation of the obtaining of Hollow PBA NPs (**2-h**) through the dissolution of the gold core of $\text{Au}@K^+/Ni^{2+}/[Fe^{II}(CN)_6]^{4-}$ NPs. Down: images of the $\text{Au}@K^+/Ni^{2+}/[Fe^{II}(CN)_6]^{4-}$ NPs solution at the addition of cyanide ions (T₀, left) and 24h latter (T₀+24h, right).

The presence of the PBA network for the obtained solid is attested by IR spectroscopy. The characteristic cyanide stretching vibration band located at 2094 cm^{-1} , corresponding to the $\text{Fe}^{\text{II}}-\text{C}\equiv\text{N}-\text{Ni}^{\text{II}}$ linkage³⁸⁻⁴³ is observed, such as for the core-shell $\text{Au}@K^+/\text{Ni}^{2+}/[\text{Fe}^{\text{II}}(\text{CN})_6]^{4-}$ NPs. The remaining of the PBA structure is also attested by the stretching vibration band located at 589 cm^{-1} , and the bending vibration band located at 460 cm^{-1} , characteristic of the $\text{Fe}^{\text{II}}-\text{CN}$ linkage^{42,43}. The presence of crystallized water molecules in the PBA structure³⁵ is confirmed by the stretching vibration band located at 3415 cm^{-1} , and the bending vibration band located at 1626 cm^{-1} . Furthermore, the shoulder at 3587 cm^{-1} , attributed to coordinated water molecules⁴³, is a proof of the lacunar structure of the PBA shell, as for the initial core-shell NPs (figure 49).

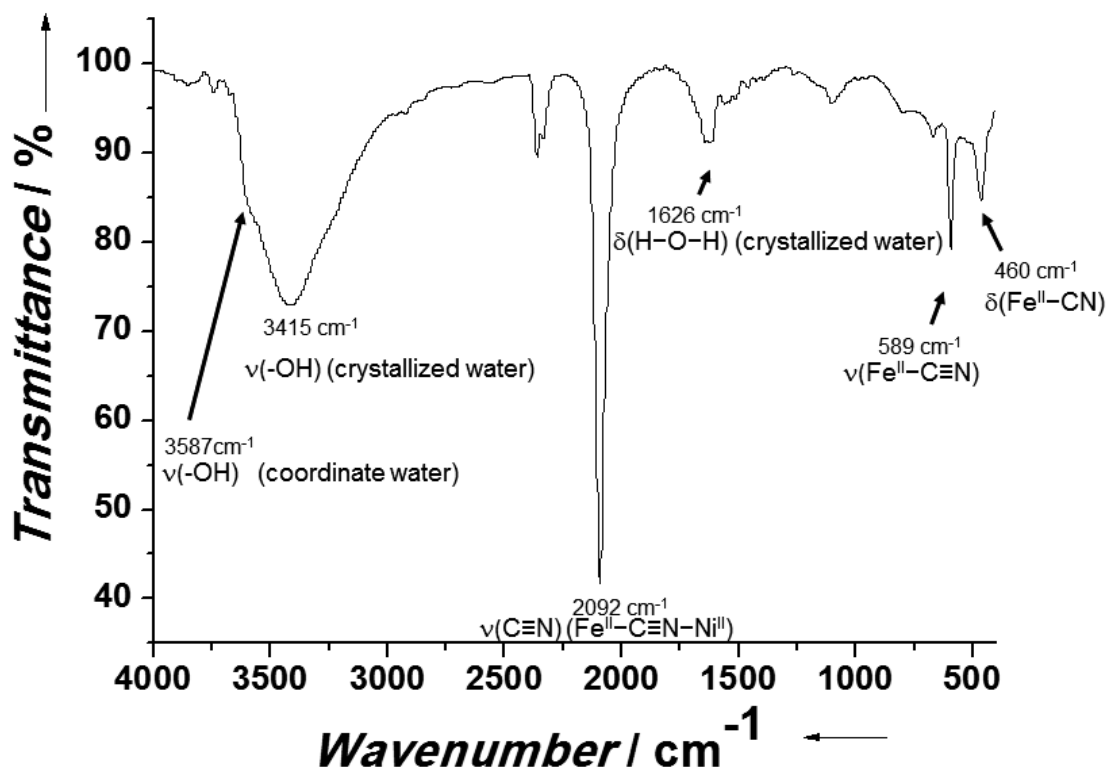


Figure 49: IR spectrum of the hollow $K^+/\text{Ni}^{2+}/[\text{Fe}^{\text{II}}(\text{CN})_6]^{4-}$ NPs.

PXRD pattern confirms that the PBA structure keeps its integrity, with the presence of peaks observed at 17.7 , 25.1 , 37.7 , 51.2 , 55.6 and 58.9° , characteristic of $\text{Ni}_2[\text{Fe}^{\text{II}}(\text{CN})_6]$ structure, and indexed in the $F4-3m$ space group ($01-075-0037$), with a cell parameter of $a_{\text{NiFe}} = 10.04\text{ \AA}$ (figure 50). Moreover, no peak corresponding to the gold structure is observed, comparatively to the original $\text{Au}@K^+/\text{Ni}^{2+}/[\text{Fe}^{\text{II}}(\text{CN})_6]^{4-}$ NPs, which corroborates the dissolution of the gold core to form hollow nanostructures. The size of the crystallites given by the Debye-Scherrer calculator has a value of 20.6 nm , which is in accordance with the size of the original core-shell NPs, and then corresponds to the expected size of the hollow NPs.

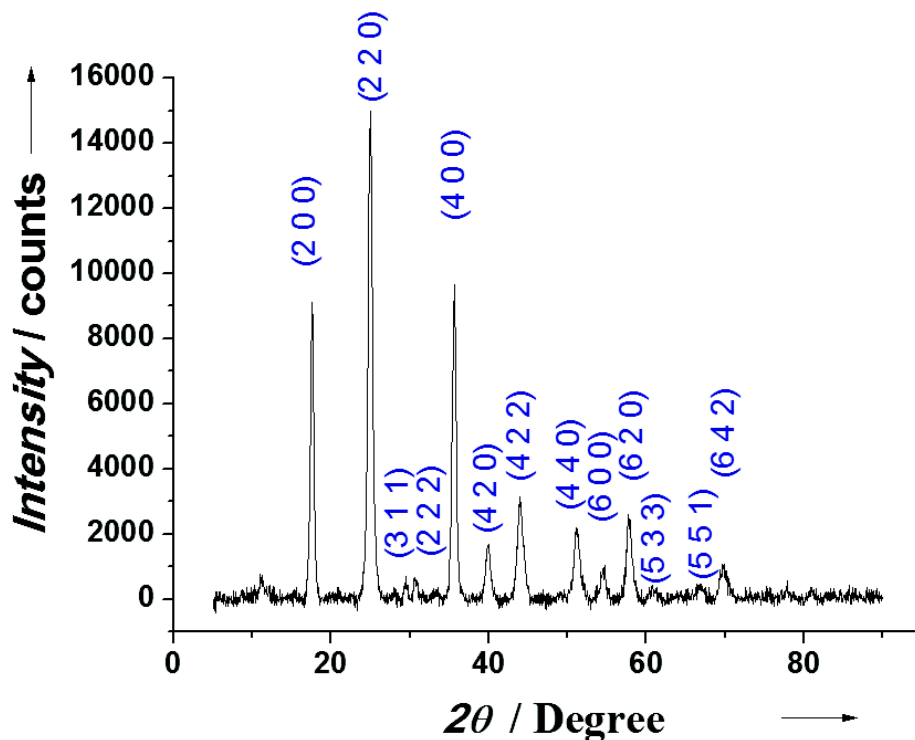


Figure 50: Room temperature PXRD pattern for the hollow $K^+/Ni^{2+}/[Fe^{II}(CN)_6]^{4-}$ NPs, with the Miller indices (h k l) corresponding to the $Ni_2[Fe^{II}(CN)_6]$ PBA structure.

The formation of the targeted hollow nanostructures is confirmed by the TEM images. All gold cores have vanished, remaining only the hollow cyano-bridged framework (figure 51). Their size distribution is 53.8 ± 5.2 nm, which is close to the initial NPs, confirming the integrity of the shell.

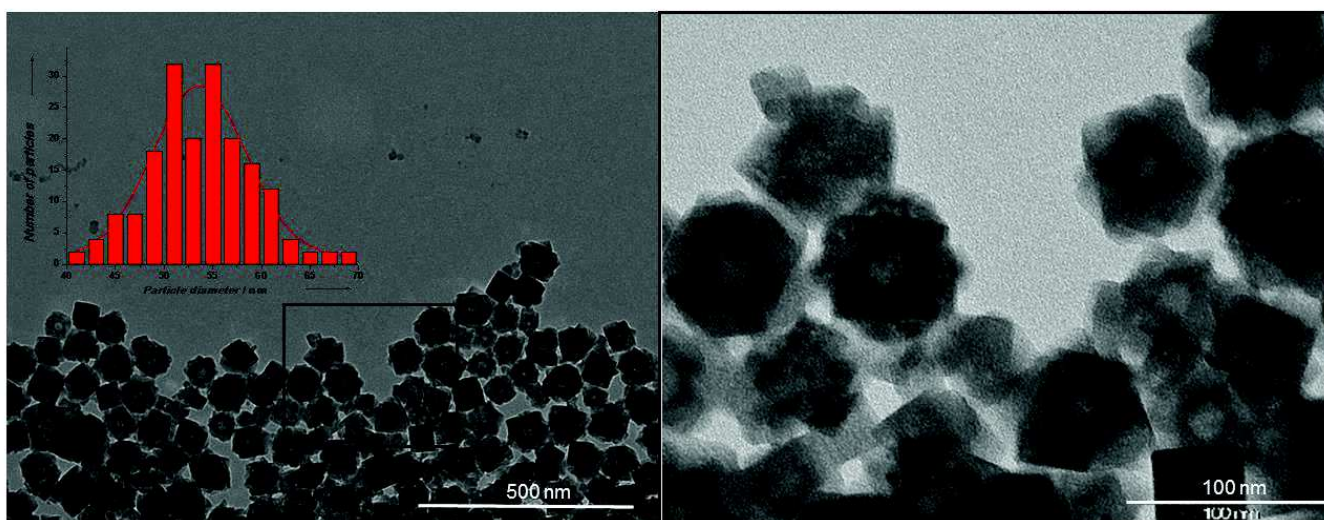


Figure 51: Left: TEM image of the hollow $K^+/Ni^{2+}/[Fe^{II}(CN)_6]^{4-}$ NPs. Inset: size distribution of the NPs. Right: Magnification of the hollow NPs.

The progressive vanishing of the color during the synthesis of the hollow NPs corresponds to a gradual modification of the SPR band, before to completely disappearance, due to dissolution of the gold core. This phenomenon is followed by UV-Vis monitoring (figure 52). The decrease of the maximum of absorbance of the band with time is observed, confirming the observations during the synthesis, the red-color solution becoming colorless in only two hours, but a trouble persisting during several hours. During the discoloration period, a blue-shift of the maximum of absorbance occurs, characteristic of the size diminution of the gold core. Indeed, the size is one of the most important parameters influencing the SPR band^{8,9}, and its decrease leads to such phenomenon. That also confirms the gradual dissolution of the Au@KNiFe core, leading to smaller gold NPs until their complete disappearance.

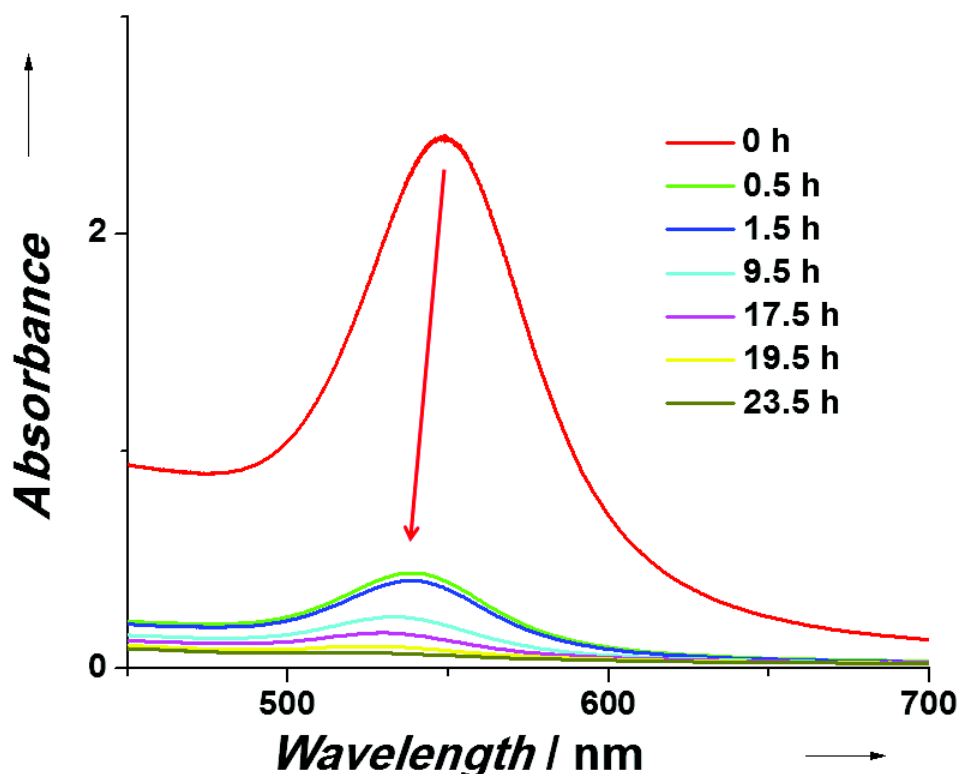


Figure 52: UV-Vis modification of the SPR band during the etching process leading to the $K^+/Ni^{2+}/[Fe^{II}(CN)_6]^{4-}$ hollow NPs (2-h).

Thus, we can obtain hollow PBA NPs by totally removing the gold core of the $Au@K^+/Ni^{2+}/[Fe^{II}(CN)_6]^{4-}$ nano-heterostructures. However, this method presents some difficulties. The dissolution of the gold core requires important amount of core-shell NPs with a well-formed structure of the cyano-bridged polymer layer. Several times, in same conditions, the attempts to remove the gold core were followed by a complete desegregation of the coordination polymer framework, leading to PBA fragments, which reveals the difficulty to control the reaction. Moreover, this reaction is limited to the initial quantity of the core-shell NPs used, and the yield is only 47%. Indeed, according to the elemental analysis, the gold represents 41.3% of the weight of the NPs, and then, the removing the gold core leads to a loss of weight for the hollow NPs. Thus it is difficult to obtain large amount of these hollow NPs, due to both the synthesis of sufficient quantities of the initial $Au@NiFe$ NPs, requiring time, and the etching of the gold, which is difficult to control and leads to few quantities of final product. Nevertheless, this process has the advantage to be effectuated in less-strict conditions than for the hollow PB NPs described in the literature^{70,71}.

III.7 Conclusion

In this chapter, we described a new and a rational approach to obtain core-shell $\text{Au}@K^+/Ni^{2+}/[Fe^{II}(CN)_6]^{4-}$ NPs, their structural and textural characterizations, to understand the growing mechanism of these core-shell heterostructures and to extend the approach to other PBA shells. The synthesis consists in a two steps method including 1) the formation of the cyanide-stabilized gold NPs in aqueous solution by reduction of the dicyanoaurate precursor $[\text{Au}(\text{CN})_2]^-$ with potassium borohydride, and 2) the growth of the PBA shell on the surface of the gold, performed by a slow addition of the precursors. First of all we focalized on the synthesis of $\text{Au}@K^+/Ni^{2+}/[Fe^{II}(CN)_6]^{4-}$ NPs by using the $\text{NiCl}_2 \cdot 6\text{H}_2\text{O}$ and the $\text{K}_3[\text{Fe}^{III}(\text{CN})_6]$ as PBA precursors.

The as-obtained core-shell nano-heterostructures were characterized by using several techniques. IR spectroscopy confirmed the formation of the cyano-bridged network shell, but the $[\text{Fe}^{III}(\text{CN})_6]^{3-}$ moiety was clearly reduced to $[\text{Fe}^{II}(\text{CN})_6]^{4-}$, because of residual KBH_4 in the reaction media. XRD patterns have revealed the presence of both the gold and the PBA crystalline structures. Elemental analysis provided the formula of the NPs, which is $\text{Au}_{1.08}@\text{K}_{1.20}\text{Ni}[\text{Fe}(\text{CN})_6]_{0.80} \cdot 3.2\text{H}_2\text{O}$. The TEM images show the formation of well-defined core-shell heterostructure $\text{Au}@K^+/Ni^{2+}/[Fe^{II}(\text{CN})_6]^{4-}$ NPs, with a single core of 19.5 ± 4.3 nm coated with a homogenous shell of cyano-bridged coordination polymer, for a total size of 52.4 ± 8.6 nm. TEM, HRTEM and STEM have bring several information's of the shape and the structure of the NPs. DLS measurements confirm the good dispersion of the NPs in water, and the value of the Zeta potential, -23.6 ± 4.3 mV, indicates remaining of reactive $[\text{Fe}^{II}(\text{CN})_6]^{4-}$ moieties at the surface of the PBA layer. The UV-visible measurements revealed the optical properties of the nano-objects, which exhibit an intense SPR band at 537 nm. The reduction of the Fe^{III} to Fe^{II} in the PBA structure leads to a paramagnetic behavior of the NPs. Thus, the $\text{Au}@K^+/Ni^{2+}/[Fe^{II}(\text{CN})_6]^{4-}$ NPs exhibit a multifonctionality by combination of the paramagnetism and plasmonic properties.

To better understand the mechanism of the NPs formation, we investigated the first stage of the NPs formation: the behavior of the cyanide-stabilized Au NPs when the bivalent metal ion ($M^{2+} = \text{Ni}^{2+}$) is added in the reaction media. After addition of drops of Ni^{2+} in a gold NPs solution, DLS measurements indicated that an increase of the hydrodynamic diameter occurs, and Zeta potential measurements revealed a modification of the Zeta potential with first a decrease, then an increase until a positive value, due to the presence of positive charges at the gold NPs surface. The modification of the SPR band in the electronic spectra with the addition of Ni^{2+} in a gold NPs solution confirmed the occurrence of a particular affinity between the bivalent metal ion and the cyanide-stabilized gold NPs. Raman spectroscopy performed on gold NPs solution with the addition of Ni^{2+} revealed a blue-shift of the cyanide stretching vibration band, indicating the coordination of the Ni^{2+} to the cyanide bounded to the gold NPs, to form a $\text{Au}^1\text{-C}\equiv\text{N-Ni}^{2+}$ bond, which may be the origin of the anchoring of the PBA shells. Other bivalent metal ions ($M = \text{Co}, \text{Cu}, \text{Fe}, \text{Mn}, \text{Zn}$) were investigated in the aim to extend our approach to other PBA shell. However, similar results to Ni^{2+} were observed only in the case of Co^{2+} , with the increase of the hydrodynamic radius, the decrease then the increase of the Zeta-potential until

appearance of positive charges at the gold NPs surface, and the red-shift of the SPR band, after the addition of few quantities of Co^{2+} solution. A weak effect was also observed in UV-Vis for the Zn^{2+} ions, with a red-shift of the SPR band of 3 nm. Finally, we also investigated the shell growth of the $\text{Au}@K^+/Ni^{2+}/[Fe^{II}(CN)_6]^{4-}$ NPs: TEM measurements revealed a regular but not uniform growth of the shell on the gold core.

The comprehension of the mechanism of the formation of the core-shell $\text{Au}@K^+/Ni^{2+}/[Fe^{II}(CN)_6]^{4-}$ NPs has permitted to perform the control of the gold core size and the PBA shell thickness. The control of the core size is induced by the modification of the temperature during the formation of the cyanide-stabilized NPs. Then, the temperature is raised to 25° during the addition of the PBA shell precursors. Core-shell nano-heterostructures were obtained, and the gold core size was increased with the increase of the temperature. However, these nano-objects are less-defined than the original $\text{Au}@K^+/Ni^{2+}/[Fe^{II}(CN)_6]^{4-}$ NPs. Except for the core-shell NPs synthesized at 32°C , the NPs present similar optical properties, which is due to both the gold core size and the PBA shell thickness. On other hand the control of the shell was performed by controlling the quantity of cyano-bridged coordination polymer precursors added. The core-shell $\text{Au}@K^+/Ni^{2+}/[Fe^{II}(CN)_6]^{4-}$ NPs obtained have similar gold core size, but shell thicknesses ranging from 4.0 ± 1.3 nm to 16.4 ± 2.7 nm. The increase of the shell thickness induced a progressive red-shift of the SPR band of the core-shell NPs. Then, the size of the shell thickness is clearly tunable, and able to modify the optical properties, by regularly increasing the local refractive index around the gold core.

The effect of the nature of the counter-ions, K^+ and Cl^- , was investigated. In this aim, $Ni(NO_3)_2 \cdot 6H_2O$ was used as bivalent metal precursor instead of $NiCl_2 \cdot 6H_2O$, while $Na_3[Fe(CN)_6]$ was used as hexacyanometallate instead of $K_3[Fe(CN)_6]$, and KBH_4 was used as reducing agent instead of $NiCl_2 \cdot 6H_2O$, and $Na[Au(CN)_2]$ instead of $K[Au(CN)_2]$. Moreover, the use of a Au^{III} precursor, $HAuCl_4$, was performed instead of $K[Au(CN)_2]$. Similar core-shell NPs are obtained with varying the nature of the PBA precursors' counter-ions, the reducing agent and the dicyanoaurate precursor. However, the use of Na^+ as counter-ion for the hexacyanometallate, the reducing agent and the dicyanoaurate precursor together did not yield to heterostructures. Moreover, the nature of the counter-ions seems to have an effect on the size of the PBA shell thickness, inducing a size reduction of the cyano-bridged coordination polymer layer. On other hand, the use of $HAuCl_4$ did not lead to the targeted heterostructure, confirming the role of the cyanide ions at the gold surface in the formation of the PBA shell.

Several attempts were performed to modulate the properties of the PBA shell, such as ferromagnetic behavior. Then, using a similar two-steps approach, the growth of a different PBA shell on the gold NPs was performed. However, no heterostructure was obtained, except with the use of Co^{2+} , which permits to realize less-defined NPs, with an important amount of single $K^+/Co^{2+}/[Fe^{II}(CN)_6]^{4-}$ NPs. The synthesis of $\text{Au}@K^+/Co^{2+}/[Fe^{II}(CN)_6]^{4-}$ NPs was optimized by using a delay between the addition of the Co^{2+} precursor and the $[Fe^{III}(CN)_6]^{3-}$ precursor, to favor the heterostructure formation instead of the $K^+/Co^{2+}/[Fe^{II}(CN)_6]^{4-}$ NPs nucleation. These $\text{Au}@K^+/Co^{2+}/[Fe^{II}(CN)_6]^{4-}$ NPs

are well-formed and observed for the most part (80%), however $K^+/Co^{2+}/[Fe^{II}(CN)_6]^{4-}$ NPs are still present (20%). The NPs have similar size comparatively with the $Au@K^+/Ni^{2+}/[Fe^{II}(CN)_6]^{4-}$ NPs, with a gold core of 20.0 ± 3.3 nm, a $K^+/Co^{2+}/[Fe^{II}(CN)_6]^{4-}$ shell thickness of 16.2 ± 3.5 nm, for a total size of 52.3 ± 7.0 nm. These $Au@K^+/Co^{2+}/[Fe^{II}(CN)_6]^{4-}$ NPs are also subject to the same reduction process than for $Au@K^+/Ni^{2+}/[Fe^{II}(CN)_6]^{4-}$ NPs, and display a similar paramagnetic behavior. Then the variations of the PBA shell do not seem to be a good way to simply modify the magnetic properties. Nevertheless, that proves the possibility to transpose the approach to other PBA to obtain core-shell heterostructures. The main synthetic problems, such as the kinetic of the PBA shell formation or the concentration of the precursors, may be optimized.

Finally, the synthesis of the hollow $K^+/Ni^{2+}/[Fe^{II}(CN)_6]^{4-}$ NPs was performed by removing the gold core using an etching process. Indeed, in the presence of the cyanides, it was dissolved to reform the dicyanoaurate precursor $[Au^I(CN)_2]^-$. IR spectroscopy and PXRD showed no alteration on the cyano-bridged coordination network. TEM images revealed the formation of the hollow NPs with size distribution of 53.8 ± 5.2 nm. The removing of the gold core is followed by UV-visible, the SPR band disappearing with the dissolution of the gold NPs, complete after 23 h.

The nano-objects designed present multifunctionality, with the paramagnetic behavior, due to the reduction of the $[Fe^{III}(CN)_6]^{3-}$ moiety. However, such property doesn't target future applications, which require strong response from an external stimuli. Then, we should implement magnetic properties, as ferromagnetic properties. The presence of reactive cyanide molecules in the shell surface may permit to grow another layer of a different PBA.

References

- 1 M. C. Daniel, D. Astruc, *Chem. Rev.*, **2004**, *104*, 293; M. B. Gawande, A. Goswami, T. Asefa, H. Guo, A. V. Biradar, D.-L. Peng, R. Zboril and R. S. Varma, *Chem. Soc. Rev.*, **2015**, DOI: 10.1039/c5cs00343a.
- 2 S. Phadtare, A. Kumar, V. P. Vinod, C. Dash, D. V. Palaskar, M. Rao, P. G. Shukla, S. Sivaram, M. Sastry, *Chem. Mater.*, **2003**, *15*, 1944; A. R. Kortan, R. Hull, R. L. Opila, M. G. Bawendi, M. L. Steigerwald, P. J. Carroll, L. E. Brus, *J. Am. Chem. Soc.*, **1990**, *112*, 1327.
- 3 L. Babes, B. Denizot, G. Tanguy, J. J. Le Jeune, P. Ballet, *J. Colloid Interface Sci.*, **1999**, *212*, 474; P. M. A. De Farias, B. S. Santos, F. D. Menezes, A. G. Brasil Jr, R. Ferreira, M. A. Motta, A. G. Castro-Neto, A. A. S. Vieira, D. C. N. Silva, A. Fontes, C. L. Cesar, *Appl. Phys. A: Mater. Sci. Process.*, **2007**, *89*, 957; F. D. de Menezes, A. G. Brasil Jr., W. L. Moreira, L. C. Barbosa, C. L. Cesar, R. D. C. Ferreira, P. M. A. de Farias, B. S. Santos, *Microelectron. J.*, **2005**, *36*, 989; A. K. Gupta, M. Gupta, *Biomaterials*, **2005**, *26*, 3995; B. Schreder, T. Schmidt, V. Ptatschek, L. Spanhel, A. Materny, W. J. Kiefer, *Cryst. Growth*, **2000**, *214*, 782.
- 4 F. Caruso, *Adv. Mater.*, **2001**, *13*, 11.
- 5 L. Babes, B. Denizot, G. Tanguy, J. J. Le Jeune, P. Ballet, *J. Colloid Interface Sci.* **1999**, *212*, 474 ; P. M. A. De Farias, B. S. Santos, F. D. Menezes, A. G. Brasil Jr, R. Ferreira, M. A. Motta, A. G. Castro-Neto, A. A. S. Vieira, D. C. N. Silva, A. Fontes, C. L. Cesar, *Appl. Phys. A: Mater. Sci. Process.*, **2007**, *89*, 957; F. D. de Menezes, A. G. Brasil Jr., W. L. Moreira, L. C. Barbosa, C. L. Cesar, R. D. C. Ferreira, P. M. A. de Farias, B. S. Santos, *Microelectron. J.*, **2005**, *36*, 989; A. K. Gupta, M. Gupta, *Biomaterials*, **2005**, *26*, 3995; B. Schreder, T. Schmidt, V. Ptatschek, L. Spanhel, A. Materny, W. J. Kiefer, *Cryst. Growth*, **2000**, *214*, 782.
- 6 N. Sounderya, Y. Zhang, *Recent Pat. Biomed. Eng.*, **2008**, *1*, 34. A. K. Gupta, M. Gupta, *Biomaterials*, **2005**, *26*, 3995; J. K. Jaiswal, H. Mattoussi, J. M. Mauro, S. M. Simon, *Nat. Biotechnol.*, **2003**, *21*, 47; X. Michalet, F. F. Pinaud, L. A. Bentolila, J. M. Tasy, S. Doose, J. J. Li, G. Sundaresan, A. M. Wu, S. S. Gambhir, S. Weiss, *Science*, **2005**, *307*, 538.
- 7 K. M. Mayer, J. H. Hafner, *Chem. Rev.*, **2011**, *111*, 3828.
- 8 C. J. Murphy, A. M. Gole, S. E. Hunyadi, C. J. Orendorff, *Inorg. Chem.*, **2006**, *45*, 7544.
- 9 J. Gong, F. Zhou, Z. Li, Z. Tang, *Langmuir*, **2012**, *28*, 8959.
- 10 L. M. Liz-Marzan, M. Giersig, P. Mulvaney, *Langmuir*, **1996**, *12*, 4329.
- 11 R. T. Tom, A. Sreekumaran Nair, N. Singh, M. Aslam, C. L. Nagendra, R. Philip, K. Vijayamohan, T. Pradeep, *Langmuir*, **2003**, *19*, 2439.
- 12 S. B. Kim, C. Cai, S. Sun, D. A. Sweigart, *Angew. Chem.*, **2009**, *121*, 2951; *Angew. Chem. Int. Ed.* **2009**, *48*, 2907.

- 13 H.-L. Jiang, B. Liu, T. Akita, M. Haruta, H. Sakurai, Q. Xu, *J. Am. Chem. Soc.*, **2009**, *131*, 11302.
- 14 J. Son, H. J. Lee, M. Oh, *Chem. Eur. J.*, **2013**, *19*, 6546.
- 15 S. Hermes, M.-K. Schröter, R. Schmid, L. Khodeir, M. Muhler, A. Tissler, R.W. Fischer, R. A. Fischer, *Angew. Chem.*, **2005**, *117*, 6394; *Angew. Chem. Int. Ed.* **2005**, *4*, 6237.
- 16 H. J. Lee, W. Cho, M. Oh, *Chem. Commun.*, **2012**, 48,221.
- 17 C. Jo, H. J. Lee, M. Oh, *Adv. Mater.*, **2011**, *23*, 1716.
- 18 J. Du, J. Qi, D. Wang, Z. Tang, *Energy Environ. Sci.*, **2012**, *5*, 6914.
- 19 K. C.-F. Leung, S. Xuan, X. Zhu, D. Wang, C.-P. Chak, S.-F. Lee, W. K.-W. Ho, B. C.-T. Chung, *Chem. Soc. Rev.*, **2012**, *41*, 1911.
- 20 Y. Yin, R. M. Rioux, C. K. Erdonmez, S. Hughes, G. A. Somorjai, A. P. Alivisatos, *Science*, **2004**, *304*, 711.
- 21 C. Levin, C. Hofmann, T. A. Ali, A. T. Kelly, E. Morosan, P. Nordlander, K. H. Whitmire, N. J. Halas, *ACS Nano.*, **2009**, *3*, 1379.
- 22 L. Carbone, P. D. Cozzoli, *Nano Today*, **2010**, *5*, 449.
- 23 M. B. Cortie, A. M. McDonagh, *Chem. Rev.*, **2011**, 3173.
- 24 Z. Xu, Y. Hou, S. Su, *Phys. Rev. Lett.*, **2006**, *96*, 167402.
- 25 Z. Xu, Y. Hou, S. Sun, *J. Am. Chem. Soc.* **2007**, *129*, 8698.
- 26 S. Tomita, T. Kato, S. Tsunashima, S. Iwata, M. Fujii, S. Hayashi, *Phys. Rev. Lett.*, **2006**, *96*, 167402.
- 27 P. K. Jain, Y. Xiao, R. Walsworth, A. E. Cohen, *Nano Lett.*, **2009**, *9*, 1644.
- 28 F. Pineider, C. de Julian Fernandez, V. Videtta, E. Carlino, A. al Hourani, F. Wilhelm, A. Rogalev, P. D. Cozzoli, P. Ghigna, C. Sangregorio, *ACS Nano.* **2013**, *7*, 857.
- 29 P. Horcajada, R. Gref, T. Baati, P. K. Allan, G. Maurin, P. Couvreur, G. Férey, R. E. Morris, C. Serre, *Chem. Rev.*, **2012**, *112*, 1232.
- 30 K. M. L. Taylor, A. Jin, W. Lin, *Angew. Chem. Int. Ed.*, **2008**, *47*, 7722.
- 31 A. M. Spokoyny, D. Kim, A. Sumrein, C. A. Mirkin, *Chem. Soc. Rev.*, **2009**, *38*, 1218.
- 32 S. Kotagawa, R. Kitaura, S.I. Noro, *Angew. Chem. Int. Ed.* **2004**, *43*, 2334.
- 33 J.-D. Qiu, H.-Z. Peng, R.-P. Liang, J. Li, and X.-H. Xia, *Langmuir*, **2007**, *23*, 2133.

- 34 L. Jing, X. Liang, Z. Deng, S. Feng, X. Li, M. Huang, C. Li, Z. Dai, *Biomaterials*, **2014**, *35*, 5814.
- 35 G. Maurin-Pasturel, J. Long, Y. Guari, F. Godiard, M.-G. Willinger, C. Guérin, J. Larionova, *Angew. Chem. Int. Ed.*, **2014**, *53*, 3872.
- 36 C.-C. Huang, W.-C. Lai, C.-Y. Tsai, C.-H. Yang, C.-S. Yeh, *Chem. Eur. J.*, **2012**, *18*, 4107.
- 37 M. A. Rawashdeh-Omary, M. A. Omary, H. H. Patterson, *J. Am. Chem. Soc.*, **2000**, *122*, 10371.
- 38 J. Larionova, Y. Guari, C. Sangregorio and C. Guerin, *New J. Chem.*, **2009**, *33*, 1177.
- 39 E. Chelebaeva, Y. Guari, J. Larionova, A. Trifonov and C. Guerin, *Chem. Mater.*, **2008**, *20*, 1367.
- 40 D. Asakura, C. H. Li, Y. Mizuno, M. Okubo, H. Zhou and D. R. Talham, *J. Am. Chem. Soc.*, **2013**, *135*, 2793.
- 41 O. N. Risset, E. S. Knowles, S. Ma, M. W. Meisel and D. R. Talham, *Chem, Mater.*, **2013**, *25*, 42.
- 42 S. N. Gosh, *J. Inor. Nucl. Chem.*, **1974**, *36*, 2465.
- 43 J. Lejeune, J. B. Brubach, P. Roy and A. Bleuzen, *C. R. Chimie*, **2014**, *17*, 534.
- 44 K. M. Jeerage, W. A. Steen, and D. T. Schwartz, *Chem. Mater.*, **2002**, *14*, 530.
- 45 Infrared and Raman Spectra of Inorganic and Coordination Compounds, first edition, K. Nakamoto, 1963, Wiley.
- 46 L. Laurentius, S. R. Stoyanov, S. Gusarov, A. Kovalenko, R. Du, G. P. Lopinski, and M. T. McDermott, *ACS Nano*, **2011**, *5*, NO. 5, 4219.
- 47 V. Hornok, I. Dékány, *J. Colloid Interface Sci.*, **2007**, *309*, 176.
- 48 H. Jans, Q. Huo, *Chem. Soc. Rev.*, **2012**, *41*, 2849.
- 49 J. S. Ovens, K. N. Truong, D. B. Leznoff, *Inorg. Chim. Acta*, **2013**, *403*, 127.
- 50 J. Lefebvre, F. Callaghan, M. J. Katz, J. E. Sonier, and D. B. Leznoff, *Chem. Eur. J.*, **2006**, *12*, 6748.
- 51 L. H. Jones, *Inorg. Chem.*, **1964**, *11* (3), 1581.
- 52 R. J. Roberts, X. Li, T. F. Lacey, Z. Pan, H. H. Patterson and D. B. Leznoff, *Dalton Trans.*, **2012**, *41*, 6992.

- 53 J. R. Thompson, R. J. Roberts, V. E. Williams and D. B. Leznoff, *Cryst. Eng. Comm.*, **2013**, *15*, 9387.
- 54 J. Lefebvre, J. L. Korčok, M. J. Katz and D. B. Leznoff, *Sensors*, **2012**, *12*, 3669.
- 55 C. Y. Bhatkhande and V. D. Joglekar, *forensic science*, **1977**, *9*, 33.
- 56 L. Catala, D. Brinzei, Y. Prado, A. Glover, O. Stéphan, G. Rogez and T. Mallah, *Angew. Chem. Int. Ed.*, **2009**, *48*, 183.
- 57 M. F. Dumont, E. S. Knowles, A. Guet, D. M. Pajerowski, A. Gomez, S. W. Kycia, M. W. Weisel and D. R. Talham, *Inorg. Chem.* **2011**, *50*, 4295.
- 58 N. Dia, L. Lisnard, Y. Prado, Al. Gloter, O. Stéphan, F. Brisset, H. Hafez, Z. Saad, C. Mathonière, L. Catala, and T. Mallah, *Inorg. Chem.*, **2013**, *52*, 10264.
- 59 M. Presle, J. Lemainque, J.-M. Guigner, E. Larquet, I. Maurin, J.-P. Boilot and T. Gacoin, *New J. Chem.*, **2011**, *35*, 1296.
- 60 M. Clemente-Leon, E. Coronado, A. Lopez-Munoz, A. D. Repetto, C. Mingotaud, D. Brinzei, L. Catala and T. Mallah, *Chem. Mat.*, **2008**, *14*, 4642.
- 61 C. Delchet, A. Tokarev, X. Dumail, G. Toquer, Y. Barre, T. Guari, C. Guerin, J. Larionova and A. Grandjean, *RSC Advances*, **2012**, *13* (2), 5707.
- 62 C. Loos-Neskovic, S. Ayrault, V. Badillo, B. Jimenez, E. Garnier, M. Fedoroff, D. Jones, B. Merinov, *J. Solid State Chem.*, **2004**, *177* (6), 1817.
- 63 S. Ayrault, B. Jimenez, E. Garnier, M. Fedoroff, D. J. Jones, *J. Solid State Chem.*, **1998**, *141* (2), 475.
- 64 A. K. Jain, R. Pal Singh and C. Bala, *J. Radioanal. Chem.*, **1998**, *141* (2), 475.
- 65 H. H. Kamerbeek, A. G. Rauws, M. ten Ham and A. N. P. van Heijst, *Acta med. scand.*, **1971**, *189*, 321.
- 66 P. J. Faustino, Y. Yang, J. J. Progar, C. R. Brownell, N. Sadrieh, J. C. May, E. Leutzinger, D. A. Place, E. P. Duffy, F. Houn, S. A. Loewke, V. J. Mecozzi, C. D. Ellison, M. A. Khan, A. S. Hussain and R. C. Lyon, *J. Pharm. Biomed. Anal.*, **2008**, *47*, 114.
- 67 Y. Yang, P.J. Faustino, J. J. Progar, C. R. Brownell, N. Sadrieh, J. C. May, E. Leutzinger, D. A. Place, E. P. Duffy, L. X. Yu, M. A. Khan and R. C. Lyon, *Int. J. Pharm.*, **2008**, *353*, 187.
- 68 H. A. Hoffman, L. Chakrabarti, M. F. Dumont, A. D. Sandler and R. Fernandes, *RSC Adv.*, **2014**, *4*, 29729.
- 69 O. N. Risset, E. S. Knowles, S. Ma, M. W. Meisel, and D. R. Talham, *Chem. Mater.*, **2013**, *25*, 42.
- 70 M. Hu, S. Furukawa, R. Ohtani, H. Sukegawa, Y. Nemoto, J. Reboul, S. Kitagawa and Y. Yamauchi, *Angew. Chem. Int. Ed.*, **2012**, *51*, 984.

71 H.-Y. Lian, M. Hu, C.-H. Liu, Y. Yamauchi, K. C.-W. Wu, *Chem. Commun.*, **2012**, 5151.

Experimental part

The syntheses were carried out using commercially available reagents. All chemical reagents were purchased and used without further purification. Gold(I) potassium cyanide ($K[Au(CN)_2]$, 99%), Gold(I) Sodium cyanide ($Na[Au(CN)_2]$, 99%), silver(I) potassium cyanide ($K[Ag(CN)_2]$), Palladium chloride ($PtCl_2$, 99%), Platinum Chloride ($PdCl_2$), Chromium(III) chloride ($CrCl_3$, 98%) and Potassium cyanide (KCN, 97%) were purchased from Alfa Aesar, Potassium borohydride (KBH_4 , 98%), Ascorbic acid and Cobalt nitrate trihydrate ($Co(NO_3)_2 \cdot 3H_2O$) were purchased from Acros Organics, Sodium borohydride ($NaBH_4$, 96%) was purchased from Panreac, Zinc chloride ($ZnCl_2$) was purchased from Prolabo, Cetyltrimethylammonium bromide (CTAB, 99%, product no: H6269) was purchased from Sigma, Hydrogen tetrachloroaurate ($HAuCl_4$, 99%), Nickel nitrate hexahydrate ($Ni(NO_3)_2 \cdot 6H_2O$, 98%), Chloride cobalt hexaydrate ($CoCl_2 \cdot 6H_2O$, 98%), Chloride copper dihydrate ($CuCl_2 \cdot 2H_2O$, 99%), Iron(II) chloride hexahydrate ($FeCl_2 \cdot 6H_2O$, 99%), Gadolinium nitrate hexahydrate ($Gd(NO_3)_3 \cdot 6H_2O$), Manganese chloride tetrahydrate ($MnCl_2 \cdot 4H_2O$), Potassium hexacyanochromate ($K_3[Cr(CN)_6]$) and Potassium hexacyanocobaltate ($K_3[Co(CN)_6]$, 95%) were purchased from Aldrich.

Synthesis of core-shell $Au@Ni[Fe(CN)_6]$ (2):

Au core NPs:

In a typical experiment, KBH_4 (0.63 mmol) was added to 100 mL of an aqueous solution of $K[Au(CN)_2]$ (4.8×10^{-5} mol, 4.8×10^{-4} M) under vigorous stirring at $25^\circ C$. The colorless solution rapidly turned red, indicating the formation of NPs. After 20 min, they were used immediately in the next step.

Characterizations:

UV-visible: 517 nm (surface plasmon band of gold NPs).

Zeta potential: -33.9 ± 7.0 mV. Size by DLS measurements: 48.3 ± 26.1 nm (Pdl: 0.57).

Single layered core@shell $Au@KNi[Fe(CN)_6]$ NPs:

10mL of an aqueous solution of $K_3[Fe(CN)_6]$ (5.65 mM) and 10mL of an aqueous solution of $NiCl_2 \cdot 6H_2O$ (5.00 mM) were simultaneously added (2mL/h) to the gold colloidal suspension under vigorous stirring at $25^\circ C$. After completion of the addition, the solution was vigorously stirred for one hour. The aqueous solution of NPs was centrifuged at 20000 rpm during 15 min. The supernatant was removed and the NPs were washed with water and centrifuged again at 20000 rpm during 15 min. The supernatant was removed and the NPs were washed with ethanol and centrifuged at 20000 rpm during 10 min and were dried under vacuum. The number of core@shell NPs represent 97% of the sample as inferred from TEM images.

Characterizations:

Purple powder. FT-IR (KBr, ν , cm^{-1}): $\nu(-OH)$ (coordinate water) = 3600 cm^{-1} , $\nu(-OH)$ ((free water) = 3410 cm^{-1} , $\nu(C\equiv N)$ = 2094 cm^{-1} ($Fe^{II}-C\equiv N-Ni^{II}$), $\delta(H-O-H)$ (free water) = 1622 cm^{-1} , $\nu(Fe^{II}-CN)$ = 586 cm^{-1} , $\delta(Fe^{II}-CN)$ = 461 cm^{-1} .

Raman: $\nu(C\equiv N)$ = 2106 and 2142 cm^{-1} ($Fe^{II}-C\equiv N$), $\nu(Au-CN)$ = 388 cm^{-1} , $\nu(Fe^{II}-CN)$ = 250 cm^{-1} .

Anal. Found (at%): Au, 6.5; K, 7.2; Ni, 5.9; Fe, 4.6; C, 28; N, 28; H, 19.8. Calculated formula: $Au_{1.08}@K_{1.20}Ni[Fe(CN)_6]_{0.80} \cdot 3.35H_2O$.

Zeta potential: -23.6 ± 4.3 mV. Size by DLS measurements: 190 ± 74 nm (Pdl: 0.22). UV-visible: 537 nm (surface plasmon band of gold NPs).

Variation of the gold core's size for the single layered core@shell Au@KNi[Fe(CN)₆] NPs (2-18; 2-32; 2-40) :

KBH₄ (0,63 mmol) was added to of an aqueous solution of K[Au(CN)₂] (4.8×10⁻² mmol) under vigorous stirring at different selected temperatures (T= 18; 25; 32 or 40 °C). The colorless solution rapidly turned red, indicating the formation of NPs. After 20 min, 10 mL of an aqueous solution of K₃[Fe(CN)₆] (5.65 mM) and 10 mL of an aqueous solution of NiCl₂·6H₂O (5.0 mM) were simultaneously added (2 mL/h) to the gold NPs solution under vigorous stirring with the temperature fixed at 25 °C. After completion of the addition, the solution was vigorously stirred for one hour. The aqueous solution of NPs was centrifuged at 20000 rpm during 10 min. The supernatant was removed and the NPs were washed with water and centrifuged again at 20000 rpm during 10 min. The supernatant was removed and the NPs were washed with ethanol and centrifuged at 20000 rpm during 10 min and were dried under vacuum.

Characterizations:

Purple powder. FT-IR ((KBr, ν , cm⁻¹): ν (-OH) (coordinate water) = 3600 cm⁻¹, ν (-OH) (free water) = 3410 cm⁻¹, ν (C≡N) = 2094 cm⁻¹ (Fe^{II}-C≡N-Ni^{II}), δ (H-O-H) (free water) = 1622 cm⁻¹, ν (Fe^{II}-CN) = 586 cm⁻¹, δ (Fe^{II}-CN) = 461 cm⁻¹.

Temperature for synthesis of gold NPs	K/Fe/Ni/Au	Estimated formula
18°C	36.2/23.5/27.0/13.3	Au _{0.5} @K _{1.35} Ni[Fe(CN) ₆] _{0.85}
25°C	29.0/20.0/24.0/27.0	Au _{1.08} @K _{1.20} Ni[Fe(CN) ₆] _{0.80}
32°C	28.8/17.9/20.1/33.2	Au _{1.65} @K _{1.45} Ni[Fe(CN) ₆] _{0.88}
40°C	28.1/16.7/19.5/35.7	Au _{1.9} @K _{1.44} Ni[Fe(CN) ₆] _{0.86}

Variation of the Ni[Fe(CN)₆] shell's size for the single layered core@shell Au@KNi[Fe(CN)₆] NPs (2-1 to 2-6):

KBH₄ (0.63 mmol) was added to 100 mL of an aqueous solution of K[Au(CN)₂] (4.8×10⁻² mmol) under vigorous stirring at 25°C. The colorless solution rapidly turned red, indicating the formation of NPs. After 20 min, a volume (V=0.5; 1; 2; 4; 5; 6; 10 mL) of an aqueous solution of K₃[Fe(CN)₆] (5.65 mM) and a volume (V=0.5; 1; 2; 4; 5; 6; 10 mL) of an aqueous solution of NiCl₂·6H₂O (5.0 mM) were simultaneously added (2mL/h) to the gold NPs solution under vigorous stirring at 25°C. After completion of the addition, the solution was vigorously stirred for one hour. The aqueous solution of NPs was centrifuged at 20000 rpm during 10 min. The supernatant was removed and the NPs were washed with water and centrifuged again at 20000 rpm during 10 min. The supernatant was removed and the NPs were washed with ethanol and centrifuged at 20000 rpm during 10 min and were dried under vacuum. In the case of smaller volumes (V = 0.5; 1; 2 ml) before the centrifugation (5 minutes instead of 10) the pH of the solution of NPs was decreased close to 4 with addition of a dilute HCl solution (1M).

Characterizations:

Purple powder. FT-IR (KBr, ν , cm⁻¹): ν (-OH) (coordinate water) = 3600 cm⁻¹, ν (-OH) (free water) = 3410 cm⁻¹, ν (C≡N) = 2094 cm⁻¹ (Fe^{II}-C≡N-Ni^{II}), δ (H-O-H) (free water) = 1622 cm⁻¹, ν (Fe^{II}-CN) = 586 cm⁻¹, δ (Fe^{II}-CN) = 461 cm⁻¹.

EDX:

Volume of precursors added	EDS ratio (K/Fe/Ni/Au)	Estimated formula
0.5mL	3.5/3.2/4.4/88.9	Au _{20.2} @K _{0.8} Ni[Fe(CN) ₆] _{0.7}
1mL	5.3/4.4/5.7/84.6	Au _{14.7} @K _{0.92} Ni[Fe(CN) ₆] _{0.76}
2mL	12.1/11.8/17.4/58.7	Au _{3.4} @K _{0.7} Ni[Fe(CN) ₆] _{0.68}
4mL	16.9/13.1/18.1/51.9	Au _{2.87} @K _{0.93} Ni[Fe(CN) ₆] _{0.72}
5mL	14.1/15.4/22.3/48.2	Au _{2.16} @K _{0.63} Ni[Fe(CN) ₆] _{0.65}
6mL	19.8/16.1/23.6/40.5	Au _{1.72} @K _{0.88} Ni[Fe(CN) ₆] _{0.69}
10mL	29.3/25.5/19.5/26.7	Au _{1.08} @K _{1.20} Ni[Fe(CN) ₆] _{0.80}

Hollows KNi[Fe(CN)₆] NPs (2-h):

5 mg of dried Au@KNiFe NPs were added to 10mL of an aqueous solution of KCN (2.10⁻³ M). The mixture is let under vigorous stirring for 24h. The suspension, initially purple, becomes progressively colorless.

Characterizations:

White powder. FT-IR (KBr, ν , cm⁻¹): ν (-OH) (coordinate water) = 3600 cm⁻¹, ν (-OH) (free water) = 3412 cm⁻¹, ν (C≡N) = 2091 cm⁻¹ (Fe^{II}-CN--Ni^{II}), δ (H-O-H) (free water) = 1620 cm⁻¹, ν (Fe^{II}-CN) = 590 cm⁻¹, δ (Fe^{II}-CN) = 455 cm⁻¹.

Chapter IV

-

Epitaxial growth of a PBA shell on $\text{Au}@K^+/\text{Ni}^{2+}/[\text{Fe}^{\text{II}}(\text{CN})_6]^{4-}$ core-shell nanoparticles: a way to implement magnetic properties

IV.1 Introduction

In the previous chapter, we have reported the synthesis of core-shell $\text{Au}_{1.08}@\text{K}_{1.20}\text{Ni}[\text{Fe}(\text{CN})_6]_{0.80}$ NPs obtained using a new and rational approach consisting in: 1) the synthesis of cyanide-stabilized gold NPs in aqueous solution, and 2) the subsequent time-controlled growth of the coordination polymer shell on the surface of these gold NPs¹. These as-obtained nano-objects exhibit optical properties due to the presence of a surface plasmon resonance (SPR) band of the gold core and a paramagnetic behavior caused by the presence of the PBA shell. However, no interesting magnetic properties such as ferromagnetism, can be obtained due to the reduction of Fe^{III} to Fe^{II} in the PBA network. In this line of research, we wish to extend our approach to other core-shell systems and combines interesting magnetic properties, such as a short or long range magnetic ordering, with optical properties in order to obtain multifunctional materials. This can be performed by growing a second magnetic PBA shell of a different nature on $\text{Au}@\text{K}^+/\text{Ni}^{2+}/[\text{Fe}^{\text{II}}(\text{CN})_6]^{4-}$ NPs and combines the optical properties of the gold with the ferromagnetic or superparamagnetic properties of the second PBA²⁻⁸ shell in a nano-heterostructure.

Epitaxial growth of a cyano-bridged coordination polymer at the surface of another one with closed cell parameters has already been demonstrated in literature on surfactant-free core PBA NPs⁹⁻²⁰. This is provided by the presence of the cyanide terminated reactive $[\text{M}(\text{CN})_6]^{3-}$ moieties located at the surface of the coordination polymer NPs. In our case, the use of the core-shell $\text{Au}@\text{K}^+/\text{Ni}^{2+}/[\text{Fe}^{\text{II}}(\text{CN})_6]^{4-}$ NPs as precursor should permit to obtain double-layered core-shell $\text{Au}@\text{PBA}@\text{PBA}'$ NPs exhibiting magneto-optical properties.

We have also demonstrated that the PBA shell thickness can be finely tuned for $\text{Au}@\text{K}^+/\text{Ni}^{2+}/[\text{Fe}^{\text{II}}(\text{CN})_6]^{4-}$ NPs by varying the quantity of precursors added during the synthesis. Then, it should be possible to use a first small shell of $\text{K}^+/\text{Ni}^{2+}/[\text{Fe}^{\text{II}}(\text{CN})_6]^{4-}$ as a anchoring point for the second PBA shell and also control its thickness. That should permit to investigate the dependence of the magnetic properties and optical properties as a function of the shell thickness. Indeed, the magnetic behavior can be affected by the reduction of the shell thickness, and switching from a long magnetic ordering with the large shell size (a behavior comparable to the bulk material) to a slow magnetic relaxation leading to a superparamagnetic or a spin-glass behavior when the size of the PBA layer is lower than the magnetic domain size³⁻⁶. In parallel, optical properties of the gold core should also be affected by the shell thickness inducing the shift in the SPR position^{22,23}.

In this chapter, we describe the synthesis of double-layered core-shell $\text{Au}@\text{K}^+/\text{Ni}^{2+}/[\text{Fe}^{\text{II}}(\text{CN})_6]^{4-}@\text{PBA}'$ NPs obtained by the subsequent growth of the second shell of the selected cyano-bridged coordination polymers ($\text{PBA}' = \text{KNi}^{\text{II}}[\text{Cr}^{\text{III}}(\text{CN})_6]$, $\text{KNi}^{\text{II}}[\text{Fe}^{\text{III}}(\text{CN})_6]$, $\text{KCo}^{\text{II}}[\text{Fe}^{\text{II}}(\text{CN})_6]$ and $\text{KFe}^{\text{III}}[\text{Fe}^{\text{II}}(\text{CN})_6]$). These later were used to modulate the magnetic property, particularly for $\text{Ni}^{\text{II}}\text{Cr}^{\text{III}}$, $\text{Ni}^{\text{II}}\text{Fe}^{\text{III}}$ and $\text{Fe}^{\text{III}}\text{Fe}^{\text{II}}$ for ferro- or ferri-magnetism. The size of the first and the second shell was controlled, by keeping, as it was possible, the same size of the Au core. The multifunctionality was confirmed by observation of the remaining optical properties and appearance of new magnetic properties instead of paramagnetism. As a proof of concept, we focalized on the growth of the second $\text{Ni}^{\text{II}}\text{Cr}^{\text{III}}$ PBA layer with different thicknesses and a series of

Au@KNi^{II}Fe^{III}@KNi^{II}Cr^{III} starting from the same initial Au@K⁺/Ni²⁺/[Fe^I(CN)₆]⁴⁻ NPs was obtained. After that, we extended our research to other PBA's shells of different nature. The influence of the shell size on the optical properties was investigated by using UV-Vis spectroscopy. Secondly, we investigate the effect of the second shell size on the magnetic properties by using a SQUID magnetometer in the static (DC) and the dynamic modes (AC). In order to study their intrinsic magnetic behavior, different dilutions of the Au@KNi^{II}Fe^{III}@KNi^{II}Cr^{III} NPs in a polymer matrix were also performed, in order to reduce the dipolar interactions between the particles.

IV.2 Synthesis of double-layered core-shell $\text{Au}@K^+/Ni^{2+}/[Fe^{II}(CN)_6]^{4-}@PBA$ NPs where $PBA = KNi^{II}[Cr^{III}(CN)_6]$, $KNi^{II}[Fe^{III}(CN)_6]$, $KCo^{II}[Fe^{II}(CN)_6]$ and $KFe^{III}[Fe^{II}(CN)_6]$.

The general procedure to synthesize double-layered core-shell $\text{Au}@K^+/Ni^{2+}/[Fe^{II}(CN)_6]^{4-}@PBA$ NPs consists in realizing a subsequent growth of a new (second) PBA shell, *i.e.* to use the initial $\text{Au}@K^+/Ni^{2+}/[Fe^{II}(CN)_6]^{4-}$ NPs as seeds to grow the second PBA layer by adding the corresponding PBA precursors (figure 1). The possibility of an epitaxial growth of the cyano-bridged coordination polymer on the surface of another has already been demonstrated, with surfactant-free PBA core NPs⁹⁻²⁰, thanks to the presence of reactive $[M^{III}(CN)_6]^{3-}$ moieties at the NPs surface. As for the original core-shell $\text{Au}@K^+/Ni^{2+}/[Fe^{II}(CN)_6]^{4-}$ NPs, the size and the morphology control is achieved by controlling the precursors' addition rate and the concentration of the PBA' precursors. In order to promote the growth of the second shell and to avoid any nucleation of single PBA NPs, we used a slow addition rate (2 mL/h) and a low concentration of the PBA precursors, 5.0 mM for the transition metal ions M^{2+} and 5.65 mM for the cyanometallate ions $[M^{III}(CN)_6]^{3-}$. The size of the second PBA layer can be controlled by varying the added amount of substance of the PBA precursors (*i.e.* the volume), as already described for $\text{Au}@K^+/Ni^{2+}/[Fe^{II}(CN)_6]^{4-}$ NPs. The total size of the double-layered core-shell $\text{Au}@K^+/Ni^{2+}/[Fe^{II}(CN)_6]^{4-}@PBA$ NPs can also be controlled by the subsequent growing of a second PBA shell on the first $K^+/Ni^{2+}/[Fe^{II}(CN)_6]^{4-}$ shell with a large (shell thickness of 16.6 ± 2.7 nm) or on a thin (shell thickness of 5.9 ± 1.5 nm).

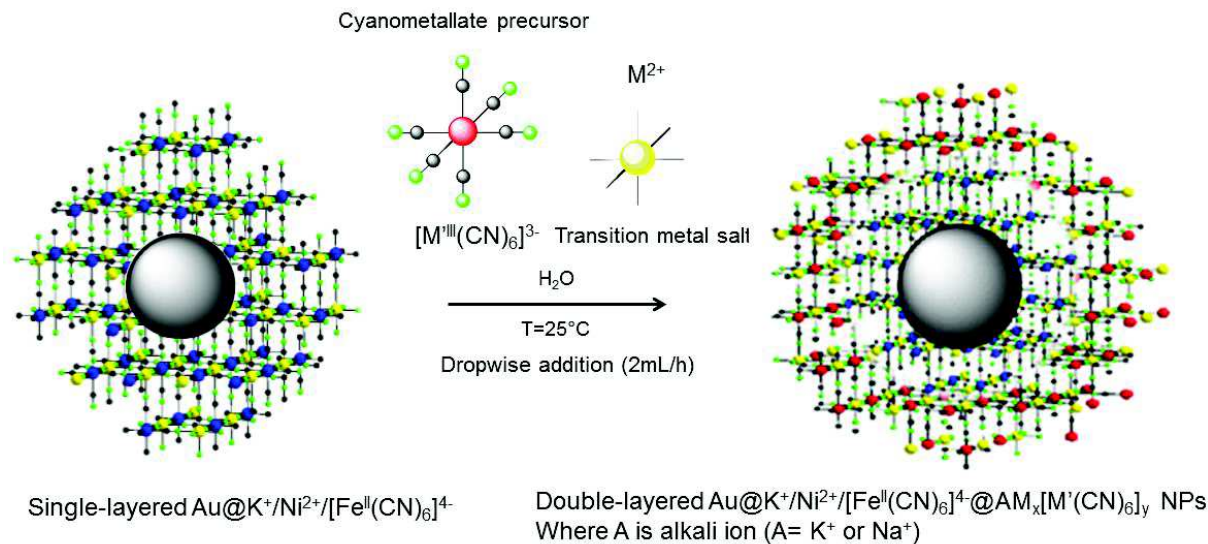


Figure 1: Schematic representation of the synthesis of the double-layered core-shell $\text{Au}@KNi^{II}Fe^{II}@KNi^{II}Cr^{III}$ NPs by subsequent growth of a PBA on the $\text{Au}@K^+/Ni^{2+}/[Fe^{II}(CN)_6]^{4-}$ NPs.

IV.2.1 Synthesis of double-layered core-shell $\text{Au}@K^+/Ni^{2+}/[Fe^{II}(CN)_6]^{4-}@KNi^{II}[Cr^{III}(CN)_6]$ NPs.

To obtain the double-layered $\text{Au}@K^+/Ni^{2+}/[Fe^{II}(CN)_6]^{4-}@KNi^{II}[Cr^{III}(CN)_6]$ core-shell NPs with the small first shell of $Ni^{II}Fe^{II}$ (shell thickness of 5.9 ± 1.5 nm, sample **2-3**), the first step consists in obtaining small $\text{Au}@K^+/Ni^{2+}/[Fe^{II}(CN)_6]^{4-}$ NPs with the addition of only 1.0×10^{-5} mol (2 mL, 1 hour of addition) of $NiCl_2 \cdot 6H_2O$ (5.0 mM) and 1.1×10^{-5} mol of $K_3[Fe(CN)_6]$ (5.65 mM). After one hour of stirring, hydrochloric acid was added in order to decrease the pH of the solution from 10 to 3-4 (control by pH-meter), to prevent any aggregation during the centrifugation by hydrolyzing the potassium borohydride in the reaction media. The supernatant was removed and the NPs were dispersed in ultrapure water to give approximately 100 mL of solution. Then the PBA precursors (transition metal salt: $NiCl_2 \cdot 6H_2O$, 5.0 mM; hexacyanometallate: $K_3[Cr^{III}(CN)_6]$, 5.65 mM) were added simultaneously at the same rate of 2 mL/h. As previously described for the first shell, the size of the second shell thickness was controlled by varying the amount of added substance of the PBA precursors (*i.e.* the volume). Then, by changing amount of added substances (1×10^{-5} , 2×10^{-5} , 3×10^{-5} or 4×10^{-5} mol) of the precursors, a series of $\text{Au}@KNi^{II}Fe^{II}@KNi^{II}Cr^{III}$ NPs with different thickness of $Ni^{II}Cr^{III}$ PBA layer (samples **11-1** to **11-4**) was synthesized.

On the other hand, to obtain double-layered NPs with a large first $Ni^{II}Fe^{II}$ shell (sample **2**), 10 mg of initial $\text{Au}@K^+/Ni^{2+}/[Fe^{II}(CN)_6]^{4-}$ NPs (first shell thickness of 16.6 ± 2.7 nm) were dispersed in 100 mL of water by sonication. Then, at 25°C and under vigorous stirring, the aqueous solutions of the transition metal salt ($NiCl_2 \cdot 6H_2O$, 4×10^{-5} mol, 10 mL) and of the hexacyanometallate ($K_3[Cr(CN)_6]$, 5.65×10^{-5} mol; 10 mL) were added simultaneously at the same rate of 2 mL/h. After addition, the solution was stirred for one hour, and then the $\text{Au}@KNi^{II}Fe^{II}@KNi^{II}Cr^{III}$ NPs (sample **11-5**) were isolated by centrifugation, washed with water and ethanol and dried under vacuum¹.

The TEM images clearly confirm the achievement of the subsequent layers growth for all samples (figures 2 and 4). TEM images revealed the presence of NPs relatively uniform in size and shape with the complex shell's morphology consisting on the presence of several cubic-like shell growths on different sides of the gold core. This is particularly visible for the sample with an important second shell thickness, such as for **11-5**. For all $\text{Au}@KNi^{II}Fe^{II}@KNi^{II}Cr^{III}$ NPs, no modification of the gold core diameter is observed, indicating that any modification of the total size occurs from the PBA shell (figure 3 and 4). It is not easy to differentiate directly two PBA layers (from the first and the second shells) using the TEM images, due to the closeness of their respective lattice parameters and their electronic densities, and then to obtain their respective size distributions. To estimate them, we performed TEM images before and after the growth of the second shell; we measured the respective total sizes of the NPs. Thus the mean size of the second PBA layer was found by subtracting the size of the core-shell NPs with the first shell from the total NPs size, considering that there is no dissolution process of the first shell.

For the series of $\text{Au}@K\text{Ni}^{\text{II}}\text{Fe}^{\text{II}}@K\text{Ni}^{\text{II}}\text{Cr}^{\text{III}}$ NPs growth from the $\text{Au}@K^+/\text{Ni}^{2+}/[\text{Fe}^{\text{II}}(\text{CN})_6]^{4-}$ NPs with the small first shell (samples **11-1** to **11-4**), the $\text{Ni}^{\text{II}}\text{Cr}^{\text{III}}$ shell thickness gradually increases from 1.6 ± 0.3 nm for **11-1** to 10.45 ± 2.6 nm for **11-4** (figure 2 and table 1), as a function of the amount of added precursors (figure 3). That clearly indicates a relative control of the second shell thickness, demonstrating that these systems may be able to be largely tuned. Moreover, that also proves that the first $K\text{Ni}^{\text{II}}\text{Fe}^{\text{II}}$ shell really serves as a point of anchoring for the second PBA shell. Indeed, while we use $\text{Au}@K^+/\text{Ni}^{2+}/[\text{Fe}^{\text{II}}(\text{CN})_6]^{4-}$ NPs with a large first shell the $\text{Au}@K\text{Ni}^{\text{II}}\text{Fe}^{\text{II}}@K\text{Ni}^{\text{II}}\text{Cr}^{\text{III}}$ NPs (sample **11-5**) with a shell thickness of 40.45 ± 8.1 nm were obtained. Then we demonstrate that we can control both, the size of the first and the second PBA layer.

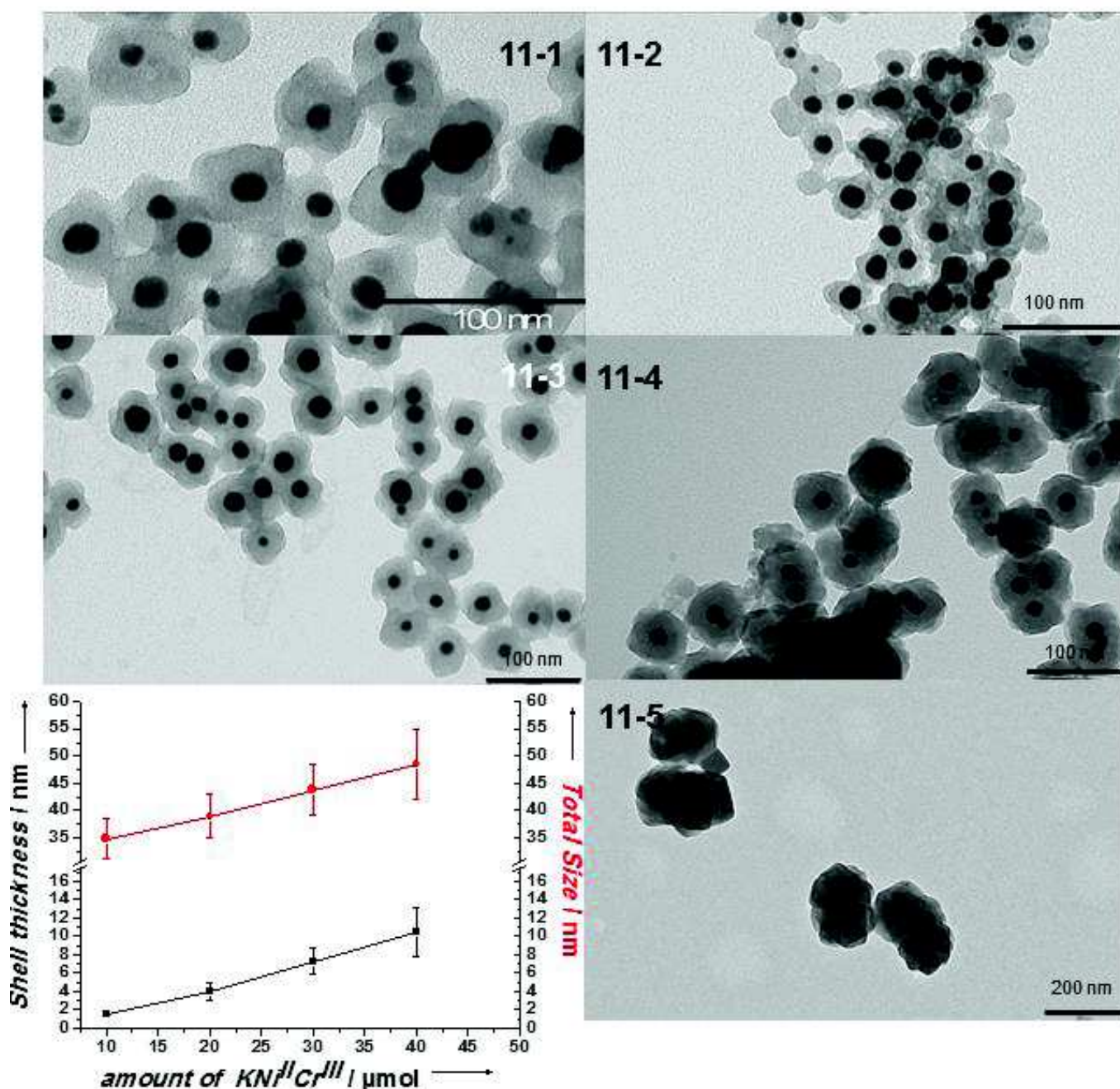


Figure 2: TEM images of a series of the double-layered core-shell $\text{Au}@K\text{Ni}^{\text{II}}\text{Fe}^{\text{II}}@K\text{Ni}^{\text{II}}\text{Cr}^{\text{III}}$ NPs. Evolution of the shell thickness of $\text{Ni}^{\text{II}}\text{Cr}^{\text{III}}$ layer (black) and the total shell size (red) as function of the amount of added precursors for $\text{Au}@K\text{Ni}^{\text{II}}\text{Fe}^{\text{II}}@K\text{Ni}^{\text{II}}\text{Cr}^{\text{III}}$ NPs.

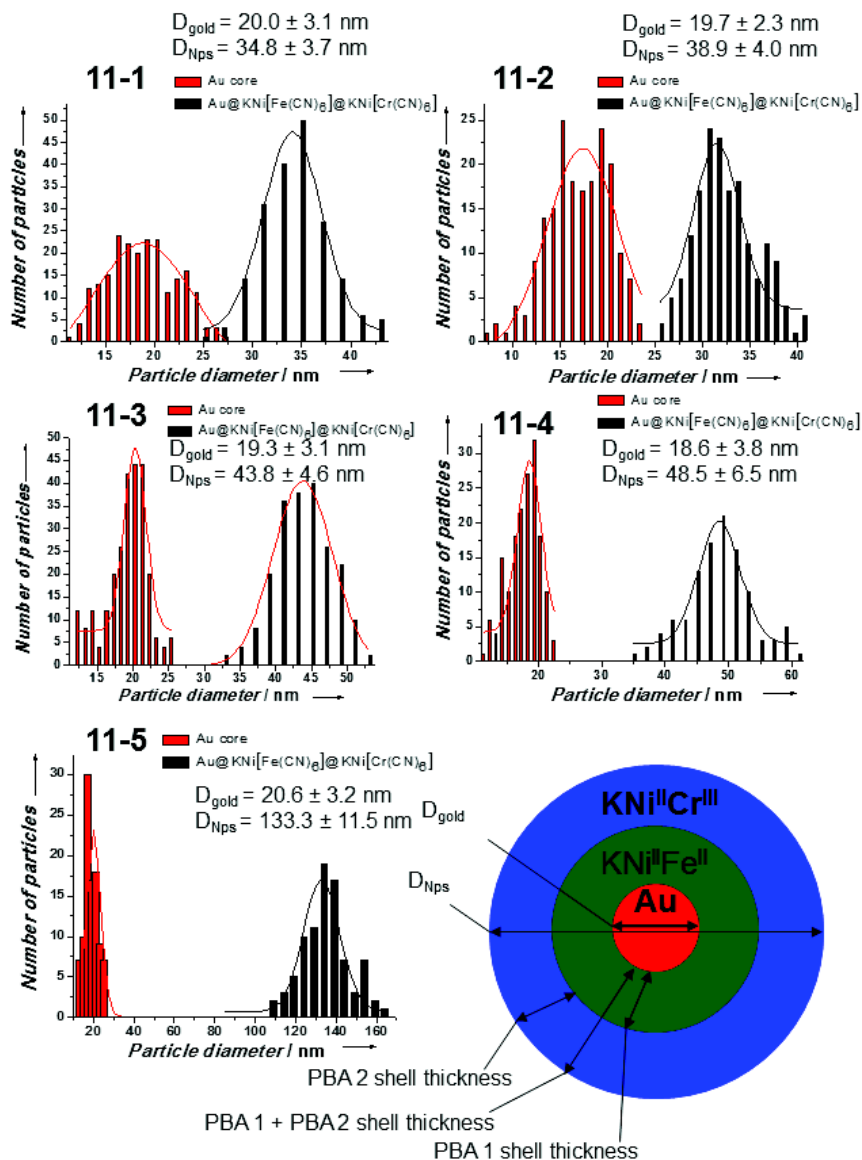


Figure 3: Size distributions of the gold core and the total size for a series of Au@KNi^{II}@KNi^{II}@Cr^{III} NPs (samples 11-1 to 11-5). Schematic representation of a double-layered core-shell NPs.

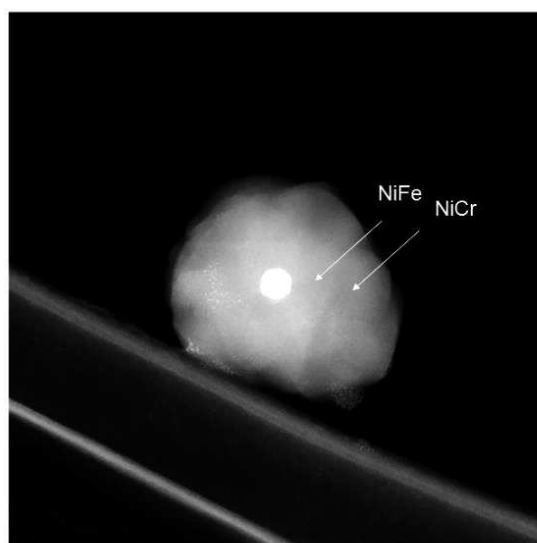


Figure 4: STEM-HAADF image of double-layered core-shell Au@KNi^{II}@KNi^{II}@Cr^{III} Cr NPs (11-5). The two PBAs layers are indicated by the arrows.

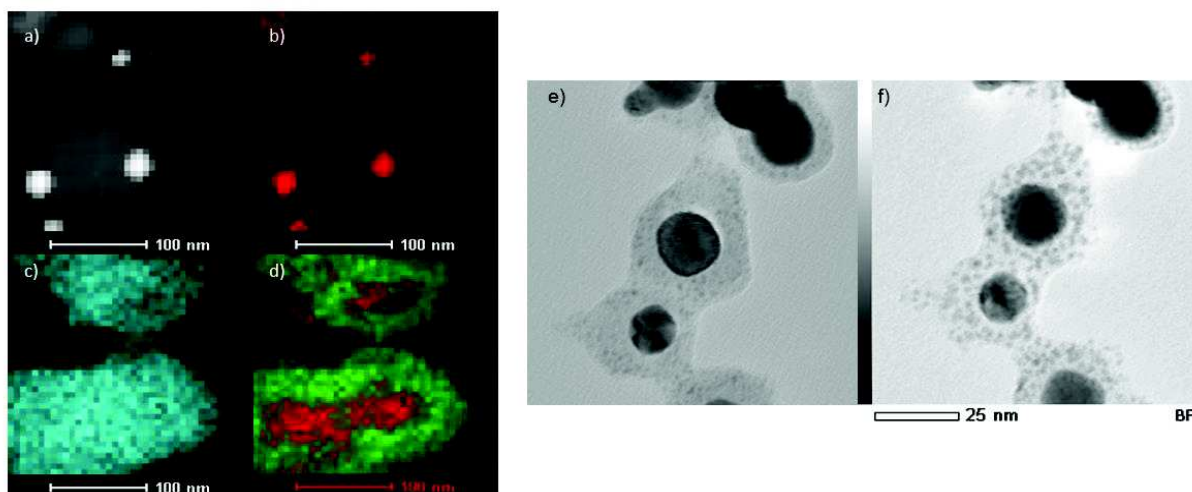


Figure 5: In left, STEM-HAADF image a) of the Au@KNi^{II}Fe^{II}@KNi^{III}Cr^{III} NPs (**11-5**) with EDS mapping for b) gold (red), c) nickel (blue) and d) iron (red) and chromium (green). In left STEM images of the Au@KNi^{II}Fe^{II}@KNi^{III}Cr^{III} NPs (**11-2**) at the beginning of the experiment e) and after few minutes f) under the electron beam. The dark spots correspond to the alteration of the PBA layer.

For all samples, IR spectroscopy confirms the formation of the second PBA layer. The values of characteristic bands for each sample are summarized in Table 1. It is possible to observe in the cyanide stretching region the band corresponding to the Fe^{II}-C≡N-Ni^{II} linkage²³, located at 2091 cm⁻¹, which is the same observed for the initial Au@K⁺/Ni²⁺/[Fe^{II}(CN)₆]⁴⁻ NPs¹, confirming the presence of the first KNi^{II}Fe^{II} layer (figure 6). This conclusion is also confirmed by the stretching and the bending vibration bands located respectively at 593 cm⁻¹ and 465 cm⁻¹, characteristic of the Fe^{II}-C linkage²³. The appearance of a new band located at 2172 cm⁻¹, corresponding to the stretching vibration of the Cr^{III}-C≡N-Ni^{II} linkage, attests the formation of the second KNi^{II}Cr^{III} shell^{3,5,6}. This is also attested by the presence of the band characteristic of the ν(Cr^{III}-CN) stretching vibration, located at 493 cm⁻¹.

Moreover, the presence of bands of the ν(-OH) vibrations and the δ(H-O-H) deformations confirms the presence of the water molecules in the samples (figure 6, table 1). The bands located respectively at 3400 cm⁻¹ and at 1610 cm⁻¹ correspond to crystallized water, involved in a hydrogen-bonded network, while the band located in the 3600-3700 cm⁻¹ range is characteristic of water molecules coordinated to the bivalent transition metal ion Ni^{II}, at the cyanometallate vacancies²⁴.

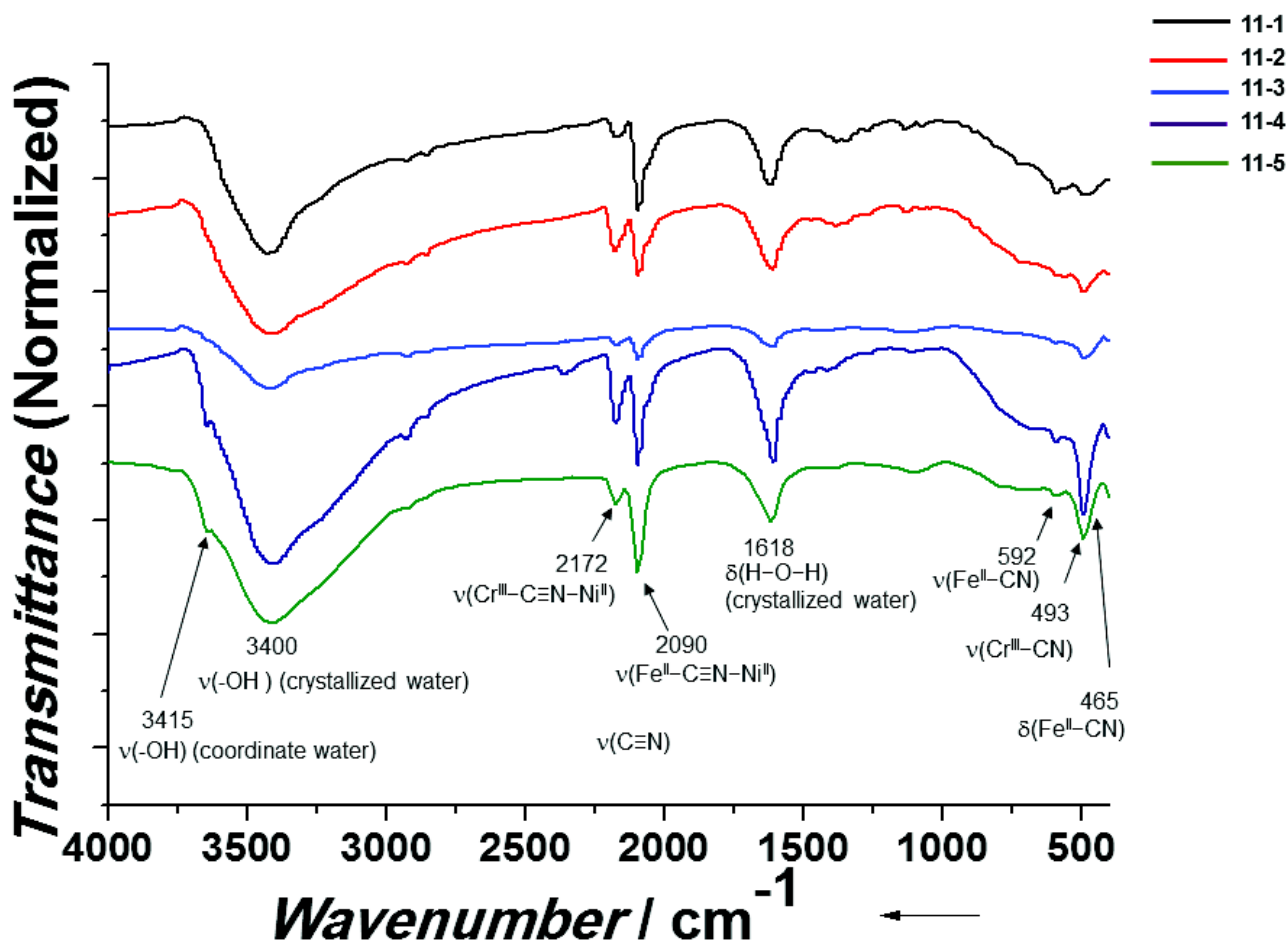


Figure 6: IR spectra of the series of double-layered core-shell Au@KNi^{II}Fe^{II}@KNi^{III}Cr^{III} NPs.

The composition of the double-layered core-shell Au@KNi^{II}Fe^{II}@KNi^{III}Cr^{III} NPs was determined, by elemental analysis for **11-5** and EDS analysis for the others. The presence of the expected elements confirms the formation of the new PBA for all the samples (table 1). With the elements ratio, the respective formulas of the Au@KNi^{II}Fe^{II}@KNi^{III}Cr^{III} NPs were calculated. However, it's not possible to determinate for each sample a precise formula giving the composition of the two PBA shells because we do not know the repartition of the elements on each layer. Indeed, for the Au@KNi^{II}Fe^{II}@KNi^{III}Cr^{III} NPs, we cannot determinate the repartition of the nickel and the potassium, which are present in both KNi^{II}Fe^{II} and KNi^{III}Cr^{III} shell. Then we have calculated their formula by fixing the formula of the first KNi^{II}Fe^{II} shell according to those calculated for similar shell size, *i.e.* K_{0.7}Ni[Fe(CN)₆]_{0.68} for the first thin KNi^{II}Fe^{II} layer (as for sample **11-3**) for sample **11-1** to **11-4** and K_{1.2} Ni[Fe(CN)₆]_{0.80} for the first large KNi^{II}Fe^{II} layer (as for sample **2**) for sample **11-5**. Then, by subtracting the amount corresponding to the first KNi^{II}Fe^{II} shell, the KNi^{III}Cr^{III} shell was estimated. A point to note is that for the series of the small Au@KNi^{II}Fe^{II}@KNi^{III}Cr^{III} NPs (samples **11-1** to **11-4**), the increase of the amount in Cr is in accordance to the regular increase of the KNi^{III}Cr^{III} shell thickness.

Main characteristics	Label				
	11-1	11-2	11-3	11-4	11-5
amount of precursors added for the synthesis of the first KNi ^{II} Fe ^{II} shell(moL)	1×10 ⁻⁵	1×10 ⁻⁵	1×10 ⁻⁵	1×10 ⁻⁵	5×10 ⁻⁵
Volume of precursors added for the synthesis of the second KNi ^{II} Cr ^{III} shell (mL)	1×10 ⁻⁵	2×10 ⁻⁵	3×10 ⁻⁵	2×10 ⁻⁵	5×10 ⁻⁵
IR ν (-OH) Coordinate water (cm ⁻¹)	3650	3674	3683	3648	3640
IR ν (-OH) Crystalized water (cm ⁻¹)	3423	3425	3425	3416	3415
IR ν (Cr ^{III} -C≡N-Ni ^{II}) (cm ⁻¹)	2172	2175	2171	2173	2172
IR ν (Fe ^{II} -C≡N-Ni ^{II}) (cm ⁻¹)	2090	2094	2098	2095	2090
IR δ (H-O-H) Crystalized water (cm ⁻¹)	1625	1611	1618	1604	1618
IR ν (Fe ^{II} -CN) (cm ⁻¹)	593	590	591	593	592
IR ν (Cr ^{III} -CN) (cm ⁻¹)	491	496	494	494	493
IR δ (Fe ^{II} -CN), (cm ⁻¹)	465	467	469	468	465
Core size (nm)	20.0 ± 3.1	19.7 ± 2.3	19.3 ± 2.9	18.6 ± 3.8	20.6 ± 3.2
First PBA shell thickness (nm)	5.8 ± 1.5	5.6 ± 1.4	5.01 ± 1.2	6.6 ± 1.7	15.9 ± 4.0
Second PBA shell thickness (nm)	1.6 ± 0.3	4.0 ± 1.0	7.3 ± 1.5	10.45 ± 2.6	40.45 ± 8.1
Total size (nm)	34.8 ± 3.7	38.9 ± 4	53.5 ± 5.5	48.5 ± 6.5	133.3 ± 11.5
Composition (atom %)	Au/K/Ni/Fe/Cr 55.3/8.0/19.7/ 8.7/8.3	Au/K/Ni/Fe/Cr 43.0/5.1/30.7/ 5.6/15.7	Au/K/Ni/Fe/Cr 55.3/3.6/23.5/ 4.1/13.4	Au/K/Ni/Fe/Cr 39.8/4.6/30.8/ 3.6/21.2	Au/K/Ni/Fe/Cr/C/ N/H 0.8/1.55/5.1/ 0.85/2.75/23.7/ 20.6/44.6
Estimated formula	Au _{5.6} @ K _{0.7} Ni[Fe(CN) ₆] _{0.68} @ K _{0.1} [Cr(CN) ₆] _{0.81}	Au _{2.8} @ K _{0.7} Ni[Fe(CN) ₆] _{0.68} @ K _{0.1} [Cr(CN) ₆] _{0.70}	Au _{4.5} @ K _{0.7} Ni[Fe(CN) ₆] _{0.68} @ K _{0.1} [Cr(CN) ₆] _{0.76}	Au _{2.3} @ K _{0.7} Ni[Fe(CN) ₆] _{0.68} @ K _{0.1} [Cr(CN) ₆] _{0.83}	Au _{0.30} @ K _{1.2} Ni[Fe(CN) ₆] _{0.80} @ K _{0.04} [Cr(CN) ₆] _{0.68}

Table 1: table summarizing the main characteristics of the different double-layered core-shell Au@KNi^{II}Fe^{II}@KNi^{II}Cr^{III} NPs and their main synthetic conditions (volume of precursors added for the first and the second shell).

The PXRD analysis was performed on sample **11-5** (figure 7). For this sample, PXRD also confirms the formation of the second PBA network on the initial Au@K⁺/Ni²⁺/[Fe^{II}(CN)₆]⁴⁻ NPs. The peaks corresponding to the *fcc* gold metal structure of the core are observed, such as for the initial Au@K⁺/Ni²⁺/[Fe^{II}(CN)₆]⁴⁻ NPs, which are indexed to the space group *Fm* $\bar{3}$ *m* with a cell parameter $a_{\text{gold}} = 4.07 \text{ \AA}$. PXRD pattern also shows the presence of two sets of distinct peaks which corresponds to two PBAs structures of KNi^{II}[Fe^{II}(CN)₆] and KNi^{II}[Cr^{III}(CN)₆], in accordance to the significant difference of their respective cell parameters, $a_{\text{NiFe}} = 10.07 \text{ \AA}$ and $a_{\text{NiCr}} = 10.46 \text{ \AA}$ (figure 7, inset)¹. Note that an important cell parameter difference is observed, with a Δa value of 0.4 \AA , which correspond to lattice misfit of 3.7 %. The peaks exhibited for both PBAs are characteristic to *fcc* structures, and they were indexed in the *F* $\bar{4}$ *3m* space group, confirming the formation of the KNi^{II}[Cr^{III}(CN)₆] structure without any modification of the initial KNi^{II}[Fe^{II}(CN)₆] one. Indeed, no peaks corresponding to a mixed phase with different lattice parameters could be detected, which confirm that the particles contain two different PBA layer. This is in accordance with the results previously obtained by EDS mapping.

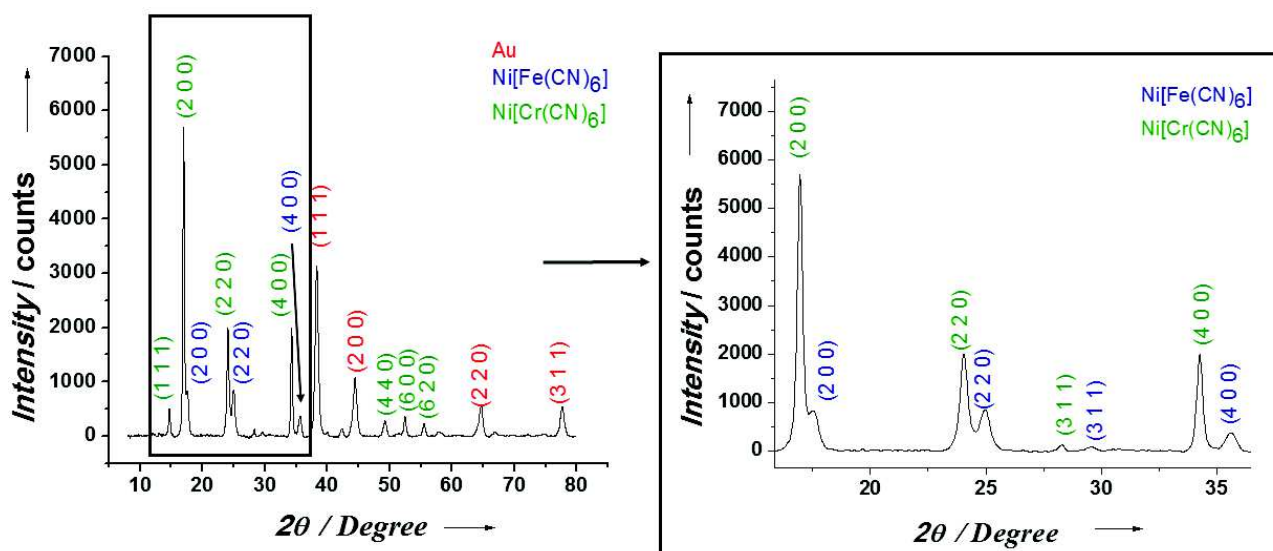


Figure 7: Left, XRD patterns of the double-layered core-shell Au@KNi^{II}Fe^{II}@KNi^{II}Cr^{III} (**11-5**). Right, magnification of the two set of distinct peaks corresponding to the two PBAs structures of KNi^{II}[Fe^{II}(CN)₆] and KNi^{II}[Cr^{III}(CN)₆].

IV.2.2 Synthesis of double-layered core-shell NPs Au@K⁺/Ni²⁺/[Fe^{II}(CN)₆]⁴⁻@PBA where PBA = KNi^{III}[Fe^{III}(CN)₆], KCo^{II}[Fe^{II}(CN)₆] and KFe^{III}[Fe^{II}(CN)₆].

The approach consisting on the subsequent growing of a second PBA on the Au@K⁺/Ni²⁺/[Fe^{II}(CN)₆]⁴⁻ NPs was extended to other PBA' second shell, such as KNi^{III}[Fe^{III}(CN)₆], KCo^{II}[Fe^{II}(CN)₆] and KFe^{III}[Fe^{II}(CN)₆]. The experimental protocols to obtain the double-layered Au@K⁺/Ni²⁺/[Fe^{II}(CN)₆]⁴⁻@PBA core-shell NPs remain the same as previously described.

The synthesis of double-layered Au@K⁺/Ni²⁺/[Fe^{II}(CN)₆]⁴⁻@PBA with the small first KNi^{III}Fe^{II} shell is the same than those previously used to obtained samples **11-1** to **11-4**, *i.e.* the synthesis of Au@K⁺/Ni²⁺/[Fe^{II}(CN)₆]⁴⁻ NPs (sample **2-3**) with the addition of only 1.0×10⁻⁵ molL (2 mL, 1 hour of addition)) of NiCl₂·6H₂O (5.0 mM) and 1.1×10⁻⁵ molL of K₃[Fe(CN)₆] (5.65 mM), then the hydrolysis of the KBH₄ remaining in the media before the centrifugation. After removing the supernatant, the NPs are dispersed in ultrapure water to obtain approximately 100 mL of solution, and the PBA precursors are added using a slow addition rate (2 mL/h). The use of NiCl₂·6H₂O and K₃[Fe(CN)₆] as PBA precursors led to Au@KNi^{III}Fe^{II}@KNi^{III}Fe^{III} NPs (sample **12-1**) and the use of CoCl₂·6H₂O and K₃[Fe(CN)₆] gave Au@KNi^{III}Fe^{II}@KCo^{II}Fe^{II} NPs (sample **13**). The synthesis of the double-layered Au@KNi^{III}Fe^{II}@KFe^{III}Fe^{II} (sample **14-1**) and Au@NaNi^{III}Fe^{II}@NaFe^{III}Fe^{II} (sample **14-2**) heterostructures were obtained by using respectively FeCl₃·6H₂O with K₄[Fe(CN)₆]·3H₂O and FeCl₃·6H₂O with Na₄[Fe(CN)₆]·10H₂O.

To obtain double-layered NPs with a large first and second shells, the protocol was the same than the one used to obtain Au@KNi^{III}Fe^{II}@KNi^{III}Fe^{III} NPs (sample **3-5**), *i.e.* the dispersion of 10 mg of dried initial Au@K⁺/Ni²⁺/[Fe^{II}(CN)₆]⁴⁻ NPs with the large first KNi^{III}Fe^{II} shell (sample **2**) in 100 mL of water, and then the slow (2 mL/h) and simultaneous addition of the aqueous solutions of the transition metal salt (5.0×10⁻⁵ mol, 10 mL) and the hexacyanometallate (5.6×10⁻⁵ mol, 10 mL). The use of NiCl₂·6H₂O and K₃[Fe(CN)₆] as PBA' precursors led to Au@KNi^{III}Fe^{II}@KNi^{III}Fe^{III} (**12-2**).

The TEM images clearly confirm the achievement of the subsequent layers growth for all samples (figure 8). As for the Au@KNi^{III}Fe^{II}@KCr^{III}Fe^{III} NPs (samples **11-1** to **11-5**), TEM images show the presence of the NPs relatively uniform in size and in shape with the complex shell's morphology consisting on the presence of several cubic-like shells growth on different sides of the gold core. As for sample **11-5**, this intricate morphology is particularly visible for samples with an important shell thickness, (all samples except **13**). For all Au@K⁺/Ni²⁺/[Fe^{II}(CN)₆]⁴⁻@PBA NPs, no modification of the gold core diameter is observed, indicating that the PBA shell growth is responsible to any modification of the total size (figure 8 and table 2).

As described previously, we observed the increase of the total size of the NPs comparatively to the size of Au@K⁺/Ni²⁺/[Fe^{II}(CN)₆]⁴⁻ NPs used as seeds. This clearly indicates that a subsequent growth of the second PBA shell occurred. To estimate the shell sizes, the mean size of the second PBA layer was found by difference between the NPs size before and after the second shell growth.

For the Au@KNi^{II}Fe^{II}@KNi^{II}Fe^{III} NPs (figure 8), the total size of both samples is close (80.4 ± 12.6 nm for **12-1** and 80.6 ± 10.5 nm for **12-2**) (figure 9 and table 2), with the second KNi^{II}Fe^{III} shell thickness of 24.8 ± 5.0 nm for **12-1** and 14 ± 2.8 nm for **12-2**. That also confirms the possibility to use the small KNi^{II}Fe^{III} as a point of anchoring of the second PBA shell.

The size of the second KCo^{II}Fe^{II} layer for sample **13** is 6.6 ± 1.4 nm. This is the thinner layer obtained in the same conditions, as other samples (figure 9 and table 2). This may be due to the kinetic of the shell formation, depending on the nature of the PBA used. Note that, for sample **5**, the shape is clearly more cubic and the nano-objects are less defined than for all other second PBA shells (figure 8).

Finally, the growth of a second Fe^{III}[Fe^{II}(CN)₆] layer leads to Au@Ni^{II}Fe^{II}@Fe^{III}Fe^{II} with a shell thickness of 12.0 ± 2.4 nm with using K⁺ as counter-ion (sample **14-1**) and of 8.1 ± 1.6 nm using Na⁺ (sample **14-2**) (figure 9 and table 2). No significant difference is observed for their morphology. This indicates a minor influence of the counter cation of the second shell growth.

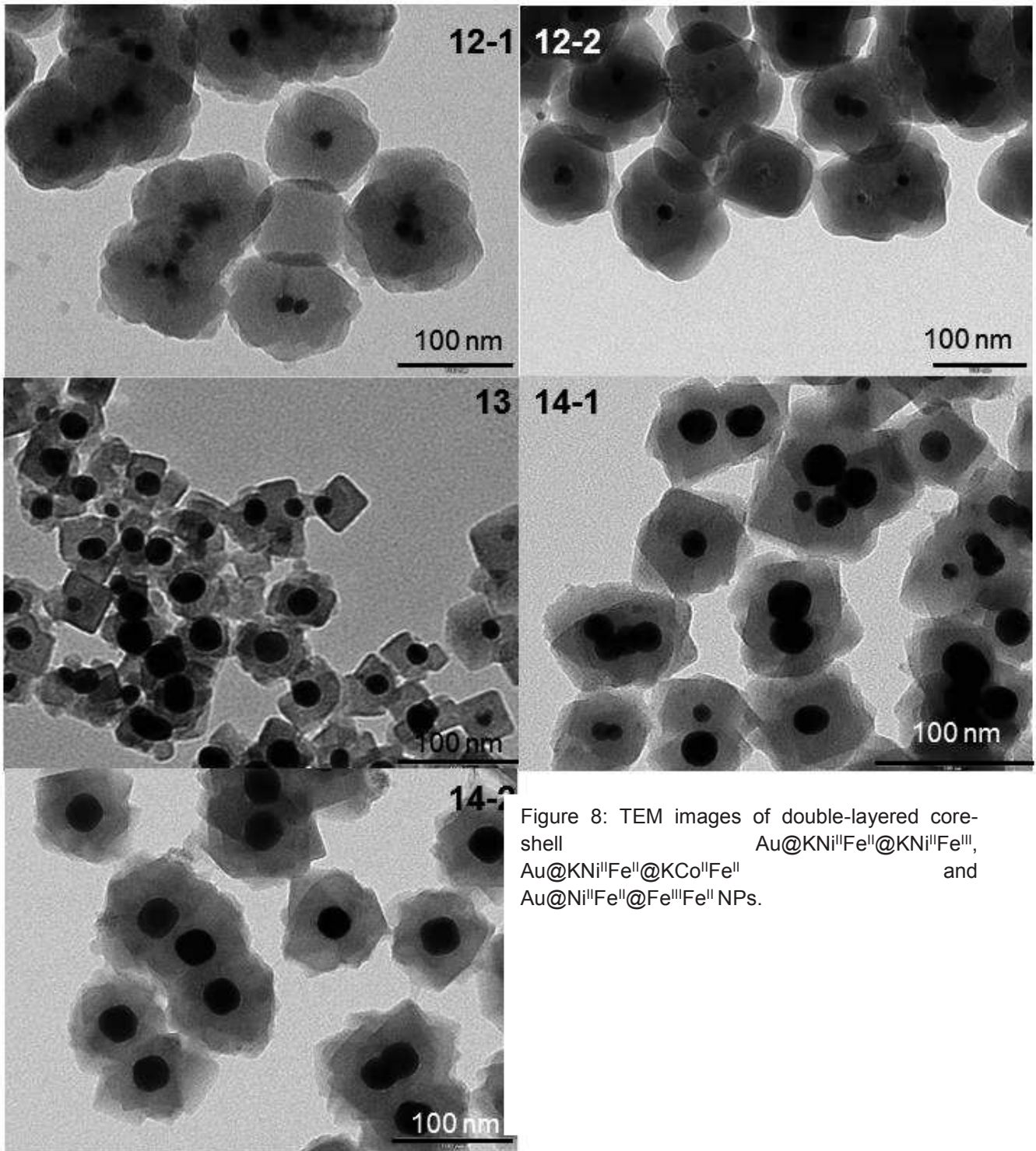


Figure 8: TEM images of double-layered core-shell $\text{Au@KNi}^{\text{II}}\text{Fe}^{\text{II}}@\text{KNi}^{\text{II}}\text{Fe}^{\text{III}}$, $\text{Au@KNi}^{\text{II}}\text{Fe}^{\text{II}}@\text{KCo}^{\text{II}}\text{Fe}^{\text{II}}$ and $\text{Au@Ni}^{\text{II}}\text{Fe}^{\text{II}}@\text{Fe}^{\text{III}}\text{Fe}^{\text{II}}$ NPs.

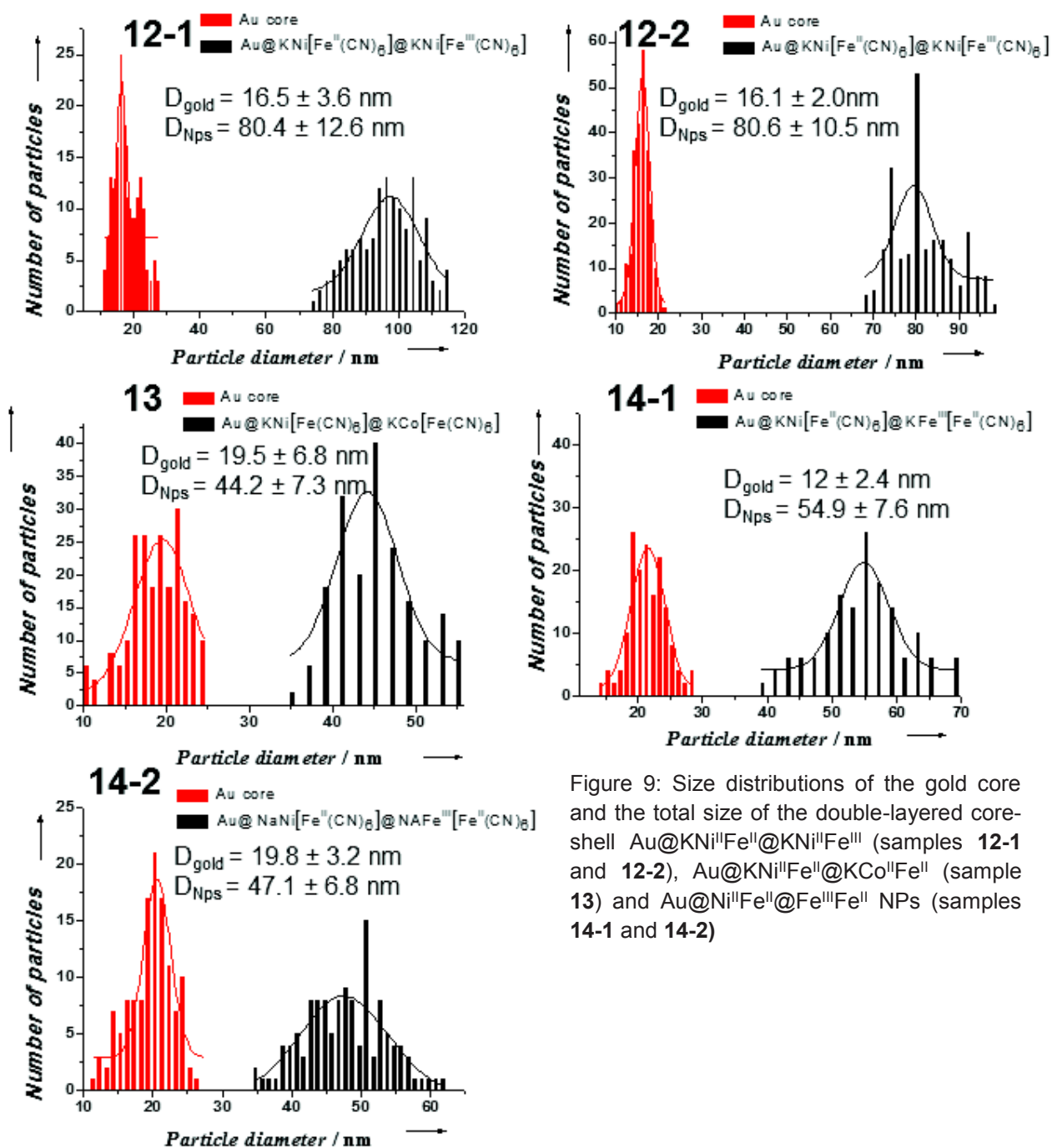


Figure 9: Size distributions of the gold core and the total size of the double-layered core-shell Au@KNi^{II}Fe^{II}@KNi^{II}Fe^{III} (samples **12-1** and **12-2**), Au@KNi^{II}Fe^{II}@KCo^{II}Fe^{II} (sample **13**) and Au@Ni^{II}Fe^{II}@Fe^{III}Fe^{II} NPs (samples **14-1** and **14-2**)

STEM, STEM-HAADF and EDS mapping were performed on Au@NaNi^{II}Fe^{II}@NaFe^{III}Fe^{II} NPs (sample **14-2**). Note that Au@KNi^{II}Fe^{II}@KCo^{II}Fe^{II} NPs (sample **13**) were not investigated due to their poor definition comparatively to others. EDS mapping was not performed on Au@KNi^{II}Fe^{II}@KNi^{II}Fe^{III} NPs for a practical reason: the nature of the metal ions are the same in both, the first and the second shell.

STEM image (figure 10a) shows clearly the complex shell's morphology of the NPs, as previously observed. The formation of two PBA shells was confirmed by EDS mapping (figure 10). The presence of a thin distribution of the Ni atoms around the gold core is observed. Moreover, while the Ni atoms seems to be only inside the particle, the Fe atoms are present in the entire NP, clearly indicating that the small KNi^{II}Fe^{II} shell is the first shell anchored on the gold, and the second shell is constituted only with iron, corresponding to the Fe^{III}Fe^{II} PB shell.

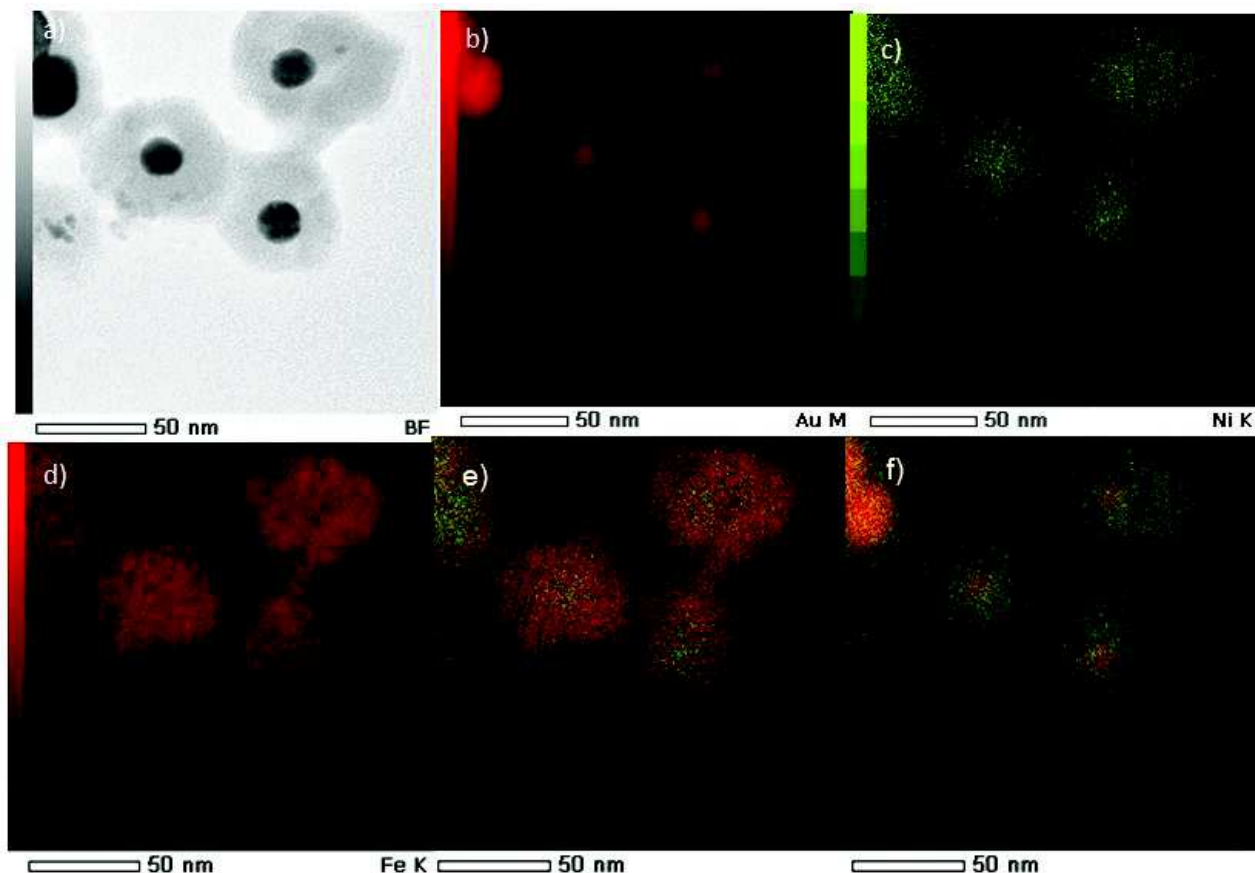


Figure 10: STEM image a) and EDS mapping of the Au@NaNi^{II}Fe^{II}@NaFe^{III}Fe^{II} NPs with the topochemical repartition for b) gold (red), c) nickel (green) d) iron (red) e) iron (red) and nickel (green) and f) gold (red) and nickel (green).

IR spectroscopy confirms the formation of the second PBA layer for all samples. The values of the characteristic bands for each sample are summarized in table 2.

For the Au@KNi^{II}Fe^{II}@KNi^{II}Fe^{III} NPs (samples **12-1** to **12-2**), it is possible to observe the stretching vibrations corresponding to the Fe^{II}-C≡N-Ni^{II} linkage²³, located at 2091 cm⁻¹, which is the same than observed for the initial Au@KNi^{II}Fe^{II} NPs, confirming the presence of the first KNi^{II}Fe^{II} layer¹. Another band, observed in the spectrum and located at 2165 cm⁻¹ is characteristic of the stretching vibrations of Fe^{III}-C≡N-Ni^{II} linkage (figure 11), indicating that the non-reduced Ni^{II}Fe^{III} PBA is present in the second layer.

For Au@KNi^{II}Fe^{II}@KCo^{II}Fe^{II} (sample **13**) and the Au@Ni^{II}Fe^{II}@Fe^{III}Fe^{II} NPs (samples **14-1** and **14-2**), we observe a single band in the cyanide stretching region, located respectively at 2081 cm⁻¹ and at 2084 cm⁻¹ (Figure 12). This band is attributed to both Fe^{II}-C≡N-Ni^{II} corresponding to the first shell and respectively to Fe^{II}-C≡N-Co^{II} (**13**) and Fe^{II}-C≡N-Fe^{III} (**14-1** and **14-2**) linkages^{23,24}, corresponding to the second shell. Indeed, the expected values for each PBA are 2090 cm⁻¹ for Fe^{II}-C≡N-Ni^{II} linkages corresponding to the first shell, and 2081 cm⁻¹ for Fe^{II}-C≡N-Co^{II} linkages (**13**) and 2080 cm⁻¹ for Fe^{II}-C≡N-Fe^{III} linkages respectively (**14-1** and **14-2**)^{23,24} corresponding to the second shell, which are too close to observe two separated bands. For the Au@KNi^{II}Fe^{II}@KCo^{II}Fe^{II} NPs, that indicates the formation of the reduced pairs Fe^{II}-C≡N-Co^{II} instead of the Fe^{III}-C≡N-Co^{II} linkage, as frequently observed for this coordination network.

The formation of the second PBA shell is also confirmed by the bands observed in the metal-carbon stretching and bending regions.

For the Au@KNi^{II}Fe^{II}@KNi^{II}Fe^{III} NPs (samples **12-1** and **12-2**), the appearance of the metal-carbon stretching and bending bands, respectively at 549 cm⁻¹ and 437 cm⁻¹ provided the formation of the non-reduced Ni^{II}Fe^{III} PBA shell²³ (figure 11).

For the Au@KNi^{II}Fe^{II}@KCo^{II}Fe^{II} NPs (sample **13**), the reduction of the Fe^{III} in Fe^{II} is also confirmed by the metal-carbon stretching band, located at 593 cm⁻¹, and the metal-carbon bending band, located at 473 and 461 cm⁻¹, corresponding to the Fe^{II}-CN linkage, and characteristic of both the Ni^{II}Fe^{II} and Co^{II}Fe^{II} PBAs^{23,24} (figure 12). The reduction of the Fe^{III} in Fe^{II} indicates that no interesting magnetic properties would be obtained in this case. Indeed, the Co^{II} in low spin configuration is paramagnetic (S= 1/2) and the Fe^{II} in low spin is diamagnetic (S = 0), then the NPs should only exhibit paramagnetic properties, instead of ferromagnetic or photomagnetic behavior.

Finally, for the Au@KNi^{II}Fe^{II}@FeFe NPs (samples **14-1** and **14-2**), the shoulder corresponding to the bending band and located at 474 cm⁻¹ is typical to the reduced Fe^{II}-CN linkage, as observed for the initial Au@K⁺/Ni²⁺/[Fe^{II}(CN)₆]⁴⁻ NPs, confirming the presence of the first KNi^{II}Fe^{II} shell (figure 12). The stretching and the bending metal-carbon bands, respectively located at 600 and 493 cm⁻¹, characteristic to the Fe^{II}-CN bond of Fe^{III}[Fe^{II}(CN)₆], also attesting the growth of the Prussian blue structure²³. No significant difference is observed between the samples **14-1** synthesized with K⁺ as counter-ion and **14-2** synthesized with Na⁺ as counter-ion.

Moreover, the presence of bands of the $\nu(-OH)$ vibration and the $\delta(H-O-H)$ deformation confirms the presence of water molecules in the samples (figures 11 and 12). The bands located respectively around 3400 cm⁻¹ and 1610 cm⁻¹ correspond to crystallized water in the sample, involved in a hydrogen-bonded network²⁴. The band located in the 3600-3700 cm⁻¹ range is characteristic to water molecules coordinated to the metal transition centers, at the cyanometallate vacancies, characteristic of a lacunar structure for the PBAs.

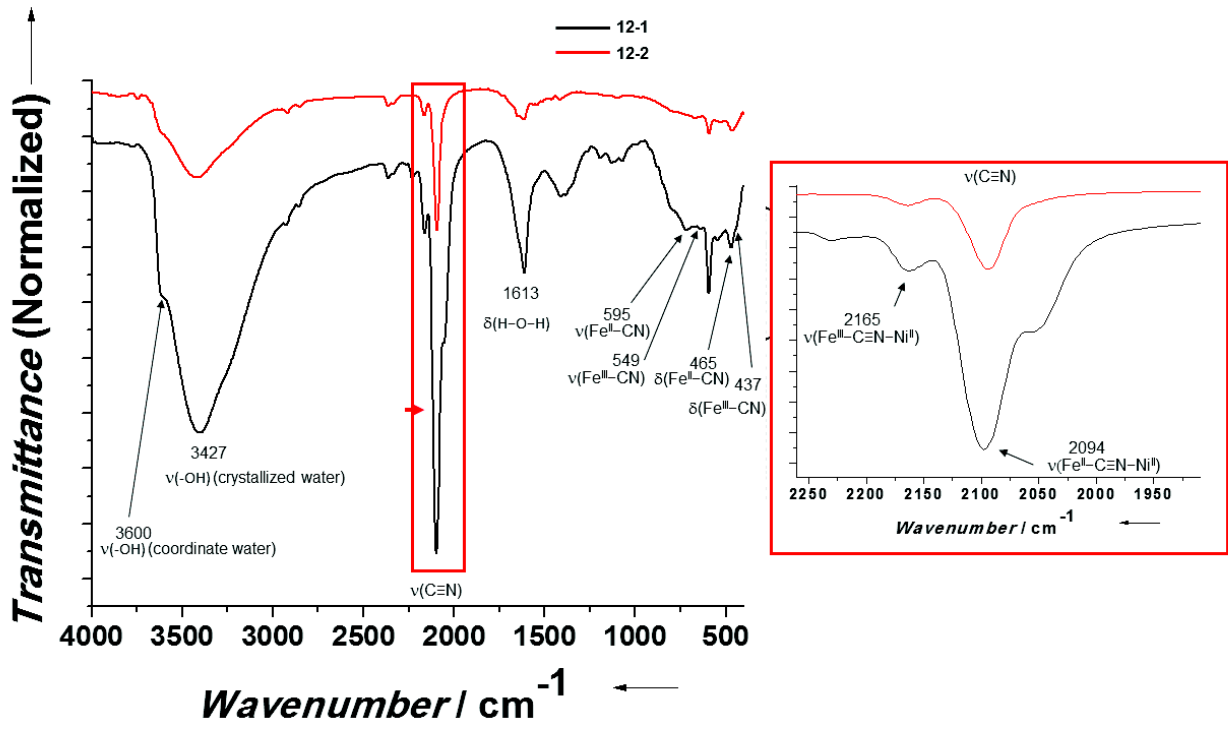


Figure 11: Left, IR spectra of the double-layered core-shell Au@KNi^{II}Fe^{II}@KNi^{II}Fe^{III} NPs. Right, magnification of the cyanide stretching region.

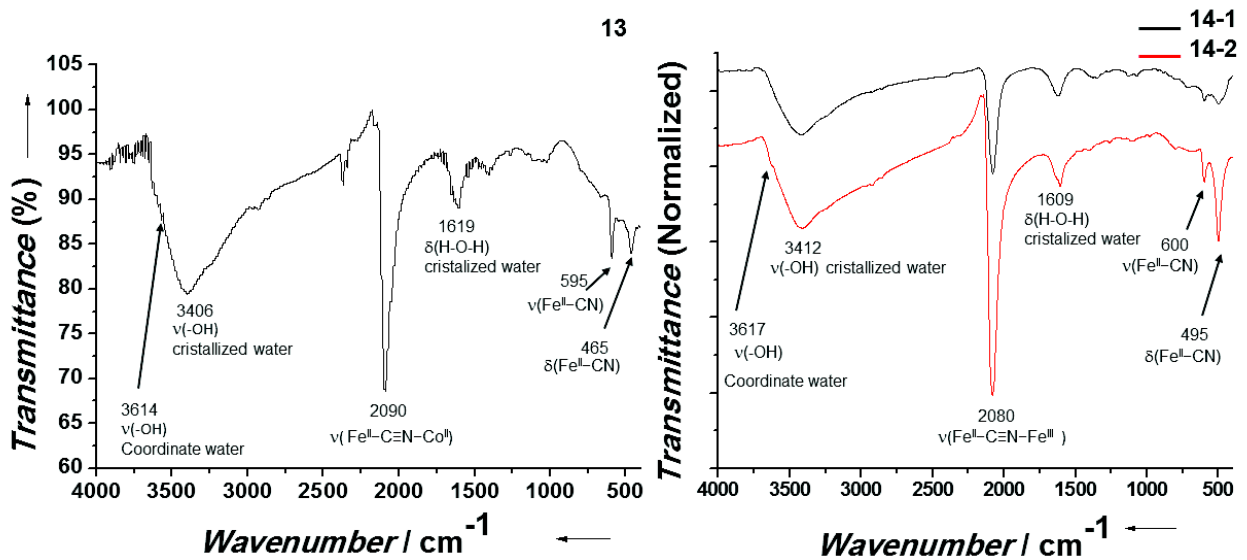


Figure 12: Left, IR spectrum of the double-layered core-shell Au@KNi^{II}Fe^{II}@KCo^{II}Fe^{II} NPs. Right, IR spectra of the double-layered core-shell Au@KNi^{II}Fe^{II}@KFe^{III}Fe^{II} (14-1) and Au@NaNi^{II}Fe^{II}@NaFe^{III}Fe^{II} (14-2) NPs.

Main characteristics	Label				
	12-1	12-2	13	14-1	14-2
	Au@K ^{II} Ni ^{II} Fe ^{II} @K ^{III} Ni ^{III} Fe ^{III}	Au@K ^{II} Ni ^{II} Fe ^{II} @K ^{III} Ni ^{III} Fe ^{III}	Au@K ^{II} Ni ^{II} Fe ^{II} @K ^{II} Co ^{II} Fe ^{II}	Au@K ^{II} Ni ^{II} Fe ^{II} @K ^{II} Fe ^{II} Fe ^{III}	Au@Na ^{II} Ni ^{II} Fe ^{II} @Na ^{II} Fe ^{II} Fe ^{III}
Cyanometallate precursor for the second shell	K ₃ [Fe(CN) ₆]	K ₃ [Fe(CN) ₆]	K ₃ [Fe(CN) ₆]	K ₄ [Fe(CN) ₆].3H ₂ O	Na ₄ [Fe(CN) ₆].10H ₂ O
Transition metal salt precursor for the second shell	NiCl ₂ .6H ₂ O	NiCl ₂ .6H ₂ O	CoCl ₂ .6H ₂ O	FeCl ₃ .6H ₂ O	FeCl ₃ .6H ₂ O
amount of precursors added for the synthesis of the first K ^{II} Ni ^{II} Fe ^{II} shell (mol/L)	1×10 ⁻⁵	5×10 ⁻⁵	1×10 ⁻⁵	1×10 ⁻⁵	1×10 ⁻⁵
amount of precursors added for the synthesis of the second PBA ^I shell (mol/L)	4×10 ⁻⁵	5×10 ⁻⁵	4×10 ⁻⁵	4×10 ⁻⁵	4×10 ⁻⁵
IR ν(-OH) Coordinate water (cm ⁻¹)	3600	3610	3614	3609	3617
IR ν(-OH) crystalized water (cm ⁻¹)	3427	3402	3406	3417	3412
IR ν(C≡N) (cm ⁻¹)	2165 (Fe ^{III} -C≡N-Ni ^{II}) 2094 (Fe ^{II} -C≡N-Ni ^{II})	2166 (Fe ^{III} -C≡N-Ni ^{II}) 2095 (Fe ^{II} -C≡N-Ni ^{II})	2090 (Fe ^{II} -C≡N-Co ^{II}) (Fe ^{II} -C≡N-Ni ^{II})	2080 (Fe ^{II} -C≡N-Fe ^{II}) (Fe ^{II} -C≡N-Ni ^{II})	2081 (Fe ^{II} -C≡N-Fe ^{II}) (Fe ^{II} -C≡N-Ni ^{II})
IR δ(H-O-H) crystalized water (cm ⁻¹)	1613	1610	1619	1624	1609
IR ν(Fe-CN) cm ⁻¹	595 Fe ^{II} -CN 549 Fe ^{III} -CN	595 Fe ^{II} -CN 551 Fe ^{III} -CN	595 Fe ^{II} -CN	600 Fe ^{II} -CN	601 Fe ^{II} -CN
IR δ(Fe-CN), (cm ⁻¹)	465 Fe ^{II} -CN 437 Fe ^{III} -CN	474 Fe ^{II} -CN 460 Fe ^{III} -CN	465 Fe ^{II} -CN	493, 474 Fe ^{II} -CN	499, 474 Fe ^{II} -CN
Core size (nm)	16.1 ± 2.0	16.5 ± 3.6	19.5 ± 6.8	21.5 ± 5	19.8 ± 3.2
First PBA shell thickness (nm)	7.5 ± 1.9	18.0 ± 4.5	5.8 ± 1.4	4.7 ± 1.2	5.6 ± 1.4
Second PBA shell thickness (nm)	24.8 ± 5.0	14.0 ± 2.8	6.6 ± 1.4	12.0 ± 2.4	8.1 ± 1.6
Total size (nm)	80.6 ± 10.5	80.4 ± 12.6	44.2 ± 7.3	54.9 ± 7.6	47.1 ± 6.8
Composition (Atom %)	Au/K/Ni/Fe 23.6/22.7/29.9/ 23.8	Au/K/Ni/Fe/C/N/H 0.6/1.8/5.3/4/23.4/ 21.6/43.3	Au/K/Ni/Fe/Co 19.8/25.5/1.10/28.3/ 25.2	Au/K/Ni/Fe 24.2/28.6/5.2/42	Au/K/Na/Ni/Fe 34.2/1/1.1/3.9/ 59.8
Estimated formula	Au _{1.6} @ K _{0.8} Ni[Fe ^{II} (CN) ₆] _{0.7} @ K _{0.7} [Fe ^{III} (CN) ₆] _{0.9}	Au _{0.25} @ K _{1.2} Ni[Fe ^{II} (CN) ₆] _{0.8} @ K _{0.2} [Fe ^{III} (CN) ₆] _{0.9}	Au _{1.58} @ K _{0.7} Ni[Fe ^{II} (CN) ₆] _{0.68} @ K _{0.9} Co[Fe ^{II} (CN) ₆] _{0.86}	Au _{1.2} @ K _{0.7} Ni[Fe(CN) ₆] _{0.68} @ K _{0.57} Fe[Fe(CN) ₆] _{0.89}	Au _{1.24} @ K _{0.7} Ni[Fe(CN) ₆] _{0.68} @ Na _{0.05} Fe[Fe(CN) ₆] _{0.95}

Table 2: table summarizing the main characteristics of the different double-layered core-shell Au@K^{II}Ni^{II}Fe^{II}@PBA NPs and their main synthetic conditions (precursors used for the second shell, volume of precursors added for the first and the second shell).

The composition of the different double-layered core-shell Au@KNi^{II}Fe^{II}@PBA NPs was determined, by elemental analysis for **12-2** and by EDS analysis for the others. The presence of the expected elements confirms the formation of the new PBA for all the samples (table 2). However, it is not possible to determinate a precise formula giving the composition of the two PBA shells because we do not know the repartition of the elements on each layer. Then, according to the method previously described for the Au@KNi^{II}Fe^{II}@KNi^{II}Cr^{III} NPs, formulas were estimated for the Au@KNi^{II}Fe^{II}@PBA NPs (table 2).

The PXRD patterns were performed on samples **12-2**, **13** and **14-2** (figure 13, 14 and 15). PXRD also confirms the formation of the second PBA network on the initial Au@K⁺/Ni²⁺/[Fe^{II}(CN)₆]⁴⁻ NPs (figure 4). For all samples, the peaks corresponding to the *fcc* gold metal structure of the core are observed, such as for the initial Au@K⁺/Ni²⁺/[Fe^{II}(CN)₆]⁴⁻ NPs, which are indexed to the space group *Fm* $\bar{3}$ *m*, with a cell parameter $a_{\text{gold}} = 4.07 \text{ \AA}$. Using the Scherrer formula, the size of the crystallites was estimated to be 16.2 nm for **12-2**, 15.6 nm for **13** and 16.2 nm for **14-2**, which is in accordance with the sizes obtained from TEM distributions.

For the Au@KNi^{II}Fe^{II}@KNi^{II}Fe^{III} NPs (sample **12-2**), the PXRD pattern exhibits only a single peak attributed to Ni₂[Fe(CN)₆] PBA (01-075-0037), indexed in the *F* $\bar{4}$ *3m* space group, with a mean cell parameter value of 10.20 Å (figure 14). This reflects the small difference in the cell parameter of PBA with $a_{\text{NiFe}^{\text{II}}} = 10.07 \text{ \AA}$ and $a_{\text{NiFe}^{\text{III}}} = 10.23 \text{ \AA}$, and confirms the formation of the non-reduced KNi^{II}[Fe^{III}(CN)₆] structure with the remaining of the initial KNi^{II}Fe^{II} structure. The size given by the Debye-Scherrer calculator is 44 nm, which is in the same order than the value obtained by TEM distribution (NiFe^{II} + NiFe^{III} = 32.0 ± 3.7 nm)

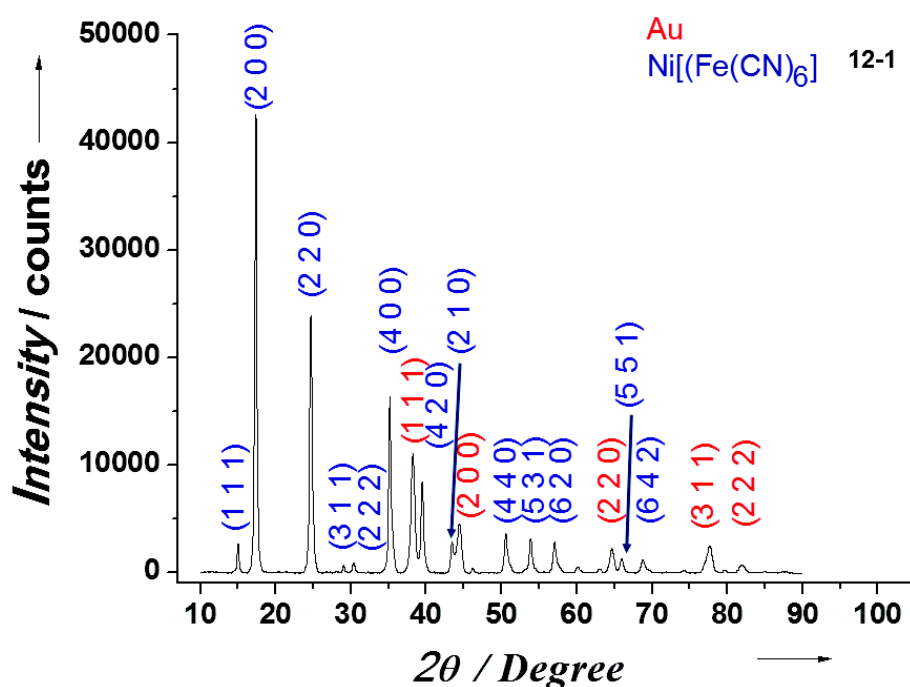


Figure 13: XRD patterns of the double-layered core-shell Au@KNi^{II}Fe^{II}@KNi^{II}Fe^{III} NPs (**12-2**).

For the Au@KNi^{II}Fe^{II}@KCo^{II}Fe^{II} NPs (sample **13**), the PXRD pattern exhibits only single peak attributed to both Ni₂[Fe(CN)₆] PBA (01-075-0037) and Co₂[Fe(CN)₆] PBA (01-075-0038), indexed in the *Fm* $\bar{3}$ *m* space group for the first and in the *F* $\bar{4}$ *3m* space group for the second, with cell parameter values of 10.13 Å and 10.09 Å respectively (figure 14). The correspondence of all peaks for both PBAs reflects the small difference in the cell parameters, except for the (1 1 1) plane only observed for Ni₂[Fe(CN)₆] PBA. As indicated by IR spectroscopy, the presence of the reduced Ni^{II}[Fe^{II}(CN)₆] and Co^{II}[Fe^{II}(CN)₆] PBAs is confirmed for the two cyano-bridged coordination polymer shells. The size of the PBA crystallite has been evaluated using the Scherrer formula, to be 15.6 nm, which is in accordance with the value obtained by TEM distribution (NiFe + CoFe = 12.4 ± 1.4 nm).

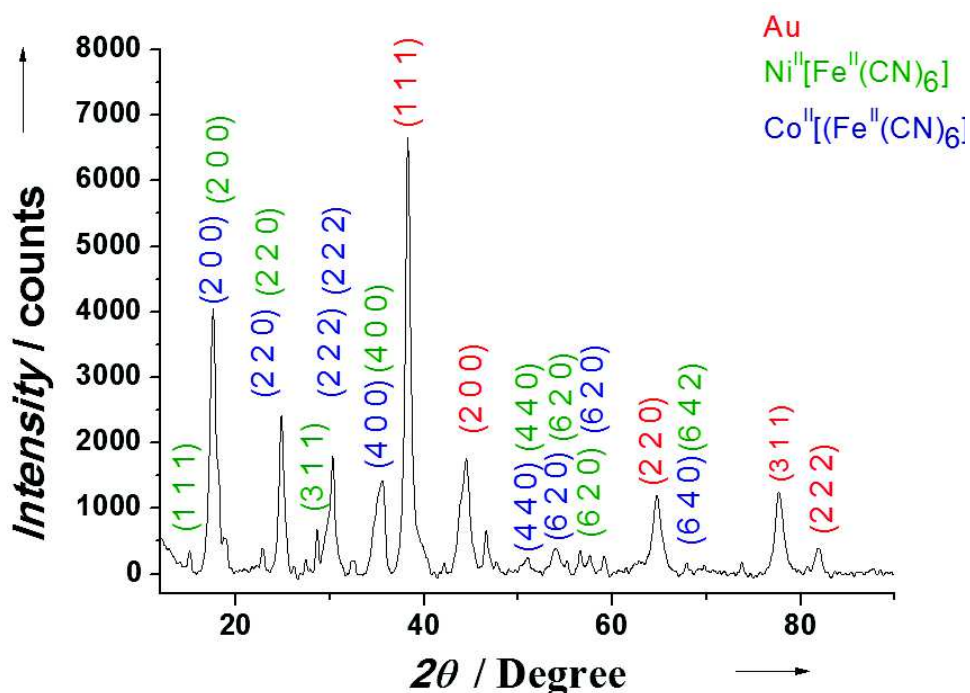


Figure 14: XRD patterns of the double-layered core-shell Au@KNi^{II}Fe^{II}@KCo^{II}Fe^{II} NPs (**13**).

For the Au@NaNi^{II}Fe^{II}@NaFe^{III}Fe^{II} NPs (sample **14-2**), the PXRD pattern exhibits also single peaks related to the structure of both Ni₂[Fe(CN)₆] PBA (01-075-0037) and PB (01-073-0687), with cell parameter value of 10.13 Å and 10.17 Å, which are indexed to the space group *Fm* $\bar{3}$ *m* (figure 15). For the PB structure, this is in accordance to the bulk material of Fe^{III}₄[Fe^{II}(CN)₆]₃, with a cell parameter of $a_{PB} = 10.16$ Å. This confirms the formation of the PB network on the initial small single-layered Au@K⁺/Ni²⁺/[Fe^{II}(CN)₆]⁴⁻ NPs. Using the Debye-Scherrer formula, the crystallite size was calculated to be 26 nm, which is in a same order than the value obtained by TEM distribution (NiFe + FeFe = 13.7 ± 1.5 nm).

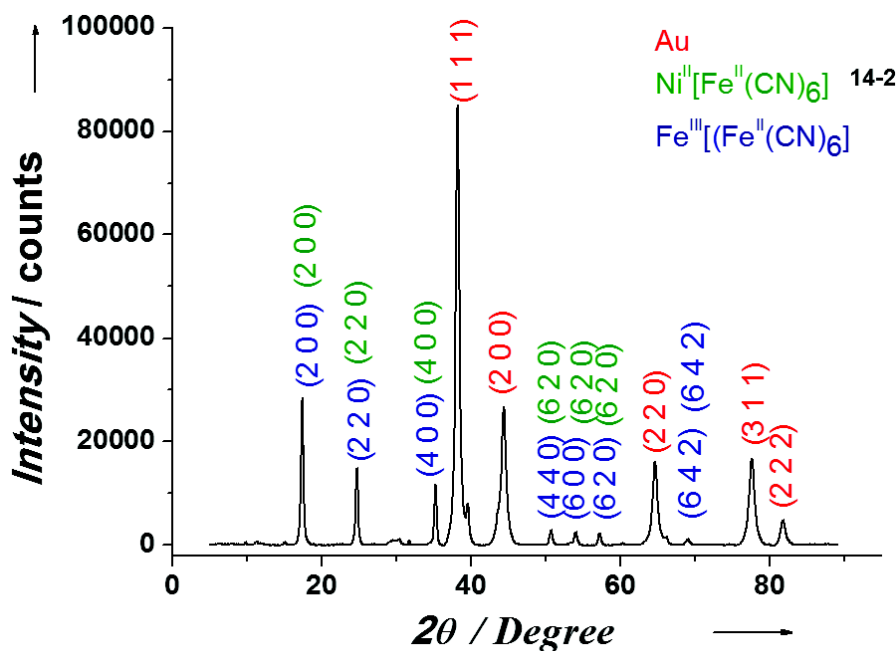


Figure 15: XRD patterns of the double-layered core-shell Au@NaNi^{II}Fe^{II}@NaFe^{II}Fe^{III} (**14-2**) NPs.

IV.2.3 Optical properties of the double-layered core-shell Au@K⁺/Ni²⁺/[Fe^{II}(CN)₆]⁴⁻@PBA NPs.

All Au@K⁺/Ni²⁺/[Fe^{II}(CN)₆]⁴⁻@PBA NPs exhibit plasmonic properties of the gold core. As a reminder, the SPR band is observed for the gold NPs at 517 nm, and it is red-shifted to 532 nm and 539 nm, respectively for the core-shell Au@K⁺/Ni²⁺/[Fe^{II}(CN)₆]⁴⁻ NPs with 5.9 ± 1.5 nm (sample **2-3**) and 16.6 ± 2.7 nm (sample **2**) shells. For a series of double-layered Au@KNi^{II}Fe^{II}@KNi^{II}Cr^{III} NPs synthesized from Au@K⁺/Ni²⁺/[Fe^{II}(CN)₆]⁴⁻ NPs with a small first shell, a regular increase of the KNi^{II}Cr^{III} layer induces a gradual red-shift of the SPR band (figure 16). The maximum shifts from 532 nm to 541 nm for sample **11-2** with the total shell thickness of 9.6 ± 1.2 nm, to 545 nm for sample **11-3** for the total shell thickness of 12.3 ± 2.8 nm, then to 547 nm for the total shell thickness of 16.7 ± 2.3 nm for sample **11-4** and to 552 nm for sample **11-5** with the shell thickness of 56.4 ± 11.3 nm (figure 15 left). This behavior is consistent with the increase of the total PBA shell thickness (Ni^{II}Fe^{II} and Ni^{II}Cr^{III}), due to the modification of the refractive index²¹ of the PBA layers, and of water, as also previously observed for KNi^{II}Fe^{II} shell (Chapter III). Note that a saturation of the SPR band is observed beyond a shell thickness of 15 nm, which is caused by the scattering effect, as described in the chapter III. The comparison for the shell thickness dependence of the SPR band maximum for Au@K⁺/Ni²⁺/[Fe^{II}(CN)₆]⁴⁻ NPs (samples **2** to **2-6**) and the Au@KNi^{II}Fe^{II}@KNi^{II}Cr^{III} NPs (samples **11-2** to **11-5**) indicates a similar evolution, but the λ_{\max} shift is higher for double layer NPs in comparison with the single layer ones even for an equivalent shell thickness. That may be explained by the difference in the refractive index between the two PBAs constituting the two distinct shells. Consequently, the PBA shell nature also influences the optical properties of the core-shell NPs, and not only the shell thickness (figure 15). The presence of the large PBA shell induces also an enlargement of the SPR band especially for sample **11-5**. As described in

literature, this phenomenon may be explained by the confinement of the free electrons within the gold metal core²², due to the important thickness ($\text{KNi}^{\text{II}}\text{Fe}^{\text{II}} + \text{KNi}^{\text{II}}\text{Cr}^{\text{III}}$) of 56.4 ± 11.3 nm or by the influence of the scattering effect which starts to mask the SPR band, as observed for core-shell systems, such as $\text{Au}@ \text{SiO}_2$. For such system, a blue-shift is observed for shell thickness superior to 50 nm²¹. It may be interesting to perform the synthesis to larger $\text{Au}@ \text{KNi}^{\text{II}}\text{Fe}^{\text{II}}@ \text{KNi}^{\text{II}}\text{Cr}^{\text{III}}$ NPs to observe if such a phenomenon occurs in this case.

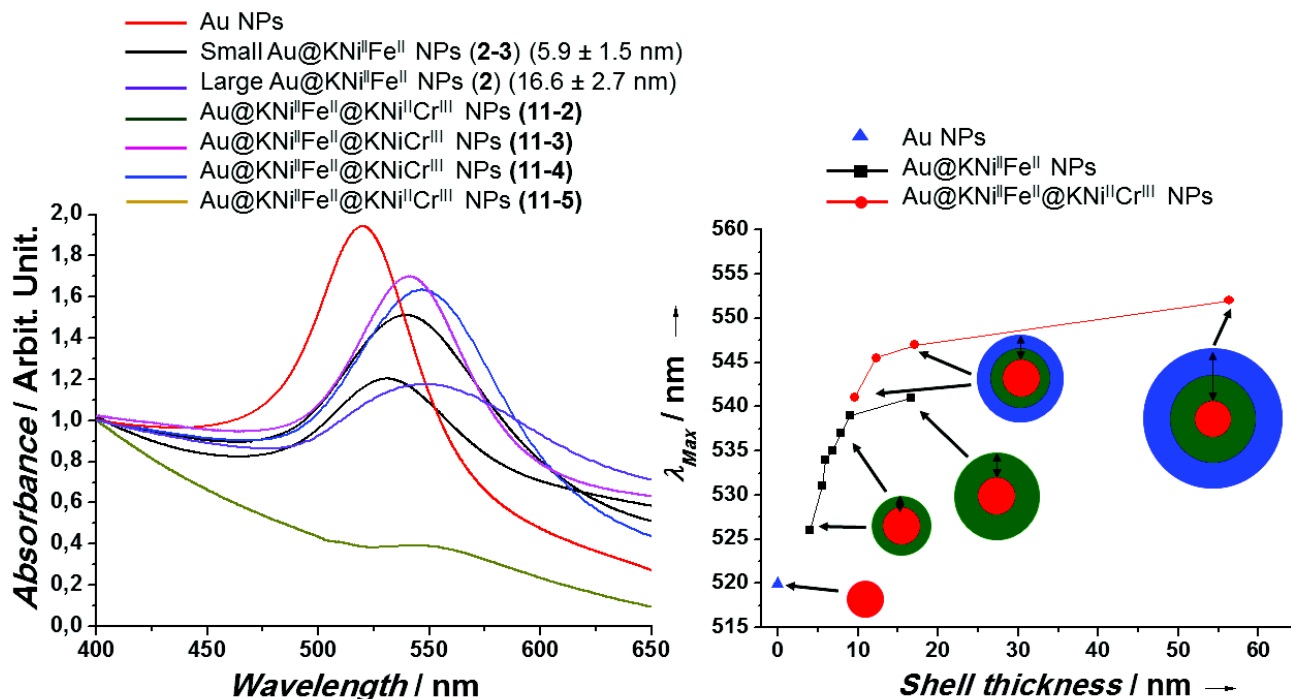


Figure 16: Left, evolution of the SPR band with the increase of the $\text{KNi}^{\text{II}}\text{Cr}^{\text{III}}$ shell thickness for the series of $\text{Au}@ \text{KNi}^{\text{II}}\text{Fe}^{\text{II}}@ \text{KNi}^{\text{II}}\text{Cr}^{\text{III}}$ NPs (11-2 and 11-3) and large shell $\text{Au}@ \text{KNi}^{\text{II}}\text{Fe}^{\text{II}}@ \text{KNi}^{\text{II}}\text{Cr}^{\text{III}}$ NPs (11-5) with comparison with the initial $\text{Au}@ \text{K}^+/\text{Ni}^{2+}/[\text{Fe}^{\text{II}}(\text{CN})_6]^{4-}$ NPs. Right, evolution of the maximum of absorbance of the SPR as a function of the shell thickness ($\text{KNi}^{\text{II}}\text{Fe}^{\text{II}} + \text{KNi}^{\text{II}}\text{Cr}^{\text{III}}$). Line is a guide for eyes.

For both double-layered $\text{Au}@ \text{KNi}^{\text{II}}\text{Fe}^{\text{II}}@ \text{KNi}^{\text{II}}\text{Fe}^{\text{III}}$ NPs (12-1 and 12-2), the SPR band is red-shifted (figure 17). The band is shifted from 532 nm to 550 nm for sample 12-1 with a total shell thickness ($\text{KNi}^{\text{II}}\text{Fe}^{\text{II}} + \text{KNi}^{\text{II}}\text{Fe}^{\text{III}}$) of 31.9 ± 6.4 nm and from 539 nm to 548 nm for sample 12-2 for the shell thickness of 32.2 ± 6.5 nm. We observed that for a nearly total shell size (first shell + second shell) the evolution of the SPR band is similar, and thus dependent of the PBA layer thickness around the gold core. Then it is rational to think that the PBA nature has no effect on the optical properties in this case. Indeed, the nature of both PBA layers is similar; the only difference is the oxidation state of the Fe. Such potential effect may be observable only for a double-layered heterostructure with two layers of two strictly different PBAs. On the other hand the presence of the second large PBA shell induces an enlargement of the SPR band for both samples. As for the $\text{Au}@ \text{KNi}^{\text{II}}\text{Fe}^{\text{II}}@ \text{KNi}^{\text{II}}\text{Cr}^{\text{III}}$ NPs (11-5) this phenomenon may be explained by confinement of the free electrons within the metal core²³, due to the important shell thickness of the $\text{KNi}^{\text{II}}\text{Fe}^{\text{II}}$ layer (< 30 nm).

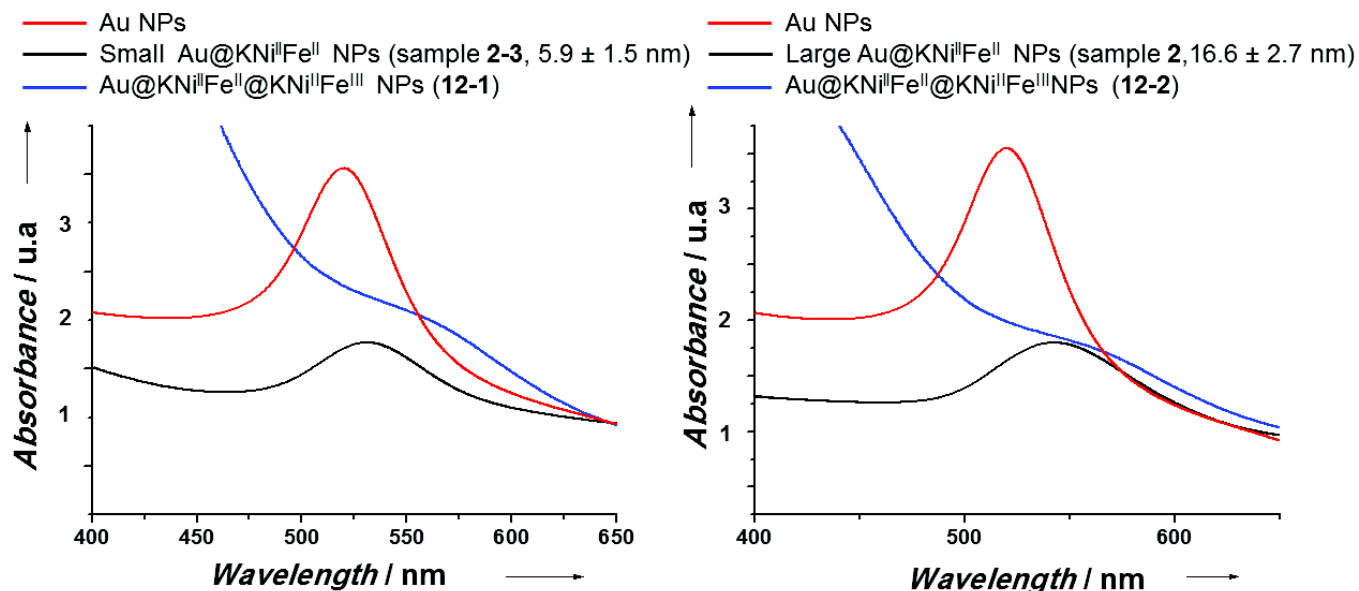


Figure 17: Right, Evolution of the SPR band of Au@KNi^{II}Fe^{II}@KNi^{II}Fe^{III} NPs obtained from small Au@K⁺/Ni²⁺/[Fe^{II}(CN)₆]⁴⁻ NPs (12-1, left) and large Au@K⁺/Ni²⁺/[Fe^{II}(CN)₆]⁴⁻ NPs (12-2, right) in the visible region, comparatively to Au and initial Au@K⁺/Ni²⁺/[Fe^{II}(CN)₆]⁴⁻ NPs.

For the Au@Ni^{II}Fe^{II}@Co^{II}Fe^{II} NPs (13), the increase of the second PBA shell thickness also induces a red-shift ($\lambda_{\max} = 536$ nm), comparatively to the initial Au@K⁺/Ni²⁺/[Fe^{II}(CN)₆]⁴⁻ NPs, due to the modification of the refractive index around the gold cores (figure 18). Comparatively to Au@K⁺/Ni²⁺/[Fe^{II}(CN)₆]⁴⁻ NPs with a close shell thickness (9.2 ± 2.0 nm and $\lambda_{\max} = 535$ nm), the Au@Ni^{II}Fe^{II}@Co^{II}Fe^{II} NPs (12.3 ± 2.4 nm) present a similar SPR band. Then that seems to confirm the total PBA shell thickness effect on the evolution of the SPR band.

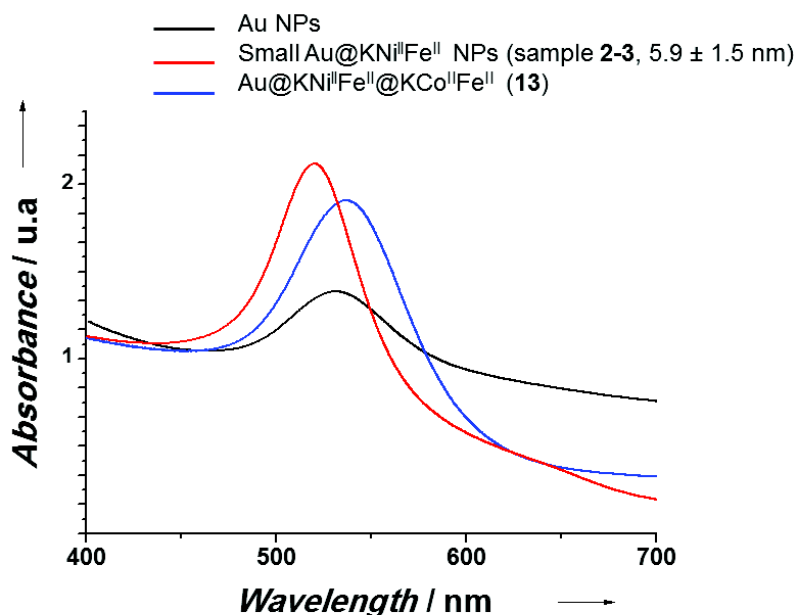


Figure 18: Evolution of the SPR absorption band of Au@Ni^{II}Fe^{II}@Co^{II}Fe^{II} NPs (13) comparatively to the initial Au@K⁺/Ni²⁺/[Fe^{II}(CN)₆]⁴⁻ NPs and the Au NPs.

The Au@Ni^{II}Fe^{II}@Fe^{II}Fe^{III} NPs also exhibit a SPR band, respectively at 538 (**14-1**) and 536 nm (**14-2**) (figure 19), which is red-shifted comparatively to the initial peak for Au@K⁺/Ni²⁺/[Fe^{II}(CN)₆]⁴⁻ NPs (sample **2-3**, $\lambda_{\text{max}} = 532$ nm). Comparatively to the Au@K⁺/Ni²⁺/[Fe^{II}(CN)₆]⁴⁻ NPs with similar size of PBA shell of 16.6 ± 2.7 nm (sample **2**), the maximum of the absorbance of the SPR band ($\lambda_{\text{max}} = 540$ nm) is quite close to those observed for these Au@Ni^{II}Fe^{II}@Fe^{II}Fe^{III} NPs, with the total shell thicknesses (Ni^{II}Fe^{II} + Fe^{III}Fe^{II}) of 16.7 ± 3.3 nm for **14-1** and 13.7 ± 2.7 nm for **14-2**). This is in accordance with the previous observation, and seems to indicate that the size increase of the layer around the gold induces the evolution of the SPR band, and not really the PBA nature.

Moreover, a very broad band is observed in the spectra of these NPs in the near-IR region, at 710 nm. This band corresponds to the absorption of the PB NPs, which is due to the intervalence charge transfer band²⁵ between Fe^{II} and Fe^{III}. This is particularly interesting for future possible applications in biology. Note that, this characteristic property of the PB NPs was recently studied, revealing promising for photoacoustic and X-ray computed tomography (CT) imaging, and also for photothermal therapy, due to this strong absorption in NIR. That is the way to the design of theragnostic agents²⁶⁻³². In our case, the combination of both gold and PB should be also interesting for such applications³³.

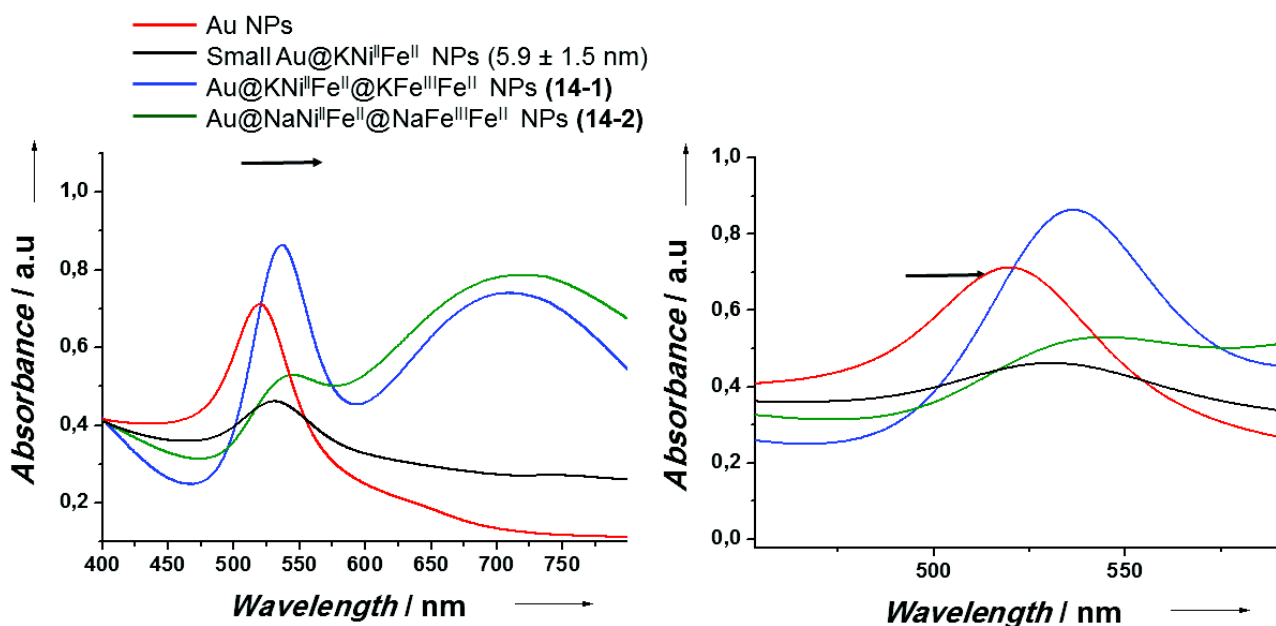


Figure 19: Evolution of the UV-visible spectra of the Au@KNi^{II}Fe^{II}@KFe^{II}Fe^{III} NPs (**14-1**) and Au@NaNi^{II}Fe^{II}@NaFe^{II}Fe^{III} NPs (**14-2**), comparatively to the initial gold NPs and core-shell Au@K⁺/Ni²⁺/[Fe^{II}(CN)₆]⁴⁻ NPs. Right, magnification of their SPR band.

Then, the optical properties of the double-layered core-shell NPs is clearly dependent on the size of the total PBA shell thickness around the gold core. This is in accordance with the previous observations made on the different sized Au@K⁺/Ni²⁺/[Fe^{II}(CN)₆]⁴⁻ NPs¹, and also with the Au@shell systems described in literature, as Au@silica²¹ or Au@metal oxide²² NPs. The maximum of the SPR absorption band was red-shifted with the increase of the shell size, until a limit thickness (figure 20), as described for Au@TiO₂²² or Au@silica²¹ NPs. However, for this last system, a blue-shift occurs when the shell thickness is higher than 50-60 nm. In our case, no blue-shift is observed for a similar size (56.4 ± 11.3 nm, **11-5**), but it may occur for a larger thickness.

It may be interesting to perform the synthesis of Au@K⁺/Ni²⁺/[Fe^{II}(CN)₆]⁴⁻@PBA NPs with shell thickness larger than 60 nm to observe, or not, a similar effect. On the other hand, the nature of the PBA shell seems to have an influence on the location of the SPR band, due to the difference of the refractive index of the two PBAs shells, particularly for the Au@KNi^{II}Fe^{II}@KNi^{II}Cr^{III} NPs. Nevertheless, only a weak influence is observed for Au@Ni^{II}Fe^{II}@Ni^{II}Fe^{III}, Au@Ni^{II}Fe^{II}@Co^{II}Fe^{II} and Au@Ni^{II}Fe^{II}@Fe^{II}Fe^{III} NPs. This may be due to the closeness of the refractive index of all these PBAs.

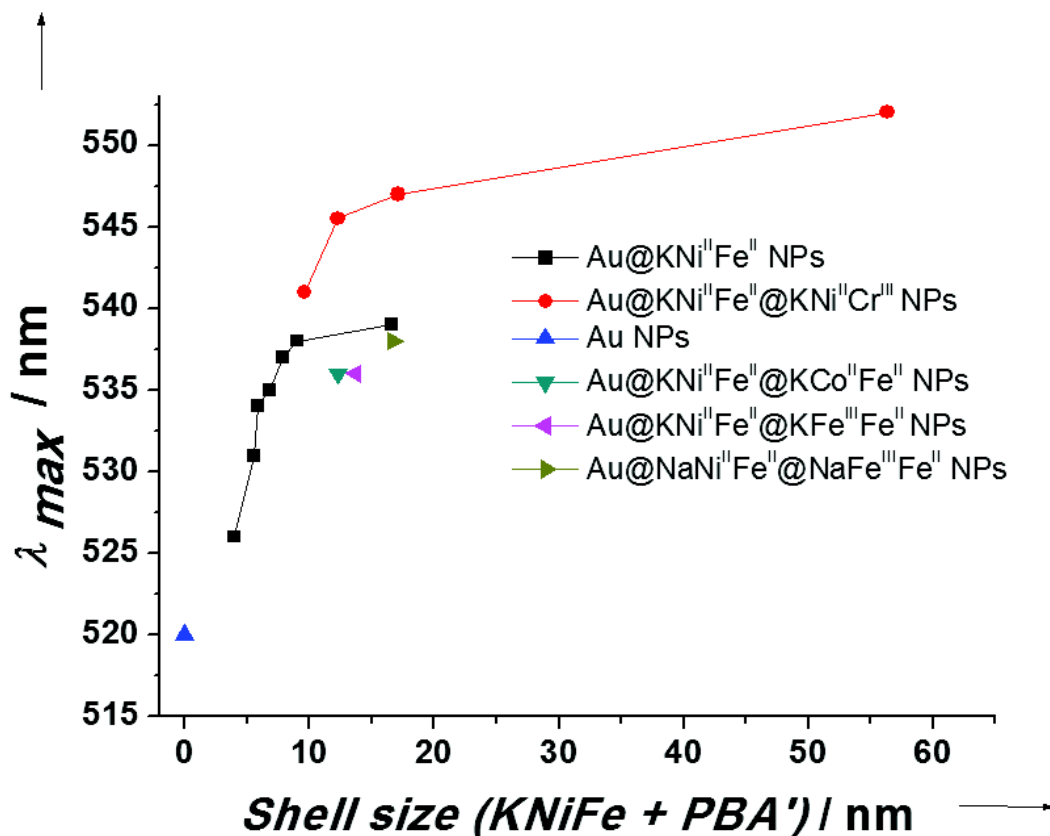


Figure 20: evolution of the maximum of absorbance of the SPR as a function of the total shell thickness. Line is a guide for eyes.

IV.3 Study of the magnetic properties of the double-layered core-shell Au@K⁺/Ni²⁺/[Fe^{II}(CN)₆]⁴⁻@PBA NPs.

The as-synthesized double-layered core-shell Au@K⁺/Ni²⁺/[Fe^{II}(CN)₆]⁴⁻@PBA NPs exhibit plasmonic properties and paramagnetism as expected. The objective of the second PBA shell growth was to implement long range or short range magnetic ordering in order to obtain magneto-optical nano-objects. In the first time we focused our study on the magnetic behavior of a series of Au@KNi^{II}Fe^{II}@KNi^{II}Cr^{III} NPs, and we investigated the evolution of the magnetic properties as a function of the shell thickness. In the second time, we were interested on magnetic properties of the other Au@K⁺/Ni²⁺/[Fe^{II}(CN)₆]⁴⁻@PBA NPs, according to the nature of the second PBA layer.

The magnetic properties of the double-layered core-shell Au@K⁺/Ni²⁺/[Fe^{II}(CN)₆]⁴⁻@PBA NPs were investigated first by using a SQUID-MPMS magnetometer working in the temperature range 1.8 – 350 K up to 7 T, by applying the zero-field-cooled/field-cooled (ZFC/FC) magnetization method. In the ZFC experiment, the samples were cooled in the absence of a static magnetic field and the magnetization was then recorded as a function of the temperature under a 100 Oe field. The FC magnetization data were collected after cooling the sample with the same field. The temperature dependence of the in-phase and the out-of-phase magnetic susceptibilities were measured in a zero dc-field with frequencies ranging from 1Hz to 1488 Hz, in alternating current (AC) mode, in order to detect possible frequency dependence, characteristic of the short range magnetic ordering induced by a superparamagnetism or a spin-glass behavior.

IV.3.1 Effect of the PBA's shell size on the magnetic properties: study on double-layered Au@KNi^{II}Fe^{II}@KNi^{II}Cr^{III} NPs.

We focused our study of the magnetic properties on the double-layered systems Au@KNi^{II}Fe^{II}@KNi^{II}Cr^{III}, presenting the higher Curie temperature ($T_C = 70$ K) in the bulk state. Firstly time, we have performed the magnetic measurements on the Au@KNi^{II}Fe^{II}@KNi^{II}Cr^{III} NPs (**11-5**).

The ZFC/FC protocol was applied for sample (**11-5**). As the temperature decreases, the ZFC curve increases brutally after 76 K (with the inflexion point at 70 K), exhibits a maximum at 60 K, and then decreases¹. The FC magnetization coincides with the ZFC curve at high temperature, separates from the ZFC at the maximum and tends to saturation as the temperature decreases (figure 21). For large Au@KNi^{II}Fe^{II}@KNi^{II}Cr^{III} NPs (**11-5**), the ZFC curve exhibits a peak with a maximum at 60 K (figure 21). This behavior corresponds to the presence of the long or short range magnetic ordering. The divergence of the ZFC/FC curve at the maximum at 65 K indicates a relatively narrow size distribution of the NPs. The field dependence of the magnetization measured at 2.5 K shows the presence of a small hysteresis effect with a coercive field H_C of 115 Oe, confirming the blocking of the magnetization (figure 21). As expected due to the relatively large KNi^{II}Cr^{III} shell size, the values obtained for both, the transition temperature and the coercive field are in accordance with those obtained for Ni^{II}[Cr^{III}(CN)₆] NPs with diameters greater than 20 nm ($T_C = 70$ K) as well as with the bulk KNi^{II}[Cr^{III}(CN)₆] exhibiting a ferromagnetic

behavior. Indeed, the size of the KNiCr shell of 40.45 ± 8.1 nm is bigger than the magnetic domain size estimated between 16 to 22 nm for this PBA^{5,6}. The presence of the long range ferromagnetic ordering is confirmed by AC susceptibility measurements showing the presence of χ' and χ'' susceptibilities peaks at 70 K without frequency dependence (figure 22).

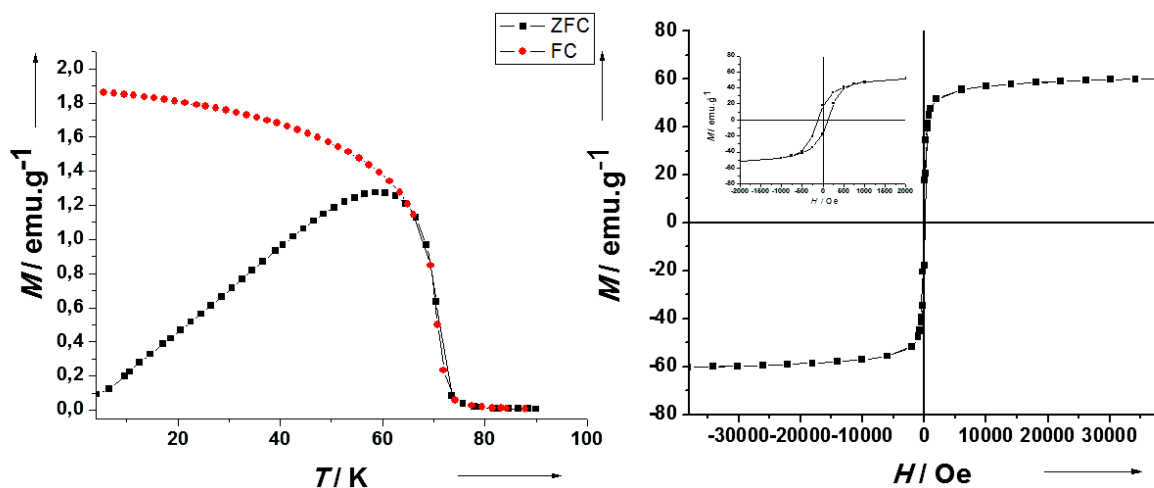


Figure 21: In left ZFC/FC curves for Au@KNi^{II}Fe^{II}@KNi^{III}Cr^{III} NPs (**11-5**) at an applied field of 100 Oe. In right, the hysteresis loop at 2.5K.

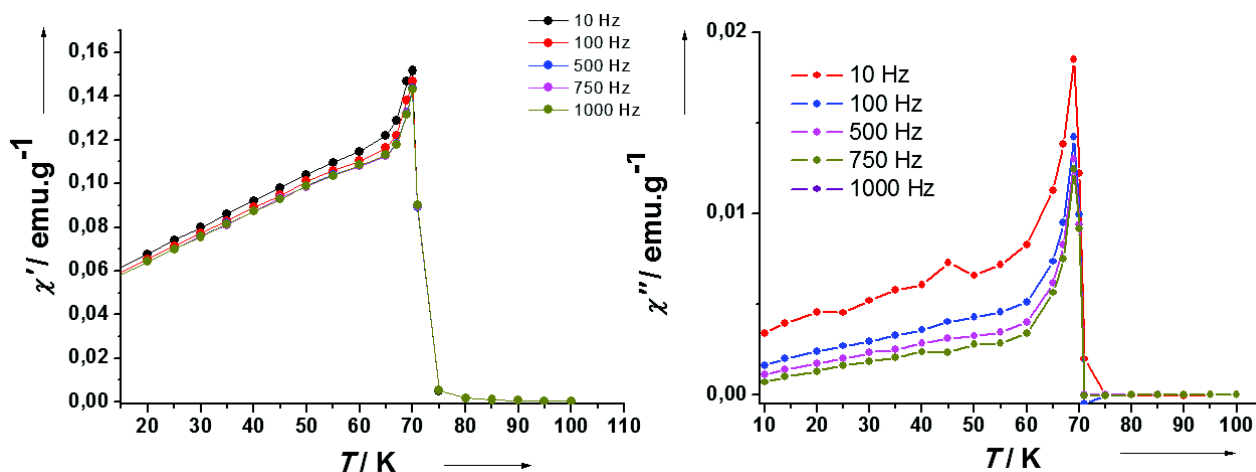


Figure 22: Temperature dependence of the in-phase (χ') and the out of phase (χ'') susceptibility with a zero dc magnetic field for Au@KNi^{II}Fe^{II}@KNi^{III}Cr^{III} NPs (**11-5**).

The Au@KNi^{II}Fe^{II}@KNi^{III}Cr^{III} NPs (**11-5**) exhibit long-range ordering with a magnetic behavior similar to the bulk material. Thus we have successfully implemented ferromagnetism to obtain multifunctional magneto-plasmonic nanoheterostructure presenting both ferromagnetism from the KNi^{III}Cr^{III} shell and plasmonic properties from the gold core.

We have previously demonstrated that it is possible to use a small first KNi^{II}Fe^{II} shell and then to grow subsequently a second magnetic KNi^{III}Cr^{III} shell, with controlled size by using a time-controlled reaction. This should permit to finely tune the magnetic properties of the designed nano-objects. Indeed, a series of previously described

Au@KNi^{II}Fe^{II}@KNi^{II}Cr^{III} NPs, with different shell thickness of the KNi^{II}Cr^{III} layer, ranging from 1.6 ± 0.3 (11-1) to 10.45 ± 2.6 (11-4), was investigated.

Firstly, the temperature dependence of the magnetization was performed following the ZFC/FC procedure for samples 11-1 to 11-4 (figure 23). For sample 11-1, the ZFC increases as the temperature decreases, presents a maximum at $T_{\max} = 11\text{K}$, then decreases. The ZFC curve coincides with the ZFC one up to 11 K, then they separate because the FC curve continues to increase slowly and tends to saturation at low temperature. The ZFC/FC curves for samples 11-2 – 11-4 present similar behavior. Figure 23 shows ZFC curves for samples 11-1 – 11-5 demonstrating that the T_{\max} (ZFC maximum) progressively decreases from 60 K for sample 11-5 to 11 K for 11-1 (table 3). The FC curves increase as the temperature decreases and reach a plateau at low temperature. The distribution size of the NPs seems to be relatively narrow, as indicated by the coincidence of the ZFC and FC curves at high temperatures, and their separation close to the blocking temperature (irreversible temperature). The KNi^{II}Cr^{III} shell size dependence of the T_{\max} is presented on Fig 25 and show an increase of the T_{\max} (freezing or blocking) temperature of the NPs with the shell size according to a $d^{4.3}$ law³⁴ excluding the sample 11-5 which have a bulk behavior.

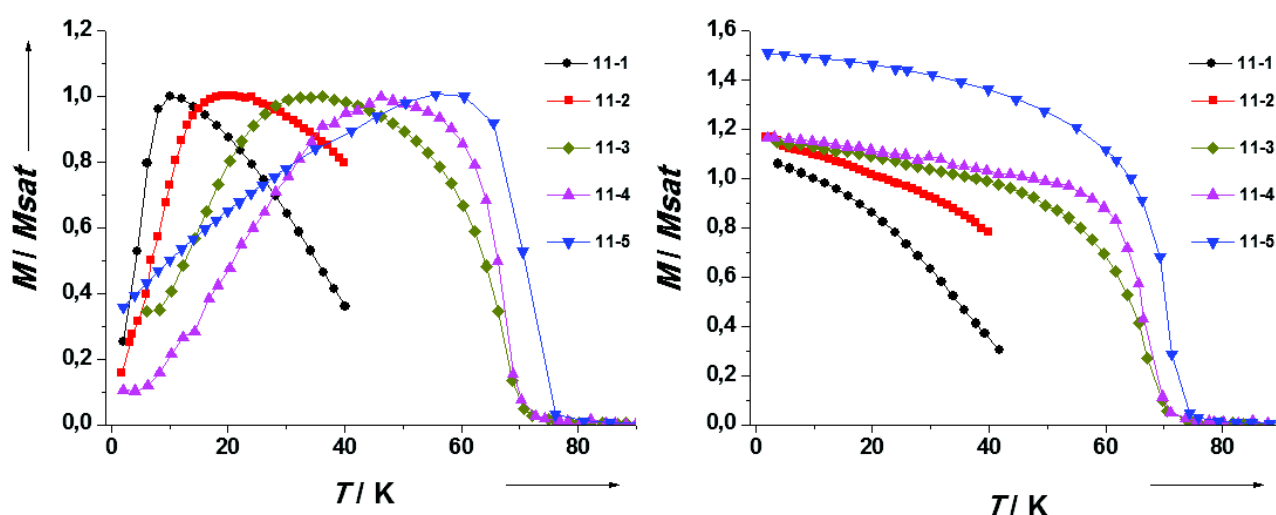


Figure 23: Evolution of the ZFC curve (left) and evolution of FC curves (right) for the different KNi^{II}Cr^{III} shell thicknesses (samples 11-1 to 11-5).

Field dependence of the magnetization performed at 2.5 K revealed the presence of a hysteresis effect for all samples, with a coercive field H_C , which confirms the blocking of the magnetization (figure 24). Moreover, the values of the magnetization at 50 kOe increase from 14.6 emu.g^{-1} (11-1) to 37.4 emu.g^{-1} (11-4) (table 3). This and the diminution of the hysteresis loop with the reduction of the shell size are in accordance with the decrease of the blocking temperature, which also validate the influence of the layer thickness on the magnetic properties (figure 25).

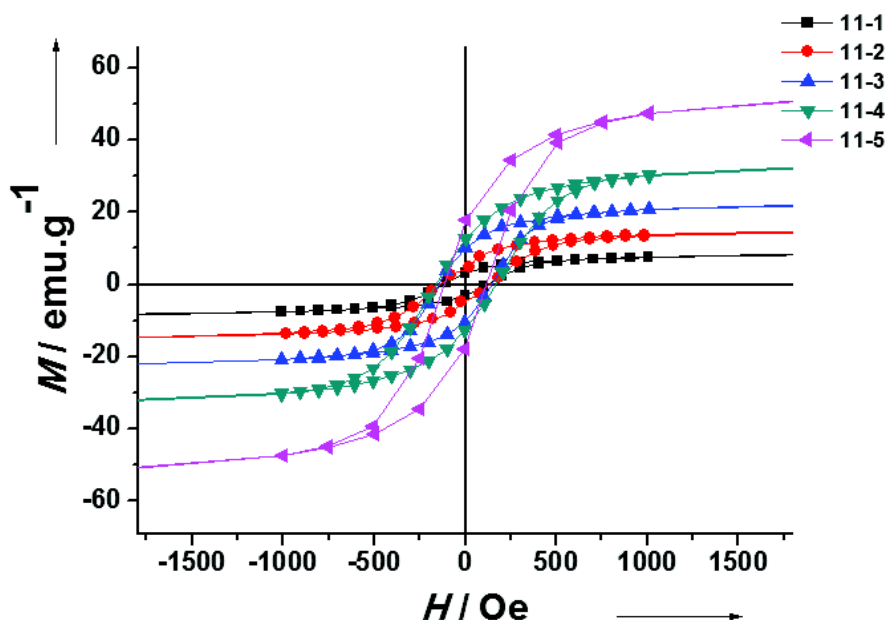


Figure 24: Evolution of the field dependence of the magnetization for the different KNi^{II}Cr^{III} shell thicknesses.

The decrease of the KNi^{II}Cr^{III} shell thickness induces the decrease of both the blocking temperature T_B and the saturation magnetization M_{sat} , as observed on figure 25. Then it is clear that the size decrease of the ferromagnetic KNi^{II}Cr^{III} PBA layer has an effect on the magnetic behavior, turning from a bulk material behavior to another behavior such as superparamagnetism or spin-glass.

Sample	T_{max} (K)	M_s (2.5K) (emu/g)	H_c (2,5K) (kOe)	Mydosh parameter ϕ	Néel law	
					E_a/k_b (K)	τ_0 (s)
11-1	10	14.6	120	0.069	426	1.77×10^{-15}
11-2	21	23.2	140	0.070	753	1.99×10^{-16}
11-3	36	29	155	No frequency dependence		
11-4	48	37.4	160			
11-5	65	60.3	115			

Table 3: Magnetic parameters for the series of Au@KNi^{II}Fe^{II}@KNi^{II}Cr^{III} NPs (11-1 to 11-5).

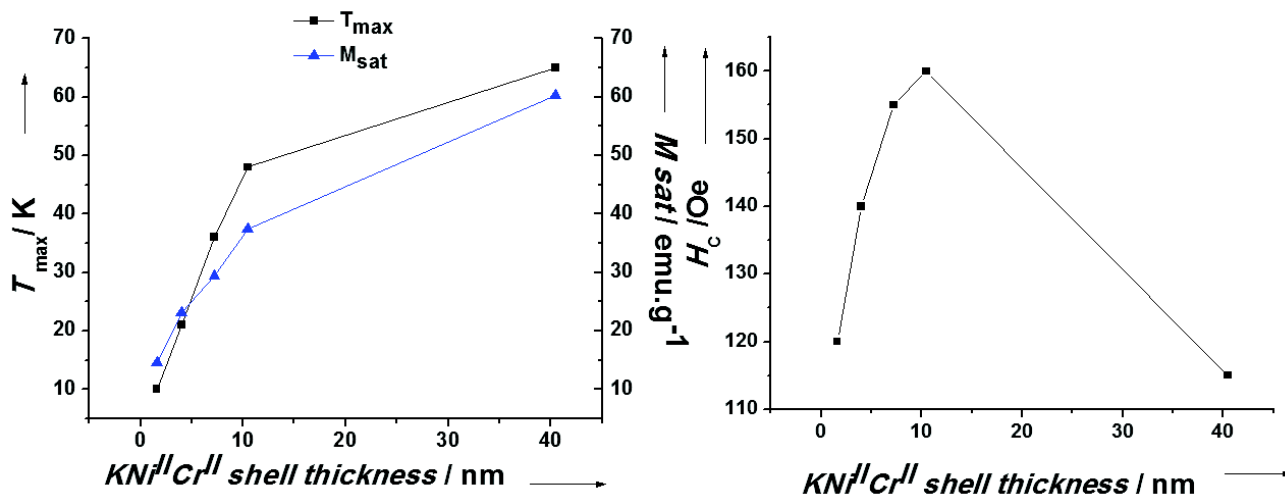


Figure 25: Left: evolution of the blocking temperature T_B and the saturation magnetization M_{sat} as a function of the KNi^{II}Cr^{III} shell thickness. Right: evolution of the coercive field H_c as a function of the KNi^{II}Cr^{III} shell thickness.

The dynamic behavior of a series of Au@KNi^{II}Fe^{II}@KNi^{II}Cr^{III} NPs was studied by AC measurements. A clear frequency dependence of both, χ' and χ'' components of the AC susceptibility is clearly evident for samples **11-1** and **11-2** (figure 26) and less pronounced for samples **11-3** and **11-4**. At 10 Hz, χ' and χ'' exhibits peaks at 19.4 K and 14.1 K respectively for **11-1** and 33.0 K and 24.5 K for **11-2**. In these cases, the peaks are shifted to higher temperature as the frequency increases.

Such behavior indicates the presence of a short range magnetic ordering and can have several origins. This could be:

- a superparamagnetic behavior of non or weakly interacting NPs³⁵
- a spin-glass transition caused by strong-interparticle interactions and magnetic disorder
- intraparticle spin-glass like behavior arising from an interface or a surface disorder³⁶.

In contrast, a weak frequency dependence of both, the in-phase (χ') and out-of-phase (χ'') susceptibilities was observed for large KNi^{II}Cr^{III} shell thicknesses (samples **11-3**: 7.2 ± 1.8 and **11-4**: 10.45 ± 2.6) (figure 27). At 10 Hz, χ' and χ'' exhibit peaks at 55 K and at 51 K respectively for **11-3** and at 58 and at 55.8 K for **11-4** (table 3).

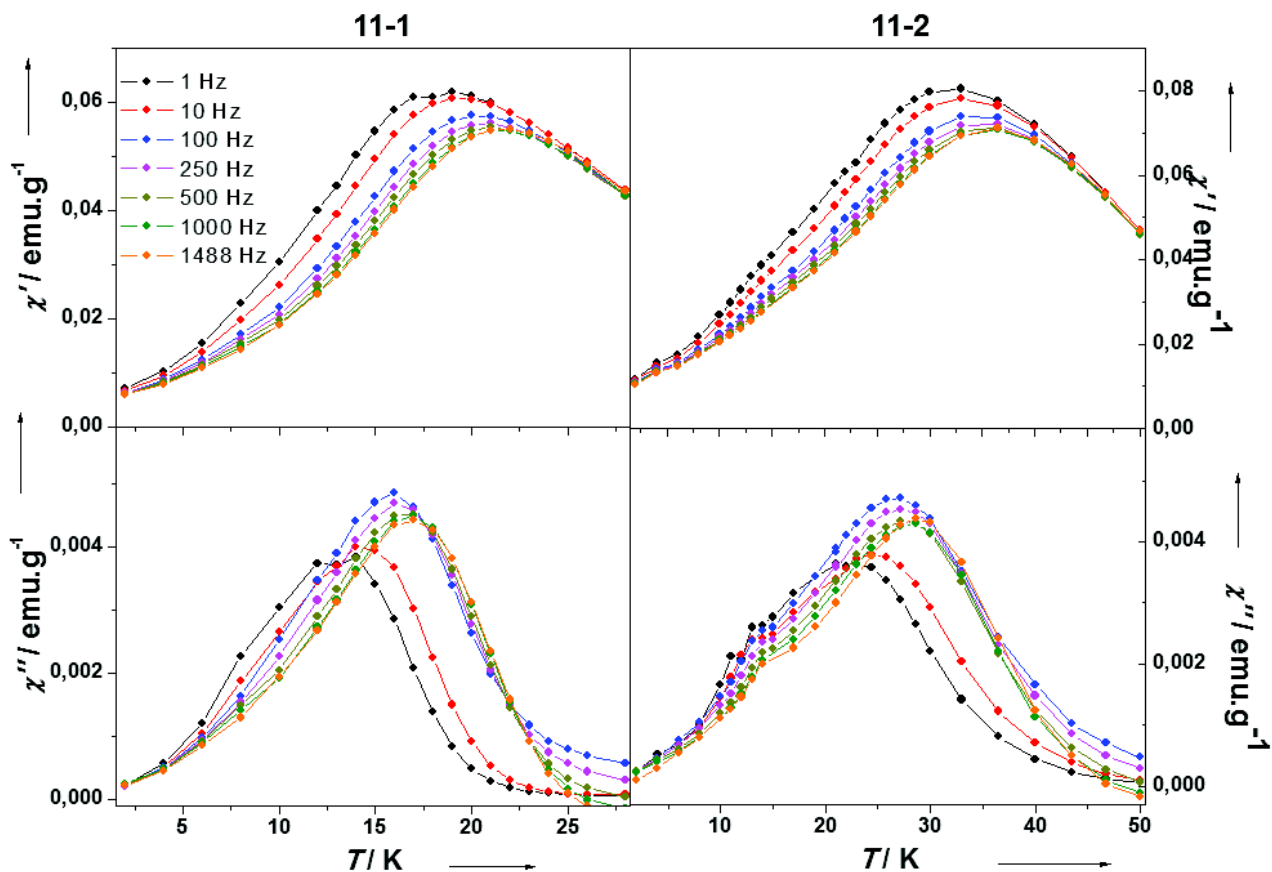


Figure 26: Temperature dependence of the in-phase, χ' , and out-of-phase susceptibility, χ'' , with a zero dc magnetic field for samples 11-2 and 11-3.

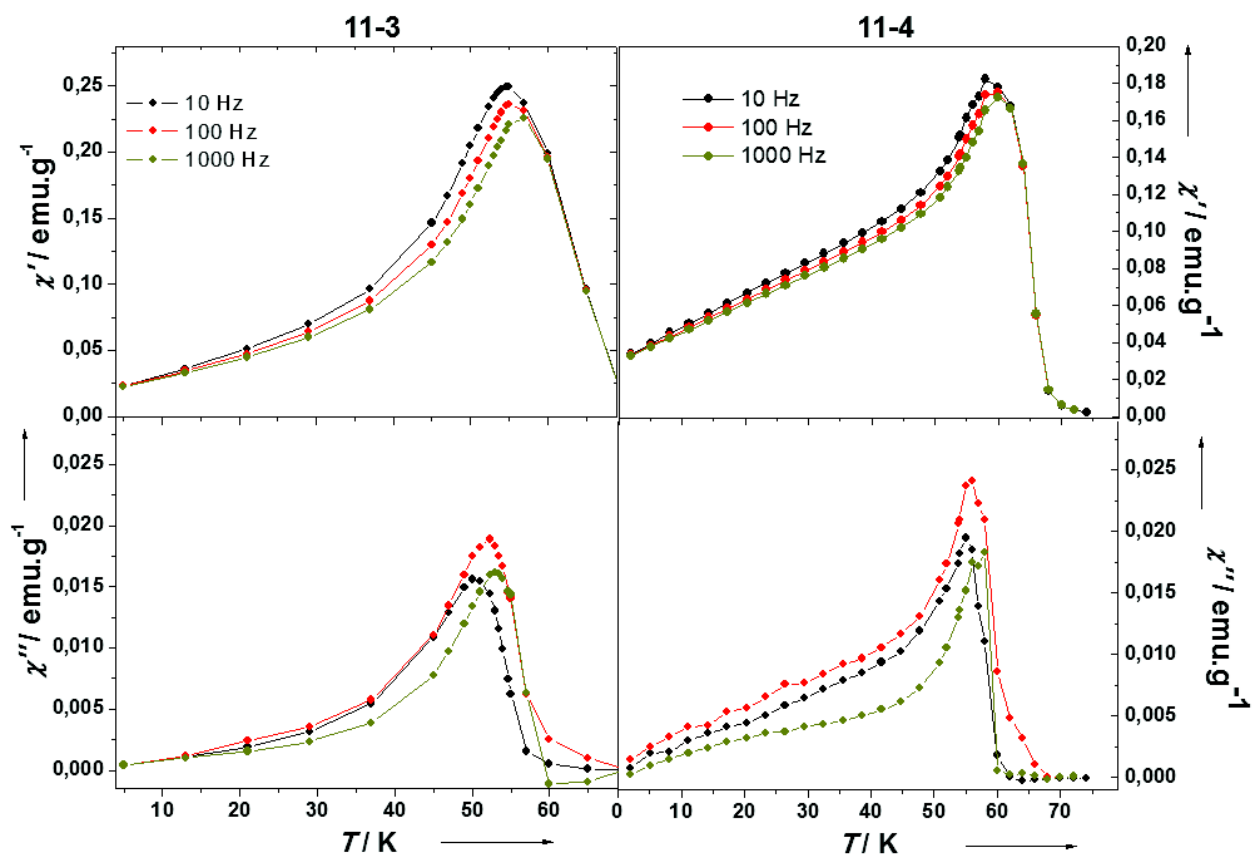


Figure 27: Temperature dependence of the in-phase, χ' , and out-of-phase susceptibility, χ'' , with a zero dc magnetic field for samples 11-3 and 11-4.

The Mydosh parameter, which is defined as $\varphi = (T_{max} - T_{min}) / (T_{max} \times \log v_{max} - \log v_{min})$ permits to qualitatively estimate the regime associated to this frequency dependence³⁶. This parameter indicates the amplitude of the out-of-phase maxima's shift with frequency. For samples **11-1** and **11-2**, we obtained respectively the φ values of 0.069 and 0.070, which are lower in comparison with the value classically observed for superparamagnets ($\varphi > 0.1$). The best explanation of this phenomenon is the presence of magnetostatic interactions between the particles. Moreover, the peak intensity of the out-of-phase susceptibility increases up to 100 Hz, then decreases for higher frequencies. This evolution is rather unusual. Indeed, a decrease of the signal intensity is classically observed for superparamagnetic systems, and an opposite behavior is usually characteristic of the presence of interparticle interactions (spin glasses). This peculiar frequency dependence seems to indicate that two different regimes may occur in our systems.

If we consider a purely superparamagnetic system, the magnetic relaxation of the NPs is thermally activated and can be model by an Arrhenius law, given according to the equation $\tau = \tau_0 \exp(E_a/kT)$, where E_a is the average energy barrier for the reversal of the magnetization, τ_0 is the attempt time and k_B is the Boltzmann constant. Applied on the **11-1** and **11-2** samples, the Arrhenius linear law fit of the blocking temperature is extracted from the maximum of the out-of-phase susceptibility, where the relaxation time is $\tau = 1/2\pi\nu$. The fit gave the values of E_a and τ_0 equal to 426 K and 1.77×10^{-15} s for **11-1** and 753 K and 1.99×10^{-16} s for **11-2** (figure 28). The obtained values of τ_0 are too low in comparison with superparamagnetic systems, which are usually between 10^{-8} and 10^{-12} s, and has no physical meaning. Moreover, such values of τ_0 are typical of strong interactions between the NPs or may be a fingerprint of a spin-glass behavior. Thus, we have tried to evaluate the strength of these dipolar interactions by using the Vogel-Fulcher relationship³⁷, $\tau = \tau_0 \exp(E_a/k(T-T_0))$, where T_0 reflects the strength of the interparticles interactions. However, the fit do not lead to weaker linear regression coefficient, with respect to the Arrhenius law. Then, this have also confirmed our hypothesis of the overlap of several magnetic relaxation processes. In the case of samples **11-3** and **11-4**, the frequency dependence is too weak to perform an acceptable Arrhenius linear fit, then their magnetic behavior is close to the those of bulk material.

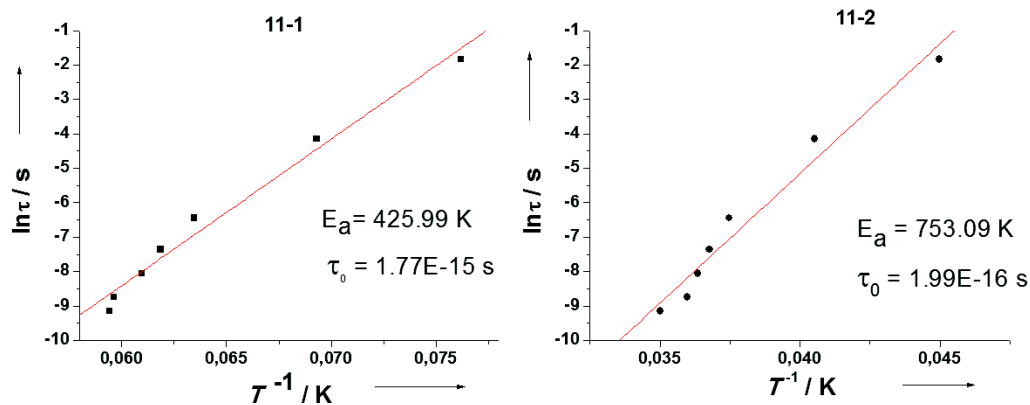


Figure 28: Fit based on Arrhenius linear law applied on the **11-1** and **11-2** samples.

To study the intrinsic magnetic behavior of the Au@KNi^{II}Fe^{II}@KNi^{II}Cr^{III} NPs, we had to reduce the dipolar interactions between the particles. The solution consists in diluting the nano-objects in a diamagnetic polymer matrix, such as Polyvinylpyrrolidone (PVP), as widely described in the literature^{3,5,6}. Then, the pristine NPs were redispersed in pure water by sonication in presence of a large amount of PVP, before being dried in vacuum at 40°C. First, we have searched to determinate the best dilution amount permitting to limit the interparticle interactions and to obtain a sufficient signal. Several dilutions were performed on sample **11-1**, with 8, 2.5 and 1% (% weight of NPs/PVP).

The effect of dilution was clearly visible on the magnetic measurements. The ZFC curves shows a shift of the maximum from 11 K for the undiluted NPs to 4.5 K for the dilution at 1% (figure 29), indicating the decrease of the blocking temperature with dilution (figure 29) and thus with decrease of the dipolar interparticle interactions. The same shift is observed for the out-of-phase susceptibility χ'' at 1000 Hz (figure 29), which shifts from 17 K to 5.6 K for the dilution at 1% (table 4).

This is also confirmed by the evolution of the field dependence of the magnetization performed at 2.5 K (figure 30): the coercive field decreases from 120 to 76 Oe with diminution of the concentration of NPs in the PVP matrix (figure 31). However, no difference is observed here between the undiluted system and the dilution at 8% (table 4). Due to the important decrease in the signal intensity, the investigations about the magnetic regime in these samples were performed on diluted samples containing 1 weight % of NPs in PVP.

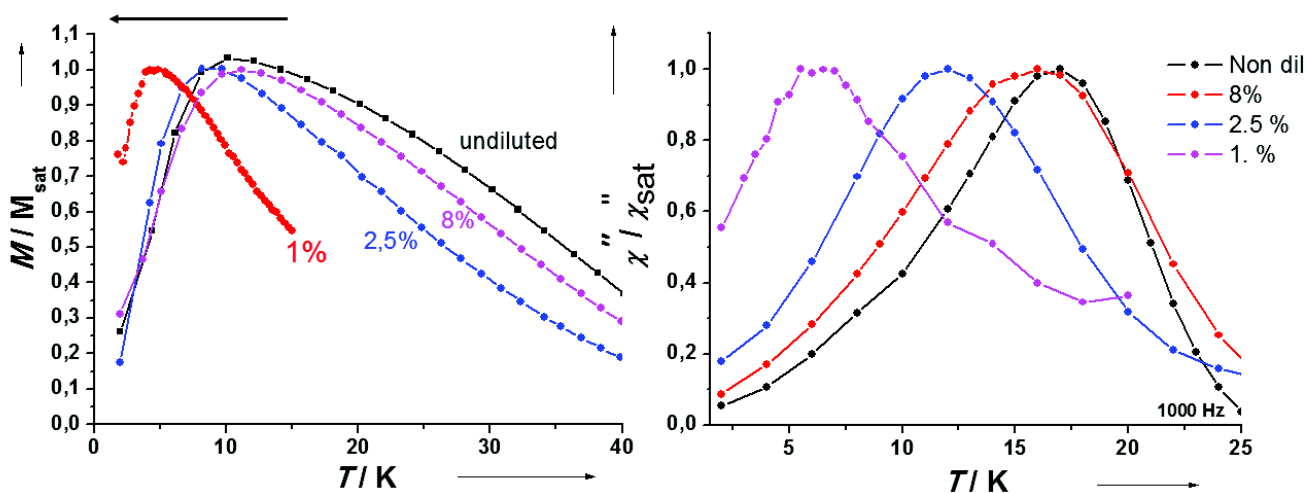


Figure 29: Evolution of the magnetization (ZFC curve, left) and the imaginary part of the magnetization (right) as function of the temperature for the different dilution rates.

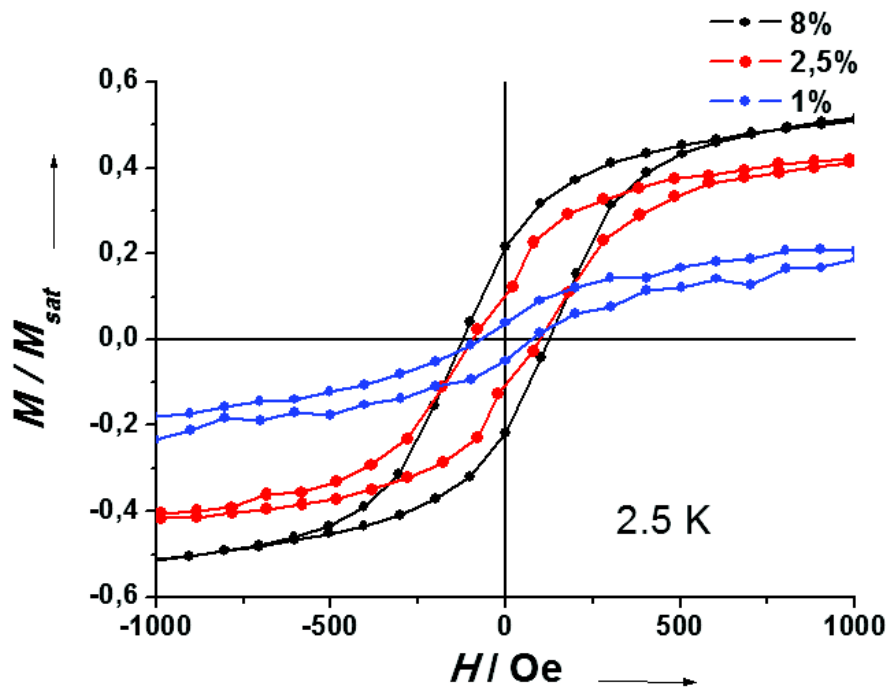


Figure 30: Evolution of the field dependence of the magnetization for sample 11-1 with different dilution wt % of NPs of 8, 2.5 and 1 %.

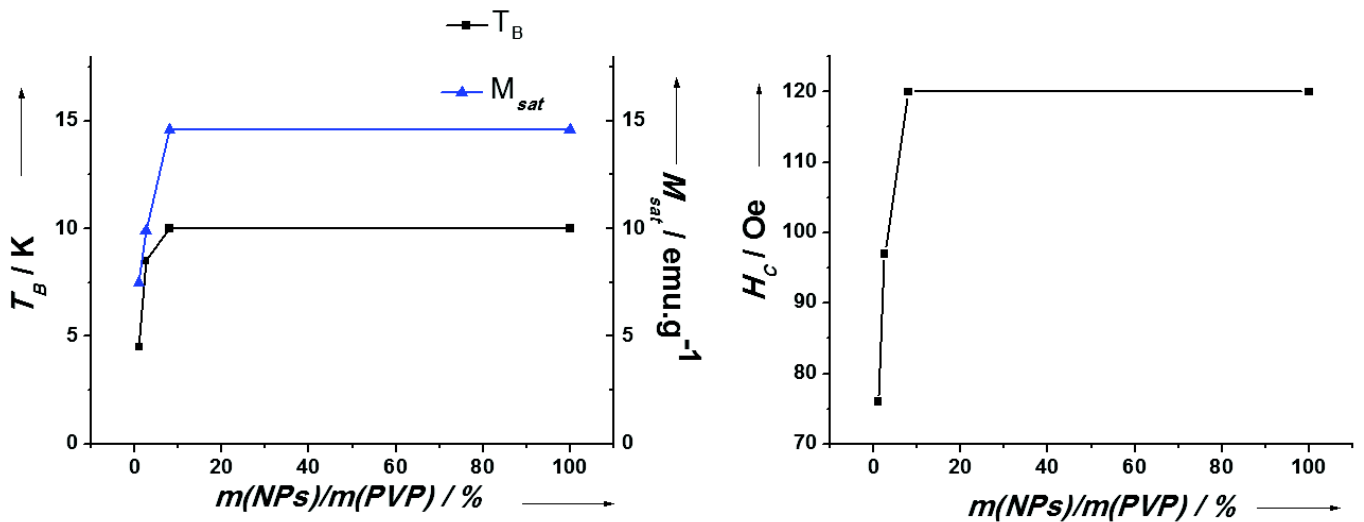


Figure 31: Evolution of the blocking temperature T_B and the saturation magnetization M_{sat} (Left) and the coercive field as functions of the % of dilution of the NPs in PVP.

Dilution rate of 11-1 (weight % on NPs/PVP)	T_{\max} (K)	M_{sat} (2.5K) (emu/g)	H_c (2,5K) (kOe)	Mydosh parameter φ	Néel law	
					E_a/k_b (K)	T_0 (s)
Undiluted	10	14.6	120	0.069	426	1.77×10^{-15}
8%	10	14.6	120	0.055	525.9	1.08×10^{-18}
2.5%	8.5	9.9	97	0.057	363.7	9.50×10^{-18}
1%	4.5	7.5	76	0.064	213.5	1.99×10^{-18}

Table 4: Magnetic values for the successive dilution of Au@KNI^{II}Fe^{II}@KNI^{II}Cr^{III} NPs performed with sample 1-1.

For all samples, except **11-3dil**, the dilution in PVP matrix induces a shift of the ZFC peaks to lower temperature, with following T_{\max} values: 4.5 K for **11-1dil**, 15.6 K for **11-2dil** and 46.5 K for **11-4dil** (figure 32). For sample **11-3dil**, we observe a shift of the ZFC peak to higher temperature, from 29 K for **11-3** to 50K for **11-3dil**. This higher value seems to be correct, because the same value is obtained for different samples, with NPs presenting the same shells' thicknesses. For now, no explanation of this increase has been advanced. As observed for the undiluted samples, the ZFC maximum temperature T_{\max} decreases as the KNI^{II}Cr^{III} shell thickness decreases for samples **11-1dil** to **11-3dil**, then tends to saturation for the larger shells, corresponding to the sample **11-4dil** (figure 33). The T_{\max} vs the shell thickness curve shows a quasi linear dependence for samples **11-1dil** to **11-3dil**, which is different in comparison to what is observed for non-diluted samples (see Figure 33).

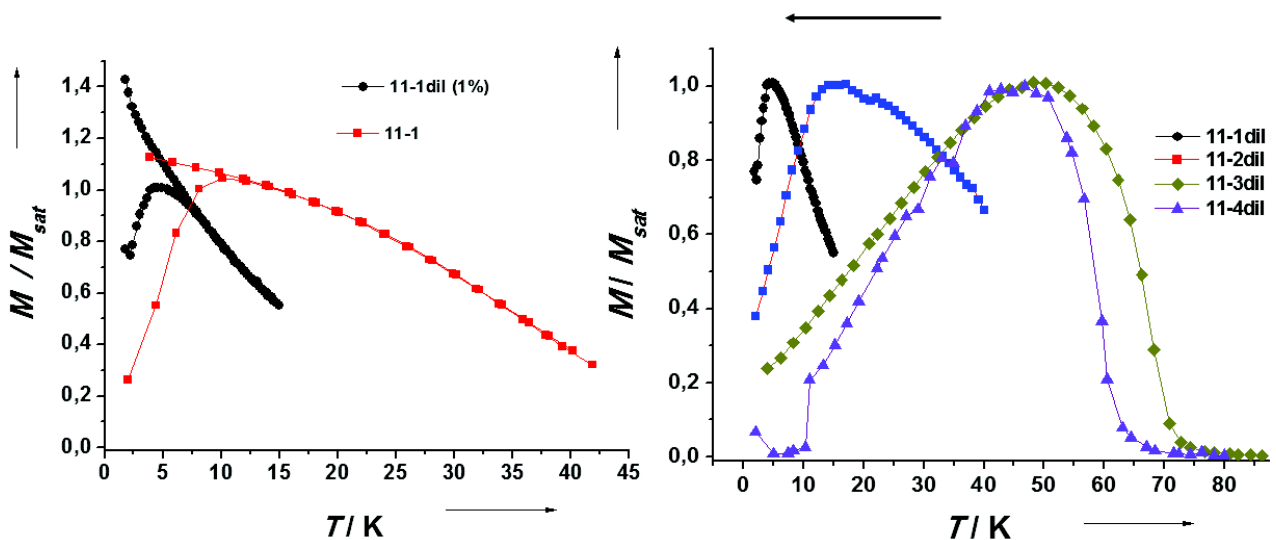


Figure 32: Left, ZFC/FC curves of 11-1 and 11-1dil (1%). Right, evolution of the ZFC curve as a function of the temperature for samples 11-1dil to 11-4dil.

We observed that T_{\max} increases as the shell thickness increases (samples **11-1dil** to **11-3dil**) with the NPs size but with a size dependence (or d dependence) slower than the d^3 law (ca. $d^{1.6}$) predicted by the Neel model for the relaxation of not interacting NPs (figure 33). By comparison with others systems, similar complex d dependences were observed for Iron/carbide Fe_3C NPs of 2.8 -15.1 nm presenting a $d^{1.6}$ law³⁴. For non-interacting Fe_3O_4 nanoparticles of 2.5 – 14 nm, a $d^{1.7}$ law has been reported³⁸, and a quasi linear T_B vs d trend was observed for interacting Fe_3O_4 nanoparticles sized from 7.8 to 17.9 nm obtained from FeOOH ³⁹. For these systems, the main responsible for such behavior is the increasing contribution of the surface to the total effective magnetic anisotropy with the decreasing of d , and this explanation may be also valid for the $\text{Au@KNi}^{\text{II}}\text{Fe}^{\text{II}}\text{@KNi}^{\text{II}}\text{Cr}^{\text{III}}$ NPs. To our knowledge, such d dependence was already observed on photomagnetic PBA NPs, but it is the first time on ferromagnetic PBA NPs. Then it is rational to think this d dependence may be originated from the contribution of the surface.

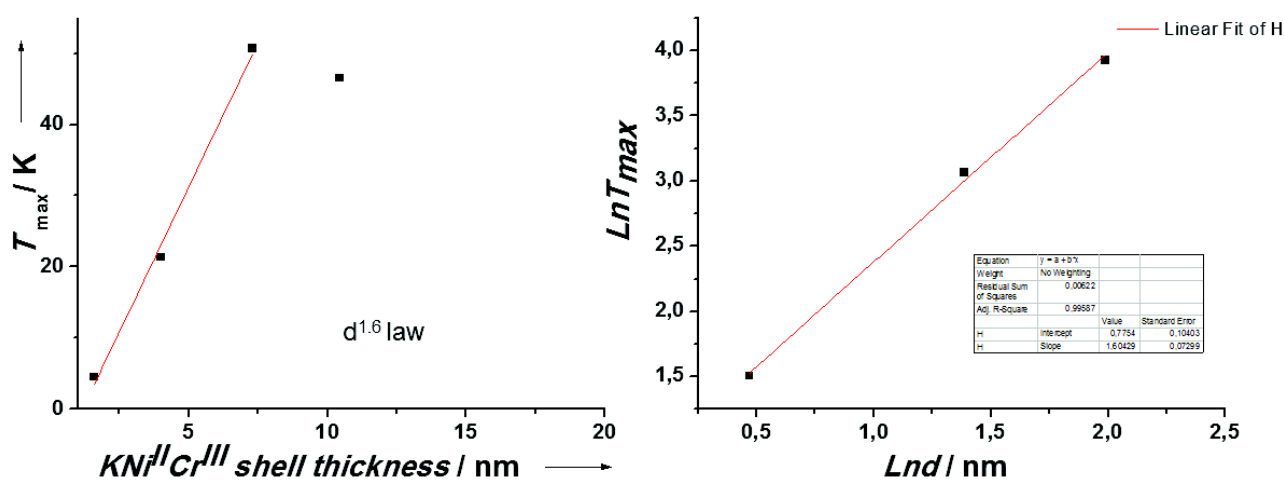


Figure 33: Left; evolution of the blocking temperature T_B as a function of the $\text{KNi}^{\text{II}}\text{Cr}^{\text{III}}$ shell thickness. Right, Size dependence of T_{\max} with a $d^{1.6}$ dependence field dependence of the magnetization for samples **11-1dil** to **11-4dil**.

On the other hand, the hysteresis loop is still observed for samples **11-1dil**, **11-2dil**, **11-3dil** and **11-4dil** at 2.5 K, confirming the blocking of the magnetization (figure 34, left; table 4). The coercive field H_C first increases from 76 to 210 Oe with the shell thickness increase (samples **11-1dil** to **11-3dil**) and then decreases for larger shell thicknesses (**11-4dil** and **11-5**). Such evolution of H_C as a function of the NPs size is usually observed for superparamagnetic NPs and can result from a transition in the magnetization switching mode and/or a demagnetization effect induced by the shape⁴⁰. Indeed, in the case of non-interacting monodomain NPs, the magnetization reverses its orientation through a coherent uniform rotation of the atomic spins giving rise to an increase of the coercive field from zero with the NPs' size, as observed on the the first part of the curve (Figure 34, right, A). After a certain limit, called the critical size, the coercive field starts to decrease, due to the crossover of the magnetization reversal process from a coherent to incoherent mode⁴⁰, typical of a bulk material (Figure 34, right, B). In our case, the profile of the curve indicates that the critical $\text{KNi}[\text{Cr}^{\text{III}}(\text{CN})_6]$ shell thickness is in the 7-10 nm thickness range. It is interesting to compare this value with the previously reported critical diameter for cubic $\text{CsNi}[\text{Cr}^{\text{III}}(\text{CN})_6]$ nanoparticles which was estimated at 20 nm⁶. The coercive field

dependence to the magnetic shell thickness in our core@shell nanoparticles is different in comparison to what has been observed in the case of superparamagnetic $\text{CsNi}[\text{Cr}(\text{CN})_6]$ nanoparticles having a cubic shape, for which H_C is little sensitive to the nanoparticles diameter with an increase from 50 to 100 Oe only for sizes ranging from 5 to 10 nm. Previously, it was demonstrated that the shape of the nanoparticles, the structural defects and the presence of different magnetic regimes, such as flower or vortex magnetic states, can significantly influence the coercive field that can explain the observed difference. In this line of thought, we investigated the dynamic behavior of the core@shell nanoparticles using ac mode measurements.

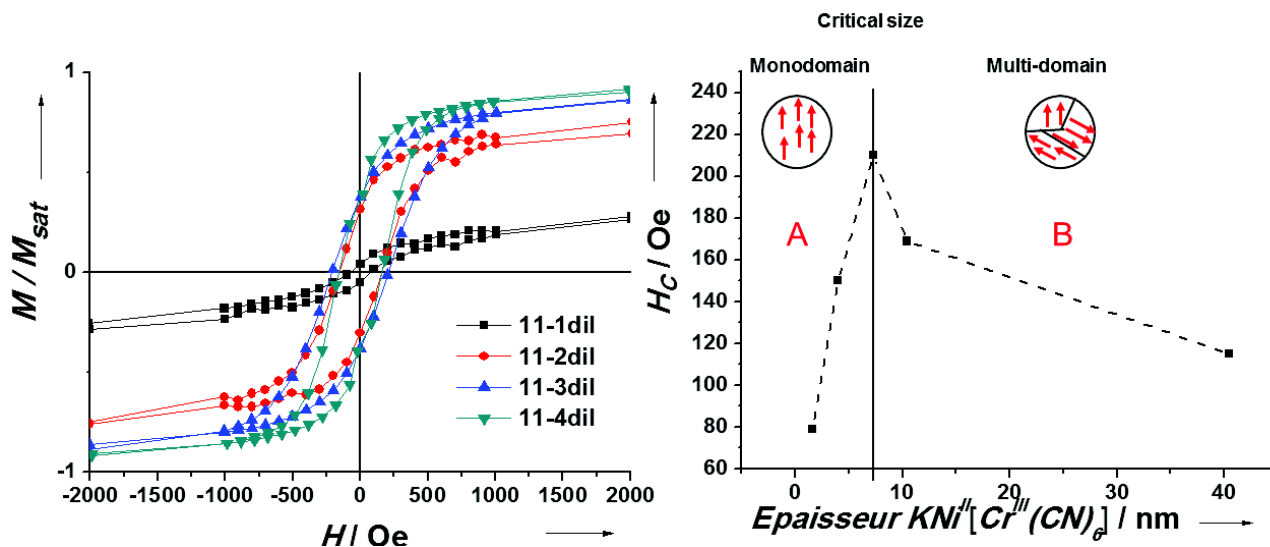


Figure 34: In left, field dependence of the magnetization performed at 2.5 K for samples **11-1dil** to **11-4dil**. In right, dependence of H_c vs vs $\text{KNi}[\text{Cr}^{\text{III}}(\text{CN})_6]$ shell thickness for samples **11-1dil** to **11-4dil** and sample **11-5dil**).

Then, the dynamic of the magnetization of the diluted samples was performed using AC modes. For **11-4dil** sample, no frequency dependence of the in-phase and out-of-phase susceptibilities is observed, which indicates a magnetic behavior similar to the bulk material (figure 37). At the opposite, samples **11-1dil**, **11-2dil** and **11-3dil** show frequency dependence (figure 35 and 37). While χ' decrease with the temperature increase, χ'' increase with the temperature increase. Note that the χ'' evolution is different for samples **11-1dil** and **11-2dil**. However, in contrast with the undiluted systems, the increase of the intensity of the out-of-phase susceptibility continuously increases with frequency, even at frequency higher than 100 Hz. As expected, this indicates that one regime has been suppressed by diluting the sample, *i.e.* by decreasing the interparticles interactions. That permitted us to observe the intrinsic magnetic behavior of such intricate systems. Indeed, the continuous increases of the χ'' for both samples is not in accordance with the purely superparamagnetic system behavior, and then may indicate a spin-glass behavior.

Calculations of the Mydosh parameters have given values of 0.064, 0.062 and 0.025 respectively for **11-1dil**, **11-2dil** and **11-3dil** (table 5). These values, close to those obtained for the undiluted systems, are still too low for pure superparamagnetic system. We have also applied the Arrhenius law which yields the fit parameters of $E_a = 203$ K and $\tau_0 = 1.99 \times 10^{-18}$ s for **11-1dil**, $E_a = 799$ K and $\tau_0 = 1.02 \times 10^{-17}$ s for **11-2dil** (figure 36) and $E_a = 3877$ K and $\tau_0 = 2.52 \times 10^{-34}$ s for **11-3dil**. These values of τ_0 are still too low to be in accordance with a superparamagnetic behavior, then that should be a spin-glass regime. This may be induced by spin frustration intrinsic to such intricate nano-object. Its origin may be due to magnetic disorder located at the surface of the particle, and to strains originated from the heterostructure shape of the nano-object. Then, to confirm the spin-glass behavior observed in the diluted samples, the critical scaling law for spin glasses was used, which is described by the relationship $\tau = \tau_0 [T_g / (T_{max} - T_g)]^{zv}$ where T_g is the glass temperature and zv is the critical exponent. By fitting the thermal variation of the relaxation time, we obtained the values of $T_g = 3.96$ K, $\tau_0 = 6.12 \times 10^{-7}$ s and $zv = 10.55$ for **11-1dil** (figure 38). τ_0 and zv values are in the range to what is usually found for spin glass system. ($10^{-8} < \tau_0 < 10^{-13}$ s; $4 < zv < 12$). However, using the same law with χ'' for dilute sample **11-2dil** did not lead to reasonable values for the fits' parameters. Moreover, by using the relaxation times extracted from χ'' , we obtained $T_g = 13.4$ K, $\tau_0 = 9.52 \times 10^{-5}$ s and $zv = 14.56$, which are also in the ranges with those generally observed for spin glass behavior. Nevertheless, the values of $T_g = 3.35$ K, $\tau_0 = 2.48 \times 10^{17}$ s and $zv = 24.5$ obtained for **11-3dil** are not in accordance with those corresponding to a spin glass behavior. Then that seems indicates an intermediate regime for sample **11-3dil**.

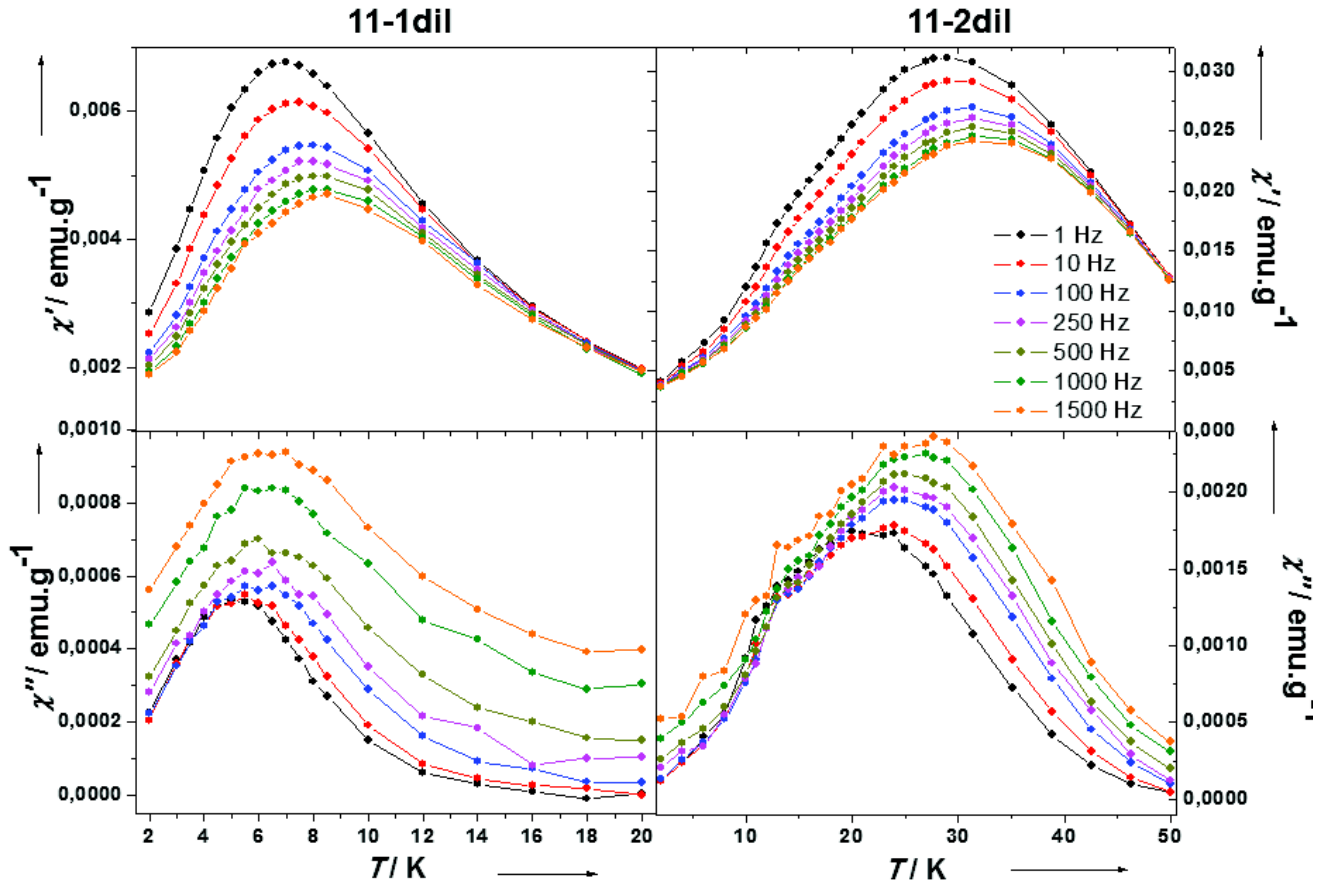


Figure 35: dependence of the in-phase, χ' , and the out-of phase susceptibility, χ'' , with a zero dc magnetic field for **11-1dil** and **11-2dil**.

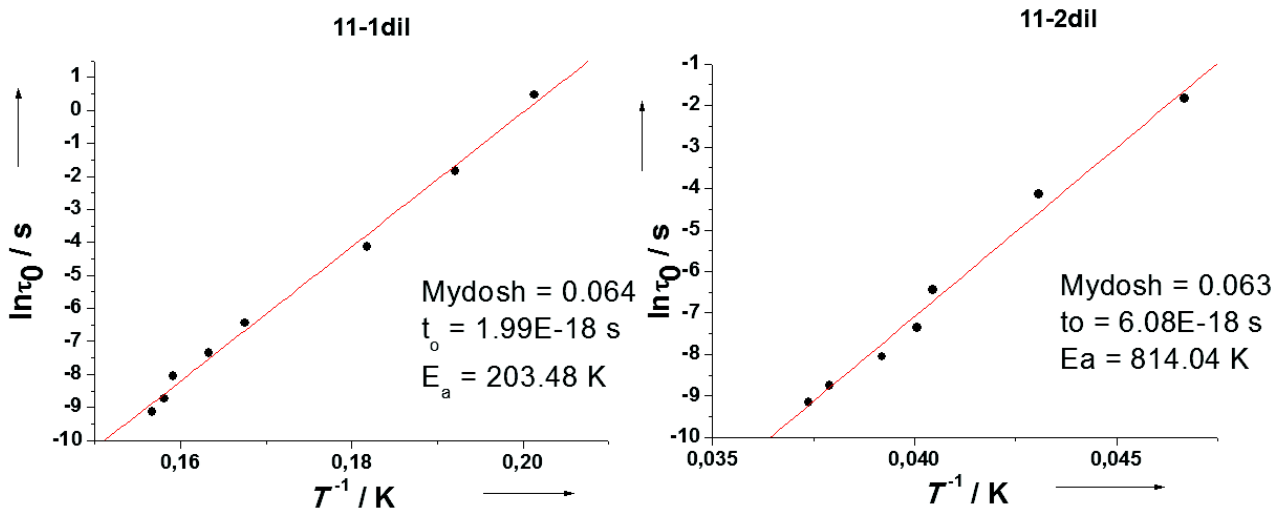


Figure 36: Fit based on Arrhenius linear law applied on the samples 11-1dil and 11-2dil.

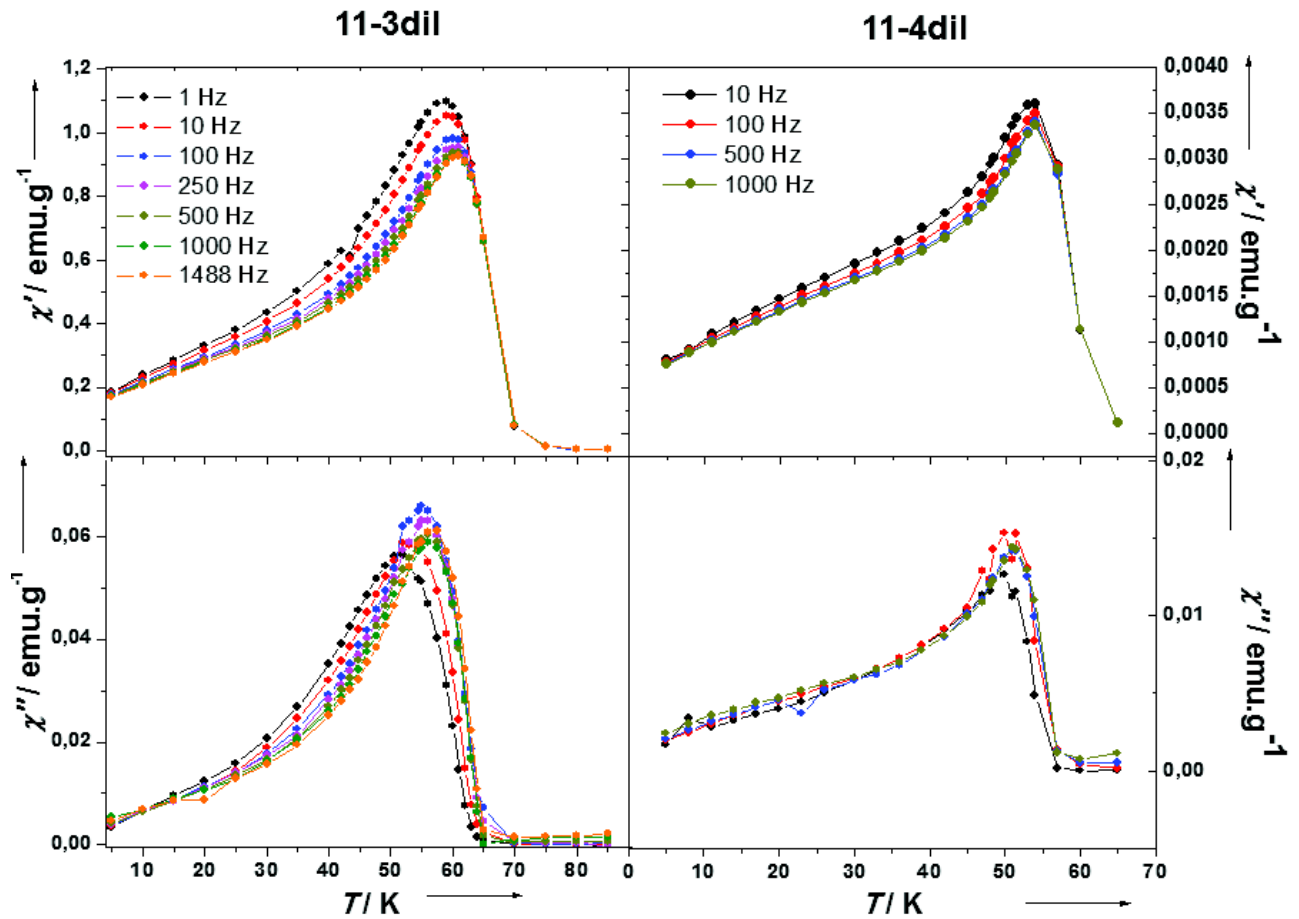


Figure 37: dependence of the in-phase, χ' , and the out-of phase susceptibility, χ'' , with a zero dc magnetic field for the samples 11-3dil and 11-4dil.

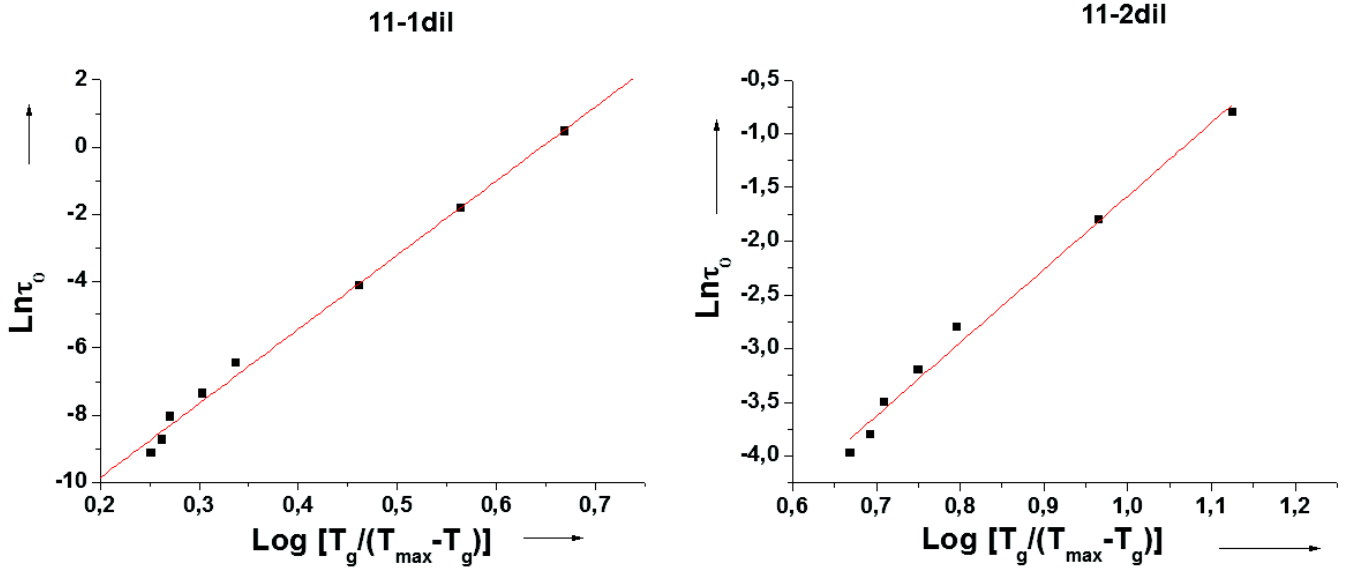


Figure 38: Fit based critical scaling law for spin glasses applied on the samples 11-1dil and 11-2dil.

Sample	T_{\max} (K)	M_{sat} (2.5K) (emu/g)	H_c (2,5K) (Oe)	Néel law			Scaling law		
				E_a/k_b (K)	τ_0 (s)	φ	T_g (K)	τ_0 (s)	$z\nu$
11-1	13.1	14.6	120	426	1.77×10^{-15}	0.069	22.8	5.79×10^{24}	0.92
11-1dil	4.5	7.5	76	203	1.99×10^{-18}	0.064	3.96	6.12×10^{-7}	10.55
11-2	22.2	23.2	150	753	1.99×10^{-16}	0.07	21.7	3.71×10^{28}	0.94
11-2dil	21.4	7	150	799	1.02×10^{-17}	0.064	13.4	1.13×10^{-4}	14.56
11-3	36	29.5	150	No frequency dependence					
11-3dil	50.5	28	203	3387	2.52×10^{-41}	0.024	28.4	1.13×10^{-4}	33.99
11-4	48	37.4	160	No frequency dependence					
11-4dil	46.5	0.05	169						
11-5	65	60.3	115						

Table 5: Magnetic parameters for diluted and undiluted samples.

To ultimately confirm the spin glass behavior for these systems, we have performed measurements of the field dependence of the AC susceptibility with an oscillating field at a frequency of 100 Hz (figures 39 and 40). For sample **11-1dil**, we observed that the temperature maximum of χ' remains almost constant with applying small DC magnetic fields, and the temperature maximum of χ'' is clearly shifted to lower temperature, to finally disappear for fields larger than 100 Oe. Usually, classical spin-glass behavior is characterized by a shift to lower temperature of both χ' and χ'' susceptibilities upon the increase of the magnetic field, which is not the case for **11-1dil**. At the opposite, the shift to lower temperature of both maxima of χ' and χ'' when the magnetic field increases is observed for samples **11-2dil** and **11-3dil**, which indicates a spin glass behavior (figures 39 and 40). Moreover, the temperature dependence of the maximum of χ' follows the Almeida-Thouless equation, which is $H \propto (1-T_{max}/T_f)^{3/2}$, where T_f is the freezing temperature. That is often considered as a spin glass signature and confirms the previous results. Then, the extrapolation of the AT line at zero field have led to $T_f = 5.3$ K, 23.7 K and 56.5 K respectively for **11-1dil**, **11-2dil** and **11-3dil** (figures 41 and 42). By comparison with T_{max} (respectively $T_{max} = 4.5$ K, 15.5 K and 50.5 K) and T_g (respectively $T_{max} = 4.55$ K, 13.4 K and 28.4 K), the values obtained for T_f are in the same magnitude for the samples **11-1dil** and **11-2dil**. Then that seems to confirm a spin glass behavior for these samples, which correspond to the smallest double-layered core-shell Au@KNi^{II}Fe^{II}@KNi^{II}Cr^{III} NPs. For sample **11-3dil** the value obtained for T_f is in accordance with T_{max} which indicate also a spin-glass behavior, but not with T_g , which seems indicate that this range of shell thicknesses is at the limit between a spin-glass behavior and an incoherent mode.

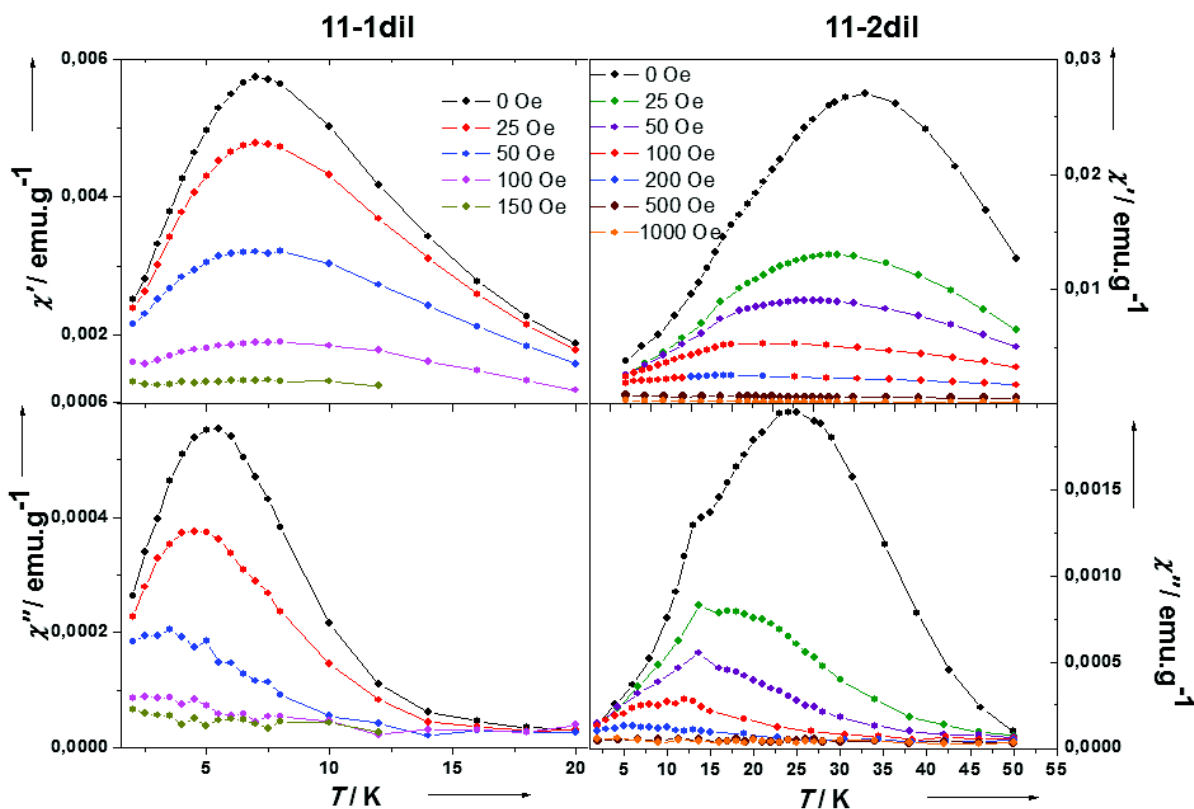


Figure 39: Dependence of the in-phase, χ' , and the out-of phase susceptibility, χ'' , with various dc fields for **11-1dil** and **11-2dil**.

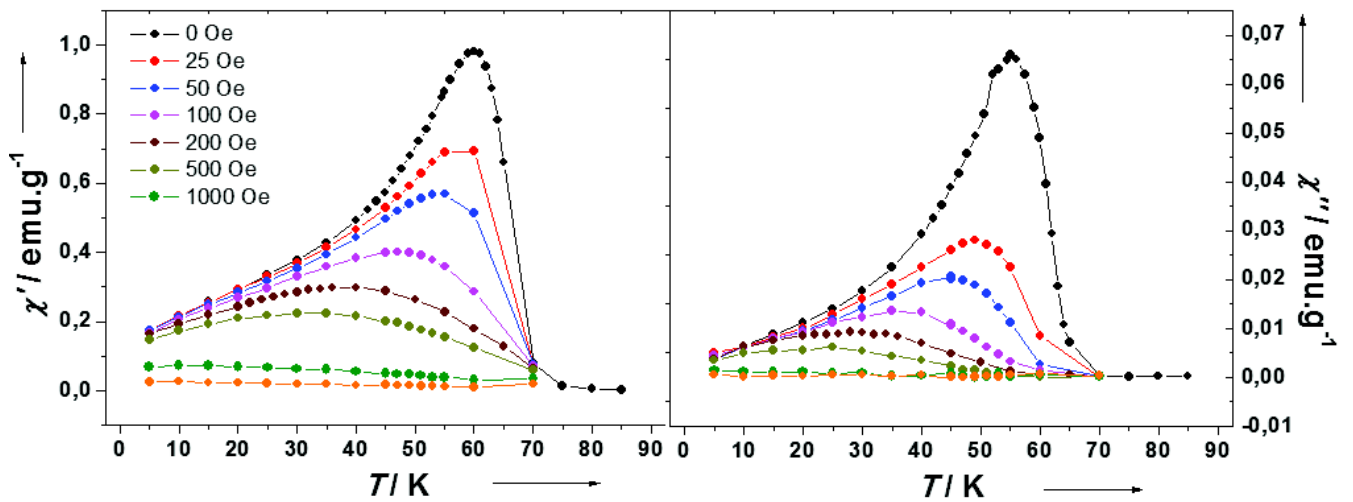


Figure 40: Dependence of the in-phase, χ' , and the out-of phase susceptibility, χ'' , with various dc fields for the 11-3dil NPs.

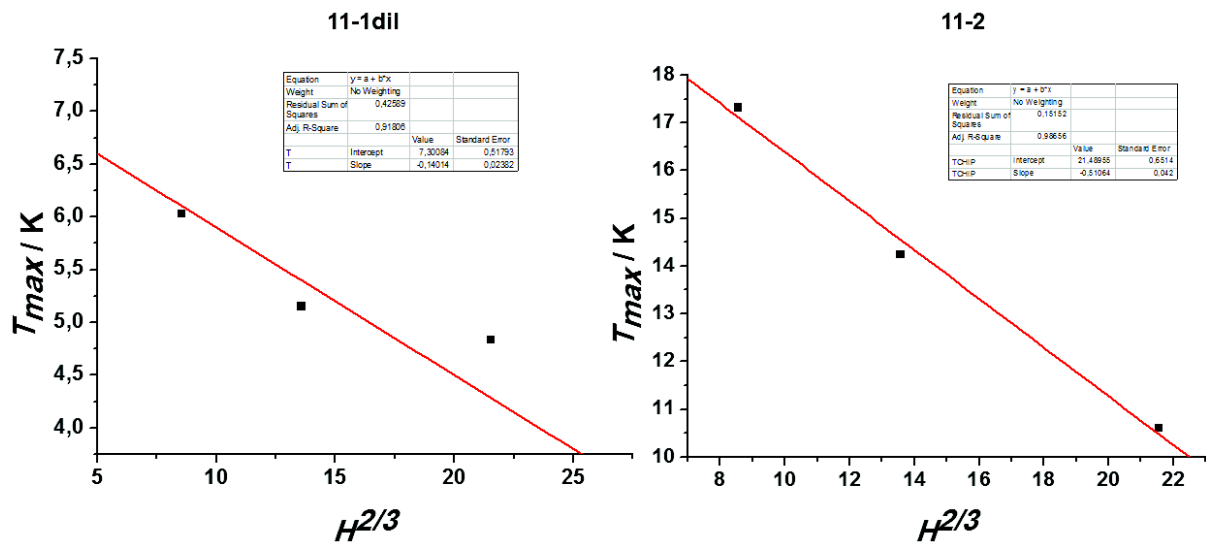


Figure 41: Extrapolation of the AT line performed with the Almeida-Thouless equation on samples 11-1dil and 11-2dil.

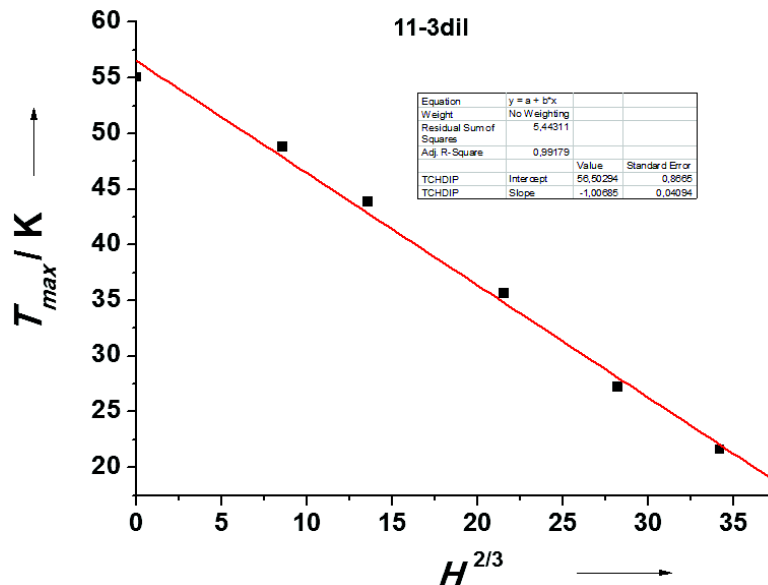


Figure 42: extrapolation of the AT line performed with the Almeida-Thouless equation on sample 11-3dil.

To conclude, this study clearly revealed that no pure superparamagnetic behavior is observed for all samples, even at high dilution rate. Nevertheless, the dilution of samples permitted to decrease significantly the interparticle interactions, permitting to point out that the spin glass behavior is visibly caused by spin frustration of each shell of nanoparticles. Furthermore, the variation of the shell thickness seems to lead to different and relatively complex magnetic behaviors. These latter observed for the different shell thickness are probably due to the intrinsic structure of the intricate NPs, and then size and shape dependent. Notably, these behaviors are different from those previously published for CsNi[Cr(CN)₆] NPs presenting a superparamagnetic behavior, for sizes lower or equal to 22 nm^{5,6}.

In order to compare with these results, we have estimated the volume of the magnetic Ni[Cr(CN)₆] material in the double-layered core@shell NPs (table 5). Because they present nearly the same magnetic volume of the magnetic Ni[Cr(CN)₆] material with sample **11-1**, the CsNi[Cr(CN)₆] NPs with a size of 22 nm can be taken as a benchmark. In comparison, sample **11-1** present a spin-glass-like regime with a freezing temperature equal to 4.5K which is lower than the blocking temperature of the superparamagnetic CsNi[Cr(CN)₆] NPs (21K), but its coercitive field of 75 Oe is higher (49 Oe for the CsNi[Cr(CN)₆] NPs). This difference may originate from a particular morphology of the magnetic shell, the presence of several interfaces, as well as from the presence of the KNi[Fe^{II}(CN)₆] intermediate paramagnetic layer that most likely affect the overall magnetic properties of the core-shell NPs. Indeed, a spin glass behavior means a disorder of the spins in the material.

First, it seems clear that the growth on different of the gold cores to form several interconnected cubic-like magnetic shells leads to the appearance of a particular anisotropic morphology of the magnetic shell. Such intricate morphology certainly impacts the shape anisotropy which should in turn influence the values of the coercitive field and the blocking/freezing temperature. Furthermore, due to their respective cell parameters values significantly different, the growth of the two PBA shells should generate the presence of structural constraints. Such structural constraints generate the appearance of a structural disorder at the two interfaces: first interface between the gold core and the first KNi[Fe^{II}(CN)₆] layer; second interface between the first KNi[Fe^{II}(CN)₆] and second KNi[Cr^{III}(CN)₆] layer. This structural disorder and spin frustration at the interface and/or on the surface of the magnetic KNi[Cr^{III}(CN)₆] layer may explain the appearance of a spin glass-like behavior. Finally, we have previously shown that the first KNi[Cr^{III}(CN)₆] layer present a paramagnetic behavior. This layer is situated directly in contact with the magnetic KNi[Cr^{III}(CN)₆] shell, and then some magnetic interactions can arise from this common interface, and may have an influence on the spin orientation at the interface especially at low temperatures. To determine the contribution of the probable effect arising from the interface, it may be interesting to get free from this first shell by growing directly the ferromagnetic shell on the gold nanoparticles.

Samples	11-1	11-2	11-3	11-4	11-5
Magnetic volume of KNi ^{II} Cr ^{III} estimated (nm ³)	10560	29361	57672	93060	2224716
Diameter for an equivalent cube of KNi ^{II} Cr ^{III} (nm)	21.8	30.9	36.6	45.3	130

Table 6: table presenting the estimated volume of magnetic KNi^{II}Cr^{III} and their equivalent diameter for a simple cube of KNi^{II}Cr^{III}.

IV.3.2 Magnetic properties of the double-layered core-shell Au@K⁺/Ni²⁺/[Fe^{II}(CN)₆]⁴⁻@PBA NPs.

After our study of the magnetic properties of the Au@KNi^{II}Fe^{II}@KNi^{II}Cr^{III}, and the effect of the KNi^{II}Cr^{III} shell thickness decrease on their magnetic behavior, we investigated the magnetic properties of others Au@K⁺/Ni²⁺/[Fe^{II}(CN)₆]⁴⁻@PBA (PBA = KNi^{II}Fe^{III} and KFe^{II}Fe^{II}) NPs. The nature of the PBA may modify the magnetic properties, then different magnetic behavior than those already observed were expected.

For Au@KNi^{II}Fe^{II}@KNi^{II}Fe^{III} NPs (**12-2**), the ZFC curve exhibits a peak at 17 K corresponding to the ordering temperature of the mean size NPs, with the FC continuous increases as the temperature decreases. (Figure 43). The value obtained for the ordering temperature is slightly lower than those usually observed for the bulk analogous² ($T_c = 23$ K), indicating a similar magnetic behavior. Then, that corresponds to a ferromagnetic behavior. The sharp increase observed at very low temperature for both, ZFC and FC curves, is due to the blocking temperature of the first reduced PBA KNi^{II}Fe^{II} shell, as observed for the original Au@K⁺/Ni²⁺/[Fe^{II}(CN)₆]⁴⁻NPs. This is caused by magnetic interactions between the Ni^{II} ions through the diamagnetic [Fe^{II}(CN)₆]⁴⁻ bridges. The field dependence of the magnetization exhibits a hysteresis loop with a coercive field at 1300 Oe, which confirmed the blocking of the magnetization. As for the large Au@KNi^{II}Fe^{II}@KNi^{II}Cr^{III} NPs (**11-5**), no frequency dependence of the in-phase (χ') and out of phase (χ'') susceptibilities as function of the temperature is observed, confirming the magnetic behavior similar as the bulk material (figure 44).

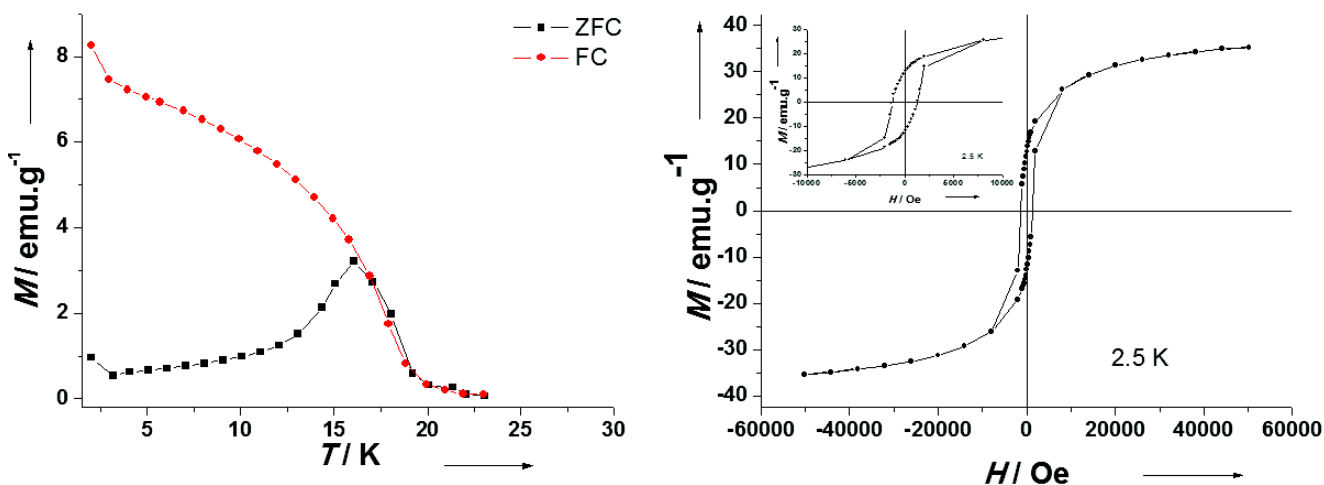


Figure 43: In left ZFC/FC curves for Au@KNiFe^{II}@KNiFe^{III} NPs (**12-2**) at an applied field of 100 Oe. In right, the hysteresis loop at 2.5K.

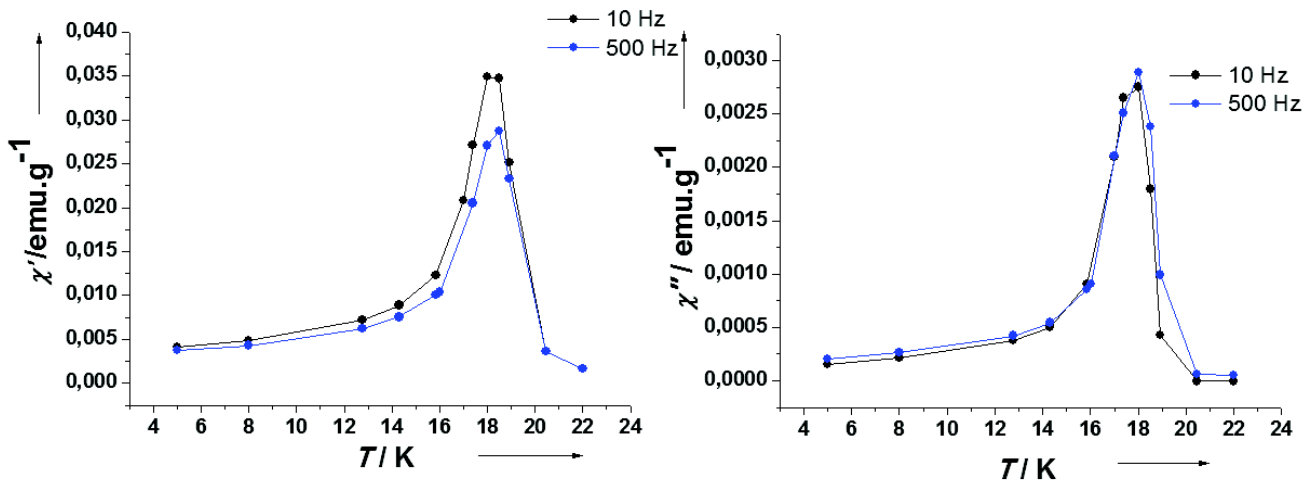


Figure 44: Temperature dependence of the in-phase (χ') and the out of phase (χ'') susceptibility with a zero dc magnetic field for Au@KNiFe^{II}@KNiFe^{III} NPs (12-2).

For the Au@KNiFe^{II}@KFe^{III}Fe^{II} NPs (14-2), the ZFC curve shows a large peak with a maximum at 4K, and the ordering temperature of the NPs is observed at similar value than for bulk material^{41,42} ($T_C = 5.5$ K) (figure 45). The ZFC curve, decreasing, and the FC curve, increasing continuously, began to separate close to the ordering temperature, which indicates a relatively narrow distribution size for the NPs. The presence of a really sharp hysteresis loop, with a coercive field of 12 Oe, seems confirm to the blocking of the magnetization. Finally, the measures of the temperature dependence of the in-phase (χ') and out of phase (χ'') susceptibilities revealed no frequency dependence, which is in accordance with a magnetic behavior as the bulk material (figure 46).

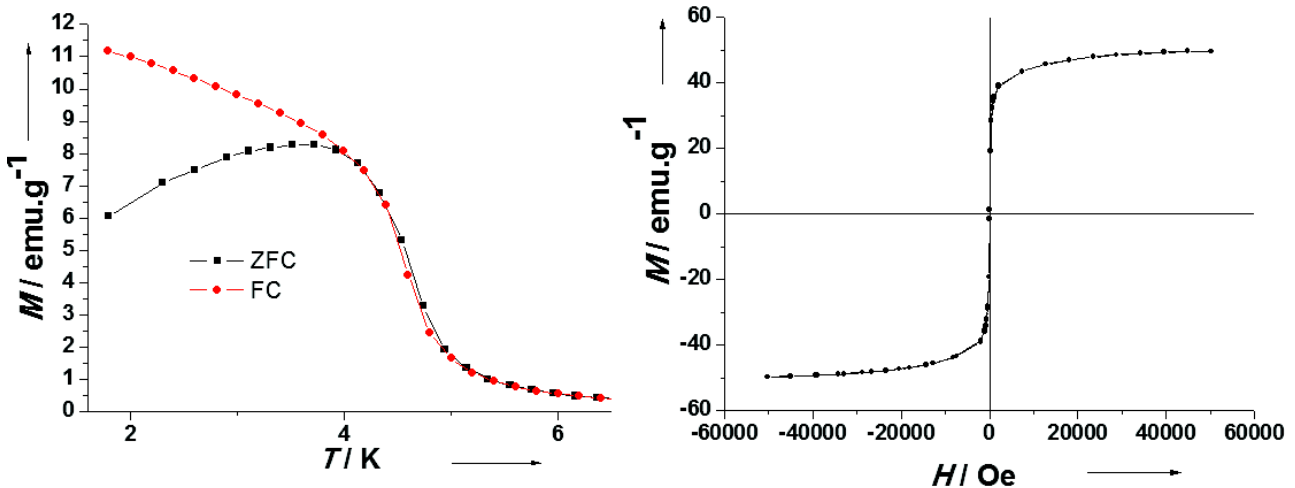


Figure 45: In left ZFC/FC curves for Au@KNiFe^{II}@KFe^{III}Fe^{II} NPs (14-2) at an applied field of 100 Oe. In right, the hysteresis loop at 2.5K.

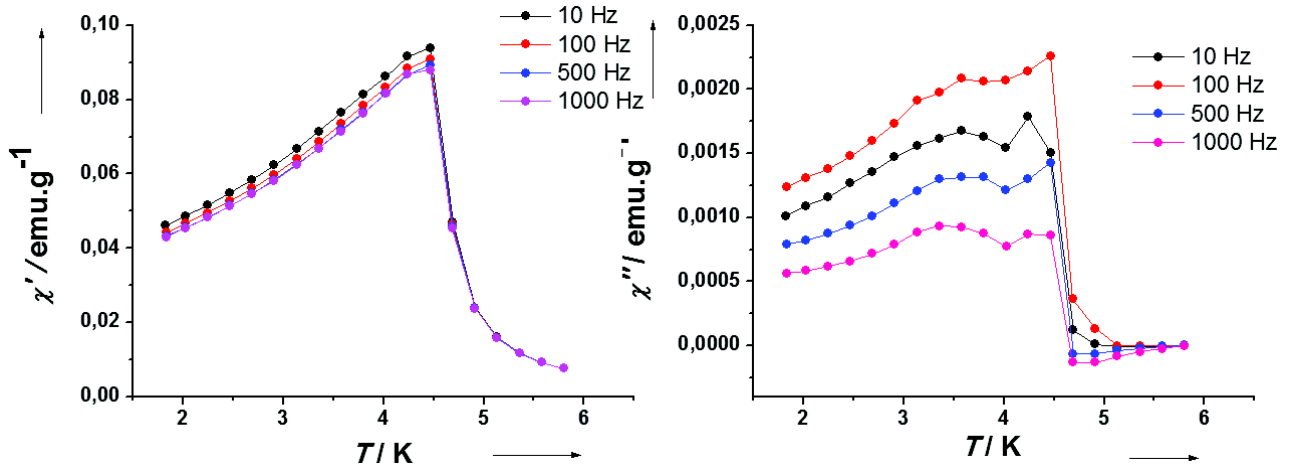


Figure 46: Temperature dependence of the in-phase (χ') and the out of phase (χ'') susceptibility with a zero dc magnetic field Au@KNiFe^{II}@KFe^{III}Fe^{II} NPs (14-2).

Then, the growth of a second shell clearly permits to implement ferromagnetic properties, leading to nano-objects exhibiting magneto-plasmonic properties. By combining the properties of both gold core and PBA shell, these core-shell NPs may be considered as multifunctional. Moreover, the use of a selected PBA for the second shell permits to finely tune the magnetic properties of to design double layered core-shell Au@K⁺/Ni²⁺/[Fe^{II}(CN)₆]⁴⁻@PBA NPs, allowing to use them for various applications, such as imaging.

IV.4 Conclusion

In this chapter, we have described the synthesis of double-layered core-shell $\text{Au@K}^+/\text{Ni}^{2+}/[\text{Fe}^{\text{II}}(\text{CN})_6]^{4-}@PBA$ performed by subsequent growing on single-layered $\text{Au@K}^+/\text{Ni}^{2+}/[\text{Fe}^{\text{II}}(\text{CN})_6]^{4-}$ NPs. Indeed, the epitaxial growth of a new PBA shell on the initial NPs is possible due to the closeness of their respective cell parameters. The double-layered core-shell $\text{Au@K}^+/\text{Ni}^{2+}/[\text{Fe}^{\text{II}}(\text{CN})_6]^{4-}@PBA$ NPs have been obtained by adding slowly the PBA precursors to a solution of $\text{Au@K}^+/\text{Ni}^{2+}/[\text{Fe}^{\text{II}}(\text{CN})_6]^{4-}$ NPs. Several PBA have been used, as $\text{Ni}^{\text{II}}\text{Cr}^{\text{III}}$, $\text{Ni}^{\text{II}}\text{Fe}^{\text{II}}$, $\text{Co}^{\text{II}}\text{Fe}^{\text{II}}$ and $\text{Fe}^{\text{III}}\text{Fe}^{\text{II}}$. Furthermore, by varying the precursor addition time, it is possible to control the size of both, the first and the second PBA layer. Moreover, a series of double layered core-shell $\text{Au@Ni}^{\text{II}}\text{Fe}^{\text{II}}@Ni^{\text{II}}\text{Cr}^{\text{III}}$ NPs was obtained on single layered $\text{Au@K}^+/\text{Ni}^{2+}/[\text{Fe}^{\text{II}}(\text{CN})_6]^{4-}$ NPs presenting small first $\text{Ni}^{\text{II}}\text{Fe}^{\text{II}}$ shell of 4.0 ± 1.3 nm. The as obtained NPs were characterized using several techniques which have confirmed the formation of the new PBA layer on the $\text{Au@K}^+/\text{Ni}^{2+}/[\text{Fe}^{\text{II}}(\text{CN})_6]^{4-}$ NPs.

As for the initial single-layered core-shell $\text{Au@K}^+/\text{Ni}^{2+}/[\text{Fe}^{\text{II}}(\text{CN})_6]^{4-}$ NPs, the different double-layered core-shell $\text{Au@K}^+/\text{Ni}^{2+}/[\text{Fe}^{\text{II}}(\text{CN})_6]^{4-}@PBA$ NPs exhibit interesting optical properties originated from the SPR band of the gold core. The comparison between the $\text{Au@K}^+/\text{Ni}^{2+}/[\text{Fe}^{\text{II}}(\text{CN})_6]^{4-}@PBA$ and $\text{Au@K}^+/\text{Ni}^{2+}/[\text{Fe}^{\text{II}}(\text{CN})_6]^{4-}$ NPs of which the former are respectively originated, revealed a red-shift of the SPR band. For all systems, such red-shifts are dependent of the total shell ($\text{Ni}^{\text{II}}\text{Fe}^{\text{II}} + \text{PBA}$) increase, which induces an increase of the local refractive index, and this is in agreement with the behavior observed for the shell increase of $\text{Au@K}^+/\text{Ni}^{2+}/[\text{Fe}^{\text{II}}(\text{CN})_6]^{4-}$ NPs, and for other systems described in literature. The nature of the PBA shells can also influence the evolution of the SPR band, due to the difference between the refractives indexes of both layers. Moreover, the enlargement of the SPR band is observed for a total shell thickness larger than 30 nm. This behavior may be explained by the confinement of the free electrons within the metal core or the increase of the scattering phenomenon, as observed in literature.

On the other hand, we have studied the magnetic properties implemented with the subsequent growing of the second PBA layer of the $\text{Au@K}^+/\text{Ni}^{2+}/[\text{Fe}^{\text{II}}(\text{CN})_6]^{4-}$ NPs. In the first time, we have investigated the effect of the shell thickness on the magnetic properties on the series of $\text{Au@Ni}^{\text{II}}\text{Fe}^{\text{II}}@Ni^{\text{II}}\text{Cr}^{\text{III}}$ NPs with different shell size. We have observed the decrease of the maximum temperature (blocking or freezing), the coercive field and the saturation magnetization with the decrease of the shell thickness. The $\text{Au@Ni}^{\text{II}}\text{Fe}^{\text{II}}@Ni^{\text{II}}\text{Cr}^{\text{III}}$ NPs with the larger $\text{Ni}^{\text{II}}\text{Cr}^{\text{III}}$ thickness (40.45 ± 8.1 nm) clearly present a long range ferromagnetic ordering, with no frequency dependence. However, the other NPs present frequency dependence, weak for the larger (7.3 ± 1.5 nm and 10.45 ± 2.6) and strong for the thinner (1.6 ± 0.3 and 4.0 ± 1.0 nm), which indicate the presence of a short range magnetic ordering. To determinate precisely their magnetic behavior, several models were used (Neel and Vogel-Vulcher laws). These models indicates that the smallest NPs have a superparamagnetic or spin glass behavior, and then we have focalized our investigations on these samples. However, strong interparticle interactions were preventing any possibility to validate one or the other magnetic behavior. Then to limit these interactions, the pristine NPs were diluted in a

PVP matrix. According to the different dilution rates performed, we have determined that 1% of NPs in PVP matrix is the best dilution rate to limit the interparticle interactions. Indeed, dilution decreases the blocking temperature, the coercitive field. This has also been confirmed by fitting with several models (scaling law and Almeida-Thouless equation). Nevertheless, the variation of the Ni^{II}Cr^{III} shell thickness seems to induce different magnetic behavior since the data cannot be fitted using the same model. This phenomenon is probably due to the contribution of the surface disorder and the disorder that originates from the interface between the two KNi^{II}Fe^{II} and Ni^{II}Cr^{III} coordination shells, which the value of their cell parameters are significantly different.

We have also investigated the magnetic behavior of the others Au@K⁺/Ni²⁺/[Fe^{II}(CN)₆]⁴⁻@PBA NPs. The Au@KNi^{II}Fe^{II}@KNi^{II}Fe^{III} NPs and the Au@KNiFe^{II}@KFe^{III}Fe^{II} NPs present both long range ordering, which correspond to the magnetic behavior observed for the bulk analogous. This is also provided by the absence of frequency dependence.

Then, double-layered core-shell Au@K⁺/Ni²⁺/[Fe^{II}(CN)₆]⁴⁻@PBA NPs exhibiting both plasmonic, and magnetic properties, such as ferromagnetic behavior, have been synthesized, leading to nano-objects presenting a multifunctionality. Such nano-objects may be use for future applications such as imaging.

References

- 1 G. Maurin-Pasturel, J. Long, Y. Guari, F. Godiard, M.-G. Willinger, C. Guérin, J. Larionova, *Angew. Chem. Int. Ed.*, **2014**, *53*, 3872.
- 2 Y. Mizuno, M. Okubo, K. Kagesawa, D. Asakura, T. K. Haoshen Zhou, K. Oh-ishi, A. Okazawa and N. Kojima, *Inorg. Chem.*, **2012**, *51*, 10311.
- 3 D. Brinzei, L. Catala, N. Louvain, G. Rogez, O. Stephan, A. Gloter and Talal Mallah, *J. Mater. Chem.*, **2006**, *16*, 2593.
- 4 E. Chelebaeva, Y. Guari, J. Larionova, A. Trifonov and C. Guerin, *Chem. Mater.*, **2008**, *20*, 1367.
- 5 Y. Prado, L. Lisnard, D. Heurtaux, G. Rogez, A. Gloter, O. Stephan, N. Dia, E. Riviere, L. Catala and T. Mallah, *Chem. Commun.*, **2011**, *47*, 1051.
- 6 Y. Prado, S. Mazerat, E. Riviere, G. Rogez, A. Gloter, O. Stephan, L. Catala and T. Mallah, *Adv. Funct. Mater.*, **2014**, *24*, 5402.
- 7 E. Pinilla-Cienfuegos, S. Kumar, S. Mañas-Valero, J. Canet-Ferrer, L. Catala, T. Mallah, A. Forment-Aliaga and E. Coronado, *Part. Part. Syst. Character.*, **2015**, *32*, 693.
- 8 L. Catala, D. Brinzei, Y. Prado, A. Gloter, O. Stephan, G. Rogez and T. Mallah, *Angew. Chem.*, **2009**, *48*, 183.
- 9 O. N. Risset, P. A. Quintero, T. V. Brinzari, M. J. Andrus, M. W. Lufaso, M. W. Meisel and D. R. Talham, *J. Am. Chem. Soc.*, **2014**, *136*, 15660.
- 10 C. H. Li, M. K. Peprah, D. Asakura, M. W. Meisel, M. Okubo and D. R. Talham, *Chem. Mater.*, **2015**, *27*, 1524.
- 11 D. M. Pajerowski, B. Ravel, C. H. Li, M. F. Dumont and D. R. Talham, *Chem. Mater.*, **2014**, *26*, 2586.
- 12 N. Dia, L. Lisnard, Y. Prado, A. Gloter, O. Stéphan, F. Brisset, H. Hafez, Z. Saad, C. Mathonière, L. Catala, and T. Mallah, *Inorg. Chem.*, **2013**, *52*, 10264.
- 13 M. F. Dumont, E. S. Knowles, A. Guiet, D. M. Pajerowski, A. Gomez, S. W. Kycia, M. W. Meisel, and D. R. Talham, *Inorg. Chem.*, **2011**, *50*, 4295.
- 14 D. Asakura, C. H. Li, Y. Mizuno, M. Okubo, H. Zhou and D. R. Talham, *J. Am. Chem. Soc.*, **2013**, *135*, 2793.
- 15 C.H. Li, Y. Nanba, D. Asakura, M. Okubo and D. R. Talham, *RSC Adv.*, **2014**, *4*, 24955.
- 16 M. Ishizaki, Y. Sajima, S. Tsuruta, A. Gotoh, M. Sakamoto, T. Kawamoto, H. Tanaka, and M. Kurihara, *Chemistry Letters*, **2009**, No. 11 (Vol.38), 1059.

- 17 M. Presle, J. Lemainque, J.-M. Guigner, E. Larquet, I. Maurin, J.-P. Boilot and T. Gacoin, *New J. Chem.*, 2011, **35**, 1296.
- 18 M. Presle, I. Maurin, F. Maroun, R. Cortès, L. Lu, R. S. Hassan, E. Larquet, J.-M. Guigner, E. Rivière, J. P. Wright J.-P. Boilot and T. Gacoin, *J. Phys. Chem. C*, **2014**, *118*, 13186.
- 19 O. N. Risset and D. R. Talham, *Chem. Mater.*, **2015**, *27*, 3838.
- 20 P. Bhatt, S. Banerjee, S. Anwar, M. D. Mukadam, S. S. Meena, and S. M. Yusuf, *ACS Appl. Mater. Interfaces*, **2014**, *6*, 17579.
- 21 L. M. Liz-Marzan, M. Giersig, P. Mulvaney, *Langmuir*, **1996**, *12*, 4329.
- 22 R. T. Tom, A. Sreekumaran Nair, N. Singh, M. Aslam, C. L. Nagendra, R. Philip, K. Vijayamohanam, T. Pradeep, *Langmuir*, **2003**, *19*, 2439.
- 23 S. N. Gosh, *J. Inor. Nucl. Chem.* **1974**, *36*, 2465.
- 24 J. Lejeune, J. B. Brubach, P. Roy and A. Bleuzen, *C. R. Chimie*, **2014**, *17*, 534.
- 25 K. Itaya and I. Uchida, *Inorg. Chem.*, **1986**, *25*, 389.
- 26 X. Liang, Z. Deng, L. Jing, X. Li, Z. Dai, C. Li and M. Huang, *Chem. Commun.*, **2013**, *49*, 11029.
- 27 10 X. Jia, X. Cai, Y. Chen, S. Wang, H. Xu, K. Zhang, M. Ma, H. Wu, J. Shi, and H. Chen, *ACS Appl. Mater. Interfaces*, **2015**, *7*, 4579.
- 28 11 X. Cai, X. Jia, W. Gao, K. Zhang, M. Ma, S. Wang, Y. Zheng, J. Shi, and H. Chen, *Adv. Funct. Mater.*, **2015**, DOI: 10.1002/adfm.201403991.
- 29 G. Fu, Wei Liu, S. Feng and X. Yue, *Chem. Commun.*, **2012**, *48*, 11567.
- 30 H. A. Hoffman, L. Chakrabarti, M. F. Dumont, A. D. Sandler and R. Fernandes, *RSC Adv.*, **2014**, *4*, 29729.
- 31 Z. Li, Y. Zeng, D. Zhang, M. Wu, L. Wu, A. Huang, H. Yang, X. Liu and J. Liu, *Mater. Chem. B*, **2014**, *2*, 3686.
- 32 Y. Li, C. Li and D.R. Talham, *Nanoscale*, **2015**, DOI: 10.1039/C4NR06481J.
- 33 L. Jing, X. Liang, Z. Deng, S. Feng, X. Li, M. Huang, C. Li, Z. Dai, *Biomaterials*, **2014**, *35*, 5814.
- 34 A. Demortière, P. Panissod, B. P. Pichon, G. Pourroy, D. Guillon, B. Donnio, S. Begin-Colin, *Nanoscale*, **2011**, *3*, 225.
- 35 L. Néel, *Adv. Phys.*, **1995**, *4*, 191.
- 36 J. A. Mydosh, *Spin Glasses*: Taylor and Francis, Washington DC, **1993**.

- 37 M. A. Girtu, *J. Optoelectron. Adv. Mater.*, **2002**, 4, 85.
- 38 L. Lartigue, J. Long, X. Dumail, S. I. Nikitenko, C. Cau, Y. Guari, L. Stievano, M. T. Sougrati, C. Guerin, C. Sangregorio, J. Larionova, *J. Nanopart. Res.*, **2013**, 15, 1490.
- 39 C.R. Lin, R. K. Chiang, J. S. Wang, T. W. Sung, *J. Appl. Phys.*, **2006**, 99 (08), 710.
- 40 A. López-Ortega, E. Lottini, C. d. J. Fernández, C. Sangregorio, *Chem. Mater.* **2015**, 27, 4048.
- 41 M. Shokouhimehr, E. S. S., A. Khitrin, S. Basu, S. D. Huang, *Inorg. Chem. Commun.*, **2010**, 13, 58.
- 42 P. Day, Allan E. Underhill: *Metal-organic and Organic Molecular Magnets*, Royal Society of Chemistry, **1999**.

Experimental part:

The syntheses were carried out using commercially available reagents. All chemical reagents were purchased and used without further purification. Potassium hexacyanoferrate(II) trihydrate ($K_4[Fe(CN)_6] \cdot 3H_2O$) was purchased from Acros Organics, Sodium hexacyanoferrate(II) decahydrate ($Na_4[Fe(CN)_6] \cdot 10H_2O$) was purchased from Alfa Aesar, Iron(III) chloride hexahydrate ($FeCl_3 \cdot 6H_2O$, 97%) and Polyvinylpyrrolidone (PVP, Mw = 10000g/mol) were purchased from Aldrich.

Synthesis of double layered Au@KNi[Fe(CN)₆]@KNi[Cr(CN)₆] core@shell NPs (1-5):

10mL of an aqueous solution of $K_3[Cr(CN)_6]$ (5.65 mM) and 10 mL of an aqueous solution of $NiCl_2 \cdot 6H_2O$ (5.0 mM) were simultaneously added (2 mL/h) to Au@KNi[Fe(CN)₆] core@shell NPs (10 mg) redispersed in 50 mL of water under vigorous stirring at 25°C. After completion of the addition, the solution was vigorously stirred for one additional hour. The colloidal suspension of NPs was centrifuged at 20000 rpm during 15 min. The supernatant was removed and the NPs were washed with water and centrifuged again at 20000 rpm during 15 min. The supernatant was removed and the NPs were washed with ethanol and centrifuged at 20000 rpm during 10 min and were dried under vacuum.

Characterizations:

Mauve powder. FT-IR (KBr, ν , cm^{-1}): $\nu(-OH)$ (coordinate water) = 3640 cm^{-1} , $\nu(-OH)$ (free water) = 3415 cm^{-1} , $\nu(C\equiv N)$ = 2172 cm^{-1} ($Cr^{III}-C\equiv N-Ni^{II}$), $\nu(C\equiv N)$ = 2094 cm^{-1} ($Fe^{II}-C\equiv N-Ni^{II}$), $\delta(H-O-H)$ (free water) = 1618 cm^{-1} , $\nu(Fe^{II}-CN)$ = 592 cm^{-1} , $\nu(Cr^{III}-CN)$ = 493 cm^{-1} , $\delta(Fe^{II}-CN)$ = 465 cm^{-1} . Anal.found (wt%): Au, 9.4; K, 3.6; Ni, 18.1; Fe, 2.8; Cr, 8.5; C, 16.8; N, 16.6; H, 2.6.

Calculated formula: $Au_{0.15}@K_{0.3}Ni[Fe(CN)_6]_{0.2}[Cr(CN)_6]_{0.5} \cdot 4.35 H_2O$.

UV-visible: 545 nm (surface plasmon band of gold NPs).

Synthesis of double layered Au@KNi[Fe(CN)₆]@KNi[Fe(CN)₆] core@shell NPs (12-2) :

10 mL of an aqueous solution of $K_3[Fe(CN)_6]$ (5.65 mM) and 10 mL of an aqueous solution of $NiCl_2 \cdot 6H_2O$ (5.0 mM) were simultaneously added (2 mL/h) to Au@KNi[Fe(CN)₆] core@shell NPs (10 mg) redispersed in 50 mL of water under vigorous stirring at 25°C. After the addition, the solution was vigorously stirred for one hour. The aqueous solution of NPs was centrifuged at 20000 rpm during 15 min. The supernatant was removed and the NPs were washed with water and centrifuged again at 20000 rpm during 15 min. The supernatant was removed and the NPs were washed with ethanol and centrifuged at 20000 rpm during 10 min and were dried under vacuum.

Characterizations:

Mauve powder. FT-IR (KBr, ν , cm^{-1}): $\nu(-OH)$ (coordinate water) = 3600 cm^{-1} , $\nu(-OH)$ (free water) = 3427 cm^{-1} , $\nu(C\equiv N)$ = 2165 cm^{-1} ($Fe^{III}-C\equiv N-Ni^{II}$), $\nu(C\equiv N)$ = 2094 cm^{-1} ($Fe^{II}-C\equiv N-Ni^{II}$), $\delta(H-O-H)$ (free water) = 1613 cm^{-1} , $\nu(Fe^{II}-CN)$ = 595 cm^{-1} , $\nu(Fe^{III}-CN)$ = 549 cm^{-1} , $\delta(Fe^{II}-CN)$ = 480 cm^{-1} , $\delta(Fe^{III}-CN)$ = 465 cm^{-1} .

Anal.found (wt%): Au, 7.3; K, 4.1; Ni, 17.8; Fe, 12.7; C, 15.9; N, 17.1; H, 2.5. Calculated formula: $Au_{0.125}@K_{0.32}Ni[Fe^{II}(CN)_6]_{0.19}[Fe^{III}(CN)_6]_{0.52} \cdot 3.85H_2O$.

UV-visible: 530 nm (surface plasmon band of gold NPs).

Synthesis of double layered Au@KNi[Fe(CN)₆]@KNi[Fe(CN)₆] core@shell NPs with small single layered Au@KNi[Fe(CN)₆] core@shell NPs (12-1):

In the first time, KBH₄ (0.63 mmol) was added to 100 mL of an aqueous solution of K[Au(CN)₂] (4.8×10⁻⁵ mol, 4.8×10⁻⁴ M) under vigorous stirring at 25°C. The colorless solution rapidly turned red, indicating the formation of NPs. After 20 min, 2 mL of an aqueous solution of K₃[Fe(CN)₆] (5.65 mM) and 2 mL of an aqueous solution of NiCl₂·6H₂O (5.00 mM) were simultaneously added (2 mL/h) to the gold NPs solution under vigorous stirring at 25°C. After completion of the addition, the solution was vigorously stirred for one hour. After completion of the addition, the solution was vigorously stirred for one hour, then the pH of the solution of NPs was decreased close to 4 with addition of a dilute HCl solution (1 M), and the solution sonicated for 5 min.

In the second time, After sonication, 8 mL of an aqueous solution of K₃[Fe(CN)₆] (5.65 mM) and 8 mL of an aqueous solution of NiCl₂·6H₂O (5.0 mM) were simultaneously added (2 mL/h) under vigorous stirring at 25°C. After the addition, the solution was vigorously stirred for one hour. The aqueous solution of NPs was centrifuged at 20000 rpm during 10 min. The supernatant was removed and the NPs were washed with water and centrifuged again at 20000 rpm during 10 min. The supernatant was removed and the NPs were washed with ethanol and centrifuged at 20000 rpm during 10 min and were dried under vacuum.

Characterizations:

Purple powder. FT-IR (KBr, ν , cm⁻¹): ν (-OH) (coordinate water) = 3610 cm⁻¹, ν (-OH) (free water) = 3402 cm⁻¹, ν (C≡N) = 2166 cm⁻¹ (Fe^{III}-C≡N-Ni^{II}), ν (C≡N) = 2095 cm⁻¹ (Fe^{II}-C≡N-Ni^{II}), δ (H-O-H) (free water) = 1610 cm⁻¹, ν (Fe^{II}-CN) = 595 cm⁻¹, ν (Fe^{III}-CN) = 551 cm⁻¹, δ (Fe^{II}-CN) = 474 cm⁻¹, δ (Fe^{III}-CN) = 465 cm⁻¹.

EDS: 22.6/23.7/29.8/23.55 (K/Fe/Ni/Au).

UV-visible: 546 nm (surface plasmon band of gold NPs).

Synthesis of double layered Au@KNi[Fe(CN)₆]@K[FeFe(CN)₆] core@shell NPs with small single layered Au@KNi[Fe(CN)₆] core@shell NPs (14-1):

In the first time, KBH₄ (0.63 mmol) was added to 100 mL of an aqueous solution of K[Au(CN)₂] (4.8×10⁻⁵ mol, 4.8×10⁻⁴ M) under vigorous stirring at 25°C. The colorless solution rapidly turned red, indicating the formation of NPs. After 20 min, 2 mL of an aqueous solution of K₃[Fe(CN)₆] (5.65 mM) and 2 mL of an aqueous solution of NiCl₂·6H₂O (5.00 mM) were simultaneously added (2 mL/h) to the gold NPs solution under vigorous stirring at 25°C. After completion of the addition, the solution was vigorously stirred for one hour. After the addition, the solution was vigorously stirred for one hour, and then the pH of the solution of NPs was decreased close to 4 with addition of HCl (1 M). The aqueous solution of NPs was centrifuged at 20000 rpm during 5 min. The supernatant was removed and the NPs dispersed in some water and re-filled until 100 ml.

Secondly, 8 mL of an aqueous solution of K₄[Fe(CN)₆]·3H₂O (5.65 mM) and 8 mL of an aqueous solution of FeCl₃·6H₂O (5.0 mM) were simultaneously added (2 mL/h) under vigorous stirring at 25°C. After the addition, the solution was vigorously stirred for one hour. The aqueous solution of NPs was centrifuged at 20000 rpm during 10 min. The supernatant was removed and the NPs were washed with water and centrifuged again at 20000 rpm during 10 min. The supernatant was removed and the NPs were washed with ethanol and centrifuged at 20000 rpm during 10 min and were dried under vacuum.

Characterizations:

Dark Blue powder. FT-IR (KBr, ν , cm^{-1}): $\nu(\text{-OH})$ (coordinate water) = 3609 cm^{-1} , $\nu(\text{-OH})$ (free water) = 3417 cm^{-1} , $\nu(\text{C}\equiv\text{N}) = 2080 \text{ cm}^{-1}$ ($\text{Fe}^{\text{III}}\text{-C}\equiv\text{N-Fe}^{\text{II}}$), $\delta(\text{H-O-H})$ (free water) = 1624 cm^{-1} , $\nu(\text{Fe}^{\text{II}}\text{-CN}) = 600 \text{ cm}^{-1}$, $\delta(\text{Fe}^{\text{II}}\text{-CN}) = 493 \text{ cm}^{-1}$ and 474 cm^{-1} .

EDS: 28.6/42/5.25/24.15 (K/Fe/Ni/Au). UV-visible: 536 nm (surface plasmon band of gold NPs), 710 nm (intervalence absorption band $\text{Fe}^{\text{II}}\text{-CN-Fe}^{\text{III}} \rightarrow \text{Fe}^{\text{III}}\text{-CN-Fe}^{\text{II}}$).

Synthesis of double layered $\text{Au@Na[NiFe(CN)}_6\text{]@Na[FeFe(CN)}_6\text{]}$ core@shell NPs with small single layered $\text{Au@NaNi[Fe(CN)}_6\text{]}$ core@shell NPs (14-2):

The NPs are obtained using the same protocol than the $\text{Au@KNi[Fe(CN)}_6\text{]@K[FeFe(CN)}_6\text{]}$ core@shell NPs by changing the nature of the counter-ions precursors, in the first time $\text{Na}_3[\text{Fe(CN)}_6]$ is used instead of $\text{K}_3[\text{Fe(CN)}_6]$, and in the second time $\text{Na}_4[\text{Fe(CN)}_6]\cdot 10\text{H}_2\text{O}$ instead $\text{K}_4[\text{Fe(CN)}_6]\cdot 3\text{H}_2\text{O}$.

Characterizations:

Dark Blue powder. FT-IR (KBr, ν , cm^{-1}): $\nu(\text{-OH})$ (coordinate water) = 3617 cm^{-1} , $\nu(\text{-OH})$ (free water) = 3412 cm^{-1} , $\nu(\text{C}\equiv\text{N}) = 2080 \text{ cm}^{-1}$ ($\text{Fe}^{\text{III}}\text{-C}\equiv\text{N-Fe}^{\text{II}}$), $\delta(\text{H-O-H})$ (free water) = 1609 cm^{-1} , $\nu(\text{Fe}^{\text{II}}\text{-CN}) = 600 \text{ cm}^{-1}$, $\delta(\text{Fe}^{\text{II}}\text{-CN}) = 495 \text{ cm}^{-1}$ and 474 cm^{-1} .

EDS: 1.05/0.95/59.8/3.95/34.25 (Na/K/Fe/Ni/Au). UV-visible: 545 nm (surface plasmon band of gold NPs), 730 nm (intervalence absorption band $\text{Fe}^{\text{II}}\text{-CN-Fe}^{\text{III}} \rightarrow \text{Fe}^{\text{III}}\text{-CN-Fe}^{\text{II}}$).

Synthesis of double layered $\text{Au@KNi[Fe(CN)}_6\text{]@KCo[Fe(CN)}_6\text{]}$ core@shell NPs with small single layered $\text{Au@K[NiFe(CN)}_6\text{]}$ core@shell NPs (13):

The NPs are obtained using the same protocol than the $\text{Au@KNi[Fe(CN)}_6\text{]@KFe[Fe(CN)}_6\text{]}$ core@shell NPs by changing the nature of the precursors in the second time, $\text{CoCl}_2\cdot 6\text{H}_2\text{O}$ is used instead of $\text{FeCl}_3\cdot 6\text{H}_2\text{O}$ and $\text{K}_3[\text{Fe(CN)}_6]$ instead of $\text{K}_4[\text{Fe(CN)}_6]\cdot 3\text{H}_2\text{O}$.

Characterizations:

Dark cobalt blue powder. FT-IR (KBr, ν , cm^{-1}): $\nu(\text{-OH})$ (coordinate water) = 3621 cm^{-1} , $\nu(\text{-OH})$ (free water) = 3386 cm^{-1} , $\nu(\text{C}\equiv\text{N}) = 2084 \text{ cm}^{-1}$ ($\text{Co}^{\text{II}}\text{-C}\equiv\text{N-Fe}^{\text{II}}$, $\text{Ni}^{\text{II}}\text{-C}\equiv\text{N-Fe}^{\text{II}}$), $\delta(\text{H-O-H})$ (free water) = 1603 cm^{-1} , $\nu(\text{Fe}^{\text{II}}\text{-CN}) = 593 \text{ cm}^{-1}$, $\delta(\text{Fe}^{\text{II}}\text{-CN}) = 473 \text{ cm}^{-1}$, $\delta(\text{Fe}^{\text{II}}\text{-CN}) = 463 \text{ cm}^{-1}$.

EDS: 25.55/28.25/25.2/1.10/19.85 (K/Fe/Co/Ni/Au). UV-visible: 542 nm (surface plasmon band of gold NPs).

Synthesis of double layered $\text{Au@KNi[Fe(CN)}_6\text{]@KNi[Cr(CN)}_6\text{]}$ core@shell NPs with small single layered $\text{Au@KNi[Fe(CN)}_6\text{]}$ core@shell NPs (11-1 to 11-4):

The NPs are obtained using the same protocol than the $\text{Au@KNi[Fe(CN)}_6\text{]@KFe[Fe(CN)}_6\text{]}$ core@shell NPs by changing the nature of the precursors in the second time, $\text{NiCl}_2\cdot 6\text{H}_2\text{O}$ is used instead of $\text{FeCl}_3\cdot 6\text{H}_2\text{O}$ and $\text{K}_3[\text{Cr(CN)}_6]$ instead of $\text{K}_4[\text{Fe(CN)}_6]$, and by changing the volume of the precursors solution for the second shell. Thus, a volume ($V = 2; 4; 8; 10$ mL) of the aqueous solution of $\text{K}_3[\text{Cr(CN)}_6]$ (5,65 mM) and a volume ($V = 2; 4; 10$ mL) of the aqueous solution of $\text{NiCl}_2\cdot 6\text{H}_2\text{O}$ (5.0 mM) is added.

Characterizations:

Mauve powder. FT-IR (KBr, ν , cm^{-1}): $\nu(\text{-OH})$ (coordinate water) = 3649 cm^{-1} , $\nu(\text{-OH})$ (free water) = 3423 cm^{-1} , $\nu(\text{C}\equiv\text{N}) = 2172 \text{ cm}^{-1}$ ($\text{Cr}^{\text{III}}\text{-C}\equiv\text{N-Ni}^{\text{II}}$), $\nu_{\text{C}\equiv\text{N}} = 2095 \text{ cm}^{-1}$ ($\text{Fe}^{\text{II}}\text{-C}\equiv\text{N-Ni}^{\text{II}}$), $\delta(\text{H-O-H})$ (free water) = 1622 cm^{-1} , $\nu(\text{Fe}^{\text{II}}\text{-CN}) = 598 \text{ cm}^{-1}$, $\nu(\text{Cr}^{\text{III}}\text{-CN}) = 493 \text{ cm}^{-1}$, $\delta(\text{Fe}^{\text{II}}\text{-CN}) = 470 \text{ cm}^{-1}$.

Dilution of Au@K₃[Fe(CN)₆]@K₃[Cr(CN)₆] NPs in polymer matrix for SQUID measurements:

The Au@K₃[Fe(CN)₆]@K₃[Cr(CN)₆] NPs (GM552,GM592) were redispersed in ultrapure water with large amount of Polyvinylpyrrolidone (Mw=10000 g/mol, 10, 5 and 1% w/t of nanoparticles/PVP), before being dried under vacuum at 40°C under vigorous stirring.

Synthesis of Na₃[Fe(CN)₆]·3H₂O:

10 g of K₃[Fe(CN)₆] are dissolved in 50 mL of ultrapure water. The solution is passed through a resin exchange ion «Dowex®50WX8 hydrogen form» (Sigma-Aldrich) to obtain H₃[Fe(CN)₆]. The resin has been previously washed several times with a HCl solution (4M) then rinsed with ultrapure water to obtain neutral pH. The pH of the obtained H₃[Fe(CN)₆] solution is neutralized with addition of a NaOH solution (1M). The solution is concentrated then filtered warm on cotton. After 1 week, red-orangey crystals of Na₃[Fe(CN)₆]·3H₂O are obtained and washed quickly with cold water.

Characterizations:

Red-orangey powder. FT-IR (KBr, ν , cm⁻¹): $\nu(-OH)$ (free water) = 3590 and 3532 cm⁻¹, $\nu(C\equiv N)$ = 2120, 2084 and 2066 cm⁻¹ (Fe^{III}-C≡N), $\delta(H-O-H)$ (free water) = 1612 cm⁻¹, $\nu(Fe^{III}-CN)$ = 508 cm⁻¹, $\delta(Fe^{III}-CN)$ = 400 cm⁻¹.

Elemental analysis: O: 7.51%; Fe: 16.6%; Na: 19.16%; N: 26.82%; C: 22.47%; H: 1.41%.

CHAPTER V

-

$^{201}\text{Tl}^+$ -labeled Prussian Blue and core-shell Au@Prussian Blue NPs for bio-imaging.

V.1 Introduction

In the previous chapter, we have described the synthesis of double-layered core-shell nano-heterostructures $\text{Au}@K^+/\text{Ni}^{2+}/[\text{Fe}^{\text{II}}(\text{CN})_6]^{4-}@PBA$ exhibiting magneto-plasmonic properties and obtained by subsequent growing of a new PBA shell on single-layered core-shell $\text{Au}@K^+/\text{Ni}^{2+}/[\text{Fe}^{\text{II}}(\text{CN})_6]^{4-}$ NPs. Both optical and magnetic properties of these nano-objects are tunable, by varying the PBA shell thickness for the optical properties, and by varying the nature of the selected PBA and the PBA shell thickness for the magnetic properties. Such multifunctionality is interesting for applications, and particularly for biomedical applications, such as imaging.

On one hand, gold NPs are some of the most extensively studied nanomaterial for medicines, for their intrinsic optical properties due to the presence of a strong Surface Plasmon Resonance (SPR) phenomenon. Gold NPs are able to absorb and scatter light intensively at its SPR wavelength region, which can be used as optical probes for sensing applications, such as light absorption or light scattering techniques (biosensors)¹⁻³. Due to their strong light absorption properties, gold NPs are also very promising contrast agents for photothermal (PT) and photoacoustic (PA) imaging^{1,4}, based on the laser-induced heating of the material, with the detection of a heat for the former and the detection of acoustic waves generated by thermal expansion of air surrounding the material for the latter. Moreover, gold NPs can absorb X-ray radiation and be used to increase imaging contrast in diagnostic computed tomography (CT)¹.

On the other hand, a particular attention has been recently devoted to the design of PB and PBA NPs stabilized in aqueous solution with biocompatible stabilizing agents for imaging. Such NPs can be used as potential contrast agents for magnetic resonance imaging (MRI) due to their intrinsic magnetic properties⁵⁻⁸. As for gold NPs, the presence of a strong light absorption band for PB NPs, due to the large intervalence charge-transfer band ($\text{Fe}^{\text{III}}-\text{NC}-\text{Fe}^{\text{II}} \rightarrow \text{Fe}^{\text{II}}-\text{NC}-\text{Fe}^{\text{III}}$) make them promising for PT and PA imaging⁹⁻¹¹. Moreover, based on the PB and PBA ability to capture selectively Cs^+ and Tl^+ ions^{12,13}, these NPs were synthesized in the team and employed as carriers of radioisotopes (^{201}Tl) to be used as nano-radiotracers for Single-Photon Emission Computed Tomography imaging (SPECT). Indeed, $^{201}\text{Tl}^+$ -based SPECT is a powerful diagnostic technique used in a nuclear medicine. However, the usual administration by intravenous (*iv*) of an aqueous TlCl solution leads to the clearing of 90% of the radioactive thallium ions from the blood and only 10% of the injected activity is used for imaging^{14,15}. Thus, the quick clearance of the contrast agents limits the time and efficiency of imaging. Then, the entrapment of the radioactive ions coupled with the presence of different stabilizing agents used to functionalize the NPs surface may permit to modify the biokinetics of the $^{201}\text{Tl}^+$ into the organism¹⁶, improving the efficiency of the contrast agent.

Pursuing in this line of thought, the double-layered core-shell heterostructures Au@NaNi^{II}Fe^{II}@NaFe^{II}Fe^{III} described in the previous chapter were used as nanoprobcs for SPECT/CT imaging. In the first time, similar-sized Na⁺/Fe³⁺/[Fe^{II}(CN)₆]⁴⁻ PB NPs were synthesized by self-assembly reaction without using stabilizing agents then post-synthetically grafted, as for the second approach described in chapter II, in order to compare the effect of gold to enhance the imaging contrast in CT. To select the stabilizing agents used in the *in vivo* studies, several organic molecules and polymers were grafted at the surface of the BP NPs, then the efficiency of the grafting was determined by IR spectroscopy. The stabilizing agents selected were also grafted on the double-layered core-shell Au@NaNi^{II}Fe^{II}@NaFe^{II}Fe^{III} NPs surface. The capacity of both NPs to entrap TI⁺ was studied, to determine the kinetic of the entrapment and the maximum adsorption capacity. Finally, the grafted PB and Au@NaNi^{II}Fe^{II}@NaFe^{II}Fe^{III} NPs were injected in mice and SPECT/CT images were acquired at different times, to determine the evolution of the NPs distribution in the organism. The effect of shape, composition, size and grafting of both the NPs (single PB or core-shell NPs) were investigated, and compared with the previous works on ultra-small PB NPs¹⁶.

V.2 Preparation, post-synthetic grafting and entrapment of Tl^+ of the $^{201}\text{Tl}^+$ nano-carriers.

V.2.1 Synthesis and characterization of the $\text{Na}^+/\text{Fe}^{3+}/[\text{Fe}^{\text{II}}(\text{CN})_6]^{4-}$ NPs.

As for the series of the larger $\text{K}^+/\text{Ni}^{2+}/[\text{Fe}(\text{CN})_6]^{3-}$ NPs obtained in the chapter II, the $\text{Na}^+/\text{Fe}^{3+}/[\text{Fe}^{\text{II}}(\text{CN})_6]^{4-}$ NPs were obtained by the two steps reaction consisting in first the self-assembly reaction between $\text{FeCl}_3 \cdot 6\text{H}_2\text{O}$ and $\text{K}_3[\text{Fe}(\text{CN})_6]$, in water at 25°C without stabilizing agents (figure 1) and secondly by a post-synthetic anchoring of the stabilizing agents at the NPs surface. Several stabilizing agents being tested, this latter step will be described latter. The first step consists in the dropwise addition at 2 mL/h of the aqueous solutions of $\text{FeCl}_3 \cdot 6\text{H}_2\text{O}$ (10 mM, 10 mL) and $\text{Na}_4[\text{Fe}(\text{CN})_6] \cdot 10\text{H}_2\text{O}$ (11.25 mM, 10 mL) simultaneously in 100 mL of ultrapure water under stirring. The formation of an intense and a turbid blue coloration indicates the formation of $\text{Na}^+/\text{Fe}^{3+}/[\text{Fe}^{\text{II}}(\text{CN})_6]^{4-}$ NPs (sample **15**). After addition, the solution was stirred one hour and the NPs were isolated by centrifugation, washed with water and ethanol, and finally dried under vacuum to give a blue powder. These NPs are re-dispersible in water and the as obtained suspensions are stable in water for several hours.

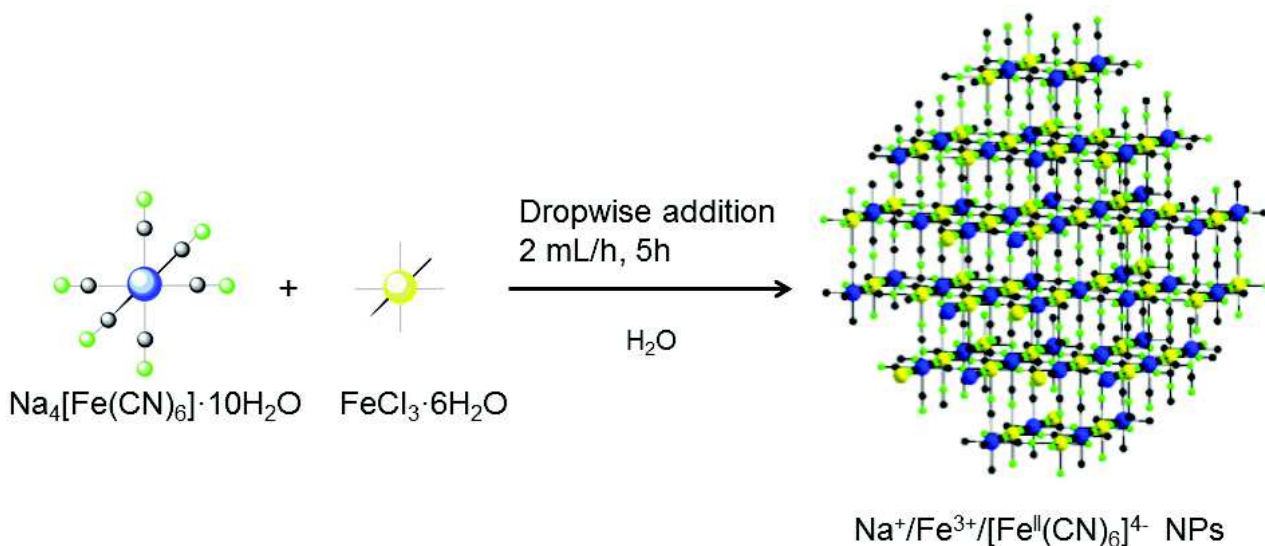


Figure 1: Schematic representation of the self-assembly reaction for the synthesis of $\text{Na}^+/\text{Fe}^{3+}/[\text{Fe}^{\text{II}}(\text{CN})_6]^{4-}$ NPs (sample **15**).

IR spectroscopy confirms the formation of the cyano-bridged network (figure 2). The broad band observed at 2080 cm^{-1} is characteristic of the $\text{Fe}^{\text{II}}-\text{C}\equiv\text{N}-\text{Fe}^{\text{III}}$ linkage, and is situated at the same value as the bulk analogous¹⁷. This is also provided by the presence of two bands, situated at 601 cm^{-1} and at 496 cm^{-1} , corresponding respectively to the stretching and the bending vibration of the $\text{Fe}^{\text{II}}-\text{CN}$ linkage typical to the PB structure¹⁷. The presence of water in the sample is attested by the presence of characteristic bands located in the $3700\text{--}3000\text{ cm}^{-1}$ region¹⁸. A very broad band at 3418 cm^{-1} corresponds to the $-\text{OH}$ stretching vibration of crystalized water molecules. A sharp band, located at 3631 cm^{-1} , is attributed to the water molecules coordinated to the metallic ions of the cyano-bridged

network, indicating the presence of several vacancies in the PB structure¹⁸. Finally, the bending vibration band corresponding to H-O-H linkage confirms the presence of crystalized water molecules in the structure.

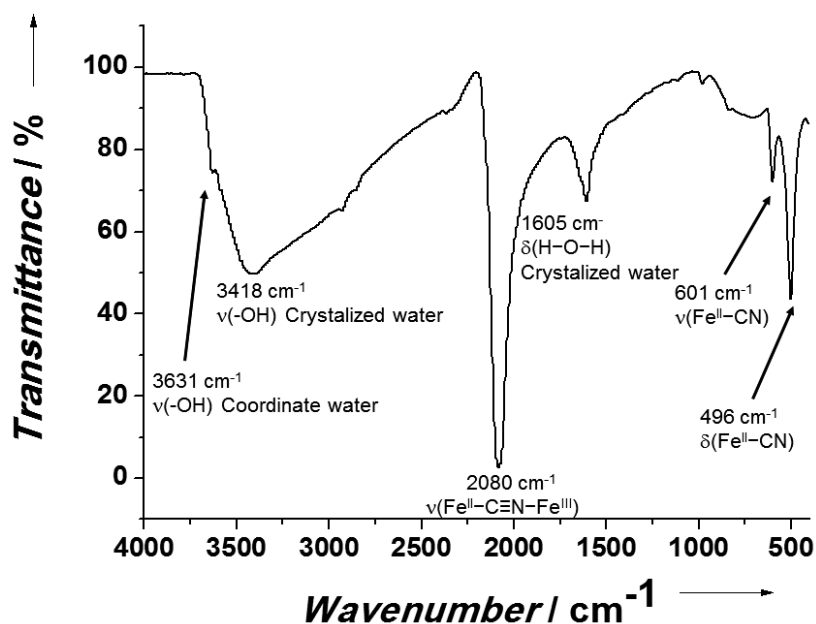


Figure 2: IR spectrum of $\text{Na}^+/\text{Fe}^{3+}/[\text{Fe}^{\text{II}}(\text{CN})_6]^{4-}$ NPs.

The composition of the $\text{Na}^+/\text{Fe}^{3+}/[\text{Fe}^{\text{II}}(\text{CN})_6]^{4-}$ NPs was determined by EDS, giving the metal amount, respectively 10.65 at.% of Na and 89.35 at.% of Fe. According to the general PB formula $\text{A}_{1-x}\text{Fe}[\text{Fe}(\text{CN})_6]_{1-(x/4)}$, the formula of the $\text{Na}^+/\text{Fe}^{3+}/[\text{Fe}^{\text{II}}(\text{CN})_6]^{4-}$ NPs was determined to be $\text{Na}_{0.1}\text{Fe}[\text{Fe}(\text{CN})_6]_{0.77}$.

The experimental XRD pattern performed on the $\text{Na}^+/\text{Fe}^{3+}/[\text{Fe}^{\text{II}}(\text{CN})_6]^{4-}$ NPs also confirms the formation of the PB structure (figure 3). Diffraction peaks observed at 15.15° , 17.5° , 24.9° , 35.3° , 39.65° , 43.6° , 50.7° , 54.1° and 57.3° are characteristics of the *fcc* PB structure (04-073-0687), which was indexed with the $Fm\bar{3}m$ space group. A value of 10.12 Å was obtained for the cell parameter using the (2 0 0) reflexion peak. The value of the crystallite size obtained using the Scherrer formula is 56 nm.

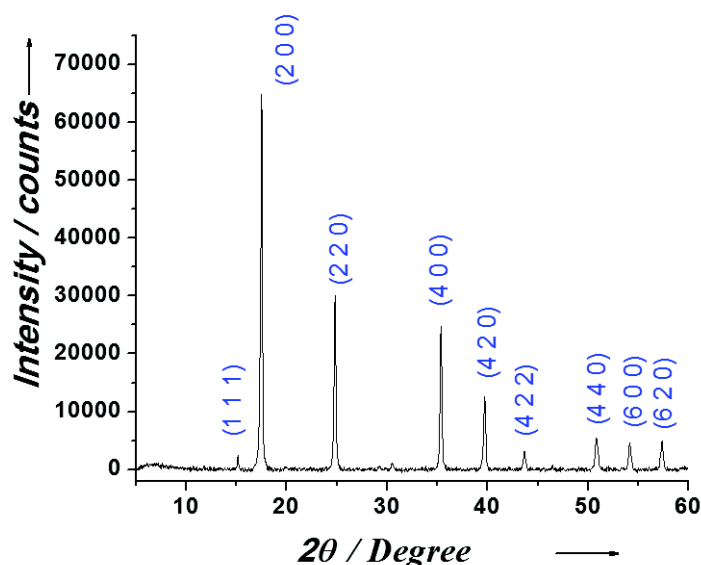


Figure 3: Powder X-Ray diffraction pattern of the $\text{Na}^+/\text{Fe}^{3+}/[\text{Fe}^{\text{II}}(\text{CN})_6]^{4-}$ NPs.

TEM images show the formation of well-defined and cubic $\text{Na}^+/\text{Fe}^{3+}/[\text{Fe}^{\text{II}}(\text{CN})_6]^{4-}$ NPs (figure 4). The size distribution of the NPs performed from the TEM images is 63.0 ± 8.7 nm, which is in a range closed to the $\text{Au}@[\text{NaNi}^{\text{II}}\text{Fe}^{\text{II}}]@[\text{NaFe}^{\text{II}}\text{Fe}^{\text{III}}]$ NPs used for the study (47.1 ± 6.8 nm).

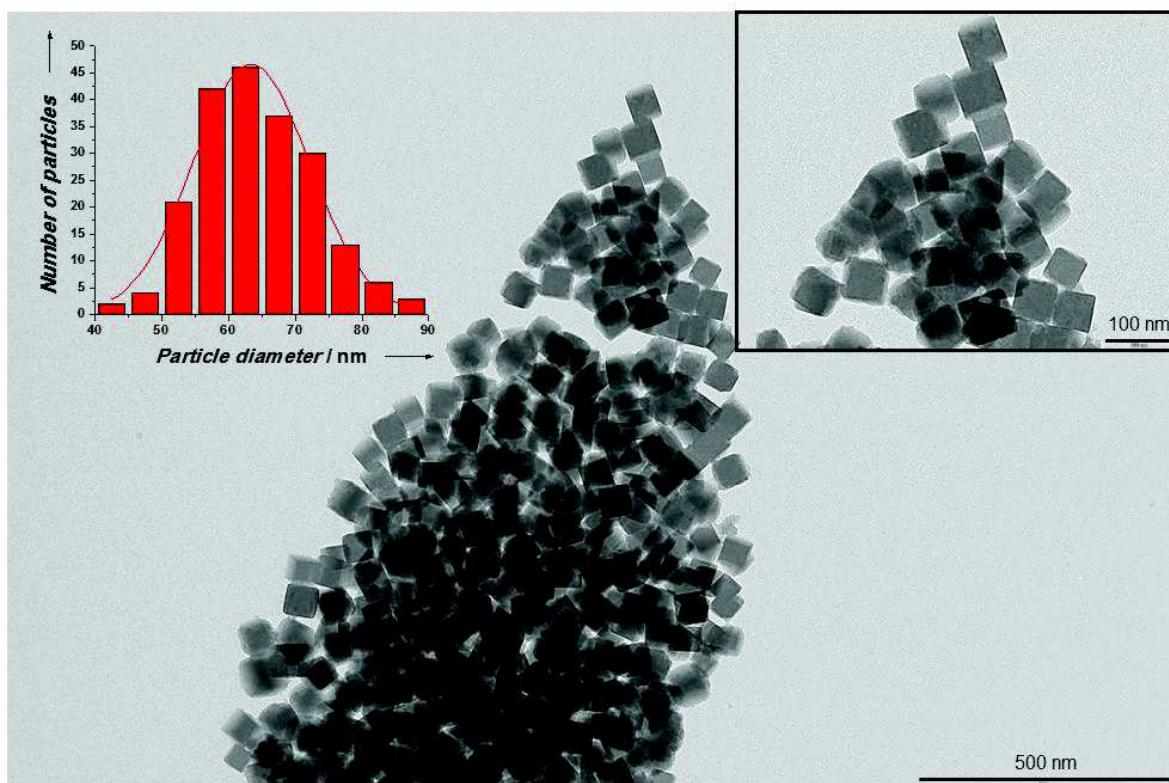


Figure 4: TEM images of the $\text{Na}^+/\text{Fe}^{3+}/[\text{Fe}^{\text{II}}(\text{CN})_6]^{4-}$ NPs.

Dynamic light-scattering (DLS) and zeta-potential measurements were performed on the $\text{Na}^+/\text{Fe}^{3+}/[\text{Fe}^{\text{II}}(\text{CN})_6]^{4-}$ NPs (**15**), first in water. DLS measurements give a value of the NPs hydrodynamic radius of 190 nm with a polydispersity index (PDI) of 0.2. The presence of a single and a narrow distribution of the hydrodynamic radius indicates no aggregation of the NPs in pure water. The value obtained for the Zeta potential is -32 mV, which is close to the value observed in the literature¹⁹, indicating a negative charge at the NPs surface, originated from the negatively charged $[\text{Fe}(\text{CN})_6]^{4-}$ moieties. This charge ensures the stabilization of the NPs and permits their dispersion in water. Then DLS and Zeta potential measurements were also performed in a saline solution (NaCl 0.9%), to be close to the *in vivo* conditions. DLS measurements give us a value of 1443 nm (PDI = 0.21) for the hydrodynamic radius of the $\text{Na}^+/\text{Fe}^{3+}/[\text{Fe}^{\text{II}}(\text{CN})_6]^{4-}$ NPs (**15**), which clearly indicates the presence of an aggregation. On the other hand, the $\text{Na}^+/\text{Fe}^{3+}/[\text{Fe}^{\text{II}}(\text{CN})_6]^{4-}$ NPs (**15**) exhibit a Zeta potential of -25 mV, which also provides the presence of the negative charges at the surface, due to the $[\text{Fe}^{\text{II}}(\text{CN})_6]^{4-}$ moieties. These results are similar to those obtained for the double-layered core-shell $\text{Au}@[\text{NaNi}^{\text{II}}\text{Fe}^{\text{II}}]@[\text{NaFe}^{\text{II}}\text{Fe}^{\text{III}}]$ NPs (**14-2**), with which we will compare the respective effects in imaging. In saline solution, these $\text{Au}@[\text{NaNi}^{\text{II}}\text{Fe}^{\text{II}}]@[\text{NaFe}^{\text{II}}\text{Fe}^{\text{III}}]$ NPs have a hydrodynamic radius of 1247 nm (PDI = 0.15) which also indicates the presence of an aggregation, and a Zeta potential of -15.3 mV which is coherent with the presence of $[\text{Fe}^{\text{II}}(\text{CN})_6]^{4-}$ moieties at the surface. As indicated by

the DLS/ Zeta potential measurements for both cases, the NPs dispersion are not really stable in saline media, which can be explained by the strength ionic effect. Indeed, contrary to the results obtained in pure water, the presence of ion salts in solution masks the surface charges, destabilizing the dispersion. Then it is necessary to stabilize these NPs by using stabilizing agents, as organic molecules or polymers. Moreover, these stabilizing agents may have an effect on the biodistribution of the NPs for *in vivo* experiments.

The $\text{Na}^+/\text{Fe}^{3+}/[\text{Fe}^{\text{II}}(\text{CN})_6]^{4-}$ NPs exhibit a strong absorption band in the near infrared region, from 500 to 900 nm, with a maximum of absorbance at 692 nm (figure 5). This broad band is originated from the intervalence charge-transfer band $\text{Fe}^{\text{III}}\text{-NC-Fe}^{\text{II}} \rightarrow \text{Fe}^{\text{II}}\text{-NC-Fe}^{\text{III}}$ occurring under the emitting-light source²⁰.

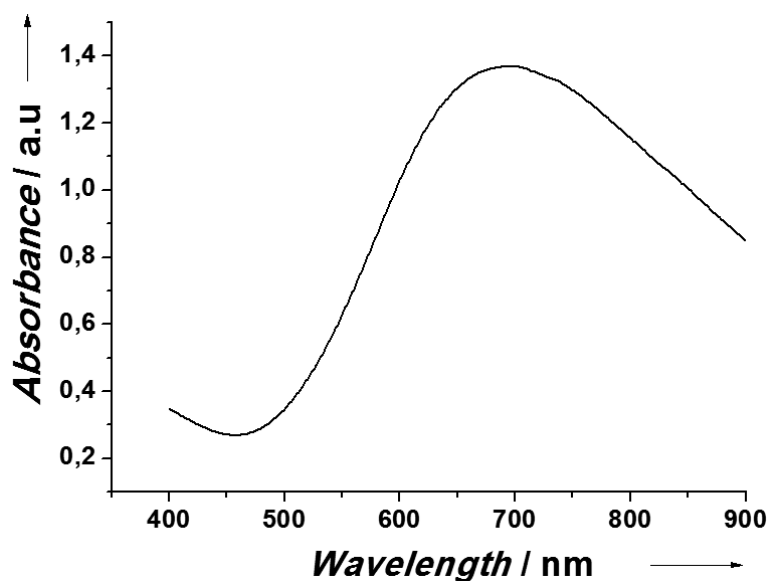


Figure 5: Electronic spectrum of the $\text{Na}^+/\text{Fe}^{3+}/[\text{Fe}^{\text{II}}(\text{CN})_6]^{4-}$ NPs.

Main characteristics	Na ⁺ /Fe ³⁺ /[Fe ^{II} (CN) ₆] ⁴⁻ NPs (15)	Au@NaNi ^{II} Fe ^{II} @NaFe ^{II} Fe ^{III} NPs (14-2)
FT-IR ν (-OH) (coordinate water) (cm ⁻¹)	3631	3617
FT-IR ν (-OH) (crystalized water) (cm ⁻¹)	3418	3412
FT-IR ν (Fe ^{II} -C≡N-Fe ^{III}) (cm ⁻¹)	2080	2081
FT-IR δ (H-O-H) (crystalized water) (cm ⁻¹)	1605	1609
FT-IR ν (Fe ^{II} -CN) (cm ⁻¹)	601	601
FT-IR δ (Fe ^{II} -CN) (cm ⁻¹)	496	499
EDS amount	Na/Fe 10.65/89.35	Au/K/Na/Ni/Fe 34.2/1/1.1/3.9/59.8
formula	Na _{0.1} Fe[Fe(CN) ₆] _{0.77}	Au _{8.7} @K _{0.24} Na _{0.27} Ni[Fe(CN) ₆] _{0.63} @Fe _{8.3} [Fe(CN) ₆] _{6.2}
Lattice parameter (Å)	10.12	a _{Gold} = 4.07 a _{PB} = 17.17
Debye Scherrer size (nm)	56	d _{Gold} = 16.5 d _{PB} = 26
TEM size (nm)	63.0 ± 8.7	Core = 19.8 ± 3.2 Total size = 47.1 ± 6.8
Hydrodynamic radius (in saline solution, nm)	1443 (PDI = 0.20)	1247 (PDI = 0.15)
Zeta potential (in saline solution, mV)	-25.0	-15.3
Maximum of absorbance (nm)	692 intervalence absorption band Fe ^{II} -CN-Fe ^{III} → Fe ^{III} -CN-Fe ^{II}	538 SPR band 710 intervalence absorption band Fe ^{II} -CN-Fe ^{III} → Fe ^{III} -CN-Fe ^{II}

Table 1: Table summarizing the main characteristics of the Na⁺/Fe³⁺/[Fe^{II}(CN)₆]⁴⁻ NPs (15). To compare with the Au@NaNi^{II}Fe^{II}@NaFe^{II}Fe^{III} NPs (14-2) used in the study, the main characteristics are also summarized in the table.

V.2.2 Post-synthetic grafting of the $\text{Na}^+/\text{Fe}^{3+}/[\text{Fe}^{\text{II}}(\text{CN})_6]^{4-}$ and the $\text{Au}@\text{NaNi}^{\text{II}}\text{Fe}^{\text{II}}@\text{NaFe}^{\text{II}}\text{Fe}^{\text{III}}$ NPs.

As described in chapter II, the post-synthetic grafting of stabilizing agents was performed for the $\text{Na}^+/\text{Fe}^{3+}/[\text{Fe}^{\text{II}}(\text{CN})_6]^{4-}$ NPs (**15**) and $\text{Au}@\text{NaNi}^{\text{II}}\text{Fe}^{\text{II}}@\text{NaFe}^{\text{II}}\text{Fe}^{\text{III}}$ NPs (**14-2**). This step was achieved by mixing the NPs with the stabilizing agents in the stoichiometry 1:1, in water under stirring for 24h. Preliminary, the NPs were dispersed in water by sonication, to avoid any aggregation of the particles, permitting the maximal dispersibility to favor the grafting. After 24h, the grafter NPs were centrifuged and washed several times with water to remove any trace of ungrafted stabilizing agents, then dried under vacuum.

To select the stabilizing agents used later and after for imaging, several molecules and polymers were grafted on the surface of $\text{Na}^+/\text{Fe}^{3+}/[\text{Fe}^{\text{II}}(\text{CN})_6]^{4-}$ NPs (**15**), and the efficiency was investigated using IR spectroscopy, before the grafting of the $\text{Au}@\text{NaNi}^{\text{II}}\text{Fe}^{\text{II}}@\text{NaFe}^{\text{II}}\text{Fe}^{\text{III}}$ NPs (**14-2**) with the selected stabilizing agents. We have selected two sugars, Sucrose and D-Mannitol, two polymers, Dextran 6000 g/mol and PEG-NH₂ 1500 g/mol, which are biocompatibles²¹⁻²⁴ (figure 6). Moreover, in collaboration with Dr. Cyrille Boyer from school of Chemical Engineering, University of New South Wales, Sydney, Australia, two polymers recently developed, and which may present biological interest, were grafted on the surface of the $\text{Na}^+/\text{Fe}^{3+}/[\text{Fe}^{\text{II}}(\text{CN})_6]^{4-}$ NPs (figure 7).

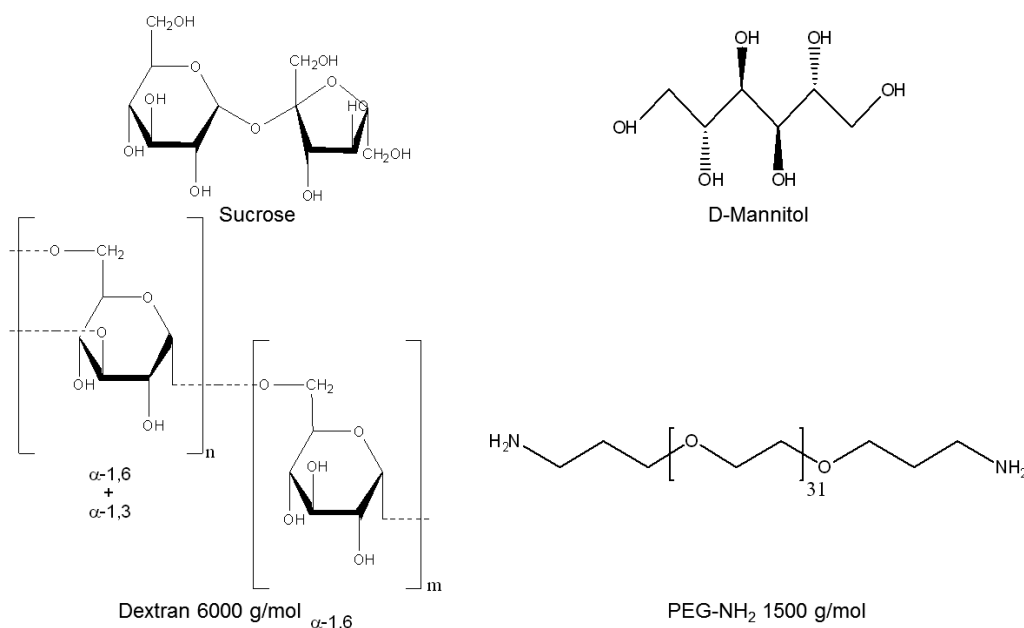


Figure 6: molecular structures of the organic molecules and polymers selected.

IR spectra of all the grafted $\text{Na}^+/\text{Fe}^{3+}/[\text{Fe}^{\text{II}}(\text{CN})_6]^{4-}$ NPs confirm the presence of the cyano-bridged network of the PB NPs with the same bands observed previously and summarized in table 1, as particularly the band located at 2080 cm^{-1} corresponding to the $\text{Fe}^{\text{II}}-\text{C}\equiv\text{N}-\text{Fe}^{\text{III}}$ linkage (figures 8 to 12). This indicates that the PBA structure remains unchanged during the grafting step.

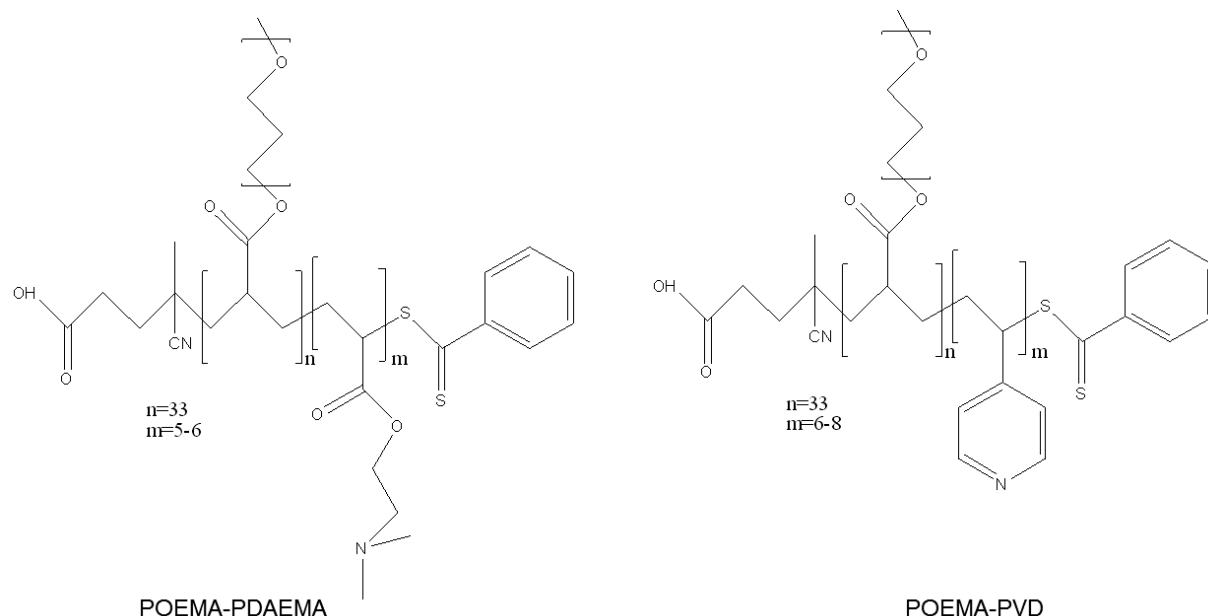


Figure 7: molecular structures of the polymers synthesized by Dr. Cyrille Boyer, and used in collaboration for the grafting of the $\text{Na}^+/\text{Fe}^{3+}/[\text{Fe}^{\text{II}}(\text{CN})_6]^{4-}$ NPs.

The achievement of the grafting at the surface of the $\text{Na}^+/\text{Fe}^{3+}/[\text{Fe}^{\text{II}}(\text{CN})_6]^{4-}$ NPs (**15**) is attested for all the organic molecules/polymers used, by the presence of several characteristic bands, summarized in table 2. For all grafted NPs, two bands are observed at around 2920 and 2850 cm^{-1} , corresponding to the stretching vibration of C-H bonds. The presence of is provided by the presence of the stretching vibration band of C-O bond located at 1136 cm^{-1} and 1079 cm^{-1} can be attribute to ether groups (sucrose, dextran), ethylene glycol groups (PEG-NH₂, POEMA-PDAEMA, POEMA-PVD), primary and secondary alcohol groups (sucrose, D-mannitol, dextran) or ester/carboxylic acid groups (POEMA-PDAEMA, POEMA-PVD). The bands observed in the $1000\text{-}700\text{ cm}^{-1}$ region are attributed to C-C linkage, corresponding to the carbon skeleton, and the bending vibration band at around 720 cm^{-1} , corresponding to $-\text{CH}_2$ groups, are typical of the aliphatic chain, which also provides the grafting of the organic molecules/polymers at the NPs surface.

The grafting of the sucrose is also provided by bands corresponding to the bending vibration of O-H bonds located at 1350 and 1260 cm^{-1} , characteristic of the primary and secondary alcohol groups (figure 8). Similar bands, observed at 1364 and 1265 cm^{-1} , also confirmed the presence of the D-mannitol (figure 9) and Dextran (figure 10) at the NPs surface.

The stretching vibration band of C-N bond visible at 1234 cm^{-1} , and the stretching vibration band of N-H at 1643 cm^{-1} are characteristic of the primary amino groups, and then confirm the grafting of the $\text{Na}^+/\text{Fe}^{3+}/[\text{Fe}^{\text{II}}(\text{CN})_6]^{4-}$ NPs (**15**) by PEG-NH₂ (figure 11).

Finally, the grafting with the POEMA-PDAEMA and POEMA-PVD polymers is confirmed with the presence in both case of the stretching vibration band at 1388 cm^{-1} , characteristic of C=S bond and attributed to the dithioester groups. Moreover, the presence of the stretching vibration band at 1723 cm^{-1} corresponding to the C=O bonds of ester/carboxylic acid groups, and the stretching vibration band of C=C bonds, characteristic of the aromatic rings, clearly provides the obtaining of $\text{Na}^+/\text{Fe}^{3+}/[\text{Fe}^{\text{II}}(\text{CN})_6]^{4-}$ /grafted POEMA-PDAEMA NPs (figure 12) and POEMA-PVD NPs (figure 13).

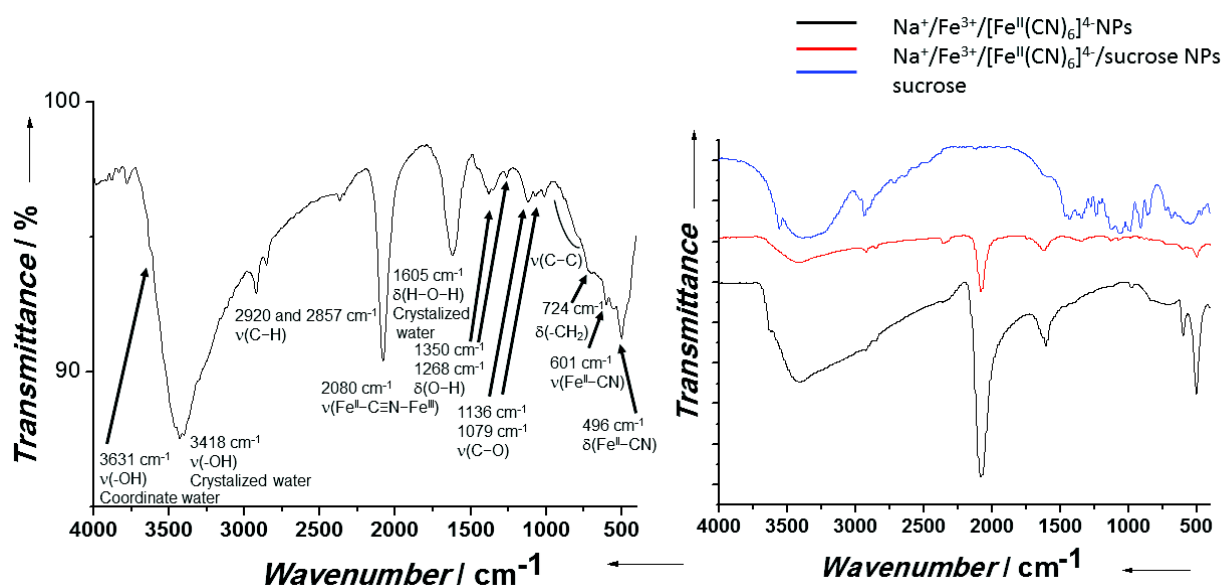


Figure 8: Left: IR spectrum of the $\text{Na}^+/\text{Fe}^{3+}/[\text{Fe}^{\text{II}}(\text{CN})_6]^{4-}$ /grafted Sucrose NPs. Right: comparison of the IR spectra of sucrose, the ungrafted and the grafted $\text{Na}^+/\text{Fe}^{3+}/[\text{Fe}^{\text{II}}(\text{CN})_6]^{4-}$ NPs (15).

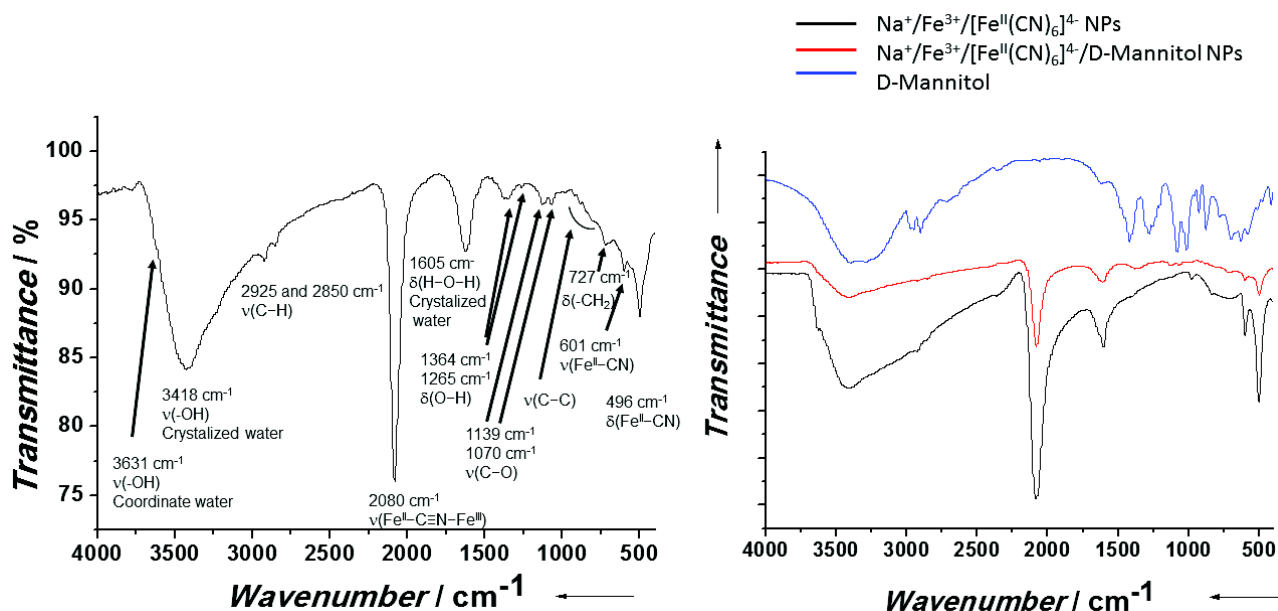


Figure 9: Left: IR spectrum of the $\text{Na}^+/\text{Fe}^{3+}/[\text{Fe}^{\text{II}}(\text{CN})_6]^{4-}$ /grafted D-Mannitol NPs. Right: comparison of the IR spectra of D-Mannitol, the ungrafted and the grafted $\text{Na}^+/\text{Fe}^{3+}/[\text{Fe}^{\text{II}}(\text{CN})_6]^{4-}$ NPs (15).

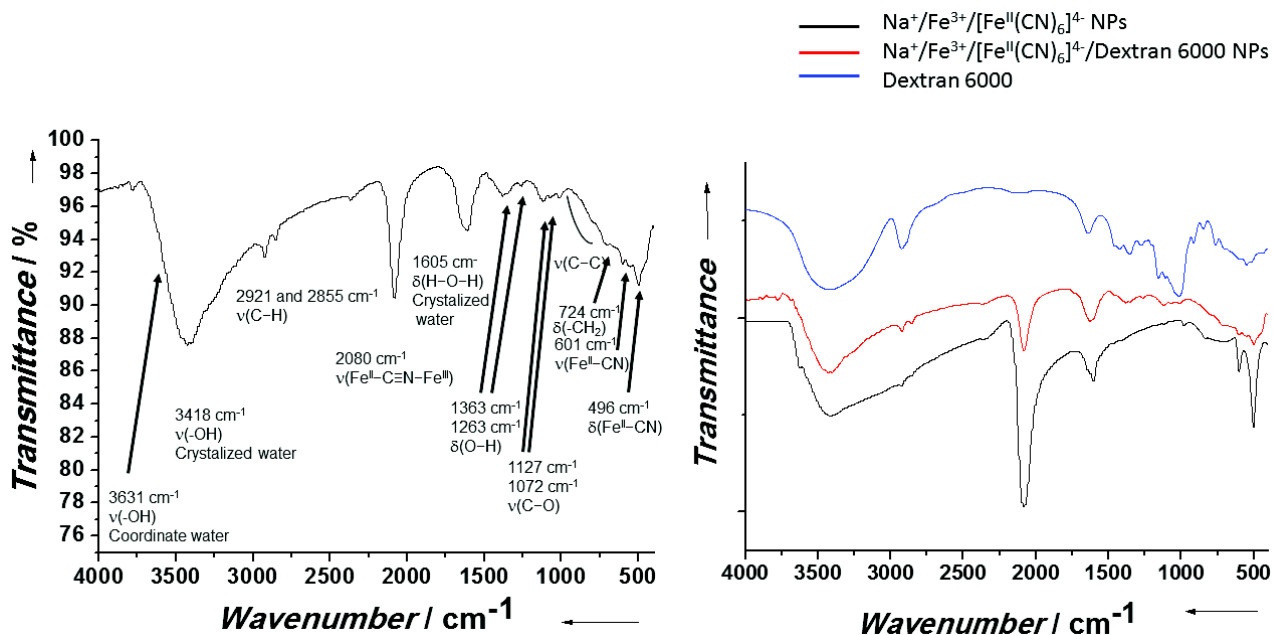


Figure 10: Left: IR spectrum of the $\text{Na}^+/\text{Fe}^{3+}/[\text{Fe}^{\text{II}}(\text{CN})_6]^{4-}$ /grafted Dextran 6000 g/mol NPs. Right: comparison of the IR spectra of Dextran 6000 g/mol, the ungrafted and the grafted $\text{Na}^+/\text{Fe}^{3+}/[\text{Fe}^{\text{II}}(\text{CN})_6]^{4-}$ NPs (15).

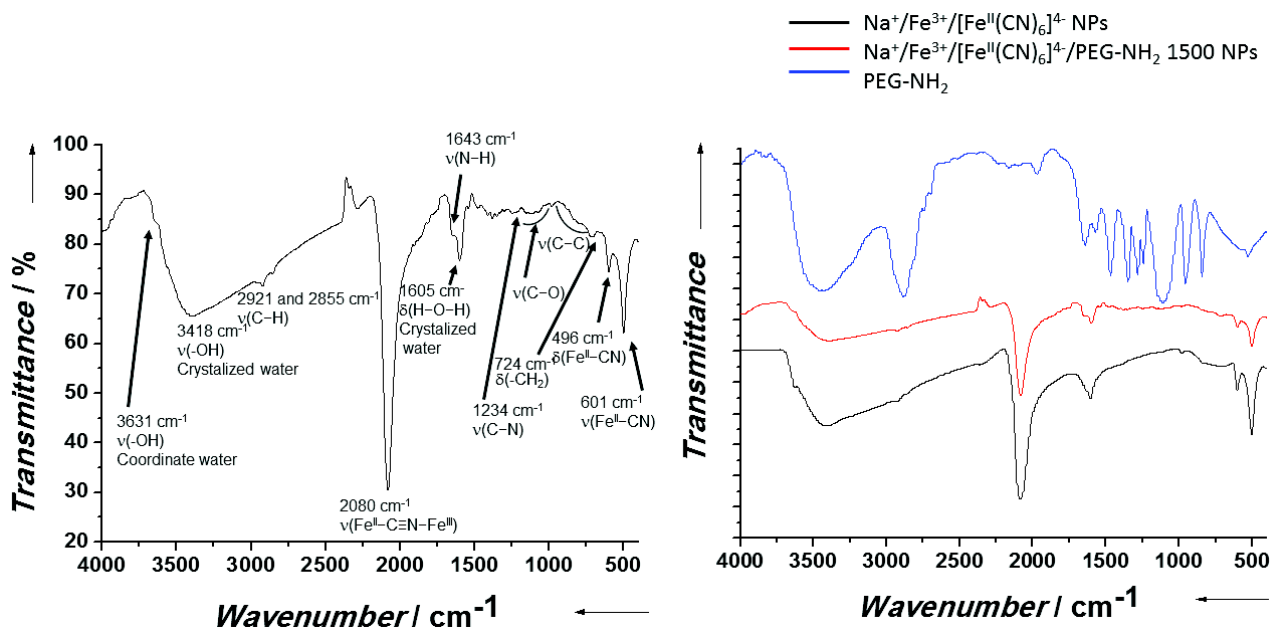


Figure 11: Left: IR spectrum of the $\text{Na}^+/\text{Fe}^{3+}/[\text{Fe}^{\text{II}}(\text{CN})_6]^{4-}$ /grafted PEG-NH₂ 1500 g/mol NPs. Right: comparison of the IR spectra of PEG-NH₂ 1500 g/mol, the ungrafted and the grafted $\text{Na}^+/\text{Fe}^{3+}/[\text{Fe}^{\text{II}}(\text{CN})_6]^{4-}$ NPs (15).

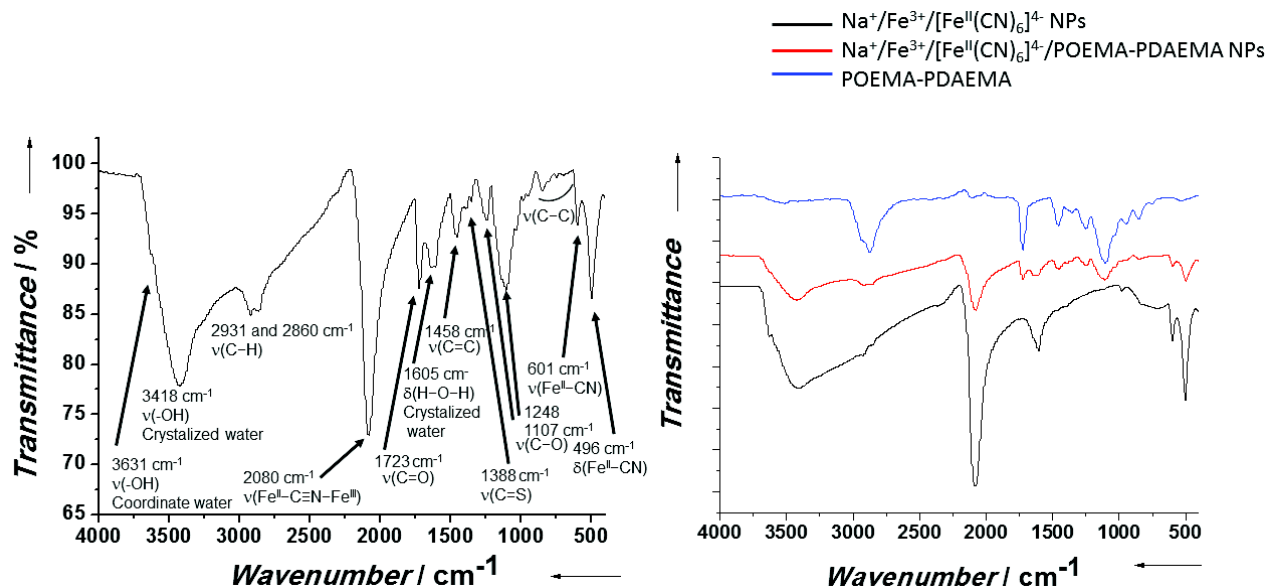


Figure 12: Left: IR spectrum of the $\text{Na}^+/\text{Fe}^{3+}/[\text{Fe}^{\text{II}}(\text{CN})_6]^{4-}$ /grafted POEMA-PDAEMA NPs. Right: comparison of the IR spectra of POEMA-PDAEMA the ungrafted and the grafted $\text{Na}^+/\text{Fe}^{3+}/[\text{Fe}^{\text{II}}(\text{CN})_6]^{4-}$ NPs (15).

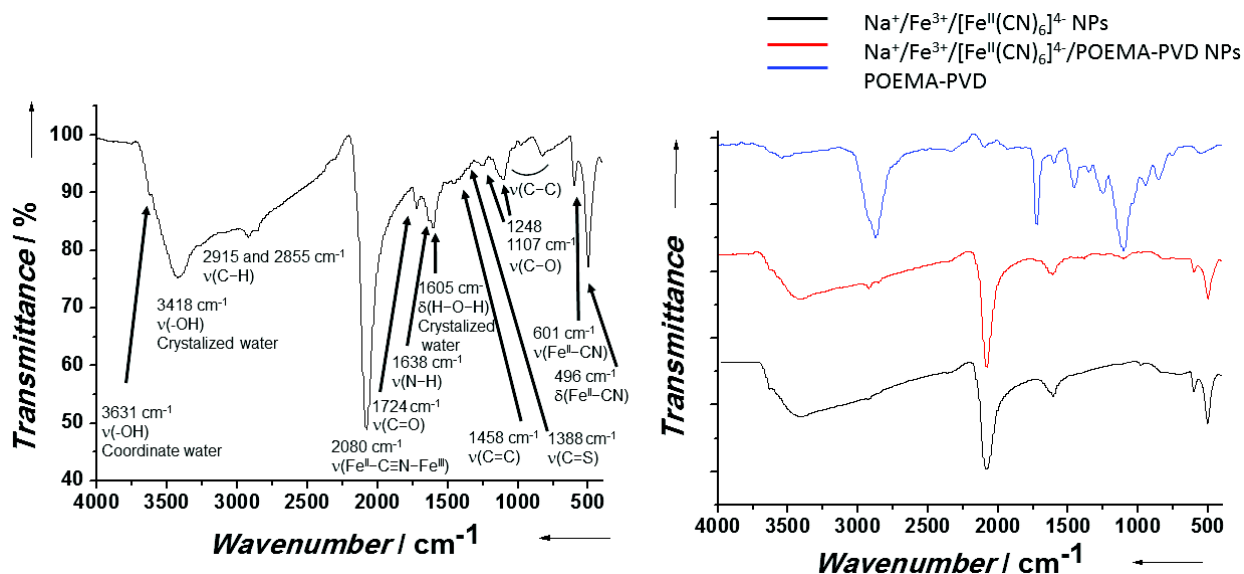


Figure 13: Left: IR spectrum of the $\text{Na}^+/\text{Fe}^{3+}/[\text{Fe}^{\text{II}}(\text{CN})_6]^{4-}$ /grafted POEMA-PVD NPs. Right: comparison of the IR spectra of POEMA-PVD, the ungrafted and the grafted $\text{Na}^+/\text{Fe}^{3+}/[\text{Fe}^{\text{II}}(\text{CN})_6]^{4-}$ NPs (15).

FT-IR bands	PB/grafted Sucrose NPs.	PB/grafted D-Mannitol NPs	PB/grafted Dextran 6000 g/mol NPs	PB/grafted PEG-NH ₂ 1500 g/mol NPs	PB/grafted POEMA-PDAEMA NPs	PB/grafted POEMA-PVD NPs
$\nu(\text{C-H})$ (cm^{-1})	2920 and 2857	2925 and 2850	2921 and 2855	2926 and 2851	2931 and 2860	2915 and 2855
$\nu(\text{C-O})$ (cm^{-1})	1136 and 1079 (alcohol and ether groups)	1139 and 1070 (alcohol groups)	1127 and 1072 (alcohol and ether groups)	1200, 1157 and 1072 (ethylene glycol groups)	1248 and 1107 (ethylene glycol and ester/carboxylic acids groups)	1248 and 1107 (ethylene glycol and ester/carboxylic acids groups)
$\nu(\text{C-C})$ (cm^{-1})	987, 920, 887, 851 and 812	982, 927 and 887	1012	987, 917 and 880	992 and 852	822
$\delta(-\text{CH}_2)$ (cm^{-1})	724	727	721	711		
$\delta(\text{O-H})$ (cm^{-1})	1350 and 1268 (alcohol groups)	1364 and 1265 (alcohol groups)	1363 and 1263 (alcohol groups)			
$\nu(\text{C-N})$ (cm^{-1})				1234 (primary amino groups)		
$\nu(\text{N-H})$ (cm^{-1})				1643 (primary amino groups)		1638 primary amino groups)
$\nu(\text{C=O})$ (cm^{-1})					1723 (ester/carboxylic acids groups)	1724
$\nu(\text{C=C})$ (cm^{-1})					1458 and 1353 (aromatic rings)	1463 aromatic rings)
$\nu(\text{C=S})$ (cm^{-1})					1388 (dithioester groups)	1388 (dithioester groups)

Table 2: Table summarizing the main FT-IR bands characteristic of the organic molecules/ polymers grafted at the surface of the $\text{Na}^+/\text{Fe}^{3+}/[\text{Fe}^{\text{II}}(\text{CN})_6]^{4-}$ NPs (**15**).

For all the stabilizing agents used, the comparison between the spectra of respectively the ungrafted $\text{Na}^+/\text{Fe}^{3+}/[\text{Fe}^{\text{II}}(\text{CN})_6]^{4-}$ NPs, the organic molecules/the polymers and the grafted NPs provided the achievement of the grafting, by the appearance of the same bands corresponding to the organic molecule/the polymer on the IR spectrum of the grafted $\text{Na}^+/\text{Fe}^{3+}/[\text{Fe}^{\text{II}}(\text{CN})_6]^{4-}$ NPs. However, the relative intensities of the bands corresponding to the PB NPs and the organic molecules/polymers are different according to the stabilizing agent use, which may indicate that the surface of the NPs is not totally grafted. It may be confirmed by quantitative techniques, such as elemental analysis or thermogravimetric analysis (TGA). Note that, according to the IR spectra, the grafting of the NPs surface with small molecules as sugars (Sucrose and D-Mannitol) seems to be incomplete and not sufficient to stabilize the NPs in aqueous media. Even if the grafting is incomplete, the use of PEG-NH₂ is efficient and has previously been provided on $\text{K}^+/\text{Ni}^{2+}/[\text{Fe}^{\text{III}}(\text{CN})_6]^{3-}$ NPs in the chapter II, and PEG are known to be used in biomedical applications since several years²¹⁻²⁴. However, recent studies have revealed the drawback of the PEGylated polymers, and their potential toxicity is still discussed²⁴. At the opposite, the Dextran, which is biocompatible and presents no toxicity, is a promising stabilizing agent for biomedical applications and has already been used to stabilize NPs²⁵⁻³¹. Moreover, the IR spectroscopy showed us that the grafting of Dextran at the surface of the NPs is effective. On the other hand, the polymers POEMA-PDAEMA and POEMA-PVD studied in collaboration with Dr. Cyrille Boyer may present biological activity, with the presence of carboxylic acid, tertiary amino and cyano groups. Both polymers can be used as stabilizing agents to graft the NPs surface, as indicated by the IR spectra, however the POEMA-PVD seems to present a certain toxicity. Then, accordingly to these considerations, we have selected Dextran 6000 g/mol and POEMA-PDAEMA for our *in vivo* studies.

As for the $\text{Na}^+/\text{Fe}^{3+}/[\text{Fe}^{\text{II}}(\text{CN})_6]^{4-}$ NPs, the $\text{Au}@\text{NaNi}^{\text{II}}\text{Fe}^{\text{II}}@\text{NaFe}^{\text{II}}\text{Fe}^{\text{III}}$ NPs (**14-2**) were grafted with Dextran 6000 g/mol and POEMA-PDAEMA using the same protocol. IR spectroscopy confirms the grafting of the $\text{Au}@\text{NaNi}^{\text{II}}\text{Fe}^{\text{II}}@\text{NaFe}^{\text{II}}\text{Fe}^{\text{III}}$ NPs with both the Dextran (figure 14) and the POEMA-PDAEMA (figure 15). As for the grafted $\text{Na}^+/\text{Fe}^{3+}/[\text{Fe}^{\text{II}}(\text{CN})_6]^{4-}$ NPs two bands are observed at 2931 and 2860 cm^{-1} , in the C-H stretching region. The presence of bands in the 1050-1200 cm^{-1} region, corresponding to the stretching vibration of C-O bond, indicates the presence of the ether and alcohol groups of Dextran, Polyethylene glycol groups and ester/carboxylic acid groups for the POEMA-PDAEMA. Several stretching vibration bands are observed in the 1000-700 cm^{-1} , characteristic of the carbon skeleton, and the bending vibration band located at 724 cm^{-1} is typical of the $-\text{CH}_2$ groups, providing the presence of the organic molecules/polymers at the NPs surface. For the Dextran, the bending vibration bands of O-H at 1378 and 1263 cm^{-1} also provide the presence of the alcohol groups. For the POEMA-PDAEMA, the stretching vibration band of the C=O bond, characteristic of the ester and carboxylic acid groups is observed at 1730 cm^{-1} . The double C=C bond of the aromatic ring are attested by the stretching vibration band at 1458 cm^{-1} , and the band at 1388 cm^{-1} may be attributed to the dithioester groups, confirming the efficiency of the grafting.

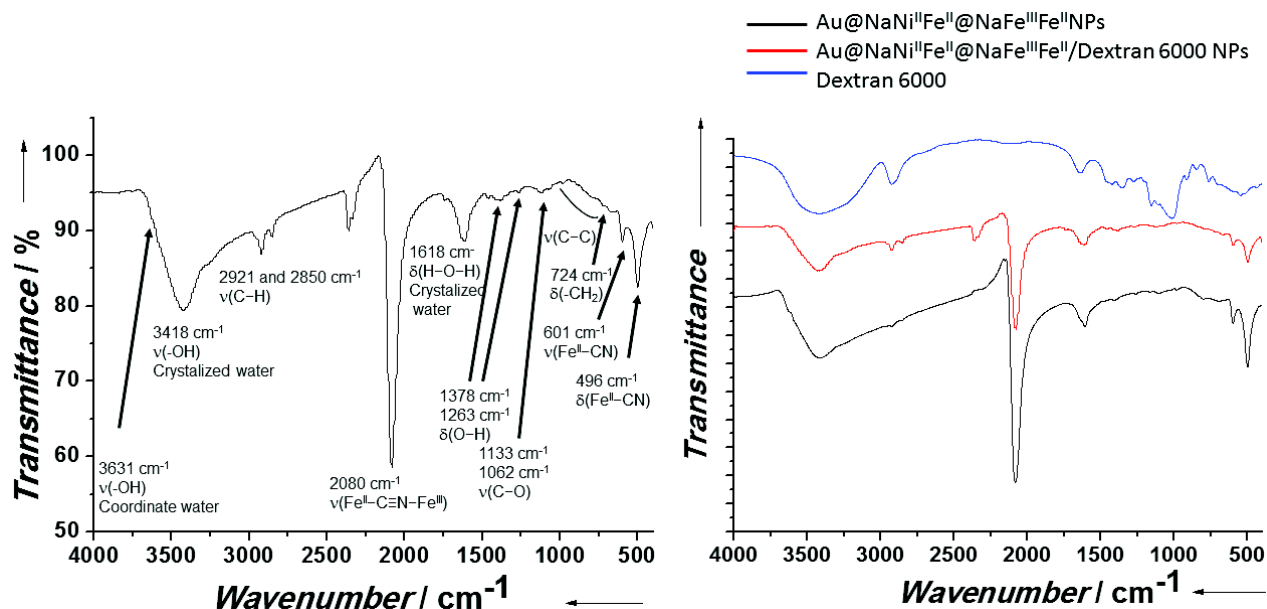


Figure 14: Left: IR spectrum of the Au@NaNi^{II}Fe^{II}@NaFe^{III}Fe^{III}/ grafted Dextran 6000 g/mol NPs. Right: comparison of the IR spectra of Dextran 6000 g/mol, the ungrafted and the grafted Au@NaNi^{II}Fe^{II}@NaFe^{III}Fe^{III} NPs (14-2).

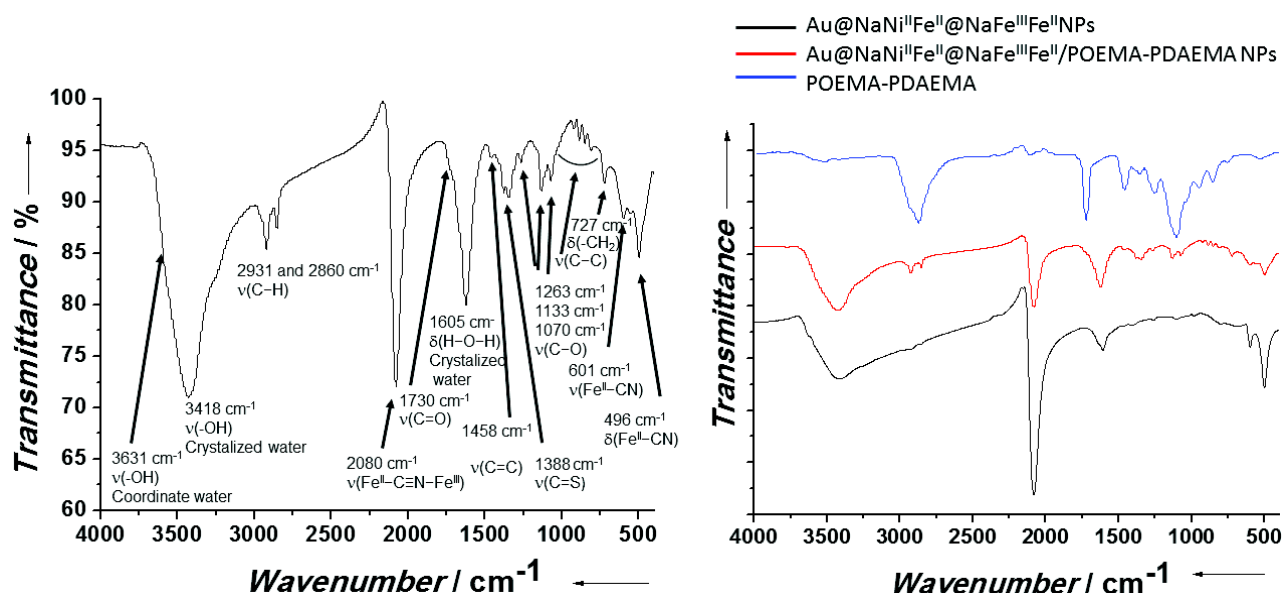


Figure 15: Left: IR spectrum of the the Au@NaNi^{II}Fe^{II}@NaFe^{III}Fe^{III}/POEMA-PDAEMA NPs. Right: comparison of the IR spectra of POEMA-PDAEMA, the ungrafted and the grafted Au@NaNi^{II}Fe^{II}@NaFe^{III}Fe^{III} NPs (14-2).

DLS and Zeta potential measurements can also give indication on the efficiency of the grafting step and the effect of the stabilizing agents on the NPs dispersibility in aqueous solution. As previously, all the measurements were performed in saline solution (NaCl 0.9%) to be close to the *in vivo* conditions. Previously, the DLS measurements have given us a value of 1443 nm (PDI = 0.21) for the hydrodynamic radius of the Na⁺/Fe³⁺/[Fe^{II}(CN)₆]⁴⁻ NPs (15), which clearly indicates the presence of aggregation. The presence of Dextran and POEMA-PDAEMA at the NPs surface leads to values of the hydrodynamic radius of respectively 765 nm (PDI = 0.26) and 154 nm (PDI = 0.2). On other hand, the Zeta potential measured after the grafting step indicates -20.7 mV for Na⁺/Fe³⁺/[Fe^{II}(CN)₆]⁴⁻/grafted Dextran and -1.0 mV for Na⁺/Fe³⁺/[Fe^{II}(CN)₆]⁴⁻/grafted POEMA-PDAEMA. Comparatively to the Na⁺/Fe³⁺/[Fe^{II}(CN)₆]⁴⁻ NPs (-25 mV), the increase

of the Zeta potential is in accordance with the masking of the negative charges at the NPs surface by the stabilizing agents. Then, that provides the efficiency of the grafting step, confirming the results obtained by IR spectroscopy. Moreover, the decrease of the hydrodynamic radius before and after grafting shows an improvement of the stabilization of the NPs dispersion. The comparison between the effect of Dextran and POEMA-PDAEMA seems indicates for both hydrodynamic radius and Zeta potential values that the latter is more efficient than the former to stabilize the dispersion in saline solution. This may be originated from the amount of polymer chains grafted at the surface, and to the nature and the strength of the bonds permitting to anchor the stabilizing agent to the surface. Similar results were also obtained for the Au@NaNi^{II}Fe^{II}@NaFe^{II}Fe^{III} NPs (**14-2**). The grafting of both Dextran and POEMA-PDAEMA induces a decrease of the hydrodynamic radius and the Zeta potential, with values of 918.6 nm (PDI = 0.12) and -11.2 mV for Au@NaNi^{II}Fe^{II}@NaFe^{II}Fe^{III}/grafted Dextran NPs and 241.7 nm (PDI = 0.25) and -1.7 mV for Au@NaNi^{II}Fe^{II}@NaFe^{II}Fe^{III}/grafted POEMA-PDAEMA NPs. Comparatively to the Au@NaNi^{II}Fe^{II}@NaFe^{II}Fe^{III} NPs (hydrodynamic radius of 1247 nm (PDI = 0.15) and Zeta potential of -15.3 mV), these results confirm the surface modification of the Au@NaNi^{II}Fe^{II}@NaFe^{II}Fe^{III}, and are in agreement with those obtained for the Na⁺/Fe³⁺/[Fe^{II}(CN)₆]⁴⁻ NPs.

The higher ability of the POEMA-PDAEMA to stabilize the NPs dispersion, comparatively to the Dextran, may have an influence on the *in vivo* experiments. Nevertheless, the stabilization of the NPs dispersion is sufficient to use this nano-objects for imaging applications.

Finally, the grafting of the NPs surface with Dextran 6000 g/mol was provided by using STEM and EDS mapping. On the STEM image of the Na⁺/Fe³⁺/[Fe^{II}(CN)₆]⁴⁻/grafted Dextran 6000 g/mol NPs, the presence of the organic matrix at the surface of the Na⁺/Fe³⁺/[Fe^{II}(CN)₆]⁴⁻ NPs is clearly visible, indicating the achievement of the post-synthetic grafting (figure 16). Moreover, the EDS mapping of Fe and C performed on the Na⁺/Fe³⁺/[Fe^{II}(CN)₆]⁴⁻/grafted Dextran 6000 g/mol NPs and the Au@NaNi^{II}Fe^{II}@NaFe^{II}Fe^{III}/Dextran 6000 g/mol NPs shows the presence of a thin thickness of a carbon-based material at the surface of the NPs (figures 16 and 17). PB is composed by both, iron and carbon, then this difference is explained by the presence of the organic material, the Dextran, at the surface of the particles.

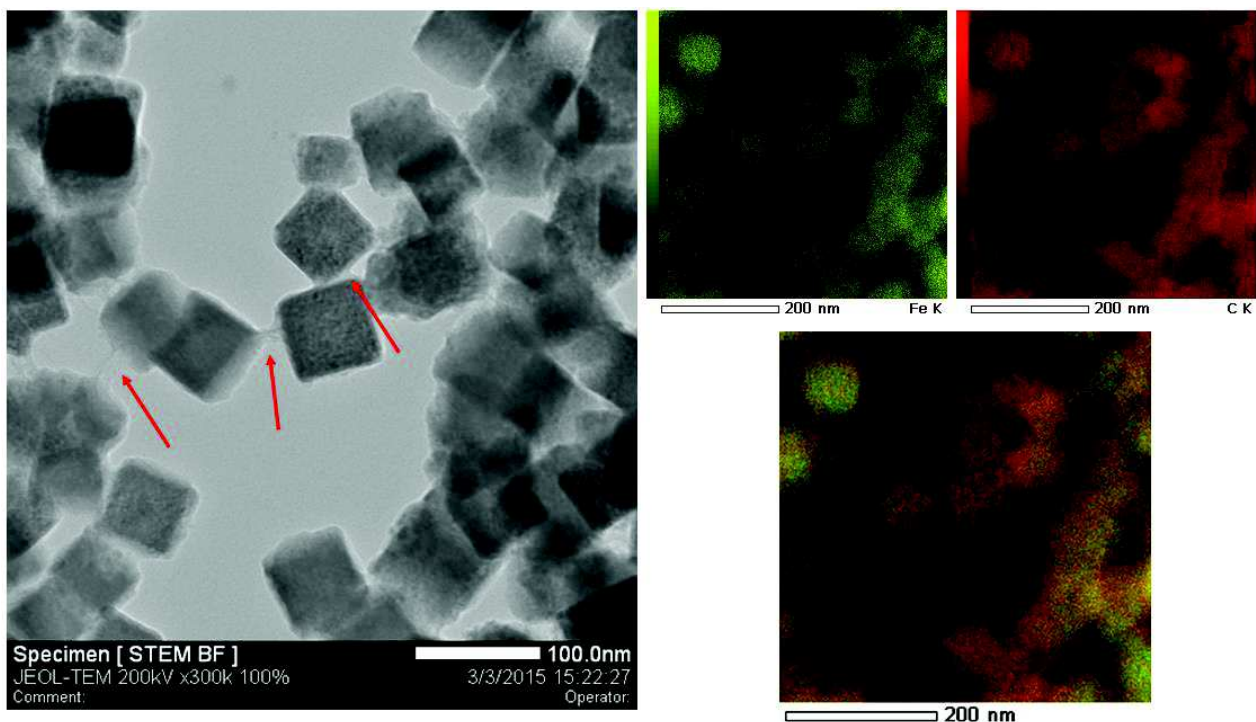


Figure 16: Left: STEM image of $\text{Na}^+/\text{Fe}^{3+}/[\text{Fe}^{\text{II}}(\text{CN})_6]^{4-}$ /grafted Dextran 6000 g/mol NPs. Right: Topochemical repartition of the Fe (green) and C (red) in the grafted NPs, and overlay of these two elements.

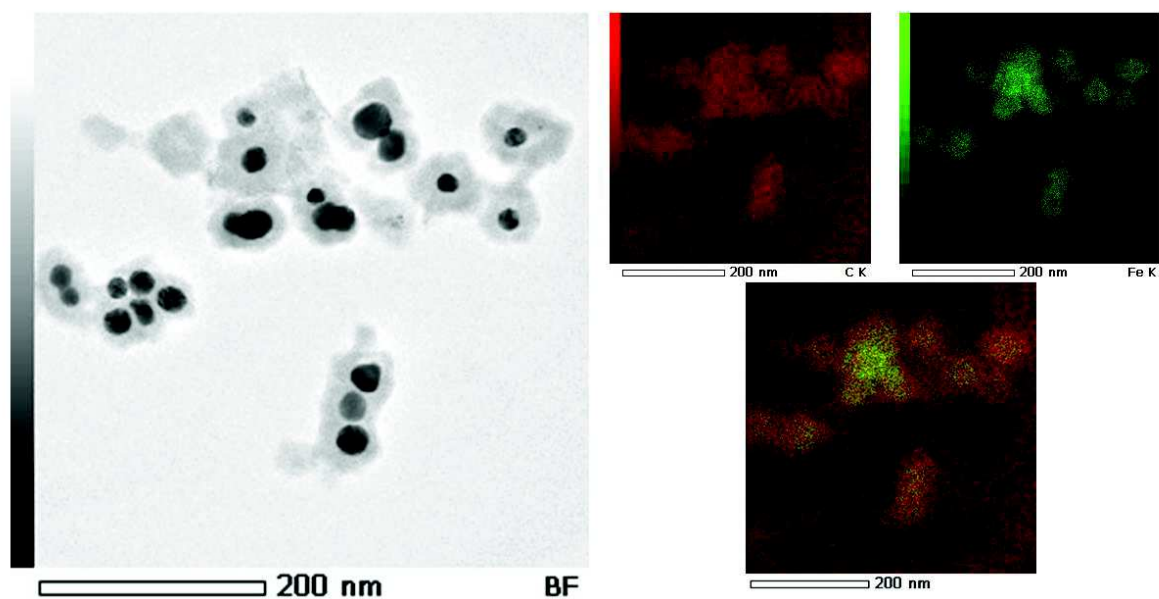


Figure 17: Left: $\text{Au}@\text{NaNi}^{\text{II}}\text{Fe}^{\text{II}}@\text{NaFe}^{\text{II}}\text{Fe}^{\text{III}}$ /Dextran 6000 g/mol NPs. Right: Topochemical repartition of the Fe (green) and C (red) in the grafted NPs, and overlay of these two elements.

To conclude, the stabilization of the NPs in aqueous media have been performed by using Dextran 6000 g/mol and POEMA-PDAEMA as stabilizing agents grafted in the post-synthetic grafting step at the NPs surface. These polymers may ensure the circulation and the non-aggregation in the organism without avoiding the capture of Ti^+ ions by the PB structure.

V.2.3 Post-synthetic sequestration of Tl^+ into the grafted $Na^+/Fe^{3+}/[Fe^{II}(CN)_6]^{4-}$ and $Au@NaNi^{II}Fe^{II}@NaFe^{II}Fe^{III}$ NPs.

The Tl^+ capture by the grafted $Na^+/Fe^{3+}/[Fe^{II}(CN)_6]^{4-}$ and $Au@NaNi^{II}Fe^{II}@NaFe^{II}Fe^{III}$ NPs was first investigated using a non-radioactive isotope in water. The insertion of the thallium ions into the cyano-bridged network of PB was performed by simply mixing of the $Na^+/Fe^{3+}/[Fe^{II}(CN)_6]^{4-}$ grafted Dextran NPs (figure 18) and $Au@NaNi^{II}Fe^{II}@NaFe^{II}Fe^{III}$ grafted Dextran NPs (figure 19) with a $TlNO_3$ aqueous solution¹⁶.

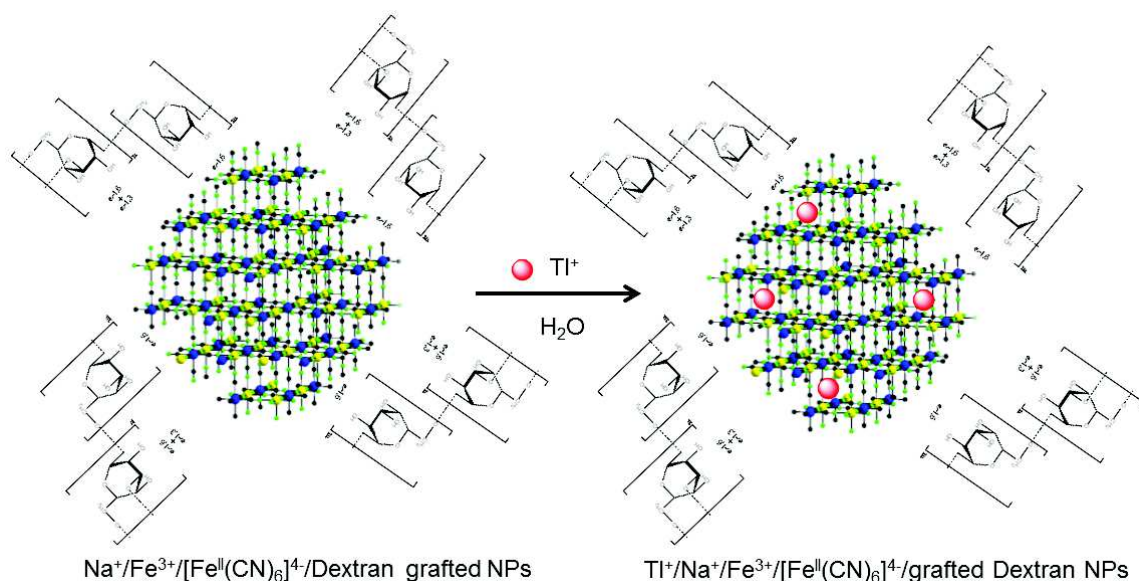


Figure 18: Schematic representation of the Tl^+ sequestration of $Na^+/Fe^{3+}/[Fe^{II}(CN)_6]^{4-}$ /grafted Dextran NPs.

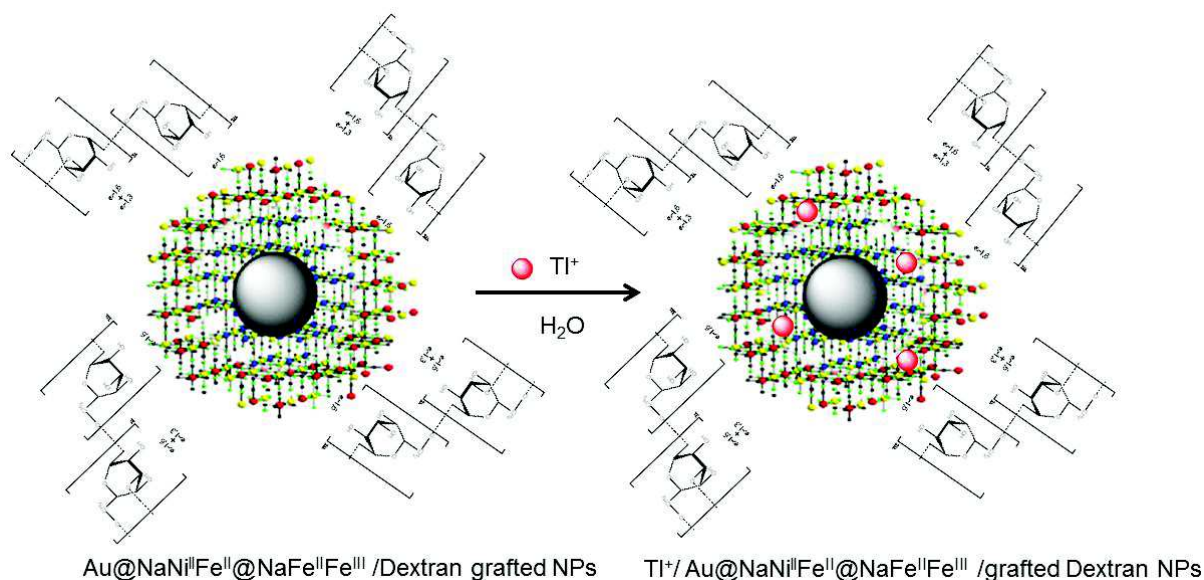


Figure 19: Schematic representation of the Tl^+ sequestration into $Au@NaNi^{II}Fe^{II}@NaFe^{II}Fe^{III}$ /grafted Dextran NPs.

The evolution of the Tl^+ kinetic sorption was followed during 24 hours by using an aqueous solution of $TlNO_3$ at 6.0×10^{-4} M and at 4.0×10^{-4} M respectively for the $Na^+/Fe^{3+}/[Fe^{II}(CN)_6]^{4-}$ /grafted Dextran NPs and the $Au@NaNi^{II}Fe^{II}@NaFe^{II}Fe^{III}$ /grafted Dextran NPs (figures 20 and 21, left). The amounts of Tl in the solid were measured using EDS. For both systems, the capture process is quite fast and the equilibrium is reached at approximatively 4 hours. The adsorption isotherm was also performed for both systems using different $TlNO_3$ concentration solutions during 24 hours, from 3.0×10^{-4} M to 8.4×10^{-3} M for the $Na^+/Fe^{3+}/[Fe^{II}(CN)_6]^{4-}$ /grafted Dextran NPs and from 4.0×10^{-4} M to 5.0×10^{-3} M for the $Au@NaNi^{II}Fe^{II}@NaFe^{II}Fe^{III}$ /grafted Dextran NPs. For both samples, the concavity of the curves relatively to the concentration clearly shows the strong affinity of the PB NPs for the Tl^+ sorption in a wide range of concentrations. At low concentration, the curves are linear, which signify that all Tl^+ is inserted into the cyano-bridged network. A plateau is observed for the $Au@NaNi^{II}Fe^{II}@NaFe^{II}Fe^{III}$ /grafted Dextran NPs, indicating that the maximum adsorption capacity is reached. The maximum adsorption capacity (Q_{max}), which characterizes the efficiency of the materials in capturing thallium ion is determined from this plateau, and is equal to 0.21 at %. That corresponds to the adsorption of 0.12 mole of Tl^+ per mole of iron. A similar behavior is observed for the $Na^+/Fe^{3+}/[Fe^{II}(CN)_6]^{4-}$ /grafted Dextran NPs at low concentration, however no plateau are clearly observable and it may possible to insert more Tl^+ in the structure. Nevertheless, at highest concentration used (8.4×10^{-3} M) the quantity of Tl^+ inserted in the structure is quite similar than for the $Au@NaNi^{II}Fe^{II}@NaFe^{II}Fe^{III}$ /grafted Dextran NPs, *i.e.* 0.12 mole of thallium per mole of iron and the chemical formula given by the EDS ratio is $Tl_{0.22}Na_{0.03}Fe[Fe(CN)_6]_{0.81}$.

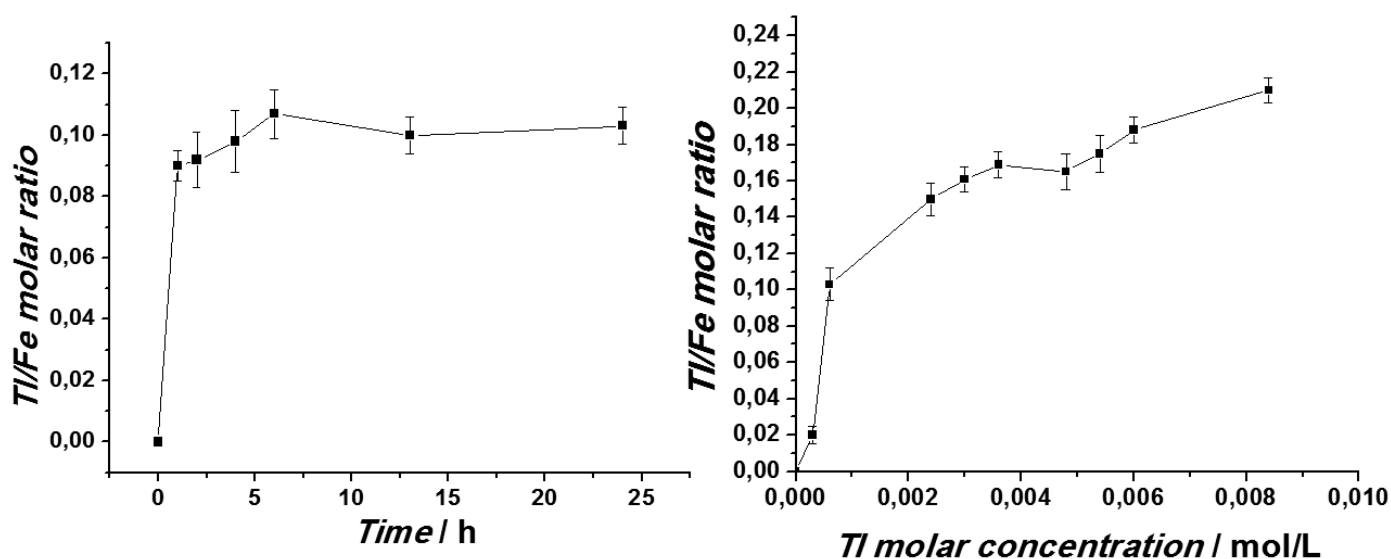


Figure 20: Left: Kinetic of Tl^+ sorption by $Na^+/Fe^{3+}/[Fe^{II}(CN)_6]^{4-}$ /grafted Dextran NPs at different times. Right: Isotherm of Tl^+ sorption by $Na^+/Fe^{3+}/[Fe^{II}(CN)_6]^{4-}$ /grafted Dextran NPs for different Tl^+ solution concentrations.

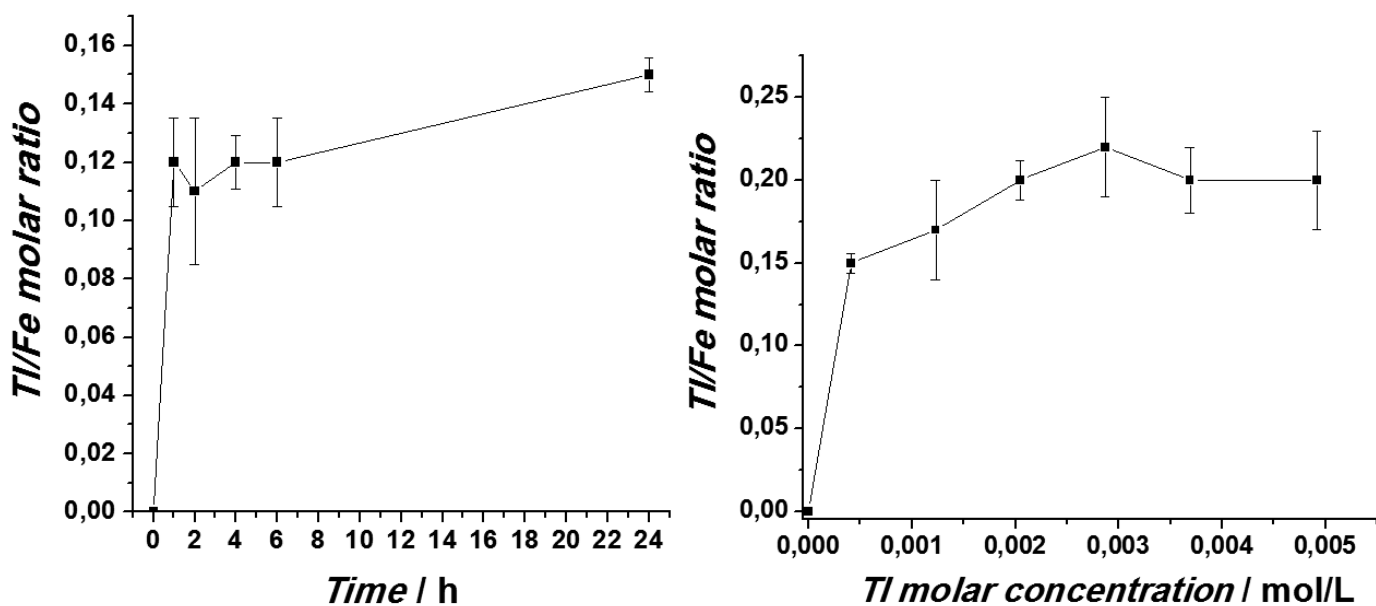


Figure 21: Left: Kinetic of TI⁺ sorption by Au@NaNi^{II}Fe^{II}@NaFe^{II}Fe^{III}/grafted Dextran NPs at different times. Right: Isotherm of TI⁺ sorption by Au@NaNi^{II}Fe^{II}@NaFe^{II}Fe^{III}/grafted Dextran NPs for different TI⁺ solution concentrations.

The IR spectra of both Na⁺/Fe³⁺/[Fe^{II}(CN)₆]⁴⁻/grafted Dextran NPs (figure 22) and Au@NaNi^{II}Fe^{II}@NaFe^{II}Fe^{III}/grafted Dextran NPs (figure 23) after TI⁺ insertion show similar bands as for the pristine NPs, such as the stretching vibration band of the Fe^{II}-C≡N-Fe^{III} linkage situated at the same value of 2080 cm⁻¹. Then no structural modification occurs with the capture of TI⁺ in the cyano-bridged coordination polymer structure.

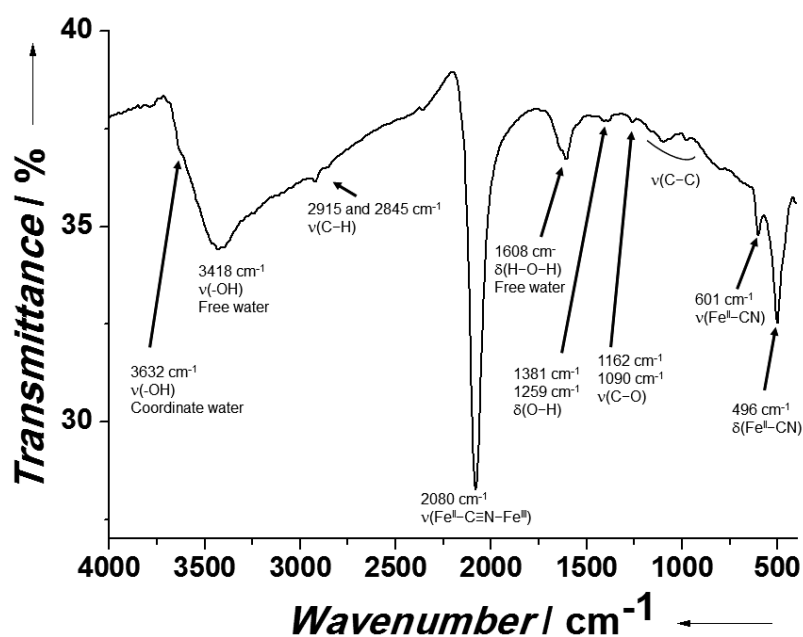


Figure 22: IR spectrum of the Na⁺/Fe³⁺/[Fe^{II}(CN)₆]⁴⁻/grafted Dextran NPs after TI⁺ insertion in the PB structure.

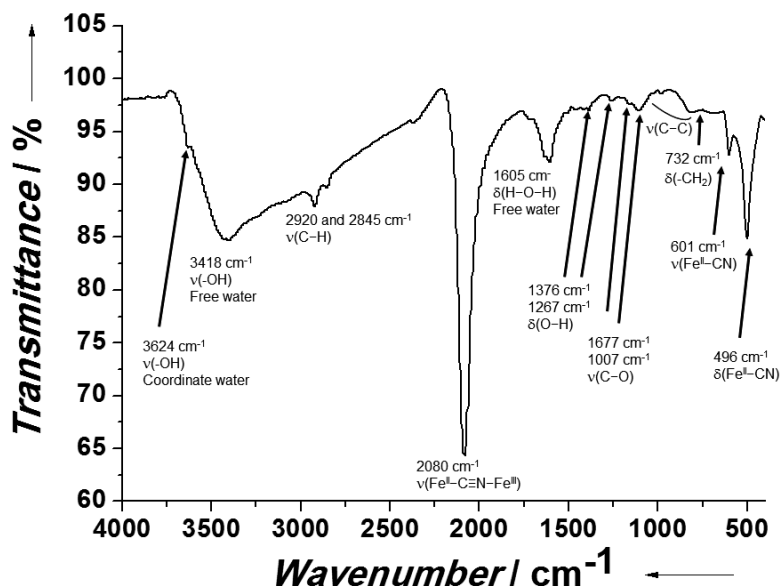


Figure 23: IR spectrum of the Au@NaNi^{II}Fe^{II}@NaFe^{III}Fe^{III}/grafted Dextran NPs after TI⁺ insertion in the PB structure.

TEM images of both Na⁺/Fe³⁺/[Fe^{II}(CN)₆]⁴⁻/grafted Dextran NPs and Au@NaNi^{II}Fe^{II}@NaFe^{III}Fe^{III}/grafted Dextran NPs performed after thallium capture indicate no change in the textural aspects of the NPs. Moreover, EDS mapping clearly show that the thallium is inserted in the cyano-bridged polymer structure, the topochemical repartition of iron and thallium being the same in both NPs (figures 24 and 25). However, it is not possible to know if the thallium is present in all the NP structure or only in a thin layer at the surface, due to the technique used (by transmission) and the shape of the nano-objects.

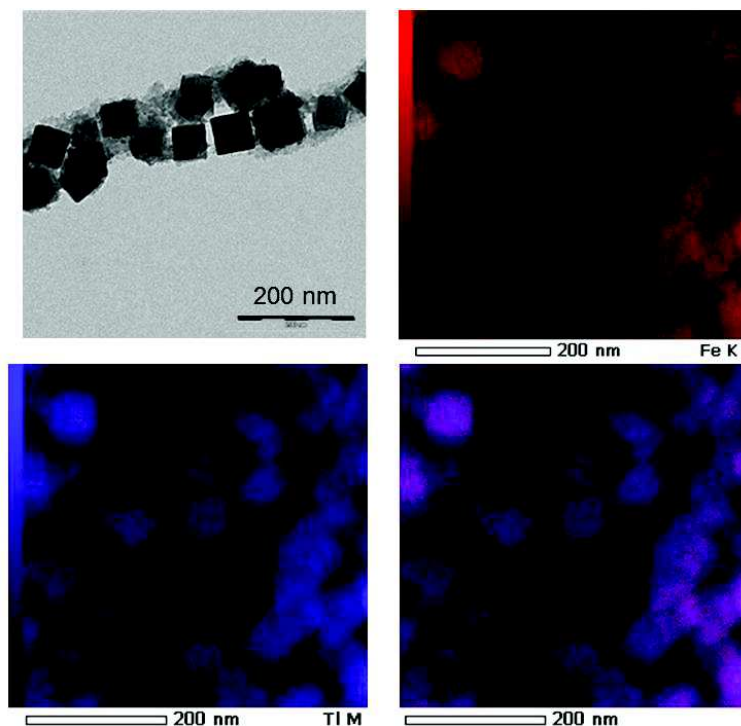


Figure 24: TEM image and topochemical repartition in the Na⁺/Fe³⁺/[Fe^{II}(CN)₆]⁴⁻/grafted Dextran NPs of Fe (red), TI (blue) and overlay of the two elements.

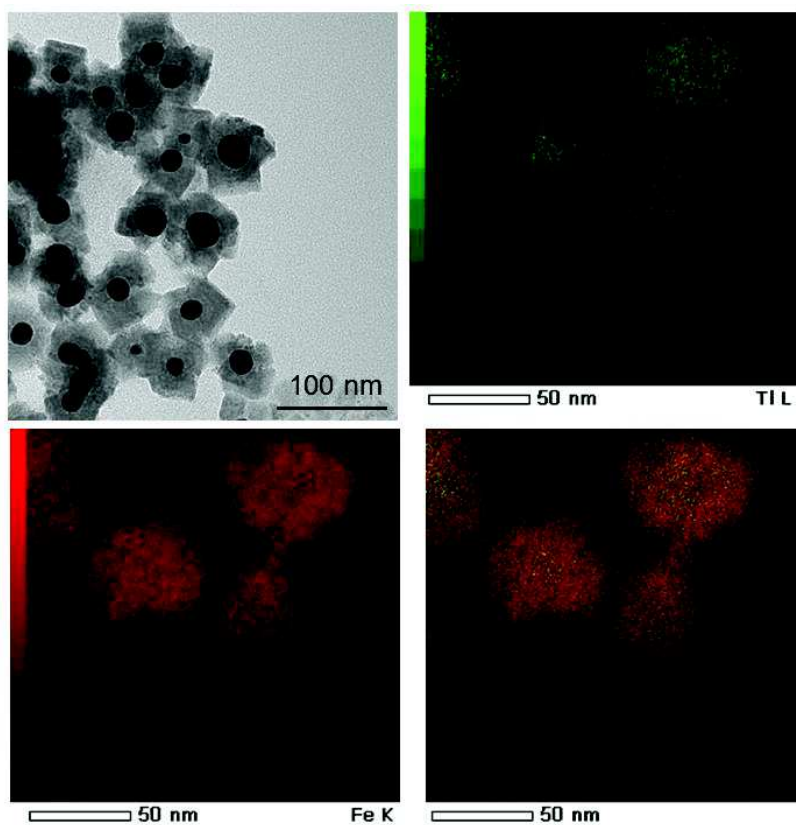


Figure 25: TEM image and topochemical repartition in the Au@NaNi^{II}Fe^{II}@NaFe^{II}Fe^{III}/grafted Dextran NPs of Fe (red), TI (green) and overlay of the two elements.

To conclude, we have demonstrated that both Na⁺/Fe³⁺/[Fe^{II}(CN)₆]⁴⁻/grafted Dextran NPs and Au@NaNi^{II}Fe^{II}@NaFe^{II}Fe^{III}/grafted Dextran NPs are able to capture Tl⁺ ions in solution, without any modification of the NPs and its grafting. Then, these systems can be used as radiotracers for ²⁰¹-thallium-based scintigraphy imaging.

V.3 Use of the $\text{Na}^+/\text{Fe}^{3+}/[\text{Fe}^{\text{II}}(\text{CN})_6]^{4-}$ /grafted and $\text{Au}@/\text{NaNi}^{\text{II}}\text{Fe}^{\text{II}}@/\text{NaFe}^{\text{II}}\text{Fe}^{\text{III}}/\text{grafted}$ NPs as $^{201}\text{Tl}^+$ nano-carriers for SPECT/CT imaging.

We have previously shown that the $\text{Na}^+/\text{Fe}^{3+}/[\text{Fe}^{\text{II}}(\text{CN})_6]^{4-}$ /grafted and $\text{Au}@/\text{NaNi}^{\text{II}}\text{Fe}^{\text{II}}@/\text{NaFe}^{\text{II}}\text{Fe}^{\text{III}}/\text{grafted}$ NPs can be used as $^{201}\text{Tl}^+$ nano-carriers 201-thallium-based imaging. The main interest of this study is to compare on one hand the effect of the stabilizing agent nature on the biodistribution of the NPs in time, and possibly passive targeting of the cancer cells. To this aim, we have selected two polymers as stabilizing agents, Dextran 6000 g/mol and POEMA-PDAEMA, to graft the NPs surface. Moreover, in collaboration with Estelle Rascol and Pr. Joel Chopineau from MACS, ICGM, Université de Montpellier, the encapsulation of the $\text{Na}^+/\text{Fe}^{3+}/[\text{Fe}^{\text{II}}(\text{CN})_6]^{4-}$ NPs and the $\text{Au}@/\text{NaNi}^{\text{II}}\text{Fe}^{\text{II}}@/\text{NaFe}^{\text{II}}\text{Fe}^{\text{III}}$ NPs with lipids bilayers was performed, and these systems were also used for the *in vivo* study. Then, three different stabilizing agents were investigated. On the other hand, the effect of the NPs morphology and composition, and particularly the interest of the gold from the core-shell NPs, was investigated. Indeed, gold is known for its properties to absorb the X-ray radiation, and then the presence of the gold core may enhance the contrast of CT images, improving the quality of the measurements¹. Then, in the first time, before any *in vivo* tests, we have performed CT imaging of the two type of NPs *in vitro*, to determinate the influence of the gold. The *in vitro* and *in vivo* experiments were performed by Dr. Muriel Buisson and Dr. Samuel Sevestre from the Institut de Recherche en Cancérologie de Montpellier (IRCM), INSERM.

V.3.1 Comparison between $\text{Na}^+/\text{Fe}^{3+}/[\text{Fe}^{\text{II}}(\text{CN})_6]^{4-}$ NPs and $\text{Au}@/\text{NaNi}^{\text{II}}\text{Fe}^{\text{II}}@/\text{NaFe}^{\text{II}}\text{Fe}^{\text{III}}$ NPs on CT imaging.

To investigate the influence of gold on the CT imaging, several solutions of different concentrations (2, 5, 10, 15, 20 mg/mL) of $\text{Na}^+/\text{Fe}^{3+}/[\text{Fe}^{\text{II}}(\text{CN})_6]^{4-}$ /grafted Dextran NPs and $\text{Au}@/\text{NaNi}^{\text{II}}\text{Fe}^{\text{II}}@/\text{NaFe}^{\text{II}}\text{Fe}^{\text{III}}$ /grafted Dextran NPs were prepared and the X-ray CT images were acquired using a 4-head multiplexing multipinhole Nano SPECT camera (Bioscan Inc., Washington, USA). The reconstructed data from CT were visualized using the dedicated software, Invivoscope®.

For both systems, the CT values increase linearly as the NPs concentration increase (figure 26). A similar linear increase was already observed for $\text{Au}@/\text{PB}$ NPs developed for photoacoustic/CT bimodal imaging application³². However, the increase is more important for the $\text{Au}@/\text{NaNi}^{\text{II}}\text{Fe}^{\text{II}}@/\text{NaFe}^{\text{II}}\text{Fe}^{\text{III}}$ /grafted Dextran NPs than for the $\text{Na}^+/\text{Fe}^{3+}/[\text{Fe}^{\text{II}}(\text{CN})_6]^{4-}$ /grafted Dextran NPs, to become consequent at 20 mg/mL. This difference is clearly due to the presence of the gold core, which absorb the X-ray radiation and enhances the contrast on the images. That demonstrates the interest in the use of the core-shell $\text{Au}@/\text{NaNi}^{\text{II}}\text{Fe}^{\text{II}}@/\text{NaFe}^{\text{II}}\text{Fe}^{\text{III}}$ NPs. However this requires to inject highly concentrated solutions to improve the contrast, which can cause embolism and may lead to the death of the subject. In our case, we will inject NPs solutions at a concentration of 2mg/mL. Even if the best contrast is observed for the $\text{Au}@/\text{NaNi}^{\text{II}}\text{Fe}^{\text{II}}@/\text{NaFe}^{\text{II}}\text{Fe}^{\text{III}}$ /grafted Dextran NPs, the difference at this concentration is insignificant. Then the effect of the gold core of the $\text{Au}@/\text{NaNi}^{\text{II}}\text{Fe}^{\text{II}}@/\text{NaFe}^{\text{II}}\text{Fe}^{\text{III}}$ /grafted Dextran NPs to enhance the contrast for CT imaging is clearly observed by comparison with the $\text{Na}^+/\text{Fe}^{3+}/[\text{Fe}^{\text{II}}(\text{CN})_6]^{4-}$ /grafted Dextran NPs, but at the working concentration for *in vivo* imaging, this effect must be relativized.

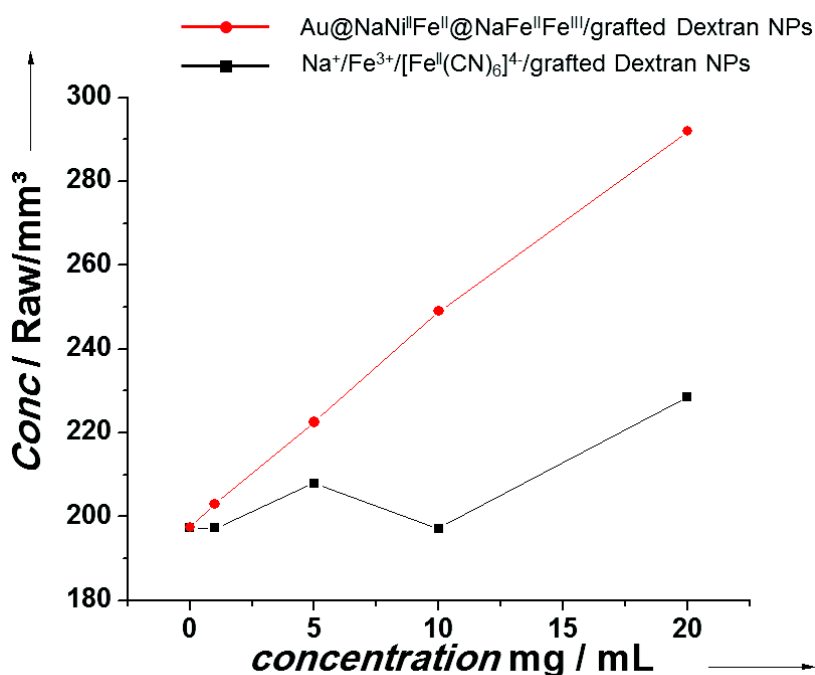
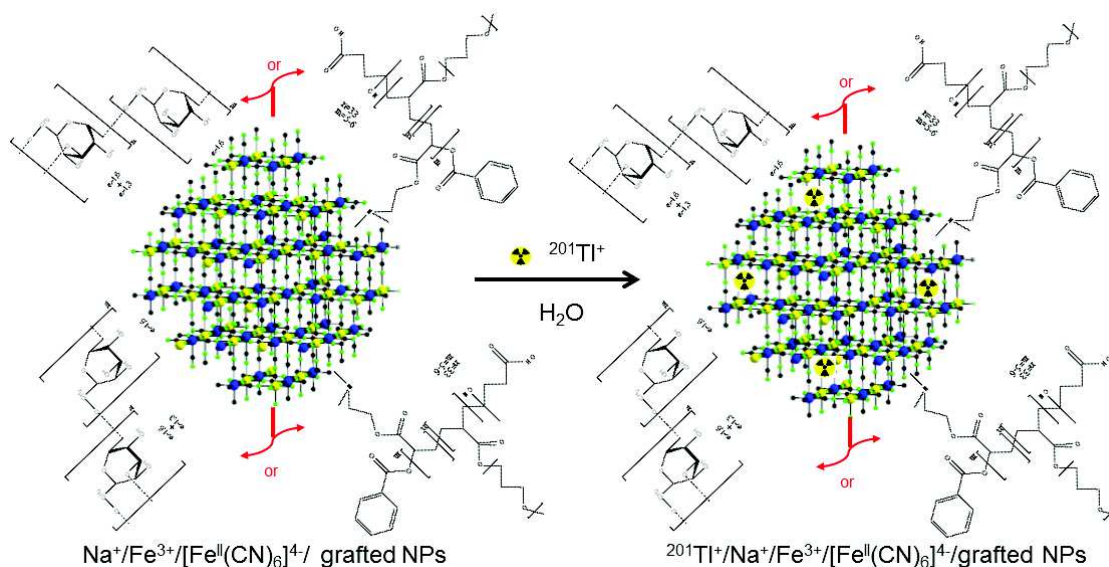


Figure 26: X-ray attenuation intensity as a function of the concentration of the $\text{Na}^+/\text{Fe}^{3+}/[\text{Fe}^{\text{II}}(\text{CN})_6]^{4-}$ /grafted Dextran NPs and the $\text{Au}@/\text{NaNi}^{\text{II}}\text{Fe}^{\text{II}}@/\text{NaFe}^{\text{II}}\text{Fe}^{\text{III}}$ /grafted Dextran NPs.

V.3.2 Use of the ^{201}Tl -labelled NPs as tracking agents for *in vivo* SPECT/CT imaging on mice.

The preparation of the ^{201}Tl -labelled NPs to be used as tracking agent for *in vivo* SPECT/CT imaging was performed by mixing the NPs powder (2 mg) with 2 mL of a $^{201}\text{TlCl}$ solution having an activity of $10\text{ MBq}\cdot\text{mL}^{-1}$ to obtain the $^{201}\text{Tl}/\text{Na}^+/\text{Fe}^{3+}/[\text{Fe}^{\text{II}}(\text{CN})_6]^{4-}$ /grafted Dextran NPs, the $^{201}\text{Tl}/\text{Na}^+/\text{Fe}^{3+}/[\text{Fe}^{\text{II}}(\text{CN})_6]^{4-}$ /grafted POEMA-PDAEMA NPs and the $\text{Au}@/\text{Na}^+/\text{Fe}^{3+}/[\text{Fe}^{\text{II}}(\text{CN})_6]^{4-}$ /grafted Dextran NPs¹⁶. The $^{201}\text{Tl}/\text{Na}^+/\text{Fe}^{3+}/[\text{Fe}^{\text{II}}(\text{CN})_6]^{4-}$ /lipid bilayers NPs requiring to stay in aqueous media for the lipid bilayers integrity, 250 μL of a saline solution of $\text{Na}^+/\text{Fe}^{3+}/[\text{Fe}^{\text{II}}(\text{CN})_6]^{4-}$ /lipid bilayers NPs (0.9% NaCl aqueous solution, 8 mg/mL) was mixed to 750 μL of a $^{201}\text{TlCl}$ solution to obtain the $^{201}\text{Tl}/\text{Na}^+/\text{Fe}^{3+}/[\text{Fe}^{\text{II}}(\text{CN})_6]^{4-}$ /lipid bilayers NPs. These radio-labelled NPs were *iv* injected into the tail vein of mice and the SPECT-CT images were acquired at different times over 48h.



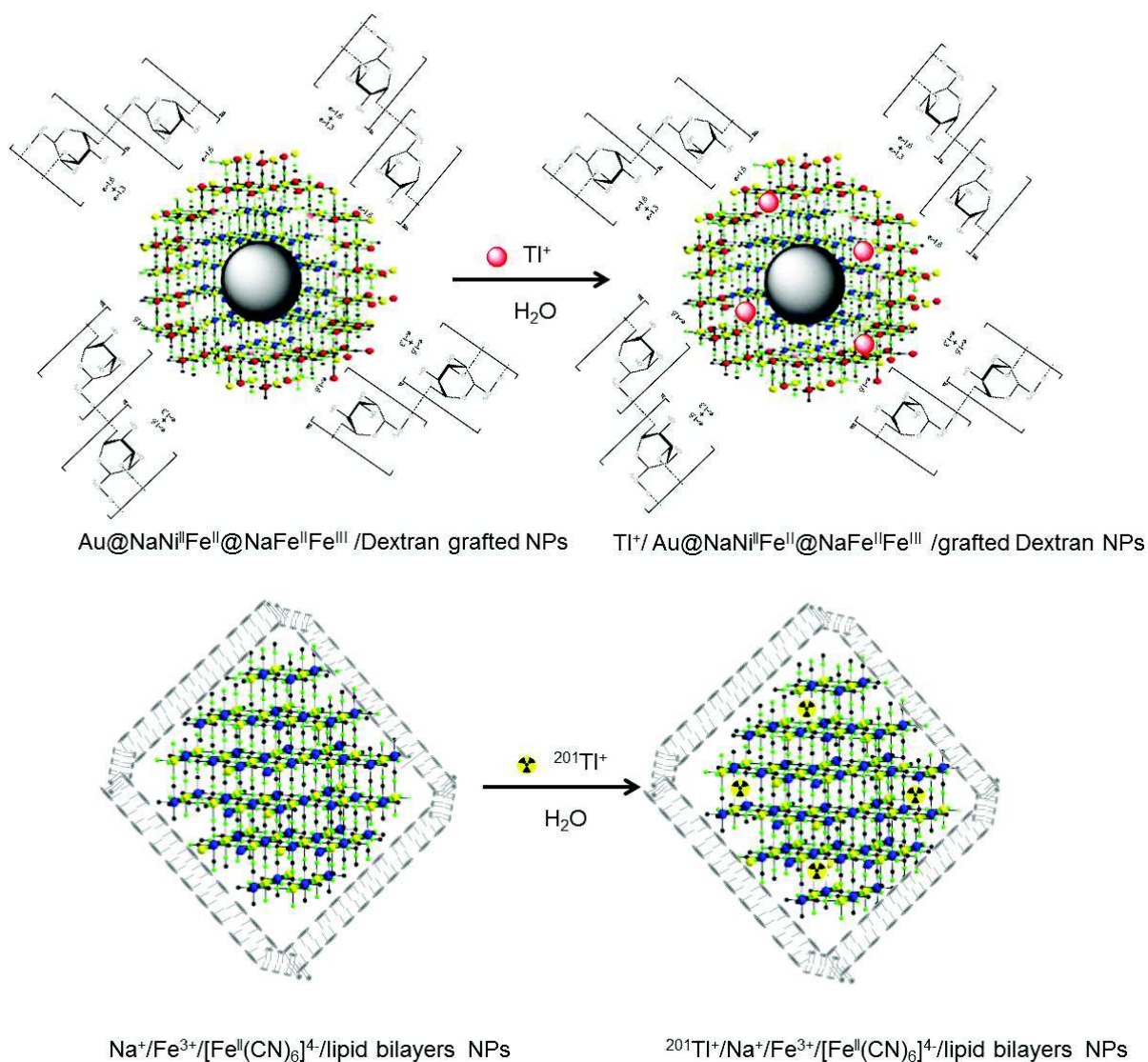


Figure 27: Schematic representation of the sequestration of $^{201}\text{Tl}^+$ into the selected NPs and the different stabilizing agents used to obtain radio-labelled NPs.

In the first time, we have investigated the effect on the stabilizing agent nature on healthy mice. $^{201}\text{Tl}/\text{Na}^+/\text{Fe}^{3+}/[\text{Fe}^{\text{II}}(\text{CN})_6]^{4-}$ NPs with three selected stabilizing agents were injected and the SPECT-CT images were acquired. The 3D quantification by segmentation using dedicated software (Inviscope®) was performed in order to recover the informations about *in vivo* uptake by organs. Maximum Intensity Projections (MIPs) images of the longitudinal plane show the transient passage of the radiolabeled NPs into the organs (figure 28). However, the observed biodistribution revealed some differences. Indeed, while the $^{201}\text{Tl}/\text{Na}^+/\text{Fe}^{3+}/[\text{Fe}^{\text{II}}(\text{CN})_6]^{4-}/\text{grafted POEMA-PDAEMA NPs}$ and $^{201}\text{Tl}/\text{Na}^+/\text{Fe}^{3+}/[\text{Fe}^{\text{II}}(\text{CN})_6]^{4-}/\text{lipid bilayers NPs}$ are successively present in the liver (1h) and the kidneys, the $^{201}\text{Tl}/\text{Na}^+/\text{Fe}^{3+}/[\text{Fe}^{\text{II}}(\text{CN})_6]^{4-}/\text{grafted Dextran NPs}$ are observed in the lungs (1h) then into the kidneys (3h). Moreover, this activity in the lungs is observable during 6h. As already observed with small ^{201}Tl -labelled PB NPs¹⁶, the biodistributions for these systems are clearly different from the commercial $^{201}\text{TlCl}$ used as a reference and which is located immediately in the kidneys. Moreover, an effect of the stabilizing agent nature on the biodistribution activity is clearly observed. The passage through the pulmonary

compartment was observed for the $^{201}\text{Tl}/\text{Na}^+/\text{Fe}^{3+}/[\text{Fe}^{\text{II}}(\text{CN})_6]^{4-}/\text{grafted Dextran NPs}$ before their clearance by natural means (liver and kidneys). At the opposite, the $^{201}\text{Tl}/\text{Na}^+/\text{Fe}^{3+}/[\text{Fe}^{\text{II}}(\text{CN})_6]^{4-}/\text{grafted POEMA-PDAEMA NPs}$ and $^{201}\text{Tl}/\text{Na}^+/\text{Fe}^{3+}/[\text{Fe}^{\text{II}}(\text{CN})_6]^{4-}/\text{lipid bilayers NPs}$ are rapidly localized into the liver, then the kidneys, for the faster glomerular elimination from the organism.

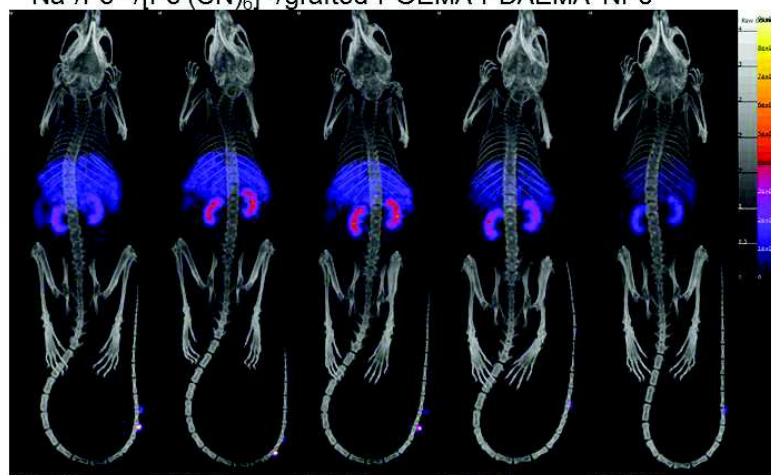
To compare data from different animals and to overcome the heterogeneity of *iv* injections, quantification data were normalized and the recorded activity of the whole body was considered to be 100% for each acquisition. The uptake kinetics by the organs of interest (lungs, liver, kidneys) and the whole body at different times after the *iv* injection of the nanoprobe are presented in figure 29. Comparative data confirm the difference previously observed on the MIPs images for the three nanoprobe used. While the activity in the whole body and the kidneys are similar for the three systems, the $^{201}\text{Tl}/\text{Na}^+/\text{Fe}^{3+}/[\text{Fe}^{\text{II}}(\text{CN})_6]^{4-}/\text{grafted Dextran NPs}$ exhibit a significant activity in the lungs for the first 3h, before the pass through the liver and the kidneys. At the opposite, a high activity of the $^{201}\text{Tl}/\text{Na}^+/\text{Fe}^{3+}/[\text{Fe}^{\text{II}}(\text{CN})_6]^{4-}/\text{grafted POEMA-PDAEMA NPs}$ is observed in the liver, indicating the massive retention of the NPs and the beginning of their organism elimination. Then, the use of Dextran as stabilizing agent for the NPs seems to permit the improvement of the pass through the lungs. This is in accordance with the properties of Dextran to target lungs, as described in the literature, and may permit to image this organ²⁸.

On the other hand, the elimination of the $^{201}\text{Tl}^+$ entrapped in the Prussian Blue NPs was evaluated and compare with that of the commercial radiotracer by recording over 48 h post *iv* injection. The excretion from the body by glomerular filtration is operational for all the ^{201}Tl -labeled NPs and the commercial $^{201}\text{TlCl}$, as attested by the whole body activity as function of the time. The biological half-life was estimated to be around 40 hours, which is a little higher than those observed for the small PB NPs studied in the team (36 h), and the commercial aqueous solution of $^{201}\text{TlCl}$ ¹⁶.

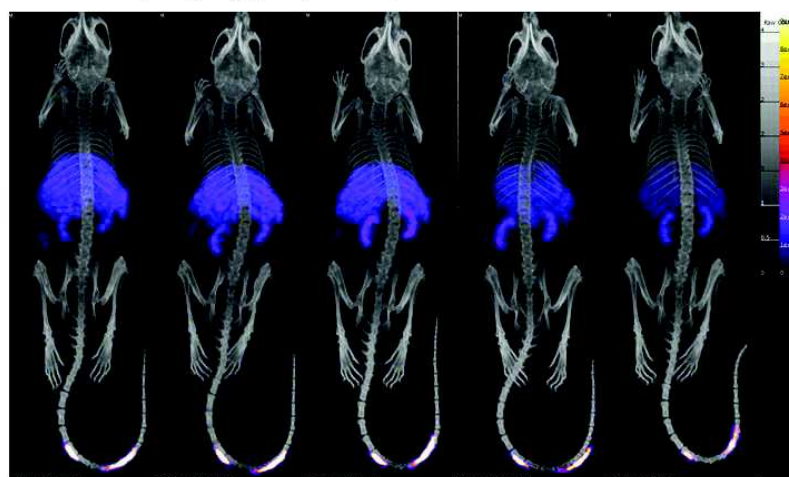
i.v post-injection time

1h 3h 6h 24h 48h

$\text{Na}^+/\text{Fe}^{3+}/[\text{Fe}^{\text{II}}(\text{CN})_6]^{4-}/\text{grafted POEMA-PDAEMA NPs}$



$\text{Na}^+/\text{Fe}^{3+}/[\text{Fe}^{\text{II}}(\text{CN})_6]^{4-}/\text{Lipid bilayers NPs}$



$\text{Na}^+/\text{Fe}^{3+}/[\text{Fe}^{\text{II}}(\text{CN})_6]^{4-}/\text{grafted Dextran NPs}$

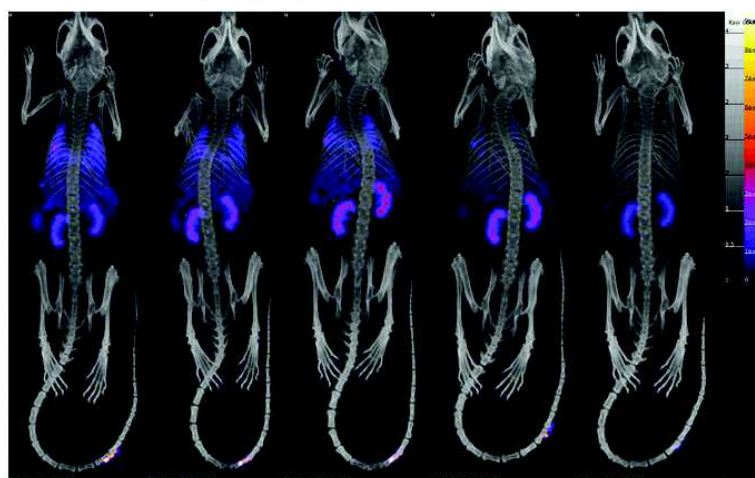


Figure 28: MIPs images of the mice after the iv injection of the $^{201}\text{Tl}/\text{Na}^+/\text{Fe}^{3+}/[\text{Fe}^{\text{II}}(\text{CN})_6]^{4-}$ NPs with the three different stabilizing agents (Dextran, POEMA-PDAEMA and lipid bilayers) for different periods of time: 1h, 3h, 6, 24h and 48 h.

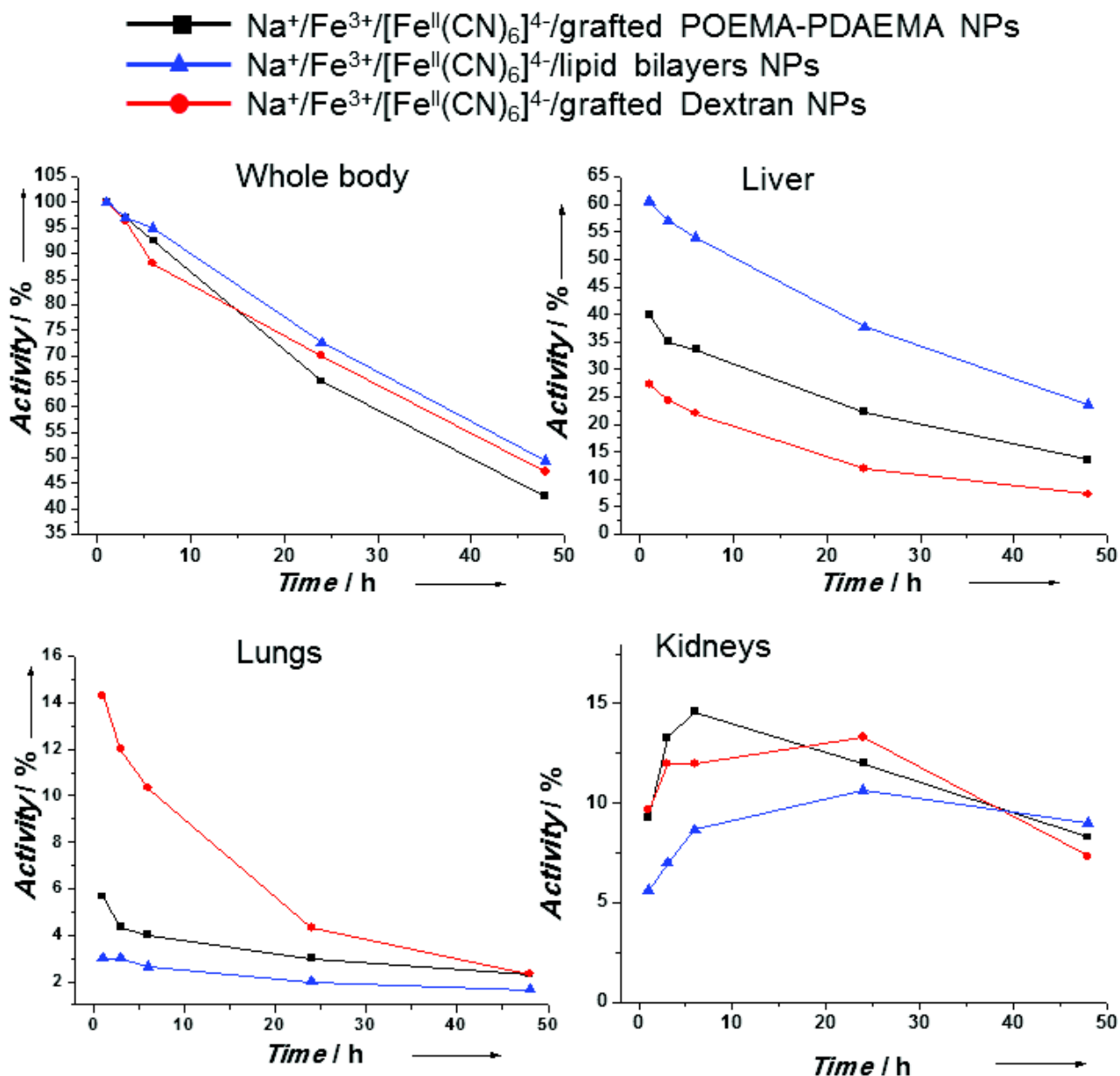


Figure 29: Captation of $^{201}\text{Tl}/\text{Na}^+/\text{Fe}^{3+}/[\text{Fe}^{\text{II}}(\text{CN})_6]^{4-}$ NPs with the three different stabilizing agents (Dextran, POEMA-PDAEMA and lipid bilayers) by organs of interest in times after *iv* injection.

The Dextran improving the lungs imaging, comparatively to the others stabilizing agents, we have used it to stabilize the $\text{Au}@/\text{NaNi}^{\text{II}}\text{Fe}^{\text{II}}@/\text{NaFe}^{\text{II}}\text{Fe}^{\text{III}}$ to prepare $\text{Au}@/\text{NaNi}^{\text{II}}\text{Fe}^{\text{II}}@^{201}\text{Tl}/\text{NaFe}^{\text{II}}\text{Fe}^{\text{III}}/\text{grafted Dextran NPs}$, in order to compare a possible effect of the NPs morphology and composition on the biodistribution. Then, injection of the $\text{Au}@/\text{NaNi}^{\text{II}}\text{Fe}^{\text{II}}@^{201}\text{Tl}/\text{NaFe}^{\text{II}}\text{Fe}^{\text{III}}/\text{grafted Dextran NPs}$ were injected into healthy mice and sick mice, presenting tumor (HT-29 cells) (figure 30).

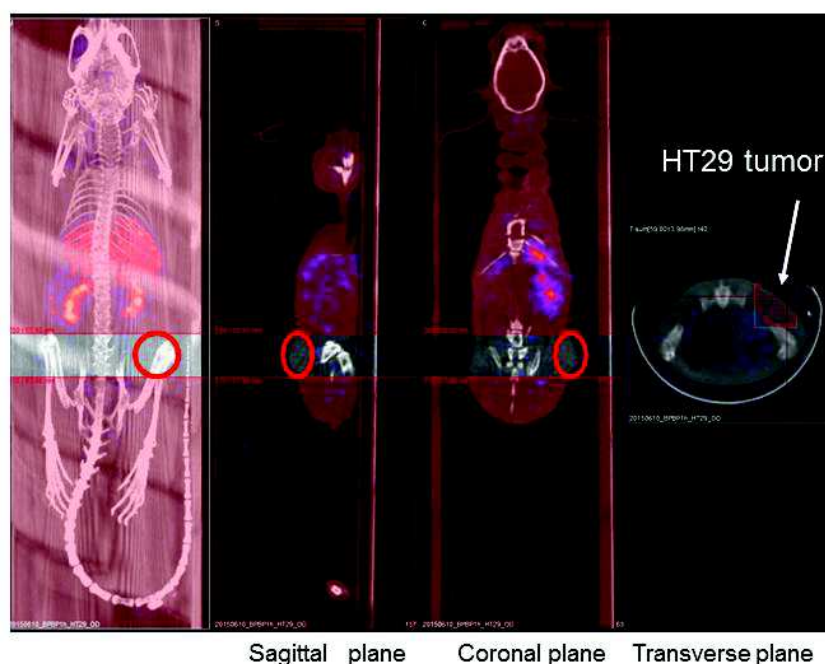


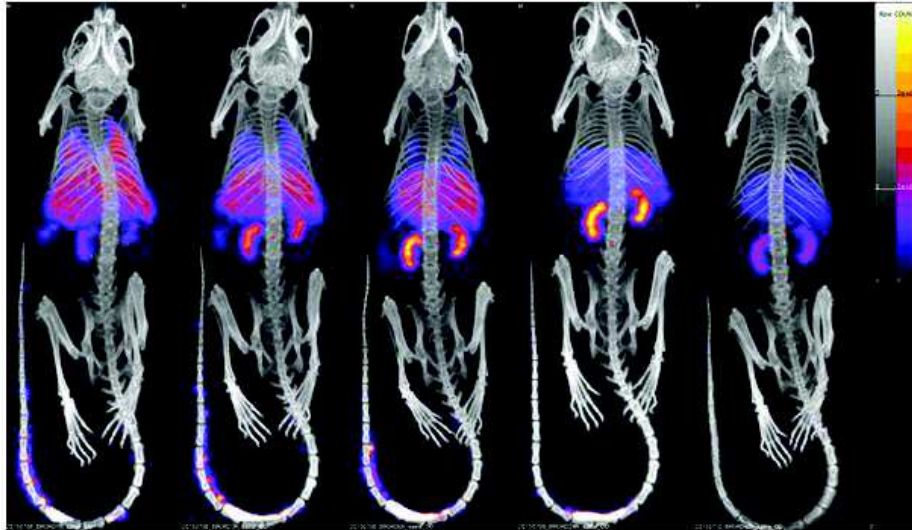
Figure 30: MIP image and different planes showing the HT29 tumor.

As for the $^{201}\text{Tl}/\text{Na}^+/\text{Fe}^{3+}/[\text{Fe}^{\text{II}}(\text{CN})_6]^{4-}/\text{grafted}$ Dextran NPs, the MIPs images reveal that the $\text{Au}@/\text{NaNi}^{\text{II}}\text{Fe}^{\text{II}}@^{201}\text{Tl}/\text{NaFe}^{\text{II}}\text{Fe}^{\text{III}}/\text{grafted}$ Dextran NPs exhibit a similar passage through the pulmonary compartment (1), before their clearance by passing through the liver and the kidneys (figure 31). The comparative data show that the $\text{Au}@/\text{NaNi}^{\text{II}}\text{Fe}^{\text{II}}@^{201}\text{Tl}/\text{NaFe}^{\text{II}}\text{Fe}^{\text{III}}/\text{grafted}$ Dextran NPs have a similar biodistribution activity as a function of time either for healthy mice than for sick mice (figure 32). Moreover, the activity observed is close to those observed for the $^{201}\text{Tl}/\text{Na}^+/\text{Fe}^{3+}/[\text{Fe}^{\text{II}}(\text{CN})_6]^{4-}/\text{grafted}$ Dextran NPs. On other hand, no sign of activity is detected in the tumor. This indicates that no EPR effect is observed. EPR effect is a physiology-based phenomenon where large molecules (< to 40 kDa) and small particles selectively accumulate in the tumor tissues³³⁻³⁵. This phenomenon is already used to target cancer, for imaging or therapy, and is also called “passive targeting”. However, such effect is not observed in our case. Thus, an active targeting with using specific molecules, anchored at the NPs surface, are needed to target the cancer cells.

Au@NaNi^{II}Fe^{II}@NaFe^{II}Fe^{III}/grafted Dextran NPs

i.v post-injection time

1h 3h 6h 24h 48h
Sane mouse



Sick mouse

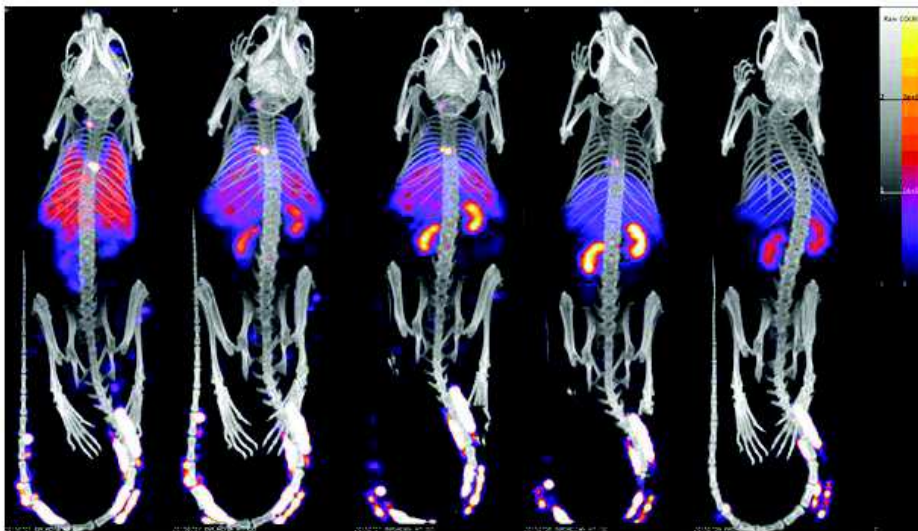


Figure 31: MIPs images of the sane and sick mice after the *iv* injection of the Au@NaNi^{II}Fe^{II}@²⁰¹Tl/NaFe^{II}Fe^{III}/grafted Dextran NPs for different periods of time: 1h, 3h, 6, 24h and 48 h.

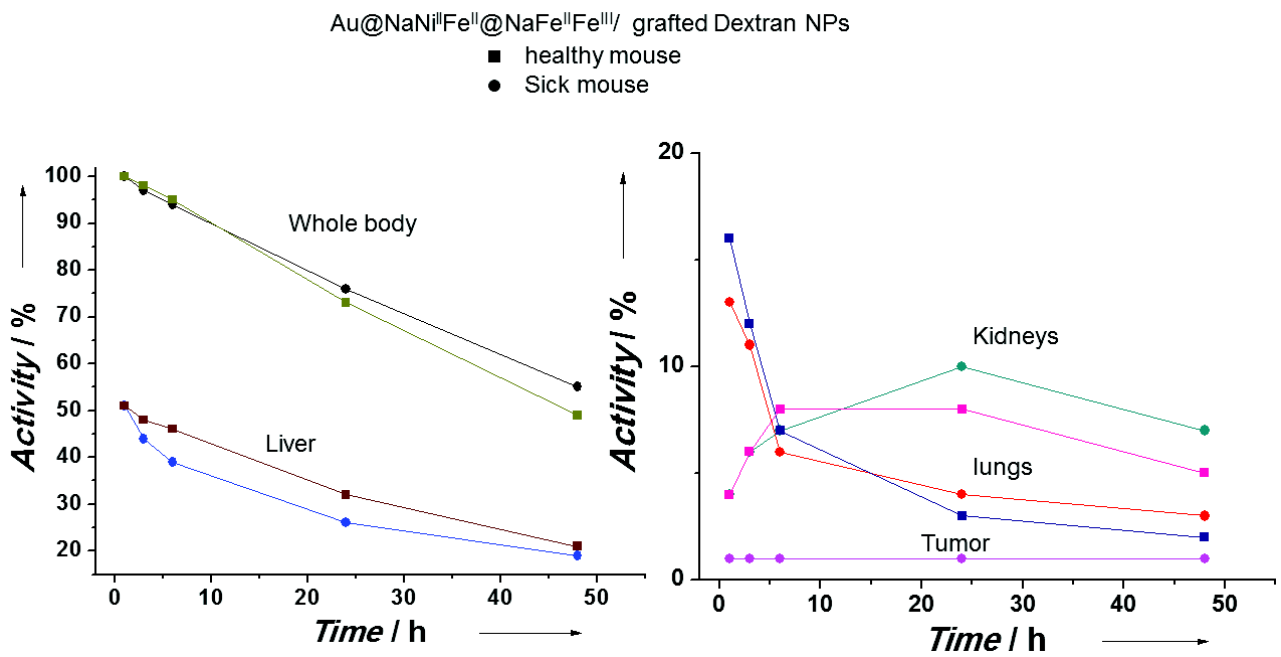


Figure 32: Captation of Au@NaNi^{II}Fe^{III}@²⁰¹Ti/NaFe^{II}Fe^{III}/grafted Dextran NPs by organs of interest in times after *iv* injection for sane and thick mice.

To conclude, the experiments have revealed the effect of the stabilizing agent nature of the biodistribution, as observed for the NPs grafted with Dextran. Moreover, the morphology of the NPs seems have no influence on the biodistribution. However, no passive targeting of the tumor is observed for these systems. It may interesting to perform an active targeting to mark the tumor, permitting to image it.

V.4 conclusion

In this chapter, we have described the synthesis of $\text{Na}^+/\text{Fe}^{3+}/[\text{Fe}^{\text{II}}(\text{CN})_6]^{4-}$ NPs obtained according to a self-assembly reaction of the precursors. IR spectroscopy and XRD pattern confirm the formation of the cyano-bridged coordination network. TEM images show cubic NPs with a mean size of 63.0 ± 8.7 nm. The size is in a similar range than for the $\text{Au}@ \text{NaNi}^{\text{II}}\text{Fe}^{\text{II}}@ \text{NaFe}^{\text{II}}\text{Fe}^{\text{III}}$ NPs (47.1 ± 6.8 nm) and which permits to compare the properties of both systems for bioimaging applications.

To avoid any aggregation as injected, the NPs surface was grafted with stabilizing agents. Several molecules and polymers were grafted at the surface of $\text{Na}^+/\text{Fe}^{3+}/[\text{Fe}^{\text{II}}(\text{CN})_6]^{4-}$ NPs and the efficiency of the grafting was investigated by IR spectroscopy. According to the results, we have selected Dextran and POEMA-PDAEMA, a new polymer synthesized by Dr. Cyrille Boyer from School of Chemical Engineering, University of New South Wales, Sydney, Australia. The Dextran has also been chosen because its ability to target lungs, as described in literature. These stabilizing agents were grafted at the surface of the $\text{Au}@ \text{NaNi}^{\text{II}}\text{Fe}^{\text{II}}@ \text{NaFe}^{\text{II}}\text{Fe}^{\text{III}}$ NPs and the efficiency of this step was confirmed by IR spectroscopy. DLS and Zeta potential measurements have confirmed the presence of the stabilizing agents at the NPs surface for all systems and the improvement of the stabilization has been demonstrated. Finally, STEM images and EDS mapping have shown the presence of the organic material at the NPs surface.

To check that these NPs can be used as $^{201}\text{Tl}^+$ -labelled nanoprobe, the insertion of Tl^+ ions in the cyano-bridged coordination polymer structure was performed in water. The evolution of the Tl^+ kinetic sorption revealed that the Tl^+ capture process is quite fast and the equilibrium is reached at approximately 4 hours in both cases. Moreover, the adsorption isotherms performed on both systems using different TlNO_3 concentrations during 24 hours indicated that the maximum adsorption capacity (Q_{max}) corresponds to the adsorption of 0.12 mole of Tl^+ per mole of iron for both cases. IR spectroscopy and TEM images show that the structural and textural characteristics remain the same before and after Tl^+ insertion.

Before the use of these NPs for *in vivo* imaging applications, we have investigated the interest for the CT imaging by comparing the *in vitro* evolution of the contrast as a function of the concentration of the $\text{Na}^+/\text{Fe}^{3+}/[\text{Fe}^{\text{II}}(\text{CN})_6]^{4-}$ NPs and the $\text{Au}@ \text{NaNi}^{\text{II}}\text{Fe}^{\text{II}}@ \text{NaFe}^{\text{II}}\text{Fe}^{\text{III}}$ NPs. As expected the presence of the gold core enhances the X-ray radiation absorption and improves the contrast of the $\text{Au}@ \text{NaNi}^{\text{II}}\text{Fe}^{\text{II}}@ \text{NaFe}^{\text{II}}\text{Fe}^{\text{III}}$ NPs by comparison with the $\text{Na}^+/\text{Fe}^{3+}/[\text{Fe}^{\text{II}}(\text{CN})_6]^{4-}$ NPs.

For the SPECT-CT imaging, realized by Dr. Muriel Buisson and Dr. Samuel Sevestre from the Institut de Recherche en Cancérologie de Montpellier (IRCM), INSERM, the different systems studied were labelled with $^{201}\text{Tl}^+$ and *iv* injected into mice. In the first time, we have investigated the effect of the stabilizing agent nature on the biodistribution with using the $\text{Na}^+/\text{Fe}^{3+}/[\text{Fe}^{\text{II}}(\text{CN})_6]^{4-}$ NPs with the three selected stabilizing agents at the NPs surface (Dextran, POEMA-PDAEMA, and lipid bilayers, performed in collaboration with Estelle Rascol and Pr. Joel Chopineau from MACS, ICGM, Université de Montpellier).

The MIPs images show that the nanoprobe with Dextran at the NPs surface presented a transient passage in the pulmonary compartments and liver before their clearance by kidneys, while the nanoprobe with POEMA-PDAEMA and lipid bilayers at the NPs surface were directly situated in the liver, then in the kidneys. This effect is confirmed by the comparative data of the quantified activity, which indicated similar evolution of the activity for all systems in the different organs of interest (whole body, liver, kidney, lungs), but an higher activity in the lungs for $\text{Na}^+/\text{Fe}^{3+}/[\text{Fe}^{\text{II}}(\text{CN})_6]^{4-}$ NPs/grafted Dextran is observed. Such effect is in accordance with the use of Dextran to target lungs, as described in literature. Then we have selected Dextran as stabilizing agent to investigate the effect of the morphology on the biodistribution. $\text{Au}@(\text{Ni}^{\text{II}}/\text{Fe}^{\text{II}})/\text{NaFe}^{\text{II}}\text{Fe}^{\text{III}}/\text{grafted Dextran}$ NPs were $^{201}\text{Tl}^+$ -labelled and *iv* injected into sane and sick mice. The MIPs images and the comparative data of the quantified activity indicated a similar behavior for both systems, and confirm the effect of the Dextran on the retention in the lungs during the first 3h after injection. However, no activity is detected in the tumor, which indicated that these NPs were not accumulated in the tumor according to the EPR effect. Then, the absence of the “passive targeting” for the nanoprobe avoid the possibility to mark the tumor cells. This clearly shows the necessity to perform an active targeting by using molecules able to be detected by the tumor cells receptors.

References

- 1 E. C. Dreaden, A. M. Alkilany, X. Huang, C. J. Murphy and Mostafa A. El-Sayed, *Chem. Soc. Rev.*, **2012**, *41*, 2740.
- 2 A. Llevota and D. Astruc, *Chem. Soc. Rev.*, **2012**, *41*, 242.
- 3 H. Jansa and Q. Huo, *Chem. Soc. Rev.*, **2012**, *41*, 2849.
- 4 N. Li, P. Zhao, and D. Astruc, *Angew. Chem. Int. Ed.*, **2014**, *53*, 2.
- 5 G. Paul, Y. Prado, N. Dia, E. Riviere, S. Laurent, M. Roch, L. V. Elst, R. N. Muller, L. Sancey, P. Perriat, O. Tillement, T. Mallah and L. Catala, *Chem. Commun.*, **2014**, *50*, 6740.
- 6 M. Shokouhimehr, E. S. Soehnlén, A. Khitrin, S. Basu, S. D. Huang, *Inorg. Chem. Commun.*, **2010**, *13*, 58.
- 6 M. Shokouhimehr, E. S. Soehnlén, J. Hao, M. Griswold, C. Flask, X. Fan, J. P. Basilion, S. Basu and S. D. Huang, *J. Mater. Chem.*, **2010**, *20*, 5251.
- 7 Z. Li, Y. Zeng, D. Zhang, M. Wu, L. Wu, A. Huang, H. Yang, X. Liu and J. Liu, *J. Mater. Chem. B*, **2014**, *2*, 3686.
- Y. Li, C. H. Li, D. R. Talham, *Nanoscale*, **2015**, DOI: 10.1039/C4NR06481J.
- 8 M. F Dumont, S. Yadavilli, R. W. Sze, J. Nazarian, R. Fernandes, *Int. J. Nanomedicine*, **2014**, *9*, 2581.
- 9 X. Liang, Z. Deng, L. Jing, X. Li, Z. Dai, C. Li and M. Huanga *Chem. Commun.*, **2013**, *49*, 11029.
- 10 X. Jia, X. Cai, Y. Chen, S. Wang, H. Xu, K. Zhang, M. Ma, H. Wu, J. Shi, and H. Chen, *ACS Appl. Mater. Interfaces*, **2015**, *7*, 4579.
- 11 X. Cai , X. Jia , W. Gao , K. Zhang , M. Ma , S. Wang , Y. Zheng ,J. Shi , and H. Chen, *Adv. Funct. Mater.*, **2015**, DOI: 10.1002/adfm.201403991.
- 12 P. J. Faustino , Y. Yang , J. J. Progar , C. R. Brownell , N. Sadrieh , J. C. May, E. Leutzinger, D. A. Place , E. P. Duffy ,F. Houn, S. A. Loewke , V. J. Mecozi , C. D. Ellison, M. A. Khan, A. S. Hussain and R. C. Lyon, *J. Pharm. Biomed. Anal.* **2008**, *47*, 114.
- 13 Y. Yang , P.J. Faustino, J. J. Progar, C. R. Brownell, N. Sadrieh, J. C. May, E. Leutzinger, D. A. Place, E. P. Duffy, L. X. Yu, M. A. Khan and R. C. Lyon, *Int. J. Pharm.* **2008**, *353*, 187.
- 14 H. F. Weich, H. W. Strauss and B. Pitt, *Circulation*, **1977**, *56*, 188.
- 15 E. Lebowitz, M. W. Greene, R. Fairchild, P. R. Bradely-Moore, H. L. Atkins, A. N. Ansari, P. Richards and E. Belgrave, *J. Nucl. Med.*, **1975**, *15*, 151.

- 16 M. Perrier, M. Buisson, G. Massasso, J. Long, V. Boudousq, J.-P. Pouget, S. Peyrottes, Ch. Perigaud, C. Porredon-Guarch, J. de Lapuente, M. Borrás, J. Larionova and Y. Guari, *Nanoscale*, **2014**, *6*, 13425.
- 17 S. N. Gosh, *J. Inor. Nucl. Chem.* **1974**, *36*, 2465.
- 18 J. Lejeune, J. B. Brubach, P. Roy and A. Bleuzen, *C. R. Chimie*, **2014**, *17*, 534.
- 19 V. Hornok, I. Dékány, *J. Colloid Interface Sci.*, **2007**, *309*, 176.
- 20 K. Itaya and I. Uchida, *Inorg. Chem.*, **1986**, *25*, 389.
- 21 T. Maldiney, C. Richard, J. Seguin, N. Wattier, M. Bessodes and D. Scherman, *ACS nano*, **2011**, *5*, 854.
- 22 Q. He, Z. Zhang, F. Gao, Y. Li and J. Shi, *small*, **2011**, *7*, No. 2, 271.
- 23 C. Allen, N. Dos Santos, R. Gallagher, G. N. C. Chiu, Y. Shu, W. M. Li, S. Johnstone, A. S. Janoff, L. D. Mayer, M. S. Webb and M. B. Bally, *Bioscience Reports*, **2002**, *22*, 225.
- 24 K. Knop, R. Hoogenboom, D. Fischer, and U. S. Schubert, *Angew. Chem. Int. Ed.* **2010**, *49*, 6288.
- 25 S. Glišić, M. Cakic, G. Nikolic and B. Danilovic, *J. Mol. Struct.*, **2015**, *1084*, 345.
- 26 H. Zhang, Y. Xue, J. Huang, X. Xia, M. Song, K. Wen, X. Zhang, X. Luo, N. Cai, S. Long and F. Yu, *Mater Sci*, 2015, *50*, 2429.
- 27 M. Ajaz Hussain, A. Shah, I. Jantan, M. N. Tahir, M. R. Shah, R. Ahmed and S. N. A. Bukhari, *J Nanobiotechnology*, **2014**, *12*, 53.
- 28 R. Bornya, T. Lechleitnerb, T. Schmiedingerb, M. Hermannc, R. Tessadrid, G. Redhammer, J. Neumüllerf, D. Kerjaschkig, G. Berzaczya, G. Ermana, M. Popovica, J. Lammera and M. Funovicsa, *Contrast Media Mol. Imaging*, **2015**, *10*, 18.
- 29 L. De Backer, K. Braeckmans, M. C.A. Stuart, J. Demeester, S. C. De Smedt and K. Raemdonck, *J. Controlled Release*, **2015**, *206*,177.
- 30 E. Cho, M. N. Tahir, J. M. Choi, H. Kim, J.-H. Yu, S. Jung, *Carbohydr. Polym.*, **2015**, *133*, 221.
- 31 S. Ma, J. Zhou, A. Roshan, M. Wali, Y. He, X. Xu, J. Zhenggui Tang and Z. Gu, *J Mater Sci: Mater Med*, **2015**, *26*, 219.
- 32 L. Jing, X. Liang , Z. Deng, S. Feng, X. Li, M. Huang, C. Li, Z. Dai, *Biomaterials*, **2014**, *35*, 5814.
- 33 J. Fang, H. Nakamura and H. Maeda, *Adv. Drug Deliv. Rev.*, **2011**, *63*,136.
- 34 H. Maedaa, J. Wua, T. Sawaa, Y. Matsumurab and K. Horic, *J. Controlled Release*, **2000**, *65*, 271.
- 35 A. K. Lyer, G. Khaled, J. Fang and H. Maeda, *Drug Discovery Today*, **2006**, *11*,17.

Experimental part:

The syntheses were carried out using commercially available reagents. All chemical reagents were purchased and used without further purification. Thallium nitrate (TlNO_3 , 88.99%), D-Mannitol and Dextran ($M_w=6000\text{g/mol}$) were purchased from Aldrich and Sucrose was purchased from Alfa Aesar. Polymers POEMA-PDAEMA and POEMA-PVD were synthesized by Dr. Cyrille Boyer from school of Chemical Engineering, the University of New South Wales, Sydney, Australia. Encapsulation of $\text{Na}^+/\text{Fe}^{3+}/[\text{Fe}^{\text{II}}(\text{CN})_6]^{4-}$ NPs and $\text{Au}@\text{Na}^+/\text{Ni}^{2+}/[\text{Fe}^{\text{II}}(\text{CN})_6]^{4-}@\text{Na}^+/\text{Fe}^{3+}/[\text{Fe}^{\text{II}}(\text{CN})_6]^{4-}$ core@shell NPs in lipids bilayers was realized by Estelle Rascol, PhD in MACS team, Institute Charles Gerhardt, University of Montpellier, France.

Synthesis of 60 nm $\text{Na}^+/\text{Fe}^{3+}/[\text{Fe}^{\text{II}}(\text{CN})_6]^{4-}$ NPs (15):

At room temperature, an aqueous solution of $\text{FeCl}_3 \cdot 6\text{H}_2\text{O}$ (10 mM, 10mL) and $\text{Na}_4[\text{Fe}(\text{CN})_6] \cdot 10\text{H}_2\text{O}$ (11.25 mM, 10 mL) were added simultaneously to 100 mL of pure water at a 2 mL/hour rate, using a syringe pump. After completion of the addition, the mixture is stirred one additional hour before being centrifuged at 20000 rpm during 10 minutes. The supernatant was removed and the NPs were washed with water and centrifuged again at 20000 rpm during 10 min. The supernatant was removed and the NPs were washed with ethanol and centrifuged at 20000 rpm during 10 min and were dried under vacuum.

Characterizations:

FT-IR (KBr, ν , cm^{-1}): $\nu(-\text{OH})$ (coordinate water) = 3631 cm^{-1} , $\nu(-\text{OH})$ (crystalized water) = 3418 cm^{-1} , $\nu(\text{C}\equiv\text{N})$ = 2080 cm^{-1} ($\text{Fe}^{\text{II}}-\text{C}\equiv\text{N}-\text{Fe}^{\text{III}}$), $\delta(\text{H}-\text{O}-\text{H})$ (crystalized water) = 1605 cm^{-1} , $\nu(\text{Fe}^{\text{II}}-\text{CN})$ = 601 cm^{-1} , $\delta(\text{Fe}^{\text{II}}-\text{CN})$ = 496 cm^{-1} .

EDS: 10.65/89.35 (Na/Fe). Estimated formula: $\text{Na}_{0.1}\text{Fe}[\text{Fe}(\text{CN})_6]_{0.77}$.

UV-visible: 725 nm (intervalence absorption band $\text{Fe}^{\text{II}}-\text{CN}-\text{Fe}^{\text{III}} \rightarrow \text{Fe}^{\text{III}}-\text{CN}-\text{Fe}^{\text{II}}$). Zeta potential: -32 mV. Size by DLS measurements: 190 nm (Pdl: 0.2).

Post-synthetic grafting of $\text{Na}^+/\text{Fe}^{3+}/[\text{Fe}^{\text{II}}(\text{CN})_6]^{4-}$ NPs with stabilizers:

The $\text{Na}^+/\text{Fe}^{3+}/[\text{Fe}^{\text{II}}(\text{CN})_6]^{4-}$ NPs were grafted (Sucrose, D-Mannitol, PEG-Amine 1500 g/mol, Dextran 6000g/mol, Polymers POEMA-PDAEMA and POEMA-PVD with a stoichiometry 1:1 in water for 24 hours, before being centrifuged at 20000 rpm during 10 min. The supernatant was removed and the NPs were washed with water and centrifuged again at 20000 rpm during 10 min, for 2 times, then the NPs were dried under vacuum.

Characterizations:

$\text{Na}^+/\text{Fe}^{3+}/[\text{Fe}^{\text{II}}(\text{CN})_6]^{4-}/\text{Sucrose}$:

FT-IR (KBr, ν , cm^{-1}): $\nu(-\text{OH})$ (coordinate water) = 3600 cm^{-1} , $\nu(-\text{OH})$ (crystalized water) = 3415 cm^{-1} , $\nu(\text{C}-\text{H})$ = 2920 and 2857 cm^{-1} , $\nu(\text{C}\equiv\text{N})$ = 2080 cm^{-1} ($\text{Fe}^{\text{II}}-\text{C}\equiv\text{N}-\text{Fe}^{\text{III}}$), $\delta(\text{H}-\text{O}-\text{H})$ (crystalized water) = 1611 cm^{-1} , $\delta(\text{O}-\text{H})$ = 1350 and 1268 cm^{-1} , $\nu(\text{C}-\text{O})$ = 1136 and 1079 cm^{-1} , $\nu(\text{C}-\text{C})$ = 987 , 920 , 887 , 851 and 812 cm^{-1} , $\delta(-\text{CH}_2)$ = 724 cm^{-1} , $\nu(\text{Fe}^{\text{II}}-\text{CN})$ = 603 cm^{-1} , $\delta(\text{Fe}^{\text{II}}-\text{CN})$ = 500 cm^{-1} .

$\text{Na}^+/\text{Fe}^{3+}/[\text{Fe}^{\text{II}}(\text{CN})_6]^{4-}/\text{D-Mannitol}$:

FT-IR (KBr, ν , cm^{-1}): $\nu(-\text{OH})$ (coordinate water) = 3600 cm^{-1} , $\nu(-\text{OH})$ (crystalized water) = 3437 cm^{-1} , $\nu(\text{C}-\text{H})$ = 2925 and 2850 cm^{-1} , $\nu(\text{C}\equiv\text{N})$ = 2080 cm^{-1} ($\text{Fe}^{\text{II}}-\text{C}\equiv\text{N}-\text{Fe}^{\text{III}}$), $\delta(\text{H}-\text{O}-\text{H})$ (crystalized water) = 1623 cm^{-1} , $\delta(\text{O}-\text{H})$ = 1364 and 1265 cm^{-1} , $\nu(\text{C}-\text{O})$ = 1139 and 1070 cm^{-1} , $\nu(\text{C}-\text{C})$ = 982 , 927 and 887 cm^{-1} , $\delta(-\text{CH}_2)$ = 727 cm^{-1} , $\nu(\text{Fe}^{\text{II}}-\text{CN})$ = 600 cm^{-1} , $\delta(\text{Fe}^{\text{II}}-\text{CN})$ = 502 cm^{-1} .

Na⁺/Fe³⁺/[Fe^{II}(CN)₆]⁴⁻/PEG-Amine 1500 g/mol:

FT-IR (KBr, ν , cm⁻¹): ν (-OH) (crystalized water) = 3402 cm⁻¹, ν (C-H) = 2926 and 2851 cm⁻¹, ν (C≡N) = 2083 cm⁻¹ (Fe^{II}-C≡N-Fe^{III}), ν (N-H) = 1643 cm⁻¹, δ (H-O-H) (crystalized water) = 1600 cm⁻¹, ν (C-N) = 1234 cm⁻¹, ν (C-O) = 1200, 1157 and 1072 cm⁻¹, ν (C-C) = 987, 917 and 880 cm⁻¹, δ (-CH₂) = 711 cm⁻¹, ν (Fe^{II}-CN) = 601 cm⁻¹, δ (Fe^{II}-CN) = 498 cm⁻¹.

Na⁺/Fe³⁺/[Fe^{II}(CN)₆]⁴⁻/Dextran:

FT-IR (KBr, ν , cm⁻¹): ν (-OH) (coordinate water) = 3611 cm⁻¹, ν (-OH) (crystalized water) = 3427 cm⁻¹, ν (C-H) = 2921 and 2855 cm⁻¹, ν (C≡N) = 2084 cm⁻¹ (Fe^{II}-C≡N-Fe^{III}), δ (H-O-H) (crystalized water) = 1623 cm⁻¹, δ (O-H) = 1363 and 1263 cm⁻¹, ν (C-O) = 1127 and 1072 cm⁻¹, ν (C-C) = 1012 cm⁻¹, δ (-CH₂) = 721 cm⁻¹, ν (Fe^{II}-CN) = 600 cm⁻¹, δ (Fe^{II}-CN) = 497 cm⁻¹.

Na⁺/Fe³⁺/[Fe^{II}(CN)₆]⁴⁻/POEMA-PDAEMA:

FT-IR (KBr, ν , cm⁻¹): ν (-OH) (coordinate water) = 3621 cm⁻¹, ν (-OH) (crystalized water) = 3426 cm⁻¹, ν (C-H) = 2931 and 2860 cm⁻¹, ν (C≡N) = 2080 cm⁻¹ (Fe^{II}-C≡N-Fe^{III}), ν (C=O) = 1723 cm⁻¹, δ (H-O-H) (crystalized water) = 1618 cm⁻¹, ν (C=C) = 1458 and 1353 cm⁻¹, ν (C=S) = 1388 cm⁻¹, ν (C-O) = 1248 and 1107 cm⁻¹, ν (C-C) = 992 and 852 cm⁻¹, ν (Fe^{II}-CN) = 601 cm⁻¹, δ (Fe^{II}-CN) = 496 cm⁻¹.

Na⁺/Fe³⁺/[Fe^{II}(CN)₆]⁴⁻/POEMA-PVD:

FT-IR (KBr, ν , cm⁻¹): ν (-OH) (coordinate water) = 3627 cm⁻¹, ν (-OH) (crystalized water) = 3431 cm⁻¹, ν (C-H) = 2915 and 2855 cm⁻¹, ν (C≡N) = 2081 cm⁻¹ (Fe^{II}-C≡N-Fe^{III}), ν (C=O) = 1724 cm⁻¹, ν (N-H) = 1638 cm⁻¹, δ (H-O-H) (crystalized water) = 1618 cm⁻¹, ν (C=C) = 1463 cm⁻¹, ν (C=S) = 1388 cm⁻¹, ν (C-O) = 1248 and 1107 cm⁻¹, ν (C-C) = 822 cm⁻¹, ν (Fe^{II}-CN) = 601 cm⁻¹, δ (Fe^{II}-CN) = 502 cm⁻¹.

Post-synthetic grafting Au@NaNi^{II}Fe^{II}@NaFe^{II}Fe^{III} NPs with stabilizers:

The Au@Na⁺/Ni²⁺/[Fe^{II}(CN)₆]⁴⁻@Na⁺/Fe³⁺/[Fe^{II}(CN)₆]⁴⁻ NPs were grafted (Dextran, POEMA-PDAEMA according to the same protocol than the post-grafting of Na⁺/Fe³⁺/[Fe^{II}(CN)₆]⁴⁻ NPs.

Characterizations:

Au@NaNi^{II}Fe^{II}@NaFe^{II}Fe^{III}/Dextran:

FT-IR (KBr, ν , cm⁻¹): ν (-OH) (coordinate water) = 3631 cm⁻¹, ν (-OH) (crystalized water) = 3426 cm⁻¹, ν (C-H) = 2921 and 2850 cm⁻¹, ν (C≡N) = 2080 cm⁻¹ (Fe^{II}-C≡N-Fe^{III}), δ (H-O-H) (crystalized water) = 618 cm⁻¹, δ (O-H) = 1378 and 1263 cm⁻¹, ν (C-O) = 1127 and 1067 cm⁻¹, ν (C-C) = 982 cm⁻¹, δ (-CH₂) = 722 cm⁻¹, ν (Fe^{II}-CN) = 597 cm⁻¹, δ (Fe^{II}-CN) = 496 and 473 cm⁻¹.

Au@NaNi^{II}Fe^{II}@NaFe^{II}Fe^{III}/POEMA-PDAEMA:

FT-IR (KBr, ν , cm⁻¹): ν (-OH) (crystalized water) = 3431 cm⁻¹, ν (C-H) = 2931 and 2850 cm⁻¹, ν (C≡N) = 2080 cm⁻¹ (Fe^{II}-C≡N-Fe^{III}), δ (H-O-H) (crystalized water) = 1623 cm⁻¹, ν (C=C) = 1458 cm⁻¹, ν (C=S) = 1378 cm⁻¹, ν (C-O) = 1263, 1133 and 1062 cm⁻¹, ν (C-C) = 927, 887 and 857 cm⁻¹, δ (-CH₂) = 727 cm⁻¹, ν (Fe^{II}-CN) = 601 cm⁻¹, δ (Fe^{II}-CN) = 502 cm⁻¹ and 478 cm⁻¹.

Incorporation of TI in Na⁺/Fe³⁺/[Fe^{II}(CN)₆]⁴⁻/Dextran NPs:

The NPs are dispersed in ultrapure water (1mg/mL), and then mixed with a varying concentration of an aqueous solution of TiNO₃. The solution is stirred for a determine time (1h, 2h, 4h, 12h, 24h), then centrifuged at 20000 rpm during 10 min. The supernatant was removed and the NPs were washed with water and centrifuged again at 20000 rpm during 10 min. The supernatant was removed and the NPs were washed with ethanol and centrifuged at 20000 rpm during 10 min and were dried under vacuum.

Incorporation of TI in Au@NaNi^{II}Fe^{II}@NaFe^{II}Fe^{III}/Dextran NPs:

Ti is incorporated in Au@Na⁺/Ni²⁺/[Fe^{II}(CN)₆]⁴⁻@Na⁺/Fe³⁺/[Fe^{II}(CN)₆]⁴⁻/Dextran NPs according to the same protocol than the incorporation of TI in Na⁺/Fe³⁺/[Fe^{II}(CN)₆]⁴⁻/Dextran NPs, by modifying the varying concentration of aqueous solution of TiNO₃.

Incorporation of TI in Na⁺/Fe³⁺/[Fe^{II}(CN)₆]⁴⁻/Lipid bilayers NPs:

Ti is incorporated in Na⁺/Fe³⁺/[Fe^{II}(CN)₆]⁴⁻/Lipid bilayers NPs according to the same protocol than the incorporation of TI in Na⁺/Fe³⁺/[Fe^{II}(CN)₆]⁴⁻/Dextran NPs.

Incorporation of TI in Au@NaNi^{II}Fe^{II}@NaFe^{II}Fe^{III}/Lipid bilayers NPs:

Ti is incorporated in Au@Na⁺/Ni²⁺/[Fe^{II}(CN)₆]⁴⁻@Na⁺/Fe³⁺/[Fe^{II}(CN)₆]⁴⁻/Lipid bilayers NPs according to the same protocol than the incorporation of TI in Na⁺/Fe³⁺/[Fe^{II}(CN)₆]⁴⁻/Lipid bilayers NPs.

Nanoparticles ²⁰¹Ti⁺/ Na⁺/Fe³⁺/[Fe^{II}(CN)₆]⁴⁻/grafted Dextran, ²⁰¹Ti⁺/ Na⁺/Fe³⁺/[Fe^{II}(CN)₆]⁴⁻/grafted POEMA-PDAEMA, ²⁰¹Ti⁺/ Na⁺/Fe³⁺/[Fe^{II}(CN)₆]⁴⁻/lipid bilayers and Au@NaNi^{II}Fe^{II}@²⁰¹Ti⁺Fe^{II}Fe^{III}/grafted Dextran for SPECT/CT measurements.

²⁰¹TiCl was obtained from CisBio, and nanoparticles were radio-labelled at the activity of 10 MBq per mg of NP.

In a typical experiment, 2 mg of the studied nanoparticles, either Na⁺/Fe³⁺/[Fe^{II}(CN)₆]⁴⁻/grafted Dextran, Na⁺/Fe³⁺/[Fe^{II}(CN)₆]⁴⁻/grafted POEMA-PDAEMA, and Au@NaNi^{II}Fe^{II}@Fe^{II}Fe^{III}/grafted Dextran was treated with 10MBq.mL⁻¹ ²⁰¹TiCl aqueous solution in order to obtain ²⁰¹Ti⁺/Na⁺/Fe³⁺/[Fe^{II}(CN)₆]⁴⁻/grafted Dextran, ²⁰¹Ti⁺/Na⁺/Fe³⁺/[Fe^{II}(CN)₆]⁴⁻/grafted POEMA-PDAEMA, and Au@NaNi^{II}Fe^{II}@²⁰¹Ti⁺Fe^{II}Fe^{III}/grafted Dextran nanoprobles.

Nanoparticles ²⁰¹Ti⁺/ Na⁺/Fe³⁺/[Fe^{II}(CN)₆]⁴⁻/lipid bilayers:

In a typical experiment, a solution of 2 mg of the studied nanoparticles, Na⁺/Fe³⁺/[Fe^{II}(CN)₆]⁴⁻/lipid bilayers in 250μL of 0.9 % NaCl was treated with 750 μL of a 10 MBq.mL⁻¹ ²⁰¹TiCl aqueous solution in order to obtain ²⁰¹Ti⁺/ Na⁺/Fe³⁺/[Fe^{II}(CN)₆]⁴⁻/lipid bilayers nanoprobles.

SPECT-CT imaging:

All animal experiments were performed in compliance with the guidelines of the French government and the standards of Institut National de la Santé et de la Recherche Médicale for experimental animal studies (agreement C34-172-27).

Mice (Nude athymic FoxN1) were obtained from Harlan Laboratories and were acclimated for one week before experimental use. They were housed at 22°C and 55% humidity with a light–dark cycle of 12 h. Food and water were available ad libitum.

Whole-body SPECT/CT images were acquired at various times (20 min, 1h20, 3h20, 7h20, 26h, 48h) after tail vein injection of 8 MBq of radio-labelled Na⁺/Fe³⁺/[Fe^{II}(CN)₆]⁴⁻/grafted

Dextran, $\text{Na}^+/\text{Fe}^{3+}/[\text{Fe}^{\text{II}}(\text{CN})_6]^{4-}$ /grafted POEMA-PDAEMA, $^{201}\text{Tl}^+/\text{Na}^+/\text{Fe}^{3+}/[\text{Fe}^{\text{II}}(\text{CN})_6]^{4-}$ /lipid bilayers and $\text{Au}@[\text{Ni}^{\text{II}}\text{Fe}^{\text{II}}@[\text{Fe}^{\text{II}}\text{Fe}^{\text{III}}]]$ /grafted Dextran nanoprobe. Mice were anesthetized with 2% isoflurane and positioned on the bed of 4-head multiplexing multipinhole NanoSPECT camera (Bioscan Inc., Washington, USA). Energy window was centered at 73 keV with $\pm 20\%$ width, acquisition times were defined to obtain 30 000 counts for each projection with 24 projections. Images and maximum intensity projections (MIPs) were reconstructed using the dedicated software Invivoscope® (Bioscan, Inc., Washington, USA) and Mediso InterViewXP® (Mediso, Budapest Hungary). Concurrent microCT whole-body images were performed for anatomic co-registration with SPECT data. Reconstructed data from SPECT and CT were visualized and co-registered using Invivoscope®. *In vivo* experiments were repeated three times, and quantification on whole body images provided semi-quantitative data.

General conclusion

For several years, the design of multifunctional nano-objects has particularly attracted the researchers. Such systems combine the properties of different materials, exhibiting diverse responses when subjected to various stimuli, and sometimes leading to the appearance of interesting new properties or synergistic effects. This work has been devoted to the combination of two materials, gold and Prussian Blue and its analogous, to elaborate magneto-optical nano-heterostructures.

The second chapter was dedicated to the synthesis of Prussian Blue Analogous nanoparticles such as $\text{Ni}_3[\text{Fe}(\text{CN})_6]_2$ presenting different and controlled sizes in order to better understand the evolution of their characteristics with the size reduction. They were obtained using two different approaches. Ultra-small nanoparticles were synthesized in presence of stabilizing agents. The other sized-nanoparticles were elaborated without any stabilizing agents, then post-synthetically grafted with polymers. The nanoparticles, ranging from 2 nm to 180 nm, present various morphologies depending on their size: below 14 nm, like-sphere shape is observed, and under this critical size, truncated cubes are obtained. The different characterization techniques used have revealed an increase of the $\text{Fe}^{\text{II}}/\text{Fe}^{\text{III}}$ ratio with the size reduction. Using ^{57}Fe Mössbauer spectroscopy, the Debye temperature has been estimated, indicating an increase of the rigidity with the size reduction, which is in accordance to a “nano” behavior which occurs for size below 10 nm.

In the third chapter, we have focused on the synthesis of core-shell $\text{Au}@\text{K}^+/\text{Ni}^{2+}/[\text{Fe}^{\text{II}}(\text{CN})_6]^{4-}$ NPs obtained according to a new and rational approach consisting in i) the formation of the cyanide-stabilized gold nanoparticles and ii) the growth of the Prussian Blue analogous shell on the gold surface. The nanoparticles obtained are well-defined and present a single gold core of around 20 nm coated by a homogeneous shell of cyano-bridged coordination polymer for a total size of around 50 nm. These nano-objects exhibit both optical properties of the gold core and paramagnetic properties of the PBA shell. The mechanism of the nanoparticles formation was investigated using diverse techniques. According to the results, it may be rational to think that a coordination phenomenon occurs between the surface of the cyanide-stabilized gold nanoparticles and the divalent transition metal precursor inducing the shell growth process. The control of both the gold core size and the cyano-bridged coordination polymer shell was performed by varying respectively the temperature and the quantity of precursors added. The size modification of the gold core and the PBA layer induces a variation of the Surface Plasmon phenomenon. However, only the control of the shell thickness clearly permits to finely tune the optical properties. Different variations in the synthesis were performed, in order to improve our rational approach. First, we have shown that the modification of the counter ion nature of the PBA precursors and the reducing agent also permits to obtain the targeted heterostructures, contrary to the use of different gold precursors. The modulation of the PBA nature was also performed, in order to implement different magnetic properties than paramagnetism, such as ferromagnetism. Diverse cyano-bridged coordination polymers were used but heterostructures were obtained only for $\text{Co}_2[\text{Fe}(\text{CN})_6]$, leading to $\text{Au}@\text{K}^+/\text{Co}^{2+}/[\text{Fe}^{\text{II}}(\text{CN})_6]^{4-}$ NPs. These nano-objects also present paramagnetism, but that prove the possibility to transpose the synthetic approach to other PBA to obtain core-shell to obtain heterostructures. Finally, by etching the gold core of the core-shell nanoparticles with using cyanide ions, hollow nano-objects were synthesized, without any modification of

the cyano-bridged coordination network. This strategy can be viewed as an alternative to design such hollow PBA nanoparticles.

The fourth chapter was devoted to the synthesis of double-layered core-shell nanoparticles obtained by the subsequent growing of a new PBA shell on the single-layered core shell nanoparticles. Several cyano-bridged coordination polymer were used, such as $\text{Ni}^{\text{II}}\text{Cr}^{\text{III}}$, $\text{Ni}^{\text{II}}\text{Fe}^{\text{III}}$, $\text{Co}^{\text{II}}\text{Fe}^{\text{II}}$ and $\text{Fe}^{\text{III}}\text{Fe}^{\text{II}}$ to obtain new heterostructures. Moreover, a series of double-layered core-shell $\text{Au}@\text{Ni}^{\text{II}}\text{Fe}^{\text{II}}@\text{Ni}^{\text{II}}\text{Cr}^{\text{III}}$ NPs with different second shell thickness was obtained by varying the quantity of precursors added. These nano-objects exhibit optical properties originated from the Surface Plasmon Resonance phenomenon due to the gold core. The increase of the total shell thickness induces a modification of the optical properties, originated from the increase of the local refractive index around the gold core and from a confinement of the free electrons within the core. The magnetic properties of the double-layered nanoparticles were studied. First, we investigated the effect of the shell size on the evolution of the magnetic properties with using the series of $\text{Au}@\text{Ni}^{\text{II}}\text{Fe}^{\text{II}}@\text{Ni}^{\text{II}}\text{Cr}^{\text{III}}$ NPs. While the larger shells present long range ordering behavior, the smallest present short range magnetic ordering. On these latter, several models were used, indicating a superparamagnetic or spin glass behavior. However, strong interparticle interactions were preventing any possibility to validate one or the other magnetic behavior. These interactions were limited by diluting the nanoparticles in a PVP matrix, revealing different magnetic behavior according to the variation of the $\text{Ni}^{\text{II}}\text{Cr}^{\text{III}}$ shell thickness. This phenomenon is probably due to the contribution of the surface disorder and the disorder originate from the interface between the two Prussian Blue analogous shell. Then we also investigated the properties of the others systems synthesized, which present a long range ordering, corresponding to the magnetic behavior of their bulk analogous.

In the fifth chapter, we have evaluated the potential of the core-shell nanoparticles to be used as contrast agents for SPECT-CT imaging. In order to compare the effect of the morphology and composition on the nanoparticles biodistribution and kinetic, simple cubic Prussian Blue nanoparticles with similar size than the $\text{Au}@\text{K}^+/\text{Ni}^{2+}/[\text{Fe}^{\text{II}}(\text{CN})_6]^{4-}@\text{K}^+/\text{Fe}^{3+}/[\text{Fe}^{\text{II}}(\text{CN})_6]^{3-}$ nanoparticles evaluated were synthesized. As the core-shell nano-objects, these nanoparticles exhibit a strong intervalence charge-transfer band. Then, both of these systems were post-synthetically grafted to ensure their stability in aqueous media. Several stabilizing agents, as organic molecules and polymers, were tested. We finally chose Dextran and POEMA-PDAEMA polymers (synthesized by Dr. Cyrille Boyer from school of Chemical Engineering, University of New South Wales, Sydney, Australia) for our study. Moreover, in collaboration with Estelle Rascol and Pr. Joel Chopineau from MACS, ICGM, Université de Montpellier, the nanoparticles were covered by lipid bilayers, and then three stabilizing agents were evaluated to compare the effect of the functionalization on the biodistribution and kinetic. The different systems (two types of nanoparticles, three types of functionalization) were $^{201}\text{Tl}^+$ -labelled and injected in vivo into sane and mice with tumor. The images comparative data of the quantified activity indicated a rapid clearance of the nanoprobes into the liver and the lungs, except for the Dextran which present an interesting activity in the lungs for 3h. However, no activity in the tumor was detected, revealing no passive targeting for the nanoprobes.

We have successively obtained magneto-plasmonic core-shell nano-objects combining both gold as core and PBA as shell. However, the implement of properties as ferromagnetism with using cyano-bridged coordination polymers as Ni^{II}Cr^{III} remains dependent from the presence of a first paramagnetic Ni^{II}Fe^{III} used as anchoring point. As outlook, it may be interesting to get free from this first shell by growing directly the ferromagnetic shell on the gold nanoparticles, with maybe the apparition of new synergistic effect arising from the direct interface between the gold and the ferromagnetic PBA shell, as for examples the enhancement of the SPR phenomenon at temperature below T_C (originating from the magnetostriction of the magnetic material) or the modification of the magnetic properties under irradiation in the SPR wavelength. We have also attempted to modify the plasmonic properties by changing the shape or the metal used for the core. It may be really interesting to persevere in this sense to target different properties, as for example the implement of a Surface Plasmon Resonance Band in the near IR, which is more efficient for biomedical applications. Concerning the applications of the core-shell nanoparticles for bioimaging, results may be more convincing by performing an active targeting with using molecules able to be detected by the tumor cells receptors, permitting to image the cancer.

Annexes

Annex 1: General instrumentation.

The infrared spectra in transmission mode were recorded in a dried (oven, 60°C) KBr matrix formatted as disks on a Nicolet Model 510P spectrophotometer. For viscous polymers, the measures were performed with using the ATR accessory on the Nicolet Model 510P spectrophotometer. A background without the sample was recorded.

Raman spectroscopic analyses were performed in reflectance mode with a LabRAM ARAMIS IR² (Horiba Jobin Yvon) on solid samples and on solutions. For the measurements in solutions, a glass cuve has been used and the focus was performed at 50 μm under the surface.

UV-Vis spectra were collected on a Specord 210 UV-VIS spectrophotometer in transmission modes. A reference background was registered with the solvent (generally ultrapure water).

X-Ray Powder Diffraction patterns (XRPD) for all materials were recorded in the interval $2\theta = 5-90^\circ$ at room temperature with the XPERTpro Panalytical diffractometer mounted in a Debye-Scherrer configuration and equipped with a Cu K α radiation. For all samples, the XRDP planar configuration with fixed samples and rotating diffraction angle was used.

The DLS/Zeta potential measurements were performed on a Zetasizer Nano ZS (Malvern Instrument). For the measurement on gold and core-shell nanoparticles, the material refractive index and absorption used are those correspondent of gold, *i.e.* RI = 1.50 and Absorption = 0.001.

Elemental analyses were performed by the Service Central d'analyse (CNRS, Villeurbanne, FRANCE).

EDX measurements were performed on a FEI Quanta FEG 200 instrument. The powders were deposited on an adhesive carbone film and analyzed under high vacuum. The quantification of the heavy elements was carried out with the INCA software with a dwell time of 3 μs .

Transmission Electron Microscopy (TEM) observations were carried out on a microscope JEOL 1200 EXII operated at 100 kV. The samples were prepared by deposition of a drop of the dispersion (generally in water or ethanol) on copper grid and air-drying. The NPs' size distribution histograms were determined using enlarged TEM micrographs taken at magnification of 100K on a statistical sample of ca. 300 NPs. HRTEM measurements were performed on a JEOL 2200FS at 200 kV and equipped with a STEM module, a BF and a HAADF detector.

Magnetic susceptibility data were collected with a Quantum Design MPMS-XL SQUID magnetometer working in the temperature range 1.8 – 350 K and up to 7 T, by applying the zero-field-cooled/field-cooled (ZFC/FC) magnetization method. In the ZFC experiments, the samples were cooled in the absence of a static magnetic field and the magnetization was then recorded as a function of the temperature under a 100 Oe field. The FC magnetization data were collected after cooling the sample with the same field. The temperature dependence of the in-phase and the out-of-phase magnetic susceptibilities

were measured in a zero dc-field with frequencies ranging from 1 Hz to 1488 Hz, in alternating current (AC) mode. The field dependence of the AC in-phase and out-of-phase magnetic susceptibilities were measured with an oscillating field at a frequency of 100 Hz.

Annex 2: Supplementary information of chapter II.

2.1 Synthesis of ultra-small $K^+/Cu^{2+}/[Fe(CN)_6]^{3-}/PEG-NH_2$ NPs using the first approach.

Ultra-small $K^+/Cu^{2+}/[Fe(CN)_6]^{3-}/PEG-NH_2$ NPs (**16**) are obtained using the first approach as $K^+/Ni^{2+}/[Fe(CN)_6]^{3-}/PEG-NH_2$ by self-assembly reaction in water between an hexacyanometallate precursor, $K_3[Fe(CN)_6]$, and a divalent transition metal ion Cu^{2+} in the presence of PEG-NH₂, which prevents the infinite growth of the tridimensional cyano-bridged network by coordination with the metal ions (figure 1). The used stoichiometry of PEG-NH₂/ M^{2+} is equals to 0.5/1. The synthesis consists in adding the aqueous solution of divalent transition metal salt ($Ni(NO_3)_2 \cdot 6H_2O$ or $Cu(NO_3)_2 \cdot 3H_2O$) containing half of the amount of PEG-NH₂ into the aqueous solution of the hexacyanometallate precursor ($K_3[Fe(CN)_6]$) containing the other half amount of PEG-NH₂. The self-assembly reaction leads to a dark red-copper solution. After reaction, the solution was filtered through a filter syringe (0.45 μm , PTFE), then precipitated with acetone, centrifuged, washed and dried under vacuum.

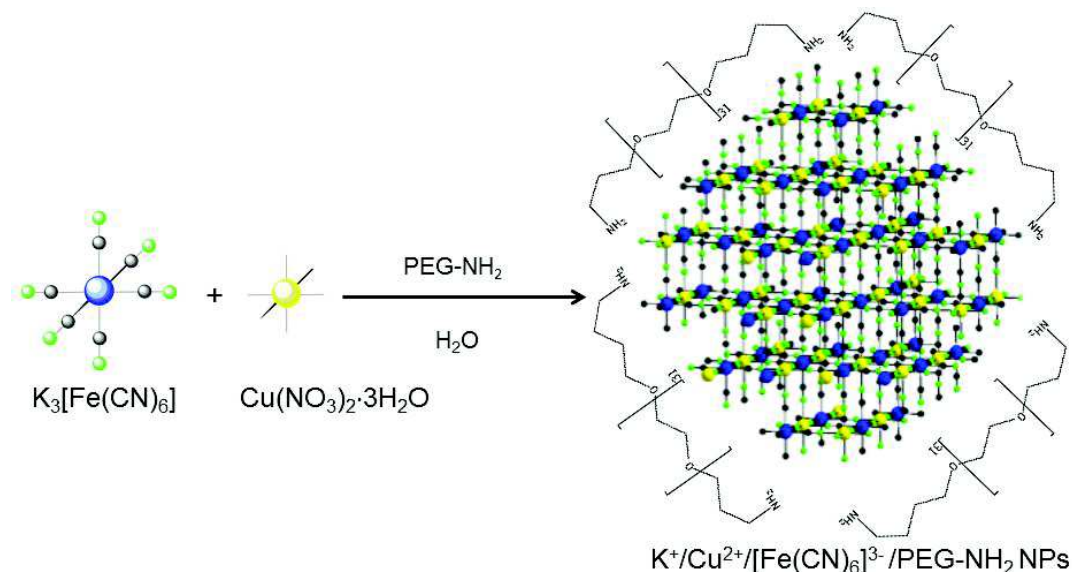


Figure 1: Schematic representation of synthesis of $K^+/Cu^{2+}/[Fe(CN)_6]^{3-}/PEG-NH_2$ NPs (**16**).

The structural characteristics of the $K^+/Cu^{2+}/[Fe(CN)_6]^{3-}/PEG-NH_2$ NPs were obtained using IR spectroscopy. The formation of PBA cyano-bridged network is confirmed with the presence of the stretching vibration of the bridging cyano-groups¹⁻⁶ (figure 2). These bands, located at 2168 cm^{-1} and 2012 cm^{-1} are characteristic of respectively $Fe^{III}-C \equiv N-Cu^{II}$ and $Fe^{II}-C \equiv N-Cu^{II}$. As for the $K^+/Ni^{2+}/[Fe(CN)_6]^{3-}/PEG-NH_2$ NPs, that indicates the presence of both Fe^{III} and Fe^{II} in the structure, due to the reduction of a part of the ferric ions Fe^{3+} , in ferrous ions Fe^{2+} in the PBA's network. The reduction is also attested by the metal-carbon bond stretching vibration with the presence of a band at 593 cm^{-1} for

Fe^{II}-CN linkages. No trace of the band corresponding to metal-carbon bond stretching vibration of the Fe^{III}-CN linkage is observed, indicating a large amount in Fe^{II} in the structure¹⁶⁻¹⁸. Finally, the metal-carbon bending vibration at 480 cm⁻¹, attributed to Fe^{II}-CN, confirms once more a large ratio of Fe^{II} in the NPs⁵⁻⁷.

As for K⁺/Ni²⁺/[Fe(CN)₆]³⁻/PEG-NH₂ NPs, the presence of water is indicated by characteristic bands located in 3700-3000 cm⁻¹, corresponding to -OH vibration band. The very broad band at 3423 cm⁻¹ corresponds to crystalized water molecules, involved in a hydrogen-bonded network⁶. The shoulder located at 3632 cm⁻¹ corresponds to water molecules coordinated to the metallic ions of the cyano-bridged network⁶ (Figure 24). This water is coordinated to the Cu²⁺ ions to complete their coordination sphere, due to the presence of several vacancies originated from the absence of a part of the [Fe(CN)₆]³⁻ moieties. The presence of a band located at 1621 cm⁻¹ region, attributed to the bending vibration of H-O-H linkage confirms the presence of crystalized water molecules.

On other hand, the presence of the stabilizer is confirmed by several characteristic bands^{8,9} (figure 2). Two bands located at 2924 cm⁻¹ and 2889 cm⁻¹ are attributed to CH₂ and CH₃ stretching vibration. Several bands, corresponding to C-C stretching vibrations, are located at 1463 cm⁻¹, 1350 cm⁻¹ and 943 cm⁻¹. C-N stretching vibrations bands, observed at 1293 and 1259 cm⁻¹, prove the presence of the terminal-amino groups of PEG-NH₂. The bands located at 1088 cm⁻¹ have been assigned to C-O stretching vibration band, corresponding to the polyethylene glycol groups in the PEG-NH₂.

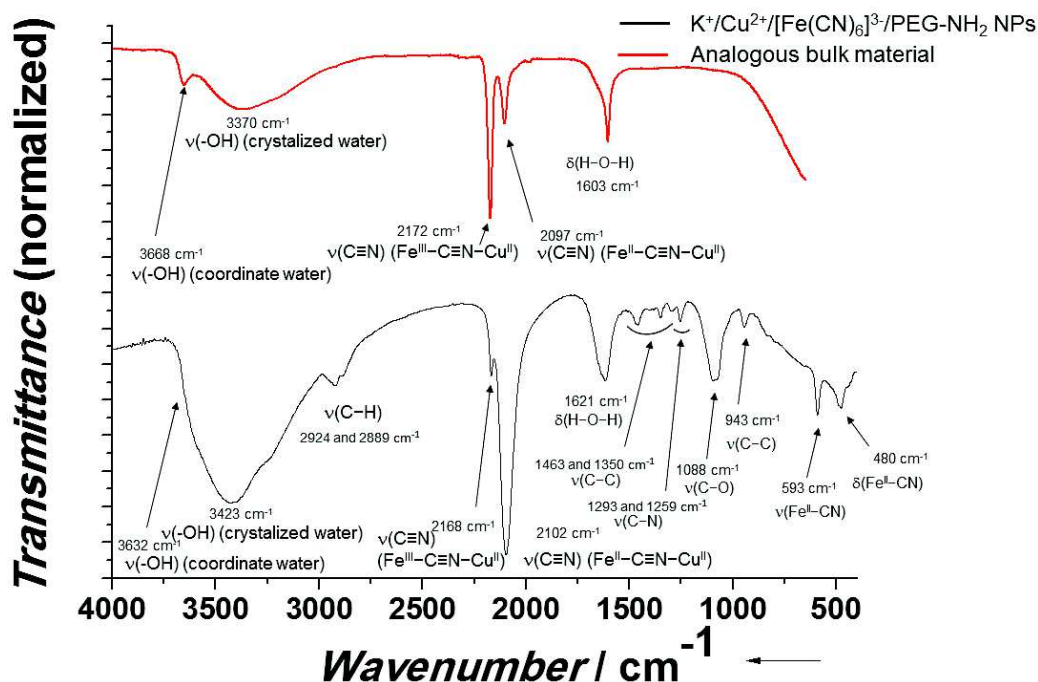


Figure 2: IR spectra of K⁺/Cu²⁺/[Fe(CN)₆]³⁻/PEG-NH₂ NPs and the analogous bulk material.

As for the K⁺/Ni²⁺/[Fe(CN)₆]³⁻ NPs, the size reduction of the particles leads to the increase of the amount in Fe^{II}. That is revealed by the respective intensity two bands corresponding respectively to the Fe^{III}-C≡N-Cu^{II} and Fe^{II}-C≡N-Cu^{II} linkages, by comparison with the IR spectrum of the analogous bulk material (figure 2). Indeed, the band located at 2168 cm⁻¹ (Fe^{III}-C≡N-Cu^{II}) is more intense for the analogous bulk material than the band located at 2102 cm⁻¹ (Fe^{II}-C≡N-Cu^{II}), but it is the contrary for the ultra-small

$\text{K}^+/\text{Cu}^{2+}/[\text{Fe}(\text{CN})_6]^{3-}/\text{PEG-NH}_2$ NPs. The quantification, by calculating the areas under the respective bands, gives values of the $\text{Fe}^{\text{II}}/\text{Fe}^{\text{III}}$ ratio, of 0.85 for the analogous bulk material and 216 for the ultra-small NPs. As for the $\text{K}^+/\text{Ni}^{2+}/[\text{Fe}(\text{CN})_6]^{3-}$ -NPs, that indicates a large amount in Fe^{II} , which is probably located at the NPs surface, due to the increase of the number of atoms at the surface with the size reduction.

The ultra-small $\text{K}^+/\text{Cu}^{2+}/[\text{Fe}(\text{CN})_6]^{3-}/\text{PEG-NH}$ NPs and the analogous bulk material were characterized using Raman spectroscopy^{10,11} (figure 3). As for the $\text{K}^+/\text{Ni}^{2+}/[\text{Fe}(\text{CN})_6]^{3-}$ -NPs, the Raman spectra indicate for the analogous bulk material the presence of a broad band located around 2201 cm^{-1} corresponding to the stretching vibrations of the $\text{Fe}^{\text{III}}-\text{C}\equiv\text{N}$ linkage and two low-wavenumbers bands characteristic of the $\text{Fe}^{\text{II}}-\text{C}\equiv\text{N}$ linkage¹², located at 2070 cm^{-1} and 2114 cm^{-1} . For the ultra-small $\text{K}^+/\text{Cu}^{2+}/[\text{Fe}(\text{CN})_6]^{3-}/\text{PEG-NH}_2$ NPs, the stretching vibrations of the $\text{Fe}^{\text{III}}-\text{C}\equiv\text{N}$ linkage is observed at 2166 cm^{-1} , but a broad band is observed at 2105 cm^{-1} instead of the two low-wavenumbers bands characteristic of the $\text{Fe}^{\text{II}}-\text{C}\equiv\text{N}$ linkage, larger than the bands observed for the bulk analogous. Moreover, while the band corresponding to the $\text{Fe}^{\text{III}}-\text{C}\equiv\text{N}$ linkage is really larger than the two low-wavenumbers bands characteristic of the $\text{Fe}^{\text{II}}-\text{C}\equiv\text{N}$ linkage¹² for the bulk material, their respective intensities are clearly modified for the ultra-small NPs, where the band corresponding to the $\text{Fe}^{\text{III}}-\text{C}\equiv\text{N}$ linkage is more intense but less larger than those attributed to the $\text{Fe}^{\text{II}}-\text{C}\equiv\text{N}$ linkage. That confirms that the size reduction induces an increase of the amount in Fe^{II} , as observed for the $\text{K}^+/\text{Ni}^{2+}/[\text{Fe}(\text{CN})_6]^{3-}$ -NPs.

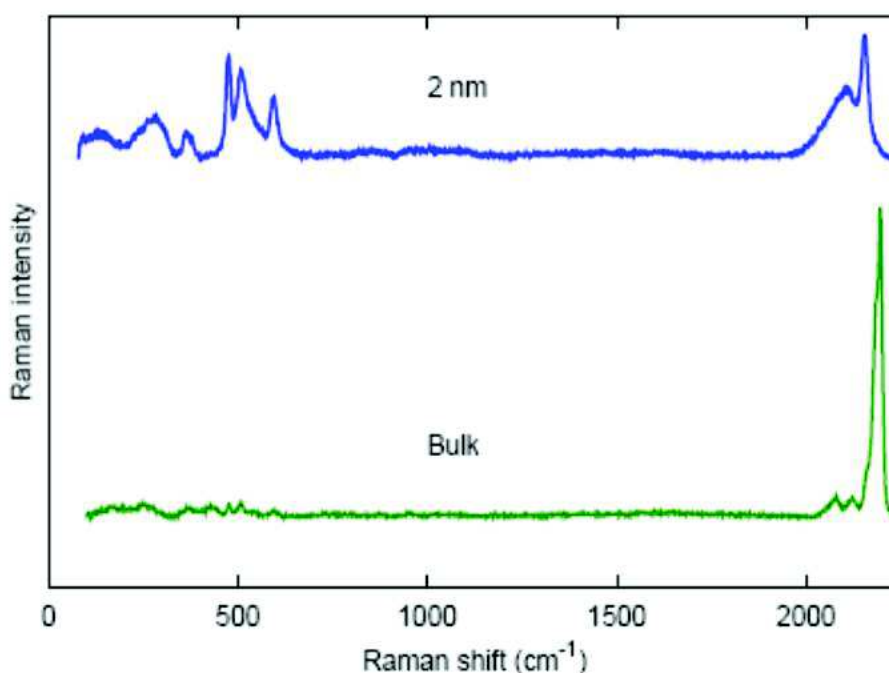


Figure 3: Raman spectra of the $\text{K}^+/\text{Cu}^{2+}/[\text{Fe}(\text{CN})_6]^{3-}/\text{PEG-NH}_2$ NPs and the analogous bulk material at room temperature¹¹.

EDS analysis gives the ratio in metal and alkali ions, permitting to calculate the composition of the $\text{K}^+/\text{Cu}^{2+}/[\text{Fe}(\text{CN})_6]^{3-}/\text{PEG-NH}_2$ NPs. The expected $\text{Cu}^{2+}/\text{Fe}^{3+}$ ratio for the NPs should be close to 1.5, because it is the value observed for bulk of formula $\text{M}_3[\text{Fe}(\text{CN})_6]\cdot\text{XH}_2\text{O}$ ¹³. However, this experimental ratio is relatively far from the theoretical ratio, with a value of 1.3 for the $\text{K}^+/\text{Cu}^{2+}/[\text{Fe}(\text{CN})_6]^{3-}/\text{PEG-NH}_2$ NPs. This difference can be explain by the presence of a non-negligible amount of Fe^{II} instead of Fe^{III} in the NPs,

confirmed by the IR and the Raman spectroscopies. Then, using the calculation method described in annex 1.2, the composition of the $\text{K}^+/\text{Cu}^{2+}/[\text{Fe}(\text{CN})_6]^{3-}/\text{PEG-NH}_2$ NPs have been determined, to be $\text{K}_{0.25}\text{Cu}[\text{Fe}^{\text{II}}(\text{CN})_6]_{0.39}[\text{Fe}^{\text{III}}(\text{CN})_6]_{0.23}$. As for the $\text{K}^+/\text{Ni}^{2+}/[\text{Fe}(\text{CN})_6]^{3-}$ NPs, an important amount of Fe^{II} is observed in the NPs.

TEM analysis revealed the formation of ultra-small $\text{K}^+/\text{Cu}^{2+}/[\text{Fe}(\text{CN})_6]^{3-}/\text{PEG-NH}_2$ NPs into the stabilizing agents with a mean size distribution of 2.0 ± 0.7 nm (figure 4). Their spherical morphology may be close to icosahedron shape, because it's the most stable shape at smaller size (< 10 nm), which maximize the cohesion energy and minimize the surface energy¹⁴.

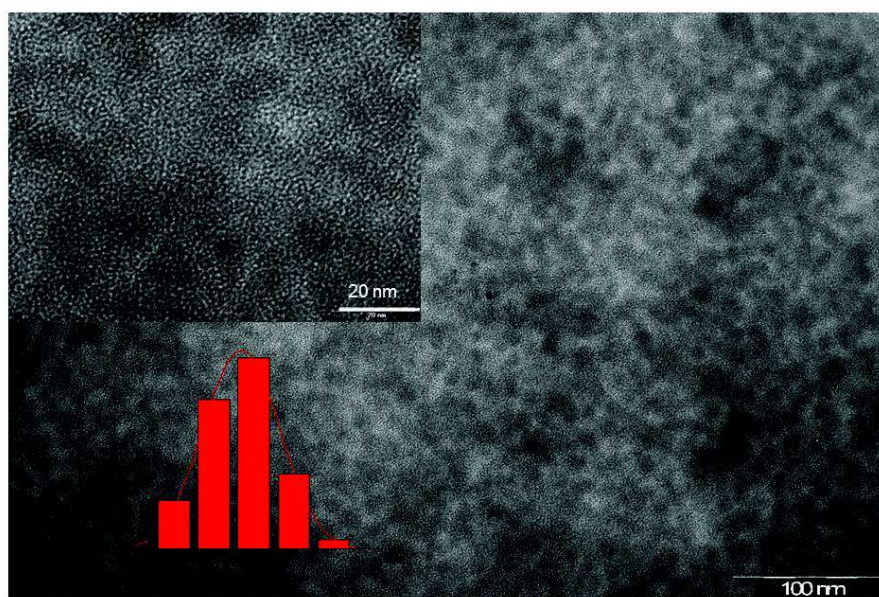


Figure 4: TEM images of the $\text{K}^+/\text{Cu}^{2+}/[\text{Fe}(\text{CN})_6]^{3-}/\text{PEG-NH}_2$ NPs (down). Inset, magnification of the ultra-small NPs (up) and corresponding histogram of the size distribution.

^{57}Fe Mössbauer measurements were performed on the $\text{K}^+/\text{Cu}^{2+}/[\text{Fe}(\text{CN})_6]^{3-}/\text{PEG-NH}_2$ NPs and the analogous bulk material (figure 5). The spectrum corresponding of the bulk material presents a doublet characteristic of Fe^{III} ions. At the opposite, a singlet is observed for the ultra-small NPs, indicating the presence of only Fe^{II} ions in the PBA network. Then, as for the $\text{K}^+/\text{Ni}^{2+}/[\text{Fe}(\text{CN})_6]^{3-}$ NPs, the size reduction induces the increase of the amount in Fe^{II} , which is probably located at the surface.

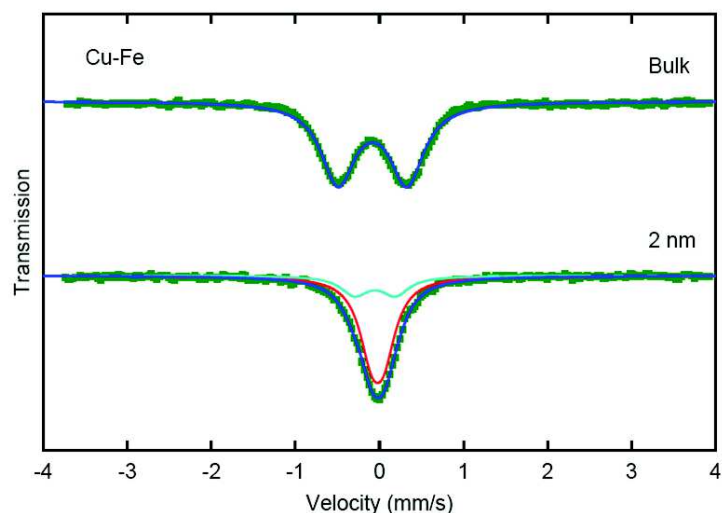


Figure 5: ^{57}Fe Mössbauer spectrum of $\text{K}^+/\text{Cu}^{2+}/[\text{Fe}(\text{CN})_6]^{3-}$ at 80 K for different particle sizes (2 nm and bulk)¹¹.

Using the ^{57}Fe Mössbauer spectroscopy, the Debye temperature of the $\text{K}^+/\text{Cu}^{2+}/[\text{Fe}(\text{CN})_6]^{3-}/\text{PEG-NH}_2$ NPs and the analogous bulk material were estimated, as for $\text{K}^+/\text{Ni}^{2+}/[\text{Fe}(\text{CN})_6]^{3-}$ NPs. The Debye temperature increases with the size reduction, consequently of the hardening of the material¹⁰ (figure 6). That confirms the evolution of the rigidity as a function of the size of the particles, as observed for the $\text{K}^+/\text{Ni}^{2+}/[\text{Fe}(\text{CN})_6]^{3-}$ NPs. It should be interesting to performed a complete study with a series of different sized $\text{K}^+/\text{Cu}^{2+}/[\text{Fe}(\text{CN})_6]^{3-}$ NPs to observed precisely the evolution, as for the $\text{K}^+/\text{Ni}^{2+}/[\text{Fe}(\text{CN})_6]^{3-}$ NPs.

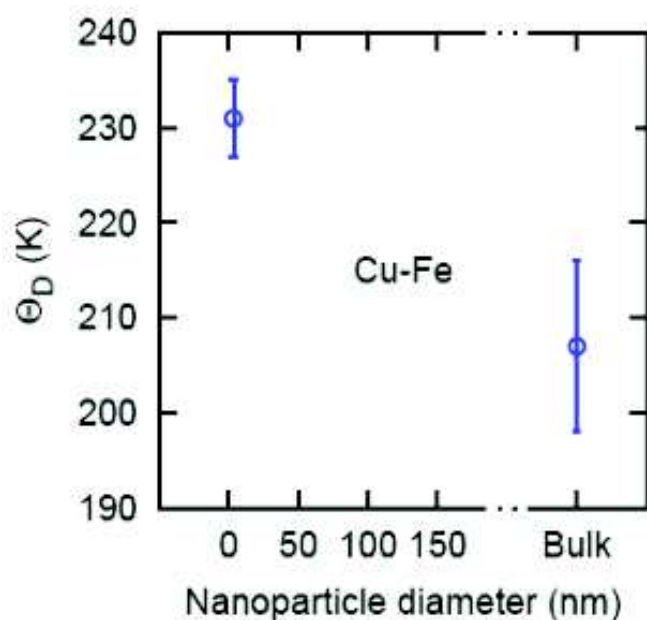


Figure 6: Evolution on the Debye temperature for $\text{K}^+/\text{Cu}^{2+}/[\text{Fe}(\text{CN})_6]^{3-}$ NPs as a function of their average size (2 nm, bulk material)¹⁰.

2.2: Calculation model of the $K^+/M^{2+}/[Fe(CN)_6]^{3-}$ formula.

Due to the presence of both Fe^{II} and Fe^{III} valence state on the PBA structure, it's difficult to obtain a balanced formula for the $K^+/M^{2+}/[Fe(CN)_6]^{3-}$ NPs. Then we have try to determinate by calculation formula presenting respective amount of Fe^{II} and Fe^{III} . This calculation method is based on the fact that the final formula must satisfy the electroneutrality rule. Then, for a PBA structure of $K^+_c/M^{2+}_d/[Fe^{II}(CN)_6]^{4-}_a/[Fe^{III}(CN)_6]^{3-}_b$, the electroneutrality can be expressed by the equation:

$$c + d = 4a + 3b \text{ (Equation 1)}$$

with c is the proportion of alkali ions, d the proportion of M^{2+} , and $4a$ and $3b$ corresponding to the negative charges of the cyanometallate moieties, respectively four for $[Fe^{II}(CN)_6]^{4-}$ and three for $[Fe^{III}(CN)_6]^{3-}$.

Then, the proportion of iron given by EDS analysis are corresponding to both Fe^{II} and Fe^{III} . Mathematically, that can be resume to:

$$aFe^{II} + bFe^{III} = \text{proportion of Fe gives by EDS analysis. (Equation 2)}$$

To simplify the Equation 2, using the EDS amounts of the elements, the M^{2+} is set to have a stoichiometry coefficient of one, then the others elements proportions are given by calculating the EDX ratio with M^{2+} , Fe/M^{2+} and K/M^{2+} . The equations become:

$$aFe^{II} + bFe^{III} = Fe/Ni \text{ (Equation 1)}$$

and

$$c + 2 = 4a + 3b \text{ (Equation 2),}$$

where c is K/M^{2+} .

By solving this linear system of two equations with two unknowns, estimated formula for the $K^+/M^{2+}/[Fe^{II}(CN)_6]^{4-}/[Fe^{III}(CN)_6]^{3-}$, NPs are obtained.

2.3 DLS/Zeta potential measurements.

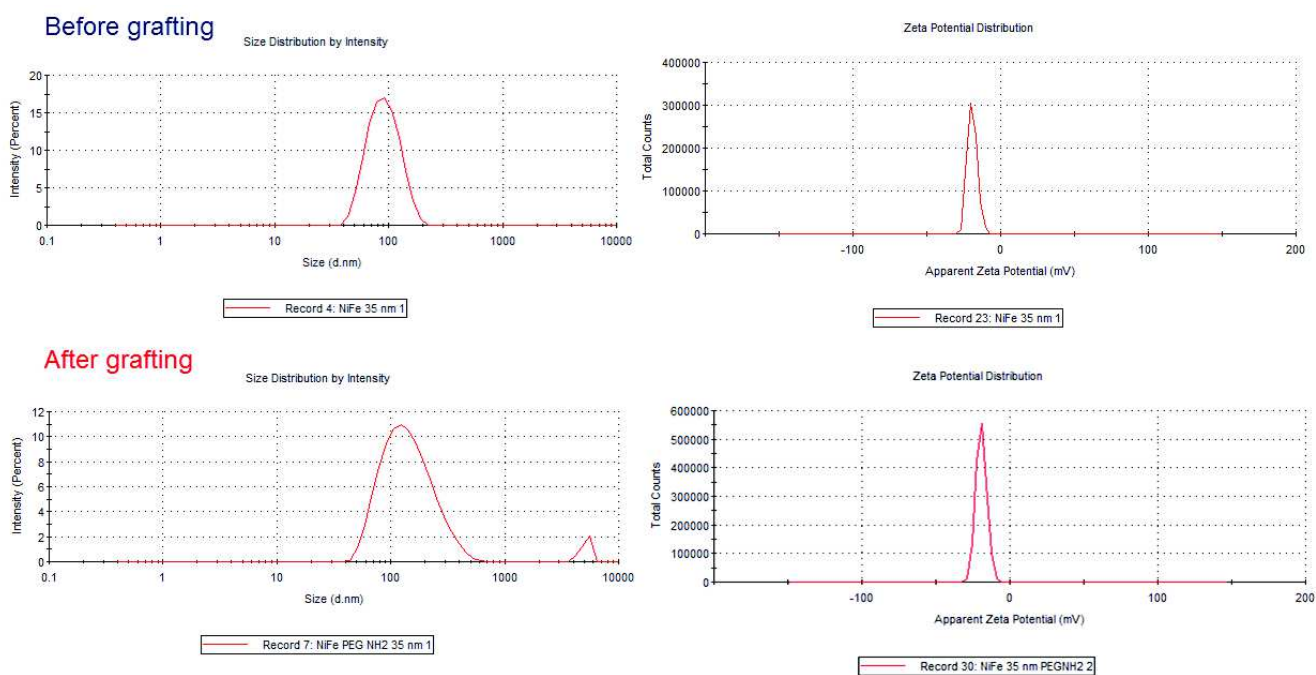


Figure 7: Size distribution of the hydrodynamic radius (in left) and Zeta potential measures (in right) of the 35 nm $K^+/Ni^{2+}/[Fe(CN)_6]^{3-}$ NPs (sample 1-3) before grafting (up) and after grafting (down).

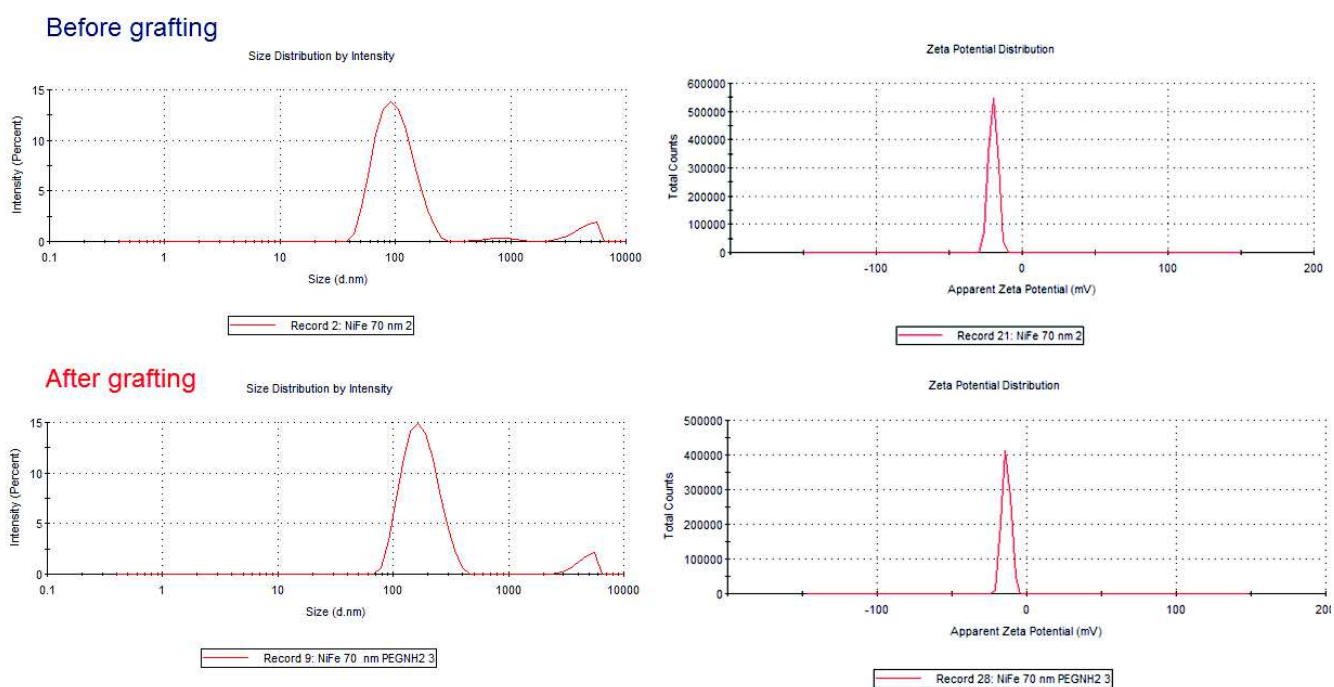


Figure 8: Size distribution of the hydrodynamic radius (in left) and Zeta potential measures (in right) of the 70 nm $K^+/Ni^{2+}/[Fe(CN)_6]^{3-}$ NPs (sample 1-4) before grafting (up) and after grafting (down).

Annex 3: Supplementary information of chapter III.

3.1 Study of the kinetic of the gold NPs formation: UV-Visible monitoring.

Previously, we have reported that the temperature is one of the main parameters able to modify the size of the cyanide-stabilized gold NPs. However, it is not easy to quantify the effect of the temperature on the formation of the gold NPs. A technique which may permit to follow the formation of the gold NPs is the electronic spectroscopy. Indeed, the gold NPs present an intense SPR band, which is extremely sensitive to many factors, such as size or shape of the NPs^{16,17}. By the way, the size and shape are dependent of some parameters, such as the temperature. Then using UV-Visible monitoring, we have investigated the kinetic of the formation of the cyanide-stabilized gold NPs.

At the beginning of the reaction between $\text{K}[\text{Au}(\text{CN})_2]$ and KBH_4 , 0.5 mL of the mixture of the gold NPs was put in a cuve, under stirring. In this reactor, the reaction was monitored by taking UV-visible measurements at regular interval. At 25°C, the SPR band increases rapidly to a value of absorbance of 1.9, then decreases rapidly until 0.7 at 20 min, and then the decrease is slowed down until the total disappearance of the band after 24h, indicating the total dissolution of the gold NPs according to the etching process. The addition of the PBA precursors coincides with the period when the value of the absorbance decreases slowly. After 5 min reaction, the maximum of absorbance is located at 525 nm, then a blue-shift is observed to 520 nm. This indicates the size reduction of the NPs^{16,17}. Then, the maximum of absorbance remains relatively stable between 20 min to 3 hours, which may significate a relative size stabilization of the gold NPs (figure 47). On the other hand, we can observed at 5 min a short band located at 760 nm. This band correspond to another SPR band, and reveals the presence of other gold NPs shape in the solution. This is also observable at 10 min with a shoulder at 650 nm, but not at 20 minutes. Then, at 20 min, only spherical NPs remain in the solution, the anisotropy of the particle shape has vanished, which seems to be the optimal period to perform the growth of the PBA shell, to obtain well-defined core-shell NPs.

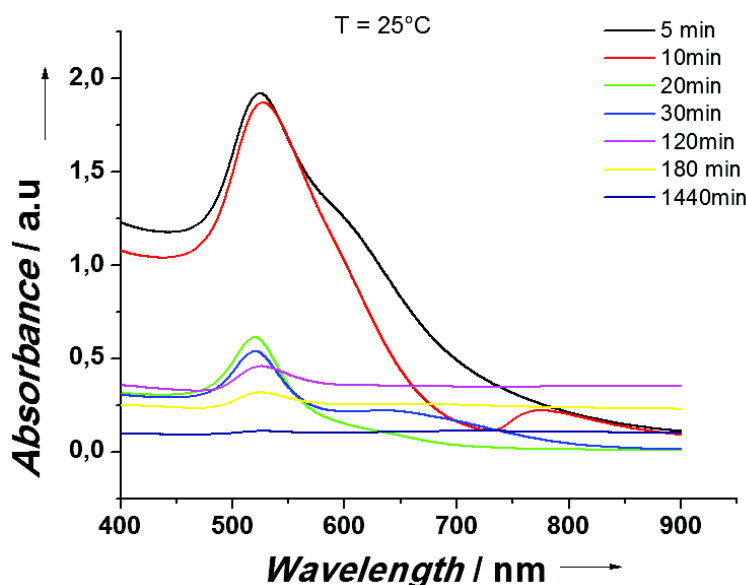


Figure 9: Evolution of the SPR band in the time by UV-Visible spectroscopy monitoring, at 25°C.

The same reaction performed at other temperatures reveals a different kinetic behavior, as shown on the UV-visible monitoring (figure 10). At 10°C, the absorbance of the SPR band increases more slowly than at 25°C, with the highest value of 1.1 obtained at 15 min instead of 5 min. After this, the absorbance decreases really slowly, and remains at 1.05 after 145 min. The red-shift of the maximum of absorbance from 524 nm at 5 min to 532 nm at 15 min indicates the size increase of the gold NPs, larger than 20 nm comparatively to those observed at 25°C. Then the blue-shift occurring until 145 min, to a value of 523 nm is due to the size reduction of the NPs originated from the dissolution of gold to reform the dicyanoaurate precursor, with a similar size obtained at 25°C. No other band is observed, contrary to those observed at 25 °C, then no different size or shape of the gold NPs is formed during the synthesis, only spherical particles.

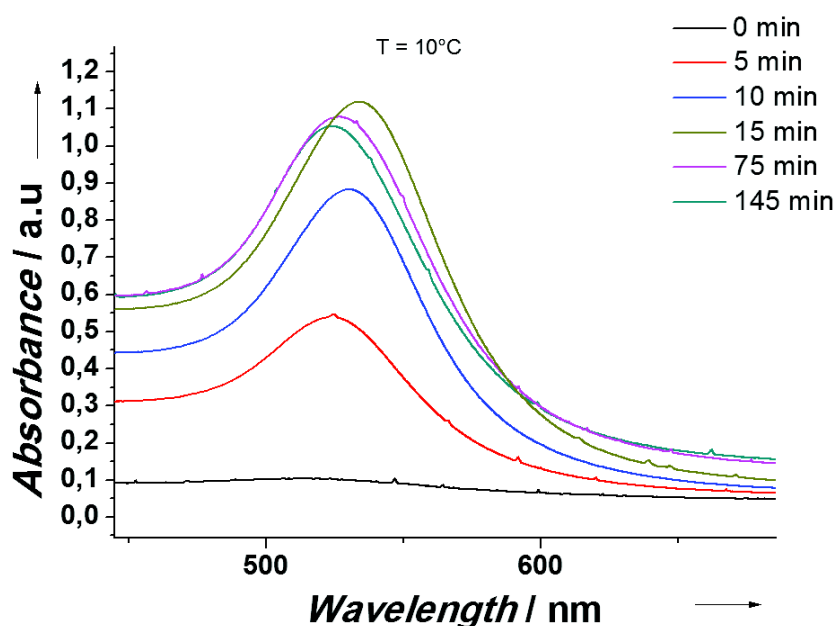


Figure 10: Evolution of the SPR band in the time by UV-Visible spectroscopy monitoring at 10°C.

At 40°C, the increase of the SPR absorption band is more gradual than at 25°C, from the beginning of the reaction to the first hour, then the absorbance remains stable, at a high value, for the second hour of the reaction (figure 11). Moreover, the maximum of absorbance is located at 540 nm, indicating the formation of gold NPs larger than 20 nm. The value of the maximum of absorbance remains stable during the first hour, then a blue-shift occurs to 535 nm at 145 min, indicating a decrease of the NPs size. As observed at 10°C, no other band is observed, only spherical gold NPs were formed during the reaction.

Then the kinetic of the formation of the cyanide-stabilized gold NPs by UV-Visible spectroscopy shows clearly that the temperature is an essential parameter affecting the size and the shape of the gold NPs. At 25°C, the stabilization of the SPR band maximum of absorbance and its value of absorbance seem to have a role to obtain well-defined nano-heterostructures. Indeed, attempts to perform the same reaction with adding the PBA precursors before and after 20 min did not lead to well-defined core-shell NPs. As shown by the UV-Visible monitoring, different gold NPs sizes seems to be accessible by working at different temperature. Thus, it may be interesting to perform the synthesis of core-shell Au@K⁺/Ni²⁺/[Fe^{II}(CN)₆]⁴⁻ NPs at different temperature, to modulate the size of the gold core.

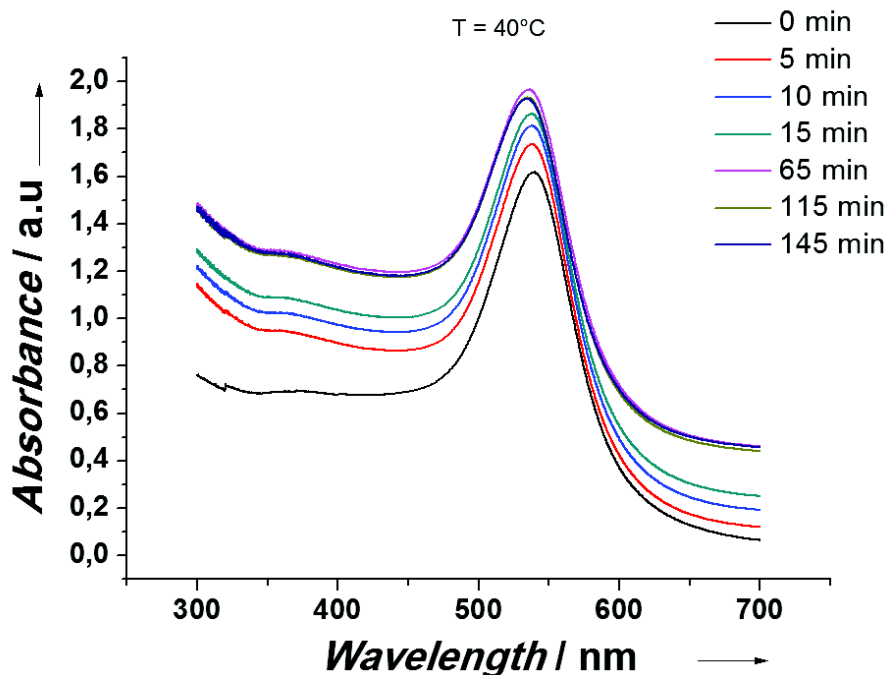


Figure 11: Evolution of the SPR band in the time by UV-Visible spectroscopy monitoring at 40°C.

3.2 Modification of the nature and the shape of the core.

Even if the $\text{Au}@K^+/Ni^{2+}/[Fe^{II}(CN)_6]^{4-}$ NPs exhibit interesting optical properties, with the presence of the intense SPR band, we have tried to modulate it, in order to target other applications. To change the location of the SPR band, we can either change the nature of the inorganic core or the shape of the gold NPs.

3.2.a modification of the nature of the core.

Firstly, we interested to change the nature of the metallic core. Indeed, it is known that other metals than gold can exhibit localized SPR phenomenon. Some metal as Ni, and noble metal as Pd, Pt or especially Ag are studied for their optical properties^{16,18,19}. The idea consists to transpose the synthesis of the $\text{Au}@K^+/Ni^{2+}/[Fe^{II}(CN)_6]^{4-}$ using a $[M(CN)_2]^-$ cyanometallate precursor (with $M = Ag$) or $[M(CN)_4]^{2-}$ (with $M = Pd, Pt, Ni$) instead of the dicyanoaurate $[Au(CN)_2]^-$, in order to form a different inorganic core (figure 12).

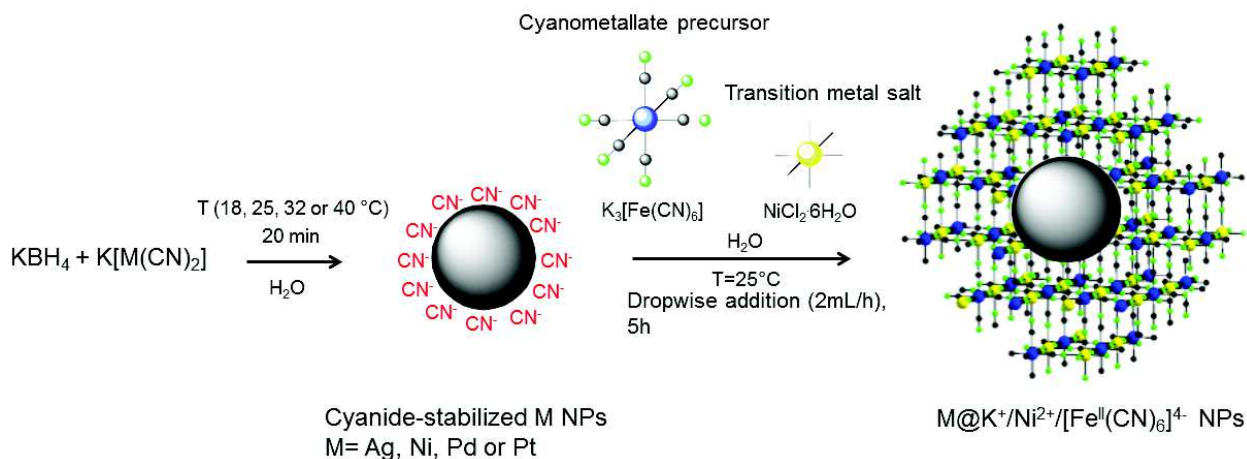


Figure 12: schematic representation of the approach to obtain $M@K^+/Ni^{2+}/[Fe^{II}(CN)_6]^{4-}$ NPs.

Several attempts were performed using $K[Ag(CN)_2]$, $K[Ni(CN)_4]$, $K_2[Pd(CN)_4]$ and $K_2[Pt(CN)_4]$. For each try, the metal precursor was mixed with potassium borohydride in aqueous solution, in the same concentration and volume than for the reaction with the $[Au(CN)_2]^-$. A trouble of the solution appeared in several minutes for the reaction with the silver precursor, and a yellow-orange color after 45 min, indicating the formation of NPs. For the other metals, the solution remained clear, no sign of the formation of NPs was observed. The TEM images, realized 1h before the beginning of the reaction, revealed the formation of cyanide-stabilized Ag NPs (figure 13). Several shapes are visible, as spheres and spheroids. Their size-dimension is under 10 nm. Even if the shape of these cyanide-stabilized Ag NPs are less uniform than for the gold NPs obtained with the same approach, it seems rational to consider the possibility to synthesize $Ag@K^+/Ni^{2+}/[Fe^{II}(CN)_6]^{4-}$ NPs.

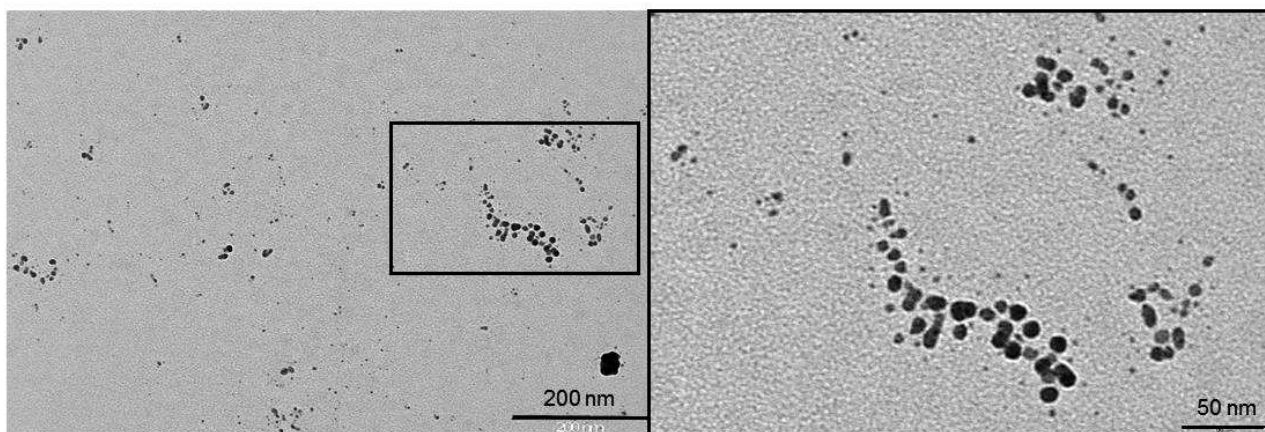


Figure 13: Left: TEM image of cyanide-stabilized Ag NPs. Right: magnification of the different shapes obtained.

The Ag NPs exhibit a SPR band, as confirmed by UV-Vis measurements (figure 14). After 10 min, an intense band in the near ultra-violet^{16,20,21} located at 385 nm is detected, indicating that the NPs are already present in the reaction media. After 45 min, this band is shifted at 392 nm, and two others band, at 369 and 568 nm were appeared. The transition between one single band to three indicates that the NPs are relatively homogenous in size and shape during the first minutes of the reaction, then an anarchical growth of the Ag NPs occurs, leading to several shape and/or size repartition, as indicated by the apparition of a broad SPR band at 568 nm, which explains the yellow-orange color in the aqueous solution.

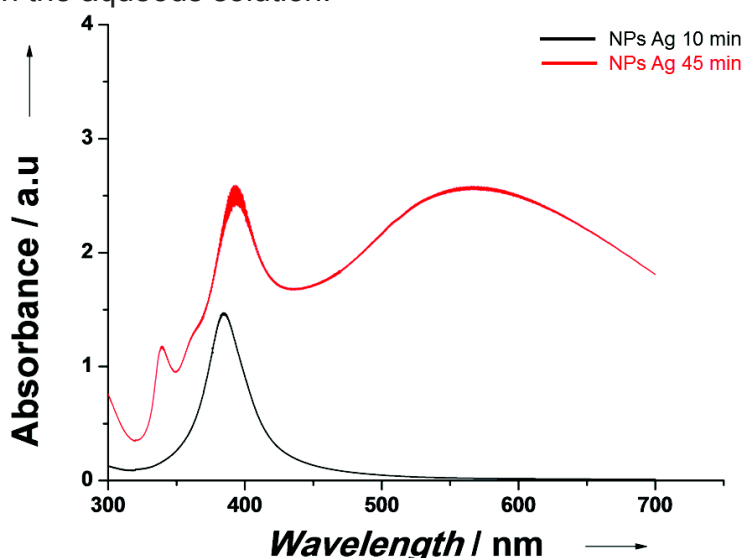


Figure 14: UV-visible spectra of cyanide-stabilized Ag NPs at 10 min (in black) and 45 min (in red) after the beginning of the reaction.

According to the results obtained with UV-visible, the most appropriate time to add the PBA precursors seems to be between 10 minutes, when the SPR band is well-defined, and the first appearance of the others SPR bands, visible at 30 min. We have selected to add the PBA precursors at 20 min, as for the original synthesis. Then the protocol is the same than for Au@ K⁺/Ni²⁺/[Fe^{II}(CN)₆]⁴⁻ NPs, with the simultaneous drop wise addition of the K₃[Fe(CN)₆] and NiCl₂·6H₂O. However, no core-shell Ag@ K⁺/Ni²⁺/[Fe^{II}(CN)₆]⁴⁻ NPs was obtained (figure 15), the PBA does not anchoring at the Ag NPs surface. That may indicates a different behavior of the cyanide-stabilized silver NPs, and a different affinity with the PBA precursors, contrary to those observed with the gold NPs.

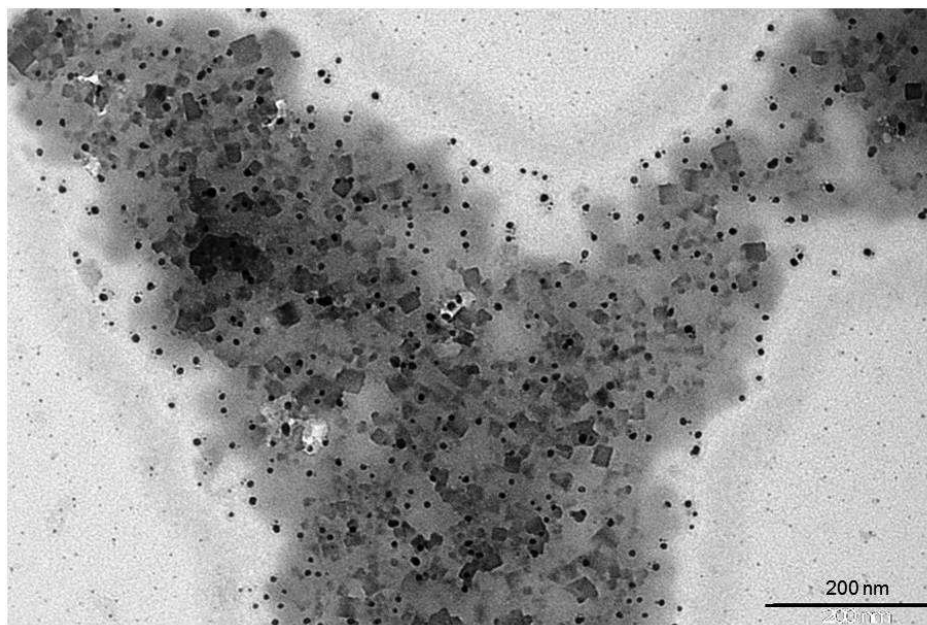


Figure 15: TEM image of the attempt to obtain Ag@ K⁺/Ni²⁺/[Fe^{II}(CN)₆]⁴⁻ heterostructures, with the presence of two distinct populations of respectively Ag and K⁺/Ni²⁺/[Fe^{II}(CN)₆]⁴⁻ NPs.

3.2.b Modification of the shape of the gold core.

The other route to modulate the plasmonic properties of the gold NPs consists to change their shape. Indeed, the shape is an important parameter modulating the location of the SPR band^{16,18,22-24}. One of the most example studied in the last twenty years is the gold nanorod^{16,25-27}. Indeed, gold nanorods exhibit two SPR bands, due to the anisotropy of the shape, with a longitudinal SPR band and a transverse SPR band. The location of the transverse band is generally around 520 nm, as for the Au@ K⁺/Ni²⁺/[Fe^{II}(CN)₆]⁴⁻ NPs, but the longitudinal band can be tuned and is located in the near infrared, between 700 and 900 nm, until 1500 nm for high–aspect ratio nanorods^{26,27}. This band is really interesting for potential biomedical imaging, because the human tissues don't absorb the wavelength in the range of the near-infrared, permitting to scan deeply in the organism^{28,29}. If the synthesis of Au@K⁺/Ni²⁺/[Fe^{II}(CN)₆]⁴⁻ could be transposed to use gold nanorods instead of spherical NPs as the core, that should present a considerable interest for bioimaging applications. Moreover, the shape of the gold core inducing the shape of the shell, that should permit to design interesting and high intricate morphology, which possibly affect the PBA shell properties.

The method of the synthesis of Au_{nanorods}@ K⁺/Ni²⁺/[Fe^{II}(CN)₆]⁴⁻ was inspired from the original synthesis of the Au@ K⁺/Ni²⁺/[Fe^{II}(CN)₆]⁴⁻. The nanorods were previously synthesized, using a seed-mediated method, according to the literature^{30,31}. That consists

to obtain small spherical NPs by the reduction of HAuCl_4 in an excess of stabilizers, as CTAB. These small NPs are used in a second step as seeds to growth the nanorods, in mild conditions, the Au^{III} requiring the presence of the seeds to be reduced to Au^0 (the ascorbic acid used only reduces Au^{III} to Au^{I}). The shape is induced by the cationic surfactants as CTAB, and by the Ag^+ ion, the Au binding only on the same (111) facets, favoring the growth in a single direction^{16,18,25}. Then, after obtaining the nanorods, they were washed several time to remove the excess of CTAB, and dispersed in aqueous solution. To permit the precursors of the PBA to anchor at the surface, 2mL of potassium cyanide (10^{-3} M) were added (figure 16). After 30 min under stirring, the $\text{K}_3[\text{Fe}(\text{CN})_6]$ and $\text{NiCl}_2 \cdot 6\text{H}_2\text{O}$ were added simultaneously at the same rate than the original synthesis.

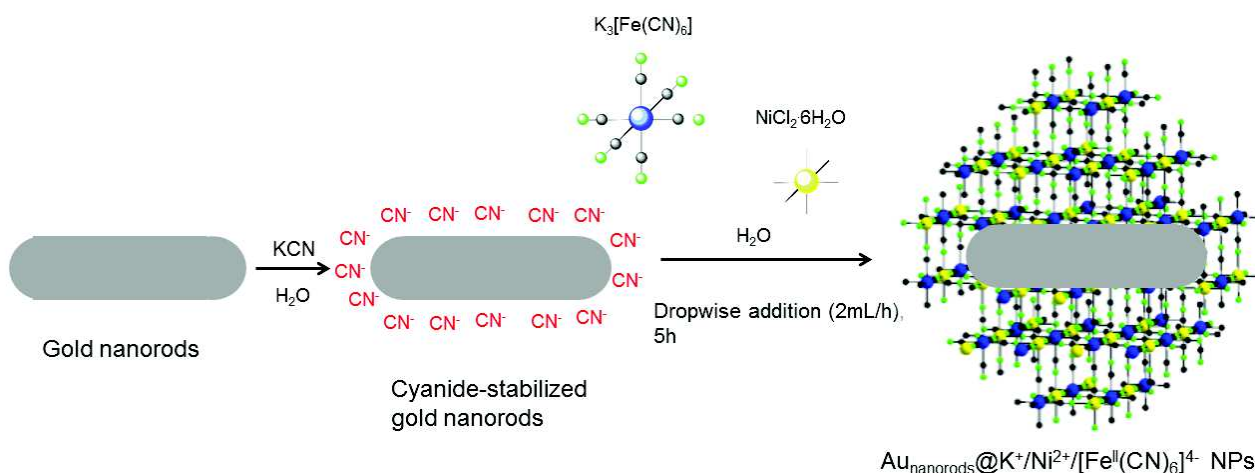


Figure 16: schematic representation of the approach to obtain $\text{Au}_{\text{nanorods}}@ \text{K}^+/\text{Ni}^{2+}/[\text{Fe}^{\text{II}}(\text{CN})_6]^{4-}$ NPs.

The TEM images show the presence of few gold nanorods and large PBA NPs (figure 17). The observation of these NPs suggests there is still CTAB in the gold nanorods solution. The remaining surfactant molecules may avoid the possibility to the metal precursors to anchor at the surface of the nanorods, not allowing the synthesis of $\text{Au}_{\text{nanorods}}@ \text{K}^+/\text{Ni}^{2+}/[\text{Fe}^{\text{II}}(\text{CN})_6]^{4-}$ nano-heterostructures. Unfortunately, to our knowledge, it is not possible to remove all the surfactants without leading to an aggregation on the NPs. Several methods were tested, washing with different solvents, dialysis, but that always leads to the apparition of aggregates. Nevertheless, that may confirm the necessity to have only a cyanide-stabilized gold NPs to grow a cyano-bridged coordination polymer layer.

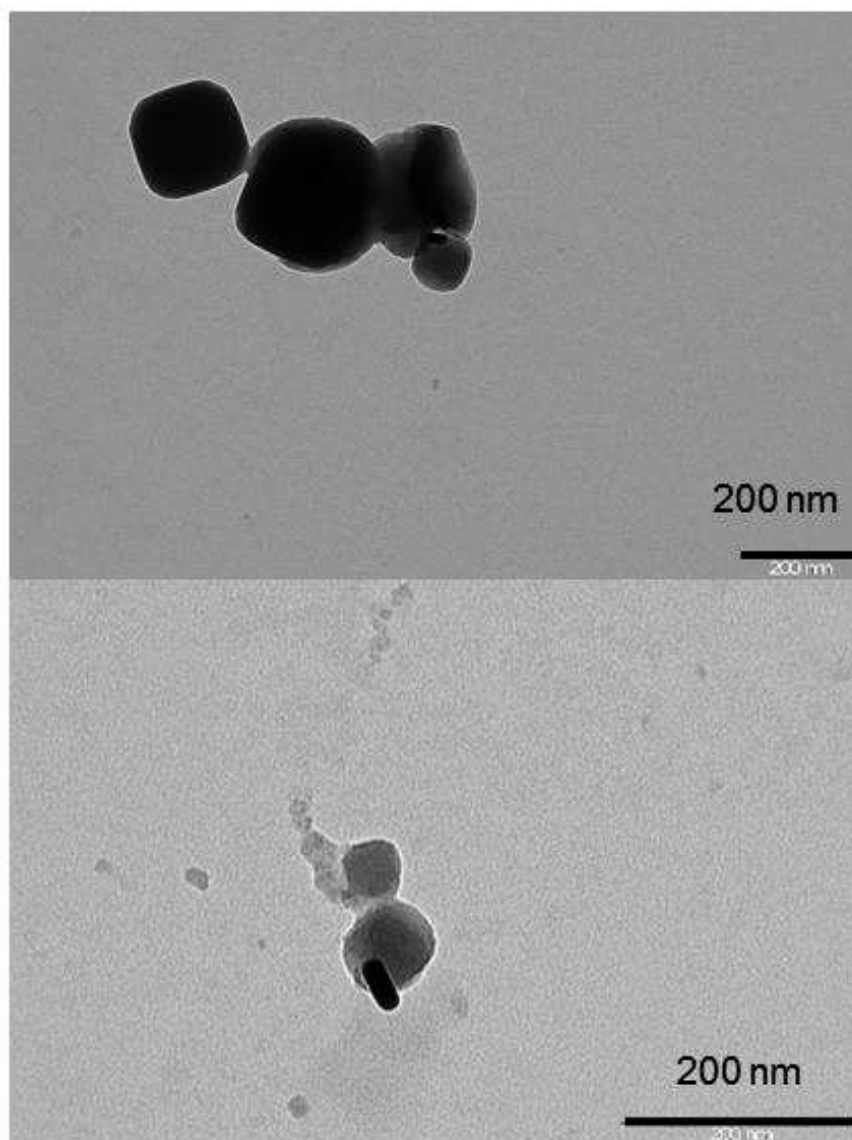


Figure 17: TEM images of the attempts to performed $\text{Au}_{\text{nanorods}}@ \text{K}^+/\text{Ni}^{2+}/[\text{Fe}^{\text{II}}(\text{CN})_6]^{4-}$ with the presence of two distinct nano-objects as gold nanorods and $\text{K}^+/\text{Ni}^{2+}/[\text{Fe}^{\text{II}}(\text{CN})_6]^{4-}$ NPs.

References

- 1 J. Larionova, Y. Guari, C. Sangregorio and C. Guerin, *New J. Chem.*, **2009**, 33, 1177.
- 2 E. Chelebaeva, Y. Guari, J. Larionova, A. Trifonov and C. Guerin, *Chem. Mater.*, **2008**, 20, 1367.
- 3 C.H. Li, Y. Nanba, D. Asakura, M. Okubo and D. R. Talham, *RSC Adv.*, **2014**, 4, 24955.
- 4 D. Asakura, C. H. Li, Y. Mizuno, M. Okubo, H. Zhou and D. R. Talham, *J. Am. Chem. Soc.*, **2013**, 135, 2793.
- 5 S. N. Gosh, *J. Inor. Nucl. Chem.*, **1974**, 36, 2465.
- 6 J. Lejeune, J. B. Brubach, P. Roy and A. Bleuzen, *C. R. Chimie*, **2014**, 17, 534.
- 7 P. Higuél, F. Villain, M. Verdaguer, E. Rivière and A. Bleuzen, *J. Am. Chem. Soc.*, **2014**, 136, 6231.
- 8 Y. Guari, J. Larionova, K. Molvinger, B. Folch, C. Guerin, *Chem. Commun.*, **2006**, 2613.
- 9 B. Folch, Y. Guari, J. Larionova, C. Luna, C. Sangregorio, C. Innocenti, A. Caneschi, C. Guerin, *New J. Chem.*, **2008**, 32, 273.
- 10 G. Félix, W. Nicolazzi, L. Salmon, G. Molnar, M. Perrier, G. Maurin-Pasturel, J. Larionova, J. Long, Y. Guari, and A. Bousseksou, *Phys. Rev. Lett.*, **2013**, 110, 235701.
- 11 Supplementary material of (20).
- 12 K. M. Jeerage, W. A. Steen, and D. T. Schwartz, *Chem. Mater.*, **2002**, 14, 530.
- 13 Y. Mizuno, M. Okubo, K. Kagesawa, D. Asakura, T. Kudo, H. Zhou, K. Oh-ishi, A. Okazawa, and N. Kojima, *Inorg. Chem.*, **2012**, 51, 10311.
- 14 M. Lahmani, C. Bréchinac, P. Houdy, *Les nanosciences*, Belin, **2006**, Vol.2, *Nanomateriaux et nanochimie*.
- 15 K. M. Mayer, J. H. Hafner, *Chem. Rev.* **2011**, 111, 3828.
- 16 C. J. Murphy, A. M. Gole, S. E. Hunyadi, C. J. Orendorff, *Inorg. Chem.*, **2006**, 45, 7544.
- 17 E. C. Dreaden, A. M. Alkilany, X. Huang, C. J. Murphy and M. A. El-Sayed, *Chem. Soc. Rev.*, **2012**, 41, 2740.
- 18 B. Nikoobakht and M. A. El-Sayed, *Chem. Mater.*, **2003**, 15, 1957.

- 19 B. D. Busbee, S. O. Obare and C. J. Murphy, *Adv. Mater.* **2003**, *15* (5), 414.
- 20 M. Rycenga, C. M. Cobley, J. Zeng, W. Li, C. H. Moran, Q. Zhang, D. Qin and Y. Xia, *Chem. Rev.*, **2011**, *111*, 3669.
- 21 N. R. Jana, L. Gearheart, and C. J. Murphy, *J. Phys. Chem. B*, **2001**, *105*, 4065.
- 22 A. M. Smith, M. C. Mancini and S. Nie, *Nat. Nanotechnol.*, **2009**, *4*, 710.
- 23 R. Weisleder, *Nat. Biotechnol.*, **2001**, *19*, 316.
- 24 K. A. Kozek, K. M. Kozek, W.-C. Wu, Su. R. Mishra, and J. B. Tracy, *Chem. Mater.*, **2013**, *25*, 4537.
- 25 D. K. Smith, N. R. Miller, and B. A. Korgel, *Langmuir*, **2009**, *25* (16), 9518.
- 26 M. Hu, S. Furukawa, R. Ohtani, H. Sukegawa, Y. Nemoto, J. Reboul, S. Kitagawa and Y. Yamauchi, *Angew. Chem.*, **2012**, *124*, 1008.
- 27 M. Hu, A. A. Belik, M. Imura, Y. Yamauchi, *J. Am. Chem. Soc.*, **2013**, *51*, 384.
- 28 X. Cai , X. Jia , W. Gao , K. Zhang , M. Ma , S. Wang , Y. Zheng ,J. Shi and H. Chen, *Adv. Funct. Mater.*, **2015**, DOI: 10.1002/adfm.201403991.
- 29 X. Jia, X. Cai, Yu Chen, Shige Wang, H. Xu, Kun Zhang, M. Ma, H. Wu, J. Shi, and H. Chen, *Appl. Mater. Interfaces*, **2015**, *7*, 4579.
- 30 M. Hu, N. L. Rorad, Y. Yamauchi, *Eur. J. Inorg. Chem.*, **2012**, 4795.
- 31 M. A. Rawashdeh-Omary, M. A. Omary, H. H. Patterson, *J. Am. Chem. Soc.*, **2000**, *122*, 10371.

Résumé

Synthèse de nano-objets
multifonctionnels à base moléculaire: vers
des applications biomédicales

Depuis plusieurs décennies, l'un des principaux domaines de la chimie moderne réside dans l'élaboration de nanomatériaux. En effet, la diminution de la taille jusqu'à l'échelle nanométrique entraîne de profonds changements des propriétés physiques et chimiques des matériaux. De telles modifications sont généralement issues de l'augmentation de la contribution de la surface par rapport à celle de l'intérieur de l'objet. Les propriétés qui en découlent se sont révélées prometteuses et ont particulièrement suscité l'attrait des chercheurs qui se sont en premier lieu concentrés sur l'élaboration de nanoparticules composées d'un seul matériau. Une grande variété de nanomatériaux (à base de silice, de métaux, d'oxydes métalliques, de polymères de coordination) ont été développés et présentent un intérêt majeur pour une grande variété d'applications telles que entre autres, la catalyse, le stockage de données, la dépollution de l'environnement, les capteurs, les systèmes photovoltaïques et optiques, ou encore la médecine. Le contrôle de certains paramètres, tels que la forme ou la taille des objets, est obtenu en modifiant les conditions de synthèse, ce qui nous permet de moduler les propriétés des nanoparticules. De cette manière il est possible de concevoir des nanomatériaux adaptés pour des applications spécifiques.

Depuis quelles années, l'élaboration de nanocomposites hétérogènes s'est révélé être une voie particulièrement prometteuse dans le but d'apporter une multifonctionnalité à l'échelle nanométrique. Cela peut s'obtenir en combinant deux ou plusieurs matériaux différents dans une seule nanoparticule qui ainsi, va présenter au minimum, la somme des propriétés intrinsèques de chacun de ses constituants, et ainsi présenter des réactions différentes lorsqu'elle sera soumise à des excitations externes diverses. Cependant, pour certains de ces systèmes complexes, il est possible d'observer l'apparition de nouvelles propriétés ou d'une synergie entre les propriétés de ces matériaux.

C'est dans cette optique que nous avons porté notre attention sur la conception d'hétérostructures nanoscopiques qui combinent les propriétés de deux matériaux différents. Dans notre cas, nous nous sommes tout particulièrement intéressés à l'élaboration de nano-objets cœur-coquilles magnéto-optiques. Dans ce but, deux types de matériaux ont attiré notre attention.

Tout d'abord, nous nous sommes intéressés au Bleu de Prusse et à ses analogues. Ces matériaux font partie de la famille des polymères de coordination, et sont constitués de cations de métaux de transition ou de lanthanides reliés entre eux par des cyanures pontant, formant de la sorte un réseau tridimensionnel. De formule générale $A_xM_y[M'(CN)_6]_z$ où M et M' sont des métaux de transition ou des lanthanides et A un métal alcalin, ces polymères de coordination peuvent présenter deux structures limites. La première structure est dite de type « lacunaire » : à cause de briques cyanometallates vacantes dans le réseau, les ions métalliques se coordinent à des molécules d'eau pour compléter leur sphère de coordination, comme présenté sur la figure 1a). La seconde structure est de type 1:1:1 et incorpore des cations monovalents (tel que K^+ , Na^+ , NH_4^+ ,...) dans les sites tétraédriques, tel que l'on peut le voir sur la figure 1b). Ces matériaux sont généralement obtenus par l'auto-assemblage de sels métalliques et d'hexacyanometallates, et présentent à l'état massif des propriétés physiques et

chimiques intéressantes, telles que des propriétés magnétiques, optiques, de photo-commutation, catalytiques ou d'intercalations, utilisables dans toute une gamme de domaines. L'exemple le plus connu est l'utilisation du Bleu de Prusse comme agent de décontamination lors d'empoisonnement au Césium ou au Thallium radioactif, résultant de la capture sélective de ces éléments dans sa structure (Radiogardase®).

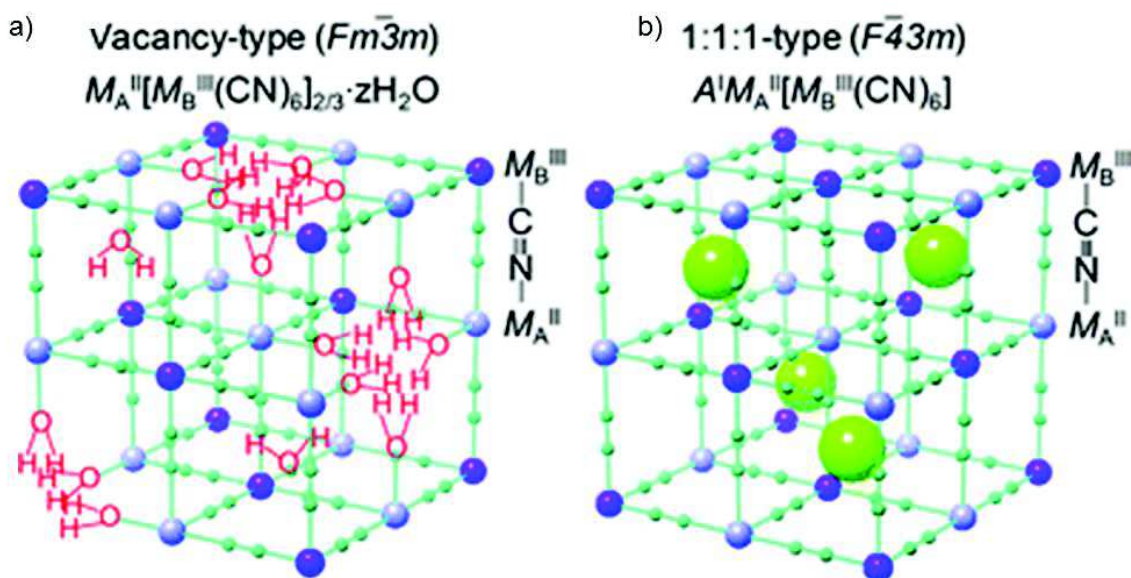


Figure 1 : Représentation de la structure cristallographique des analogues du Bleu de Prusse avec a) la structure de type « lacunaire » incorporant des molécules d'eau coordonnées aux cations métalliques et b) la structure de type 1:1:1 incorporant des cations monovalent dans les sites tétraédriques¹.

Durant les deux dernières décennies, ces polymères de coordination cyano-pontés ont été utilisés pour concevoir des nanoparticules. Plusieurs procédés ont été mis au point pour obtenir des nano-objets de taille et de forme contrôlées et présentant des propriétés intéressantes, tout particulièrement des propriétés magnétiques (figure 2, de a jusqu'à d). Des architectures plus complexes, telles que des nanoparticules cœur-coquilles ont également été obtenues récemment (figure 2, de e jusqu'à f). Ces hétérostructures combinent deux ou plusieurs analogues de Bleu de Prusse, présentant ainsi les propriétés de chacun. Il a également été observé des effets de synergie des propriétés. Le cas le plus étudié consiste en des nanoparticules cœur-coquille composées d'un analogue de Bleu de Prusse ferromagnétique et d'une autre photo-commutable. On observe alors une modification des propriétés magnétiques après irradiation des composés. D'autres types de morphologie complexes peuvent être obtenus, tels que des nanoparticules creuses obtenues par des procédés de lixiviation qui dissolvent sélectivement l'intérieur de la structure du matériau, permettant la formation d'une cavité dans la nanoparticule. De manière générale, ces composés sont tout à fait adaptés pour concevoir des nano-objets multifonctionnels, car ils présentent des propriétés intéressantes, notamment des propriétés magnétiques, qui peuvent être contrôlées, et ils peuvent être obtenus par des voies de synthèses simples.

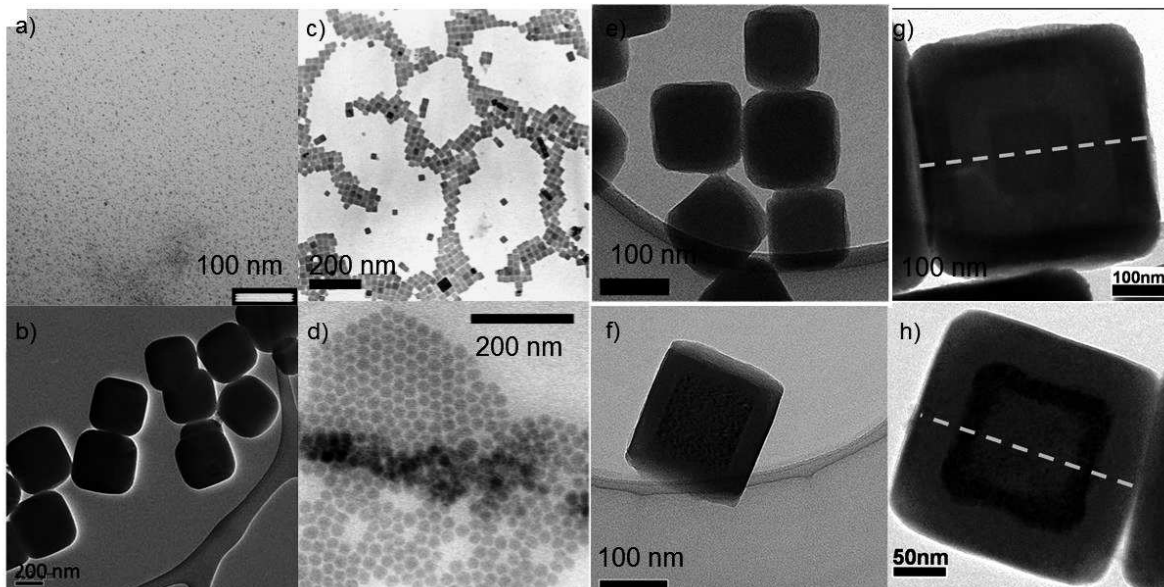


Figure 2: A droite, images de microscopie électronique à transmission de nanoparticules de Bleu de Prusse et ses analogues obtenues par diverses méthodes expérimentales, à base de $\text{Ni}^{2+}/[\text{Fe}(\text{CN})_6]^{3-}$ a)², de $\text{KNi}[\text{Fe}(\text{CN})_6]$ b), et de $\text{Co}_2[\text{Fe}(\text{CN})_6]$ de forme cubique c) et sphéroïdale d)³. A gauche : images de microscopie électronique à transmission de nanoparticules cœur-coquille à base d'analogues de Bleu de Prusse, avec des hétérostructures de $\text{KNiCo}@ \text{KNiCr}$ e)⁴, de $\text{RbCoFe}@ \text{KCoCr}$ f)⁵, de $\text{KNiCr}/\text{RbCoFe}/\text{KNiCr}$ g) et de $\text{RbCoFe}/\text{KNiCr}/\text{RbCoFe}$ h)⁶.

D'autre part, nous nous avons été attirés par les propriétés des nanoparticules d'or. En effet, la réduction de la taille entraîne l'apparition d'un phénomène appelé plasmon de surface, à l'origine des formidables propriétés optiques de ces nanoparticules. Ce phénomène, ainsi que les propriétés qui en découlent, est particulièrement dépendant de la forme et de la taille des particules (figure 2). Il est donc possible d'obtenir les propriétés optiques désirées en contrôlant ces paramètres.

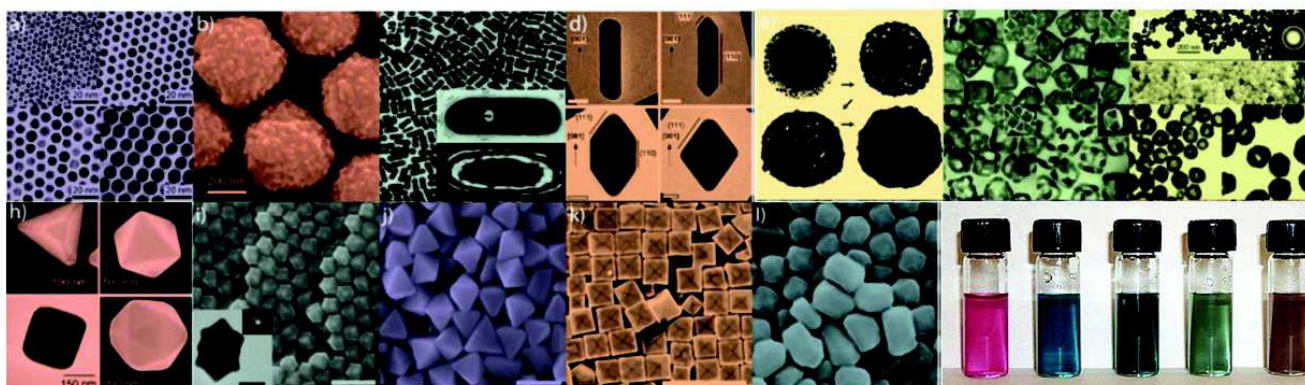


Figure 3 : Images de microscopie électronique à transmission de nanoparticules d'or de formes différentes⁷, avec des nanosphères de petites a) et de grandes tailles b), des nanobâtonnets c), des nanobâtonnets pointus d), des nanocoquilles e), des nanocages f) des nanosphères creuses g), des tétraèdres/octaèdres/cubes/icosaèdres h), des dodécaèdres rhombiques i), des octaèdres j), des nanocubes concaves k) et des tetrahexaèdres l). Image de solutions de nanoparticules d'or de formes différentes qui présentent des propriétés optiques différentes⁸.

Les nanoparticules d'or ont d'ailleurs été utilisées pour obtenir des hétérostructures avec une grande variété de matériaux (silice, métaux, oxydes métalliques, polymères de coordination). Ces hétérostructures présentent d'intéressantes modifications de leurs propriétés optiques par rapport à des nanoparticules d'or simples, ainsi que parfois l'apparition de synergies, notamment entre les propriétés optiques de l'or et les propriétés magnétiques de nanoparticules métalliques ou d'oxydes de fer.

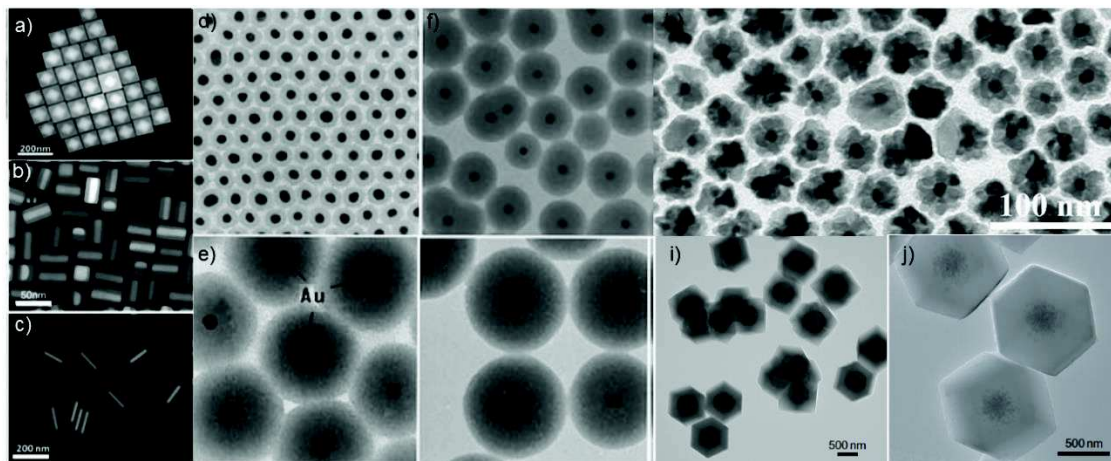


Figure 3 : Images de microscopie électronique à transmission de nanoparticules cœur-coquilles comprenant de l'or, combiné avec des métaux tel que l'argent a-c)⁹, de la silice d-g)¹⁰, d'oxydes métalliques tel que Fe₃O₄ h)¹¹, et des polymères de coordination de type Métal-Organic Framework (MOFs) tel que le ZIF-8¹².

Dans ce travail, nous avons donc cherché à concevoir des nano-objets hétérostructurés combinant à la fois les propriétés optiques de l'or et les propriétés magnétiques des analogues du Bleu de Prusse, dans le but d'obtenir des nanoparticules cœur-coquilles multifonctionnelles. De tels systèmes présentent un véritable intérêt pour plusieurs domaines tel que l'imagerie médicale ou les systèmes magnéto-optiques. De plus, une telle combinaison demeure relativement inédite, un seul exemple ayant été rapporté dans la littérature.

Dans un premier temps, nous avons cherché à mieux comprendre les modifications des propriétés structurales se produisant avec la réduction de la taille sur les analogues de Bleu de Prusse en utilisant un système modèle, de formule générale $K^+/Ni^{2+}/[Fe^{III}(CN)_6]^{3-}$. Pour cela, nous avons préparé une série de nanoparticules à base de cet analogue de Bleu de Prusse. En contrôlant les conditions de synthèse, nous avons obtenu plusieurs échantillons, chacun présentant des tailles différentes allant de 2 nm jusqu'à 180 nm (figure 4). Les différentes techniques de caractérisation ont confirmé la structure de ces nanoparticules qui correspond à celle du polymère de coordination cyanopontés. De plus, il a été observé une augmentation de la teneur en cations Fe(II) dans la structure par rapport à celle de Fe(III). Ce phénomène peut s'expliquer par l'augmentation de la contribution de la surface, les ions Fe(II) réduits se trouvant majoritairement en surface. D'autre part, nous avons pu observer une augmentation de la rigidité du matériau avec la réduction de la taille, en estimant la température de Debye par spectroscopie Mössbauer, dans le cadre d'une collaboration avec le Laboratoire de Coordination de Toulouse¹³. De cette manière, nous avons mis en évidence l'apparition d'un comportement « nano » se produisant pour des tailles inférieures à 10 nm pour ce type de matériau.

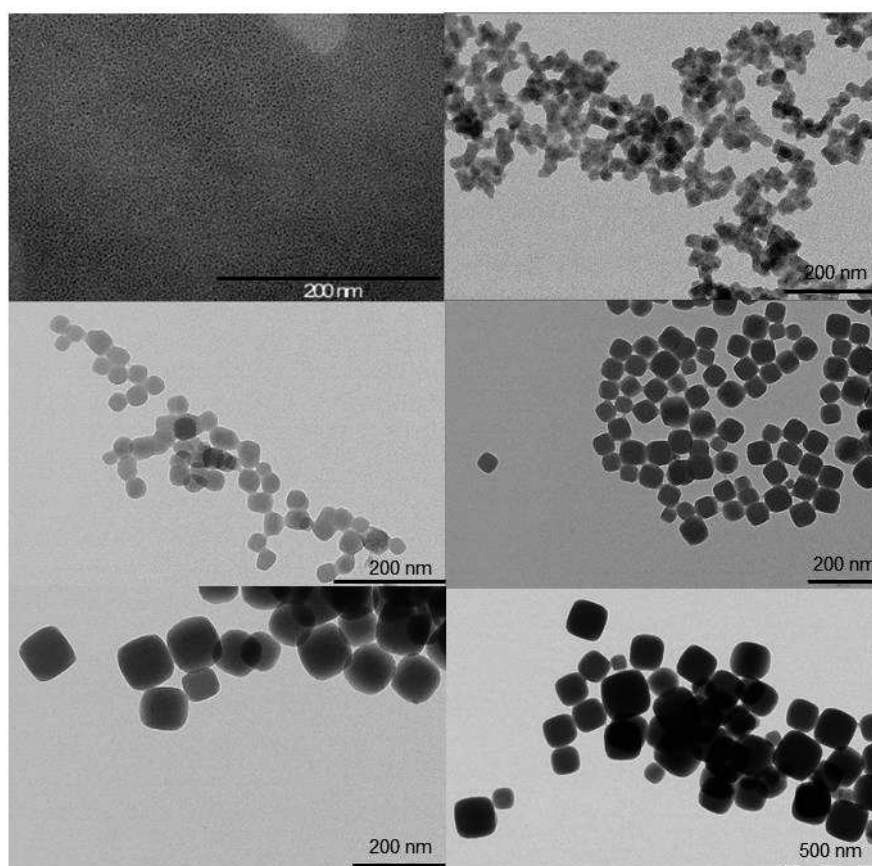


Figure 4 : Images de microscopie électronique en transmission de nanoparticules de $K^+/Ni^{2+}/[Fe^{II}(CN)_6]^{3-}$ de différentes tailles, respectivement 2 nm a) 14 nm b), 37 nm c) 70 nm d), 110 nm e) et 180 nm f).

Dans un deuxième temps, nous nous sommes focalisés sur la conception de nanoparticules cœur-coquilles à base d'or et d'analogues de Bleu de Prusse. Pour cela, nous avons développé une approche de synthèse nouvelle et rationnelle qui consiste en 1) la synthèse de nanoparticules d'or en solution aqueuse, obtenues par réduction de dicyanoaurate de potassium et stabilisées uniquement par des ions cyanures, puis 2) la croissance d'une coquille d'analogue de Bleu de Prusse par l'addition lente et contrôlée des précurseurs (sel métallique bivalent et hecyanometallate). De cette manière, nous avons obtenu des nanoparticules cœur-coquilles d' $Au@K^+/Ni^{2+}/[Fe^{II}(CN)_6]^{4-}$, composées par une seule nanoparticule d'or au cœur, entourée d'une coquille uniforme de polymère de coordination¹⁴. Ces nano-hétérostructures présentent des propriétés optiques dues à la bande de plasmon de surface du cœur d'or, qui sont différentes des celles des nanoparticules d'or de départ. Elles présentent aussi des propriétés paramagnétiques, et non pas ferromagnétiques comme attendu, suite à la réduction totale des centres Fe(III) en Fe(II) diamagnétiques. Cette réduction s'explique par l'excès d'entités réductrices présentes dans le milieu réactionnel.

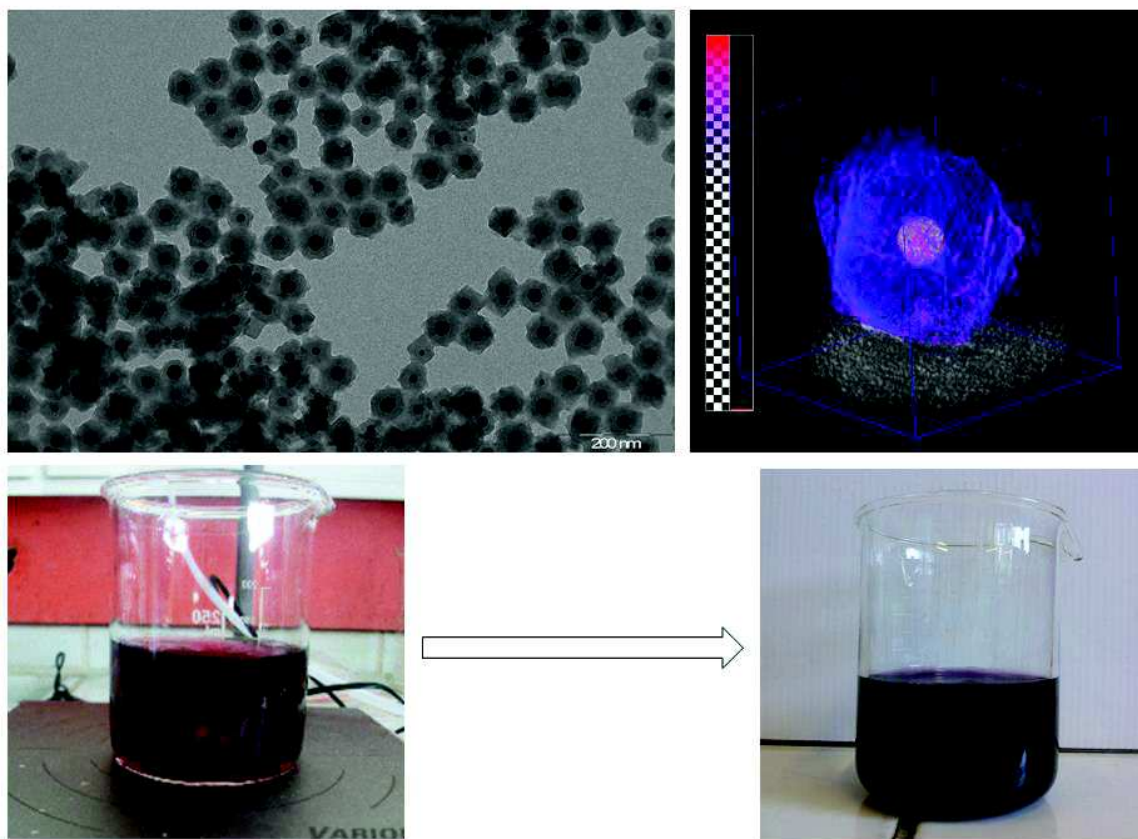


Figure 5 : En haut à gauche, image de microscopie électronique en transmission des nanoparticules cœur-coquille d' $\text{Au@K}^+/\text{Ni}^{2+}/[\text{Fe}^{\text{II}}(\text{CN})_6]^{4-}$. En haut à droite, reconstruction tridimensionnelle d'une nanoparticule obtenue par tomographie en microscopie électronique en transmission haute résolution. En bas, modification de la coloration de la solution des nanoparticules d'or avant croissance de la couche d'analogue de Bleu de Prusse (à gauche) et après croissance (à droite), illustrant la modification des propriétés optiques.

En utilisant différentes techniques, nous avons cherché à comprendre le mécanisme de formation de ces nanoparticules complexes. Au vu des résultats, il semble probable que la coquille se forme par coordination du Ni^{2+} à la surface des nanoparticules d'or, servant ainsi de point de fixation à partir duquel se forme la coquille d'analogue de Bleu de Prusse. Celle-ci croît de manière régulière au fur et à mesure de l'addition des précurseurs. Par ailleurs il est possible de contrôler la taille du cœur d'or et l'épaisseur de la coquille en modifiant les paramètres, respectivement la température de synthèse et la quantité de précurseurs ajoutés (figure 6). De cette manière, il est possible de modifier les propriétés optiques dues à l'or par la modification de la taille des cœurs métalliques ou par la variation de l'épaisseur de la coquille. Cependant, seule cette dernière permet vraiment de contrôler les propriétés optiques. En effet, la modification de la température affecte à la fois la taille du cœur et celle de la coquille, conduisant à des nanoparticules de tailles différentes mais ayant des propriétés optiques très proches.

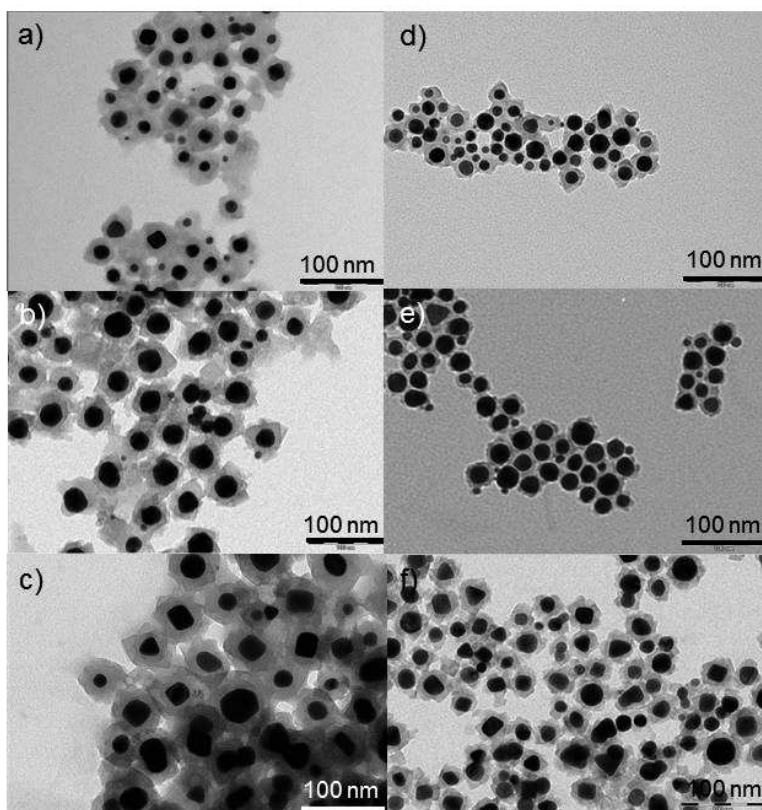


Figure 6 : Images de microscopie électronique en transmission de nanoparticules cœur-coquille de taille de cœur d'or différentes obtenues à 18°C a), 32°C, b) et 40°C, ainsi que d'épaisseurs de coquille différentes obtenus après 30 min d), 1h e) et 2h30 f) d'addition des précurseurs d'analogue de Bleu de Prusse.

Nous avons poursuivi notre étude en cherchant à transposer notre approche à d'autres systèmes. Tout d'abord nous avons utilisé les mêmes précurseurs avec des contre-ions de nature différente. Mise à part pour les précurseurs d'or, le changement de la nature des contre-ions n'affecte pas la morphologie des nanoparticules. Par la suite, nous avons essayé de changer la nature de l'analogue de Bleu de Prusse utilisé pour la coquille, afin de moduler les propriétés apportées. Ainsi, plusieurs polymères de coordination présentant des propriétés magnétiques différentes ont été utilisés. Il s'avère que cette méthode a permis d'obtenir uniquement des nanoparticules cœur-coquilles d' $\text{Au}@K^+/\text{Co}^{2+}/[\text{Fe}^{\text{II}}(\text{CN})_6]^{4-}$. Le même phénomène de réduction des centres Fe(III) en Fe(II) se produit dans ce cas, ce qui devrait conduire à des propriétés paramagnétiques similaires. L'apport de propriétés magnétiques différentes n'a donc pas été concluant. Cependant, cela montre clairement la possibilité de transposer notre approche, et l'utilisation d'autres analogues de Bleu de Prusse pour former des hétérostructures demeure accessible à condition d'arriver à optimiser la méthode de synthèse. D'autre part, nous avons aussi conçu une méthode simple à partir des nanoparticules cœur-coquille pour obtenir des nanoparticules creuses (figure 7). Pour cela nous dissolvons le cœur d'or par lixiviation en utilisant des ions cyanures, la perte de la coloration rouge due à l'or confirmant la réussite de l'opération. Cette méthode est ainsi une nouvelle alternative pour la conception de nanoparticules creuses d'analogue de Bleu de Prusse.

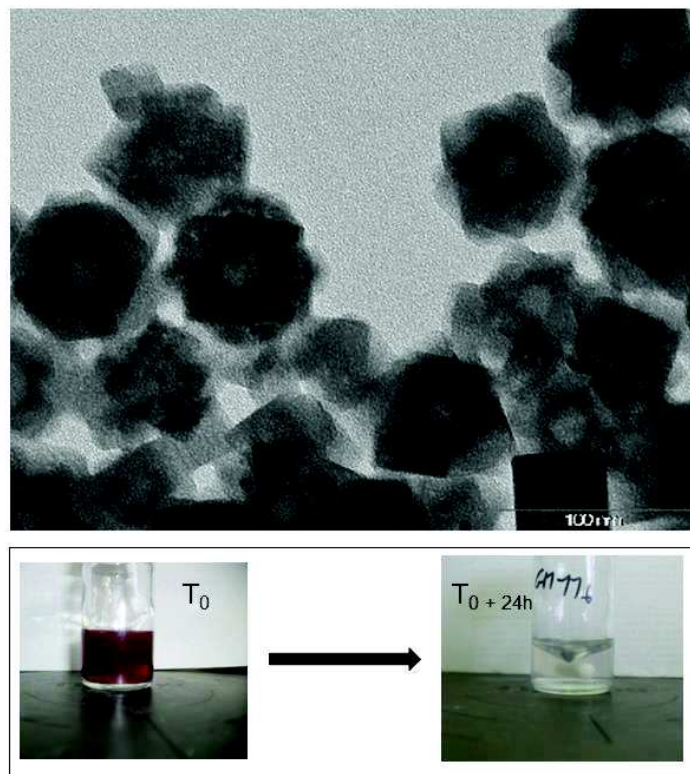


Figure 7 : En haut, image de microscopie électronique en transmission de nanoparticules creuses obtenues par dissolution du cœur d'or par lixiviation. En bas, la perte de la coloration de la solution indique la dissolution progressive du cœur d'or.

Les nano-objets que nous avons ainsi conçus présentent bien une multifonctionnalité magnéto-optique. Cependant, d'autres propriétés magnétiques, telles qu'un comportement ferromagnétique ou superparamagnétique, seraient bien plus intéressantes à combiner avec les propriétés optiques de l'or. Pour ajouter de telles propriétés, nous avons fait croître une nouvelle couche d'analogue de Bleu de Prusse sur les nanoparticules cœur-coquilles, obtenant ainsi des nanoparticules cœur-doubles coquilles. Cette croissance additionnelle est rendue possible par le fait que la surface de la couche de polymères de coordination cyano-pontés demeure réactive en raison de la présence des cyanométallates de surface en l'absence de stabilisants organiques, la stabilisation des nano-objets résultant uniquement de la présence d'interactions électrostatiques. En utilisant différents analogues de Bleu de Prusse, nous avons ainsi obtenu plusieurs combinaisons différentes, telles qu' $\text{Au@KNi}^{\text{II}}\text{Fe}^{\text{II}}@\text{KNi}^{\text{II}}\text{Cr}^{\text{III}}$, $\text{Au@KNi}^{\text{II}}\text{Fe}^{\text{II}}@\text{KNi}^{\text{II}}\text{Fe}^{\text{III}}$, $\text{Au@KNi}^{\text{II}}\text{Fe}^{\text{II}}@\text{KCo}^{\text{II}}\text{Fe}^{\text{II}}$, $\text{Au@KNi}^{\text{II}}\text{Fe}^{\text{II}}@\text{KFe}^{\text{III}}\text{Fe}^{\text{II}}$ et $\text{Au@NaNi}^{\text{II}}\text{Fe}^{\text{II}}@\text{NaFe}^{\text{III}}\text{Fe}^{\text{II}}$ (figure 8). En contrôlant la quantité de précurseurs ajoutés, il est possible de contrôler la taille de la 2^e couche de polymère de coordination cyano-pontés. De cette manière, une série de nanoparticules d' $\text{Au@KNi}^{\text{II}}\text{Fe}^{\text{II}}@\text{KNi}^{\text{II}}\text{Cr}^{\text{III}}$, avec des épaisseurs de la 2^e couche différentes, ont été obtenues. Quelle que soit la nature de l'analogue de Bleu de Prusse utilisé pour la deuxième couche, on observe des propriétés optiques qui changent selon l'épaisseur totale de la couche autour du cœur d'or. D'autre part, la présence de la 2^e couche d'analogues de Bleu de Prusse permet bien d'apporter les propriétés magnétiques recherchées. De plus, une étude poussée sur la série de nanoparticules d' $\text{Au@KNi}^{\text{II}}\text{Fe}^{\text{II}}@\text{KNi}^{\text{II}}\text{Cr}^{\text{III}}$ a montré que les propriétés magnétiques étaient dépendantes de la taille de la couche magnétique. En effet, pour des épaisseurs importantes, on observe un ordre magnétique à longue distance qui est proche du

comportement du matériau massif. A l'inverse, un ordre magnétique à courte distance caractérise les tailles de couche magnétiques de polymères de coordination cyanopontées les plus faibles. Cependant, aucun des modèles théoriques utilisés ne permettent d'identifier à quel comportement correspond cet ordre à courte distance, à cause d'interactions interparticulaires fortes. Pour les réduire, les nanoparticules ont été diluées dans une matrice polymère. Les données magnétiques ont alors révélé un comportement de type verre de spin pour les couches les plus faibles. Ce type de comportement magnétique est probablement dû à l'anisotropie de la particule, puisqu'un comportement superparamagnétique est observé pour des particules de volumes similaires, mais de forme cubique. Les nanoparticules obtenues présentent donc bien la multifonctionnalité recherchée, avec la possibilité de moduler les propriétés optiques et magnétiques en modifiant l'épaisseur de la 2^e couche d'analogues de Bleu de Prusse.

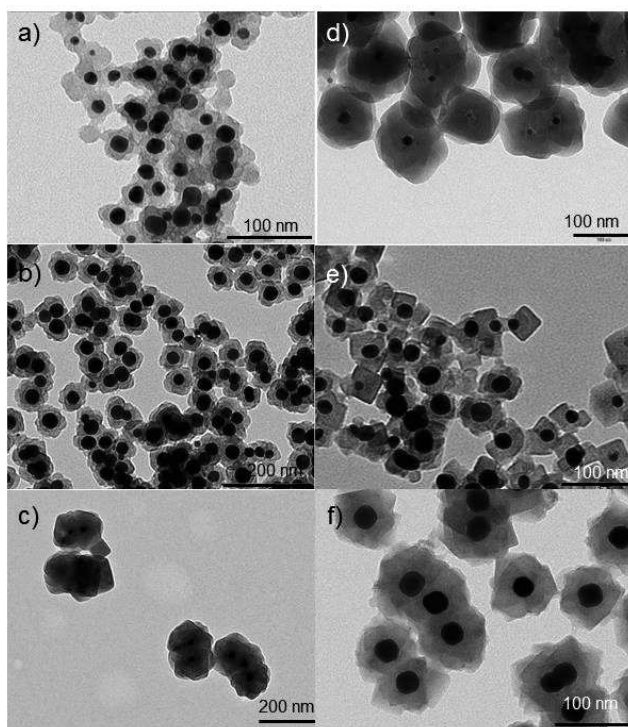


Figure 8 : Images de microscopie en transmission des nanoparticules cœur-double coquilles d'Au@KNi^{II}Fe^{II}@KNi^{II}Cr^{III} de différentes tailles a), b) et c), d'Au@KNi^{II}Fe^{II}@KNi^{II}Fe^{III} d), d'Au@KNi^{II}Fe^{II}@KCo^{II}Fe^{II} e) et d'Au@NaNi^{II}Fe^{II}@NaFe^{III}Fe^{II} f).

Au vu des propriétés intéressantes des nanomatériaux obtenus, nous avons voulu évaluer leur potentiel pour l'imagerie médicale. Nous avons choisi d'utiliser les nanoparticules d'Au@NaNi^{II}Fe^{II}@NaFe^{III}Fe^{II} comme agents de contraste pour la scintigraphie, en les marquant par insertion de Thallium radioactif dans la structure du Bleu de Prusse. Afin de comparer l'effet de la composition chimique et de la morphologie sur la biodistribution des nano-objets dans l'organisme, des nanoparticules cubiques de Bleu de Prusse de taille similaire ont été préparées. Pour assurer leur stabilité en milieu aqueux, leur surface a été fonctionnalisée en greffant des polymères organiques tels que le Dextrane ou le POEMA-PDAEMA (polymères synthétisés par le Dr. Cyrille Boyer de l'université de Nouvelle Galles du Sud, à Sydney, Australie). De plus, pour évaluer l'effet de la fonctionnalisation sur la biodistribution des nano-objets dans l'organisme, des nanoparticules ont été recouvertes de bicouches lipidiques (en collaboration avec Estelle

Rascoli et le Pr. Joël Chopineau, de l'équipe MACS de l'Université de Montpellier, France). Nous avons ensuite évalué la capacité des nanoparticules à incorporer du Thallium en les mettant en présence de solution de $TiNO_3$. Nous avons ainsi mesuré la quantité de Thallium incorporé en fonction du temps d'immersion des nanoparticules, ainsi qu'en fonction de la concentration de la solution en Thallium au bout de 24h. Il s'est avéré que la majeure partie du Thallium s'insère dans le structure du Bleu de Prusse en environ 4h. Pour finir, nous avons évalué les capacités de ces nanoparticules à être utilisées en tant que nano-sondes. Des mesures *in vitro* ont montré que la présence du cœur d'or des nanoparticules cœur-coquille augmente le contraste sur les images, par rapport à celles composées uniquement de Bleu de Prusse. Cependant, la concentration requise pour observer cet effet est nettement supérieure à celle utilisée pour les manipulations *in vivo*. Les différents systèmes (nanoparticules de Bleu de Prusse, cœur-coquilles) avec les différents types de fonctionnalisation (Dextrane, POEMA-PDAEMA, bicouches lipidiques) ont ensuite été injectés dans des souris saines. Les résultats ont montré que, hormis pour les nanoparticules fonctionnalisées au Dextrane, les nano-sondes s'accumulent rapidement dans le foie, puis dans les reins, où elles sont éliminées. Dans le cas du Dextrane, une activité notable est observée dans les poumons pendant environ 3h. Par ailleurs le même comportement est observé pour les nanoparticules de Bleu de Prusse et celles cœur-coquille, indiquant aucun effet de la morphologie sur la biodistribution dans l'organisme. Par la suite, les images après l'injection des nanoparticules dans des souris cancéreuses n'ont révélé aucune activité notable permettant d'imager la tumeur (figure 9), ce qui montre l'absence de ciblage passif, et par conséquent l'intérêt d'utiliser des molécules bioactives capable de cibler les récepteurs tumoraux.

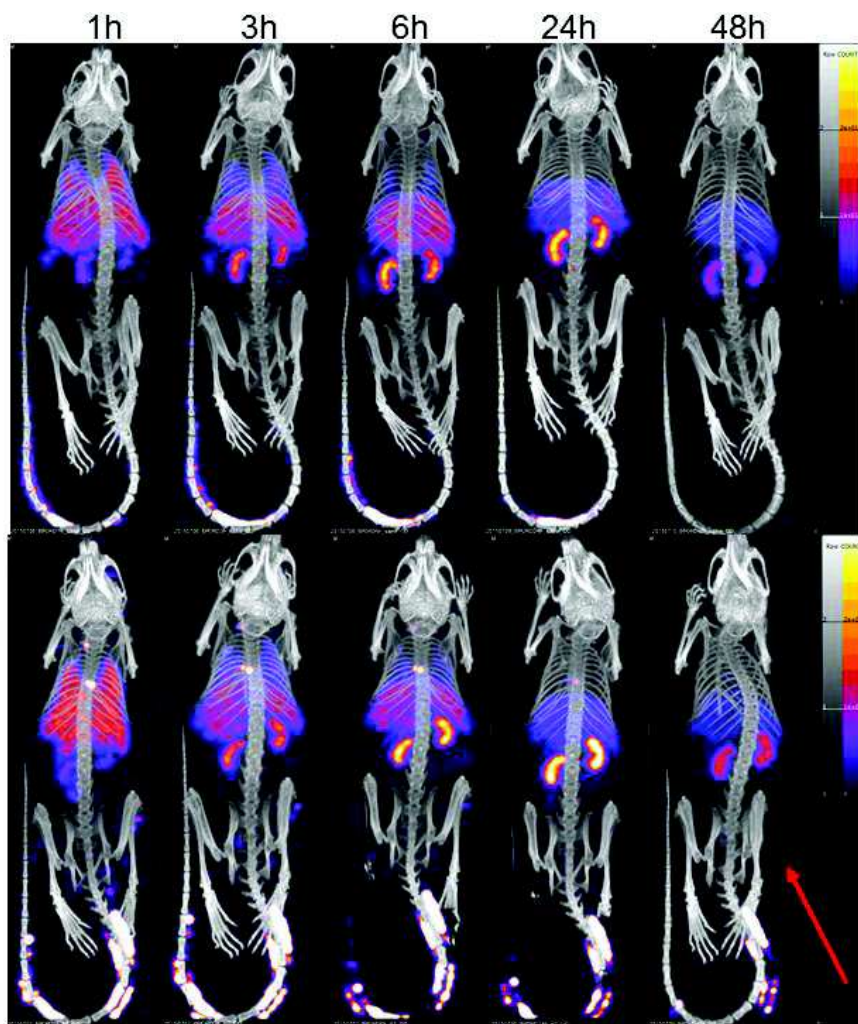


Figure 9 : Images de projection du maximum d'intensité obtenues par imagerie SPECT-CT après injection par intraveineuse d'une solution de nanoparticules cœur-coquilles d' $\text{Au@NaNi}^{\text{II}}\text{Fe}^{\text{II}}\text{@NaFe}^{\text{III}}\text{Fe}^{\text{II}}$ enrobées de Dextrane sur une souris saine (en haut) et atteinte d'une tumeur (en bas). La flèche rouge indique la position de la tumeur.

Dans ce travail, nous avons donc réussi à élaborer des nanoparticules cœur-coquilles à base d'or et d'analogues de Bleu de Prusse présentant une multifonctionnalité magnéto-optique. Il est possible de moduler leurs propriétés optiques en modifiant aussi bien la taille du cœur d'or ou l'épaisseur de la couche de polymère de coordination cyanopontés. Il est également possible d'obtenir ces nanoparticules en changeant la nature des contre-ions des précurseurs, ou aussi en changeant la nature de l'analogue de Bleu de Prusse utilisé. A partir de ces nano-objets, il est possible d'obtenir des nanoparticules creuses en dissolvant le cœur d'or par lixiviation. Il est également possible de faire croître à nouveau une seconde couche d'analogue de Bleu de Prusse, pour ajouter des propriétés magnétiques autre que du paramagnétisme, tel que des propriétés ferromagnétiques. Nous avons montré que le comportement magnétique était fortement dépendant de la taille de la 2^e couche magnétique de l'analogue de Bleu de Prusse. De plus, on observe un ordre magnétique à courte distance, qui s'est révélé être un comportement de type verre de spin. Celui-ci est probablement dû à la morphologie anisotrope des particules. Finalement, les nanoparticules cœur-coquilles ont montré un certain potentiel à être utilisées en tant que nano-sondes pour la scintigraphie en insérant du Thallium radioactif dans la structure de la coquille, cependant l'absence de ciblage passif de la tumeur a montré la nécessité d'un ciblage actif à l'aide de biomarqueurs.

Bibliographie

1. H. Tokoro, S.-i Ohkishi, *Dalton Trans.*, **2011**, *40*, 6825.
2. C.H. Li, Y. Nanba, D. Asakura, M. Okubo and D. R. Talham, *RSC Adv.*, **2014**, *4*, 24955.
3. E. Chelebaeva, Yannick Guari, J. Larionova, A. Trifonov, and C. Guérin, *Chem. Mater.*, **2008**, *20* (4), 1367.
4. O. N. Risset, P. A. Quintero, T. V. Brinzari, M. J. Andrus, M. W. Lufaso, Mark W. Meisel, and D. R. Talham, *J. Am. Chem. Soc.*, **2014**, *136*, 15660.
5. O. N. Risset and D. R. Talham, *Chem. Mater.*, **2015**, *27*, 3838.
6. M. F. Dumont, E. S. Knowles, A. Guiet, D. M. Pajerowski, A. Gomez, S. W. Kycia, M. W. Meisel, and D. R. Talham, *Inorg. Chem.*, **2011**, *50*, 4295.
7. E. C. Dreaden, A. M. Alkilany, X. Huang, C. J. Murphy and M. A. El-Sayed, *Chem. Soc. Rev.*, **2012**, *41*, 2740.
8. C. J. Murphy, T. K. Sau, A. Gole, and C. J. Orendorf, *MRS Bulletin*, **2005**, *30*, 349.
9. S. Gómez-Graña, B. Goris, T. Altantzis, C. Fernández-López, E. Carbó-Argibay, A. Guerrero-Martínez, N. Almora-Barrios, N. López, I. Pastoriza-Santos, J. Pérez-Juste, S. Bals, G. Van Tendeloo, and L. M. Liz-Marzán, *J. Phys. Chem. Lett.*, **2013**, *4*, 2209.
10. C. Loo, A. Lin, L. Hirsch, M. Lee, J. Barton, N. Halas, J. West, R. Drezek, *Technol. Cancer Res. Treat.*, **2004**, *3*, 33.
11. F. Pineider, C. de Julian Fernandez, V. Videtta, E. Carlino, A. al Hourani, F. Wilhelm, A. Rogalev, P. Davide Cozzoli, P. Ghigna, C. Sangregorio, *ACS Nano*, **2013**, *7*, 857.
12. G. Lu, S. Li, Z. Guo, O. K. Farha, B. G. Hauser, X. Qi, Y. Wang, X. Wang, S. Han, X/Liu, J. S. DuChene, H. Zhang, Q. Zhang, X. Chen, J. Ma, S. Chye, J. Loo, W. D. Wei, Y. Yang, J. T. Hupp, and F. Huo, *Nat. Chem.*, **2012**, *4*, 310.
13. G. Félix, W. Nicolazzi, L. Salmon, G. Molnar, M. Perrier, G. Maurin-Pasturel, J. Larionova, J. Long, Y. Guari, and A. Bousseksou, *Phys. Rev. Lett.*, **2013**, *110*, 235701.
14. G. Maurin-Pasturel, J. Long, Y. Guari, F. Godiard, M.-G. Willinger, C. Guérin, J. Larionova, *Angew. Chem. Int. Ed.*, **2014**, *53*, 3872.

ABSTRACT

One of the most studied fields of modern material chemistry concerns the elaboration of functional nanomaterials reserved for a wide range of applications. For several years, researchers have been particularly attracted by the design of multifunctional systems combining in a single system the properties of different materials and exhibiting diverse physical responses when subjected to various stimuli. This work describes the combination of both optical properties of gold and magnetic properties of coordination polymers such as Prussian Blue analogous to form magneto-optical nano-heterostructures presenting an intricate core-shell architecture.

Firstly, we have synthesized a series of Prussian Blue Analogous nanoparticles such as $\text{Ni}_3[\text{Fe}(\text{CN})_6]_2$ presenting different and controlled sizes, in order to better understand the evolution of their characteristics upon the size reduction from the micro- to the nanoscale.

Secondly, we focalized on the design of heterostructured nano-objects composed by a gold core coated with a uniform $\text{K}^+/\text{Ni}^{2+}/[\text{Fe}^{\text{II}}(\text{CN})_6]^{4-}$ Prussian Blue analogous shell based on a new and rational approach. These core-shell $\text{Au}@K^+/\text{Ni}^{2+}/[\text{Fe}^{\text{II}}(\text{CN})_6]^{4-}$ nanoparticles exhibit both optical properties of the gold core and paramagnetic properties originating from the cyano-bridged coordination polymer layer. Using several techniques, we have investigated the growing mechanism of such intricate system. The optical responses of these nanoparticles can be modulated by controlling the gold core size and the Prussian Blue analogous shell thickness by modifying the experimental parameters. Then we extended the used synthetic approach to other gold core containing heterostructures with $\text{K}^+/\text{Co}^{2+}/[\text{Fe}^{\text{II}}(\text{CN})_6]^{4-}$ shell. We have also investigated an original way to design hollow nanoparticles by etching the gold core.

The implement of different magnetic behavior, such as ferromagnetism or superparamagnetism, can be achieved by the subsequent growing of a new Prussian Blue Analogous shell on the $\text{Au}@K^+/\text{Ni}^{2+}/[\text{Fe}^{\text{II}}(\text{CN})_6]^{4-}$ nanoparticles. In this aim, several Prussian Blue analogous were selected to form the second layer. These double-layered nanoparticles exhibit optical properties originating from the gold core. Additionally, ferromagnetic properties have been successively implemented, proving the multifunctionality of these nano-objects. Particularly, a study on the evolution of the magnetic properties according to the shell thickness of the Prussian Blue analogous was performed on a series of different-sized $\text{Au}@K^+/\text{Ni}^{2+}/[\text{Fe}^{\text{II}}(\text{CN})_6]^{4-}@K^+/\text{Ni}^{2+}/[\text{Cr}^{\text{III}}(\text{CN})_6]^{3-}$ nanoparticles in order to demonstrate the influence of the core-shell architecture on the nature of the magnetic properties.

Finally, we evaluated the potential of these nanoparticles for the medical imaging by scintigraphy. Simple Prussian Blue and core-shell $\text{Au}@K^+/\text{Ni}^{2+}/[\text{Fe}^{\text{II}}(\text{CN})_6]^{4-}@K^+/\text{Fe}^{3+}/[\text{Fe}^{\text{II}}(\text{CN})_6]^{3-}$ nanoparticles were synthesized and post-synthetically grafted by organic molecules (commercial dextran, biopolymers or lipidic bilayer) to ensure their dispersibility in aqueous media. These nanoparticles have been loaded by radioactive $^{201}\text{Tl}^+$ ions in order to investigate their behavior in the living organism by using SPECT-CT tomography in vivo and establish the influence of the nanoparticles composition, the morphology and the functionalization on the nanoparticles biodistribution and kinetic.

RÉSUMÉ

L'élaboration de nanomatériaux fonctionnels destinés à une large gamme d'applications est l'un des domaines les plus étudiés de la chimie des matériaux modernes. L'intérêt des chercheurs porte sur la conception de nanomatériaux multifonctionnels combinant dans un unique système les propriétés de différents matériaux et présentant diverses réponses physiques lorsque soumis à différents stimuli. Ce travail décrit la combinaison des propriétés optiques de l'or et des propriétés magnétiques de polymères de coordination tels que les analogues de Bleu de Prusse, pour obtenir des hétérostructures nanoscopiques magnéto-optiques présentant une architecture de type cœur-coquille.

Dans un premier temps, nous avons préparé une série de nanoparticules à base d'un analogue du Bleu de Prusse tel que $\text{Ni}_3[\text{Fe}(\text{CN})_6]_2$ de différentes tailles et de manière contrôlée, afin de mieux comprendre l'évolution de leurs caractéristiques physiques avec la réduction de la taille jusqu'à une l'échelle nanométrique.

Deuxièmement, nous nous sommes focalisés sur la conception de nano-objets hétérostructurés composés par un cœur d'or décoré par une coquille uniforme d'analogue du Bleu de Prusse $\text{K}^+/\text{Ni}^{2+}/[\text{Fe}^{\text{II}}(\text{CN})_6]^{4-}$ suivant une approche rationnelle et innovante. Ces nanoparticules cœur-coquilles d' $\text{Au}@K^+/\text{Ni}^{2+}/[\text{Fe}^{\text{II}}(\text{CN})_6]^{4-}$ présentent à la fois les propriétés optiques du cœur d'or et le comportement paramagnétique provenant de la couche de polymère de coordination cyanoponté. Une étude a été menée sur le mécanisme de croissance de ce système complexe. Les propriétés optiques peuvent être modulées en contrôlant la taille du cœur d'or et l'épaisseur de la couche d'analogue de cyanometallate, en modifiant les paramètres de synthèse. Nous avons ensuite étendu cette approche de synthèse à d'autres hétérostructures contenant un cœur d'or et une coquille de $\text{K}^+/\text{Co}^{2+}/[\text{Fe}^{\text{II}}(\text{CN})_6]^{4-}$. Nous avons également recherché une voie originale pour obtenir des nanoparticules creuses d'analogue du Bleu de Prusse en dissolvant le cœur d'or par lixiviation.

Des propriétés magnétiques différentes, telles que le ferromagnétisme ou le superparamagnétisme, peuvent être apportées par la croissance additionnelle d'une seconde coquille d'analogue du Bleu de Prusse sur les nanoparticules de $\text{Au}@K^+/\text{Ni}^{2+}/[\text{Fe}^{\text{II}}(\text{CN})_6]^{4-}$. Pour cela, différents analogues du Bleu de Prusse ont été sélectionnés. Les nanoparticules avec une double-couche d'analogues du Bleu de Prusse présentent les propriétés optiques dues au cœur d'or. Des propriétés de ferromagnétisme ont bien été ajoutées, démontrant la multifonctionnalité de ces nano-objets. En particulier, une étude a été menée sur une série de nanoparticules d' $\text{Au}@K^+/\text{Ni}^{2+}/[\text{Fe}^{\text{II}}(\text{CN})_6]^{4-}@K^+/\text{Ni}^{2+}/[\text{Cr}^{\text{III}}(\text{CN})_6]^{3-}$ de différentes tailles de manière à démontrer l'influence de l'architecture cœur-coquille sur la nature des propriétés magnétiques.

Finalement, nous avons évalué les potentialités de ces nanoparticules pour l'imagerie médicale par scintigraphie. Des nanoparticules composées de Bleu de Prusse ou de type $\text{Au}@K^+/\text{Ni}^{2+}/[\text{Fe}^{\text{II}}(\text{CN})_6]^{4-}@K^+/\text{Fe}^{3+}/[\text{Fe}^{\text{II}}(\text{CN})_6]^{3-}$ ont été préparées, puis greffées par des molécules organiques (dextrane commercial, biopolymères ou bicouches lipidiques) pour assurer leur dispersion en milieu aqueux. Ces nanoparticules ont été chargées en ions $^{201}\text{Tl}^+$ et leur comportement in vivo a été déterminé par tomographie SPECT-CT, de manière à établir l'influence de la composition chimique, de la morphologie et de la fonctionnalisation de ces nanoparticules sur leur biodistribution dans l'organisme.